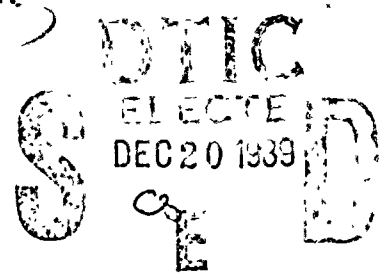
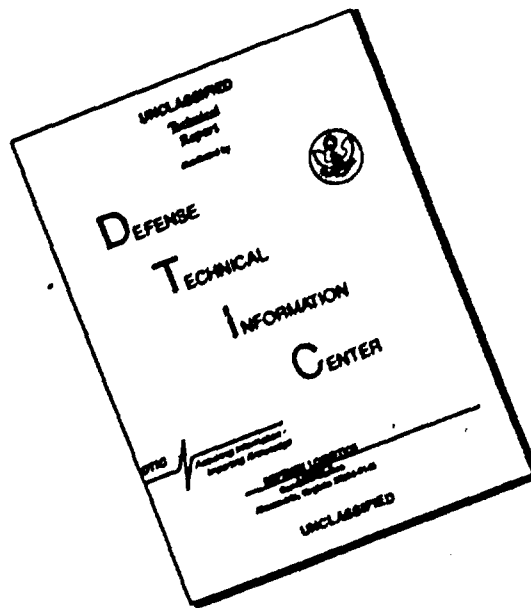


AD-A216 094

REPORT DOCUMENTATION PAGE			Form Approved OMB No. 0704-0188	
<small>Public reporting burden for this collection of information is estimated to average 1 hour per response, including the time for reviewing instructions, searching existing data sources, gathering and maintaining the data needed, and completing and reviewing the collection of information. Send comments regarding this burden estimate or any other aspect of this collection of information, including suggestions for reducing the burden, to Washington Headquarters Service, Directorate for Information Operations and Reports, 1215 Jefferson Davis Highway, Suite 1204, Arlington, VA 22202-4302, and to the Office of Management and Budget, Paperwork Reduction Project (0704-0188), Washington, DC 20503.</small>				
1. AGENCY USE ONLY (Leave blank)	2. REPORT DATE June 19, 1989	3. REPORT TYPE AND DATES COVERED Technical - June 1988 - June 1989		
4. TITLE AND SUBTITLE (U) AFOSR/ONR Contractors Meeting - Combustion, Rocket Propulsion, Diagnostics of Reacting Flow		5. FUNDING NUMBERS PE - 61102F PR - 2308		
6. AUTHOR(S) J M Tishkoff, M A Birkan, G S Roy, and S G Lekoudis				
7. PERFORMING ORGANIZATION NAME(S) AND ADDRESS(ES) Air Force Office of Scientific Research Building 410 Bolling AFB DC 20332-6448 Office of Naval Research, Arlington VA 22217-5000		8. PERFORMING ORGANIZATION REPORT NUMBER AFOSR-TR-89-1711		
9. SPONSORING/MONITORING AGENCY NAME(S) AND ADDRESS(ES) AFOSR/NA Building 410 Bolling AFB DC 20332-6448		10. SPONSORING/MONITORING AGENCY REPORT NUMBER		
11. SUPPLEMENTARY NOTES F49600-86-K-0022				
12a. DISTRIBUTION/AVAILABILITY STATEMENT Approved for public release; distribution is unlimited			12b. DISTRIBUTION CODE	
13. ABSTRACT (Maximum 200 words) Abstracts are given for research on airbreathing combustion, rocket propulsion, and diagnostics of reacting flow supported by the Air Force Office of Scientific Research and the Office of Naval Research. <div style="text-align: right;">  </div>				
14. SUBJECT TERMS Combustion, Shear Layer, Supersonic, Soot, Sprays, Boron, Lasers, Rocket, Scramjet, Nitramines, Turbulence, Plasmas, Instability, Flames, Propulsion			15. NUMBER OF PAGES 370	
			16. PRICE CODE	
17. SECURITY CLASSIFICATION OF REPORT Unclassified	18. SECURITY CLASSIFICATION OF THIS PAGE Unclassified	19. SECURITY CLASSIFICATION OF ABSTRACT Unclassified	20. LIMITATION OF ABSTRACT UL	

89 12 20 016

DISCLAIMER NOTICE



**THIS DOCUMENT IS BEST
QUALITY AVAILABLE. THE COPY
FURNISHED TO DTIC CONTAINED
A SIGNIFICANT NUMBER OF
PAGES WHICH DO NOT
REPRODUCE LEGIBLY.**

AFOSR/ONR CONTRACTORS' MEETING

**COMBUSTION
ROCKET PROPULSION
DIAGNOSTICS OF
REACTING FLOW**

19 - 23 JUNE 1989



THE UNIVERSITY OF MICHIGAN

**DEPARTMENT OF AEROSPACE ENGINEERING
ANN ARBOR, MICHIGAN 48109**

CONTRACTORS' MEETING IN PROPULSION

sponsored by

AIR FORCE OFFICE OF SCIENTIFIC RESEARCH
OFFICE OF NAVAL RESEARCH
and
THE UNIVERSITY OF MICHIGAN

Ann Arbor Inn, Ann Arbor, Michigan
19-23 June 1989

TABLE OF CONTENTS

I. AGENDA	6
II. PRESENTATIONS	14
IIa. MONDAY	
A Study of Mixing and Combustion in Supersonic Flows, C T Bowman, R K Hanson, M G Mungal and W C Reynolds	14
Investigations Into the Shock-Induced Enhancement of Mixing and Combustion in Supersonic Burners, F E Marble and E E Zukoski	18
High-Speed Reacting Flows: Research to Understand Processes in Supersonic Combustors, H Krier, J P Renie and J C Dutton	22
Fundamental Combustion Processes of Particle-Laden Shear Flows in Solid Fuel Ramjets, K K Kuo, V Yang, T A Litzinger, S T Thynell and W H Hsieh	26
Prediction of Infrared Emission From Combustion Tests, K D Annen	30
Turbulent Mixing in Exponential Transverse Jets, R E Breidenthal	33
Chemical Reactions in Turbulent Mixing Flows, P E Dimotakis, J E Broadwell and A Leonard	37
Opposed Jet Turbulent Diffusion Flames, L Talbot	41
Scramjet Combustion Mixing Improvements Using Pulsed Transverse Fuel Jets, A D Vakili and J M Wu	45
Experimental and Computational Studies of Swirling Flows in Dump Combustors, A S Nejad, S A Ahmed and R S Boray	49
IIb. TUESDAY	
The Effects of Compressibility on a Supersonic Mixing Layer, D Nixon	53

AIR FORCE OFFICE OF SCIENTIFIC RESEARCH (AFOSR)
 Propulsion Division
 AFOSR-TR-89-1711
 and is
 130-12

Instability and Transition in Supersonic Shear Layers, J J Riley and D S Eberhardt	57
Theories of Turbulent Combustion in High Speed Flows, P A Libby and F A Williams	61
IIc. WEDNESDAY	
Chemical Kinetic and Aerodynamic Structures of Flames, C K Law	65
Premixed Turbulent Flame Propagation, D A Santavicca	69
Local Extinction Mechanisms in Non-Premixed Turbulent Combustion, S M Correa and A Gulati	73
Combustion Research, W M Roquemore	77
Numerical Investigation of Turbulent Flame Sheets, S B Pope	81
Time Dependent Simulation of Turbulent Combustion, H R Baum and R G Rehm	85
Numerical Simulation of Turbulent Combustion Using Vortex Methods, A F Ghoniem	89
Fundamental Studies on Spray Combustion and Turbulent Combustion, W A Sirignano, G S Samuelsen and R H Rangel	93
Physical State Dependence and Mechanistic Relationships Between Decomposition and Combustion, S A Shackelford	97
The Heat Flow/Chemistry Interface in Fast-Heated Energetic Materials, T B Brill	107
Structure of Laminar Premixed $\text{CH}_4/\text{N}_2\text{O}$ and $\text{CH}_2\text{O}/\text{N}_2\text{O}$ Flames, M C Branch	111
High Pressure Combustion Kinetics of Propellants, T Edwards	115
Solid Fuel Combustion, J S T'ien and N A Messaoudene	118
AFOSR Sponsored Research in Airbreathing Combustion, J M Tishkoff	122
AFOSR Sponsored Research in Diagnostics of Reacting Flow, J M Tishkoff	125
IId. THURSDAY	
Numerical Simulation of Control of Supersonic Shear Layers, L N Sankar	128
Instabilities in Supersonic Turbulent Mixing Layers, S A Ragab and J-L Wu	132
Destabilization of Supersonic Free Shear Layers by Parametric Excitation, C K W Tam	136
Mixing in Supersonic Shear Layers, M Samimy	140

Mixing Control in Supersonic Shear Layers, P J Morris, D K McLaughlin and G S Settles	144
A Review of Combustion Instabilities in Propulsion Systems, F E C Culick	148
A Perturbation Study of Acoustic Propagation in a Low Mach Number Shear Flow, D R Kassoy	151
Numerical Investigation of Energy Exchange Mechanisms Between the Mean and Acoustic Flow Fields in Solid Rocket Combustion Chambers, J D Baum	155
Flame-Acoustic Wave Interactions During Axial Solid Rocket Instabilities, B T Zinn, B R Daniel and U G Hegde	159
Fractal Image Compression of Rayleigh, Raman, LIF and LV Data in Turbulent Reacting Flow, W C Strahle and J I Jagoda	163
Plume Technology, D P Weaver and D H Campbell	167
Ile. FRIDAY	
Advancements in Plasma Propulsion, R Vondra	170
Laser Thermal Propulsion, D Keefer	175
Plasma Scaling Mechanisms for Continuous Wave Laser Propulsion, H Krier and J Mazumder	179
Transport Processes in Beamed Energy Propulsion Systems, R A Beddini	183
Coupling Between Gas Dynamics and Microwave Energy Absorption, M M Micci	187
Heating of a Liquid/Vapor Mixture by a Pulsed Electric Discharge, R L Burton and B K Hilko	191
The Physics of High Voltage Solar Arrays in Contact With the Space Plasma, D E Hastings	195
Fundamental Research on the ECR Plasma Thruster, F E C Culick and J C Sercel	199
Basic Processes of Plasma Propulsion, H O Schrade	203
Nonequilibrium and Radiation in MPD Plasmas: Two Fluid Numerical Simulations, M Martinez-Sanchez	207
Fundamental Research on Erosion in Magnetoplasmadynamic Thrusters, V V Subramaniam and J W Rich	211
Propulsion Research on the Hybrid Plume Plasma Rocket, T F Yang, F R Chang-Diaz, X Yao, S Y Peng, W A Krueger and J Urbahn	215
MPD Thrust Chamber Flow Dynamics, P J Turchi, J F Davis and N F Roderick	219

III. WORK NOT PRESENTED 223

IIIa. AIR BREATHING COMBUSTION UNITS

The Modeling of Drop-Containing Turbulent Eddies, J Belian	223
Fuel Additive Effects in Sooting Flames, P A Bonczyk	227
Computer Modeling of Soot Formation Comparing Free Radical and Ionic Mechanism, H F Calcote	231
Determination of Rate-Limiting Steps During Soot Formation, M B Colket III	235
Dense-Spray Structure and Phenomena, G M Faeth	239
Ignition and Modification of Reaction by Energy Addition: Kinetic and Transport Phenomena, F E Fendell, M-S Chou and T J Zukowski	243
Computer Modeling of Soot Formation Comparing Free Radical and Ionic Mechanisms, M Frenklach	247
Kinetic Studies of Metal Combustion in Propulsion, A Fontijn and A G Slavejkov	251
Fuels Combustion Research, I Glassman and K Brezinsky	255
The Combustion of Hydrogen and Hydrocarbons in Fluorine, M Kaufman	259
Asynchronous Optical Sampling for Laser-Based Combustion Diagnostics in High Pressure Flames, G B King, N M Laurendeau and F E Lytle	263
Two- and Three-Dimensional Measurements in Flames, M B Long	267
Investigation of Combustion in Large Vortices, F E Marble and E E Zukowski	271
Investigations of the Applications of Laser-Induced Exciplex Fluorescence to Fuel Spray and Single Droplet Vaporization, L A Melton	275
Coupling Between Gasdynamics and Microwave Energy Absorption, C L Merkle	279
Ignition and Combustion Enhancement by Multiphoton Photochemical Means, A W Miziolek, B E Forch and C N Merrow	283
Combustion Enhancement by High Energy Electron Impact Processes, R B Peterson	287
A Systematic Approach to Combustion Model Reduction and Lumping, H Rabitz and F Dryer	291
Transport Phenomena and Interfacial Kinetics in Multiphase Combustion Systems, D E Rosner	293
Fuel Structure and Pressure Effects on the Formation of Soot Particles in Diffusion Flames, R J Santoro	297
Chemical Kinetic Data Base for Propellant Combustion, W Tsang	301

AGENDA

AFOSR/ONR CONTRACTORS' MEETING

19-23 June 1989

Monday, 19 June 1989

8:15 - 8:30 Welcome and Administrative Announcements

SUPERSONIC COMBUSTION EXPERIMENTS

Chair: K C Schadow
Naval Weapons Center

8:30 - 9:15 A Study of Mixing and Combustion in Supersonic Flows
C T Bowman, R K Hanson, M G Mungal and W C Reynolds
Stanford University

9:15 - 10:00 Investigations Into the Shock-Induced Enhancement of Mixing and
Combustion in Supersonic Burners
F E Marble and E E Zukoski
California Institute of Technology

10:00 - 10:30 High-Speed Reacting Flows: Research to Understand Processes in
Supersonic Combustors
H Krier, J P Renie and J C Dutton
University of Illinois at Urbana-Champaign

10:30 - 11:00 BREAK

11:00 - 11:30 Fundamental Combustion Processes of Particle-Laden Shear Flows
in Solid Fuel Ramjets
K K Kuo, V Yang, T A Litzinger, S T Thynell and W H Hsieh
The Pennsylvania State University

11:30 - 12:00 Prediction of Infrared Emission From Combustion Tests
K D Annen, Aerodyne Research, Inc.

12:00 - 12:30 Turbulent Mixing in Exponential Transverse Jets
R E Breidenthal, University of Washington

12:30 - 1:30 LUNCH

SUPERSONIC COMBUSTION (Cont'd)

Chair: E J Mularz

Army Aviation Research and Technology Activity

- 1:30 - 2:15 Chemical Reactions in Turbulent Mixing Flows
P E Dimotakis, J E Broadwell and A Leonard
California Institute of Technology
- 2:15 - 2:45 Compressible Turbulent Shear Layers and Stability of Burning Jets
A Roshko, California Institute of Technology
- 2:45 - 3:15 Opposed Jet Turbulent Diffusion Flames
L Talbot, University of California at Berkeley
- 3:15 - 3:45 Scramjet Combustion Mixing Improvements Using Pulsed
Transverse Fuel Jets
A D Vakili and J M Wu
The University of Tennessee Space Institute
- 3:45 - 4:15 BREAK
- 4:15 - 4:45 Aerothermal-Mechanical Studies of Supersonic Combustion
G Sullins and P Waltrup, Johns Hopkins University
- 4:45 - 5:15 Compressible Shear-Flow Dynamics in the Presence of Shock Waves
K C Schadow, Naval Weapons Center
- 5:15 - 5:45 Experimental and Computational Studies of Swirling Flows in
Dump Combustors
A S Nejad, S A Ahmed and R S Boray
USAF Advanced Propulsion Division

TUESDAY, 20 JUNE 1989

SUBSONIC AND SUPERSONIC COMBUSTION

THEORY AND COMPUTATIONS

Chair: E S Oran

Naval Research Laboratory

- 8:30 - 9:00 The Effects of Compressibility on a Supersonic Mixing Layer
D Nixon, Nielsen Engineering and Research, Inc.
- 9:00 - 9:30 Instability and Transition in Supersonic Shear Layers
J J Riley and D S Eberhardt, University of Washington
- 9:30 - 10:00 Theories of Turbulent Combustion in High Speed Flows
P A Libby and F A Williams
University of California at San Diego
- 10:00 - 10:30 BREAK

- 10:30 - 11:00 Fundamentals of Combustion
A K M F Hussain and R W Metcalfe, University of Houston
- 11:00 - 11:30 Numerical Simulations of Transitional and Turbulent Reactive Flows
F Grinstein, Naval Research Laboratory
- 11:30 - 12:00 Numerical Simulations of Coherent Structures in Non-Circular
Cross Section
W H Jou, Flow Research Corporation
- 12:00 - 1:30 LUNCH

1:30 - 5:00 WORKSHOPS (Locations to be Announced)

- Boron
 - Soot
 - Droplets and Sprays
 - Compressible Turbulence
-

WEDNESDAY, 21 JUNE 1989

REACTING FLOW

Chair: A S Nejad

Air Force Wright Aeronautical Laboratories

- 8:00 - 8:30 Chemical Kinetic and Aerodynamic Structures of Flames
C K Law, Princeton University
- 8:30 - 9:00 Premixed Turbulent Flame Propagation
D A Santaviceca, The Pennsylvania State University
- 9:00 - 9:30 Local Extinction Mechanisms in Non-Premixed Turbulent
Combustion
S M Correa and A Gulati
General Electric Corporate Research and Development Center
- 9:30 - 10:00 Combustion Research
W M Roquemore, USAF Aero Propulsion and Power Laboratory
- 10:00 - 10:30 BREAK
- 10:30 - 11:00 Numerical Investigation of Turbulent Flame Sheets
S B Pope, Cornell University

- 11:00 - 11:30 Time Dependent Simulation of Turbulent Combustion
H R Baum and R G Rehm
National Institute of Standards and Technology
- 11:30 - 12:00 Numerical Simulation of Turbulent Combustion Using Vortex Methods
A F Ghoniem, Massachusetts Institute of Technology
- 12:00 - 12:30 Fundamental Studies on Spray Combustion and Turbulent Combustion
W A Sirignano, G S Samuelsen and R H Rangel
University of California at Irvine
- 12:30 - 2:00 LUNCH

2:00 - 5:00 ADMINISTRATIVE SESSION
Contractors are required to attend (see page 10)

WEDNESDAY, 21 JUNE 1989

ENERGETIC MATERIALS

Chair: G Vogt
Air Force Astronautics Laboratory

-
- 8:30 - 9:30 PHYSICAL STATE DEPENDENCE AND MECHANISTIC
RELATIONSHIPS BETWEEN DECOMPOSITION AND
COMBUSTION
Scott A Shackelford
Major, United States Air Force
Frank J Seiler Research Laboratory
-
- 9:30 - 10:00 The Heat Flow/Chemistry Interface in Fast-Heated Energetic
Materials
T B Brill, University of Delaware
- 10:00 - 10:30 Structure of Laminar Premixed $\text{CH}_4/\text{N}_2\text{O}$ and $\text{CH}_2\text{O}/\text{N}_2\text{O}$ Flames
M C Branch, University of Colorado
- 10:30 - 11:00 BREAK
- 11:00 - 11:30 High Pressure Combustion Kinetics of Propellants
T Edwards, USAF Astronautics Laboratory
- 11:30 - 12:00 Solid Fuel Combustion
J S T'ien and N A Messaoudene
Case Western Reserve University

12:00 - 12:30 High Speed Laser Photography of Burning Solid Fuel
R Becker, University of Dayton

12:30 - 2:00 LUNCH

2:00 - 5:00 ADMINISTRATIVE SESSION
Contractors are required to attend (see below)

ADMINISTRATIVE SESSION

2:00 - 2:15 Michael J Salkind, Director of Aerospace Sciences, Air Force
Office of Scientific Research

2:15 - 2:35 I. AFOSR Sponsored Research in Airbreathing Combustion
II. AFOSR Sponsored Research in Diagnostics of Reacting Flow
Julian M Tishkoff, Air Force Office of Scientific Research/NA

2:35 - 3:05 Mitat A Birkan, Air Force Office of Scientific Research/NA

3:05 - 3:25 BREAK

3:25 - 3:45 Spiro Lekoudis, Office of Naval Research

3:45 - 4:15 Gabriel Roy, Office of Naval Research

4:15 - 5:00 General Questions

5:00 - 6:00 Business Meetings - AFOSR and ONR Contractors and Grantees only

7:00 - ? BANQUET

THURSDAY, 22 JUNF 1989

COMPRESSIBLE TURBULENCE

Chair: S Lekoudis
Office of Naval Research

8:15 - 8:45 Direct Numerical Simulation of Compressible Turbulence and
Aerodynamic Noise
P Moin, Stanford University

8:45 - 9:15 Numerical Simulation of Control of Supersonic Shear Layers
L N Sankar, Georgia Institute of Technology

- 9:15 - 9:45 Instabilities in Supersonic Turbulent Mixing Layers
S A Ragab and J-L Wu
Virginia Polytechnic Institute and State University
- 9:45 - 10:15 Destablization of Supersonic Free Shear Layers by Parametric
Excitation
C K W Tam, Florida State University
- 10:15 - 10:45 BREAK
- 10:45 - 11:15 Mixing in Supersonic Shear Layers
M Samimy, The Ohio State University
- 11:15 - 11:45 Mixing Control in Supersonic Shear Layers
P J Morris, D K McLaughlin and G S Settles
The Pennsylvania State University
- 11:45 - 12:15 Experimental Study of the Growth Rate Enhancement of Compressible
Turbulent Free Shear Layers
D Dolling, University of Texas at Austin

THURSDAY, 22 JUNE 1989

8:30 - 12:00

WORKSHOPS:

- Liquid Rocket Combustion Instability
Chair: W A Sirlignano
University of California
- Chemi-ionization in Flames
Chair: B Ganguly
Wright Research and Development Center

12:00 - 1:00

LUNCH

INSTABILITY

Chair: P Kessel

Air Force Astronautics Laboratory

1:00 - 2:00

A REVIEW OF COMBUSTION INSTABILITIES IN PROPULSION SYSTEMS

F E C Culick
California Institute of Technology

- 2:00 - 2:30 A Perturbation Study of Acoustic Propagation in a Low Mach Number Shear Flow
D R Kassoy, University of Colorado
- 2:30 - 3:00 Numerical Investigation of Energy Exchange Mechanisms Between the Mean and Acoustic Flow Fields in Solid Rocket Combustion Chambers
J D Baum, Scientific Applications International Corporation
- 3:00 - 3:30 BREAK
- 3:30 - 4:00 Flame-Acoustic Wave Interactions During Axial Solid Rocket Instabilities
B T Zinn, B R Daniel and U G Hegde
Georgia Institute of Technology
- 4:00 - 4:30 Fractal Image Compression of Rayleigh, Raman, LIF and LV Data in Turbulent Reacting Flow
W C Strahle and J I Jagoda, Georgia Institute of Technology
- 4:30 - 5:00 Plume Technology
D P Weaver and D H Campbell
USAF Astronautics Laboratory

FRIDAY, 23 JUNE 1989

PLASMA PROPULSION

Chair: D Byers
NASA Lewis Research Center

-
- 8:30 - 9:30 ADVANCEMENTS IN PLASMA PROPULSION
Robert Vondra
W J Schafer Associates
-
- 9:30 - 9:55 Laser Thermal Propulsion
D Keefer, University of Tennessee Space Institute
- 9:55 - 10:20 Plasma Scaling Mechanisms for Continuous Wave Laser Propulsion
H Krier and J Mazumder
University of Illinois at Urbana-Champaign
- 10:20 - 10:40 BREAK
- 10:40 - 11:05 Transport Processes in Beamed Energy Propulsion Systems
R A Beddin¹, University of Illinois at Urbana-Champaign
- 11:05 - 11:30 Coupling Between Gas Dynamics and Microwave Energy Absorption
M M Micci, The Pennsylvania State University

- 11:30 - 11:55 Heating of a Liquid/Vapor Mixture by a Pulsed Electric Discharge
R L Burton and B K Hilko, GT-Devices, Inc.
- 11:55 - 1:30 LUNCH
- 1:30 - 1:55 The Physics of High Voltage Solar Arrays in Contact With the Space Plasma
D E Hastings, Massachusetts Institute of Technology
- 1:55 - 2:20 Fundamental Research on the ECR Plasma Thruster
F E C Culick and J C Sercel, California Institute of Technology
- 2:20 - 2:45 Basic Processes of Plasma Propulsion
H O Schrade, University of Stuttgart
- 2:45 - 3:10 Nonequilibrium and Radiation in MPD Plasmas: Two Fluid Numerical Simulations
M Martinez-Sanchez, Massachusetts Institute of Technology
- 3:10 - 3:40 BREAK
- 3:40 - 4:05 Fundamental Research on Erosion in Magnetoplasma dynamic Thrusters
V V Subramaniam and J W Rich, The Ohio State University
- 4:05 - 4:30 Propulsion Research on the Hybrid Plume Plasma Rocket
T F Yang, F R Chang-Diaz, X Yao, S Y Peng,
W A Krueger and J Urbahn
Massachusetts Institute of Technology
- 4:30 - 4:55 MPD Thrust Chamber Flow Dynamics
P J Turchi, J F Davis and N F Roderick, R & D Associates

A STUDY OF MIXING AND COMBUSTION IN SUPERSONIC FLOWS

Air Force Contract No. F49620-86-K-0022

Principal Investigators: C. T. Bowman, R. K. Hanson, M. G. Mungal, and W. C. Reynolds

Department of Mechanical Engineering
Stanford University
Stanford, CA 94305

SUMMARY/OVERVIEW:

An experimental and computational investigation of supersonic combustion flows is being conducted to gain a more fundamental understanding of mixing and chemical reaction in supersonic flows. The research effort comprises three interrelated elements: (1) an experimental study of mixing and combustion in a supersonic mixing layer; (2) development of laser-induced fluorescence techniques for time-resolved, two-dimensional imaging of species concentration, temperature and velocity; and (3) numerical simulations of compressible reacting flows.

TECHNICAL DISCUSSION:

Advanced air-breathing propulsion systems offer the potential of higher performance than conventional rocket engines for hypersonic flight. Of particular interest are propulsion systems in which combustion occurs in supersonic flow. However, our current understanding of the fundamental aspects of supersonic reacting flows is inadequate to support the development of these propulsion systems. To help achieve this understanding, we are conducting a coordinated experimental and computational investigation of compressible reacting flows. The individual elements of this investigation and recent results are described below.

Experiments on Mixing and Reaction in Supersonic Flow

An experimental study of mixing and combustion in supersonic flows is being conducted in a two-stream, supersonic mixing layer facility, Fig. 1. The facility is capable of providing a high-speed Mach 2 airstream and a low-speed stream of up to Mach 1, with variable stagnation temperatures. Our initial experiments have focused on measurement of the detailed structure of the mixing layer under compressible conditions at a convective Mach number of 0.6. The primary diagnostics have been short-time-exposure Schlieren images and planar laser Mie scattering images from alcohol droplets seeded into one stream to mark the mixing region. Fig. 2 shows a typical instantaneous planar Mie scattering image of the initial region of the mixing layer, with the laser sheet cutting the centerline of the flow. In this figure there is evidence of organization that is seen in Schlieren images together with a considerable amount of fine detail. Similar scattering images from other viewing planes suggest a flow which is much more three-dimensional than is evident in incompressible mixing layers. In the near future, Planar Laser-Induced Fluorescence will be used to obtain additional measurements of flow structure and also the probability density function of mixture fraction.

In addition to the experimental work, we have developed a simplified flow model for a reacting supersonic mixing layer, with full chemistry. This model, which is based on the Broadwell-Breidenthal model for incompressible mixing layers, is being used to determine the range of experimental conditions to be employed in the reacting flow experiments. These experiments will employ hydrogen as a fuel.

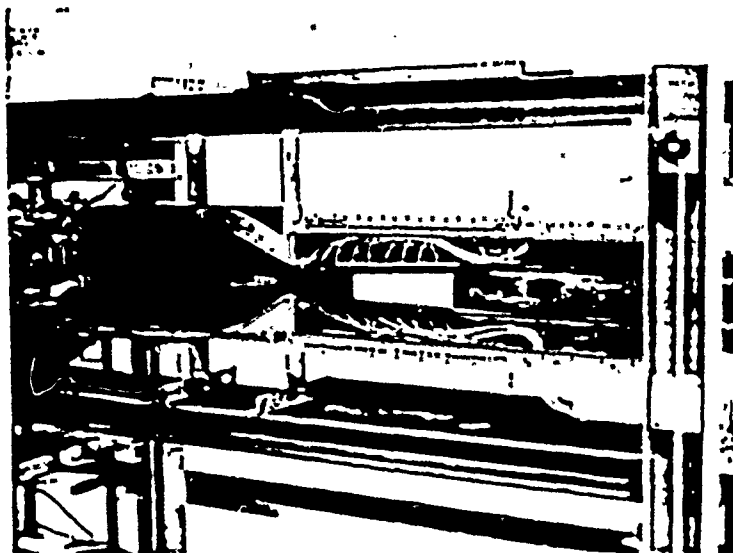


Fig. 1 Stanford Supersonic Shear Flow Facility



Fig. 2 Single-Shot Planar Mie Scattering Image of Supersonic Mixing Layer at Convective Mach Number 0.6.

Development of Supersonic Flow Diagnostics

This research is aimed at establishing flowfield imaging diagnostics based on Planar Laser-Induced Fluorescence (PLIF). Successful techniques will subsequently be applied in the supersonic mixing layer facility.

Work during the past year has been in four areas: (1) facility development; (2) imaging camera development; (3) fluorescence spectroscopy modelling; and (4) PLIF imaging.

In order to provide test environments for investigating new PLIF imaging concepts, we have built three new flow facilities: (1) a small, electrically-heated supersonic jet, which provides continuous flow capability to Mach 7 with a range of gases; (2) a 75 kW RF plasma-heated supersonic tunnel which can provide stagnation conditions of up to 4 atm and 5000 K (equilibrium temperature) in mixtures of air and argon; and (3) a pressure-driven shock tube and tunnel which can generate a wide range of pulsed-flow gas conditions and velocities. All three facilities are operational, although some difficulties remain in stabilizing undesired plasma discharges in the plasma-heated tunnel.

In the area of solid-state camera development, work was completed on two new intensified camera systems: a photodiode array camera with interchangeable 128x128 and 256x256 pixel arrays and a new video-compatible CCD array (240x512 pixels). The virtues of the photodiode

array system are its high sensitivity, variable framing rate (to 400 Hz for the 128x128 array), and frame-on-demand capability; the latter characteristic is needed in pulsed flow facilities such as the shock tube/tunnel. The CCD camera, on the other hand, operates at a fixed framing rate (60 Hz), but provides higher spatial resolution and convenient scale-up to multiple-camera systems.

With regard to spectroscopic modelling, we have continued development of computer codes for optimization and interpretation of PLIF images in O_2 , OH and NO. The code has been extended to describe excitation of NO in the $D \leftarrow X$ and $B \leftarrow X$ bands. These bands provide strong overlaps with tunable ArF lasers near 193 nm, leading to substantial improvements in SNR for PLIF imaging of NO at elevated temperatures. Recent experiments confirm that signal enhancements in excess of 20 can be achieved with this approach, leading to the ability to image low levels of NO in supersonic flow experiments.

Several new experiments involving PLIF imaging in supersonic flows have been carried out. Recent experiments have focussed on imaging NO, I_2 , O_2 and OH under a variety of conditions. As an example, Fig. 3 illustrates recent images of OH obtained in a supersonic jet of H_2 in air. The underexpanded jet of fuel exited from a 2.4 mm tube into hot air. The excitation was provided by a tunable, narrow-linewidth XeCl laser, with detection by an intensified CCD camera. Such images provide a clear determination of the turbulent flame structure, and the high SNR will enable detailed image-processing analysis for comparison with flame models. An overview of recent work on PLIF techniques in supersonic flow is given in Ref. 1.

In the area of velocity imaging, progress has been made with a new broadband laser concept. This approach allows determination of supersonic flow velocities via the Doppler effect using a single laser shot (Ref. 2). In essence, the method involves measuring the Doppler shift of a spectroscopically-accessible molecular component of the flow. Initial results have been obtained in an underexpanded N_2 jet seeded with a low level of NO. As seen in Fig. 4, the agreement between the experiment and a known correlation for the centerline velocity is good. The PLIF method yields the instantaneous velocity at a very large number of flowfield points (up to 122,800 for our current 240x512 array), which is an important advantage over various laser-marking schemes based on time-of-flight concepts.



Fig. 3 PLIF image of OH in $M = 3$ H_2 -air flame

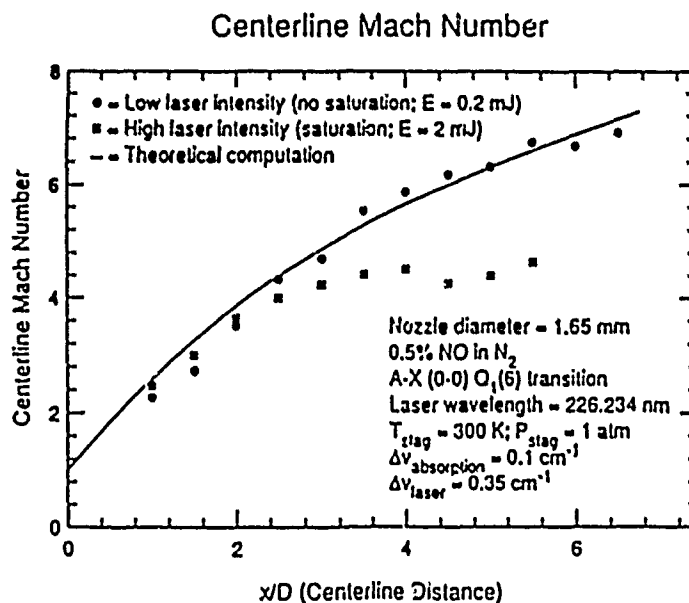


Fig. 4 PLIF velocity result for a supersonic jet

Numerical Simulation of Compressible Flow

In the simulation phase of this program, we have examined the hydrodynamic stability of supersonic mixing layers. It was found that the growth rate of the most amplified mode is a good estimator of the growth rate of the shear layer. At low convective Mach numbers, this mode is two-dimensional and leads to the familiar large-scale transverse vortices; but, above $M_c = 0.6$, three-dimensional modes dominate, which suggests that the large-scale turbulence structure will be strongly three-dimensional at high Mach numbers. This has been confirmed by direct numerical simulations, which reveal a complex three-dimensional structure involving an interwoven mesh of strong oblique and weaker transverse vortices, Fig. 5.

We are also conducting direct numerical simulations of homogeneous compressible turbulence, with the expectation that this work will lead to better understanding and modeling of the small-scale structures in supersonic shear flows that are important in the ultimate molecular mixing.

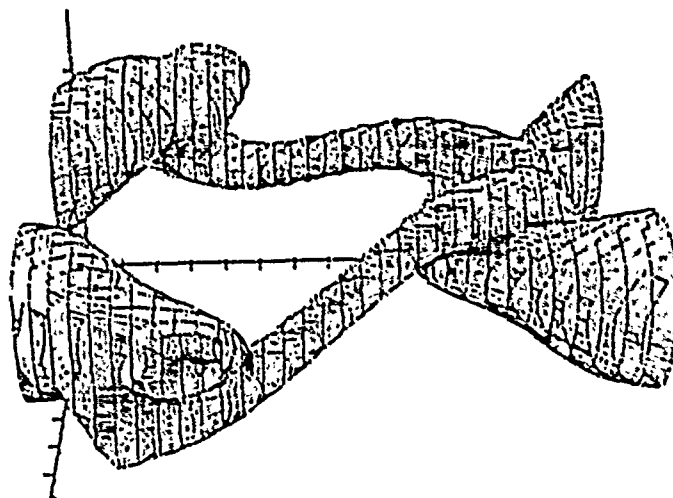


Fig. 5 Low-pressure surface in the simulated mixing layer at $M_c = 0.8$. Note the strongly oblique nature of the primary large-scale vortices.

References

1. P. H. Paul, M. P. Lee and R. K. Hanson, "Molecular Velocity Imaging of Supersonic Flows Using Pulsed Planar Laser-Induced Fluorescence of NO," Opt. Letters, May 14, 417 (1989).
2. P. H. Paul, J. M. Seitzman, M. P. Lee and R. K. Hanson, "Planar Laser-Induced Fluorescence Imaging in Supersonic Flows," AIAA-89-0059, presented at 27th Aerospace Sciences Meeting, Reno, Jan. 1989.

INVESTIGATIONS INTO THE SHOCK-INDUCED ENHANCEMENT OF MIXING AND COMBUSTION IN SUPERSONIC BURNERS

U. S. Airforce Contract No. F49620-86-C-0113

Principal Investigators: Frank E. Marble and Edward E. Zukoski

Jet Propulsion Center

California Institute of Technology

Pasadena, CA 91125

Summary/Overview:

The research reported here is directed toward producing rapid mixing and combustion between coflowing streams of hydrogen gas and air under conditions which are of interest in the combustion chamber of engines being developed for the NASA vehicle. Enhanced mixing is achieved by passing weak shock waves over masses of hydrogen embedded in much higher density air. Experimental and computational programs are described.

Technical Discussion:

The fuel used in hypersonic engines must also be used to cool the engine and vehicle and, if the coolant flow rate exceeds that required for stoichiometric combustion, the performance of the vehicle will be severely penalized. Consequently, the time available for mixing and combustion will often be limited by the allowable length of the engine and methods of enhancing the rate of mixing and combustion must be developed.

In the current project, the process of shock enhanced mixing is under study in a program which includes studies, in a 17" shock tube, of shock induced mixing between two-dimensional cylinders of helium and air, and a study of combustion in a vortex which is being carried out in a small combustion test facility. This AFOSR program has been complemented by a second program supported by NASA which has made possible a Mach 6 wind tunnel test of an injector system based on the results of the AFOSR program. This work has been supported by extensive calculations, made with an Euler code, of the shock induced mixing produced by the shock tube and nozzle flows.

The work described in the following paragraphs concerns the shock tube experiments and the accompanying calculations. The studies of vortex burning and the wind tunnel tests are described in a second abstract prepared for this meeting.

Shock Enhanced Mixing:

The mixing concept is illustrated in Figure 1, where we picture a cylindrical stream of hydrogen, flowing parallel with a supersonic air stream, intersected by a weak oblique shock wave. As a result of the large differences between the properties of hydrogen and air, strong streamwise vorticity is generated at the interface between the hydrogen and air. This vorticity distorts the cylindrical cross section within a fraction of a millisecond, see Figure 2. This process extends the interface enormously and the shear layer formed at the interface by the vorticity leads to an instability of the interface. Both processes promote rapid mixing to the molecular level which is required for chemical reaction. The left hand sketch in Figure 2 illustrates the vorticity distribution in a cylinder of helium immediately after the passage of the shock, the second two figures are a density map calculated for a time 0.3 ms after the passage of the shock and a shadowgraph obtained at the corresponding time.

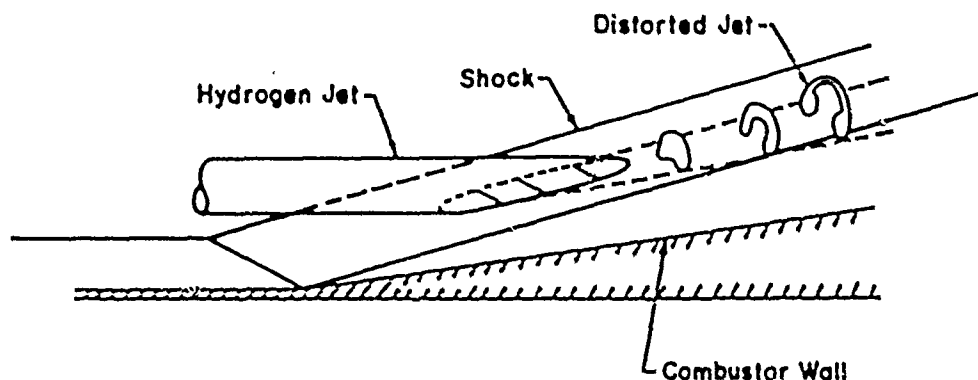


Figure 1. Distortion of Hydrogen Jet in Hypervelocity Air Stream.

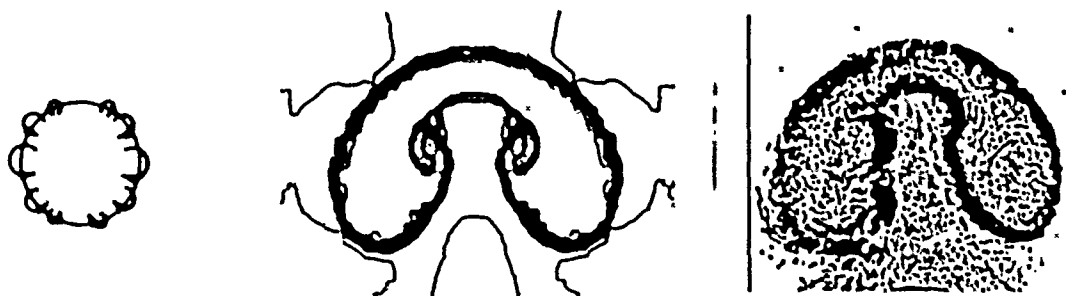


Figure 2. Vorticity Distribution, Computation and Shadowgraph of Distorted Hydrogen Jet

The possibility of examining a streamwise developing process in terms of one that develops in time allows a difficult continuous hypersonic flow experiment to be replaced with a time resolved shock tube experiment having the advantage of superior diagnostic access. The research program using the 17" shock tube had its genesis in an investigation initiated by Sturtevant in the early 1980's, culminating in a recent paper, Sturtevant and Haas (1986), concerning the scattering of shock waves by gas inhomogeneities in the atmosphere. Our program undertaken in 1986 focused on the distortion and rapid mixing of the inhomogeneity itself, interpreting time elapsed in the shock tube experiment as the distance downstream of injection, as detailed above. The principle quantitative technique employed was the laser induced fluorescence of biacetyl. Using this technique, Marble et al (1987) and Jacobs (1988), it was possible to record light gas density distributions (implying the degree of mixing between fuel and air) within a one millimeter thick cross section of the cylinder with a time resolution of a few microseconds. Extensive use was made of spark shadowgraphs, which give the local density gradient in the field, as a supplement to the fluorescence data.

The extensive research program we have pursued over the past three years has confirmed the potentiality of shock enhancement as a means of controlling and accelerating the rate of mixing between gases of very different molecular weights. Equally important, it has clarified and focused our perception of the basic issues, both scientific and technological, that control and limit the mixing process, and determine its scaling laws; issues that must be faced in the process of transferring the concept to a practical hypersonic combustor.

One of the most challenging of these is what we may refer to as stabilized stratification. In our situation, the vorticity at the interface between hydrogen and air creates an unstable shear layer which will, under usual circumstances, develop into a strong mixing layer. On the other hand, the configuration of the vortex with the lower molecular weight gas near the

center, tends to be stabilized against shear instability by a strong centripetal acceleration associated with the circulation of the vortex.

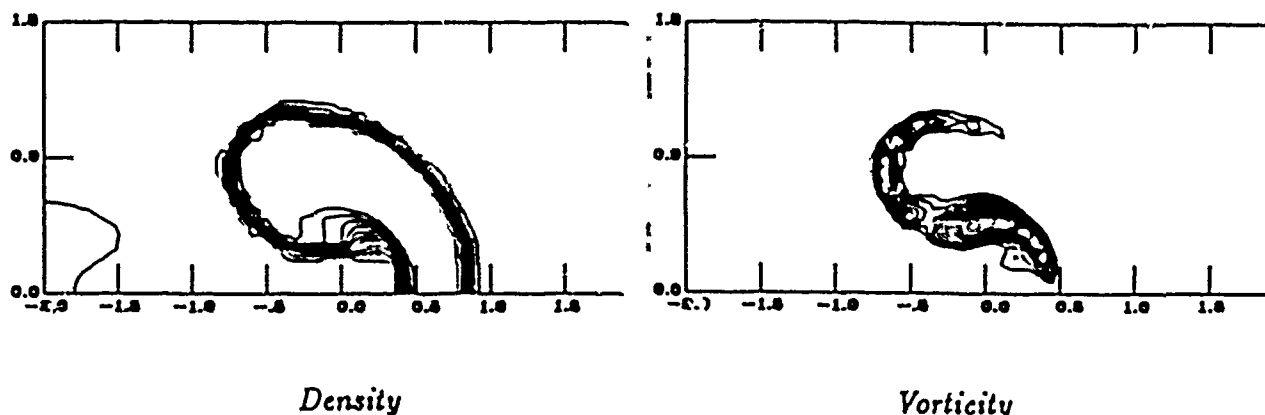


Figure 3. Density and Vorticity Contours .29 ms after Shock Impingement

The laser induced fluorescence photographs provide vital information in this regard. Initially the cylindrical cross section develops strong mixing at the interface. As the motion develops, a change takes place that can be most easily understood by examining the computations. Figure 3 shows density and vorticity contours at a time corresponding to approximately .29 ms. At about .79 ms the same physical quantities, Figure 4, show that the vorticity has, to a remarkable extent, migrated to the right-hand portion of the structure, leaving the left-hand portion largely free from vorticity. For later times, these two regions behave in completely different manners; the vorticity-free region mixes rapidly whereas the material containing the vorticity forms a symmetric vortex. The consequence is most clearly exhibited by the rates with which the helium mixes in each of these regions. Figure 5 shows that the region containing the vorticity mixes the more slowly of the two, giving weight to the contention that mixing of the region on the right is being retarded by the mechanism of stable stratification. The computations from a later stage of the process, Figure 4, confirm the symmetric vortex-like configuration of the right hand portion of the structure.

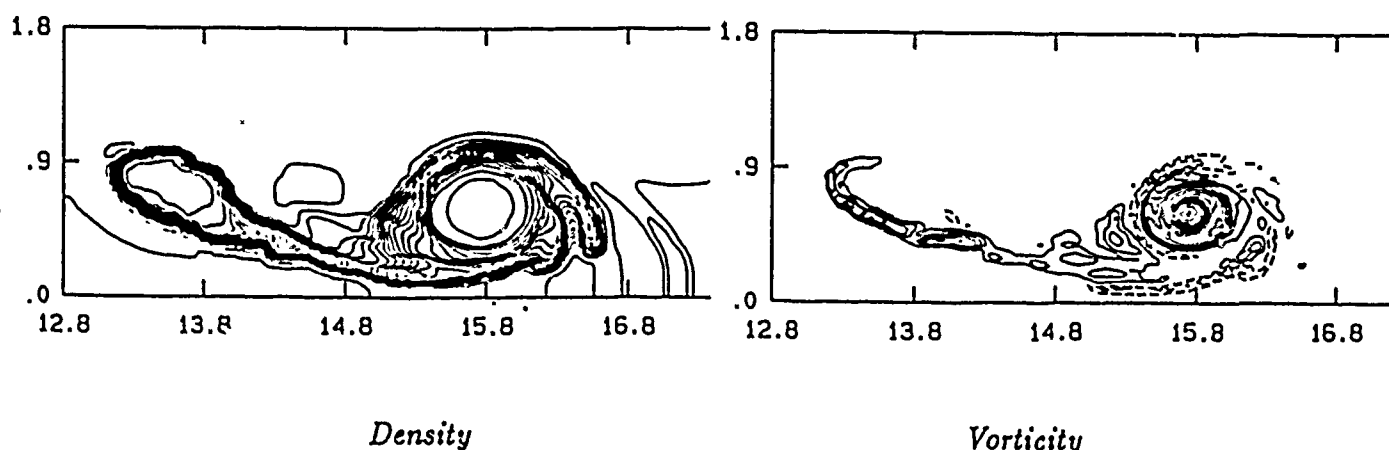


Figure 4. Density and Vorticity Contours .79 ms after Shock Impingement

We are now investigating the utilization of shock interaction to destabilize this structure through redistribution of the vorticity.

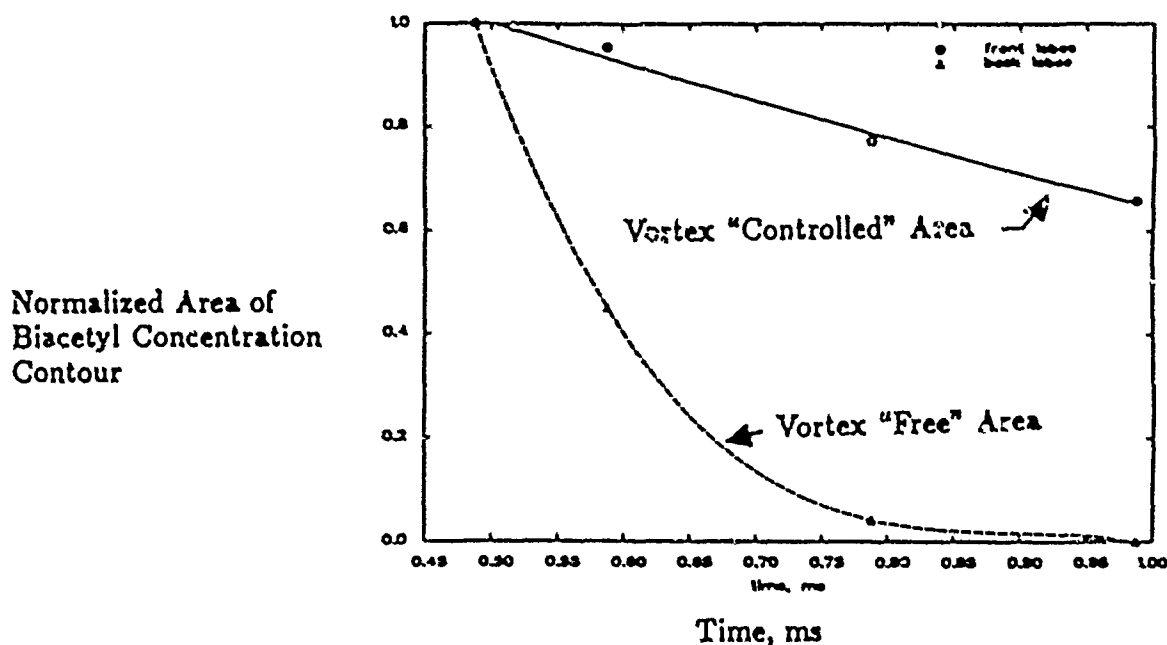


Figure 5. Mixing Histories for Non-Vortical and Vortical Regions

The experience that we have had in the conception, design and computational study of the hypersonic injector utilizing shock enhancement, has given a relevant framework within which to study basic issues of the problem that are not evident in the shock tube study. The first and most obvious of these, which was justifiably suppressed when the mechanism was being confirmed in the shock tube study, was the shear layer that develops when the hydrogen jet moves at a different velocity than the air. The boundary layer, that develops along the inlet ramp and surface of the combustor in which the injector is installed, likewise introduces a vorticity component normal to the flow direction. The interaction of vorticity component normal to the direction of flow, created by the shear, with streamwise vorticity, which we have generated by the shock interaction, is a fundamental issue that requires investigation.

A final point can not be made too emphatically. A SCRamjet engine, because of the immense difficulty of incorporating a variable geometry structure to withstand its very hostile atmosphere, must be able to adapt its internal flow mechanics to a considerable variety of internal Mach numbers, air pressure and temperature and hydrogen mixture ratio. In particular, a fixed internal configuration has poor tolerance for uncertainties in the heat release pattern along the flow path. There is, for minimizing pressure losses and heat transfer rate, an optimum heat release pattern which is different for different operating points, and may be achieved only by carefully controlled distributed injectors. It is immediately clear that shock enhancement and some variability of the injection nozzles, can provide a powerful means of controlling the heat release pattern with moving parts residing out of the high temperature regions of the combustor.

References:

- Haas, J-F., Sturtevant, B. (1988) "Interaction of Shock Waves With Cylindrical and Spherical Gas Inhomogeneities," *Jour. Fluid Mech.*, Vol. 181, p. 41.
- Jacobs, J. W. (1988), "PLIF Flow Visualization of a Shock Accelerated Transverse Helium Jet," *Physics of Fluids*, in publication.
- Marble, F. E., Hendricks, G. J. and Zukoski, E. E. (1987) "Progress Toward Shock Enhancement of Supersonic Combustion Processes," *AIAA Paper*, No. AIAA-87-1880, 23rd AIAA Joint Propulsion Conference, San Diego.

ONR Contract No. N00014-86-K-0434

Principal Investigators: H. Krier, J.P. Renie, and J.C. Dutton

Department of Mechanical and Industrial Engineering
University of Illinois at Urbana-Champaign

SUMMARY/OVERVIEW:

Major emphasis has been placed upon the study of compressible, turbulent reactive free shear layers due to the renewed interest in hypersonic, air-breathing propulsion wherein the higher flight Mach numbers require supersonic flow throughout the combustion chamber [1]. How the mixing process depends upon compressibility, as well as other parameters of the free shear layer including the freestream velocity ratio, density ratio, and heat release rate, is under investigation in an experimental study of the two-dimensional, compressible, turbulent reactive free shear layer at the University of Illinois [2-5]. Research is centered on the mixing and combustion between two high-speed streams wherein one of the streams is operated supersonically and the other is operated at either slightly supersonic or subsonic conditions. In addition, either stream may be heated by means of a nonvitrated gas-fired heat exchanger and/o. the lower Mach number stream may be supplied as either the fuel-lean or fuel-rich products of combustion from a "gas generator."

TECHNICAL DISCUSSION:

Introduction

During the past three years, the dual-stream experimental flow system has been constructed and flow visualization results and mean and turbulent velocity field data have been acquired for several operating conditions. Figure 1 schematically represents the existing airflow facility indicating the valving and plumbing necessary to supply air to both streams of the dual-stream test section. Figure 2 provides more details of the test section showing the flow conditioning and measurement equipment, nozzle blocks, splitter plate separating the two high-speed streams, and the 0.5 meter long test section with adjustable cross section. Non-intrusive, laser-based diagnostic techniques including spark and laser schlieren for flow visualization, laser doppler velocimetry (LDV) for mean and turbulence velocity measurements, planar laser-induced fluorescence (PLIF) for temperature and species concentration measurements, and particle image velocimetry (PIV) for planar velocity measurements at a given instant are being developed and employed.

Laser Doppler Velocimetry Measurements

Two-component mean and turbulent velocity field measurements of the nonreactive mixing layer have been completed for a total of four operating conditions. The LDV system has also been used to measure velocity autocorrelations and to demonstrate the behavior of fluid entrained into the mixing layer. The operating conditions of three of the four cases studied to date include velocity ratios (secondary-to-primary) of 0.79, 0.58, and 0.20 corresponding to density ratios of 0.76, 1.56, and 0.56 and convective Mach numbers of 0.20, 0.45, and 0.69, respectively. The operating conditions of a fourth case are identical to those listed for the first except that the freestream turbulence intensity of the secondary stream was higher to study the influence of this parameter. For each flow field, transverse profiles of the two-component velocity field have been measured at several axial locations including the inlet freestreams and splitter plate boundary layers to document the initial conditions. The mean and turbulent velocity field measurements have been used to examine the development, similarity, and entrainment behavior and to accurately determine growth rates of the mixing layer. In addition to the mean velocity components, higher-order moments and cross-products have also been determined from the histograms of velocity

realizations at each measurement location. A typical example of the normalized streamwise mean velocity profile development is presented in Fig. 3. The measured growth rate for the most recent case is approximately one half the value observed for incompressible mixing layers at the same velocity ratio and density ratio so that significant compressibility effects are present for this condition. A decrease in the normalized peak turbulence intensity of approximately 20% has also been observed for this case in comparison to the previous cases of this study which had a smaller convective Mach number (of value 0.20). Normalized growth rates for the cases [5] which have been examined are presented in Fig. 4.

Future LDV work will include examining additional cases, particularly those at higher convective Mach numbers. Because of the dearth of experimental information in this area, we believe that obtaining this data is crucial to improving the general state of knowledge of compressible mixing layers. Two of the future cases to be examined will have the same velocity and density ratios but different convective Mach numbers. Therefore, comparison of these cases will demonstrate the isolated effects of compressibility. Two of the other future cases will also have identical operating conditions except that for one the secondary stream will have excess fuel in order to study the effects of heat release on shear layer development. An interesting feature of these two cases is that the lower Mach number stream has a higher freestream velocity than the higher Mach number stream because the secondary is heated. However, a more fundamental difference about these cases, as compared to the others, is that the secondary stream has a higher momentum flux than the primary stream which could affect the manner in which the mixing layer develops. Comparison of one of these cases with the first case already studied will also demonstrate the isolated effects of density ratio since the velocity ratio and convective Mach number will be the same for the two cases. Finally, one of the future cases will have a supersonic convective Mach number of approximately 1.2, the highest convective Mach number that can be achieved in our facilities.

Shear Layer Combustion Experiments

A significant goal of the ongoing research program is concerned with the study of the interaction between mixing and combustion (heat release) in a quasi-two dimensional, supersonic mixing layer. To accomplish this goal, a methodology has been developed for safely producing and working with reactive gas streams in the wind tunnel facility. A basic design for a high-capacity reactive flow gas generator (RFGG) has been established and the initial phase of construction of this device has been completed. This new facility is shown as part of Fig. 1. An extensive safety check-out has been conducted, preliminary fueled firings of the RFGG have been made, and a set of trial runs has established appropriate control parameters and verified that the RFGG is capable of performing as designed. Figure 5 shows an internal cross-sectional view of the RFGG. Low temperature compressed air is supplied to a large nozzle-mixing burner at the top of the 0.60 m diameter, 3 m long cylindrical combustion chamber. The burner can operate with air flows up to 0.58 kg/s at chamber pressures up to 515 kPa absolute.

The RFGG is essentially a vitiating air heater connected in-line with the dual stream wind tunnel fueled by natural gas that can operate in either a fuel-lean or a fuel-rich mode. In the fuel-rich mode, the burner will be operated nearly stoichiometrically to convert most of the free oxygen in the air stream to carbon dioxide and water. Downstream of the burner, additional fuel will then be injected into the oxygen-deficient gas stream to generate an overall very fuel-rich mixture. In this mode (equivalence ratio above 2.5), thermochemical calculations indicate that the system will produce a high temperature, combustible gas stream composed of large amounts of hydrogen (H_2) and carbon monoxide (approximately 24% and 14% by volume, respectively). Therefore, the RFGG will supply a hot fuel-rich stream to one side of the shear layer which will mix and burn with the oxidant from the other stream.

Planar Laser Diagnostics

Recently, new nozzles have been designed and fabricated. These nozzles differ from the original ones employed in that they have narrow streamwise window slots in the upper and lower walls that enable planar diagnostic studies to be conducted within the mixing layer flow field. The quartz windows are 6.4 mm wide and 125 mm long, providing a total of almost 0.5 m of coverage in the test section downstream from the tip of the splitter plate. The nozzles themselves are designed for Mach numbers of 2.5 and 1.4. With the new nozzles, combined with the

capabilities of the new gas generator, a wide range of convective Mach numbers can be generated from wake cases, $M_c = 0$, up to $M_c = 1.2$.

Several ancillary studies have been ongoing to prepare for planar diagnostic experiments within the dual stream, wind tunnel facility. In particular, planar Mie scattering at oblique angles in the original supersonic flow test section have been performed. The oblique Mie scattering was performed since the original nozzles did not include upper and lower wall window ports. Pump source energy level and output scattered intensity were varied to investigate usable exposure levels. Also, the 15 ns pulsed dye laser source effectively froze the flow structure, yielding informative images of the turbulent mixing layer. Currently, Mie scattering experiments are concentrating on transverse illumination of the flowfield; however, oblique illumination may also provide useful information on the three-dimensionality of the mixing layer structure.

Laser-induced OH fluorescence of a bunsen burner flame has been ongoing and will continue until the test section is prepared to operate in a reacting (fuel-rich) mode. Color schlieren photography is also being developed to detect any wave phenomena present in the supersonic mixing flow. Other investigators have observed wave structure from supersonic jets [6,7] and supersonic mixing layers [8]. It is possible that some of these wave features are directly related to the convective Mach number of the flow. Due to the predominant density gradient across the supersonic mixing layer, weak wave features at angles largely different than the dominant density gradient are difficult to image with monochrome schlieren photography. In these instances, color schlieren filters, a modified two-dimensional dissection designed to highlight directionality of the density gradients [9,10], can be strategically oriented so as to generate color mixtures for the weak gradients expected for convective Mach number waves that will stand out from the dominant color scheme generated across the mixing layer. This should help to more readily visualize any wave features arising when the convective Mach number is supersonic.

REFERENCES:

1. Waltrup, P.J., "Hypersonic Airbreathing Propulsion: Evolution and Opportunities," AGARD Conference on Aerodynamics of Hypersonic Lifting Vehicles, Paper No. 12, April 1987.
2. Messersmith, N.L., J.P. Renie, J.C. Dutton, and H. Krier, "Design of a Supersonic Turbulent Reactive Free Shear Layer Flow Facility with Access for Laser Diagnostics," Technical Report No. UILU-ENG-87-4003, Department of Mechanical and Industrial Engineering, University of Illinois at Urbana-Champaign, 1987.
3. Messersmith, N.L., S.G. Goebel, W.H. Frantz, E.A. Krammer, J.P. Renie, J.C. Dutton, and H. Krier, "Experimental and Analytical Investigations of Supersonic Mixing Layers," AIAA Paper No. 88-0702, 1988, submitted as "Investigations of Supersonic Mixing Layers" to Journal of Propulsion and Power.
4. Goebel, S.G., J.C. Dutton, J.P. Renie, and H. Krier, "Measurements of a Supersonic Mixing Layer," Technical Report No. UILU-ENG-88-4007, Department of Mechanical and Industrial Engineering, University of Illinois at Urbana-Champaign, 1988.
5. Goebel, S.G., J.C. Dutton, H. Krier, and J.P. Renie, "Mean and Turbulent Velocity Measurements of Supersonic Mixing Layers," submitted to Experiments in Fluids.
6. Oertel, H., "Mach Wave Radiation of Hot Supersonic Jets Investigated by Means of the Shock Tube and New Optical Techniques," Shock Tubes and Waves, Proceedings of the 12th International Symposium on Shock Tubes and Waves, pp. 266-275, Jerusalem, 1979, Eds. Lifshitz and Rom, Magnum Press, 1980.
7. Oertel, H., "Coherent Structures Producing Machwaves Inside and Outside of the Supersonic Jet," Structure of Complex Turbulent Shear Flow, IUTAM Symposium, pp. 334-343, Marseille, 1982, Eds. Dumas and Fulachier, Springer Verlag, 1983.
8. Papamoschou, D., "Structure of the Compressible Turbulent Shear Layer," AIAA Paper No. 89-0126, Reno, Nevada, 1989.
9. Settles, G.S., "A Direction-Indicating Color Schlieren System," AIAA Journal, Vol. 8, No. 12, pp. 2282-2284, 1970.
10. Settles, G.S., "Colour-Coding Schlieren Techniques for the Optical Study of Heat and Fluid Flow," The International Journal of Heat and Fluid Flow, Vol. 6, No. 1, pp. 3-15, 1985.

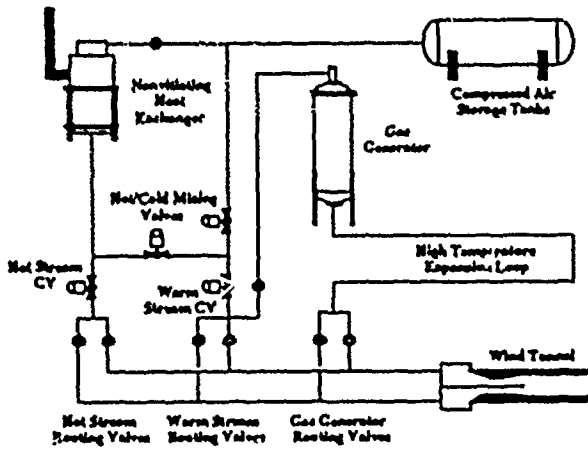


Figure 1. Gas Supply Piping for Supersonic Combustion Facility

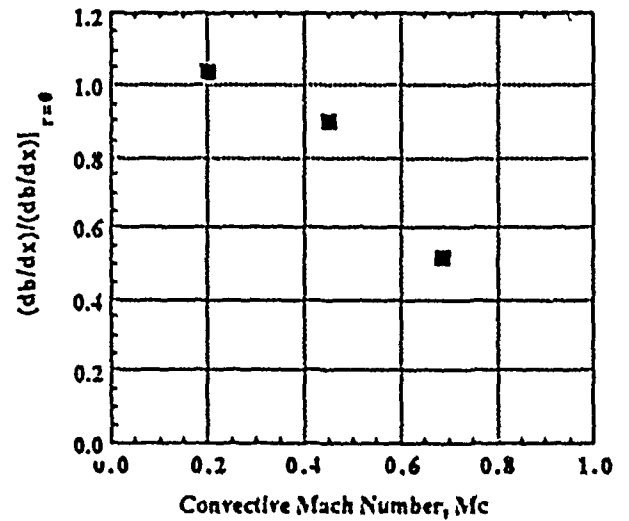


Figure 4. Normalized Growth Rates versus Convective Mach Number

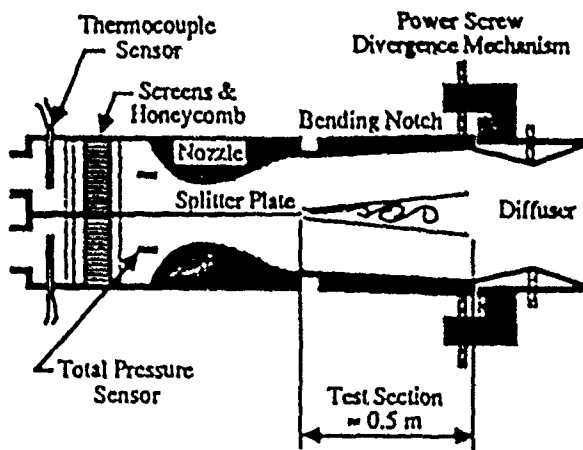


Figure 2. Test Section Schematic

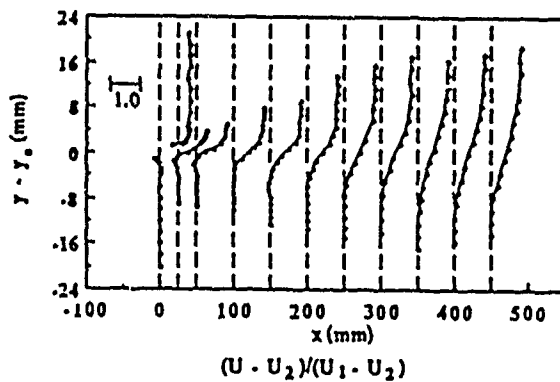


Figure 3. Normalized Velocity Profiles

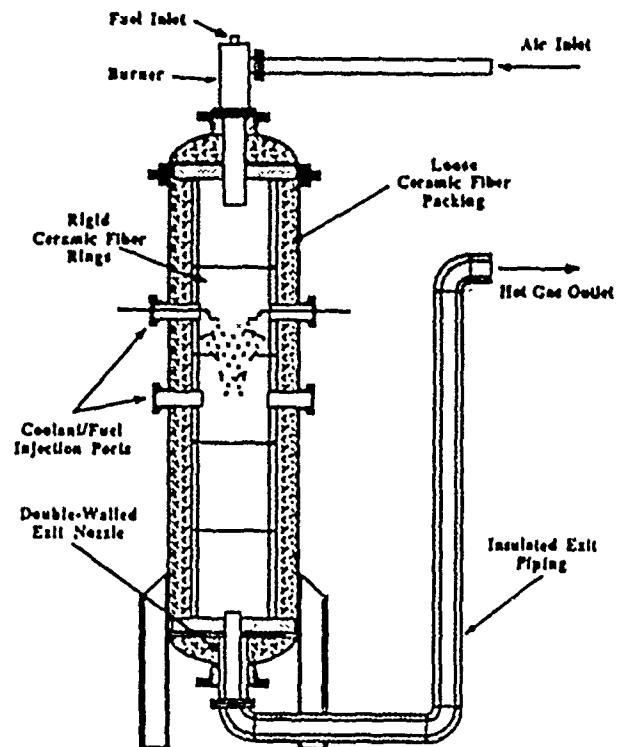


Figure 5. Gas Generator Schematic

FUNDAMENTAL COMBUSTION PROCESSES OF PARTICLE-LADEN SHEAR FLOWS IN SOLID FUEL RAMJETS

(ONR CONTRACT No. N00014-86-K-0468)

Co-Principal Investigators: K. K. Kuo, V. Yang, T. A. Litzinger
S. T. Thynell, and W. H. Hsieh

Department of Mechanical Engineering
The Pennsylvania State University
University Park, PA 16802

Solid fuels can be used in ramjet propulsion and various military applications. Three major unresolved areas regarding combustion of solid fuels under stagnant and crossflow conditions are: 1) ignition and combustion characteristics of high energy boron-based solid fuels and magnesium-based pyrotechnic materials are not well understood; 2) kinetic parameters and thermophysical properties of the above materials are not well characterized; and 3) the effects of chemical compositions and ambient flow conditions on the infrared radiation output is not fully established.

The purpose of this research project is to help answer some of the fundamental questions involved in the three areas listed above. The specific program objectives are:

- 1) to acquire a basic understanding of physical and chemical mechanisms involved in the combustion of solid fuels under strong crossflow conditions (this involves experimental testing with a supersonic blowdown wind tunnel and theoretical modeling of the two-phase fluid dynamic and combustion processes);
- 2) to characterize the thermal degradation, pyrolysis, and ignition phenomena of the specially formulated solid-fuel samples used in this project via strand burner and CO₂ laser pyrolysis studies; and
- 3) to advance the understanding of radiative heat transfer during combustion of high-energy solid fuels by determining temperature and species profiles and radiative properties of particulate matter of plumes in quiescent environments using a Fourier-Transform Interferometer (FT-IR) and numerical modeling of radiation.

Significant results obtained in the past year are summarized below.

I. Combustion of Solid Fuels under Strong Crossflow Conditions

To study both subsonic and supersonic combustion processes of high-energy metallized solid fuels, a blowdown wind tunnel facility has been designed and constructed to simulated ramjet environments. The facility is capable of simulating a broad range of flight Mach numbers and altitudes. The flow Mach number selected for supersonic combustion tests is 2.0, with a maximum mass flow rate of 9 kg/s and a test duration of 340 seconds.

The test section design allows detailed measurement of particle-laden turbulent reacting boundary-layer flows above burning solid-fuel samples. Advanced non-intrusive diagnostic instruments (including real-time x-ray radiography and image analyzer systems, Schlieren, fast wavelength tracking Smeets-George interferometer, and a Laser Doppler velocimeter) have been set up for flow measurements and visualization. In addition to these instruments, an aerodynamically shaped water-cooled gas sampling probe is online with a gas chromatograph to extract gas samples from the reacting boundary layer at the exit plane.

Boron-based solid-fuel samples have been fabricated at Penn State and were also acquired from Aerojet, UT/CSD, and NWSC for this research study.

The supersonic blowdown wind tunnel is now fully operational. The test section downstream of the wind tunnel was fully characterized by the LDV and Smeets-George interferometer. To facilitate the velocity measurements above the fuel sample, a fuel sample holder and feeding system were constructed. The position of the sample surface can be maintained at a fixed level by means of a laser-based servo-controller. A small-scale supersonic nozzle is also used to calibrate the LDV and Smeets-George interferometer.

Current efforts are focused on igniting and sustaining a stable flame above a solid fuel or propellant sample with the Mach 2 freestream flow. The Schlieren photograph in Fig. 1 shows the position of the fuel sample at 18° from the horizontal. This configuration generates a 49° oblique wave with a corresponding three-fold pressure rise across the wave. The increased pressure and a rearward-facing step contribute favorably to the ignition process, yet minimally affect the freestream velocity. Figure 2 is a Schlieren photograph of the combustion stage of a typical sample. A stable flame is held in the recirculation zone while the flame spreads upward along the sample.

II. Strand Burner Results

To study the combustion behavior of boron/(BAMO/NMMO) under no crossflow conditions, a windowed strand burner was adopted for observing the burning characteristics of fuel samples with different boron percentages in well-controlled environmental conditions. Different gaseous mixtures were used to pressurize the strand burner for studying the effect of ambient gas environment on the combustion behavior of boron/(BAMO/NMMO) fuel-rich solid propellant.

From the measured burning rate data for five boron/(BAMO/NMMO) solid fuels with different boron contents, it was found that the burning rate increases as boron weight percentage increases, until an optimum value of boron weight percentage is reached; then the burning rate starts to decrease with the increase of boron weight concentration. At the optimum value of boron weight percentage, the heat released from the combustion of boron/(BAMO/NMMO) is sufficient to increase the temperature of the boron particles to 1900 K for second-stage ignition and rapid boron oxidation, and to release a huge amount of heat of combustion from boron particles into the gas phase.

After each strand burner test, the combustion residues were collected for SEM examination and X-ray diffraction analysis. From the X-ray diffraction analysis, significant amounts of boron nitride in hexagonal crystalline form were found for the tests conducted at 1034 kPa (150 psia) with 29% boron/(BAMO/NMMO). For other tests, the amounts of BN found in combustion residues were much lower. The formation of boron nitride at high-pressure conditions can significantly reduce the total amount of energy released by the reaction of boron particles. The energy released by the reaction of boron and nitrogen (23.7 kJ/g-boron) is only half of that released by the oxidation of boron (58.7 kJ/g-boron). This indicates that the formation of boron nitride in a combustion system is highly undesirable. It is believed that the formation processes of boron nitride occurring in the combustion of boron-based solid propellants could have significant effects on the overall energy release rate. Therefore, methods for reduction or elimination of the formation of boron nitride in combustion systems should be developed.

III. Pyrolysis and Ignition of Solid Fuels

The pyrolysis and ignition characteristics of a variety of solid fuels have been investigated under radiative heating by a high-power CO_2 laser. The baseline solid fuels for the laser ignition studies have been boron/HTPB fuels with varying percentages of boron. Another fuel tested was a composition of the energetic copolymer BAMO/NMMO and boron of varying percentages. Preliminary results have also been obtained on five new fuels from the NWC. The constituents of these fuels combined with boron in various compositions and amounts included HTPB, the high-density hydrocarbons PCUD and Zecorez, boron carbide, magnesium, and two combustion aids. A pyrotechnic material (MTV) consisting of magnesium, polytetrafluoroethylene (PTFE), and Viton A has also been

extensively investigated. Recently, solid pellets composed of varying percentages of magnesium, boron, PTFE, and Viton A have been tested with promising results.

The boron/HTPB and boron/(BAMO/NMMO) solid fuels were formulated with varying percentages of boron. For the boron/HTPB fuel tests showed that the delay time for first light emission decreased as the percentage of boron increased (up to 20%) and the incident heat flux increased. Further increases in boron percentage caused an increase in delay time. However, by using a crossflow of inert gas above the sample surface to remove the two-phase mixture of pyrolysis products, it was found that the delay time decreased monotonically as the boron loading increased. This trend observed with the crossflow method was also observed for the boron/(BAMO/NMMO) solid fuels. The trend can best be explained by the effects on delay time of the volumetric specific heat of the pyrolysis products versus the effect of the absorptivity of the two-phase mixture on the rate of increase of the mixture temperature.

Tests have been performed on several solid fuels formed by pressing together powders of Mg, boron, PTFE, and Viton A into solid pellets. Figure 3 indicates that the addition of both boron and/or Viton A to a basic composition of Mg and PTFE significantly lowered the ignition delay times. Increasing the percentage of boron produced a much more vigorous, yet controlled and reproducible combustion, increasing the burning rate by about three times that of the base Mg/PTFE formulation. However, the optimum combustion of boron/Mg/PTFE fuel was found to be 35/15/50 by weight percentage, and the addition of boron beyond this composition significantly lowered the burning rate and combustion stability.

Only preliminary results have been obtained for the five new solid fuels from NWC. The usual trend of lower ignition delay times for higher heat fluxes was observed for all these boron-based solid fuels. It was also found that the two compositions with boron carbide and magnesium had significantly lower ignition delay times, roughly one-half the delay times for the three compositions based on HTPB.

IV. FT-IR Measurements and Modeling of Infrared Radiation

The first phase of the experimental study includes the use of the Fourier-Transform Interferometer (FT-IR) for performing either emission or transmission/absorption spectroscopy on plumes of burning strands confined within a low pressure, transparent test chamber. A schematic of the experimental setup for transmission/absorption measurements is shown in Fig. 4. Attached to the transparent test chamber is a computer controlled actuator, He-Ne laser, photodiode and a PC; these components will be used in a closed-loop feedback system for the purpose of maintaining the burning strand in a fixed position, such that time-independent measurements as well as measurements at different positions can be performed using the FT-IR without changing the optical alignment.

The modeling effort of radiative heat transfer in plume environments is centered around increasing the data base on radiative properties for particulate matter and to extend an available radiation code (ARC) to include the effects of scattering for all optical path lengths. In conjunction with these efforts, an exact formulation of the two-dimensional radiation problem has been completed, and an analysis on the effect of absorbing, emitting, and scattering particulate matter on the gaseous emission due to either water vapor or carbon dioxide has been determined for one-dimensional, axisymmetric plumes. The major finding of the latter study is that the particulate matter always shields the gaseous hemispherical emission for all values of the single scattering albedos and optical path lengths. However, preliminary results of a third study has revealed that an enhancement of the gaseous directional emission exists for certain ranges of the single scattering albedos and optical path lengths. This enhancement effect is due to the scattering of emitted radiant energy from small slant paths into directions of large slant paths.

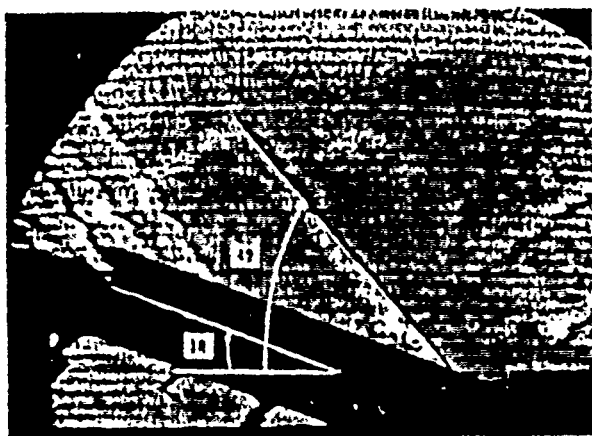


Figure 1. Schlieren Picture of Test Sample in Mach 2 Freestream Flow



Figure 2. Schlieren Photograph of Test Sample with Combustion Under Mach 2 Flow

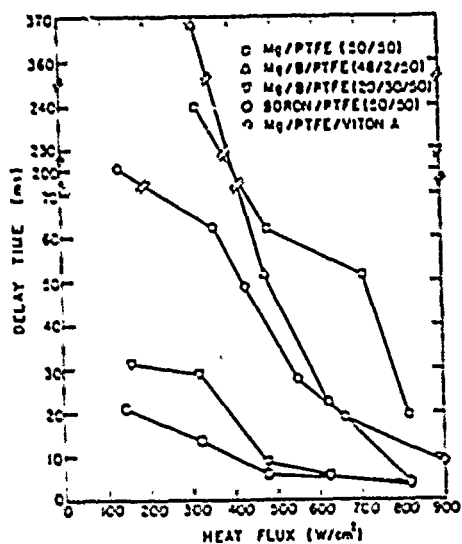


Figure 3. Effect on Ignition Delay of the Addition of Boron and Viton A to a Mg/PTFE Material (Ignition in Air at 1 Atmosphere)

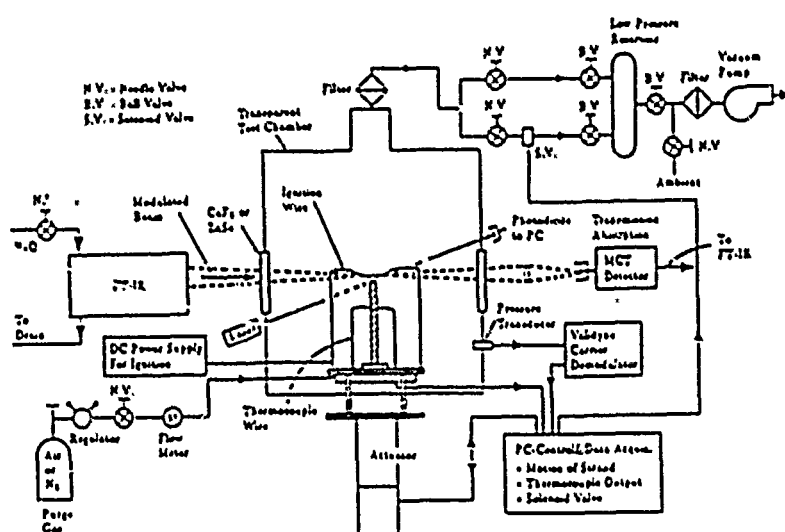


Figure 4. Schematic of Experimental Setup for Absorption Measurements Using the FT-IR with the Transparent Test Chamber

PREDICTION OF INFRARED EMISSION FROM COMBUSTION TESTS

(ONR Contract No. N00014-88-C-0492)

Principal Investigator: Kurt D. Annen

Aerodyne Research, Inc.
45 Manning Road
Billerica, MA 01821

SUMMARY/OVERVIEW:

The objective of this program is to analyze infrared (IR) emission from solid propellant combustion to obtain a better understanding of the chemical, physical, and radiative processes occurring in the combustion process. Our program interacts closely with the solid propellant combustion program of Penn State, using the spectral and radiometric IR measurements taken during their combustion tests. By comparing predictive models of IR emission with the measured data, chemical kinetic and radiative parameters used in modeling advanced propellants (such as those containing boron) can be checked, and a better understanding of the chemical and physical processes which control the rate of combustion can be obtained. In particular, we hope to obtain new information on the boron oxidation mechanism and rates occurring in boron propellant combustion and a verification of band strengths for the major boron combustion product species.

AUTHORS: K.D. Annen, J.C. Wormhoudt, and C.E. Kolb

TECHNICAL DISCUSSION:

The infrared (IR) emission produced by the products of combustion of solid propellants has considerable military significance. Both the initial combustion products and the products of the secondary combustion or "after burning", which occurs as the initial products mix with the surrounding atmosphere, are important contributors to the total IR emission. Measurements of the IR emission produced in combustion tests can allow better predictions of the IR emission produced by actual military systems, especially for advanced propellants containing boron, and can also provide a wealth of information about the chemical and fluid dynamic processes occurring in the solid propellant test.

The objective of our program is to complement the Penn State research on solid propellants. Our work will focus on analyzing the spectral and radiometric data obtained by Penn State to improve our understanding of the chemical, radiative, and fluid dynamic processes occurring in solid propellant combustion. Penn State is currently in the process of setting up a Michelson FTIR spectrometer and a transparent strand burner chamber for solid propellant tests in which the collection of spectral emission data is a major

objective. During this period, we have worked on the development of preliminary fluid dynamics, chemical kinetics, and IR radiation models which have been used to predict emission spectra for propellants to be tested by Penn State and will be used in the analysis of the spectral data when it is obtained.

An interesting propellant which has been tested by Penn State in their high pressure facilities and will be tested in the near future with spectral measurements is a formulation consisting of boron and a BAMO/NMHO binder. Preliminary predictions were made for this propellant based on the following observations and assumptions. Penn State observed in their high pressure strand burner that the boron particles in the B/(BAMO/NMHO) propellant do not burn to completion at the propellant surface, but rather are ejected from the burning surface by the decomposition of the binder. Based on this information the concentration of gas phase boron species near the surface was assumed to be small. By analogy with nitramine decomposition processes, the BAMO/NMHO binder has been assumed to decompose to CH_2O , C_2H_2 , N_2 , NO_2 , HCN , and H . Subsequent reactions to form CO , NO , and a variety of radical species occur rapidly. The peak temperature of the combustion products at a pressure of 35 psia, prior to reaction with the external atmosphere, was measured to be approximately 900 K. Higher temperatures were observed in the after-burning region of the strand combustion flowfield. The soot mole fraction in the 900 K region was assumed to be 0.01.

Figures 1 and 2 show sample predicted high resolution spectra in the CO band center and P branch region for temperatures of 900 K and 1000 K. The main features to note in these spectra are the ratios of the highest of the $v = 0$ rotational lines to the $v = 1$ "hot band" rotational lines in the vicinity of the band center. The ratio is 0.36 at 900 K and 0.55 at 1000 K. Thus, the CO line structure may be used to obtain an effective temperature for the flowfield region observed by the FTIR spectrometer.

At a typical FTIR resolution of 1 cm^{-1} , the line features would not be as sharp and temperature determination would be more difficult. In addition, calculations performed for an assumed soot mole fraction of 0.10 indicated that the baseline radiance level due to soot emission was raised to be roughly equivalent to the intensity of the $v = 1$ rotational lines near line center. While this level of soot background still allows the hot band peak heights to be measured, fluctuations in this background level will increase the uncertainty in the measurement of the hot band peak heights.

In the near future, we will incorporate chemical kinetics of the BAMO/NMHO decomposition and combustion processes into our description of the strand combustion flowfield. The model will then be compared against the Penn State measurements and further refined when the FTIR data are available.

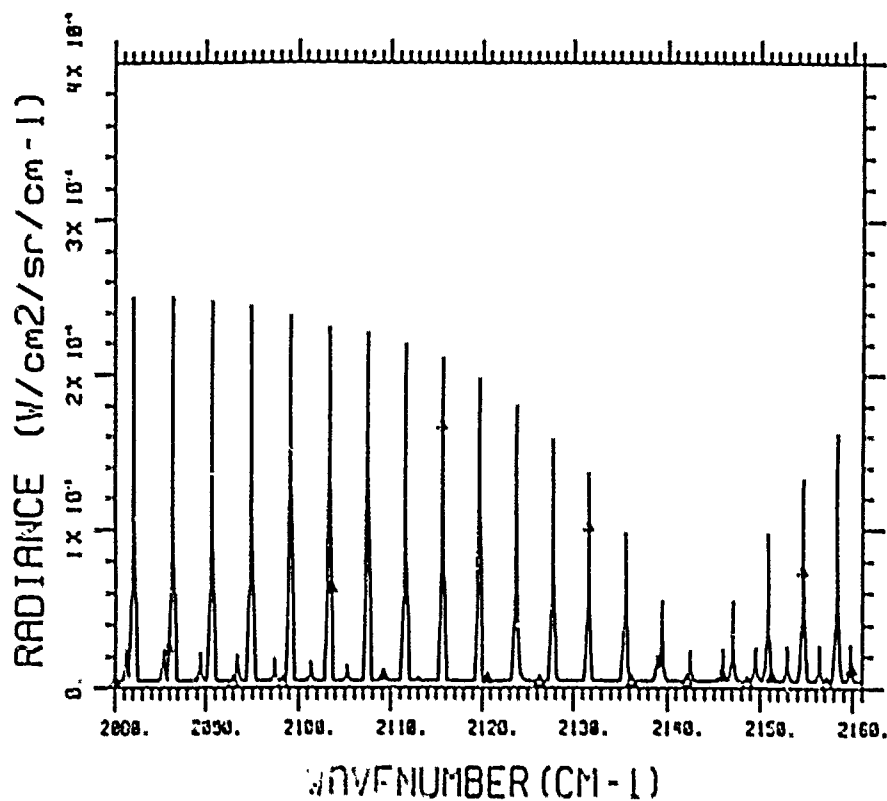


Figure 1. Predicted B/(BAHO/NMHO) emission spectra for 900 K peak temperature at 35 psia.

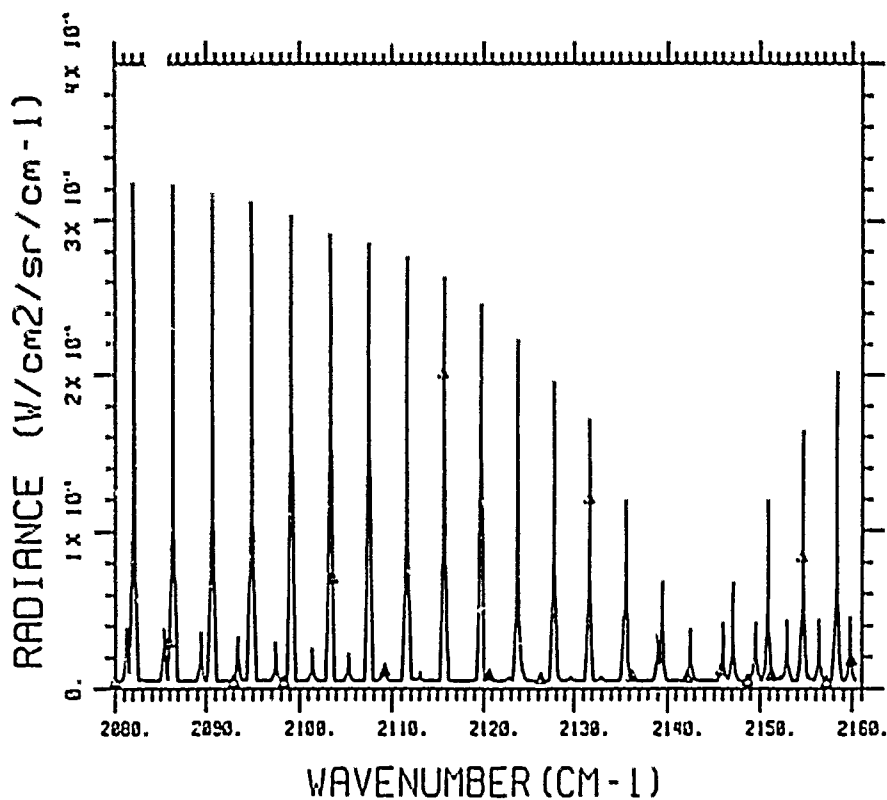


Figure 2. Predicted B/(BAHO/NMHO) emission spectra for 1000 K peak temperature at 35 psia.

TITLE: TURBULENT MIXING IN EXPONENTIAL TRANSVERSE JETS**(AFOSR Grant/Contract No. 87-0366)****Principal Investigator:**

Robert E. Breidenthal, Associate Professor
Department of Aeronautics and Astronautics
University of Washington, FS-10
Seattle, WA 98195
(Telephone: 206-545-1098)

SUMMARY/OVERVIEW:

Effects of spatial acceleration on turbulent mixing are being investigated experimentally in a new flow visualization water tunnel facility. For this purpose, an array of discrete nozzles with exponentially increasing cross-sectional area and injection speed has been constructed. Photographs of a fast chemical reaction and laser-induced-fluorescence, between the transversely injected fluid through these nozzles and the freestream, reveal the mixing characteristics of this flow. In particular, the unsteady effects due to the exponential acceleration strongly inhibit vortex growth and mixing in the near field. As an acceleration parameter is increased, the penetration of the exponential transverse jet array increases by about 50%.

TECHNICAL DISCUSSION

For all unforced free shear flows, vorticity associated with each global vortex is inversely proportional to the vortex lagrangian age. Global vorticity is diluted as pure irrotational fluid from the freestream is entrained into the vortex. Vortices grow significantly in size as they move downstream and mixing occurs rapidly.

Contrary to this, it is proposed that, under forcing, global vorticity of a particular vortex can be made constant with time. If this can be accomplished, then the vortex does not entrain ambient fluid, and mixing is inhibited as long as forcing is present. A particularly simple way of obtaining

such a flow pattern is injecting one stream transversely into another one of uniform velocity, through an array of transverse nozzles with exponentially increasing size and injection speed.

Current experiments are designed to test the validity of this hypothesis using flow visualization techniques in a new water tunnel. Under the current grant, construction of the water tunnel has been completed. Test section dimensions are 70cm x 70cm x 300cm, and maximum flow speed in the test section is 70 cm/sec. Fluorescent dye is injected through the nozzle array and a sheet of laser light illuminate a cross sectional plane at a downstream station x .

Figure 1 is a collection of such images for various values of the freestream tunnel velocity U . We define an acceleration parameter α to be the ratio of the characteristic nozzle time d_j/U_j to the e-folding time of the acceleration x_e/U . $d_j(x)$ and $V_j(x)$ are the nozzle diameter and injection speed respectively. x_e is the downstream distance over which both d_j and V_j increase by a factor of e . So

$$\alpha \equiv \frac{d_j U}{x_e V_j}$$

Figure 1 reveals that as both U and α increase, the vortex pair formed from the transverse jet is reduced in size. In part, this reduction in size results from a variation in the momentum ratio, as indicated by the reduction in absolute jet penetration. However, the vortex size even normalized by the vortex spacings markedly drops. Therefore the vortices become much smaller and closer to the injection nozzle due to the acceleration. Changes in momentum ratio are not expected to change the normalized vortex size. Experiments are in progress at constant α to confirm this.

Mixing between the primary and the injected fluids occurs in the vortex pair. As the size of the vortices is reduced, the amount of mixed fluid residing in them must also be reduced. From figure 2, the vortex cross sectional area, which goes as the square of their diameter, d decreases by a factor of about four. Acceleration dramatically inhibits mixing in the vortex pair.

Another question is the effect of acceleration on jet penetration. Figure 3 is plot of the observed penetration as a function of α , where the penetration is normalized by the assumed influence of velocity ratio $r \equiv V_j/U$ inferred from the known far-field behavior of the classical, single transverse jet. Under this normalization, the observed penetration is seen to increase in

figure 3 by about 50% as α increases. This increase is not too surprising if the vortex pair entrains less irrotational fluid and thus exchanges less transverse momentum. Again, the presumed influence of momentum ratio is currently under study.

In summary, acceleration reduces vortex size and mixing. It appears that jet penetration is concurrently increased.

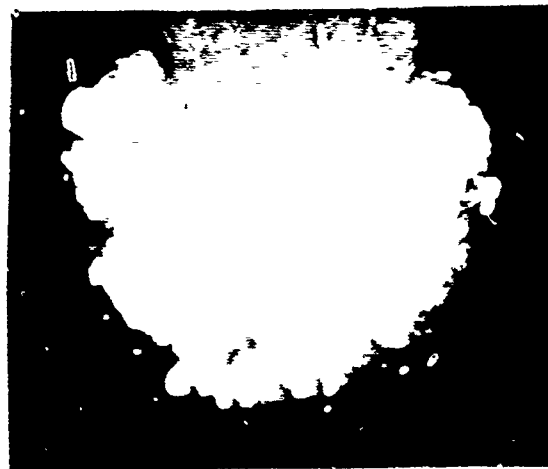
 $\alpha = 0.5$  $\alpha = 0.75$  $\alpha = 1.0$  $\alpha = 1.5$

Figure 1 Flow Visualization

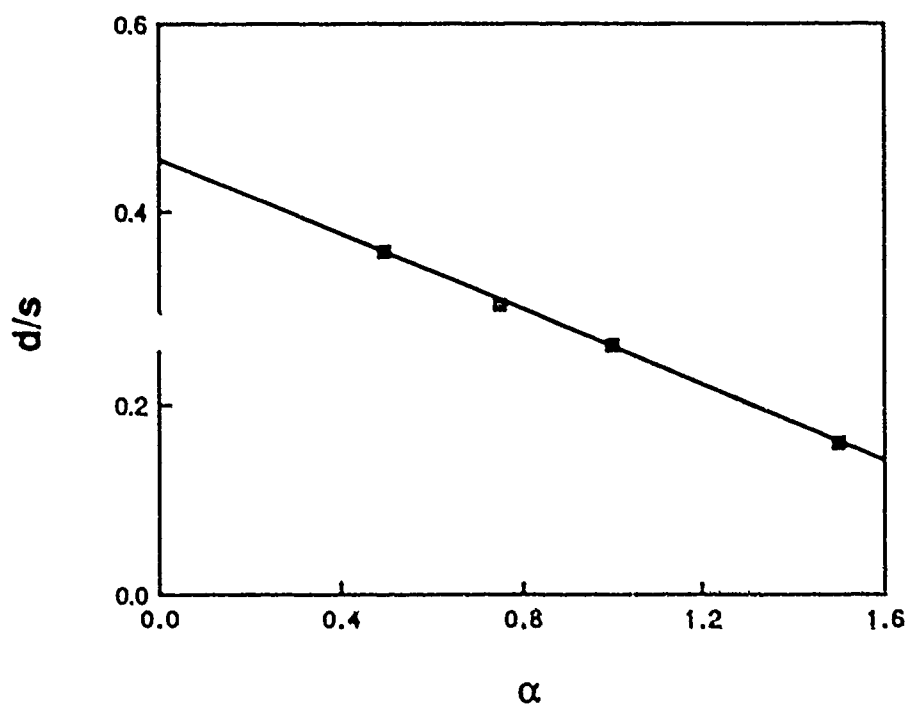


Figure 2 The effect of acceleration on vortex size

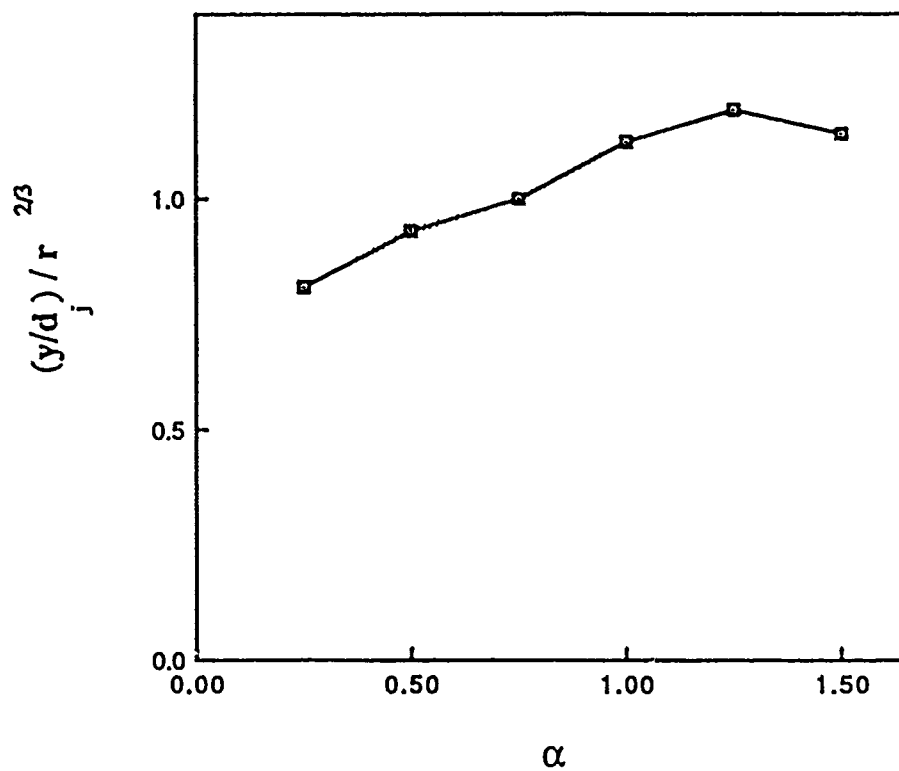


Figure 3 Penetration as a function of acceleration

CHEMICAL REACTIONS in TURBULENT MIXING FLOWS

AFOSR Grant 88-0155

P. E. Dimotakis, J. E. Broadwell and A. Leonard

*Graduate Aeronautical Laboratories
California Institute of Technology
Pasadena, California 91125*

Summary/Overview

The purpose of this research is to conduct fundamental investigations of turbulent mixing, chemical reaction and combustion processes in turbulent, subsonic and supersonic flows. Progress in this effort thus far has uncovered important deficiencies in conventional modeling of these phenomena, and offered alternative suggestions and formulations to address some of these deficiencies. This program is comprised of an experimental effort, an analytical modeling effort, a computational effort, and a diagnostics development and data-acquisition effort, the latter as dictated by specific needs of our experiments.

Our approach is to carry out a series of detailed theoretical and experimental studies primarily in two, well-defined, fundamentally important flow fields: free shear layers and axisymmetric jets. To elucidate molecular transport effects, experiments and theory concern themselves with both liquids and gases. The computational studies are, at present, focused at fundamental issues pertaining to the computational simulation of both compressible and incompressible flows.

Technical discussion

Our experimental investigations of the effects of free stream density ratio in gas phase, subsonic shear layers have been completed. A first set of findings, were reported at the National Fluid Dynamics Congress (NFDC), last July (Frieler & Dimotakis 1988). A Ph.D. thesis (Frieler 1989) documenting this effort is nearing completion at this writing.

As part of our efforts to extend these experimental studies to supersonic flow*, a review paper covering turbulent mixing and combustion in turbulent shear layers was presented at the most recent AIAA Aerospace Sciences Meeting (Reno, Nevada), and will also be presented (with some extensions) at the 9th ISABE (Athens, Greece) this coming September (Dimotakis 1989). In this review, a foreshadowing of some of the issues raised by the prospect of supersonic flow of the free streams relative to the flow structures in the turbulent mixing zone are discussed, along with implications in the context of entrainment, mixing and combustion in hypersonic propulsion.

* Co-sponsored by AFOSR (URI) Contract F49620-86-0113

At this writing, the assembly of the new supersonic combustion shear layer facility is nearing completion. Briefly, it is comprised of an atmospheric pressure test section, with a 15 cm span and a (nominally) 3.5 cm supersonic stream height. The design maximum high speed stream Mach number is $M_1 = 3.2$. At the first phase of its operation, we plan to run a subsonic low speed stream ($M_2 \leq 0.3$) in order to attain a maximum convective Mach number of $M_c \approx 2.2^{**}$. Design run time is 3 sec. The ability to accommodate the $H_2/NO/F_2$ chemical system in this facility will allow studies of supersonic chemically reacting flows in Damköhler number regimes ranging from kinetically slow to kinetically fast. In the latter case, we intend to exploit the fact that chemical product formation and measurements can serve as a quantitative measure of turbulent mixing on a molecular diffusion scale (Koochesfahani & Dimotakis 1986, Dimotakis 1989).

The first part of our compressible shear layer (linear) hydrodynamic stability calculations were completed and reported at last year's NFDC (Zhuang, Kubota & Dimotakis 1988). Our results, as well as those reported in other similar computations, suggest that the growth rate of (unbounded) shear layers, as spawned by two-dimensional disturbances, decreases to values that are much smaller than have been observed in the laboratory (Papamoschou & Roshko 1988). Other mechanisms, potentially responsible for the larger growth rates that are observed, are presently under theoretical investigation. Experiments are planned in the new supersonic shear layer facility that should elucidate this important issue.

In work recently completed in jet mixing flows[†], the experiments and behavior of the concentration field of the jet fluid in low to moderate Reynolds number ($5,000 < Re < 40,000$), gas phase flows has been documented (Dowling 1988; Dowling & Dimotakis 1988; Dowling, Lang & Dimotakis 1989), with several important new conclusions stemming from these results, briefly outlined below. All measures of the mixing process in the far field ($x/d > 20$) become self-similar when scaled by the outer flow variables. The mixing process is *not* found to be independent of the flow Reynolds number, at least in the range of Reynolds numbers investigated. The local mixing rate spans roughly *three decades*. Additionally, we also found evidence that the rate of *entrainment* of reservoir fluid is also Reynolds-number-dependent (at least for the gas phase flows and range of Reynolds numbers investigated).

Our experimental investigation of the stochastic geometric properties of the turbulent interface in low to moderate Reynolds number turbulent jets is continuing. The focus in these investigations is to characterize the dependence of the interfacial area, more specifically its surface-to-volume ratio, on the flow Reynolds number and Schmidt number, as well as other characteristics such as the spectrum of the jet fluid (conserved scalar) fluctuations at the smallest scales of the flow. We are finding no evidence in support of the notion that (constant power) fractal ideas are applicable to the description of these interfaces. These investigations, which are also designed to resolve the much smaller species diffusion scales in water, will provide an important link to the gas phase work of Dowling & Dimotakis, cited above, and the previously completed work in water[‡]. We expect this research to

^{**} Estimated assuming approximately equal pressure recovery from each stream, i.e. no shocks. See Dimotakis (1989, Sec. 2.2) for a more complete discussion.

[†] Co-sponsored by the Gas Research Institute, Contract #87-260-1467.

[‡] At lower time/space resolution, however. See Dahm, Dahm & Dimotakis 1987.

have further reaching implications, elucidating, in particular, many of the issues that must presently be accepted on faith in many of the modeling efforts currently underway.

We are proceeding with our experimental investigation of Reynolds number effects in the High Pressure Combustion Facility ($0.1 < p_0 < 10 \text{ Atm}$). A set of experiments is in progress which will initially utilize the $H_2/NO/F_2$ chemical system, permitting very low adiabatic flame temperature rise systems ($\Delta T_f < 40 \text{ K}$) to be realized. Buoyancy effects are minimized thereby, while retaining an overall reaction rate in the turbulent jet that is kinetically fast. Our first investigations are targeted at documenting the Reynolds number dependence, if any, of the flame length *over two decades in the jet Reynolds number*. This range of Reynolds numbers is sufficiently high to resolve such effects, if they exist, and has never been attained in any single combustion experiment in the past, to the best of our knowledge.

Work on the Two-Stage Lagrangian Model that has been under development for some time (Broadwell & Breidenthal 1982, Broadwell 1987 and Broadwell & Mungal 1988) is proceeding along two lines. First, under joint support from the Gas Research Institute and the Sandia Combustion Research Facility, the model for reactions in shear layers and jets is being cast in forms that allow treatment of chemical kinetics of arbitrary complexity. In its simplest form, the model consists of two inter-connected perfectly-stirred reactors. Such a model for a methane-air flame is presently operating. Methods for more realistic treatment of the flame-sheet component of the model are under study. Secondly, a possible connection between the concepts underlying the model and the idea of chaotic advection or Lagrangian turbulence are being explored. Recent work of Aref and co-workers (1989), Ottino (1988), and Rom-Hedar, Leonard, & Wiggins (1989), in particular, suggest such a connection, and in any case, point to a different way of discussing the model.

In the computational part of this program, our efforts to increase the efficiency of vortex element calculations have continued. Using hierarchical clustering techniques, targeted reductions from $O(N^2)$ to $O(N \log N)$ have in fact achieved $O(N)$ in the computational effort, where N is the number of vortex computational elements. High efficiency algorithms have been developed for — and tested on — concurrent computing machines at Caltech. In an effort to extend the numerical simulation of turbulent flows to the compressible flow regime, we have initiated an *ab initio* effort to describe the flow using lagrangian computational elements. Important new issues arising from a consistent description of the flow in the presence of shocks are under investigation, in a first pilot effort of unsteady, 1-D flow. It should be noted that the methodology under development and investigation is focusing on techniques that are extendable to unsteady flow in two and three dimensions.

References

- AREF, H. and JOUEN, S. W. [1989] "Enhanced separation of diffusing particles by chaotic advection", *Phys. Fluids A* 1 (3).
- BROADWELL, J. E. [1987] "A Model for Reactions in Turbulent Jets: Effects of Reynolds, Schmidt, and Damköhler Numbers", US-France Workshop on Turbulent Reactive Flows (Rouen, France), 7-10 July 1987. *Turbulent Reactive Flows*, (eds.) R. Borghi and S. N. B. Murthy *Lecture Notes in Engineering* 40 (Springer-Verlag, New York, 1989), 257-277.

BROADWELL, J. E. and BREIDENTHAL, R. E. [1982] "A Simple Model of Mixing and Chemical Reaction in a Turbulent Shear Layer", *J. Fluid Mech.* 125, 397-410.

BROADWELL, J. E. and MUNGAL, M. G. [1988] "Molecular Mixing and Chemical Reactions in Turbulent Shear Layers", 22nd *International Symposium of Combustion* (Seattle, Wash.), 14-18 August 1988 (to appear).

DAHM, W. J. A. [1985] *Experiments on Entrainment, Mixing and Chemical Reactions in Turbulent Jets at Large Schmidt Numbers*, Ph. D. thesis, California Institute of Technology.

DAHM, W. J. A. and DIMOTAKIS, P. E. [1987] "Measurements of Entrainment and Mixing in Turbulent Jets", *AIAA J.* 25(9), 1216-1223.

DIMOTAKIS, P. E. [1989] "Turbulent Free Shear Layer Mixing and Combustion", 9th *ISABE* (Athens, Greece), 3-9 September 1989.

DOWLING, D. R. [1983] *Mixing in gas phase turbulent jets*, Ph. D. thesis, California Institute of Technology.

DOWLING, D. R. and DIMOTAKIS, P. E. [1988] "On Mixing and Structure of the Concentration Field of Turbulent Jets", *Proceedings, First National Fluid Dynamics Congress*, 25-28 July 1988 (Cincinnati, Ohio), II, 982-988.

DOWLING, D. R., LANG, D. B. and DIMOTAKIS, P. E. [1988] "An Improved Laser-Rayleigh Scattering Photodetection System", submitted to *Exp. in Fluids*.

FRIELER, C. E. and DIMOTAKIS, P. E. [1988] "Mixing and Reaction at Low Heat Release in the Non-Homogeneous Shear Layer", *First National Fluid Dynamics Congress*, 24-28 July 1988 (Cincinnati, Ohio), AIAA Paper 88-3626.

FRIELER, C. E. [1989] *Mixing and Reaction in the Subsonic 2-D Turbulent Free Shear Layer*, Ph. D. thesis, California Institute of Technology.

KOOCHESFAHANI, M. M. and DIMOTAKIS, P. E. [1986] "Mixing and chemical reactions in a turbulent liquid mixing layer", *J. Fluid Mech.* 170, 83-112.

OTTINO, J. M. [1988] *The Kinematics of Mixing: Stretching, Chaos, and Transport* (Cambridge University Press).

PAPAMOSCHOU, D. and ROSHKO, A. [1988] "The Compressible Turbulent Shear Layer: An Experimental Study", *J. Fluid Mech.* 197, 453-477.

ROM-KEDAR, V., LEONARD, A. and WIGGINS, S. [1989] "An Analytical Study of Transport, Mixing, and Chaos in an Unsteady Vortical Flow", submitted to *J. Fluid Mech.*

ZHUANG, M., KUBOTA, T. and DIMOTAKIS, P. E. [1987] "On the Stability of Inviscid, Compressible Free Shear Layers", *Proceedings, First National Fluid Dynamics Congress*, 25-28 July 1988 (Cincinnati, Ohio), II, 768-773.

OPPOSED JET TURBULENT DIFFUSION FLAMES

(AFOSR) Grant 88-0011

Principal Investigator: Lawrence Talbot

Department of Mechanical Engineering
University of California, Berkeley, CA 94720

SUMMARY/OVERVIEW:

The laminar counter flow combustion configuration has been used extensively the past ten years [1-4] for studying fundamental combustion problems such as fuel dilution and strain rate dependence on flame extinction limit. However, very few studies have been done on the structure of turbulent opposed flow flames. The objective of this research program is to investigate experimentally the dynamics and structure of opposed jet turbulent diffusion flames, where a jet of fuel is directed counter to an oncoming airstream. This combustion configuration is of fundamental interest in exploring the effects of strain and heat release on the fluid mechanics of turbulent diffusion flames. Additionally, it exhibits some of the characteristics of boundary layer separation caused by transverse fuel injection in scramjet combustors.

TECHNICAL DISCUSSION:

The combustion configuration being investigated consists of a fuel jet exit pipe of $d=6.4\text{mm}$ in diameter directed downward toward an air jet 130mm in diameter. The velocity of the air jet is maintained at 5.5m/s . Turbulence ($u'/u = 8\%$) is generated in the air flow by a perforated plate. The vertical distance between the exit of the fuel jet and the air flow can be adjusted to vary the overall strain rate on the reaction zone structure. Hydrogen fuel with helium dilution of various levels are used to study the effect of the dilution on the extinction of the counterflow turbulent diffusion flame. To investigate the effect of combustion on the turbulent mixing, reacting and non reacting opposed jets are studied. The high speed tomography technique is based on laser sheet Mie scattering. A laser sheet of light of 60mm width and .5mm thickness is produced by a copper vapor laser which provides 5mj pulses of 10 ns width at adjustable repetition rates up to 6kHz. A high speed Fastax camera records the tomographic images. The laser is driven by the camera at 2kHz. Due to the large differences in flow rate of the fuel and air jets in order to match the Mie scattering intensity of the jet with that of air, it is necessary to seed the fuel jet with TiO_2 ; silicone oil aerosol is used for the air jet. The tomographic records are digitized and stored in a digital computer for further treatment.

RESULTS

The H_2/He diluted opposed flow has been studied with and without combustion. Both the fuel jet and air jet have been seeded separately and simultaneously. As an example, Figs. 1 and 2 show respectively the turbulent opposed jets without and with combustion. In these cases, only the fuel jet is seeded with TiO_2 particles. The fuel jet Reynolds number is 2000 in both cases. Significant differences in the scale of the wrinkles can be seen. The turbulent jet interface is clearly more convoluted in the non-reacting flow case than in the combustion case indicating significant effect of heat release on the mixing process. A fractal analysis of these edges has been done to quantify this comparison using a counter segment algorithm previously used by Gouldin [6]. A fractal curve is defined by three parameters: the inner cutoff E_i , the outer cutoff E_o and the fractal dimension D (which is found to be between 2 and 3 for a fractal surface and between 1 and 2 for a fractal curve). Physically these parameters represent respectively the smallest wrinkle scale of the curve, the largest wrinkle scale of the curve, and the scale hierarchy between the largest and the smallest. In the case of turbulent non-reacting flow for sufficiently high Reynolds number, the fractal dimension has been found to be constant and equal to 2.34 [7,8] for a surface. Typical fractal plots are presented in figs. 1 and 2 and represents a statistical analysis of the stagnation region for both reacting and non-reacting cases averaged over 30 samples. Value of $E_o=20\text{mm}$, $E_i=2\text{mm}$, $D=2.07$ are found for the reacting case, and $E_o=16\text{mm}$, $E_i=1.3\text{mm}$, $D=2.18$ for the nonreacting case. These results show clearly the large effect of the combustion on the mixing process. The wrinkles are increased at all scales by the heat release (both cutoffs E_o and E_i are larger in the combustion case). The combustion changes the scale distribution of the wrinkles and reduces significantly the fractal dimension of the jet interface. Fig. 3 shows two instantaneous images of the turbulent counter flow diffusion flame obtained at a time separation of 0.6ms. In this case both fuel and air are seeded. On these pictures the reaction zone (dark part of the images) is delineated by two jets seeded respectively with TiO_2 and silicone particles. From these images two distinct regions can be distinguished:

a) In the stagnation region the thickness of the reaction zone is between 2 and 4mm. From two consecutive pictures a wrinkle structure in a region of interest can be isolated and its successive lengths computed. The evolution of the length in time leads to the local stretch determination. In the stagnation region the stretch has been found to be 400s^{-1} for this particular example

b) The shear layer exhibits where large structures which are convected and sheared due to the mean flow velocities differences, and which produce a significant entrainment on the both sides of the flame. By isolating a vortex center the velocity and the velocity gradient between two structures can be evaluated.

As an example, for the images Fig. 3 the convection speed of typical vortex structures have been found to vary between 5m/s and 10m/s and the local strain of the turbulent flow field and the local stretch of a vortex along the reaction layer was found to be about 200s⁻¹.

CONCLUSION

Two dimensional time resolved Mie scattering imaging has been found to be very useful in providing a means to evaluate the dynamics of the flow field and of comparing it to the stretch of the reaction zone. Fractal analyses from the tomography records show clearly how significantly combustion changes the wrinkling process of the turbulent reaction zone. Further statistical treatments are still in progress (reaction zone thickness, overall strain rate of the flow field, local stretch of the reaction zone structure). In order to determine if local extinction can occur by changing the turbulence conditions (instantaneous local strain rate) or by changing the fuel composition (slowing down the chemistry) instantaneous line temperature measurements using Rayleigh scattering [9] are planned. All of these results should find application in the modeling of turbulent reacting flows.

REFERENCES

- (1) Tsuji, H. (1982), Counterflow Diffusion Flames, *Prog. Ener. Comb. Sci.*, Vol. 8, pp. 93-119.
- (2) Drake, M.C. and Blint, R.J. (1988), Structure of Laminar Opposed-Flow Diffusion Flames with CO/H₂/N₂ Fuel, *Combust. Sci and Tech.*, Vol. 61, pp. 187-224.
- (3) Kee, R.J., Miller, J.A., Evans, G.H., and Lewis, G.D. (1988), A Computational of the Structure and Extinction of Strained, Opposed Flow, Premixed Methane Air Flames, 22nd Symposium (Int) on Combustion.
- (4) Law, C.K., Zhu, D.L., and Yu, G. (1986), Propagation and Extinction of Stretched Premixed Flames, 21st Symposium (Int) on Combustion, The Combustion Institute, pp. 1419-1426.
- (5) Büger, I.W. (1976), Turbulent Jet Diffusion Flames, *Prog. Energy. Combust. Sci.*, Vol. 1, pp. 87-109.
- (6) Gouldin, F.C., Hilton, S.M., and Lamb, T. (1988), Experimental Evaluation of the Fractal Geometry of Flamelets, 22nd Symposium (Int) on Combustion.
- (7) Mandelbrot, B.B. (1975), On the Geometry of Turbulence, with Stress on Fractal Dimension of the Isosurfaces of Scalars, *J. Fluid Mech.*, Vol. 72, Part 2, pp. 401-416.
- (8) Sreenivasan, K.R., Meneveau, C. (1986), The Fractal Facets of Turbulence, *J. Fluid Mech.*, Vol. 173, pp. 357-266
- (9) Shepherd, I.G., Hubbard, G.L., and Talbot, L. (1986), The Dynamic Structure of Turbulent V-shaped Premixed Flames, 21st Symposium (Int) on Combustion, The Combustion Institute, pp. 1377-1383.

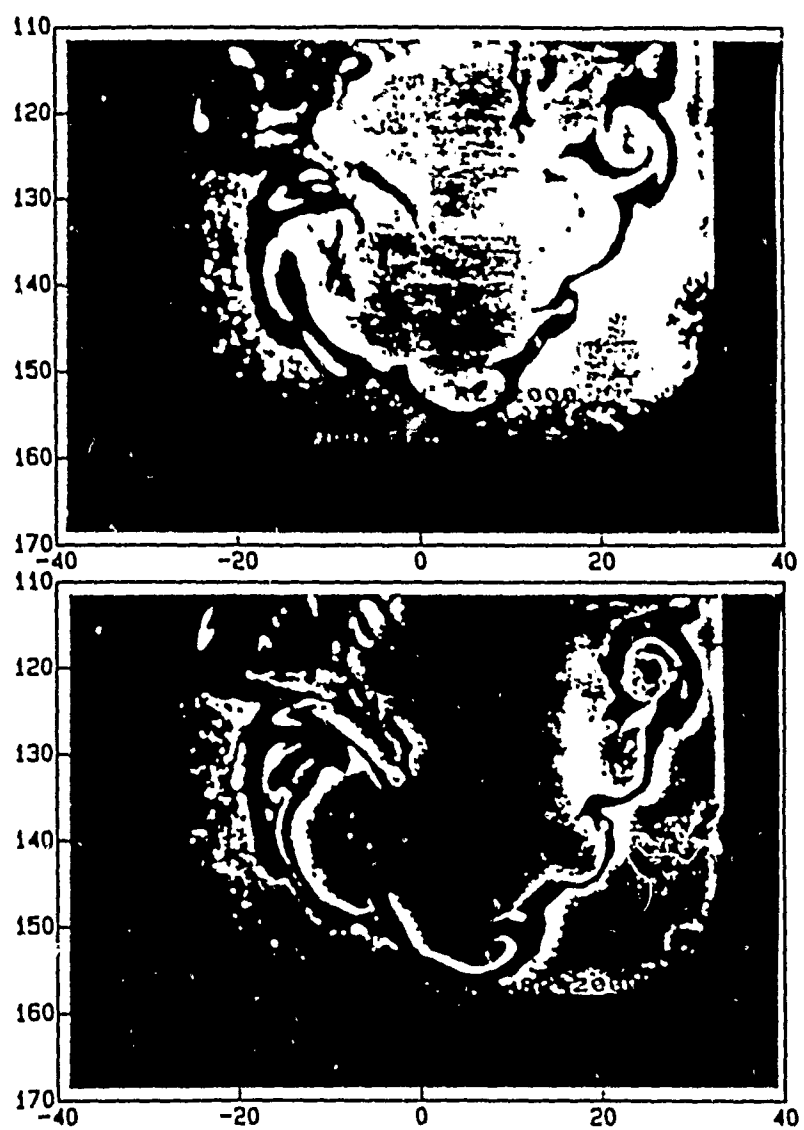


Fig.3. Successive flame
images 0.6ms apart

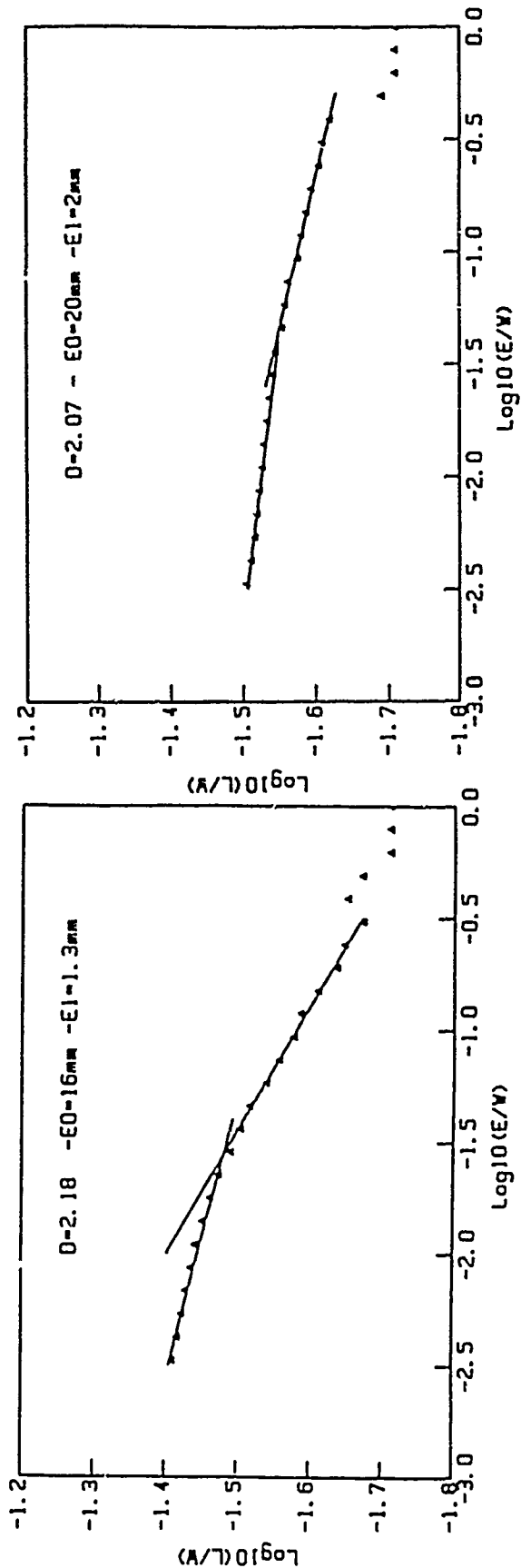
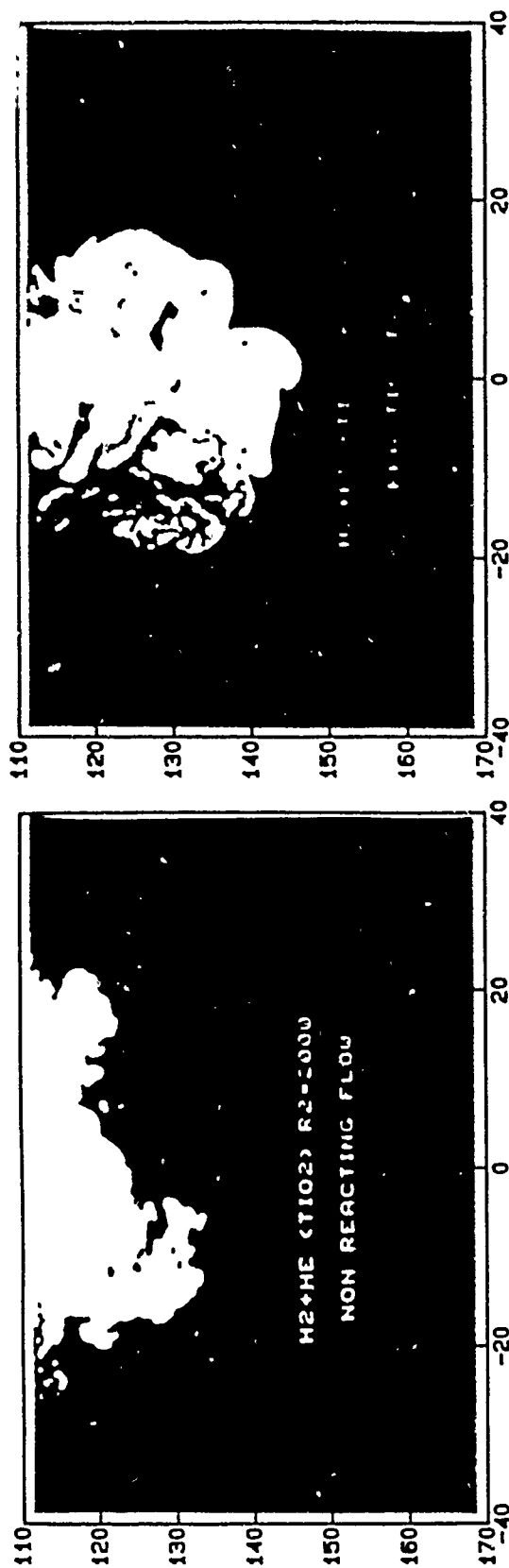


Fig. 1. Non-reacting flow

Fig. 2. Reacting flow

SCRAMJET COMBUSTION MIXING IMPROVEMENTS USING PULSED TRANSVERSE FUEL JETS

ONR Grant/Navy N00014-89-J-1696VAKILI

Principal Investigators: Ahmad D. Vakili, James M. Wu

The University of Tennessee Space Institute
Tullahoma, Tennessee 37388

SUMMARY/OVERVIEW:

Combustion process in scramjets, and to some extent in ramjets, is limited by mixing. Various concepts of mixing which are developed for ramjets are not as efficient for scramjet combustors. The development and growth of shear layer, which is responsible for mixing of fuel and air, is relatively slow in supersonic flows and cannot be effectively utilized as in ramjets. An alternate technique has been conceptually developed. Our new approach utilizes transverse injection of fuel into the mainstream in a pulsed manner to optimize the mixing between the two streams. The pulsation of fuel jets injection in a controlled manner is not only a means to improve the fuel and air mixing process but it is also a way towards controlling dump type combustors instabilities. Application of this type of transverse pulsed injection has been tested and found to eliminate the instabilities similar to the ones in ramjet dump combustors.

I. TECHNICAL DISCUSSION

In a scramjet powered flight vehicle, supersonic air is captured through an inlet geometry which decelerates the airstream to lower supersonic velocities and higher static temperatures and pressure before introducing it to the combustor section. Fuel, usually hydrogen or hydrocarbons, is injected into the air at sonic or supersonic speeds either axially or transversely. Air and fuel will mix and depending on the local static temperature, the chemical reaction and heat release may take place spontaneously. Combustor static temperatures in scramjets are usually high enough so the chemical reaction rates between hydrogen and oxygen are quite fast. Therefore, it is generally believed that the process of chemical reaction, and heat release, is mixing limited while the combustion processes are believed controlled by turbulent transport mechanisms. Obviously, the injector geometry and orientation have pronounced effects on mixing behavior in supersonic combustor design.

It would be highly desirable to provide enhanced fuel air mixing through more efficient means.

One such technique is transverse fuel injection with pulsation. Preliminary studies by our team have shown that as a result of pulsation superimposed on a jet in crossflow, the jet penetration into the cross stream increases significantly in addition to the increase in turbulence level downstream of the jet region [Ref. 1].

This study is comprised of two parts. First, through an experimental approach we would like to demonstrate the feasibility of pulsed transverse fuel injection into a fluid stream in order to improve the mixing between the fuel and air. Second, in an analytical way we would like to incorporate the pulsation flow parameters such that the physics of flow is reflected in estimating the mixing and penetration.

II. PULSATING JET IN UNIFORM LOW SPEED CROSSFLOW

Jets in uniform crossflow have been studied extensively due to their many practical aerodynamics applications [Ref. 2-4]. Introducing unsteadiness in the jet of such flows generally results in a totally different type of flow pattern and features which could be of tremendous value in improving mixing, increasing diffusion and entrainment.

Pulsating jet in crossflow represents time dependent three dimensional flow containing many vortices. Details of this study can be found in Reference 1. Jet plume centerline trajectory for various frequencies is shown in Figure I.1. As it is evidenced, there is a critical frequency for which the penetration of the jet into the crossflow is maximized. Figures I.2. and I.3. show the turbulence properties and the velocity profiles at several heights above the jet exit plane.

Pulsation in the jet was enabled by a solenoid valve in the jet supply line. A frequency generator was used to control the various frequencies at which this valve was operated. In addition to complex fluid mechanic interactions created by the pulsating jet, the penetration into the crossflow increased due to the jet pulsations. It has become clear that tremendous increase in the depth of penetration at frequency under $2Hz$. The mechanism for this flow pattern can be explained through the individual vortex rings flow pattern. The pulsating jet at low frequency generates a series of vortex rings with some spatial distance between them. This distance delays adjacent vortices from interacting with each other and hence keeps the self-pumping ability. With enough clearance between them this self-pumping characteristics resulted in the deep penetration of jet flow. The depth of penetration remains the same at pulsating frequency higher than $8Hz$.

The distance between the neighboring vortices depends on the freestream velocity or the convective velocity of each vortex ring and the frequency of the pulsating jet. For low speed flows, where this study was performed, the pulsating frequency of two Hz appears to provide the optimum desired penetration of vortices. At high freestream speeds higher frequencies are expected to be resulting in optimum penetration and mixing.

III. MEASUREMENT TECHNIQUES

Phase conditioned measurements shall be made at several points in the test section. For cold flow, these measurements will be made using dynamic pressure transducer and hot wires. Correlations between various points will indicate any coupling which may exist between the flow parameters at several points.

A fundamental requirement of this research is determination of the degree of fuel-air mixing and the extent of resulting, finite-rate reactions in supersonic flowfield. To accomplish this, laser-scattering diagnostics will be used to provide both semi-quantitative, flow visualization and, for selected, molecular species, detailed measurements of the species densities, temperatures and partial pressures. The general criteria that guide the selection of specific laser-scattering methods include [1] molecular specificity, [2] spatial and temporal resolutions that are consistent with the flowfield's spatial gradients and temporal fluctuations, respectively, and [3] the comparative robustness and ease of application to a gas-dynamics facility.

The laser-scattering measurements will be performed by the UTSI Center for Laser Applications (CLA) faculty and staff who have extensive experience in the applications

of laser-scattering diagnostics to time-dependent, reacting, flowfield studies. Their studies and the diagnostics summary of Ref. 5 demonstrate the wide range of techniques that are available for use; e.g., linear and nonlinear fluorescence, spontaneous Raman scattering (spRS), coherent anti-Stokes Raman scattering (CARS), and various pump-probe techniques.

IV. REFERENCES

1. Wu, J. M., Vakili, A. D., Yu, F. M., "Investigation of Non-symmetric Jets in Cross Flow (Discrete Wing Tip Jet Effects)," Final Report AFOSR, December 1986.
2. Wu, J. M., Vakili, A. D. and Yu, F. M., "Investigation of the Interacting Flow of Non-Symmetric Jets in Crossflow." J. of AIAA, V. 26, No. 8, pp. 940-947, 1988.
3. Abramovich, G. N., "The Theory of Turbulent Jets," MIT press, 1963.
4. McManhon, H. M., Hester, D. D. and Palfery, J. G., "Vortex Shedding From a Turbulent Jet in a Cross-Wind." Journal of Fluid Mechanics, vol. 18, Part 1, pp. 73-80, 1971.
5. Lewis, J. W. L., "Emitted Radiation from Special Engines (ERASE), Part III, Determination of Temperature and Species Number Density in the Exhaust Plume Utilizing Laser-Raman/Rayleigh Scattering," AEDC-TR-76-121, Nov. 1977.
6. Penner, S. S., Wang, C. P. and Bahadori, M. Y., "Laser Diagnostics Applied to Combustion Systems," Twentieth Symposium (International) on Combustion/ The Combustion Institute, Pittsburgh, PA, pp. 1149-1176, 1981.

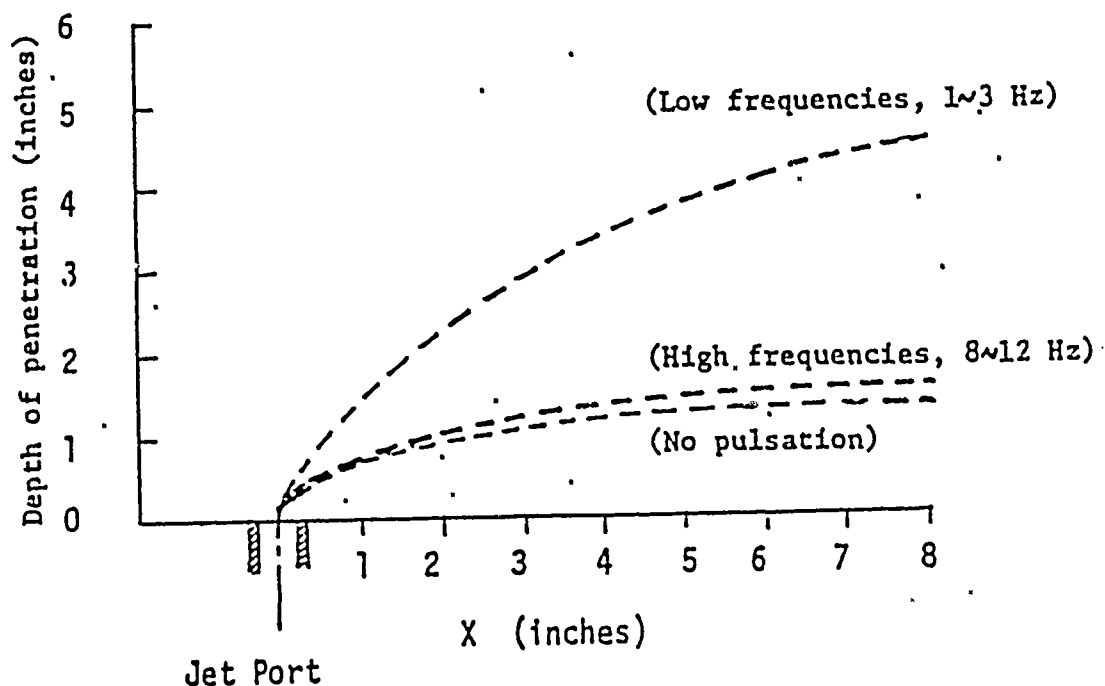


Figure 1.1 Jet plume centerline trajectory with pulsating jet stream;

$$\text{model 3, } V_j/V_\infty = 4.7, \beta = 45^\circ, Re_d = 470.$$

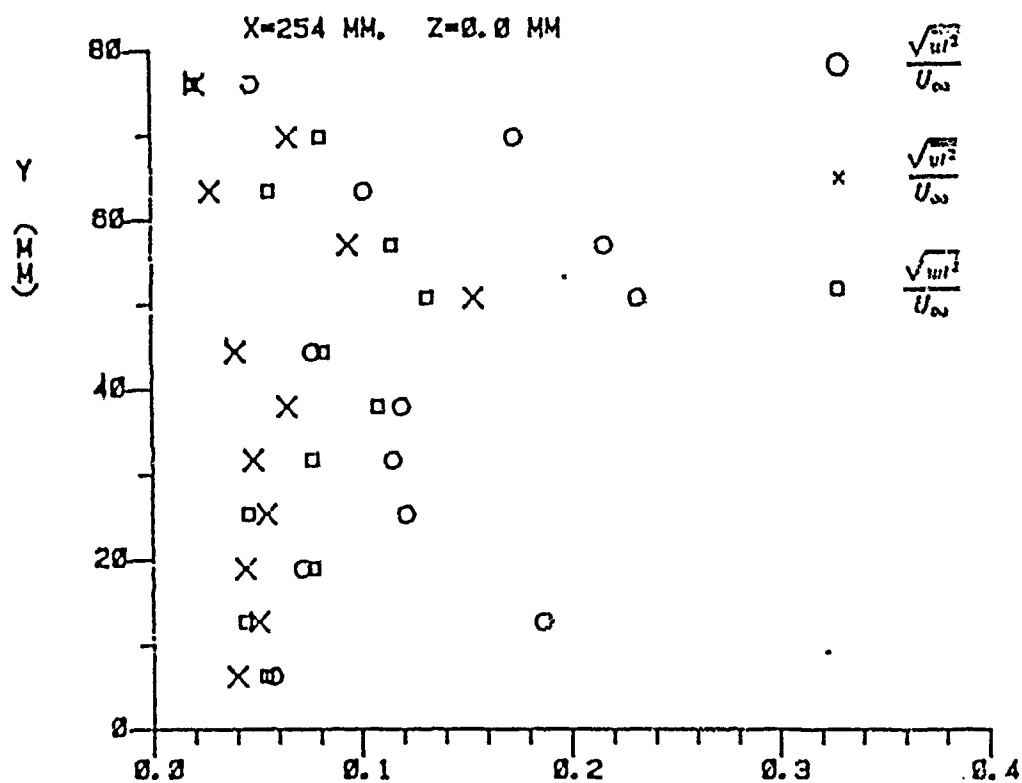


Figure I.2. Percent root mean square of normalized velocity fluctuation, two jet diameters downstream.

- * Z=12.7 MM
- Z=38.1 MM
- X Z=63.5 MM
- Z=88.9 MM

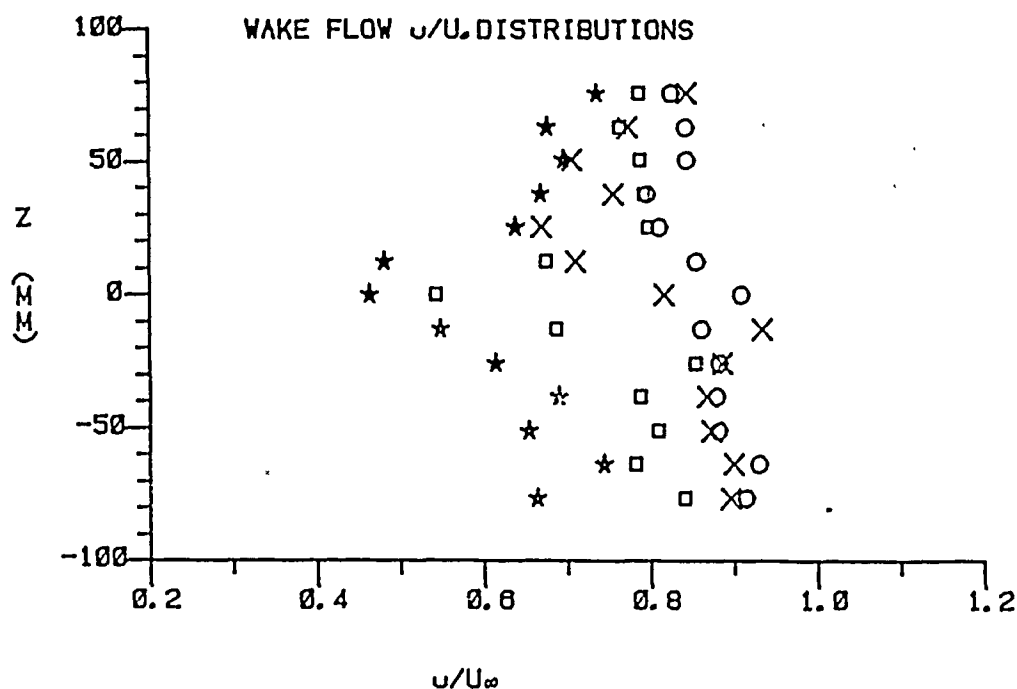


Figure I.3. The velocity distribution of u/U_∞ at various distance above the surface.

EXPERIMENTAL AND COMPUTATIONAL STUDIES OF
SWIRLING FLOWS IN DUMP COMBUSTORS

AFOSR Grant Contract No. 2308S1

Principal Investigators: A.S. Nejad, S.A. Ahmed, R.S. Boray.

Advanced Propulsion Division
Experimental Research Branch
Wright-Patterson AFB, Ohio 45433-6523

SUMMARY/OVERVIEW:

An experimental and computational investigation of confined separating flows in subsonic regime is in progress. The ultimate goal of the present effort is to gain a better fundamental understanding of the mixing process, chemical reaction, and heat release in sudden expansion flows. The current effort is comprised of three distinct but interrelated sub-tasks: 1) The experimental study of mixing and combustion in axisymmetric sudden expansion flows; 2) development of higher order computational techniques such as large eddy simulation and direct numerical simulation; 3) Development of laser based (non-intrusive) diagnostic techniques for time resolved field measurements of vector and scalar quantities (i.e., velocity, temperature, species concentration, and pressure) in highly turbulent reacting environments.

TECHNICAL DISCUSSION:

The development of mathematical models capable of predicting the turbulent behavior of reacting and non-reacting flows in complex geometries has been and continues to be the focus of many studies. The advent of large and fast super computers together with the availability of powerful post processing (graphics) routines have also popularized the numerical simulation of turbulent flows amongst the scientists. The majority of the research to date has the common goal of increasing the understanding of the behavior of turbulent flows in complex geometries and improving the accuracy of the computational methodology. Current lower order predictive codes, ones requiring turbulence models, require various assumptions in the solution of the Navier-Stokes equations. These simulations are therefore accompanied by in-depth experimental studies and require a fair amount of fine tuning for accurate duplication of the experimental observations. Higher order simulations such as direct numerical simulation (DNS) or large eddy simulation (LES) address the complex flows with more rigor. However, their use as an engineering design tool is yet to be determined. Primarily, the present study is directed towards exploring the fundamental characteristics

of sudden expansion flows. The goal is to establish a benchmark data base to assist turbulence model development and assessment. To this objective, both experimental and numerical efforts have been implemented.

During the past year work has progressed on several fronts. A series of experiments was conducted in isothermal sudden expansion flows. Different swirlers were designed and fabricated to study the effects of swirl strength (tangential to axial momentum ratio) and swirl blade geometry on the ensuing combustor flowfield. These cold flow experiments shall serve as base line reference to help understand the role of reaction and heat release on turbulent transport mechanisms. A major facility to conduct experiments with heat release has been designed and is being fabricated. The design has incorporated innovative approaches for providing optical access without disturbing the integrity of the axisymmetric flowfield. Work has also progressed towards implementation of planar laser induced fluorescence technique for vector and scalar measurements in high-speed reacting flows.

All cold flow measurements were conducted in a clear plastic flow model of a coaxial ramjet dump combustor, Figure 1. The combustor consisted of two major sections: the inlet assembly and the combustor chamber and exhaust nozzle. This modular design allowed optical access for 2-D LDV measurements while preserving the integrity of the combustor flowfield. The inlet assembly consisted of a settling chamber, inlet pipe, the associated temperature and pressure instrumentation, and the teflon swirler housing. The combustor section consisted of a plexiglas pipe which terminated in a large plexiglas rectangular chamber to aid in flow visualization studies. The unique feature of the design was the ability of positioning the dump plane relative to the combustor measurement station. Also, a 38X38mm flat quartz window was installed in the inlet pipe for measurements upstream of the swirler. Inlet flow disturbances were eliminated, when measurements in the combustor section were performed, by replacing the quartz window with a plug having the same radius of curvature as the inlet pipe. In order to study the effects of swirl number on the combustor flowfield, three constant angle swirlers ($S = 0.3, 0.4, 0.5$) were used. Also, swirlers with various blade geometry were employed which provided forced vortex, free vortex, and constant angle ($S = 0.4$) inlet flow conditions to examine the effects of different inlet swirl profiles on the ensuing combustor flowfield. Some of the results were reported earlier in references 1-3 and comparisons of normalized flow variables are shown in Figures 2-4. In summary, it was shown that swirl significantly affects the combustor flowfield. The free vortex type swirler generated a very strong central toroidal recirculation zone, which helped in improving the performance of the dump combustor. Time averaged calculations, using K-E turbulence model, were performed and the results were not promising. Work in higher

order simulation of turbulent flows has been initiated to examine the technique from two view points. First, its role in providing data for improving lower level turbulence models will be examined. Second, emphasis will be placed upon developing efficient numerical schemes to allow engineering calculations of flows of interest.

REFERENCES:

1. Nejad, A.S., Vanka, S.P., Favaloro, S.C., Samimy, M., and Langenfeld, C., "Application of Laser Velocimetry for Characterization of Confined Swirling Flow", Journal of Engineering for Gas Turbines and Power, Vol. 111, 1989, pp. 36-45.
2. Favaloro, S.C., Nejad, A.S., Ahmed, S.A., Miller, T., and Vanka, S.P., "An Experimental and Computational Investigation of Isothermal Swirling Flow in an Axisymmetric Dump Combustor", AIAA Paper No. 89-0620, 1989.
3. Ahmed, S.A., Boray, R.S., Nejad, A.S., "An Experimental Investigation of Isothermal Swirling Flow in a Model of a Dump Combustor", 9th International Symposium on Air Breathing Engines, Athens, Greece, 4-9 September 1989.

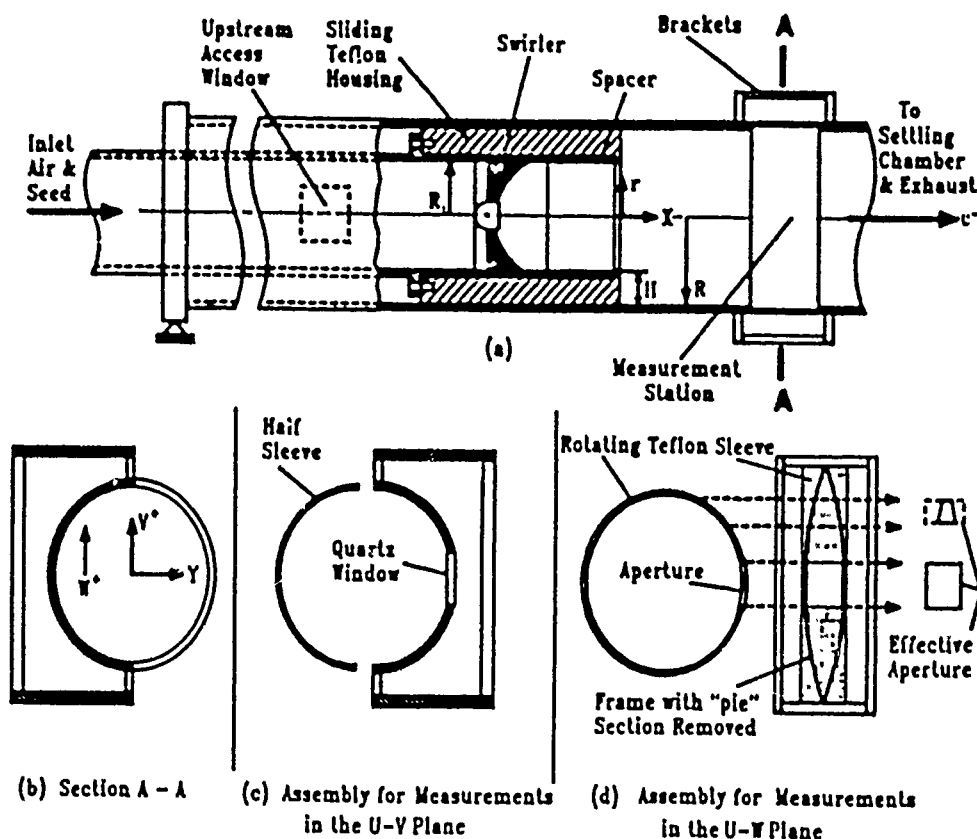


Fig. 1 Schematic of the Dump Combustor Model

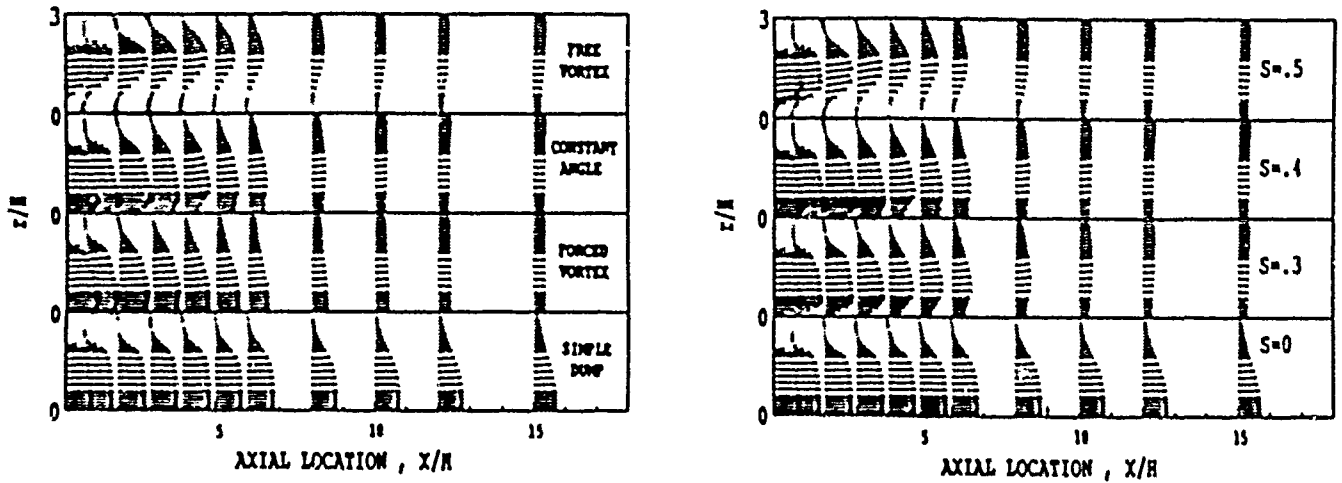


Fig. 2 Comparisons of normalized velocity vectors

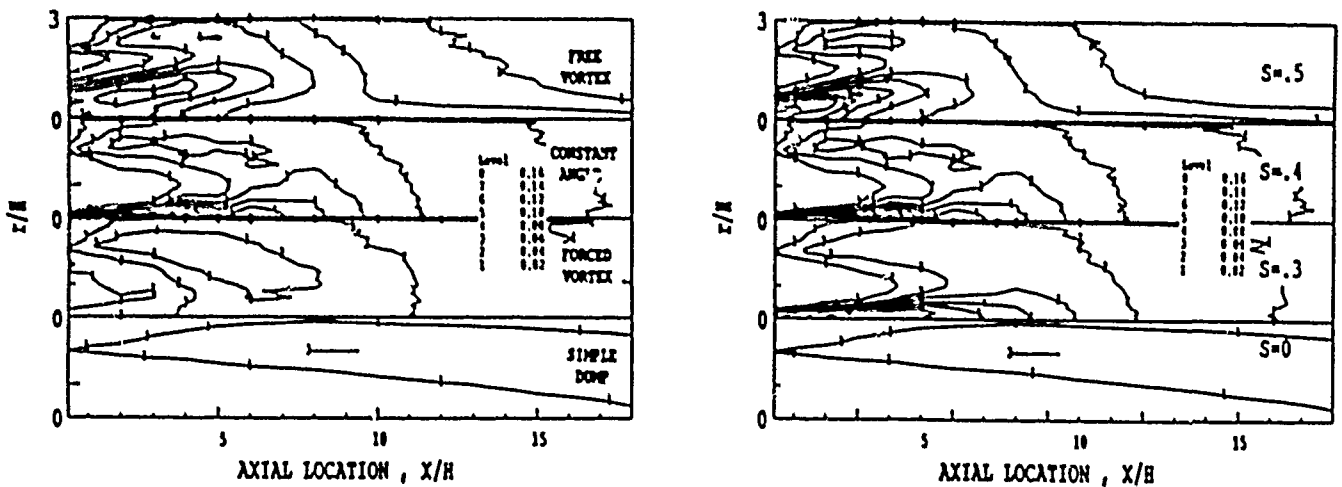
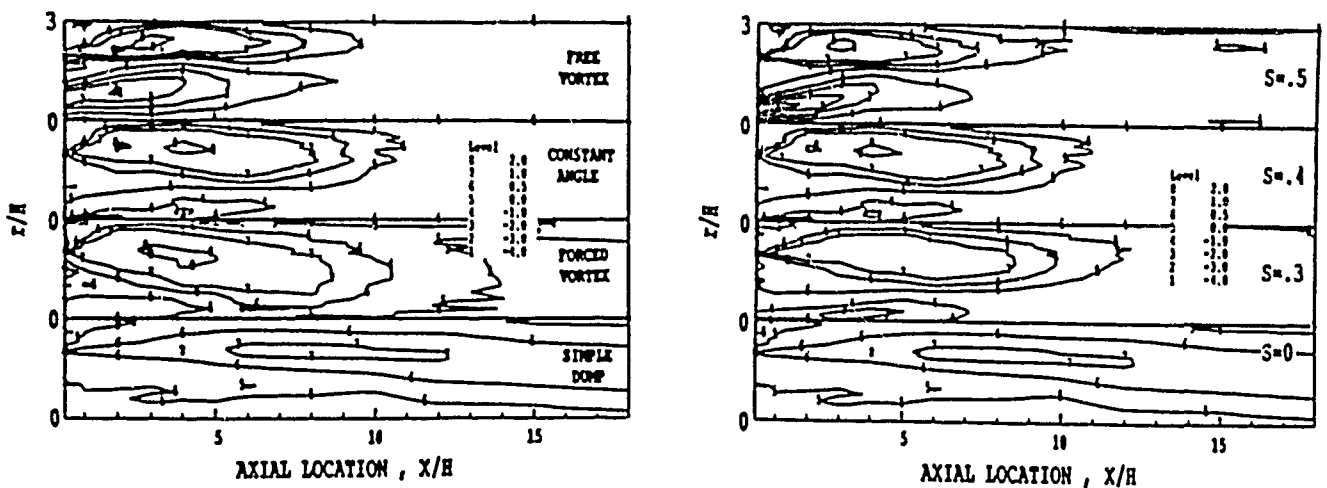


Fig. 3 Comparisons of normalized "K" contours

Fig. 4 Comparisons of normalized shear stress " $100\bar{u}\bar{v}/U_{ref}^2$ "

THE EFFECTS OF COMPRESSIBILITY ON A SUPERSONIC MIXING LAYER

AFOSR Contract No. F49620-88-C-0003

Principal Investigator: David Nixon

Nielsen Engineering & Research, Inc.
510 Clyde Avenue
Mountain View, CA 94043-2287

SUMMARY/OVERVIEW

The objective of this work is to identify the flow mechanisms that cause the decrease in the spreading rate of supersonic mixing layers and to suggest means of enhancing the mixing. Supersonic mixing layers are being studied using a numerical simulation. An analysis of the energy balance was used to derive a relation between the mixing of a shear layer and the rotational kinetic energy produced by the shear. This analysis represents many of the features of the compressible mixing layers and is used to develop a suitable computational model of the mixing. It is expected that these studies will provide important insight to the effects of compressibility on the interaction between turbulent eddies and shear layers.

TECHNICAL DISCUSSION

The objective of this work is to identify the flow mechanisms that cause the decrease in the spreading rate of supersonic mixing layers and to suggest means of enhancing the mixing. One of the possible scenarios of turbulent flow in supersonic mixing layers includes the presence of shock waves (or shocklets) which could be produced either by the fluctuating turbulent eddies or by large vortical structures, if the local flow relative to some reference frame becomes supersonic. In the case of the turbulent eddies, the induced velocities are not steady, and the shock developed will be very transient; the nature of such a transient shock/turbulent eddy interaction is not known at present.

The spreading rate of a turbulent shear layer with at least one stream supersonic has been observed to be about one quarter that of an incompressible layer at the same velocity and density ratio. Turbulent flows have been envisioned as circumscribed by a surface of relatively simple topology, which marks the instantaneous boundary between the turbulent and nonturbulent flow. Entrainment is described as the flux of nonturbulent fluid across the interface. The entrainment process can be viewed as possessing three main phases. Briefly, these phases involve induction, wherein irrotational fluid in the vicinity of the vorticity-bearing fluid is set in motion through the induced velocity field; straining, wherein a fluid element is strained until its spatial scale is small enough to make it susceptible to viscous diffusive processes; and diffusion, where other possible diffusive processes may occur. The clear demarcation between turbulent and non-turbulent fluid can be observed by various means.

A theoretical analysis of the mixing process was performed to study the effect of the convective speed of large turbulence structures on the mixing and to develop insight for the interpretation of the numerical calculations. It is assumed that a large turbulent eddy can be represented by a vortex. The vortex is caused by the shear stresses between two layers of a viscous fluid moving at different speeds. The convective Mach number, M_c of the eddy is taken to be a weighted average of the two free stream Mach numbers.

The mixing, m , is defined as the net mass flux across the boundary between the two fluid streams and is given by

$$m = \int_{-x_1}^{x_0} \rho |v| dx + \int_{x_0}^{x_2} \rho |v| dx \quad (1)$$

where ρ is the density, v is the velocity normal to the mixing boundary, x_0 denote the edges of the vortex core produced by the shear, and x_1 and x_2 are the limits of the region, sketched in Figure 1. A non-dimensional value of m , \bar{m} is obtained by dividing m by $\rho_0 u_0 s$ where ρ_0 and u_0 are representative densities and velocities respectively and s is the area through which fluid is transferred. The final result from the analysis can be expressed as

$$\bar{m}/\bar{m}_i = (\bar{m}_o/\bar{m}_{oi})^2 \left[(RKE)_{oi} / (RKE)_o \right] \quad (2)$$

where RKE is the rotational kinetic energy of the vortex, the subscript i denotes an incompressible value, the subscript o denotes a value for RKE of $(RKE)_o$.

A test of this theory was conducted in which the governing equation for the flow was taken to be the Transonic Small Disturbance equation, (see Ref. 1).

$$\frac{M_c^2}{C^2} \phi_{tt} + 2 \frac{M_c^2}{C} \phi_{xt} = (\beta^2 - k\phi_x) \phi_{xx} + \phi_{yy} \quad (3)$$

where M_c is the convective Mach number of the structure and

$$\beta^2 = (1 - M_c^2)$$

$$k = (\gamma + 1) M_c^{3/2}$$

$$C = 2X_o$$

Solutions of this equation were used to calculate the mixing, \bar{m}_o with its associated RKE, $(RKE)_o$.

Results for \bar{m}/\bar{m}_1 ; given by Equation (2) are presented in Figure 2 compared with the spreading rate of a turbulent mixing layer from Reference 2. These plots show a clear resemblance between \bar{m}/\bar{m}_1 as a function of M_c . The behavior of the mixing with M_c is due to density effects which cause the β^2 and nonlinear terms in Equation (3). Shock waves start to appear at about $M_c = 0.7$ but do not build up until much higher values of M_c . For low Mach numbers, it can be shown that the variation of \bar{m}/\bar{m}_1 is approximated by

$$\bar{m}/\bar{m}_1 = \beta^3 / (1 - M_c^2/2) \quad (4)$$

where

$$\beta^2 = 1 - M_c^2 \quad (5)$$

The curve for Equation (4) is shown for comparison in the plot of the spreading rate, Figure (3). The implication of these results is that a considerable amount of the incoming energy that would normally be converted to rotational energy is being expended in compressing the gas, thus reducing the circulation of the vortex.

REFERENCE

1. Nixon, D. (editor): Transonic Aerodynamics, Prog. in Astro and Aero., vol. 81, 1982.
2. Papamoschou, D. and Roshko, A.: Observation of Supersonic Free Shear Layers, AIAA 86-0162, January 1986, Reno, Nevada.

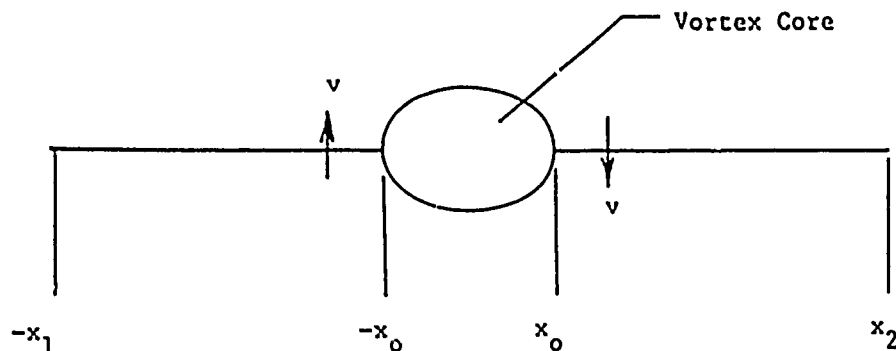


Figure 1.- Sketch of mixing due to a large structure.

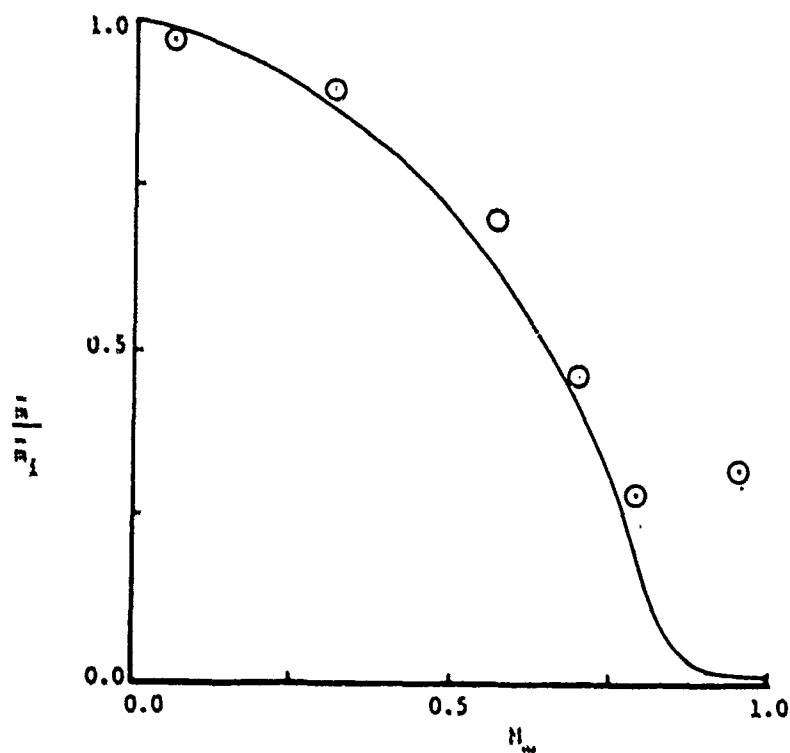


Figure 2.- Variation of the mixing parameter with Mach number. — Equation (2)
 ○ Experimental spreading rate from visual observations (Ref. 2)

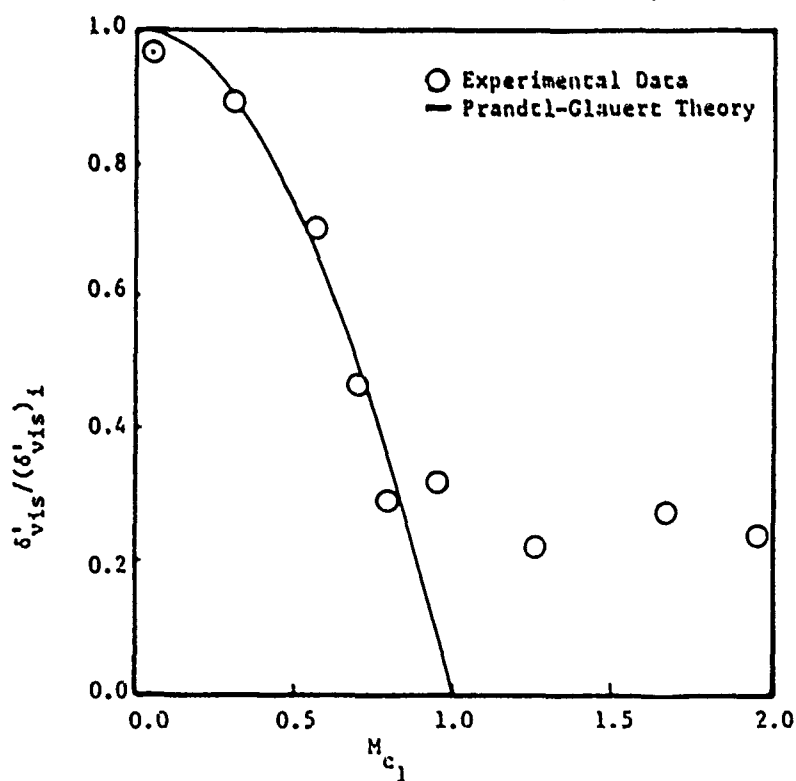


Figure 3.- Experimental spreading rate from visual observations (Ref. 2) compared with Prandtl-Glauert theory.

INSTABILITY & TRANSITION IN SUPERSONIC SHEAR LAYERS

ONR Contract No. N00014-89-J-1460

James J. Riley & D. Scott Eberhardt

University of Washington
Seattle, WA 98195

SUMMARY/OVERVIEW

The accurate prediction of supersonic combustion is an especially difficult problem, partly due to the lack of information and understanding regarding supersonic turbulent flows. And since turbulence is related to the stability properties of a flow, especially for turbulent free shear layers, we have addressed the problem of stability and transition in subsonic and supersonic shear layers. Our approach utilizes both analytical methods and direct numerical simulations. Furthermore, since supersonic shear layers are known to be very stable to two-dimensional disturbances, we have explored new scenarios for transition, including instabilities which are reinforced by confining boundaries, and instabilities which are primarily three-dimensional.

TECHNICAL DISCUSSION

We have addressed stability and transition in subsonic and supersonic free shear flows using both mathematical stability analysis and direct numerical simulations. The physical problem considered is a two-dimensional shear layer in a confined channel (see Figure 1). In order to estimate mixing we also consider a binary, single-step, diffusion-limited chemical reaction, where one reactant is initially in the top layer and the other reactant is in the bottom layer. The mathematical problem involves the Euler equations for an ideal gas, with free-slip conditions at the upper and lower boundaries. Both temporally-growing and spatially-growing instabilities have been considered. To solve for the chemical reactant and product concentrations we employ a conserved scalar.

The stability analysis has mainly involved the solution of linear eigenvalue problems to examine the stability characteristics of confined shear layers to both two- and three-dimensional disturbances. A Runge-Kutta method is used to solve the resulting ordinary differential equation, and a Newton-Raphson iteration is applied to handle the resulting nonlinear eigenvalue problem. The direct numerical simulations mainly employ an explicit, second-order Total Variation Diminishing algorithm based on the work of Yee, Warming, and Harten (1984), although spectral methods with flux correction, higher order flux-corrected methods, and compact (Padé) schemes are also being used. Unsteady two- and three-dimensional flows are simulated, and the excitation is provided by the results from the stability theory.

Three different but related problems have been addressed. The first aspect of our study addressed subsonic and supersonic free shear layers where boundary effects were not important (Soetrisno et al., 1988). Mainly two-dimensional direct numerical simulations were employed. We observed the decrease in the growth rate of the layer as the convective Mach number was increased, as predicted by previous theories, and the development of eddy shocklet for convective Mach numbers near 1. For convective Mach numbers significantly larger than 1, the layer remained relatively stable to all two-dimensional perturbations.

We next examined the effects of confining the shear layer (Greenough et al., 1989). It has been previously observed (Mack, 1984, 1989; Tam and Hu, 1988) that the effect of wall confinement can be to cause constructive Mach wave interference which results in the instability of the shear layer. As an example of this, Figure 2 gives a plot of the maximum growth rate versus Mach number for both an unbounded and a bounded vortex sheet. The unbounded vortex sheet is known to be stable to all disturbances for a convective Mach number greater than $\sqrt{2}$ (Miles, 1958), whereas, when boundaries are introduced, we find instabilities at all Mach numbers computed (Figure 2b). Direct numerical simulations have been performed to examine the nonlinear development of these "wall" modes. We find that they are highly unstable, having growth rates comparable to Kelvin-Helmholtz instabilities for low Mach number flows. The character of their development, however, is very different from the rollup produced by the Kelvin-Helmholtz instability. Instead of rollup, a sawtooth pattern develops (see Figure 3), which ultimately tends to fill the channel. Without rollup, however, this instability is apparently not as efficient at mixing.

The third aspect of our study has dealt with three-dimensional instabilities. It is well-known (Fejer and Miles, 1963) that, although vortex sheets are stable to any two-dimensional disturbance for convective Mach number above $\sqrt{2}$, they still remain unstable to three-dimensional disturbances which are at a large enough angle to the flow direction. (These disturbances see only the flow in their direction, which is subsonic.) Therefore transition due directly to three-dimensional perturbations may be important. Figure 4 gives a plot of constant contours of maximum growth rate versus streamwise and lateral wave number for a shear layer with a convective Mach number of 1.45. To the lower right the fairly smooth peak is due to oblique modes, which we find to behave as oblique Kelvin-Helmholtz modes. To the upper left are wall modes, whose behavior gives a much more complex stability diagram. We have completed a series of direct numerical simulations using both two- and three-dimensional excitation of shear layers for a range of Mach numbers, studying the behavior of isolated three-dimensional disturbances as well as their interaction with two-dimensional disturbances. At lower convective Mach numbers (< 0.75), we find results qualitative similar to previously published results for incompressible flows (e. g., Metcalfe et al., 1987; Riley et al., 1989). For higher Mach number flows, however, the results are significantly different. For example, now the three-dimensional perturbations are more unstable than the two-dimensional ones, so that the flowfield becomes three-dimensional much faster and large-scale two-dimensional structures cannot remain as coherent as they do for lower speed flows. Also two-dimensional wall modes can have significantly different phase velocities from those of oblique Kelvin-Helmholtz modes, which greatly affects their interaction. Finally, the role of the two-dimensional mode is no longer strictly catalytic, as in the subsonic case, but it strongly participates in the energetics of the interactions.

REFERENCES

- Fejer, J. A., and J. W. Miles. 1963. "On the Stability of a Plane Vortex Sheet with Respect to Three-Dimensional Disturbances", *J. Fluid Mech.*, Vol. 15, pp. 335-336.
- Greenough, J. A., J. J. Riley, M. Soetrisno, and D. S. Eberhardt. 1989. "The Effects of Walls on a Compressible Mixing Layer", AIAA Paper 89-0372.
- Mack, L. M. 1984. "Boundary Layer Linear Stability Theory", in *Special Course on Stability and Transition in Laminar Flow*, AGARD Report R-709, pp. 3-1 to 3-81.
- Mack, L. M. 1989. "On the Inviscid Acoustic-Mode Instability of Supersonic Shear Flows", in the *Proc. Fourth Symp. on Num. and Phys. Aspects of Aerodyn. Flows*, California State University, Long Beach, January.
- Metcalfe, R. W., S. A. Orszag, M. E. Brachet, S. Menon, and J. J. Riley. 1987. "Secondary Instability of a Temporally-Growing Mixing Layer", *J. Fluid Mech.*, Vol. 184, pp. 207-243.

Miles, J. W. 1958. "On the Disturbed Motion of a Plane Vortex Sheet", *J. Fluid Mech.*, Vol. 4, pp. 538-552.

Riley, J. J., P. D. Mourad, R. D. Moser, and M. M. Rogers. 1989. "Sensitivity of Mixing Layers to Three-Dimensional Forcing", in the *Proc. of the Summer Program of the Stanford/NASA Ames Center for Turbulence Research*.

Soetrismo, M., D. S. Eberhardt, J. J. Riley, and P. A. McMurtry. 1988. "A Study of Inviscid Supersonic Mixing Layers Using a Second-Order TVD Scheme", AIAA Paper 88-3677.

Tam, C. K. W., and F. Q. Hu. 1988. "Instability of Supersonic Mixing Layers Inside a Rectangular Channel", AIAA Paper 88-3767.

Yee, H. C., R. F. Warming, and A. Harten. 1984. "Implicit Total Variation Diminishing (TVD) Schemes for Steady-State Calculations", *J. Comp. Phys.*, Vol. 57, pp. 327-360.

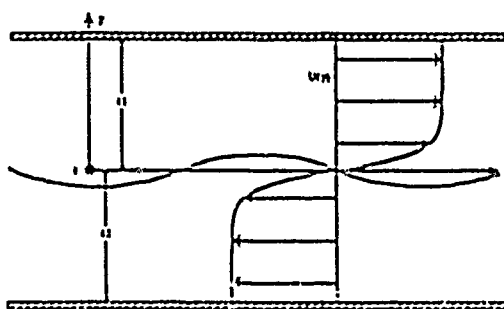


Figure 1. An idealized three-dimensional confined mixing layer.

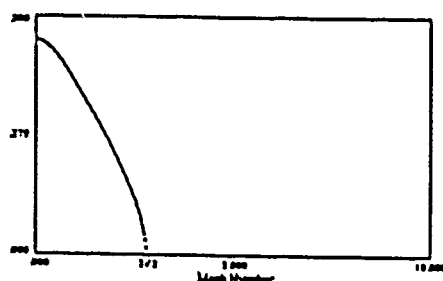


Figure 2a. Growth rate for an unbounded vortex sheet versus the relative (twice the convective) Mach number.

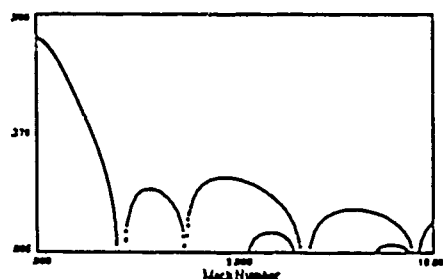


Figure 2b. Growth rate of a bounded vortex sheet versus the relative Mach number.

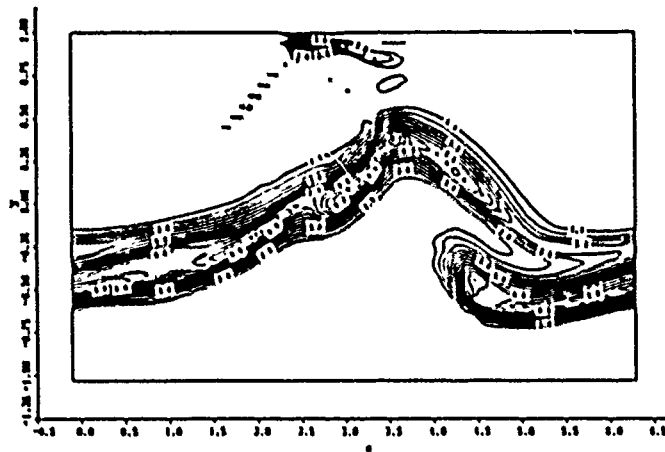


Figure 3. Vorticity field showing the sawtooth pattern for a convective Mach number of 1.45



Figure 4. Growth rate in k - l wavenumber space for a convective Mach number of 1.45.

THEORIES OF TURBULENT COMBUSTION IN HIGH SPEED FLOWS

(AFOSR Grant No. 89-0310)

Principal Investigators: P.A. Libby and F.A. Williams

Department of Applied Mechanics and Engineering Sciences
University of California, San Diego
La Jolla, CA 92093

SUMMARY/OVERVIEW

The objective of this research is to improve understanding of the chemical kinetics and fluid dynamics of turbulent combustion in high-speed flows. Supersonic combustion in hydrogen-air mixtures is being addressed by theoretical approaches that distinguish between reaction-sheet and distributed-reaction regimes. The work seeks to identify effects of compressibility in turbulent combustion, methods for including compressibility in theoretical analyses, and reduced chemical-kinetic mechanisms appropriate for supersonic combustion. The results may help to enhance capabilities of reasonable computations of high-speed turbulent reacting flows.

TECHNICAL DISCUSSION

In this newly initiated project, attention has been focused first on non-premixed hydrogen-air combustion. Previously established methods were employed with the most recent rate data for elementary steps [1] to calculate diffusion-flame structures by numerical integration. This is a first step towards identifying reduced chemical-kinetic mechanisms. Results for atmospheric pressure and initial temperatures of 300 K, at a low strain rate of 60 s^{-1} , are shown in Figs. 1-6. The nonmonotonic variation of the rate of scalar dissipation with mixture fraction, shown in Fig. 3, also has been observed for CO/H₂ flames [2] but disappears at higher strain rates.

Differential diffusion in hydrogen-containing diffusion flames introduces strong curvatures in most published plots of concentrations as functions of mixture fractions, away from regions of chemical activity. A mixture fraction suitably emphasizing the H element has been shown to remove this curvature for CO/H₂ flames [2], analyzed with a simplified 21-step mechanism [3]. The mixture fraction $Z(h)$ in Figs. 1-6 is based solely on enthalpy. Except for the curvature in the temperature profile at the fuel boundary, seen in Fig. 1, this selection may be observed from these figures to also eliminate the differential-diffusion curvature that masks chemical activity. Studies are continuing towards identifying the most appropriate definition of mixture fraction in hydrogen-air flames. Asymptotic methods, principally rate-ratio asymptotic, are then to be introduced to obtain simplified descriptions of flame structures.

Flame-structure results like these are to be used in identifying conditions under which turbulent hydrogen-air flames lie in reaction-sheet and distributed-reaction regimes. Turbulent-flame studies [4,5] have identified Fig. 7 as a plane of large-eddy Damköhler number and turbulent Reynolds number for delineating regimes of turbulent diffusion flames as well as turbulent premixed flames. An early aim is to determine where in this plane the high-speed turbulent-combustion situations of greatest interest lie. Once the regimes are ascertained, influences of kinetic energy and large pressure fluctuations on the flame structures are to be considered.

Including kinetic-energy and pressure-fluctuation terms in approaches like the Bray-Libby-Moss scheme for describing turbulent combustion involves developing understanding of pressure-velocity and pressure-concentration coupling in compressible turbulent reacting flows. A long-term objective of this research is to obtain the understanding needed for nonempirical approximation of these pressure-interaction effects so that well-founded predictive schemes can be developed.

REFERENCES

1. Chelliah, H.K. and Williams, F.A., "Aspects of the Structure and Extinction of Diffusion Flames in Methane-Oxygen-Nitrogen Systems", *Combustion and Flame*, to appear, 1989.
2. Chung, S.H. and Williams, F.A., "Asymptotic Structure and Extinction of CO/H₂ Diffusion Flames with Reduced Kinetic Mechanisms", 12th International Colloquium on Dynamics of Explosions and Reactive Systems, University of Michigan, Ann Arbor, July, 1989.
3. Rogg, B. and Williams, F.A., "Structures of Wet CO Flames with Full and Reduced Kinetic Mechanisms", Twenty-Second Symposium (International) on Combustion, The Combustion Institute, Pittsburgh, to appear, 1989.
4. Williams, F.A., "Turbulent Combustion", Chapter III of The Mathematics of Combustion (J.D. Buckmaster, editor), SIAM, Philadelphia, 1985, pp. 97-131.
5. F.A. Williams, "Structures of Flamelets in Turbulent Reacting Flows and Influences of Combustion on Turbulence Fields", Turbulent Reactive Flows (R. Borghi and S.N.B. Murthy, editors), Springer Verlag, New York, 1989, pp. 195-212.

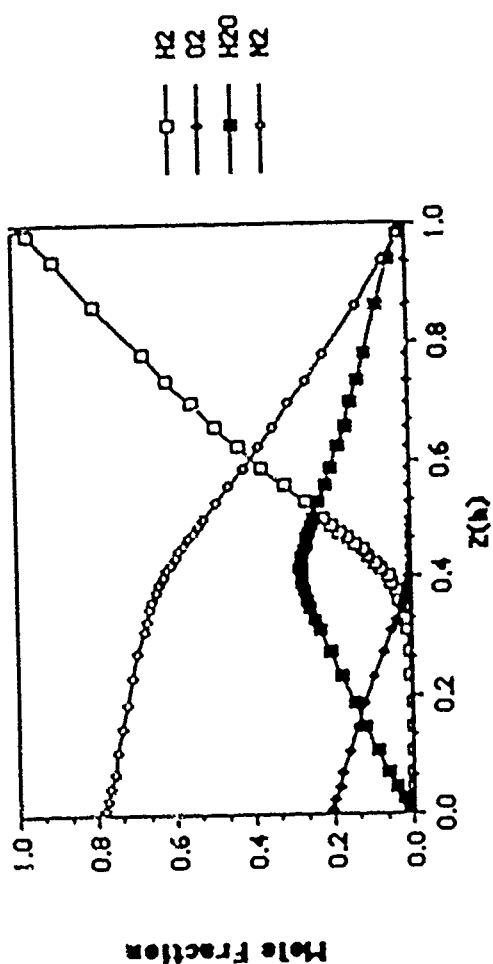


Fig. 2 Representative calculated profile of major species for hydrogen-air flame.

$a = 60 / \text{sec} : p = 1 \text{ bar}$

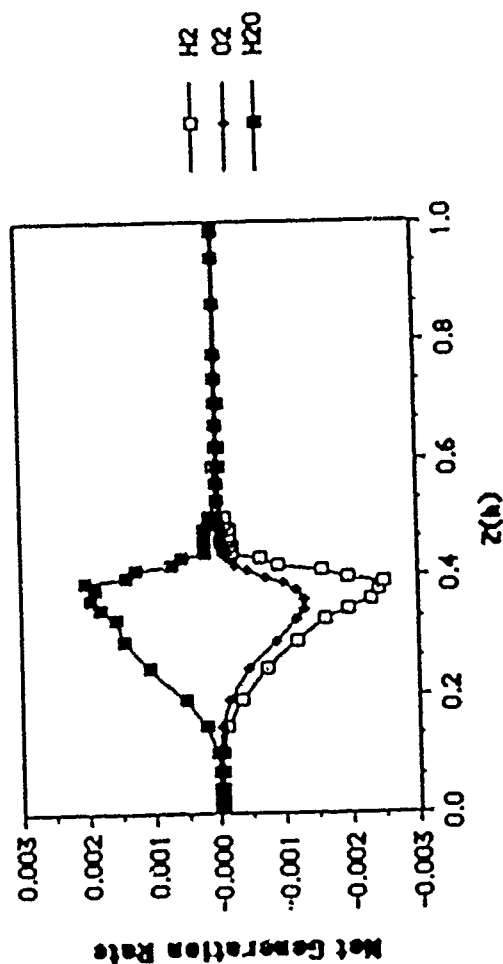


Fig. 4 Profiles of production rates of major species for hydrogen-air flame.

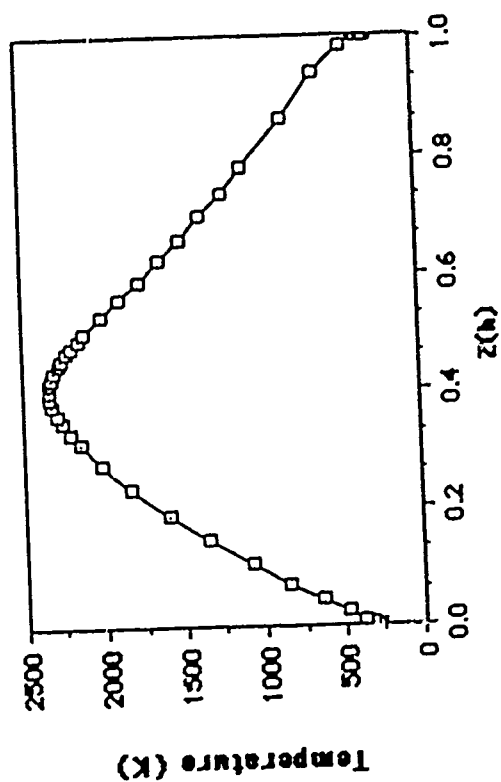


Fig. 1 Representative calculated temperature profile for hydrogen-air flame.

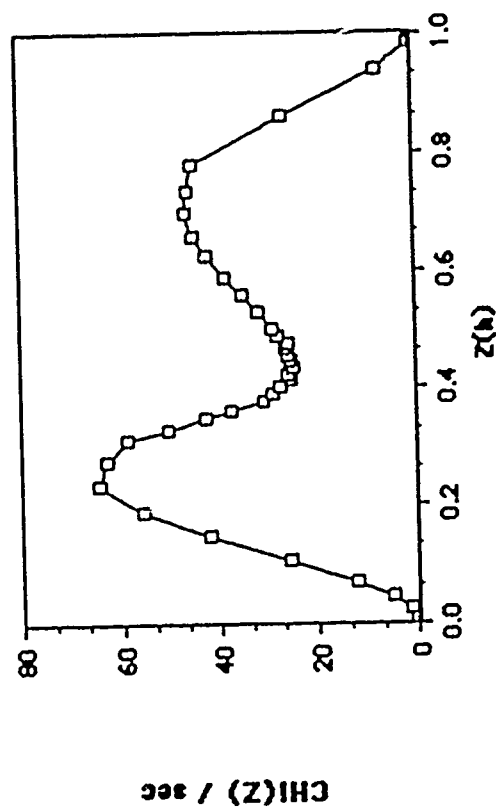


Fig. 3 Representative low-strain profile of scalar dissipation for hydrogen-air flame.

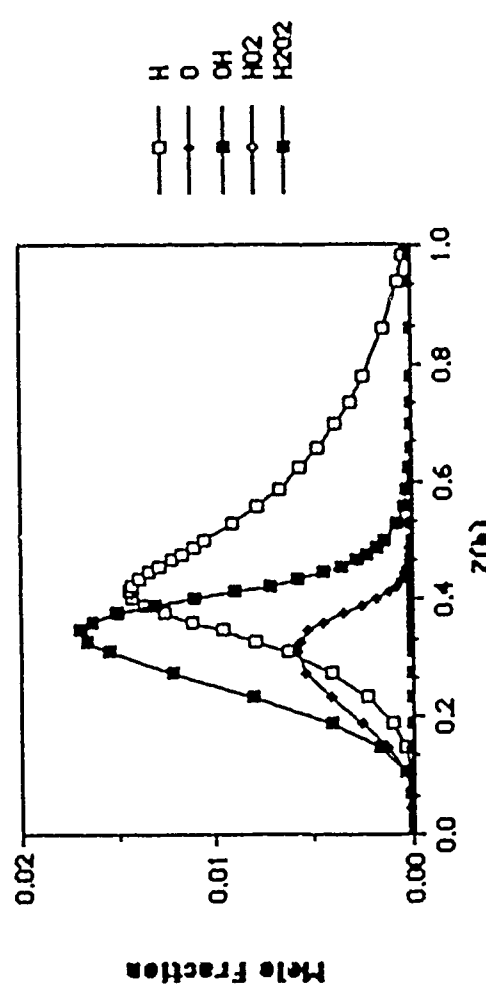


Fig. 5 Representative calculated profiles of H, O and OH for hydrogen-air flame.

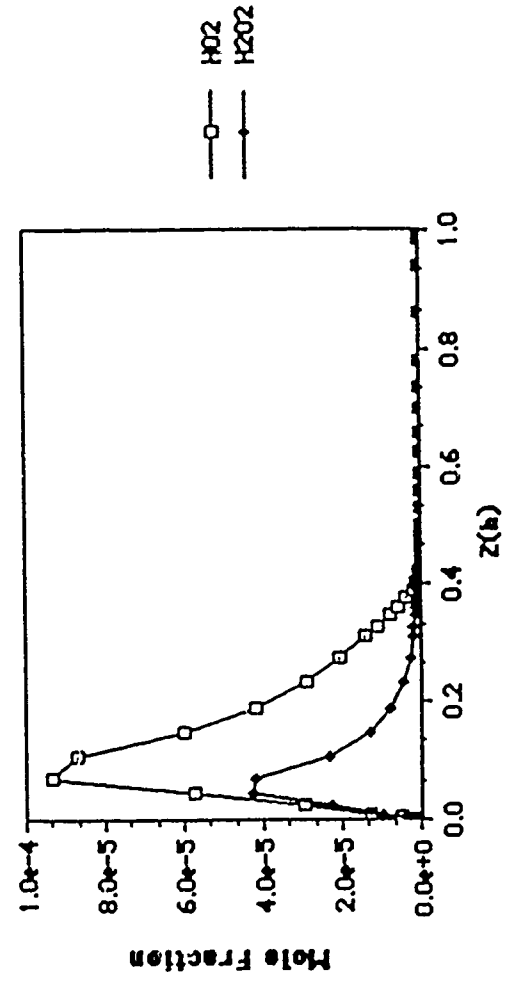


Fig. 6 Representative calculated profiles of H₂O and H₂O₂ for hydrogen-air flame.

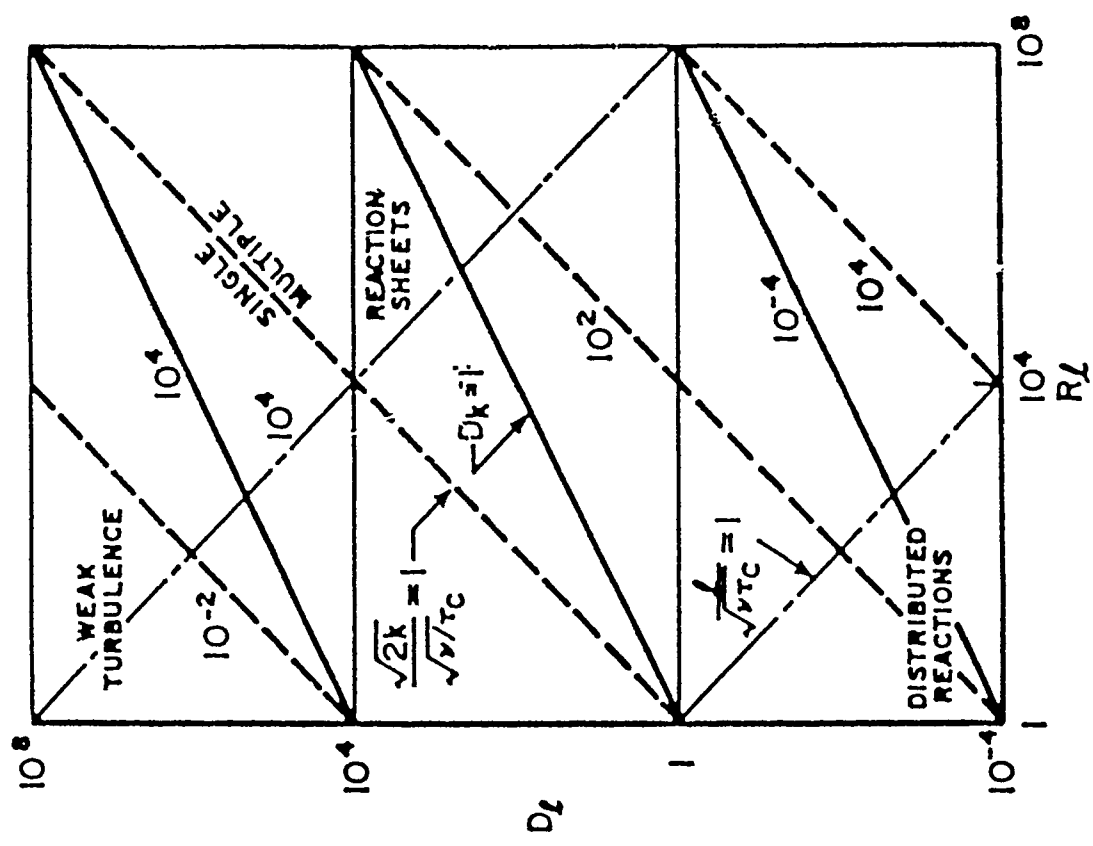


Fig. 7 Regimes of turbulent combustion in a diagram of Damköhler number and Reynolds number.

CHEMICAL KINETIC AND AERODYNAMIC STRUCTURES OF FLAMES

(AFOSR Grant No. 89-0293)

Principal Investigator: Chung K. Law

Princeton University
Princeton, NJ 08544

SUMMARY/OVERVIEW:

The objective of the present program is to study the structure of laminar premixed and diffusion flames through (a) non-intrusive experimental determination in reduced and elevated pressure environments, (b) computational simulation using detailed flame and kinetics codes, and (c) asymptotic analysis for the reduced mechanisms. During the reporting period we have (1) experimentally determined the laminar flame speeds of methane/air mixtures as functions of stoichiometry, pressure, and flame temperature, and computationally simulated their values by using various C_1 and C_2 mechanisms; (2) proposed a chemical kinetic limit for the propagation of the adiabatic, planar laminar flame; (3) experimentally determined the extinction stretch rates of diluted methane/air diffusion flames and interpreted the results on the basis of a branching-termination reaction scheme; and (4) experimentally investigated the influences of aerodynamic straining and gaseous additives on the various sooting limits of several alkane/air diffusion flames, and identified concentration modification due to preferential diffusion as a potentially important mechanism influencing soot formation.

TECHNICAL DISCUSSION

1. Laminar Flame Speeds and Reaction Mechanisms of Methane/Air Mixtures

The laminar flame speed S_u^0 is an important physico-chemical parameter of a combustible mixture because it contains the basic information regarding its diffusivity, exothermicity, and reactivity. Most of the earlier experimental determinations of S_u^0 , however, have been complicated by the coupled effects of flame stretch and preferential diffusion. These influences can cause uncertainty in the study of chemical kinetic mechanisms by using S_u^0 as a criterion for partial validation.

In an earlier study we proposed the use of the counterflow, twin-flame method to unambiguously determine the laminar flame speed S_u^0 . In the present investigation the S_u^0 of methane/"air" mixtures have been accurately and extensively determined over the stoichiometric range from very lean to very rich, the pressure range from 0.25 to 4 atm, and flame temperature range from 1,550 to 2,250 K; independent variation of the flame temperature is achieved by substituting nitrogen in the air by an equal amount of argon or carbon dioxide. Numerical simulation of the experimental flame speeds has also been conducted by using a C_1 mechanism and a full C_2 mechanism. Figures 1 and 2 respectively show the comparisons between the experimentally- and numerically-determined values of S_u^0 as a function of the equivalence ratio ϕ for mixtures with different inert gases at 1 atm (Fig. 1), and with different adiabatic flame temperatures (T_{ad}) at 1 atm. (Fig. 2). The calculated results agree well with the experimental

data, for both the C_1 and C_2 mechanisms, except for the very rich mixtures for which there is substantial overprediction by the C_2 mechanism. Further experiments and computations have been conducted for highly-diluted flames under elevated pressures. Figures 3a and 3b show typical results for the mass burning rate $m'' - \rho_u S_u^*$ and overall reaction orders n as functions of pressure and nitrogen dilution, showing that n can actually assume negative values. The above results are reported in Publication Nos. 1, 2 and 3.

2. Chemical Kinetic Limits of Laminar Flame Propagation

The objective of this investigation is to explore the potential existence of purely chemical kinetic limits for the steady propagation of the adiabatic, one-dimensional, planar laminar flame, and to explore their relation with the flammability limits of the mixture. Theoretical determination of such limits involves computing the flame structure and identifying situations under which the controlling chain termination reactions overwhelms the corresponding branching reactions. Such lean and rich limits have been determined for methane/air mixtures at various pressures, with different kinds of diluents, and with H_2 and CH_3Br additions. The values mostly agree well with the experimentally-determined flammability limits of these mixtures. This work is reported in Publication No. 4.

3. Extinction of Counterflow Diffusion Flames with Branching-Termination Chain Mechanisms

In a previous study the asymptotic structure and extinction of diffusion flames supported by a chain mechanism consisting of two two-body, thermoneutral, high-activation-energy branching reactions and a three-body, exothermic, zero-activation-energy termination reaction have been analyzed for the model problem of counterflow flames. In the present study the extinction strain rates of such a counterflow methane/ O_2/N_2 diffusion flames have been experimentally determined. Results show that the density-weighted extinction strain rates increase only linearly with increasing pressure, thereby demonstrating weakened pressure dependence due to the influence of the three-body termination reaction. This work is reported in Publication No. 5.

4. Sooting Limits of Strained Diffusion Flames and the Influence of Gaseous Additives

An experimental study has been performed with axisymmetric counterflow diffusion flames to investigate the influence of gaseous additives and aerodynamic straining on the relevant sooting limits of the lower alkanes and ethylene. The limits are defined by the critical strain rate at which either soot luminosity, soot particle scattering, or broadband fluorescence is negligible compared to the appropriate background signal. The fluorescence signal, if attributed to polycyclic aromatic precursors, yields a limit that can be interpreted as the extinction of soot precursors and is suggested to be a possible limit for identifying a completely nonsooting flame condition.

The results of the study further identify how temperature and fuel concentration influence soot particle inception, and both are found to have a potentially important influence on this crucial stage of the soot formation process. Furthermore, the critical strain rates are found to display an Arrhenius temperature dependence, a dependence that is similar for the alkanes considered.

By eliminating temperature and concentration effects, the direct chemical influence of O_2 , CO_2 , and CO on soot limits and, consequently, soot inception chemistry has been observed. Oxygen and CO_2 addition decrease the soot limits while CO addition increases them. The interpretation of these results is based

on the influence of these additives on the hydroxyl radical concentrations. That is, O_2 and CO_2 addition favors OH production while the addition of CO scavenges OH in the critical interface between the soot inception zone and the OH profile. This work is reported in Publication Nos. 6 and 7.

5. Concentration Modification Due to Preferential Diffusion

An experimental and numerical investigation has been conducted to investigate the influence of the mobility of inert additives on soot formation in propane and ethylene counterflow diffusion flames. The inerts used were helium, neon, argon, or krypton. Results show that while the mobility of the inert has practically no effect when a small amount is added to the oxidizer side, the influence is significant when added to the fuel side in that krypton, being the least mobile inert, yields the greatest soot loading while helium, being the most mobile, yields the least (Fig. 4). By relating the spatially-resolved soot volume fractions to the corresponding profiles of temperature, velocity and species concentrations, it is demonstrated that this influence on soot loading is likely caused by concentration modifications of the fuel and the soot precursors due to the different mobilities of the inert additives. This work is reported in Publication No. 8.

PUBLICATIONS

1. "Laminar Flame Speeds of Methane/Air Mixtures Under Reduced and Elevated Pressures," by F. Egolfopoulos, P. Cho, and C.K. Law, to appear in Combustion and Flame.
2. Experimental and Numerical Determination of Laminar Flame Speeds of Methane/(Ar, N_2 , CO_2)-Air Mixtures as Function of Stoichiometry, Pressure, and Flame Temperature," by D.L. Zhu, F.N. Egolfopoulos and C.K. Law, to appear in Proc. of Twenty-Second Combustion Symposium.
3. "Chain Mechanisms in the Overall Reaction Orders in Laminar Flame Propagation," by F.N. Egolfopoulos and C.K. Law, submitted.
4. "A Kinetic Criterion of Flammability Limits: Lean Limits of C-H-O-N-Br Systems," by F. Egolfopoulos and C.K. Law, 1988 Tech. Meeting of the Central Section of the Combustion Institute.
5. "Extinction of Counterflow Diffusion Flames with Branching-Termination Chain Mechanisms: Theory and Experiment," by C.K. Law, Lecture Notes in Physics Series, Vol. 299: Mathematical Modelling in Combustion Science (J. Beckmaster and T. Takeno, eds.), Springer-Verlag, pp. 147-156, (1988).
6. "Experiments on the Sooting Limits of Aerodynamically-Strained Diffusion Flames," by D.X. Du, R.L. Axelbaum, and C.K. Law, to appear in Proc. of Twenty-Second Combustion Symposium.
7. "The Influence of Gaseous Additives on the Sooting Limits of Strained Diffusion Flames," by D.X. Du, R.L. Axelbaum, and C.K. Law, 1988 Tech. Meeting of the Central Section of the Combustion Institute.
8. "Effects of Preferential Diffusion and Concentration Modification in Sooting Counterflow Diffusion Flames," by R.L. Axelbaum, C.K. Law, and W.L. Flower, to appear in Proc. of Twenty-Second Combustion Symposium.
9. "Velocity and Scalar Fields of Turbulent Premixed Flames in Stagnation Flow," by P. Cho, C.K. Law, R.K. Cheng, and I. Shepherd, to appear in Proc. of Twenty-Second Combustion Symposium.
10. "Dynamics of Stretched Flames," by C.K. Law, to appear in Proc. of Twenty-Second Combustion Symposium.

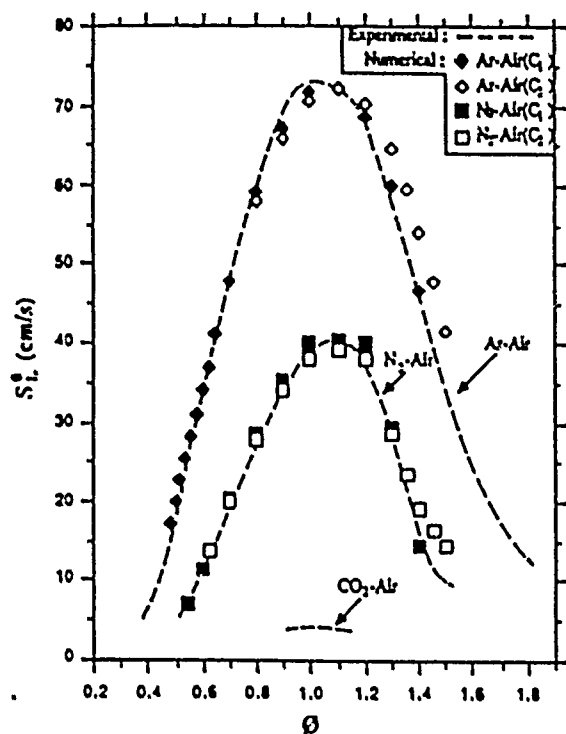


Figure 1

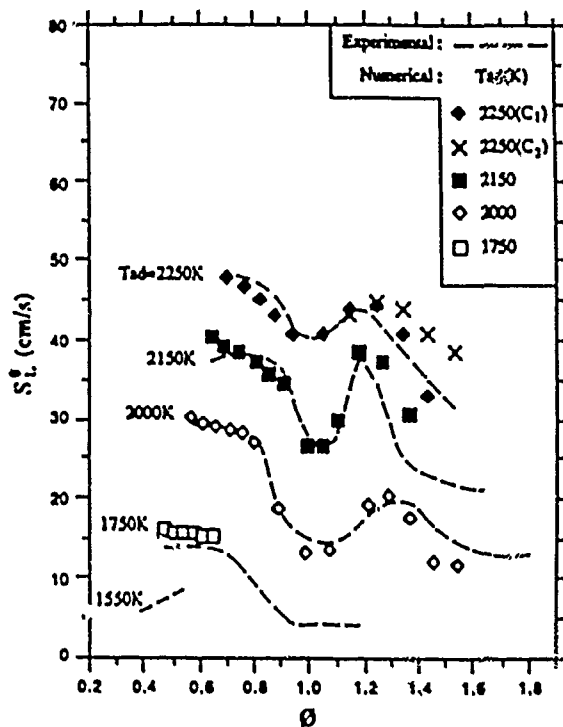


Figure 2

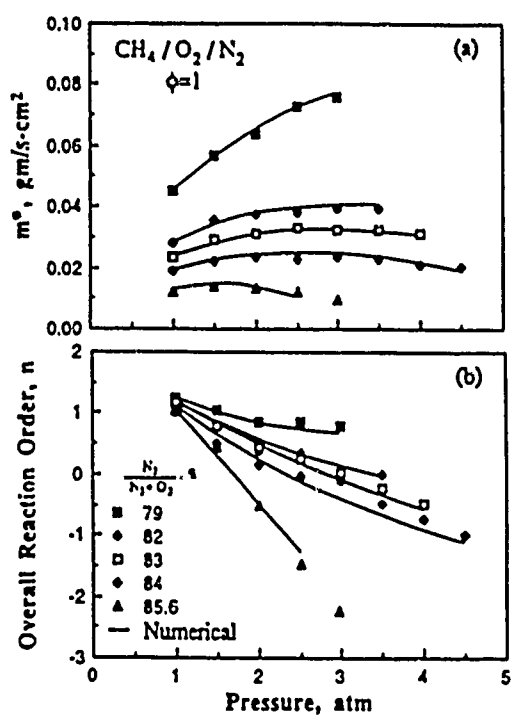


Figure 3

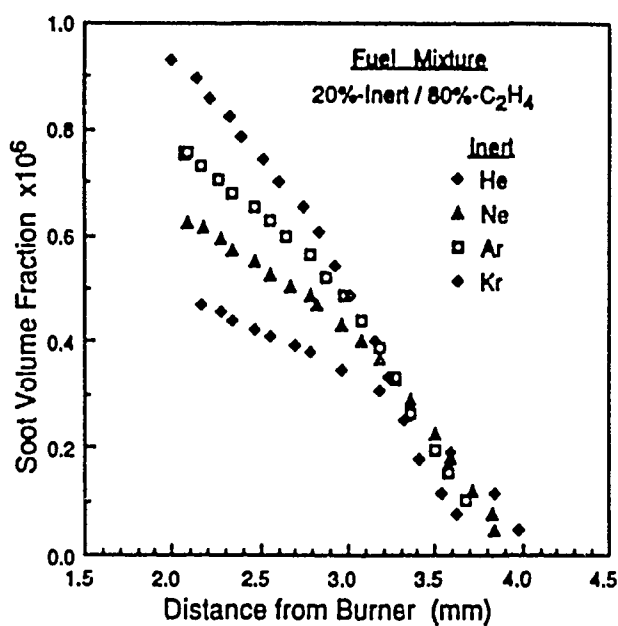


Figure 4

PREMIXED TURBULENT FLAME PROPAGATION

(AFOSR Grant No. AFOSR 87-0097)

Principal Investigator: Domenic A. Santavicca

Department of Mechanical Engineering
The Pennsylvania State University
University Park, PA 16802

SUMMARY/OVERVIEW:

The objective of this research is to develop an improved understanding of turbulence-flame interactions and their effect on turbulent flame structure, turbulent flame propagation, and flame generated turbulence in premixed turbulent flames. Measurements have been made in a freely propagating turbulent flame of the turbulence properties both upstream and downstream of the flame, including turbulence intensity, length scale, time scale, energy spectrum and Reynolds stress, as well as, of the two-dimensional flame structure. The flame structure measurements have been analyzed for fractal character and the results used to develop a heuristic model of flame structure fractal dimension. These measurements provide a comprehensive characterization of turbulence-flame interactions, new insights and understanding regarding their effect on turbulent flame propagation and flame generated turbulence, and new methods for quantifying the role of turbulent flame structure in turbulent combustion models.

TECHNICAL DISCUSSION

The turbulent flow reactor used in this research, referred to as a pulsed-flame flow reactor, was specifically designed for this study of turbulence-flame interactions in premixed turbulent flames. Turbulence is generated by forcing the fuel-air mixture through a large number of small diameter, high Reynolds number jets which are uniformly distributed over the cross-section of the flow reactor and oriented normal to the axis of the flow reactor. With this device, relative turbulence intensities as high as 70% can be achieved, which are uniform within $\pm 10\%$ over the cross-section of the flow reactor. Fuel is added to the air flow well upstream of the test section to insure complete mixing. The flame is initiated by a spark located approximately two test section diameters downstream of the measurement location. This produces a flame which freely propagates upstream through the measurement location. By cycling the fuel off and on in 2 second intervals, and by adjusting the spark timing to coincide with the arrival of each fuel-air "slug", a flame is produced every 4 seconds. Measurements can then be made over many different flame events and ensemble averaged to obtain the appropriate statistical averages.

The effect of turbulence-flame interactions on the turbulence properties of the flow both upstream and downstream of the flame front has been studied in a propane-air flame at an equivalence ratio of 1.0, a pressure of 1 atmosphere, a temperature of 300 K, a turbulence intensity of 25 cm/sec and an integral length scale of 8 mm [1]. Laser Doppler velocimetry has been used to measure the mean velocity, turbulence intensity, time scale, energy spectrum, length scale and Reynolds stress as a function of time through the propagating flame front. Velocity components and length scales are measured both normal and parallel to the mean flame front.

The turbulence intensity, normal to the mean flame front is observed to gradually increase by approximately 50% ahead of the flame and then to suddenly increase by a factor of 5 to 6 across the flame. Whereas the turbulence intensity parallel to the mean flame front shows no appreciable increase ahead of the flame and only a factor of 2 to 3 increase across the flame. Since there is a significant decrease in density across the flame, it is more appropriate to consider the density weighted turbulent kinetic energy, $\rho u'^2$, which shows a nearly three-fold increase across the flame as a result of the turbulence-flame interactions. It is important to note that the turbulence production is highly anisotropic and that any model of turbulence-flame interactions must not only account for the turbulence production but it's anisotropic nature as well.

The integral length scale measurement is a transverse length scale which is obtained from a direct two-point spatial correlation measurement. Length scales both normal and parallel to the mean flame front have been measured. The results show that the length scale increases from the

unburned to the burned gases, increasing by 50% for the length scale which is parallel to the mean flame front and by a factor of 2 for the length scale which is normal to the mean flame front. The length scale measurements also reflect the fact that the upstream turbulence is relatively isotropic, but becomes anisotropic in the post-flame gases.

The turbulence energy spectrum at 225 msec ahead of the flame shows a slope of -2.0 which indicates that the turbulence is not fully equilibrated. This is actually before the flame is ignited and therefore is a measure of the cold flow turbulence. At 75 msec before flame arrival, there is a pronounced increase in the high frequency content of the energy spectrum resulting in a slope of -1.33 . This indicates that the turbulence-flame interactions, which result in an increase in the turbulent kinetic energy of the unburned gas immediately ahead of the flame, occur selectively at high frequencies and small scales of the turbulence energy spectrum. In the burned gases behind the flame, a decrease in the high frequency content of the energy spectrum is observed resulting in a slope of -1.71 at 75 msec and 1.95 at 225 msec. The observed changes in the burned gas energy spectrum may be due to the increased viscosity in the high temperature burned gases and its dissipative effect on the small scale eddies. Additional measurements of the effect of turbulence-flame interactions on the turbulence energy spectrum are essential. Such measurements will identify the scales on which turbulence-flame interactions take place and thereby improve our understanding of the underlying fluid mechanical mechanisms.

Two-dimensional flame structure measurements in turbulent propane-air flames have been made over a range of Reynolds numbers from 50 to 1430 and Damkohler numbers from 10 to 900 [2]. This also corresponds to a range of turbulence intensity to laminar flame speed ratios from 0.25 to 12. Except for one case, all of the flame structure measurements are in what is referred to as the reaction sheet regime. At each of the operating conditions, between 15 and 35 images were recorded. Two important observations can be made from these images regarding the effect of increasing u'/S_L . One is that there is more evidence of small scale flame structure and the second is that the flame zone covers a larger portion of the field of view, i.e. it becomes more space-filling, as u'/S_L increases. These observations are consistent with the fractal analysis of the flame structure images which is used to quantitatively characterize the observed changes in flame structure.

Each of the two-dimensional flame structure images was analyzed using a fractal algorithm. These results show that there is a range of scales over which the slope is constant for each flow condition, which is a necessary and sufficient condition to show that the flame structures display fractal character. The flame surface fractal dimension is simply one minus the slope of these curves. The average fractal dimension is found to increase with increasing u'/S_L and to approach limiting values at both low and high u'/S_L . At low u'/S_L , the flame surface fractal dimension does not appear to be approaching 2.0, the Euclidean dimension of a plane, as expected. Instead, the fractal dimension is apparently approaching a slightly larger value. This behavior is most likely due to flame front instabilities, and perhaps a coupling with the turbulence. At high u'/S_L , the fractal dimension appears to be approaching a limiting value between 2.3 and 2.4.

The outer cutoff can be identified as the point where the fractal analysis curve deviates from a constant slope. This quantity is important since it is required to determine the turbulent flame speed as discussed below. The results show that the outer cutoff is not a sharp cutoff, but that there is a gradual transition. The transition, however, does occur over a narrow range of scales comparable to the integral scale for the flow conditions studied.

The inner cutoff is also required to calculate the turbulent flame speed. Based on physical arguments, there are several hypotheses regarding the proper physical scale which should be used to represent the inner cutoff including the Kolmogorov length scale, the laminar flame thickness, and the Gibson scale. The measurements in this study have not been made with sufficient spatial resolution to determine the inner cutoff, however, they do show that the inner cutoff is less than the Gibson scale.

At high Reynolds numbers, it is expected that the flame front will behave dynamically as a passive scalar surface. This occurs since the burning process is dominated by the turbulent convective action. The passive scalar fractal dimension has been determined to be approximately 2.35 [3]. In this study, the flame structure fractal dimension is found to approach this value at values of u'/S_L greater than 10.

The results of this study clearly indicate that the fractal dimension increases with increasing turbulence intensity and decreasing laminar flame speed. This can be explained in terms of two competing processes. First, the turbulent velocity fluctuations act to convectively distort the flame front at a rate proportional to the characteristic velocity scale, u' . Second, the laminar burning process acts to smooth the flame surface at a rate proportional to the laminar burning speed, S_L . The relative importance of these processes changes with u'/S_L , where the

smoothing process dominates at low values, and turbulence dominates at high values. In the region between these two limits, both effects are important. In order to quantify this behavior, a heuristic model for the fractal dimension of flame surfaces has been developed [2]. The rate of wrinkling is represented by u' , which accounts for the tendency of the turbulent motion to distort the flame surface into a passive scalar with a fractal dimension D_T . The rate of smoothing is represented by S_L , which represents the tendency of the burning process to eliminate wrinkles from the flame surface, thereby lowering the fractal dimension, towards a laminar limit, D_L . The combined effect of these processes is represented by:

$$D_f = D_L / (u' / S_L + 1) + D_T / (1 + S_L / u')$$

where D_f refers to the flame surface fractal dimension. Values of 2.05 and 2.35 have been used for the laminar flame fractal dimension and turbulent passive scalar fractal dimension, respectively. Figure 1 shows a comparison between this model and the fractal dimension measurements from this study, as well as recent measurements from other studies [4,5]. The heuristic model appears to agree well with the measured flame surface fractal dimensions over the entire range of u'/S_L from the laminar limit to the high Reynolds number limit.

In the reaction sheet regime and in the absence of flame stretch effects, the turbulent to laminar flame speed ratio is simply equal to the turbulent to laminar flame area ratio. Using the fractal description of the flame surface, this ratio is equal to

$$S_T/S_L = A_T/A_L = (\eta/L)^{2-D}$$

where the Kolmogorov scale, η , and the integral scale, L , have been used as the inner and outer cutoffs, respectively. The heuristic fractal dimension model can then be used to obtain an expression for the turbulent to laminar flame speed ratio which is a function of the turbulence intensity to laminar flame speed ratio and the Kolmogorov to integral scale ratio.

Validation of the fractal turbulent flame speed model through comparison with measured turbulent flame speeds is an important test. Despite the abundance of reported turbulent flame speed data, there are limitations to most of the measurements which preclude their use for this purpose. These limitations include the absence of information on the turbulence length scale, as well as, unwanted flow field effects associated with the various flame configurations which have been used and uncertainty in defining the unburned gas velocity with respect to the mean flame front. The flame configuration which is least affected by these problems is the freely propagating spherical flame. In this case, however, the flame propagation rate undergoes a transition from an initially laminar growth rate to a fully developed turbulent growth rate. This process is accounted for in the turbulent flame kernel model [6] described below which incorporates the heuristic flame structure fractal dimension model.

In the absence of additional ignition energy following gas breakdown, the growth rate of a spherical flame kernel is given by $(\rho_u/\rho_b)S$, where ρ_u and ρ_b are the unburned and the burned gas densities, respectively, and S is the laminar or turbulent flame speed. This expression accounts for both flame propagation and the thermal expansion due to the flame's chemical heat release. The effect of turbulence on flame kernel growth, as represented by this expression, is through changes in the flame speed S . The fundamental effects of turbulence on flame speed are much the same in a flame kernel as in a fully developed flame. The major difference between a fully developed turbulent flame and a turbulent flame kernel is that the flame kernel imposes its own characteristic time and length scales, i.e. the kernel lifetime and size, respectively. To properly account for these characteristic time and length scales, it is necessary to allow for the fact that the turbulent flow consists of a range of time and length scales and that only those turbulence scales which are smaller than the kernel's characteristic scales can affect the kernel growth rate. One approach which has been used to account for the range of turbulence time scales affecting flame kernel growth is based on the use of the turbulence energy spectrum [7], where the effective turbulence intensity at a particular time, t , is defined by the square root of the area under the energy spectrum over the range of frequency components greater than the reciprocal lifetime. The instantaneous turbulence intensity can then be used to define an instantaneous fractal dimension, which in turn can be used to predict the instantaneous turbulent flame speed. One must also, however, account for the fact the flame kernel surface can not exhibit scales larger than its size. In fact, a reasonable approximation is that the largest scale of wrinkling is equal to half the kernel radius. And finally, the instantaneous turbulent flame speed can be used to determine the instantaneous growth rate, which when integrated from the initial kernel radius, gives the kernel radius as a function of time. Figure 2 shows a comparison of the fractal model

of turbulent flame kernel growth with measurements made in a high velocity turbulent flow such that the flame kernel rapidly detaches itself from the spark electrodes [8]. In this particular case, the agreement between the model prediction and the measurement is very good.

Although the comparison shown in Figure 2 is very encouraging, a much more comprehensive evaluation of the fractal turbulent flame kernel model over a broad range of turbulence conditions is still required. In addition, measurements are still needed to identify the proper choice for the inner cutoff. Such measurements are currently being made in the pulsed-flame flow reactor.

REFERENCES

1. Videto, B. D. and Santavicca, D. A., "Flame-Turbulence Interactions in a Freely Propagating Premixed Flame," submitted to Combustion Science and Technology.
2. North, G. L. and Santavicca, D. A., "The Fractal Nature of Premixed Turbulent Flames," submitted to Combustion and Flame.
3. Hentschel, H. G. E. and Procaccia, I., A Physical Review, Vol. 29, p. 1461 (1984).
4. Mantzaras, J., Felton, P. G. and Bracco, F. V., Combustion and Flame,
5. Murayama, M. and Takeno, T., 22nd Symp. (Int'l) on Comb., (1988).
6. Santavicca, D. A., Liou, D. and North, G. L., "A Fractal Model of Turbulent Flame Kernel Growth," submitted to Combustion and Flame.
7. Abdul-Gayed, R. G., Bradley, D., Lawes, M. and Lung, F.K.-K., 21st Symp. (Int'l) on Comb., (1986).
8. Pope, S. B. and Cheng, W. K., 21st Symp. (Int'l) on Comb., (1986).

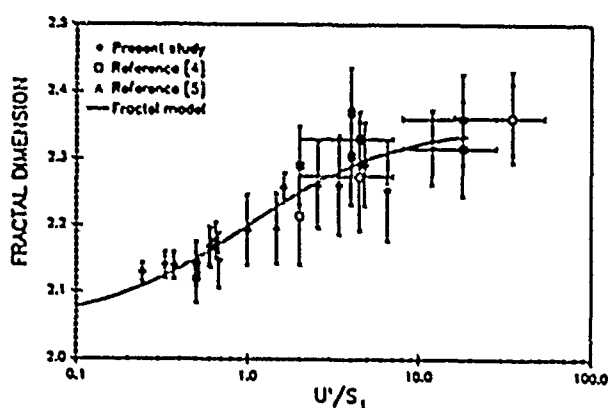


Figure 1. Comparison between the fractal dimension predicted by the heuristic model and experimentally measured values.

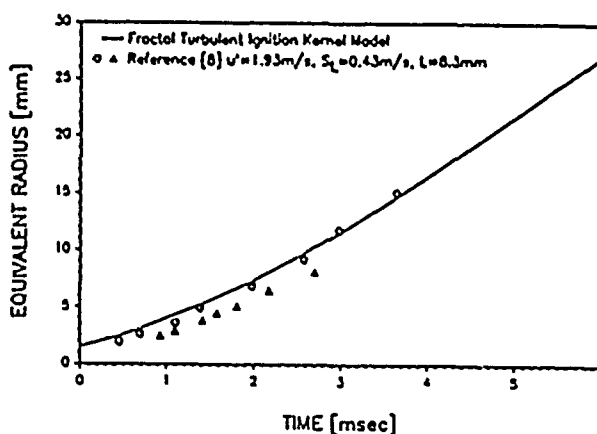


Figure 2. Comparison between the fractal turbulent flame kernel growth model and experimental data from reference [8].

LOCAL EXTINCTION MECHANISMS IN NON-PREMIXED TURBULENT COMBUSTION

AFOSR Contract No. F-49620-88-C-0066

Principal Investigators: S.M. Correa and A. Gulati

General Electric Corporate Research and Development Center

Schenectady, New York 12301

SUMMARY

This is an experimental and modeling study of gaseous flames under conditions approaching blowoff. Most recently we have investigated a non-premixed turbulent jet flame, composed volumetrically of a 40% CO/10% H₂/50% N₂ mixture called LHC (Low Hydrogen Content) gas, in co-flowing air. The high Reynolds number (15,000 based on conditions at the jet exit) necessitates stabilization, provided here by a co-annular premixed pilot flame. Pointwise measurements of (i) temperature, mixture fraction, and mole fractions of major species and (ii) velocity have been made using (i) spontaneous Raman spectroscopy and (ii) laser velocimetry, respectively. The data show significant temperature decrements due to finite-rate chemistry effects but no evidence of localized extinction. A computational model for a jet flame under such conditions has been developed. In the model, combustion chemistry is represented by two-body shuffle reactions and three-body recombination reactions. The scalar dissipation rate field is examined for a critical value below which the two-body reactions are assumed to be in partial equilibrium (p.e.) and above which they are assumed to be frozen and the gas therefore unburned. The kinetics of the recombination reactions are activated for the former fraction of the gas. This approach has been implemented in a shear-layer finite-volume averaged Navier-Stokes model with $k-\epsilon$ /assumed shape probability density function (pdf) sub-models for turbulence. Comparisons of the calculations and the data are used to make inferences regarding the nature of a flame near blowoff.

EXPERIMENTAL SETUP

The fuel (LHC gas) issues from a nozzle of diameter (d) 3.18 mm in low-turbulence co-flowing air [1-3], the flame being stabilized by a co-annular premixed pilot (Fig. 1). The LHC gas composition has been chosen to maximize the probability of local extinction, and features a critical strain rate (in a counterflow burner) of 950 s^{-1} [4]. The fluctuating strain field near the exit might be expected to result in local strain-induced extinction. The flame is attached at a jet exit Reynolds number of 15,000; time-resolved ($1 \mu\text{s}$) Schlieren photographs and shadowgraphs show no gross unsteady features or liftoff tendencies. The pilot flame consists of a premixed stoichiometric mixture of LHC gas and air, preserving the C/H/O ratios. The exit velocity of the premixed products was inferred, from laser velocimetry at $x/d = 1$, to be 15 m/s. The co-flow air velocity was 5 m/s.

The joint Rayleigh-Raman diagnostic system used in this study is similar to that used for previous studies with modifications appropriate for the more luminous LHC gas. In brief, a flashlamp-pumped dye laser, which provides pulses of $\sim 1 \text{ J}$ in $\sim 2 \mu\text{s}$ within a 0.2 nm bandpass at 488.0 nm at 1 Hz, is used to excite the scattering processes. The light scattered from the probe volume ($0.2 \times 0.2 \times 0.6$

mm) is collected by two lenses, separated in frequency by a 3/4 m polychromator and is detected by eight photomultiplier tubes at the exit plane. The system was calibrated extensively using pure gases and well-characterized premixed porous plug burners. Typically, 200 measurements were made at each flame location although 2000 shots were recorded at some locations for statistical purposes. Details are available in Refs. 4 and 5.

Laser velocimetry was used to measure the axial velocity, The 514.5 nm line from a 10 watt argon-ion laser was used to scatter light from alumina particles of 1 μm nominal diameter. These particles were used to seed the co-flowing air, the jet and the pilot flow in different combinations to provide unbiased statistics. The scattered light was collected by the same spectrometer and collection optics used for the Raman diagnostics and processed using a standard TSI signal counter. At each location 4096 instantaneous velocity data were recorded. Radial profiles of velocity, temperature and mole fractions of the major species were measured at several axial locations in the flame; $x/d \approx 1, 10, 20$ (regions of high strain), 30, 40, and 50. In addition, the centerline profile at $y=0$ was obtained.

MODEL

Several fluid mechanical time-scales characterize gaseous combustion, such as macroscopic residence time, integral scales and dissipative scales. Combustion occurs by a multi-scale chemical kinetic process, so that different types of turbulence-chemistry interactions may exist simultaneously. In the present model, combustion chemistry is represented by two-body shuffle reactions and three-body recombination reactions. We hypothesize that the two-body reactions, characterized by high activation energies and therefore spatially narrow reaction zones, occur in a flamelet manner while the recombination reactions occur in a distributed manner [5]. The two-body fast shuffle reactions therefore are not assumed to be in equilibrium throughout the flowfield: the two-body reaction zone is assumed to be either in p.e. or quenched depending on the local dissipation rate X being less or more than a critical value. Consequently, the pdf of local dissipation rate is required [6]. The kinetics of the recombination reactions are activated for the former fraction of the gas. Local extinction would arise if the strain was sufficiently high to preclude two-body reactions from occurring over sufficiently large regions. The theory is implemented with a partial-equilibrium/assumed shape pdf (over mixture fraction and radical pool reaction progress variable) for the reacting part of the gas.

The model [4,5] is an extension of the partial equilibrium model for CO/H₂-air flames. The p.e. model has been used in the past in conjunction with both $k-\epsilon$ /assumed shape pdf [e.g., Ref. 1] and full velocity-scalar joint pdf/Monte-Carlo models [3,7] with good success on velocity, temperature, major species and OH in a turbulent jet flame of medium BTU gas (40% CO, 30% H₂, 30% N₂) in air.

DISCUSSION

A temperature-mixture fraction (ξ) scattergram, using data from all radial locations at $x/d = 10$, indicates that the lean gas is near adiabatic equilibrium (Fig. 2). Near stoichiometric ($\xi_s = 0.43$), there is significant departure from equilibrium in the data: for ξ between 0.25 and 0.65 the temperature values range from 750 - 1500 K. There is no bimodality in contrast with the scattergrams in methane flames [8] or a high Reynolds number diluted H₂-Argon flame [9]. The latter, however, was not a steadily attached flame. The present data seem to deny localized extinction, but indicate significant departures from adiabatic equilibrium chemistry in the LHC flame.

Comparisons of the data with the calculations have been conducted at $x/d = 20$ (the region of large strain) and $x/d = 40$ (the equilibrated region). Here we discuss only selected results at the former station. The mean mixture fraction (Fig. 3) is predicted to decay less rapidly than measured; either

the scalar field develops differently from the velocity field or, more likely, the initial turbulence is not resolved well enough. The variance of the mixture fraction (Fig. 4) agrees very well with the predictions, with an off-axis peak centered at $r/a = 3$ (a = fuel tube radius). Figure 5 shows that the comparison for the major species N_2 and O_2 at $x/d = 20$ is fairly good. Similarly the fuel consumption is predicted well except in the fuel rich case (CO and H_2). The centerline decay of the scalar field of the jet is less than predicted as was the case for the mixture fraction. The conventionally-averaged mean temperature profile (Fig. 6) agrees fairly well. Overall, the model does a reasonable job of taking into account the departures from equilibrium chemistry.

One must explain the bimodality seen in methane flames. A contributing factor is the propensity of hydrocarbon fragments (alkyl radicals) to consume oxyhydrogen radicals. Another factor is that the flammable range in methane-air systems is narrow ($\xi_s = 0.058$), favoring flamelet-like behavior, whereas in the LHC gas flame ($\xi_s = 0.43$) the reaction zone extends from $\xi = 0.2$ to $\xi = 0.6$. Thus, in the LHC flame studied here the turbulent flame consist of distributed reaction zones, embedded within which lie thin two-body reaction zones. In such a flame, as the turbulence intensity is increased, the time scales may eventually be fast enough to be comparable to the chemical time scale of the two-body reactions, leading to their being extinguished and eventually result in global blowoff of the flame.

It appears that local extinction is not induced by strain in CO/H_2 -air flames, because the reaction zones are too broad to interact with the straining (dissipative) scales. H_2 and CH_4 flames have much narrower reaction zones, and CH_4 flames do indeed show localized extinction. H_2 flames, however, have simpler chemistry and would be worth studying in the highly turbulent regime, with pilot or bluff-body stabilization.

REFERENCES

1. Correa, S.M., Drake, M.C., Pitz, R.W. and Shyy, W., Twentieth Symposium (International) on Combustion, The Combustion Institute, p. 337, (1984).
2. Drake, M.C., Correa, S.M., Pitz, R.W., Shyy, W., and Fenimore, C.P., Combust. Flame 69, p. 347, (1985).
3. Correa, S.M., Gulati, A. and Pope, S.B., Combust. Flame, 72, p. 159, (1988).
4. Gulati, A. and Correa, S.M., AIAA Paper 87-1717, 21st Joint Propulsion Conference, San Diego, CA, (1987).
5. Correa, S.M., and Gulati, A., Twenty-second Symposium (International) on Combustion, Seattle, WA, August 1988.
6. Liew, S.K., Bray, K.N.C. and Moss, J.B., Combust. Flame 56, p. 199, (1984).
7. Pope, S.B. and Correa, S.M., Twenty-first (International) Symposium on Combustion, The Combustion Institute, p. 1341, (1986).
8. Masri, A.R., Bilger, R.W., and Dibble, R.W., "Turbulent Nonpremixed Flames of Methane near Extinction: Probability Density Functions", Combust. Flame, To appear 1988.
9. Dibble, R.W., and Magre, P., Combust. Flame, 73, p. 195, (1988).

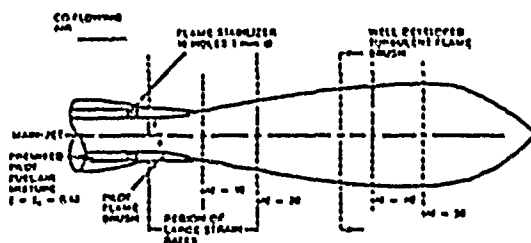


Figure 1. Burner & flame regions.

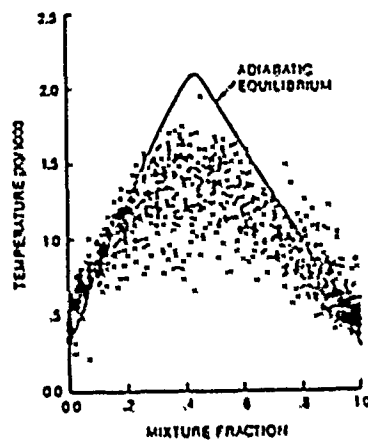


Figure 2. Scattergram at $x/d = 10$.

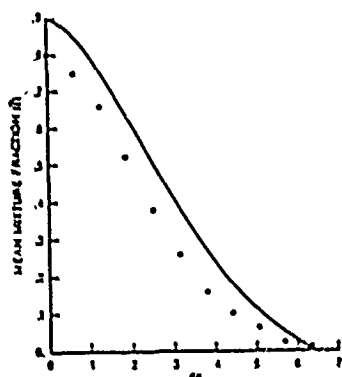


Figure 3. Mean mixture fraction at $x/d = 20$.

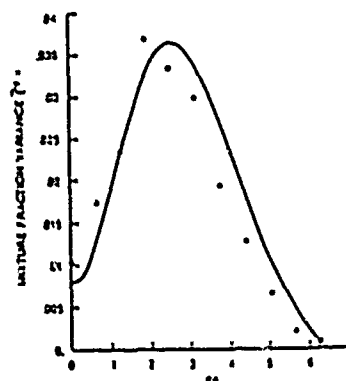


Figure 4. Variance at $x/d = 20$.

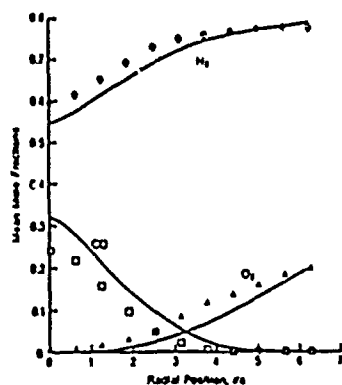


Figure 5. Selected species profiles at $x/d = 20$.

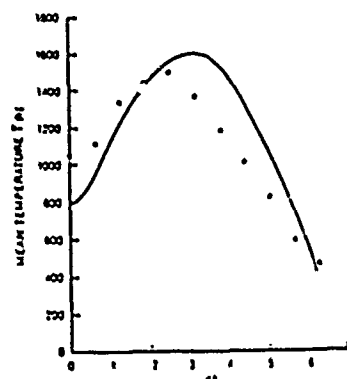


Figure 6. Temperatures at $x/d = 20$.

COMBUSTION RESEARCH

Work Unit 2308S705

W. M. Roquemore

Aero Propulsion and Power Laboratory

Wright-Patterson AFB, OH 45433-6563

SUMMARY/OVERVIEW:

Jet diffusion flames are being investigated in combined experimental and theoretical studies. The Reactive Mie Scattering (RMS) visualization technique is used in conjunction with advanced quantitative diagnostic techniques to characterize the dynamic effects that occur when fuel type, nozzle diameter and size, and flow rates are varied. The experimental studies are coupled with theoretical investigations in which time-dependent computational data bases are used to extract fundamental information about the processes occurring in jet diffusion flames. Combustion processes are primarily understood in terms of the behavior of mean properties. This research identifies and characterizes the underlying dynamic processes that contribute to the mean flow behavior involving mixing, transport, and heat release in nonpremixed jet flames.

TECHNICAL DISCUSSION:

Combustion studies are normally complicated by the numerous interactions between the fluid dynamics and chemistry effects that contribute to a measured result. Ideally, one strives to simplify the problem by studying flames that are established with simple burner geometries and by operating at conditions where the dominating processes are those of interest. Even after careful experimental design, the coupling effects are often sufficiently complex that they are hard to separate. Jet diffusion flames are often used in basic studies to gain insights into the processes that can occur in practical devices. Considerable data on statistical quantities, such as time averaged and rms values obtained with single point measurement techniques, have been obtained along with many details about the visible structure of jet flames. These data have contributed to an understanding of jet flames in terms of mean properties. Indeed, much of the current understanding of combustion is based on ideas of Reynolds averaging. Perhaps the development and utilization of computer based, Reynolds averaged models have reinforced the time averaged view. The Reynolds averaged approach has definite value for engineering applications and may be a necessity in many cases. Although this approach has proven successful, there is a danger of thinking about combustion in terms of time-averaged parameters. In some cases, it can mask the physics and chemistry that are germane to fundamental understandings. Unmixedness is a good example of this. It is masked by time averaged results and, in practical combusting devices, can cause hot streaks and reduced combustor efficiency. Our research is based on the premise that an understanding of the dynamics of processes is essential to a fundamental understanding of many combusting flows.

The long-term objective of this research program is to identify the underlying dynamic processes that are important in establishing the temperature, species concentration, and velocity fields in jet diffusion flames and develop a methodology for characterizing the conditions (fuel type, nozzle geometry, and flow rates) for which different processes are important. In addition, this program will provide powerful computational research tools that have been systematically developed and evaluated over a wide range of jet flame operating conditions and have general applicability to other burner configurations. It will provide a fundamental technical base on which

practical combustion devices, such as gas turbine combustors, can be better understood. This program is strongly coupled with other Air Force programs that link the jet flame studies with the development of combustor design models by several engine companies.

This research is being performed by scientists in several different laboratories. Experiments are being conducted at the Aero Propulsion and Power Laboratory (APPL) with part time participation of L. D. Chen from the University of Iowa; L. P. Goss, V. Vilimpoc, T. H. Chen, B. Sarka, D. D. Trump and M. E. Post of Systems Research Laboratories, Inc.; and T. A. Jackson, C. A. Obringer, and W. M. Roquemore of APPL. Two computational groups are also involved part time. They include R. W. Davis and E. F. Moore of the National Institute of Standards and Technology (NIST) who are studying propane flames and J. Ellzey, K. Laskey,⁺ and E. S. Oran of the Naval Research Laboratory who are studying hydrogen flames. Also, some experiments and analysis of the computational data are being performed at the University of Iowa under the direction of L. D. Chen. Results from some of these studies involving near laminar and turbulent flames are presented below.

The relative importance of the fluid dynamics as compared to the chemistry is a critical issue for understanding many combusting flows. This question is being addressed systematically in this program through combined experimental/computational studies. Davis and Moore at NIST have incorporated a flame sheet model with infinitely fast chemistry into a Navier-Stokes based, large-scale, time-dependent computer model that has proven to correctly describe the fluid dynamics in nonreacting flows. The combined experimental/theoretical approach is to start with a near-laminar, nonpremixed jet flame for which the flame sheet model with fast chemistry is expected to be valid. Experimental results are used to access how well the model is describing the observed dynamic processes. Likewise, the model results are used to gain insights into the dynamic processes in ways that cannot be addressed experimentally. Higher flow rate jets will be investigated in a similar manner after the experiments demonstrate that the model contains the correct physics and chemistry. Flame stretch and other effects will be added to the model as needed to describe flames for which the initial model proves incorrect. The desired result is a clearer fundamental understanding of the dynamic processes that contribute to measured results. It is believed that this combined approach will provide a more comprehensive understanding than can be achieved by independent experimental or theoretical approaches.

A buoyancy dominated near-laminar jet flame that has many distinguishing dynamic features was chosen for the initial NIST/APPL studies. The combined effort has yielded results such as those depicted in Fig. 1. The experiment consists of a 10 cm/s jet diffusion flame stabilized on a 22.5 mm diameter tube and burning a 50/50 mass mixture of propane and nitrogen. Thin-Filament Pyrometry (TFP) (Goss et al., *J. Eng. Gas Turb. and Power*, Vol. 111, pp. 46-52, 1989) is used to obtain nearly instantaneous and simultaneous radial temperature profiles at four axial locations in the flame. Good agreement between the experimental and numerical results are obtained in the first five jet diameters where the flame maintains an axisymmetric structure, Fig. 1. The digitized image of the sooting flame with background subtraction is shown in Fig. 1a along with the 15 μ m diameter SiC filaments used for TFP at four axial locations. The nearly instantaneous temperature profiles measured by the SiC filaments and those calculated by the model are overlaid on the calculated flame surface plot in Fig. 1b. The flame surface is represented by the squares. The filament measured temperature profiles are represented by the dotted curves with a lower cut-off temperature of about 1200 K. The temperature scale is from 0 to 2350 K. The phase of the experimental flame was chosen so that the shape of the experimental and theoretical flame surfaces are about the same. The agreement between the measured and calculated temperature profiles in Fig. 1b is good, but there are differences of more than 200 K at some locations that are not apparent at the compressed

⁺ Presently employed by Grumman Corporation, Space Station Program Support Division Reston, VA 22090.

temperature scale and may be the result of radiation losses and dissociation of products at high temperature.

Numerical solutions of the time dependent model are visualized by means of passive marker particles (See Fig. 1c). The numerical results show counterrotating vortex structures internal and external to the flame surface which interact and move downstream along with bulges in the flame sheet. These bulges account for one type of flame flicker. The model also predicates another type of flame flicker which occurs when the outer vortices periodically cut the tip of the flame. The predicted flicker frequency of 11 to 15 Hz is the same as that measured experimentally. When the gravitational acceleration is set to zero in the model, the outer structures disappear and the flame no longer flickers (no bulges). The predicted vortex structures bear close resemblance to those observed experimentally using the RMS laser sheet-lighting technique. However, the rate of development of the observed and theoretical flow fields is different. These and other differences are being examined in more detail at different times in the cycle of the flame motion.

The theory applicable to laminar diffusion flames has been extended to the turbulent case by conceptualizing the flame surface as wrinkled and stretched. With this approach, the turbulent flame is represented by an ensemble of stretched laminar flamelets. Takahashi et al., (Combust. Flame 48: 85-95, 1982) have shown that the transition from a laminar-like to a turbulent jet flame occurs for conditions where the turbulent fuel jet intersects the flame surface. Visualizations with the RMS technique have shown that the wrinkled appearance of a turbulent jet flame occurs when small vortices with high radial velocities "collide" with the visible flame surface (Roquemore et al., Turbulent Reactive Flows, Lecture Notes in Engineering, 40, 49-63, 1989). If the vortices have a sufficiently high velocity, they can punch a hole in the flame so that the flame sheet is no longer continuous. Recent, experiments performed by T. H. Chen et al., (AIAA-89-0153 and 0156) have provided quantitative data about the holes. The TFP method was used to make high speed radiation intensity measurements along a SiC filament located radially across a flame. Figure 2 shows a time trace sequence of these measurements in a turbulent methane jet flame operating near the flame lift-off condition. The pixel number is related to the distance across the flame. Two holes in the flame surface are evident. Events of different types were observed in measurements made higher in this flame. These events include: a sharp peak reminiscent of a thin flame sheet (i.e., a flamelet); a hole in the flame sheet; a thick flame region, or multiple, sharp temperature peaks. For this discussion, when one sharp peak per flame surface is observed the event is identified as a "flamelet". A "hole" is said to exist when no flame is present. All other events are specified as "other". The probability that these different events occur as a function of axial distances downstream are shown in Fig. 3. It is evident that the fraction of time a simple flamelet occurs decreases with downstream distance, while the fraction of time a hole occurs increases with distance. These data suggest that stretched, laminar flamelet theory might be applicable for this flame a large fraction of the time provided that provisions are made for the flame to be quenched at high strain rates. However, about 10% of a thin flamelet model could not be used and the hot zone appears to be broaden. These data also suggest that the formation of a hole by the dynamic interaction of a vortex with a reacting surface is analogous to the process of unmixedness. Finally, it is difficult to understand how theoretical descriptions of flames with intermittent holes can be fundamentally correct if they are based on theories using Reynolds averaging. Theories based on probability are more fundamentally appealing.

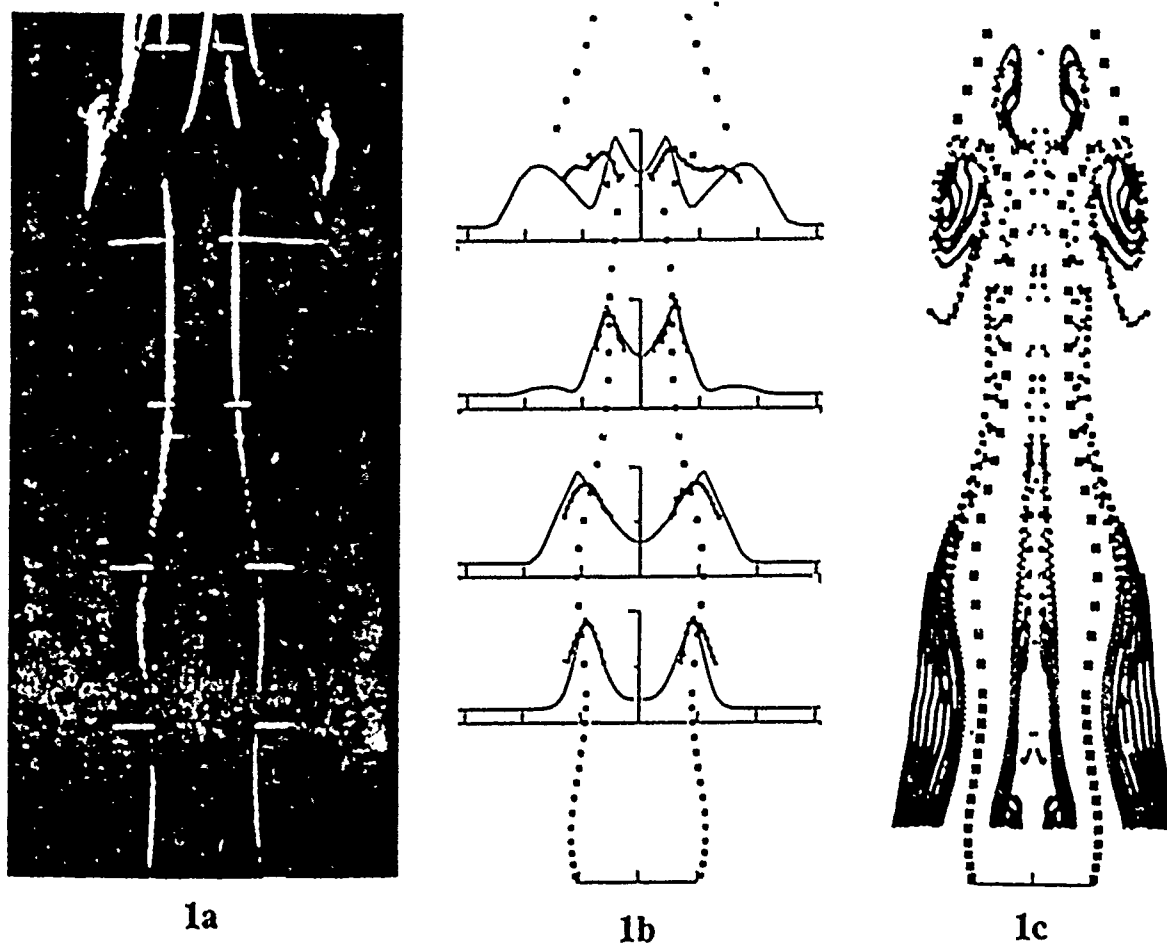


Fig. 1. 1a is a snapshot of a 50/50 propane/nitrogen mixture by mass with SiC filaments located at four axial locations. 1b is a computed flame surface with theoretical and experimental temperature profiles overlaid. 1c is a theoretical streakline plot of the flame shown in 1b.

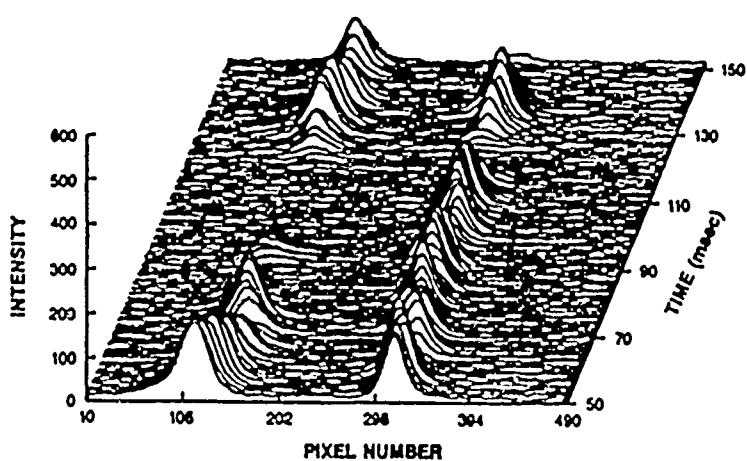


Fig. 2. Three-dimensional plot of TFP results for a near lifted methane flame.

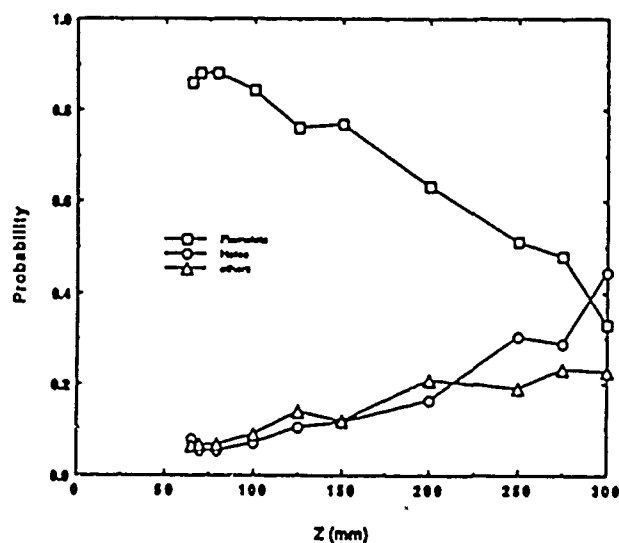


Fig. 3. Probability of flamelets, holes, and other events occurring in a near-lifted methane jet flame.

NUMERICAL INVESTIGATION OF TURBULENT FLAME SHEETS

(AFOSR - 88 - 0052)

Principal Investigator: Professor Stephen B. Pope

SUMMARY

In the flame-sheet regime, a premixed turbulent flame can be viewed as a surface that is convected, stretched and bent by the turbulence, and that propagates at the local laminar flame speed (relative to the fluid). Many of the basic processes involved are poorly understood. In this study, starting with material surfaces, we are using Direct Numerical Simulations of turbulence to study the behavior of surfaces. The two studies that have been completed this year are on the straining and curvature of material surfaces in isotropic turbulence. Work is in progress on similar studies for propagating surfaces.

TECHNICAL DISCUSSION

Introduction

An accurate physical model of a premixed flame (in the flame-sheet regime) is that combustion is confined to a thin sheet that can be regarded as a mathematical surface. This surface is convected by the fluid and propagates normal to itself at the (local) laminar flame speed. Many important questions related to the nature and evolution of these flame sheets are unanswered, because of inevitable experimental difficulties.

Our investigation starts with a simpler case: material surfaces in constant-density isotropic turbulence. While this case does not contain some essential features of premixed combustion, it is a necessary starting point for understanding the more complex circumstances.

The basic method employed is the Direct Numerical Simulation (DNS) of homogeneous, isotropic turbulence. Using a modified version of Rogallo's pseudo-spectral code, we perform 64^3 and 128^3 simulations, obtaining Taylor-scale Reynolds numbers up to $R_\lambda = 93$.

In addition to performing the Eulerian simulation, we track an ensemble (typically 8,000) of infinitesimal material area elements. Each element has a position $\mathbf{X}(t)$, an infinitesimal area $dA(t)$, an orientation ($\mathbf{N}(t)$ is the unit normal to the surface), and two principal curvatures $k_1(t)$ and $k_2(t)$ (by convention $k_1 \geq k_2$). Starting from specified initial conditions, an exact set of ordinary differential equations (Pope 1988) is solved to determine the evolution of these surface properties. These equations involve the fluid velocity and its first and second spatial derivatives following the elements. These quantities are extracted from the simulated turbulence field using the accurate cubic-spline interpolation method developed by Yeund and Pope (1988).

Straining on Material Surfaces

An essential process in turbulent combustion is the increase of surface area due to turbulent straining. For a material surface we have, simply,

$$\frac{d}{dt} dA(t) = dA(t) a(t), \quad (1)$$

where $a(t)$ is the strain-rate in the tangent plane of the surface. A material surface's area increases in time because $a(t)$ is predominantly positive. But this depends on the preferential alignment of the surface with the straining. For an arbitrarily orientated surface, the strain rate (denoted by $\alpha(t)$) is zero in the mean.

Figure 1 shows the pdf of a , $f_a^A(\hat{a})$, compared with that of α , $f_\alpha(\hat{\alpha})$, in a $R_\lambda = 93$ simulation. (All quantities are normalized by the Kolmogorov microscales.) It may be seen that the pdf of a is centered on positive values. But, nevertheless, there is 20% probability of negative (i.e. compressive) straining.

In the tangent plane of the surface there are two principal strains. When normalized by the Kolmogorov scales, these are denoted by S_1^* and S_2^* , with the convention $S_1^* \geq S_2^*$. Figure 2 shows the joint pdf of S_1^* and S_2^* . It may be seen that plane strain ($S_2^* = 0$) is more likely than axisymmetric strain ($S_1^* = S_2^*$); but there is a broad distribution without a single preferred state.

A more complete description of these results is provided by Yeung, Girimaji and Pope (1989).

Curvature of Material Surfaces

It is found that after about 15 Kolmogorov time scales, the curvature adopts a statistically-stationary distribution. In terms of the two principal curvatures ($k_1 \geq k_2$) we define the mean radius of curvature by

$$R \equiv (k_1^2 + k_2^2)^{-1/2}. \quad (2)$$

Figure 3 shows the pdf of R (normalized by the Kolmogorov length scale η). The mean value of R is 12η , and it may be seen that the distribution is essentially uniform for R less than about 10η . A consequence of this behavior is that the expectation of the mean square curvature

$$M \equiv \frac{1}{2}(k_1^2 + k_2^2), \quad (3)$$

is infinite.

The shape of area elements is characterized by

$$\theta \equiv k_s/k_\ell, \quad (4)$$

where k_s and k_ℓ are the smaller and larger (in absolute magnitude) of k_1 and k_2 . The values $\theta = 1, 0$ and -1 represent spherical, cylindrical and pseudo-spherical elements respectively. Figure 4 shows the joint pdf of θ and M . It may be seen that for moderate and large curvatures the elements are, with high probability, cylindrical.

These results, reported more fully by Pope, Yeung and Girimaji (1989) are consistent with the following, conventional, picture. Over most of the surface the straining tends to stretch the surface and to reduce its wrinkling. But in particular regions the surface is folded over, and subsequent straining increases the curvature at the fold. The line of the fold is curved much less than the curvature of the fold itself.

References

1. S. B. Pope (1988) "The evolution of surfaces in turbulence," International Journal of Engineering Science, 26, 445-469.
2. S. B. Pope, P. K. Yeung and S. S. Girimaji (1989) "The curvature of material surfaces in isotropic turbulence", submitted to Phys. Fluids A.
3. P. K. Yeung, S. S. Girimaji and S. B. Pope (1989) "Straining and scalar dissipation on material surfaces in turbulence: implications for flamelets", Combustion and Flame (to be published).
4. P. K. Yeung and S. B. Pope (1988) "An algorithm for tracking fluid particles in numerical simulations of homogeneous turbulence", J. Comput. Phys. 79, 373.

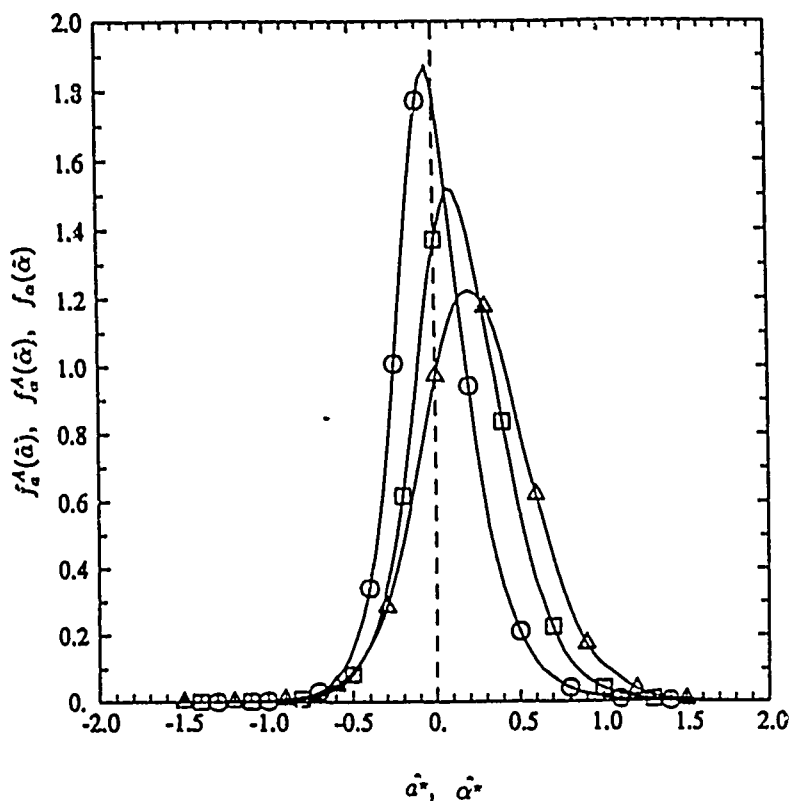


Figure 1: Probability densities of Kolmogorov-scaled strains acting on material and fixed surfaces, for the R_λ 93 case. Δ $\hat{\alpha}^*$ (area-weighted, slightly smoothed); \square $\hat{\alpha}^*$ (unweighted); \circ $\hat{\alpha}^*$ for fixed surfaces.

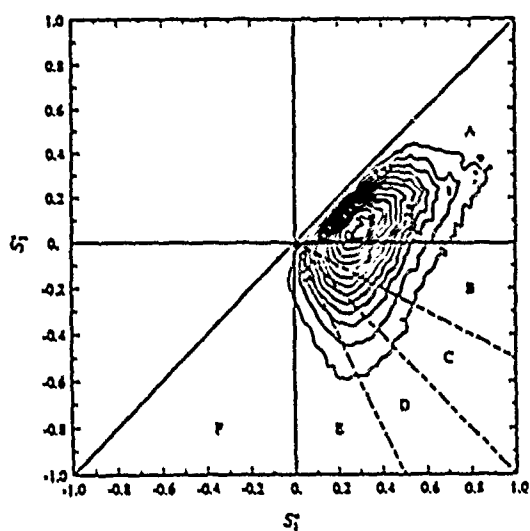


Fig. 2: Contour plot of (area-weighted) joint pdf of Kolmogorov-scaled principal surface strain components S_1^* and S_2^* from R_λ 93 data.

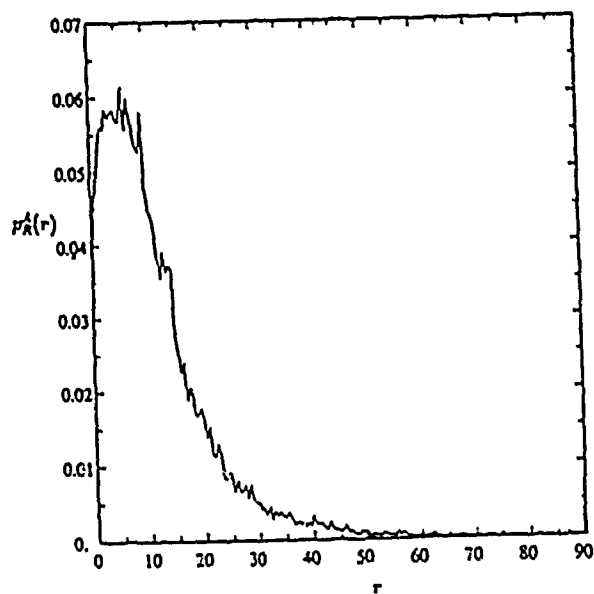


Fig. 3: Area-weighted pdf of normalized mean radius of curvature.

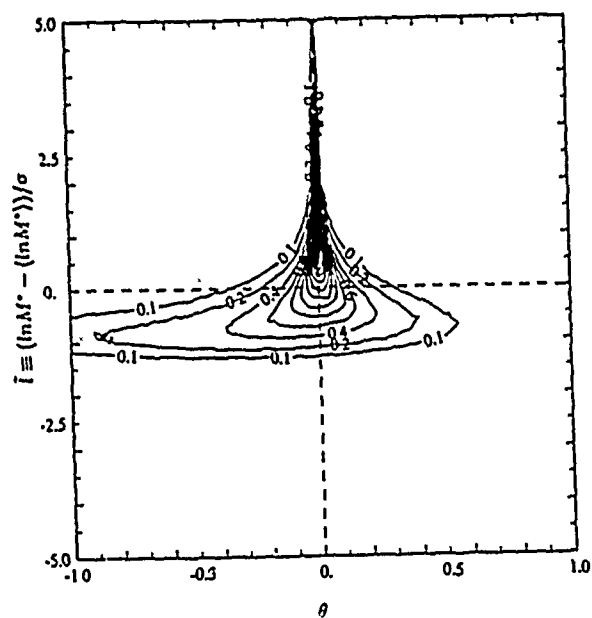


Fig. 4: Counter plot of the (unweighted) joint pdf of $\ln M^*$ and θ .

TIME DEPENDENT SIMULATION OF TURBULENT COMBUSTION

AFOSR ISSA 80-0025

Principal Investigators: Howard R. Baum and Ronald G. Rehm

National Institute of Standards and Technology
Gaithersburg, MD 20899

SUMMARY/OVERVIEW:

A mathematical model for diffusion controlled combustion in a turbulent eddy is presented. The model is intended as a computational "molecule" to be imbedded in larger scale reacting flow simulations. It consists of an exact solution of the 3-dimensional Navier Stokes equations for the vorticity field, an equation for the mixture fraction incorporating species and energy conservation, and the fluid expansion representing the feedback from the heat release. The use of models like this in conjunction with non-empirical large eddy simulations will lead to improved predictive capability for turbulent reacting flow systems.

TECHNICAL DISCUSSION:

The purpose of this work is the development of a mathematical model of diffusion controlled gas phase combustion appropriate for use in large eddy simulation of turbulent reacting flows. The basic idea is that while the large eddy simulation of necessity is highly dependent upon the geometrical and physical boundary conditions prescribed by the macroscopic problem of interest, the combustion phenomena are influenced primarily by local conditions near the fuel/oxidizer interface. Thus, by focusing attention on regions near the interface, a combustion model applicable to a wide variety of scenarios can be developed. In order to carry out such a research program, two basic tasks must be accomplished. First, the large eddy simulation must be capable of tracking a coarse-grained representation of the interface, so that a local frame of reference for the combustion analysis can be established. Second a solution to the combustion problem containing the local values of the large scale coarse grained variables as ambient parameters must be obtained. It is the latter task which is addressed in this research.

It is assumed that the fuel can be divided into a large number of subgrid scale parcels, whose location can be tracked by Lagrangian particle methods. Given an analysis capable of yielding the heat release rate for an individual fuel parcel, the composite heat release and fuel consumption rates are the sum of the locally computed rates over all fuel elements. In order to determine the rate of heat release of an individual fuel parcel, it is necessary to change the scale of the analysis and consider in detail how it burns.

The combustion process reach on the scale of an individual fuel parcel contains three essential ingredients. First, the molecular mixing of fuel and oxidizer and consequent release of heat; second, a local flow field on the scale of the fuel parcel characteristic of turbulence; finally, a mechanism

whereby the flow is modified by the combustion process. To address the first point we consider a highly idealized reaction in which fuel and oxidizer react instantly to produce carbon dioxide and water while releasing heat. We further assume that all species diffuse according to Fick's law with equal diffusivities, and that the Lewis number of the mixture is unity. These assumptions together with the equation of state allow all species mass fractions and thermodynamic variables to be uniquely related to a single mixture fraction variable. This variable is the fuel parcel and zero elsewhere.

Next, we consider an appropriate description of the local flow field. In a frame of reference moving with the large scale fluid motion, it is always possible to express the local velocity as the sum of a solenoidal (vortex-induced) flow and a potential flow. The solenoidal velocity field is assumed to be a transient vortex stretched by an imposed strainfield. This geometry is known to be characteristic of the velocity field in an individual turbulent eddy. In fact, it can be shown that the smallest length scale in this model emerges naturally as the Kolmogoroff scale. The velocity field employed is an exact solution of the constant property Navier-Stokes equations.

Finally, the feedback of the energy release on the local flow field is determined by the potential flow. The mass conservation equation relates the potential field to the local density changes. These changes, which are generated by the heat addition, lead to a non-linear relationship between the velocity potential and the mixture fraction. Thus, the final form of the combustion model is a non-linear three dimensional time dependent equation for the mixture fraction variable. The extraction of the desired heat release and fuel consumption information requires a solution of this equation subject to the initial condition stated above.

The solution to this equation is performed in two stages. First, two transformations of the dependent variable from the mixture fraction to an equivalent quantity, connected to it by different relationships on either side of the flame sheet, reduces the original mixture fraction equation to a linear diffusion-convection equation. This linear equation is the generalization to three dimensions of the constant property mixture fraction equation studied earlier. The second stage of the solution involves transforming the linear equation to a second set of Lagrangian independent variables, this one defined by the local solenoidal velocity field. This transformation of the independent variable largely eliminates the difficulties posed by the highly convoluted interface between fuel and oxidizer generated by the flow field. The solution in Lagrangian coordinates is obtained using asymptotic methods based on the assumption of large Reynolds number, together with a Fourier decomposition in terms of the cylindrical polar angular coordinate normal to the vortex direction.

Once the solution for the mixture fraction is known, the temperature and major species distributions in space and time can be readily determined. Figure 1 shows temperatures in a cross-sectional slice thru a plane perpendicular to the vortex axis half way between the center and edge of an originally spherical methane fuel element. The state relationship employed is the curve denoted "ideal" in figure 2. Also shown are experimentally determined state relationships obtained by Prof. J. Gore with differing assumptions regarding the fraction of chemical heat release radiated away x_R . Realistic fuel effects are incorporated in the model by replacing the idealized straight line (mixing only) relationships by those generated from

measurements in turbulent flames. A library of such relationships is currently being appended to the model.

As long as the fuel is burning vigorously, the above model should prove adequate for temperature and many major species. However, the role played by finite rate chemistry still needs to be addressed. Whether or not such effects can be accounted for in a one-dimensional mixture fraction state space (either transient or steady state) is an unresolved issue. A finite rate isothermal calculation based on the present author's exact solution of the self-similar "Marble problem" has been undertaken. The goal is to see the extent to which the solutions for the reactants, in this two dimensional time dependent problem can be mapped into universal curves in the state space. The reduced number of variables and parameters for this problem allow it to be accurately solved using similarity variables in Lagrangian coordinates. The outcome will provide guidance for the development of more general finite rate computations under development with NIST funds.

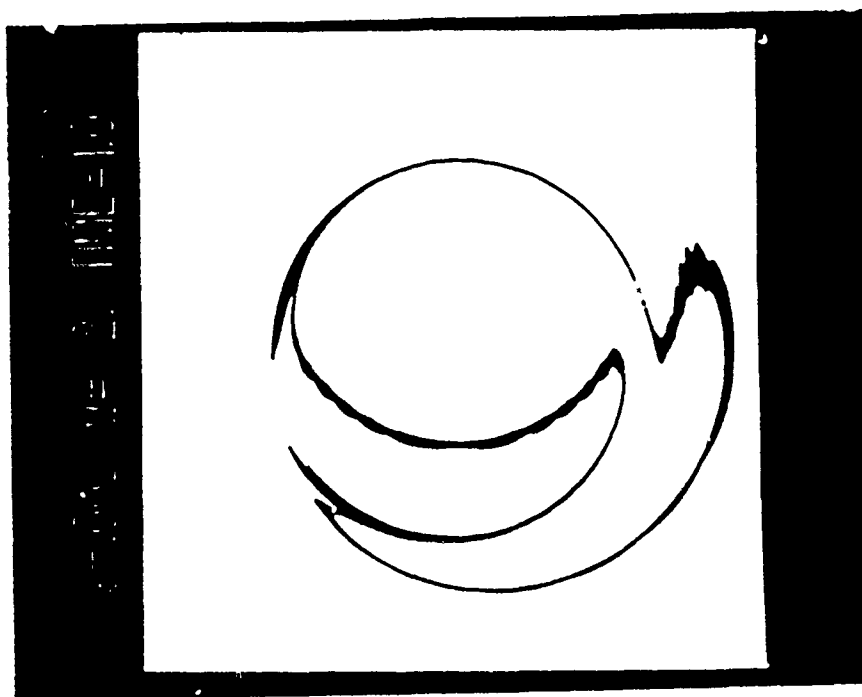


Figure 1. Temperature distribution in cross-section of turbulent eddy. Temperatures above 2000K are shown in black.

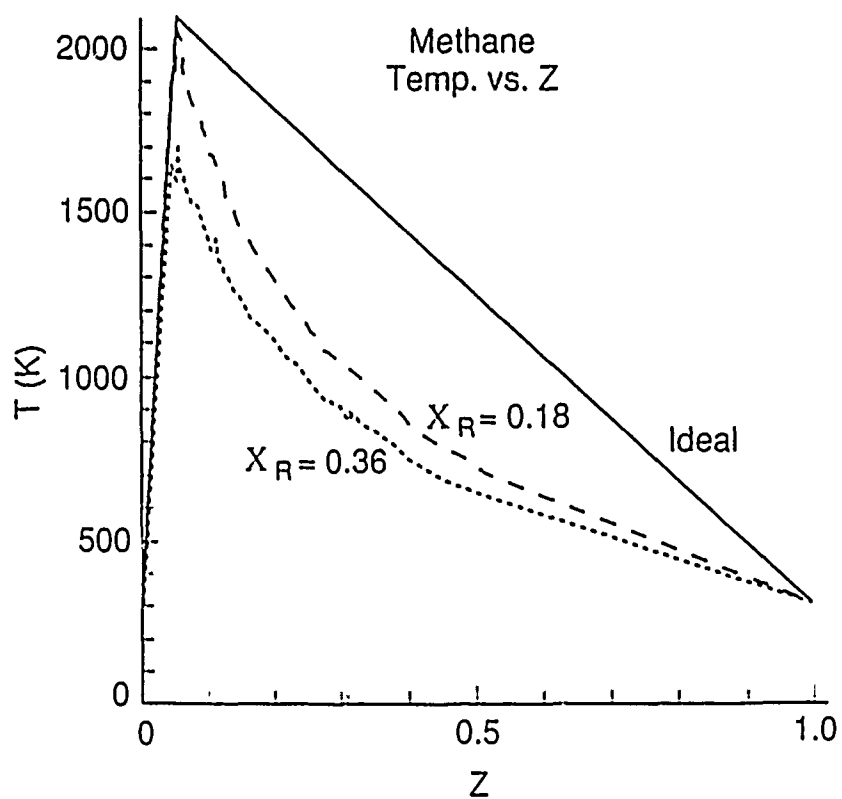


Figure 2. Ideal and experimentally determined state relations for methane.

NUMERICAL SIMULATION OF TURBULENT COMBUSTION USING VORTEX METHODS

(AFOSR Grant No. 84-0356)

Principal Investigator:

Ahmed F. Ghoniem

Department of Mechanical Engineering
Massachusetts Institute of Technology
Cambridge, MA 02139

SUMMARY/OVERVIEW:

The objectives of this research are to develop accurate numerical methods for the integration of the time-dependent, multi-dimensional Navier-Stokes equations for a chemically-reacting flow at high Reynolds number and moderate Damkohler numbers, and to apply these methods to analyze the mechanisms of flow-combustion interactions in turbulent reacting shear flow. We are working on extending the vortex element and the transport element methods, which are constructed to capture the large velocity and scalar gradients that arise in these flows, to chemically reacting steams. Attention is focused on low Mach number flows in which spatial pressure variations are neglected in the thermodynamics. Effort is also underway to extend the formulation to higher Mach number flows. In the following, we summarize some of the results obtained during the past year. Parts of the numerical methods and some of the results have been described in the publications listed at the end of the abstract.

TECHNICAL REPORT:

We have applied the transport element method [1,2,3] to study the effect of the Damkohler number on product formation in a two-dimensional reacting shear layer in which the two reacting species are initially flowing in different streams at different velocities. Analysis of the results of these two dimensional simulations was directed towards understanding the structure of the reaction zone and how the flow field affects the mode of combustion in this flow. Results of the numerical simulations reveal a strong similarity between the time-resolved spatial distribution of product concentration and vorticity. The proportionality between the product concentration, c , and the local absolute value of the vorticity, ω , depends on the Damkohler number, Da , and the Reynolds number, Re , and suggests the following relationship: $c(x,t) = f(Da, Re) \omega(x,t)$, where x and t are space coordinate and time, respectively, to describe the products field. This relationship may be used as a basis for turbulent combustion closure models.

Contour maps of the numerical results show that the product concentration is highest at the centers of the large eddies where vorticity is highest, and it is lowest within the braids between the large eddies where vorticity is lowest. In an isothermal reaction at high Damkohler number, products form at the outer edges of the eddies, within a thin reaction zone (a flame sheet), and are then entrained into the cores of the eddies by the prevailing strain field. In a temperature-dependent reaction, a similar mechanism is observed but with low reactivity between the large

eddies due to the cooling induced by the strain field and high reactivity at the centers of the eddies where the temperature is highest. At lower Damkohler numbers, the high reactivity zone moves closer to the center of the eddies and combustion takes place more in a premixed combustion mode (a distributed combustion mode [4,5]). Similar observations were made in numerical simulations of a reacting jet and a sample of the results, depicting the distributions of products, chemical reactivity and vorticity, are shown in Figure 1.

The dynamic effects of heat release at low Mach number, identified in our previous work as vorticity generation, due to baroclinic torque, and local acceleration, due heat to release, were investigated for premixed combustion in a shear layer configuration [6,7,8]. Results show that the effect of density stratification is the formation of vorticity which induces a finite convective velocity in the direction of the heavy stream (reactants), while transporting the center of the large eddies into the light stream (products) causing the entrainment into the large eddies to become biased towards the light fluid. Vorticity generation did not affect the strength of the eddies or the total rate of entrainment. Volumetric expansion, however, weakened the instability especially at high Damkohler numbers and large combustion heat release requiring the introduction of large initial perturbation to induce rollup. The reason behind this behavior is not yet clear to us although we suspect that the favorable pressure gradient associated with the flow acceleration may be important here. Similar effects are now being investigated in the diffusion flame shear layer configuration. (Note that the results in Figure 1 were obtained for compressible flow calculations, i.e. with a finite density ratio between the reactants and the products).

Three-dimensional simulations of shear layers are also being extended to a reacting compressible flow. Results for a non-reacting flow, shown in Figure 2, exhibit the interesting structure of the streamwise vorticity in a shear layer. Results show that after the maturation of the two-dimensional instability and the formation of the spanwise large vortex cores, two different instabilities are activated: (1) the translative instability which leads to the deformation of the core into/out of the streamwise and cross-stream directions and the formation of streamwise vorticity within the large cores; and, (2) the braid instability which leads to the formation streamwise vortex filaments which convolute the material surfaces within the braids while they wrap around the spanwise cores. The entrainment within the large eddies is enhanced by approximately 25% due to the onset of the three-dimensional instability. We are currently investigating the effects of density stratification and heat release on the shear layer structure. We are also computing the reacting shear layer to study the effects of the streamwise vorticity on the proposed relationship between the instantaneous, local product concentration and vorticity.

REFERENCES:

1. Ghoniem, A.F., Heidarinejad, G. and Krishnan, A. "Numerical Simulation of A Thermally-stratified Shear Layer Using the Vortex Element Method," J. Comput. Phys., 79, 1, 1988, pp. 135-166.
2. Ghoniem, A.F., Heidarinejad, G. and Krishnan, A. "Turbulence-combustion Interactions in A Reacting Shear Layer," Lecture Notes in Engineering, ed by Murthy and Borghi, Proceedings of the France-U.S.A. Joint Workshop on Turbulent Reactive Flows, July 1987, Rouen, France, Springer-Verlag, 1988.
3. Ghoniem, A.F., "Vortex Methods in Two and Three Dimensions with Application to Turbulent Shear Flows," Invited paper, Proceedings of the AIAA/ASME/SIAM/APS 1st National Fluid Dynamics Congress, Cincinnati, OH, July 24-28, 1988, p. 658.
4. Heidarinejad, G. and Ghoniem, A.F., "Vortex Simulation of the Reacting Shear Layer; Effects of the Reynolds and Damkohler Numbers," AIAA 27th Aerospace Sciences Meeting, Reno, Nevada, January 9-12, 1989, AIAA-89-0573.
5. Krishnan, A. "Turbulence-Combustion Interactions in Shear Flow," Ph.D. Thesis, Department of Mechanical Engineering, M.I.T., 1989.
6. Ghoniem, A.F. and Krishnan, A., "Origin and Manifestation of Flow-Combustion Interactions in A Premixed Shear Layer," Proceedings of the 22nd Symposium (International) on Combustion, University of Washington, Seattle, WA, August 14-19, 1988, The Combustion Institute, Pittsburgh, PA, in press.
7. Ghoniem, A.F. and Krishnan, A., "Mixing Patterns and the Generation of Vorticity in Density Stratified Flow," Proceedings of the International Workshop on the Physics of Compressible Turbulent Mixing, Princeton University, Princeton, NJ, October 24-27, 1988, in press.
8. Krishnan, A. and Ghoniem, A.F., "Numerical Simulation of the Structure of A Heated Jet in Cold Atmosphere," AIAA 27th Aerospace Sciences Meeting, Reno, Nevada, January 9-12, 1989, AIAA-89-0485.
9. Knio, O.M. and Ghoniem, A.F. "Numerical Study of A Three-dimensional Vortex Method," J. Comput. Phys., November 1988, in press.
10. Knio, O.M. and Ghoniem, A.F., "Three-dimensional Simulation of the Entrainment Augmentation Due to Streamwise Vortex Structures," AIAA 27th Aerospace Sciences Meeting, Reno, Nevada, January 9-12, 1989, AIAA-89-0574.

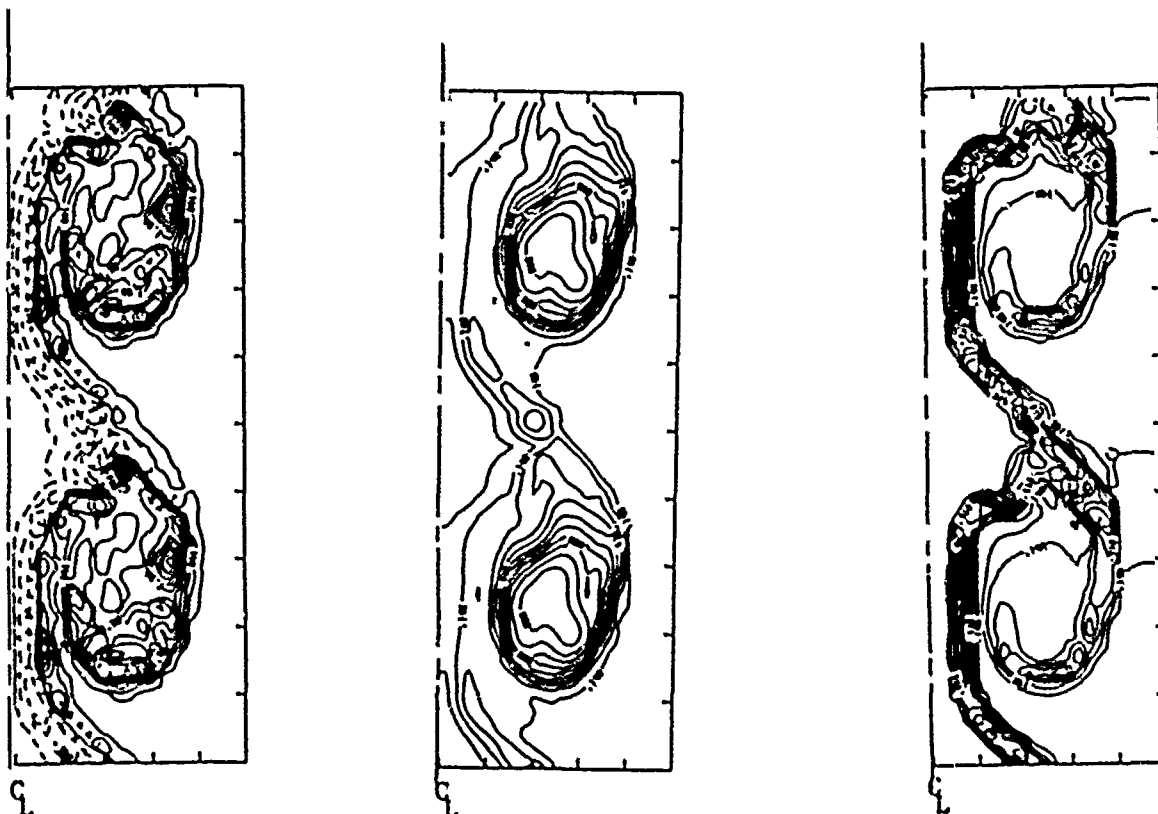


Figure 1. The vorticity, product concentration and chemical activity, shown from the left in this order, in the field of a two-dimensional reacting jet. The Damkohler is number based on the size of the eddies, the velocity ratio across the jet and the chemical time is 3.0. The reactants/products density ratio is 4.0. The figures show the right half of the jet across the centerline.

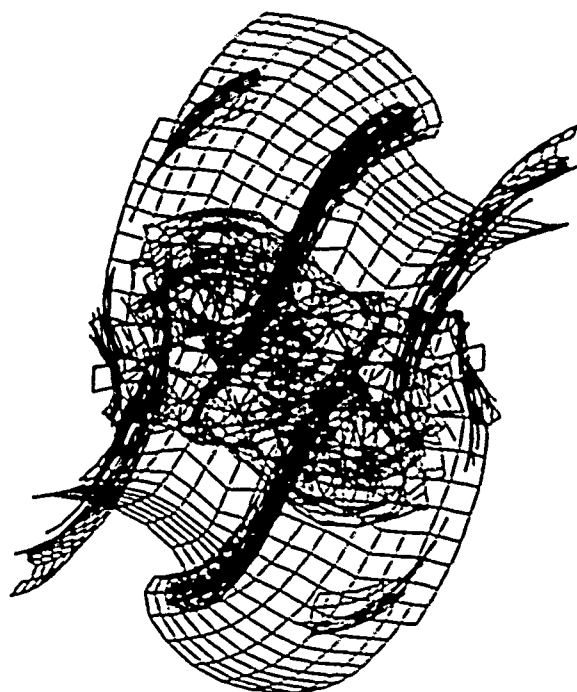


Figure 2. The shape of the material surface initially located at the mid point in a periodic shear layer at the late stages of the development of the instability showing the spanwise core after being deformed due to the translative mode, and the streamwise vortex filament within the braids due to the core deformation.

9

FUNDAMENTAL STUDIES ON SPRAY COMBUSTION
AND TURBULENT COMBUSTION

AFOSR Grant #860016D

Principal Investigators: W.A. Sirignano
G.S. Samuelsen
R.H. Rangel

Department of Mechanical Engineering
University of California, Irvine
Irvine, CA 92717

SUMMARY

The analysis of species concentration distributions in a non-reacting mixing layer continued during the current year. The new efforts were directed to improve the simulation of the effect of the splitter plate upstream of its edge and the calculation of the concentration field including the superposition of solutions for more than one vortex.

The modelling of a shear layer by an infinite row of vortices is able to explain the distortion of an initially planar interface downstream of a splitter plate. However, the presence of the splitter plate upstream of the vortices invalidates the symmetry of the flow field. Therefore, a numerical scheme that simulates the periodic birth of the vortical structures one by one in time is being undertaken to model the relative growth of the vortices as they travel downstream.

In the previous calculations of the species concentration field, only one vortex among the infinite row of vortices was taken into account in the construction of the solution by superposition of the contributions corresponding to neighboring material elements. In order to gain a better understanding of the mixing phenomena in a broader flow domain it is important to include more than one vortex in the analysis. This novel feature gives insight into the interaction between the vortical structures when molecular diffusion is taking place. The concentration field is then computed by an instantaneous tracking of the interface material elements corresponding to three vortices at the present time. The results obtained do not differ significantly from those obtained using the single vortex, generalized to more than one vortex, as it is shown in Fig. 1, for the instantaneous species concentration contours corresponding to three vortices. However, since a more realistic calculation relies on the previous knowledge of the shape of the interface, this problem is strongly coupled with the definition of the velocity field. Because of this, the development of a solution for the effect of the splitter plate will also determine the behavior of the concentration profiles.

The nonlinear analysis of entrainment and mixing in the field of pairing and merging vortical structures has continued during this

reporting period and is expected to provide useful information on entrainment rates in a developing vortical flow such as a mixing layer. The effort has been and will be concentrated on the calculation of streamlines and pathlines during the evolution of the flow field from its initial configuration as a vortex sheet to the final configuration consisting of two or more rolled-up and merged vortex structures. Realize that because of the unsteady character of the flow, it is difficult to characterize the flow pattern by using streamlines alone and therefore, the information from these as well as the other flowlines are required. Figure 2 shows the development of the streamlines for a case in which a vortex sheet evolves into two vortical structures which eventually pair. In addition to this, the diffusion of a passive scalar is calculated using a finite-difference approach with the velocity field obtained from the vortex-dynamic calculation. The effect of the pairing and merging process on the molecular diffusion process can thus be understood. The pdf analysis of the mixing process will continue during this year in order to investigate the existence or not of a preferential entrainment rate from the high speed stream. We have observed a characteristic antisymmetry of the entrainment rates and of the mixing process when looking at the temporal evolution of the layer without the effect of the downstream evolution. Some of our attention during this year will be focused on obtaining some estimates of the entrainment and mixing characteristics, in particular concerning the mixing bias, when the spacial evolution as well as the temporal one is considered. Figure 3 shows the nonlinear evolution of four vortical structures, with the two on the right (downstream) pairing before the two on the left (upstream).

PUBLICATIONS

Rangel, R.H. and Sirignano, W.A., "The Dynamics of Vortex Pairing and Merging," AIAA 27th Aerospace Sciences Meeting, Preprint No. 89-0128, 1989.

Miralles-Willhelm, F.R., Rangel, R.H., and Sirignano, W.A., "An Analysis of Molecular Diffusion in a Vortical Structure: Bias in PDF Measurement," AIAA 27th Aerospace Sciences Meeting, Preprint, No. 89-0482, 1989.

contour interval: 1.00E-01 from: 0.00E+00 to: 1.00E+00 $t = 0.25$

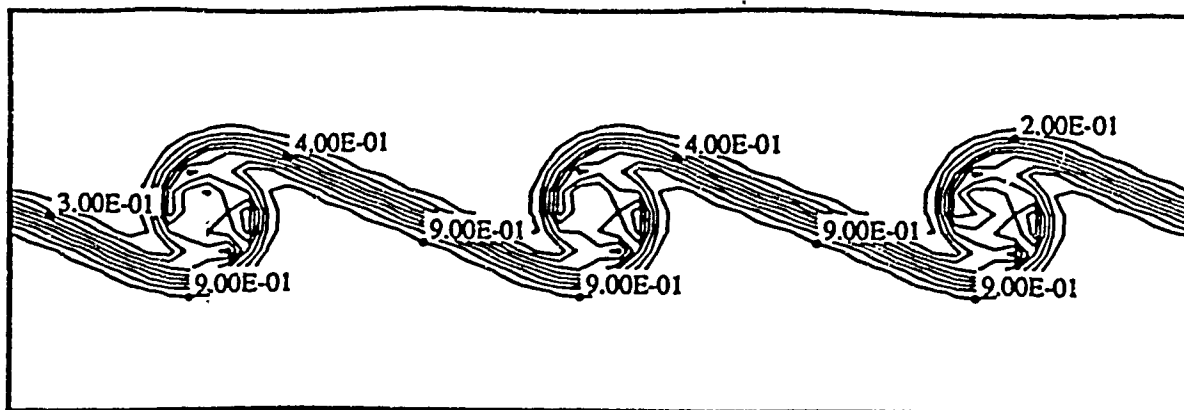


Figure 1. Caption on the next page.

contour interval: 1.00E-01 from: 0.00E+00 to: 1.00E+00 $t=0.75$

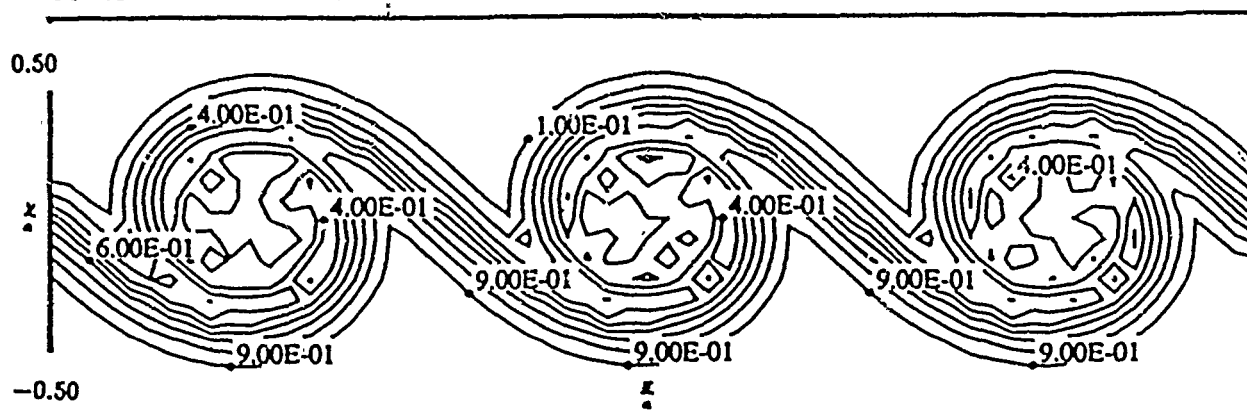
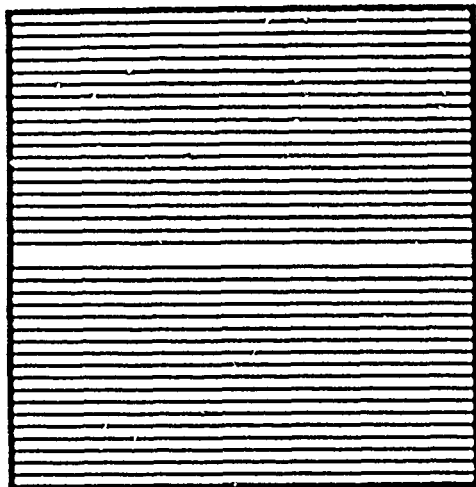
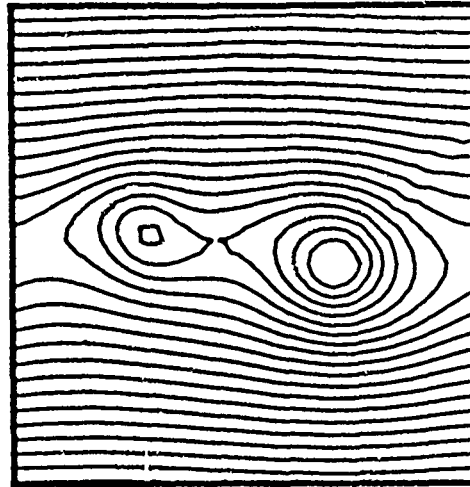


Figure 1: Species Concentration contour plots for $Re=50$ and $Sc=1$. Solution for three vortices.

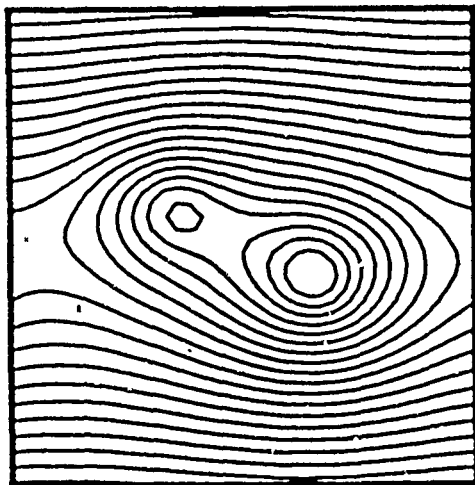
$t=0.00E+00$
contour interval: 2.50E-02 from: -4.75E-01 to: 2.50E-02



$t=1.00E+00$
contour interval: 2.83E-02 from: -5.40E-01 to: 2.51E-02



$t=2.00E+00$
contour interval: 2.89E-02 from: -5.53E-01 to: 2.43E-02



$t=3.00E+00$
contour interval: 2.98E-02 from: -5.71E-01 to: 2.58E-02

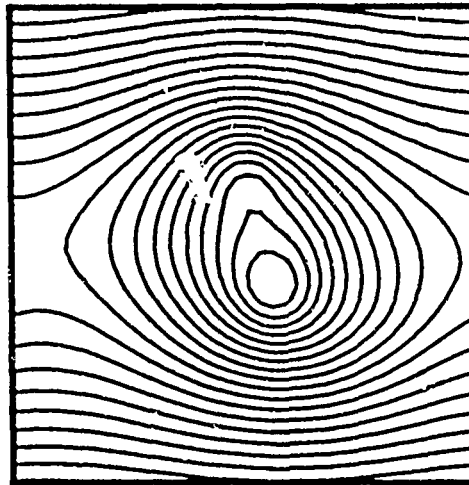


Figure 2. Streamlines during the rollup and pairing of two vortical structures

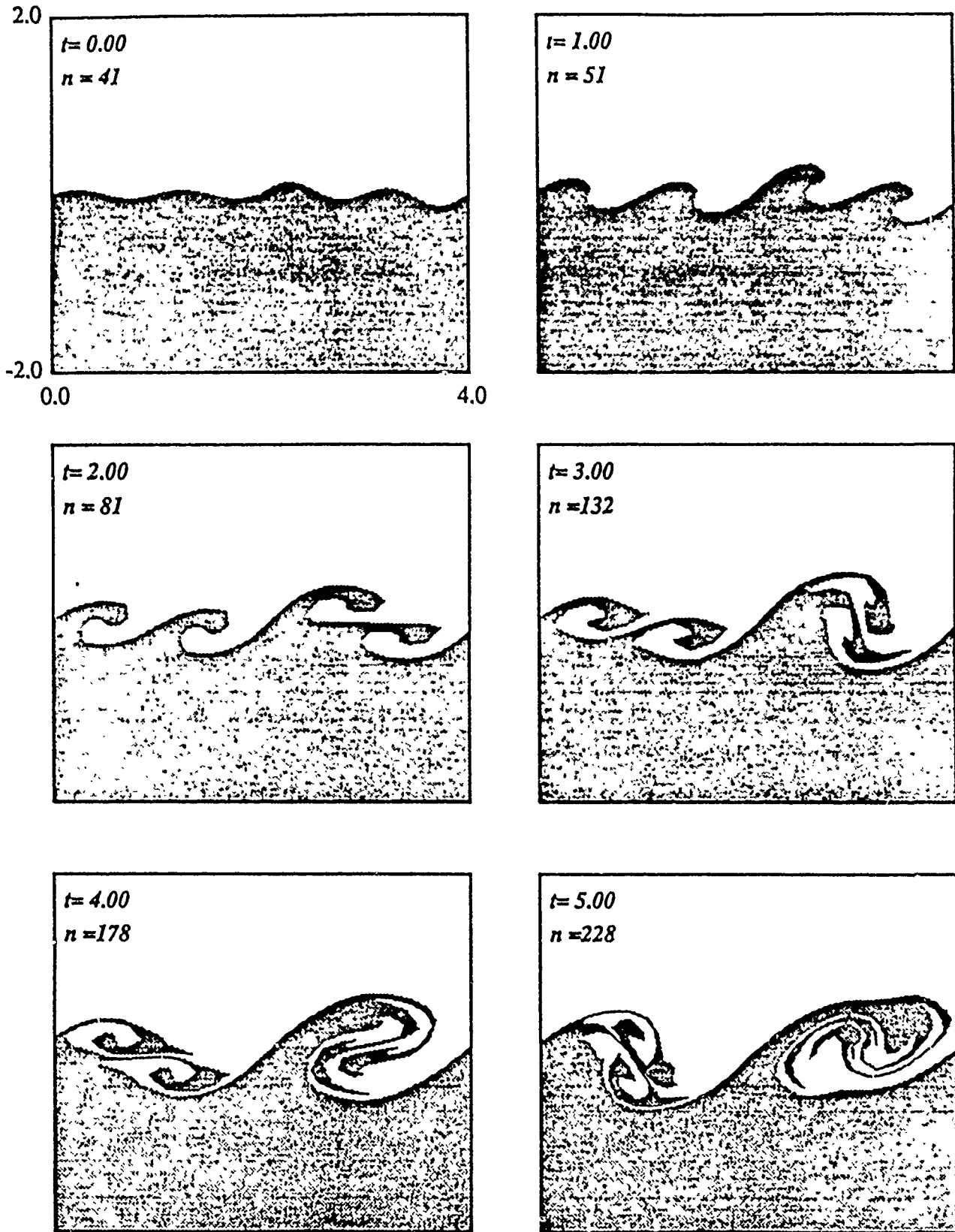


Figure 3. Nonlinear evolution of four vortical structures with induced sequential pairing by the first subharmonic.

PHYSICAL STATE DEPENDENCE AND MECHANISTIC RELATIONSHIPS BETWEEN DECOMPOSITION AND COMBUSTION

Scott A. Shackelford

Frank J. Seiler Research Laboratory (AFSC)
USAF Academy, Colorado 80840-6528

Condensed phase Kinetic Deuterium Isotope Effect (KDIE) investigations conducted with HMX and its HMX-d₈ deuterium labeled analog during their ambient pressure decomposition process, selectively defines the mechanistic feature that controls its rate of energy release,¹⁻³ and further reveals a varying mechanistic dependence upon HMX's physical state.^{1,3} Additional KDIE investigations conducted during progressively more drastic exothermic HMX incidents like pyrolytic decomposition/deflagration,¹⁻³ combustion,³ thermal explosion⁴, and detonation,² display a common thread for comparing the mechanistic similarities and differences that promote or generate these high energy incidents.⁴ While a review of the KDIE investigations conducted with HMX provides the most complete description of these high energy incidents, condensed phase KDIE investigations with the TNT/TNT-d₃,^{5,6} TATB/TATB-d₆,⁷ and RDX/RDX-d₆,^{2,8} systems also display rate-controlling mechanistic data in decomposition which correlates with key mechanistic features in combustion,⁸ thermal explosion⁷ and detonation^{2,5,6} events. When reviewed in total, these KDIE investigations produce several new insights potentially important for elucidating the critical combustion behavior of energetic materials:

- a. An energetic material's rate-controlling mechanistic feature can change as its physical state is altered.
- b. Rate-controlling mechanistic features found during an energetic material's decomposition process also can be present in its high pressure combustion event.
- c. An energetic material's combustion event can display a substantial degree of kinetic control where its inherent optimized burn rate probably can be modified or tailored only by chemically altering its rate-controlling mechanistic feature.
- d. An energetic material's rate-controlling mechanistic feature may come from a specific chemical reaction step in the combustion event's condensed phase decomposition/deflagration process which then feeds low molecular weight products to the gaseous flame oxidation process.
- e. The rate-controlling mechanistic feature that determines a pure energetic material's burn rate, can be the same as that which controls a propellant formulation's burn rate.
- f. Computational modeling development must be extended into condensed phase combustion processes in order to produce a reliable computer code which fully characterizes solid propellant behavior and accurately predicts its performance.

Conventional energetic materials associated with solid propellants and explosives can release their stored chemical energy through different types of exothermic incidents. These range from the mild ambient pressure decomposition process to the more rapid pyrolytic decomposition/deflagration process and into the progressively more hostile higher pressure/temperature events represented by combustion, thermal explosion, and

detonation. Since these latter three events must convert solid energetic materials to gaseous products, the decomposition/deflagration process must play a role in these high energy phenomena. Combustion scientists have long sought to understand the combustion event from two major perspectives. First, theoretical computational researchers seek to accurately model the combustion characteristics of an energetic material or propellant formulation in order to develop computer codes that correctly predict propulsion performance. Secondly, experimental researchers attempt to characterize and quantify combustion behavior in order to control propellant burn rates and tailor these burn rates for specific propulsion applications. In both cases, a more thorough understanding of the rate-controlling mechanistic features inherent to the combustion event's behavior and its resultant burn rate is needed, both in pure energetic materials and propellant formulations based upon them. An energetic material's chemical structure, resultant physical properties and physical state can affect its mechanistic behavior in terms of reactivity and kinetics; this presentation reviews recent experimental chemical investigations that provide new mechanistic insights relevant to a more detailed conceptual description of the combustion event. Condensed phase Kinetic Deuterium Isotope Effect (KDIE) investigation provides these new mechanistic insights when the KDIE is applied to the energetic materials like HMX and RDX.

The KDIE results from a difference in zero point vibrational energy between a compound's carbon-hydrogen (C-H) bond and its stronger analogously labeled carbon-deuterium (C-D) chemical bond as illustrated with the HMX and HMX-d₈ chemical structures (Figure 1). These dissimilar bond energies cause reaction rate differences between the two compounds, providing the C-H/C-D bond, or one in its near vicinity, ruptures in the slowest chemical reaction occurring during the complex high energy process or event.

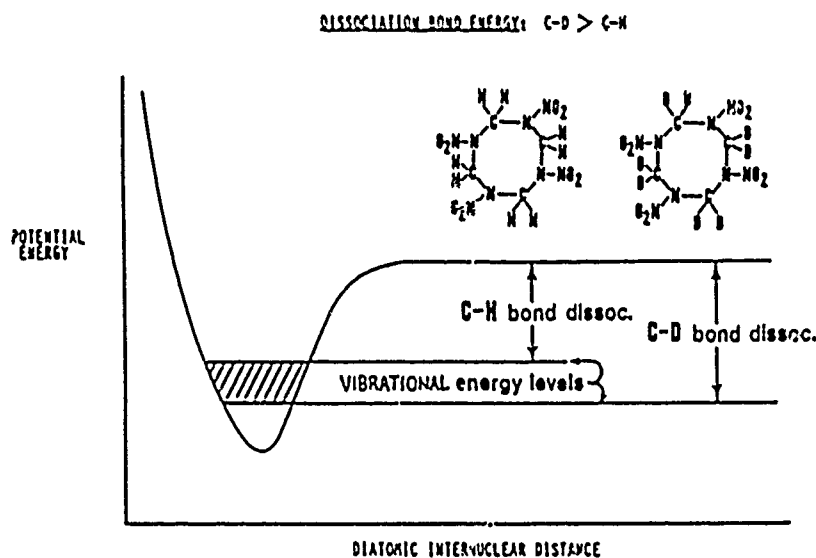


Figure 1

This slowest rate-controlling mechanistic chemical reaction or reaction step is not necessarily the first one to occur along a reaction pathway, but in some cases, can be the first step. Because this rate-controlling reaction step happens during the slowest chemical reaction occurring among many, this mechanistic feature provides the kinetic control which ultimately determines the overall rate of a high energy incident. The first application of the condensed phase KDIE with an energetic material involved an ambient pressure decomposition investigation of liquid TNT and its TNT-d₃ analog (Figure 2) using

isothermal differential scanning calorimetry (IDSC).⁵ Rupture of the methyl group's C-H bond proved to be the mechanistic rate-controlling feature; but just as importantly, this KDIE investigation revealed the rate-controlling C-H bond rupture resulted from a chemical reaction occurring only to a minor extent during in the very early stage of the entire decomposition process.

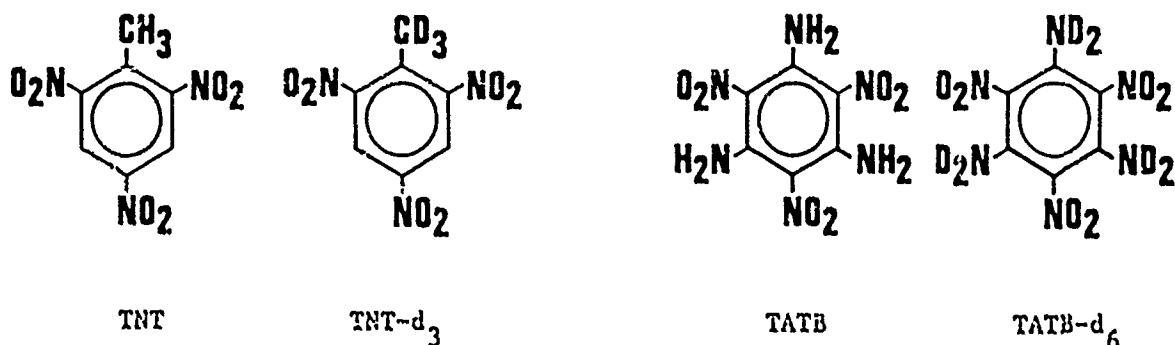


Figure 2

The overall autocatalytic decomposition process's rate for TNT is controlled by the rate at which C-H bond rupture occurs with a small concentration of TNT molecules in the bulk sample during the decomposition's induction period (Figure 3) to form a catalytic material. This chemical reaction occurs only to a limited extent, but provides a threshold concentration of catalyst which in turn promotes the exothermic autocatalytic TNT decomposition. The most prominent or obvious chemical reactions of an exothermic process, therefore, may not be those that actually control it, but instead, the rate-controlling mechanistic feature may come from a reaction which proceeds to a very low degree and with no measurable heat evolution. A similar KDIE study of solid TATB and TATB-d₆ (Figure 2) using IDSC analysis also displayed a rate-controlling feature wherein N-H bond rupture kinetically controlled its overall decomposition process in an early stage.⁷

a THERMOCHEMICAL DECOMPOSITION OF LIQUID TNT & TNT-d₃

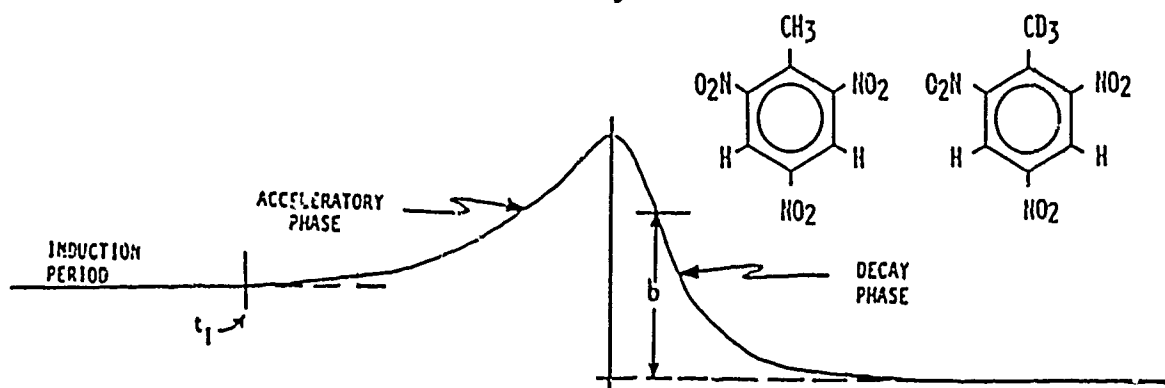


Figure 3

Because of its chemical structure, three different types of KDIE potentially could result from HMX, and each would represent a different rate-controlling feature (Figure 4). A KDIE investigation of HMX and HMX- d_8 by IDSC analysis also revealed an early rate-controlling mechanistic feature in its overall decomposition process during the induction period.¹ Three dissimilar KDIE values actually were found during the entire HMX decomposition, and each occurred in a different physical state (Figure 5).¹

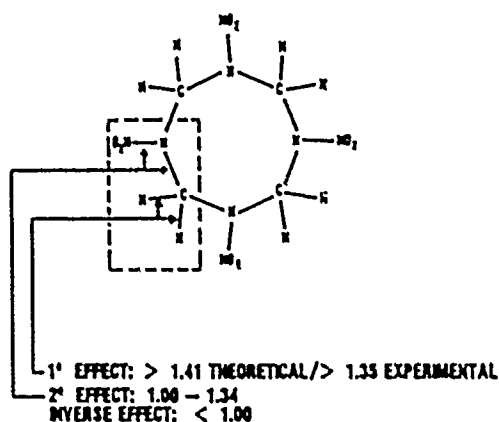


Figure 4

The early induction periods revealed a primary (1°) KDIE indicating C-H bond rupture controls solid state HMX decomposition, while a 2° KDIE revealed that ring C-N bond rupture controls liquid state decomposition. The short lived mixed melt phase afforded an apparent inverse KDIE suggesting that a thermal weakening of the intermolecular crystal

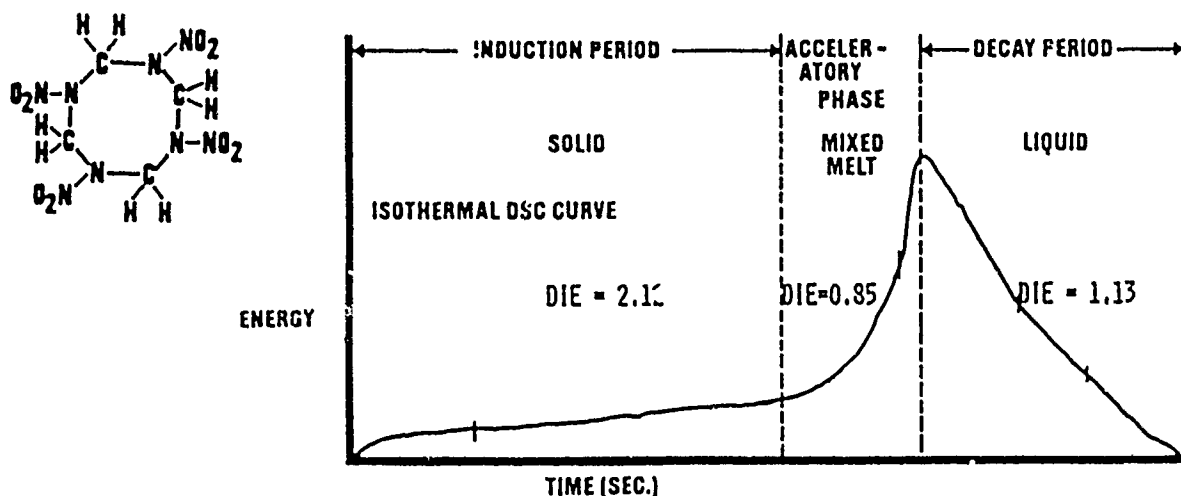


Figure 5

lattice forces constitutes its rate-controlling feature. These results show the HMX decomposition is not a single mechanistic pathway with one rate-controlling step; rather, it is a process consisting of at least three different rate-controlling mechanistic features that each are dependent upon one predominant HMX physical state.¹ Several other KDIE investigations with more hostile energetic incidents support this conclusion. A solid state pyrolytic decomposition/deflagration study produced a 1^o KDIE indicating C-H bond rupture to be this process's rate-controlling step.¹ The first KDIE investigation of energetic material sensitivity involved the thermal explosion event and permits correlation an energetic material's critical temperature to IDSC determined condensed phase KDIE values.⁷ A comparison of HMX and HMX-d₈ critical temperatures determined from thermal explosion revealed an inverse KDIE. This would mean the HMX thermal explosion event occurs primarily in the HMX mixed melt phase where the controlling mechanistic feature depends upon the rate at which the intermolecular crystal lattice forces are weakened by thermal activation.¹ A KDIE investigation of HMX and HMX-d₈ in the most hostile high energy event of all, detonation, showed HMX-d₈ required a slightly higher impact velocity than unlabeled HMX when an exploding foil initiation method is used.² This small positive (1^o or 2^o) KDIE demonstrates that like the HMX pyrolytic decomposition/deflagration process and the thermal explosion event, condensed phase mechanistic features could control the rate at which a chemical reaction process promotes or generates this detonation event. The indirect nature of this detonation KDIE does not allow quantitative differentiation between solid state C-H bond rupture (1^o KDIE) or liquid state C-N bond cleavage (2^o KDIE) as being the possible rate-controlling feature. However, recent high pressure diamond anvil cell/FTIR HMX decomposition experiments in the GPa pressure range⁹, showed HMX remains in the solid state at such extreme pressures; this result, therefore, might favor the 1^o KDIE solid state C-H bond rupture as being the detonation event's rate-controlling mechanistic feature.^{4a} This could mean the HMX pyrolytic decomposition/deflagration process and detonation event both possess some kinetic control from solid state C-H bond rupture, and that only the thermally activated thermal explosion event proceeds by a different mechanistic rate-controlling feature operating in the HMX mixed melt phase. Thus, the kinetically controlled mechanistic features found during ambient pressure decomposition can mirror those energetic events found in more drastic high energy events like thermal explosion and detonation; but is there a correlation with the combustion event?

The high energy combustion event falls in a temperature/pressure/time regime between the pyrolytic decomposition/deflagration process and the thermal explosion event. Combustion undoubtedly is a very complex phenomenon involving both chemical and physical interactive processes proceeding among various condensed and gaseous physical states. All three HMX condensed phase states (solid, mixed melt, liquid) could be present during combustion, and the far more extensively studied gas phase flame portion is represented with several flame stages and reaction zones.¹⁰⁻¹² In order to discuss the combustion event's rate-controlling mechanistic features for comparison to those processes and events already addressed, the combustion event is viewed as consisting of two major portions: (1) a condensed phase decomposition/deflagration process for producing the gaseous species found in the second process, (2) the gaseous flame oxidation process which produces the final combustion products (Figure 6).³ Each process considered separately, would have its own rate-controlling mechanistic step; but, of the two, one logically would occur more slowly.

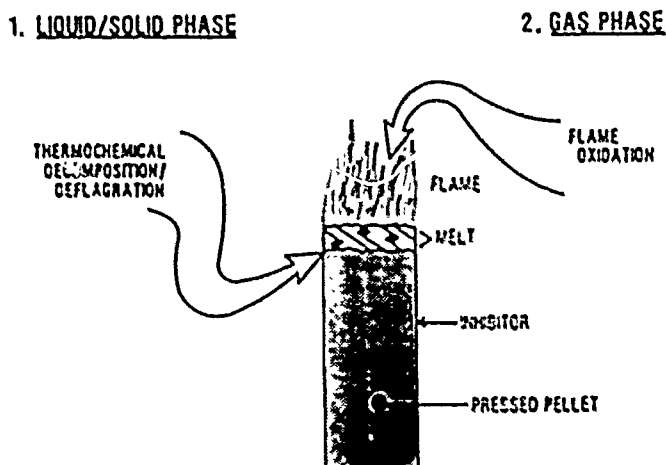


Figure 6

This slower rate-controlling feature ultimately would determine the HMX burn rate. High pressure window bomb combustion (3.6–10.4 MPa) of cylindrical pressed HMX and HMX- d_8 pellets produced significant KDIE values from comparative burn rates; this verifies a substantial degree of kinetic control for this event (Table 1).³

Table I. HMX/HMX- d_8 Combustion KDIE Values.

Temperature	500 psig (3.55 MPa)	1000 psig (6.99 MPa)	1500 psig (10.4 MPa)
Expl (553K) ¹³	1.37 ± 0.22	1.60 ± 0.16	1.24 ± 0.20
Std (298K)	3.26	3.80	2.95

The KDIE magnitudes reveal an apparent 1^o KDIE at 3.55 and 6.99 MPa pressures; the value at 10.4 MPa at first glance appears low for a 1^o KDIE, but is within the experimentally accepted minimum 1^o KDIE of 1.35¹⁴ at a 95% confidence level statistical variation. The possibility the KDIE at 10.4 MPa represents a very large 2^o KDIE and a resultant mechanistic change to a different rate-controlling step, is not discarded;^{3a} but, when the experimental KDIE values are mathematically extrapolated to standard temperature,¹³ a 1^o KDIE remains plausible when one considers the maximum 2^o KDIE at standard temperatures theoretically would be 1.74 squared or 3.03.¹⁵ The 1^o KDIE reveals that ultimately, C–H bond rupture kinetically controls the global HMX burning rate to a very large degree. When compared to the KDIE results of HMX's atmospheric pressure decomposition and pyrolytic decomposition/deflagration processes, the 1^o KDIE combustion value suggests this rate-controlling C–H bond rupture may occur in the solid state decomposition/deflagration process of the combustion event. While the gas phase flame oxidation process could have its own kinetically controlled mechanistic feature, past studies with HMX and RDX decomposition in different physical states within a similar temperature range, show an increase of rate as one proceeds from the solid to liquid to gaseous states.¹⁶ It is, therefore, quite possible that the observed kinetic rate-controlling C–H bond rupture occurs most slowly in the solid state and that condensed phase kinetics ultimately exercise substantial mechanistic control over the global HMX burn rate.³ Condensed phase HMX burn rate control also has been postulated recently from other experimental findings.¹⁷ KDIE investigations of RDX and RDX- d_8 by thermogravimetric

analysis (TGA)² and IDSC⁸ show a 1° KDIE for RDX decomposition as does a KDIE investigation of the RDX combustion event (Table II).⁸

Table II. RDX Decomposition and Combustion KDIE Values

Decomposition	1.50 (TGA) ²	1.74 ± 0.17 (IDSC) ⁸
	<u>500 psig (3.55 MPa)⁸</u>	<u>1000 psig (6.99 MPa)⁸</u>
Combustion	1.37 ± 0.16	1.46 ± 0.23

Values reported to the 95% confidence level

This could suggest RDX's burn rate may also be determined from a rate-controlling kinetic C—H bond rupture in one of its condensed phases (solid or liquid).

Recently, the first KDIE formulated nitramine propellant investigations conducted in a high pressure window bomb at 6.99 MPa, show the same rate-controlling mechanistic step as that observed for their pure HMX and RDX compounds (Table III).¹⁸

Table III. HMX and RDX Propellant Formulation Combustion KDIE Values

<u>Temp (K)</u>	<u>Pure Compd</u>	<u>KDIE</u>	<u>Propellant</u>	<u>KDIE</u>
Expl (553) ¹³	HMX	1.30 ± 0.05	HMX/CW5	1.29 ± 0.09
Std (Calc)		3.09		3.07
Expl (673) ¹⁷	RDX	1.31 ± 0.04	RDX/CW5	1.24 ± 0.05
Std (Calc)		3.73		3.53

Maximum theoretical 2° KDIE (298K) is $(1.74)^2 = 3.03^{15}$

Values reported to the 95% confidence level

While the KDIE values fall slightly below the 1.35 high temperature experimental minimum for a 1° KDIE,¹⁴ their statistical variation places them within the same 1° KDIE 95% confidence level range as those illustrated in Tables I and II. They also do exceed the upper theoretical value for a standard temperature 2° KDIE,¹⁵ a magnitude that is rarely observed. At any rate, it is clear that both the pure HMX and RDX have the same type of KDIE as their respective formulated propellants and are, therefore, kinetically controlled by the same rate-determining step.

This presentation does not imply that either physical heat feed back mechanisms nor the chemical reactions and species in the gas phase flame oxidation process are unimportant. Optimization of heat back is a necessary consideration for achieving the maximum inherent HMX burn rate with a properly designed combustion chamber and flow field pattern. The observance, however, of a large KDIE in the HMX combustion event signifies substantial kinetic control for the HMX burn rate. This verifies that even if the inherent HMX burn rate is optimized by physical design, further modification or tailoring of the pure HMX burn rate or that of HMX based propellant formulations, ultimately must be achieved by chemically altering the kinetically driven, rate-controlling C—H bond rupture, possibly in the solid state decomposition/deflagration portion of the combustion event.

Understanding the gas phase flame properties and mechanism in combustion is also necessary; however, because the combustion event is comprised of both condensed phase and gas phase chemical processes, the mechanism of each must be elucidated and their interactive nature determined. Presently, little experimental investigation and almost no theoretical computational modeling address the condensed phase process, while both experimental and theoretical investigations for the gas phase process abound. The KDIE results achieved especially by HMX, strongly suggest mechanistic condensed phase combustion characteristics can no longer be ignored, and that only by understanding the mechanistic features of both the condensed and gas phase chemical processes for a given energetic material, will adequate computational codes be developed and precise burn rate tailoring be achieved.¹⁹ Furthermore, the KDIE investigations described strongly suggest mechanistic rate-controlling features can be dependent on an energetic material's different physical states, and that these different physical states and their resultant rate-controlling mechanistic feature, might be the same in both decomposition and combustion. This would permit the careful extrapolation of mechanistic data gained in ambient pressure decomposition as a guide for conducting further mechanistic combustion studies, a viewpoint also determined from an investigation of polynitroaliphatic energetic materials.²⁵

REFERENCES AND NOTES

1. S.A. Shackelford, M.B. Coolidge, B.B. Goshgarian, B.A. Loving, R.N. Rogers, J.L. Janney, M.H. Ebinger, *J. Phys. Chem.*, **89**, 3118-3126 (1985); Deuterium Isotope Effects in Condensed Phase Thermochemical Decomposition Reactions of Octahydro-1,3,5,7-tetranitro-1,3,5,7-tetrazocine.
2. S. Bulusu, D.I. Weinstein, J.R. Autera, R.W. Velicky, *J. Phys. Chem.*, **90**, 4121-4126 (1986); Deuterium Kinetic Isotope Effect in the Thermal Decomposition of 1,3,5-Trinitro-1,3,5-triazacyclohexane and 1,3,5,7-Tetranitro-1,3,5,7-tetrazacyclooctane: Its Use as an Experimental Probe for Their Shock-Induced Chemistry.
3. (a) S.A. Shackelford, B.B. Goshgarian, R.D. Chapman, R.E. Askins, D.A. Flanigan, R.N. Rogers, *Prop., Explos., Pyrotech.*, **14**, In Press (Jun 1989); Deuterium Isotope Effects During HMX Combustion: Chemical Kinetic Burn Rate Control Mechanism Verified.
(b) S.A. Shackelford, M.B. Coolidge, B.B. Goshgarian, R.N. Rogers, J.L. Janney, M.H. Ebinger, D.A. Flanigan, R.E. Askins, *CPIA Publ 383, Vol I*, 571-580 (Oct 1983); Deuterium Isotope Effects in HMX Thermochemical Mechanisms: Decomposition, Deflagration and Combustion.
4. (a) S.A. Shackelford, "ONR Workshop on Energetic Material Initiation Fundamentals and Reaction Processes of Pure Energetic Materials", Livermore, CA (Dec 1988); KDIE Determined Chemical Mechanism Relationships in Decomposition, Combustion, and Explosion: Current Status and Future Studies.
(b) S.A. Shackelford, P.C. Trulove, R.D. Chapman, "19th Intl. Annual ICT Conference on Combustion and Detonation Phenomena", Karlsruhe, West Germany (Jun 1988); Deuterium Isotope Effects in Combustion and Explosion. Impact of Chemical Mechanism and Physical State on Energy Release.
(c) S.A. Shackelford, *J. de Physique*, **48** (C4), 193-207 (Sep 1987); In-Situ Determination of Exothermic Transient Phenomena: Isotopic Labelling Studies.

5. S.A. Shackelford, J.W. Beckmann, J.S. Wilkes, J. Org. Chem., **42**, 4201-4206 (1977); Deuterium Isotope Effects in the Thermochemical Decomposition of Liquid 2,4,6-Trinitrotoluene: Application to Mechanistic Studies Using Isothermal Differential Scanning Calorimetry.
6. S. Bulusu, J.R. Autera, J. Energetic Matls., **1**, 133-140 (1983); Deuterium Isotope Effect as an Experimental Probe.
7. R.N. Rogers, J.L. Janney, M.H. Ebinger, Thermochim. Acta, **59**, 289-298 (1982); Kinetic Isotope Effects in Thermal Explosions.
8. S.A. Shackelford, S.L. Rodgers, M.B. Coolidge, R.E. Askins, CPIA Publ. 412, Vol II, 615-621 (Oct 1984); Deuterium Isotope Effects in RDX Decomposition and Combustion Processes: A Progress Report.
9. G.J. Piermarini, S. Block, P.J. Miller, J. Phys. Chem., **91**, 3872-3878 (1987); Effects of Pressure and Temperature on the Thermal Decomposition Rate and Reaction Mechanism of β -Octahydro-1,3,5,7-tetranitro-1,3,5,7-tetrazocine.
10. (a) J. Duterque, J. Hommel, G. Lengellé, Prop. Explos., Pyrotech., **10**, 18-25 (1985); Experimental Study of Double-Base Propellants Combustion Mechanisms.
 (b) G. Lengellé, A. Bizot, J. Duterque, J.F. Trubert, "Fundamentals of Solid-Propellant Combustion", Eds. K.K. Kuo and M. Summerfield, Progress in Astronautics and Aeronautics, Vol 90, AIAA, Inc., 1984, pp. 361-407; Steady-State Burning of Homogeneous Propellants.
11. N. Kubota, Nineteenth Symposium (International) on Combustion, The Combustion Institute, 777-785 (1982); Physicochemical Processes of HMX Propellant Combustion.
12. T.B. Brill, "ONR Workshop on Energetic Material Initiation Fundamentals and Reaction Processes of Pure Energetic Materials", Livermore, CA (Dec 1988); Part I. Condensed Phase Issues Related to Combustion.
13. T.H. Lowry, K.S. Richardson, "Mechanism and Theory in Organic Chemistry", Harper and Row, 2nd Ed, NY, 1981, p 206-207. Because 553K represents the highest temperature in ref 1 for which a 1° KDIE was observed with solid state HMX, this temperature was chosen as a reference point for calculating the 1° KDIE at standard temperature.
14. (a) A. Streitweiser, R.H. Jagow, R.C. Fahey, S. Suzuki, J. Am. Chem. Soc., **80**, 2326-2332 (1958); Kinetic Isotope Effects in the Acetolyses of Deuterated Cyclopentyl Tosylates.
 (b) G. Herzberg, "Molecular Spectra and Molecular Structure", II, Van Nostrand Co., Inc., NY, 1950, p 217.
 (c) J. Bigeleisen, M. Wolfsberg, "Theoretical and Experimental Aspects of Isotope Effects in Chemical Kinetics", Adv. in Chem. Phys., Vol I, Ed. I. Prigogine, Interscience, NY, 1958, p 28 and 64.
15. (a) Reference 14c, p 28.

(b) E.K. Thorton, E.R. Thornton, "Origin and Interpretation of Isotope Effects", Eds C.J. Collins, N.S. Bowman, ACS Monogr. 167, Van Nostrand Rheinhold Co., NY, 1970, pp 215-216.

16. (a) R.A. Fifer, CPIA Publ. 366, Vol I, 311-319 (Oct 1982); Cage Effects in the Thermal Decomposition of Nitramines and Other Energetic Materials.

(b) Ibid., "Proceedings of the Jt ONR, AFOSR, ARO Workshop on Fundamental Directions for Energetic Material Decomposition Research", 153-168 (Jan 1981); A Hypothesis for the Phase Dependence of the Decomposition Rate Constants of Propellant Molecules.

17. Y. Yano, N. Kubota, Prop., Explos., Pyrotech., 11, 1-5 (1986); Combustion of HMX-CMDB Propellants (II). The 673K temperature was selected as a reference point for calculating the 1^o KDIE at room temperature since it is the maximum condensed phase temperature experimentally measured during combustion of a nitramine propellant formulation.

18. P.C. Trulove, R.D. Chapman, S.A. Shackelford, CPIA Publ. 476, Vol I, 303-308 (Oct 1987); Deuterium Isotope Effects in the Combustion of Formulated Nitramine Propellants. The propellant composition used for HMX/CW5 and RDX/CW5 is as follows: Nitramine (73.20%), Hydroxy-terminated R-18 binder (8.15%), TMETN plasticizer (16.89%), IDPI curative (1.39%), and DBTDA cure catalyst (0.01%).

19. S.A. Shackelford, P.C. Trulove, R.D. Chapman, R.N. Rogers, "1st JANNAF Combustion Subcommittee Panel on Kinetic and Related Aspects of Propellant Combustion Chemistry", Laurel, MD (May 1988); Deuterium Isotope Effects During the Nitramine Combustion Event: Possible Implications to Chemical Kinetics/Mechanisms and Predictive Modeling.

20. Y. Oyumi, T.B. Brill, Prop., Explos., Pyrotech., 11, 35-39 (1986); Thermal Decomposition of Energetic Materials. XV. Evidence that Decomposition Initiates Deflagration: High-Rate Thermolysis of FEFO, TEFO, and DITEFO.

Acknowledgement: Mrs Linda E. Pukajlo's assistance in this abstract preparation is gratefully cited.

TITLE: THE HEAT FLOW/CHEMISTRY INTERFACE IN FAST-HEATED ENERGETIC MATERIALS

AFOSR-87-0033

Principal Investigator: Thomas B. Brill

Department of Chemistry
University of Delaware
Newark, DE 19716

SUMMARY/OVERVIEW:

The chemical and physical description of the condensed phase as it transits to the gas phase at high heating rates is a frontier area of research on energetic materials experiencing combustion or explosion. Rapid-scan FTIR/temperature profiling techniques have been developed and are being employed to cast light on these problems. The goal is to determine the thermochemical changes taking place in the condensed phase simultaneously with the observation of the near surface gas products evolved so that (1) the physicochemical mechanisms of decomposition at high heating rates can be established, and (2) the near surface gas products that drive the flame can be determined as a function of the parent molecular structure. This level of understanding is input necessary for three-dimensional combustion modeling.

TECHNICAL DISCUSSION

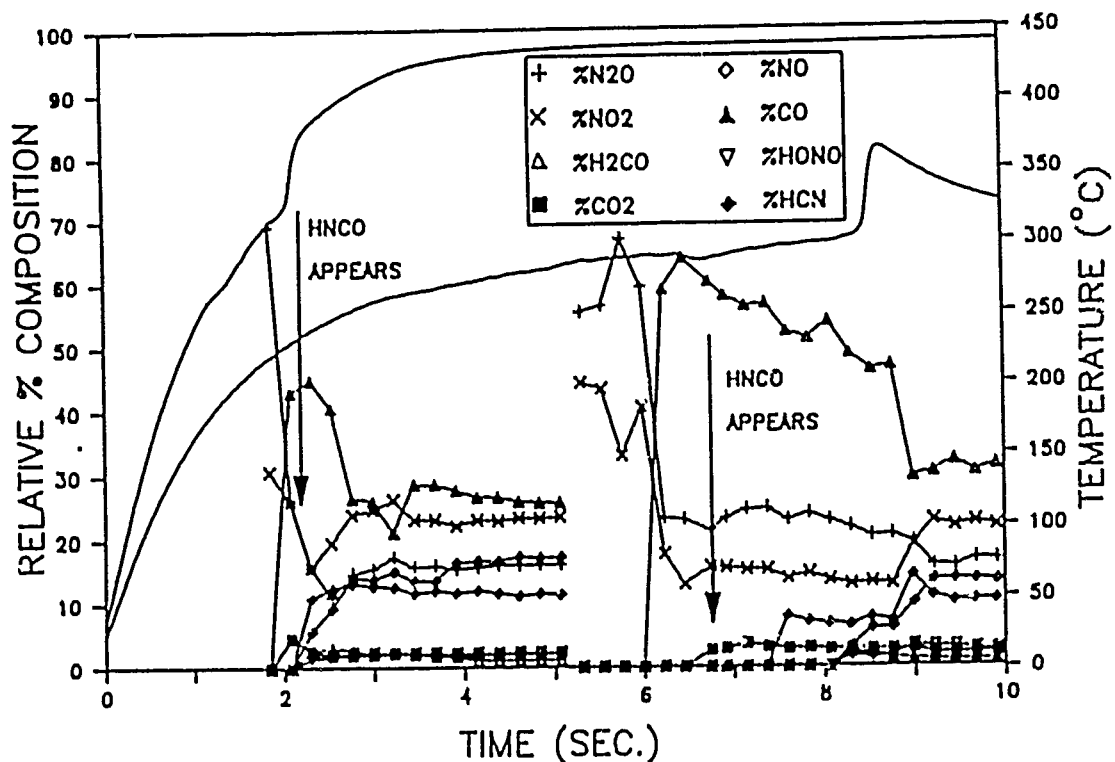
During this year significant progress has been made toward developing a new technique to give insight into chemistry along the thermal wave in a fast-heated material. By measuring the time-to-exotherm in fast-heated materials, we have found that, at temperatures well above the normal decomposition temperature, the apparent activation energy to the exotherm is dominated by the rate of heat flow rather than the rates of the chemical reactions. Thus, the apparent activation energy decreases with increasing temperature and is smallest at the burning surface. With the FTIR/temperature profiling technique, we are also able to measure the gas products at various temperatures in near real-time. By investigating various energetic materials having the most important energetic functional groups: nitramines, nitrate esters, C-NO₂, azides, tetrazoles, perchlorate, etc., we are attempting to attach chemical events to the behavior of the thermal wave.

The Approach, Progress and Future Plans figures shown here pictorially summarize the main points of this aspect of the research this year. In addition to studies of the heat flow/chemistry interface mentioned above, a detailed study of the decomposition-to-deflagration transition in trinitromethyl compounds has been completed. Studies of highly overoxidized compounds containing both the trinitromethyl group and the nitramine group have been conducted. A new experimental method in which simultaneous mass and temperature change (SMATCH/FTIR) is conducted while recording the FTIR spectra has been developed and is beginning to be applied to the fast thermolysis of binders and energetic polymers.

AIR FORCE BASIC RESEARCH

Approach

Originality: The first simultaneous thermocouple measurements of time-to-exotherms and real-time FTIR spectra of the near surface gas products at high heating rates.

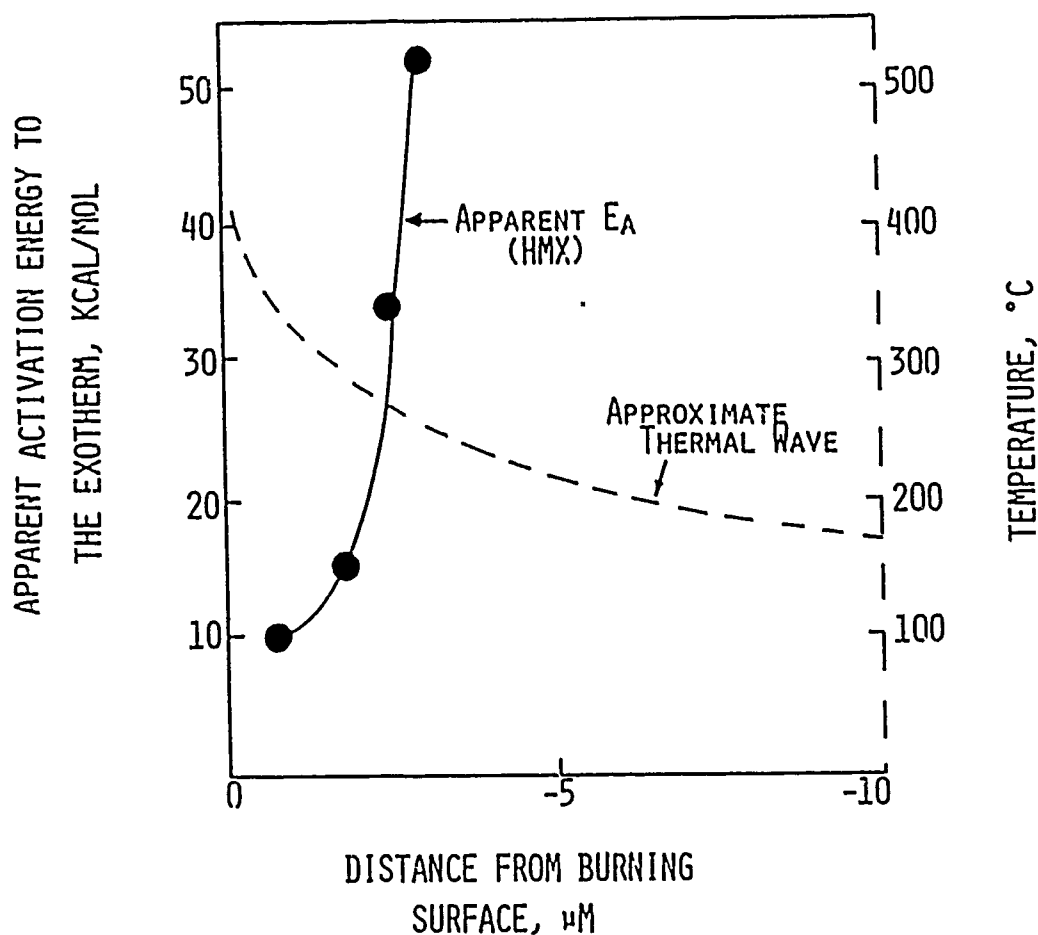


Contribution: Provides a depth (or temperature) profile in the condensed phase of the apparent activation energy revealing the combined contribution of heat flow and chemical processes during the combustion (or explosion) of an energetic material.

AIR FORCE BASIC RESEARCH

Progress

The apparent activation energy of the exotherm for the condensed phase (ignition delay) differs along the thermal wave because it reflects the sum of the heat flow and chemical rate terms. An apparent activation energy profile as a function of distance beneath the surface is shown.



Near the surface the contribution of heat flow dominates the experimental apparent activation energy, while farther from the surface the contribution of chemical processes to E_a dominates because T is lower.

AIR FORCE BASIC RESEARCH

Future Plans

Obtain simultaneous time-to-exotherm and real-time spectroscopic data on a wide variety of energetic materials.

Model processes with the TACO code (LLNL).

Obtain data on binders.

Extend the study to decomposition mechanisms of new caged nitramines.

STRUCTURE OF LAMINAR PREMIXED $\text{CH}_4/\text{N}_2\text{O}$ and $\text{CH}_2\text{O}/\text{N}_2\text{O}$ FLAMES

AFOSR Grant Number AFOSR-88-0331

Melvyn C. Branch
 Mechanical Engineering Department
 University of Colorado
 Boulder, Colorado 80309-0427

SUMMARY/OVERVIEW:

This study is part of a comprehensive investigation of the structure and chemical mechanism of gas phase flame reactions above the surface of nitramine propellants in order to assist modeling the overall combustion behavior of the propellant. We have previously reported on the measurement of the composition and temperature of stable and unstable species in $\text{CH}_4/\text{NO}_2/\text{O}_2$ and $\text{CH}_2\text{O}/\text{NO}_2/\text{O}_2$ laminar premixed flat flames. The discussion below summarizes our most recent results, including flame data for $\text{CH}_4/\text{N}_2\text{O}$ and $\text{CH}_2\text{O}/\text{N}_2\text{O}$ flames. Research which is proposed for the next year will focus on developing a consistent reaction mechanism for all of these fuel/ NO_x flames and will consider the effects of additives to increase flame burning velocities.

TECHNICAL DISCUSSION:

Flames were stabilized on a 2 cm by 8 cm burner housed in an evacuated chamber maintained at a pressure of 50 torr. Flame measurements were made of the concentration of stable species by a sampling microprobe and gas chromatographic gas analysis. Measurements of the concentration of unstable species was made by laser induced fluorescence and laser absorption using an excimer pumped dye laser system. Temperature was measured by a radiation corrected $\text{BeO}/\text{Y}_2\text{O}_3$ coated Pt-Pt/13%Rh thermocouple and compared to rotational temperature measurements. The accuracy of the stable species measurements was approximately 8%, the accuracy of the temperature measurements was about 3% and the accuracy of the unstable species measurements was estimated to be 20%.

Composition profiles for stable and unstable species measured in near stoichiometric flames of CH_4 with N_2O and of CH_2O with N_2O are given in Figures 1 and 2 respectively. Although a complete reaction mechanism for these flames is not yet available, any such mechanism should account for the overall trends in the data represented in these results. In our efforts to develop such a mechanism, we have relied heavily on several recent related studies and reviews.

These flames demonstrate that N_2O is a much more effective oxidizer than was NO_2 in our earlier investigation. In the earlier study it was necessary to add O_2 in order to produce flames that were sufficiently stable that measurements could be made. In addition, NO_2 was only partially consumed in the earlier flames whereas in this investigation, the N_2O is completely reacted. Another significant difference between these results with N_2O and the results with NO_2 is that N_2 is formed in both the CH_4 and the CH_2O flame due to the reaction



In the flames with NO_2 as oxidizer it was shown that CH was needed to form N_2 so that little N_2 was found in the CH_2O flames. Miller and Bowman have suggested that the reaction between N_2O and H can also have a seven percent yield of NO and

NH. This could account for the observed formation of NO in Figures 1 and 2.

Many differences between the CH₄ and CH₂O flames with N₂O are similar to differences between CH₄ and CH₂O flames with NO₂. More CO and H₂ are formed in the CH₂O flames due to the reactions



In the CH₄ flames the H₂ concentration was below the detection limit of the gas chromatograph and the CO maximum is about one fourth the CO maximum in the CH₂O flame.

The radical species profiles are given only for the CH₄/N₂O flame where CH, NH, CN and OH were measured. The CH is formed by successive H abstraction from CH₄ and CN is formed as a consequence of reaction between CH and NO. Since CHO does not lead to the formation of CH, the formaldehyde flames do not yield CH. We have identified OH in both flames but those measurements are not yet quantitative.

In conclusion, we have made new measurements which can supplement the limited existing data on CH₄/N₂O flames and which represent the first data on CH₂O/N₂O flames. These data are now being used in detailed flame chemistry modeling to develop a complete reaction mechanism for the complete set of fuel/NO_x flames we have investigated. Future studies will include the measurement of flame velocities of fuel/NO_x mixtures and the influence of additives such as ammonia on the burning velocity of the flames. Nitric oxide is a significant product of flames with NO₂ and ammonia is known to reduce nitric oxide exothermically.

PUBLICATIONS:

1. L. Thorne, M.C. Branch, J.A. Miller and D. Chandler, "Interaction Between Nitrogen and Carbon Species in H₂/O₂ Laminar Premixed Flames," *21st Symposium (International) on Combustion*, The Combustion Institute, Pittsburgh, pp. 965-977, 1988.
2. M. Sadeqi and M.C. Branch, "A Continuous Flow Gaseous Formaldehyde Generation System for Combustion Studies," *Combustion and Flame*, 71, pp. 325-329, 1988.
3. M.C. Branch, A.A. Alfarayedhi, M.A. Sadeqi and P.J. Van Tiggelen, "Measurements of the Structure of Laminar Premixed Flames of CH₄/NO₂/O₂ and CH₂O/NO₂/O₂ Flames", *Combustion and Flame*, in press.
4. M.C. Branch, F.N. Alasfour and M.A. Habeebullah, "Structure of Laminar Premixed CH₄/N₂O and CH₂O/N₂O Flames," *Proceedings of the Joint Meeting of the British and French sections of the Combustion Institute*, in press.

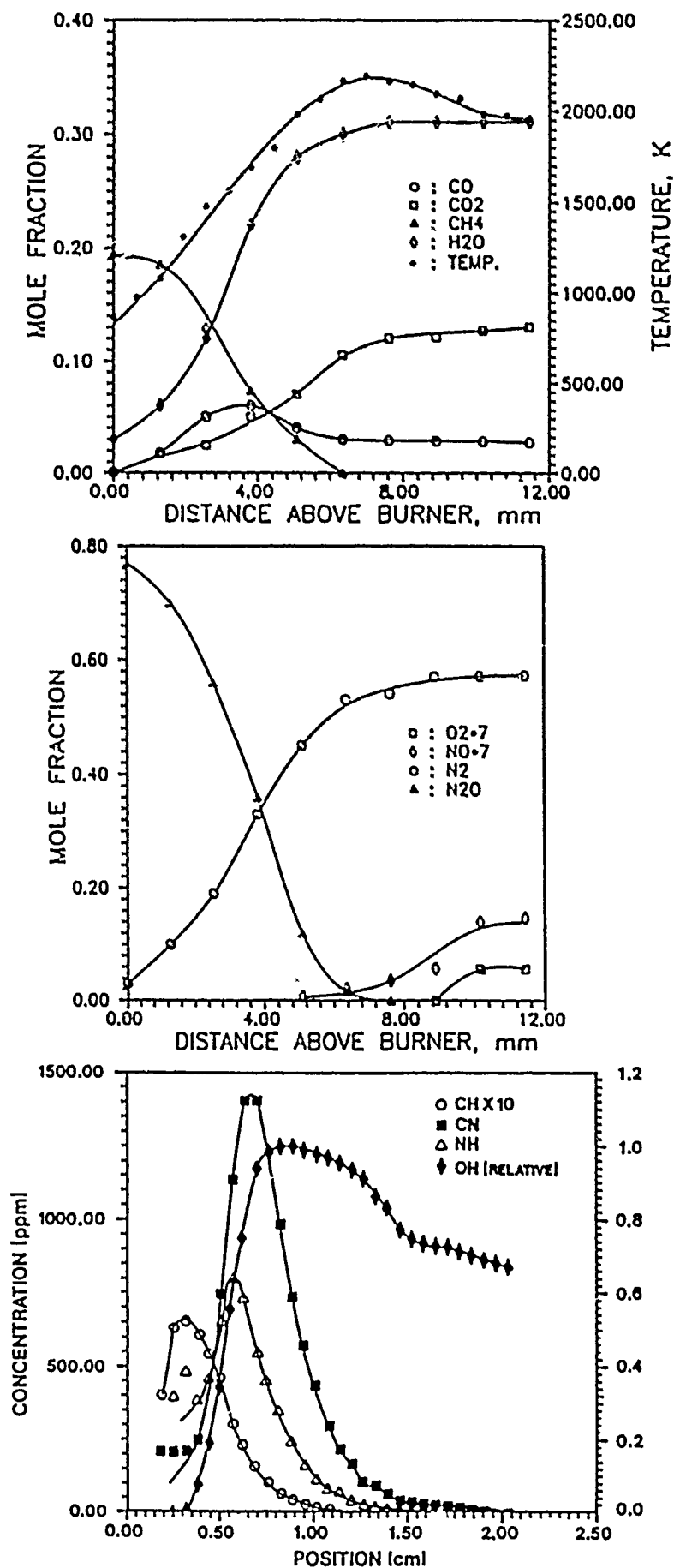


Figure 1. Measured concentration profiles in a CH₄/N₂O laminar premixed flame at 50 torr. The reactant mole fractions are 0.21 CH₄ and 0.79 N₂O and the total flowrate is 2.18 standard liters per minute.

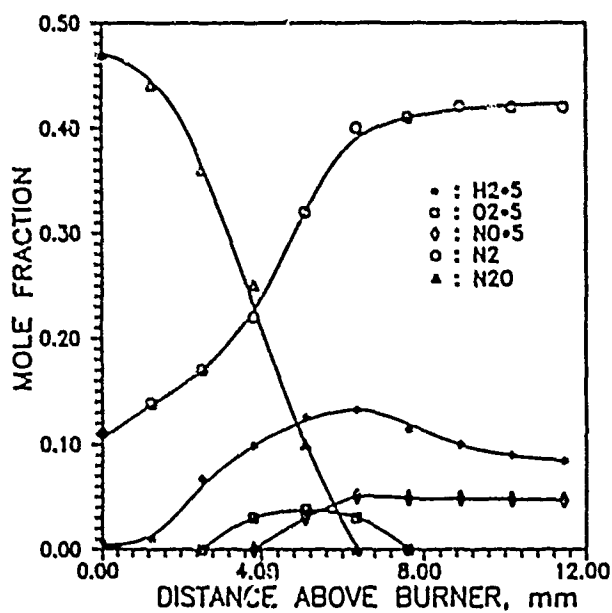
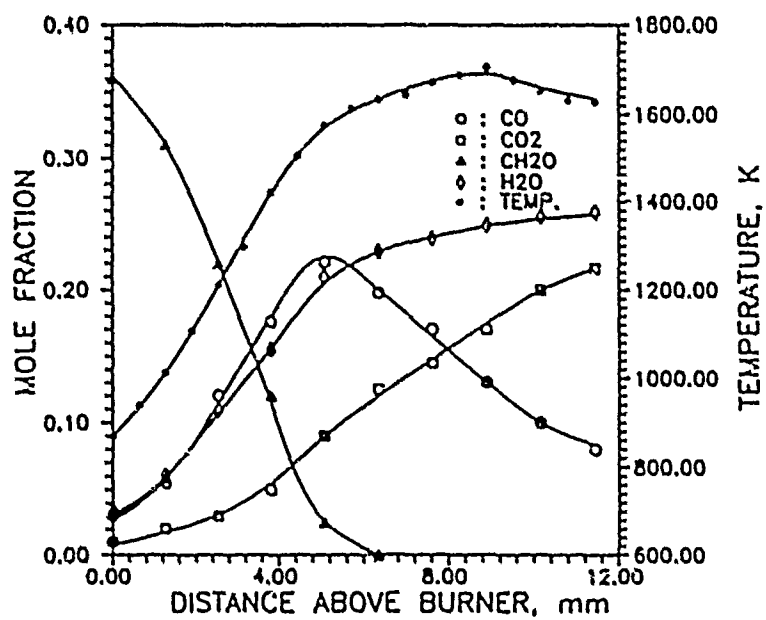


Figure 2. Measured concentration profiles in a $\text{CH}_2\text{O}/\text{N}_2\text{O}$ laminar premixed flame at 50 torr. The reactant mole fractions are 0.43 CH_2O and 0.57 N_2O and the total flowrate is 2.21 standard liters per minute.

HIGH PRESSURE COMBUSTION KINETICS OF PROPELLANTS

AFOSR PROGRAM ELEMENT 2308M1

Principal Investigator: Tim Edwards

Air Force Astronautics Laboratory (AFSC)
AL/LSCC, Edwards AFB, CA 93523-5000

SUMMARY/OVERVIEW:

This research is designed to examine the structure and reaction mechanisms of high pressure solid propellant flames. The understanding of these mechanisms is limited at present. It is believed that a better knowledge of high pressure propellant flame chemistry is needed for improvements in current propellant performance and instability models. The major experimental tools used in this research are laser-based combustion diagnostics such as laser-induced fluorescence. Simplified chemical kinetic models of the propellant flame chemistry are used to validate and direct the experimental measurements.

TECHNICAL DISCUSSION

Laser-based combustion diagnostics were originally demonstrated in laboratory flames. Relatively recently these tools [1] have been applied to the study of solid propellant flames [2,3,4]. One aspect of these diagnostics is that detailed information is obtained about species such as CN, NO, NH, N₂O, etc that is not obviously relatable to current solid propellant flame modeling. For example, which stage(s) of an HMX flame is a CN profile relevant to?

Detailed chemical kinetic models of solid flames are being developed [5,6]. The models require multiple days of VAX CPU time or a Cray-level computer. An alternative is to compare predictions from a simplified chemical kinetic models to experimental data from HMX and double-base (XLDB) propellant flames (these measurements are continuing [2]). For example, the temperature and selected species profiles for freely propagating HCN/NO₂ (modeling HMX) and CH₂O/NO₂ (modeling NG) flames at 15 atm are shown in Figures 1 and 2. The species were those seen in propellant flames with LIF [2,3]. These calculations use CHEMKIN with a 77 reaction/24 species data set [5b]. The comparison shows which species should be good diagnostic targets (those in high concentration) and shows the effect of several formulation variables on flame species. For example, the calculations show that 10⁶ times more CN could be found in an HMX flame than in a similar XLDB propellant flame. Experimentally, CN has been seen in HMX propellant flames [2,3] and has not been detected in XLDB propellant flames [2].

To be more directly applicable to propellant flames, two modifications have been made to the way CHEMKIN has been applied. The first change is to modify the stoichiometry to take into account the fuel-rich nature of propellant flames. For example, a 73% HMX/17% TMETN/10% binder propellant [2,4] was (roughly) approximated as a flame with HCN/CH₂O/NO₂ = 0.36/0.20/0.44. The results are shown in Figure 3. The broadening of the reaction zone compared to the HCN/NO₂ case is notable. This simulation made the (crude) approximation that the polyester binder formed exclusively CH₂O. A more realistic chemistry model would allow for carbon-rich binder pyrolysis products (the binder formula is

approximately $C_4H_7.5O_{2.3}$). Another step toward a more realistic chemistry model (under development) would use experimental temperature profiles [4,7] to decouple the chemistry from the energy transfer between the propellant and the flame, and is essentially the same as running CHEMKIN for a burner-stabilized flame. This type of model would give a reasonable approximation to the flame chemistry without requiring the computationally difficult energy balance equations of full models [5,6]. This simple model is useful only for situations where an experimental temperature profile is available and thus has little predictive capability. However, such a simple model can show which species are found in high concentration and thus are diagnostically accessible. Alternatively, the simple model could be compared to species profiles in propellant flames to determine if the theoretical chemistry is predicting the chemistry in a realistic way. These chemistry models are also being tested against results in a flame facility, with the goal of comparing modeling and experimental measurements in a high pressure gas flame, such as CH_4/NO_2 (see Branch's abstract in this meeting), as well as in the propellant flames.

References

1. Eckbreth, A. C., Laser Diagnostics for Combustion Temperature and Species, Abacus Press, Cambridge, 1988.
2. Edwards, T., Applied Optics, 26(17), 3496-3509 (1987); AFAL-TR-88-076, 1988.
3. Parr, T. P. and Hanson-Parr, D. M., 23rd JANNAF Comb. Mtg., Vol I, pp. 249-267, 1986, and 24th JANNAF Comb. Mtg., Vol. I, pp. 367-382, 1987.
4. Stufflebeam, J. H., CARS Measurements in Solid Propellant Flames, 25th JANNAF Comb. Mtg., 1988.
5. Hatch, R. L., 23rd JANNAF Comb. Mtg., Vol. I, pp. 157-165, 1986, and 24th JANNAF Comb. Mtg., Vol I, p.383-391, 1987.
6. Melius, C. F., 24th JANNAF Comb. Mtg., Vol. I, pp. 359-366, 1987.
7. Kubota, N., 19th Symp. on Comb., pp. 777-785, 1983.

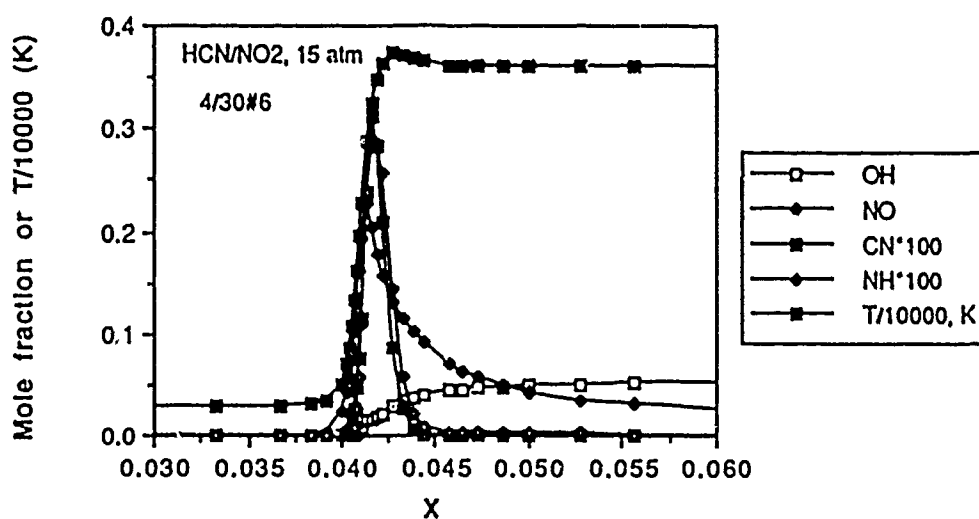


Figure 1. CHEMKIN results for freely propagating premixed HCN/NO₂ (1:1) flame, 15 atm.

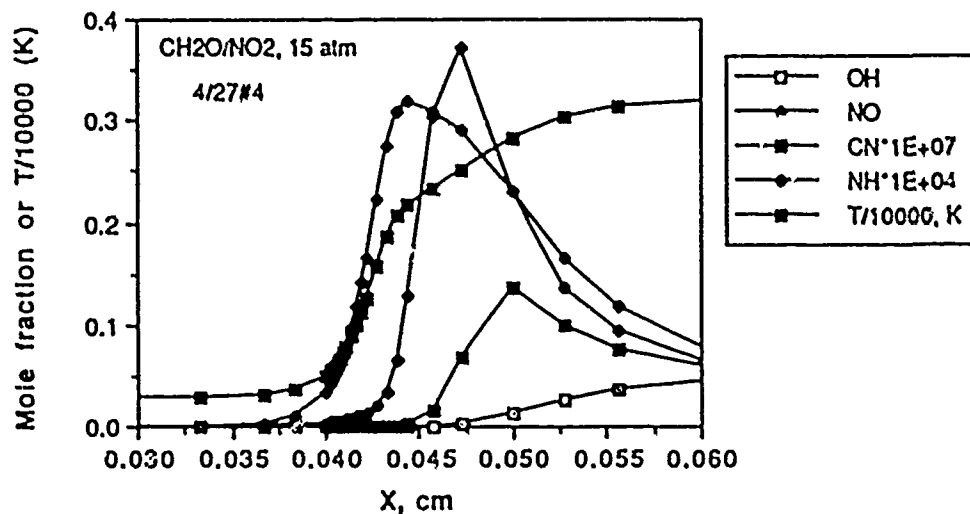


Figure 2. CHEMKIN results for freely propagating premixed CH₂O/NO₂ (1:1) flame, 15 atm.

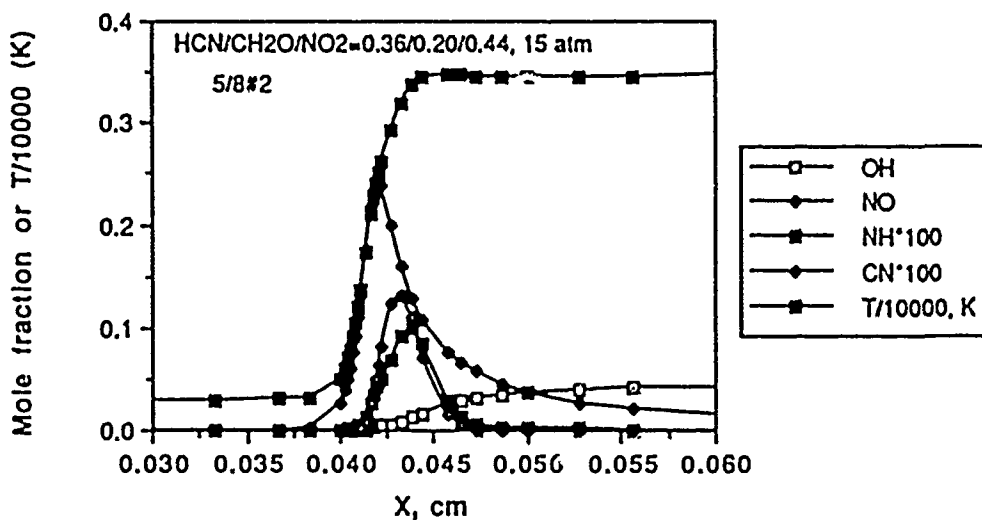


Figure 3. CHEMKIN results for freely propagating premixed HCN/CH₂O/NO₂ (0.36/0.20/0.44) flame, 15 atm.

SOLID FUEL COMBUSTION

(AFOSR Grant No. 85-0340)

Principal Investigator: J. S. T'ien
Other Professional: N. Ait Messaoudene

Department of Mechanical and Aerospace Engineering
Case Western Reserve University
Cleveland, Ohio 44106

SUMMARY/OVERVIEW

Analyses with a counterflow diffusion flame geometry are performed to study several interesting flame properties. In the first work, the flame is assumed to be laden with submicron particles, either produced in the flame or introduced from the free stream. Because of thermophoretic convection and Brownian diffusion, different particle flow patterns are produced which have a profound effect on the detailed particle concentration distribution in the flame. In the second work, the effect of gas-phase radiation on the extinction of a solid fuel diffusion flame at small flame stretch rate is also being analyzed.

TECHNICAL DISCUSSION

(1) Concentration Distribution of Particles in a Thermophoretically Affected Opposed-Flow Diffusion Flame

The behavior of submicron particles in a thermophoretically affected flow field has been investigated theoretically. Specifically, a two-dimensional counterflow diffusion flame stabilized in the forward stagnation region of porous cylinder is considered. Fuel is ejected from the cylinder with a specified blowing velocity and diffuses into an oxidizer flow of specified stagnation velocity gradient. In this configuration, particles (e. g., soot) of an assumed average dimension form at a global rate depending on the local fuel concentration and temperature. Thermophoresis gives rise to many different flow patterns for the particles depending on the flame structure and the magnitude of thermophoretic coefficient. In some cases, multiple stagnation points for particle flow exist.

Brownian diffusion needs to be included in this theoretical treatment in order to avoid singular behavior (infinite particle concentration) at the stagnation point under certain conditions. Because the Schmidt number associated with the Brownian diffusion is very large a special numerical scheme was developed to solve the mass conservation equation for the particles. The numerical scheme was implemented in two stages and allowed to integrate the

equation even in situations for multiple turning points (points where the particle velocity changes direction). This was achieved by making use of an adaptive mesh refinement scheme.

For cases along the center streamline where the particles are convected toward the stagnation point, a boundary layer behavior is observed. When the product of Prandtl number and the thermophoretic coefficient is greater than a critical value (nearly unity - slightly influenced by the chemical kinetics), a local peak of particle concentration is predicted (Fig. 1). For cases where particle velocity is from the fuel rich side toward the flame, the particles, generated in the fuel-rich side (such as soot), can leak through the flame and appear on the fuel lean side (Fig. 2). This can occur only when the stoichiometric fuel/oxidizer mass ratio is less than unity. The detailed profile of particle concentration in counterflow diffusion flames, therefore, depends on many parameters.

(2) Diffusion Flame Extinction at Small Stretch Rate: The Influence of Gas-Phase Radiation

An analysis is being made to evaluate the influence of gas-phase radiation on flame extinction at very small flame stretch rate. Previously, radiative loss from the hot surface of a solid fuel has been found to produce an extinction limit at low oxygen convective rate, but the influence of gas-phase radiative contribution is uncertain. In this analysis of a counterflow solid fuel diffusion flame the gas-phase radiation from the combustion products (H_2O and CO_2) and the fuel vapor are included using a two-flux model (soot disappears before extinction limit is reached; therefore, it is not included). The formation shows that the surface radiative loss varies inversely with the square root of the stretch rate (velocity gradient) while the gas-phase radiation varies approximately with the inverse of first power of the stretch rate. Therefore, although gas-phase radiation is negligible compared with surface radiation for small flames in moderate stretch rate, it can become increasingly important at very small stretch rate. The model is still being computed and we hope to present its results at the conference.

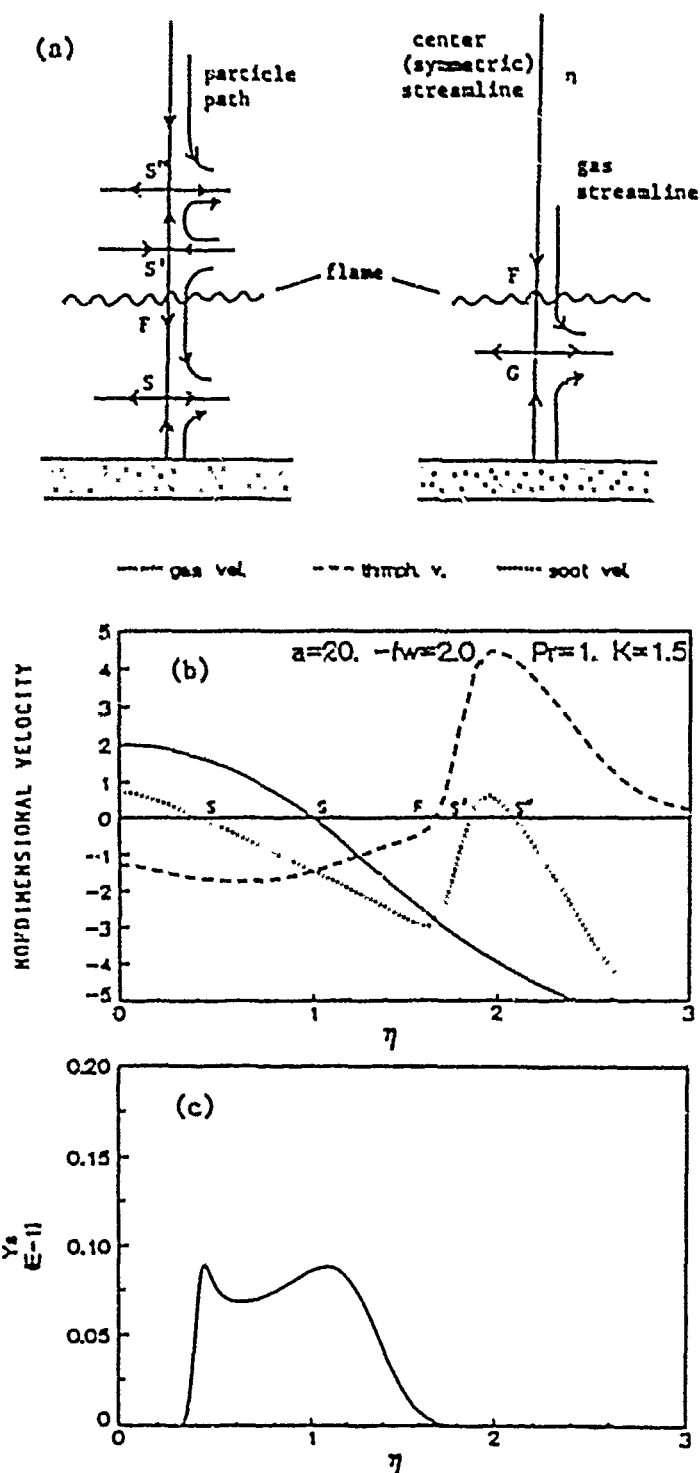


Fig. 1 Counterflow diffusion flame with $N_0 = 4$ (ratio of stoichiometric fuel/oxidizer ratio) and thermophoretic coefficient $K = 1.5$

(a) Particle path lines and gas streamlines

(b) Gas velocity, thermophoretic velocity and particle (soot) velocity along the center streamline

(c) Particle mass fraction distribution according to a production rate $w = BY_F^2 \exp(E/RT)$

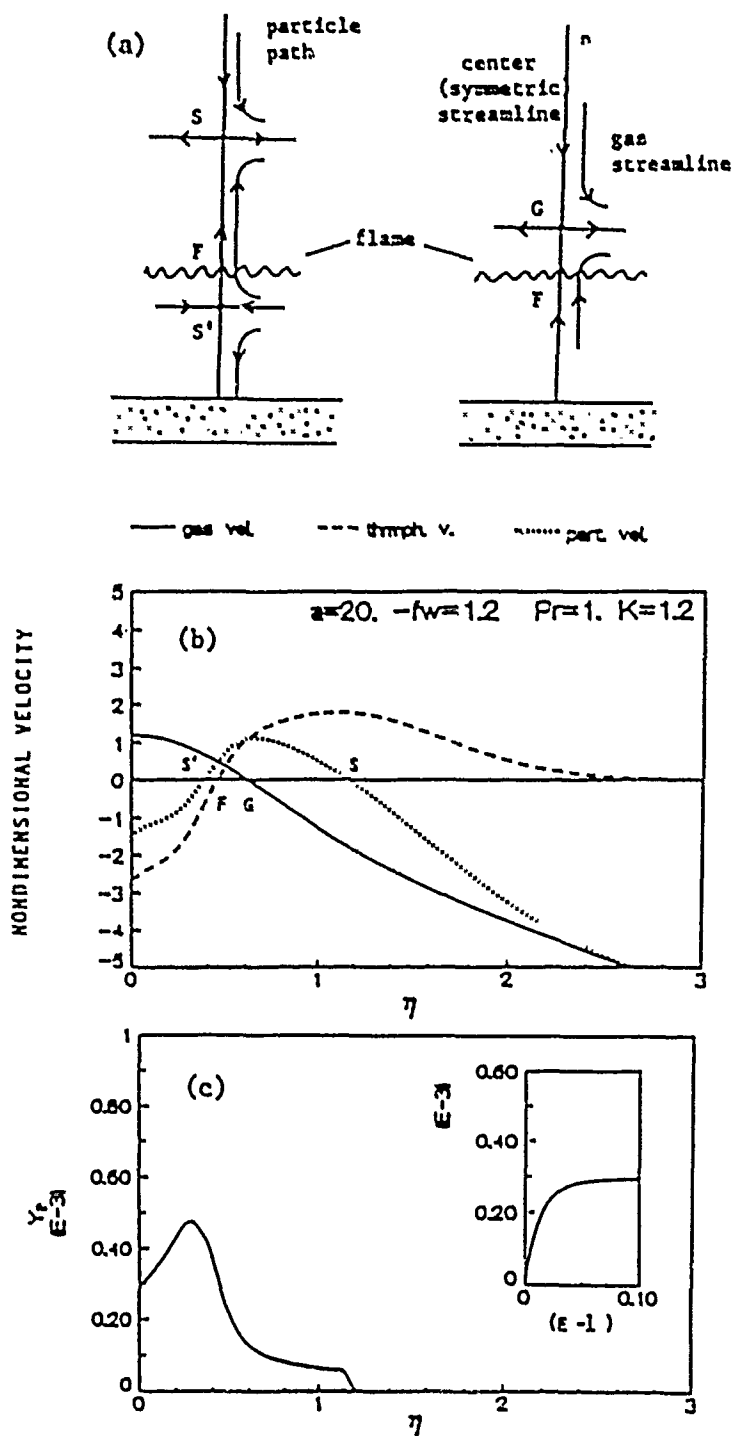


Fig. 2 Counterflow diffusion flame with $N_0 = 0.2$ (ratio of stoichiometric fuel/oxidizer ratio) and thermophoretic coefficient $K = 1.2$

(a) Particle path lines and gas streamlines

(b) Gas velocity, thermophoretic velocity and particle (soot) velocity along the center streamline

(c) Particle mass fraction distribution according to a production rate $w = BY_F^2 T \exp(E/RT)$

PROGRAM MANAGER: JULIAN M. TISHKOFF

AFOSR/NA
BOLLING AFB DC 20332-6448

SUMMARY/OVERVIEW: The Air Force Office of Scientific Research (AFOSR) program in airbreathing combustion currently is focused on six areas of study: reacting flow, soot, sprays, kinetics, boron slurries and supersonic combustion. An assessment of major research needs in each of these areas is presented.

TECHNICAL DISCUSSION

AFOSR is the single manager for Air Force fundamental research, including programs based on external proposals and in-house work at Air Force laboratories. Airbreathing combustion is assigned to the AFOSR Directorate of Aerospace Sciences along with programs in rocket propulsion, diagnostics of reacting flow, fluid and solid mechanics, and civil engineering.

Interests of the AFOSR airbreathing combustion program are given in the SUMMARY section above. Many achievements can be cited for these interests, yet imposing fundamental research challenges remain. The objective of the program is publications in the refereed scientific literature describing significant new understanding of multiphase turbulent reacting flow. Incremental improvements to existing scientific approaches, hardware development and computer codes fall outside the scope of this objective.

Decisions on support for research proposals are based on scientific opportunities and technology needs. Current AFOSR perceptions of scientific opportunities appear in Figure 1, and areas of emphasis are indicated by arrows with positive slopes. Technology needs have been defined by the results of the Forecast II exercise which the Air Force completed recently.

Included in Forecast II are two technology areas which are relevant to the AFOSR airbreathing combustion task: combined cycle engines and high performance gas turbines. The former area would provide the propulsion system for the National Aero Space Plane, and related research proposals will receive primary consideration for available support. The combined cycle engine concept has motivated significant research interest in supersonic combustion. In fiscal year 1986 (FY86) substantial research activity was initiated to study mixing and chemical reaction under supersonic flow

conditions. In FY87 new research efforts were directed at novel means for achieving ignition, combustion enhancement and low-loss flameholding in supersonic combustion. FY89 saw new research in interactive control of fluid transport processes. These opportunities reflect a generic interest in interdisciplinary efforts between researchers in control theory and fluid transport behavior. For the combined cycle engine a particular focus of interactive flow control will be the investigation of means to overcome the suppression of mixing which high Mach number flows experience in relation to subsonic flows.

The behavior of single fuel droplets has been the subject of renewed research activity. Both computational and experimental capabilities appear to be poised to expand studies of spray combustion to spatial dimensions smaller than those of the droplets themselves. A particular focus of this research activity will be the interactions between droplets and gas-phase turbulent transport processes.

The purpose of this abstract has been to communicate AFOSR perceptions of research trends to the university and industrial research communities. However, communication from those communities back to AFOSR also is desirable and essential for creating new research opportunities. Therefore, all proposals and inquiries for fundamental research are encouraged even if the content does not fall within the areas of emphasis described herein. Comments and criticisms of current AFOSR programs also are welcome.

Air Force Basic Research

Aerospace Sciences

Airbreathing Combustion

Science Area	Trend	Decrease	Increase
Reacting Flow	↑		Flow Control
Soot	↑		
Sprays	↖		Drop-Turbulence Interactions, Nondilute Sprays, Atomization
Boron Slurries	↑		
Supersonic Combustion	↑		Flow Control
Kinetics	↑		

AFOSR SPONSORED RESEARCH IN DIAGNOSTICS OF REACTING FLOW

PROGRAM MANAGER: JULIAN M. TISHKOFF

AFOSR/UA
BOLLING AFB DC 20332-6448

SUMMARY/OVERVIEW: The Air Force Office of Scientific Research (AFOSR) program in diagnostics of reacting flow currently is focused on four areas of study: gas-phase measurements; thermochemical and geometric characterization of solid surfaces; particle and droplet measurements; and plasmas. An assessment of major research needs in each of these areas is presented.

TECHNICAL DISCUSSION

AFOSR is the single manager for Air Force fundamental research, including programs based on external proposals and in-house work at Air Force laboratories. The diagnostics of reacting flows task is assigned to the AFOSR Directorate of Aerospace Sciences along with programs in rocket propulsion, airbreathing combustion, fluid and solid mechanics, and civil engineering.

Interests of the AFOSR diagnostics of reacting flow program are given in the SUMMARY section above. This program, now in its eighth year, has produced many "first-ever" laser-based measurements. The instrumentation with which these measurements were made is becoming commonly available for laboratory and bench test utilization. Measurements range from microscopic to macroscopic scales with relevance to: plasma acceleration; combustion aerothermochemistry; the behavior and synthesis of advanced energetic materials; characterization of exhaust plume formation and radiation; and dynamic control of propulsion, weapon and power generation systems.

Decisions on support for research proposals are based on scientific opportunities and technology needs. Current AFOSR perceptions of scientific opportunities appear in Figure 1. Technology needs have been defined by the results of the Forecast II exercise which the Air Force completed recently.

Included in Forecast II are four technology areas which are relevant to the AFOSR diagnostics of reacting flow task: combined cycle engines, high performance turbine engines, safe compact nuclear rockets and space-based reusable orbital transfer vehicle. The first area would provide the propulsion system for the aerospace plane. As indicated by

the orientation of the arrows in Figure 1, the task area with the greatest growth potential is gas-phase measurements relevant to plasmas.

The purpose of this abstract has been to communicate AFOSR perceptions of research trends to the university and industrial research communities. However, communication from those communities back to AFOSR also is desirable and essential for creating new research opportunities. Therefore, all proposals and inquiries for fundamental research are encouraged even if the content does not fall within the areas of emphasis described herein. Comments and criticisms of current AFOSR programs also are welcome.

Air Force Basic Research Aerospace Sciences

Diagnostics of Reacting Flow

Science Area	Trend	Decrease	Increase
Gas-Phase Measurements	↑		
Solid Surface Characterization	↘	Surface Regression, Temperature	
Particle/Droplet Measurements	↑		
Plasmas	↘		

NUMERICAL SIMULATION OF CONTROL OF SUPERSONIC SHEAR LAYERS

ONR Contract No. N00014-89-J-1319

Principal Investigator: L. N. Sankar

School of Aerospace Engineering
Georgia Institute of Technology, Atlanta, GA 30332

SUMMARY

The issue of enhancing mixing between parallel, supersonic streams is numerically investigated. An explicit time marching scheme that is second order accurate in time and fourth order accurate in space is used to study this problem. Small amplitude velocity disturbances at selected frequencies are imposed over an otherwise steady flow at the juncture of the two streams to promote mixing. It is found that disturbances are selectively amplified at certain frequencies, while disturbances at other frequencies are rapidly damped out. In studies where the relative Mach number of the disturbances relative to one of the streams is high, shocklets were found to form on one or both sides of the shear layers. In such a situation, the relative Mach numbers of the eddies were different in coordinate systems attached to the upper and the lower streams.

SCOPE OF THE PRESENT WORK

The objectives of the present work are to study the growth of supersonic free shear layers and their response to imposed acoustic disturbances through direct numerical solution of the governing equations.

The 2-D compressible Navier-Stokes equations in a strong conservation form are numerically solved, using a modified MacCormack scheme that is second order accurate in time, and fourth order accurate in space. This scheme is suitable for studying phenomena such as propagation of acoustic waves, boundary layer instability, and shear layer instability and has been previously used by several authors. The flow field is assumed to be laminar.

RESULTS AND DISCUSSION

Figure 1 shows the computational domain used. The computational domain was divided into a uniformly spaced Cartesian grid consisting of 221 nodes in the x- direction and 241 nodes in the normal direction. The typical grid spacing in the x- and y- direction were $5/3d$ and $0.4d$ units respectively, where d is the vorticity thickness of the shear layer at the inflow boundary. The grid spacing in the y- direction is fine enough to place approximately 30 points across the shear layer where the vorticity content is largest, at distances sufficiently downstream ($x > 50d$) from the inlet.

At the inflow boundary, a hyperbolic tangent mean velocity profile was specified. The v component of inflow velocity was set to zero for the mean flow. The pressure was assumed to be equal and uniform at the inflow boundary. A variety of velocity, density and temperature ratios across the shear layer have been used to study parametrically their effects on the shear layer characteristics.

The 2-D Navier-Stokes solver was used to compute the mean shear flow characteristics first. Then, forced excitation of the shear layer began. This was achieved by prescribing the normal (v -) component of velocity over the entire inflow boundary to behave as follows:

$$v(y, x=0, t) = \sum A_n f(y) \sin(x_n t + \theta_n)$$

Here the summation shown is over all the excitation frequencies; A_n is the amplitude of disturbance, x_n is the frequency of disturbance and θ_n is the associated phase angle. The function $f(y)$ determines the variation of the perturbation velocity across the shear layer. Both a Gaussian distribution and a constant magnitude distribution were attempted. The results to be presented here correspond to $f(y)$ equal to unity.

The computed flow fields after several cycles of forced excitation of the shear layer are analyzed using computer graphics and Fourier transform techniques to study the following issues of interest:

- a) Effect of convective Mach number on shear layer growth
- b) Correlation between computed convective Mach number of eddies and analytical estimates
- c) Occurrence of shocklets and their effects on shear layer growth
- d) The growth and decay of low and high frequency excitations with time and space.

The following conclusions were drawn:

a) In the case of shear layers at subsonic and supersonic convective Mach numbers, the imposition of acoustic disturbances over a large range of frequencies lead to the transfer of this energy from the high frequencies to the low frequencies, as the flow progressed from the upstream boundary to the downstream boundary. The energy content at the lowermost frequencies rapidly reached asymptotic values following which eddies in the shear layer were convected downstream with no further alteration in their structure [Figure 2].

b) In the case of shear layers at a supersonic convective Mach number, situations were found where the convective Mach number relative to the faster stream is low. This leads to a situation where shocklets arose only on the lower side of the shear layer. Conditions were also found where the convective Mach number relative to both the streams is high, leading to shocklets on either side [e.g. Figure 3]. These calculations demonstrate the same features

experimentally observed by Papamoschou and discussed based on total pressure arguments by Dimotakis.

c) The spatial growth of shear layers decreased with increasing convective Mach number.

ACKNOWLEDGEMENTS

This work was supported by the Office of Naval Research under Grant No. N00014-89-J-1319. Computer time for the numerical simulations was provided by the Pittsburgh Supercomputing Center. The authors are thankful to Prof. S. A. Ragab of Virginia Polytechnic Institute & State University for several valuable discussions.

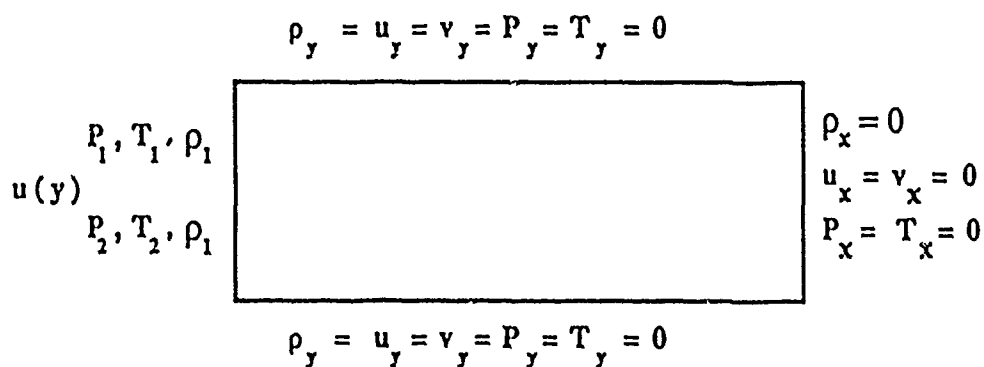


Fig. 1 Computational Domain and Boundary Conditions

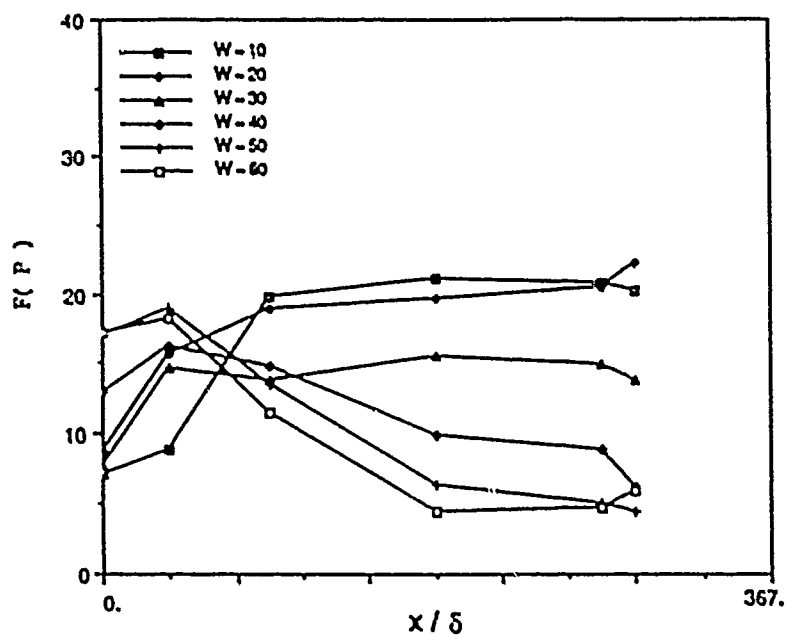


Fig. 2 Variation of Fourier Spectrum

$M_c = 0.2$, $M_1 = 4.0$, $M_2 = 2.3$, $a_1/a_2 = 2.3$, $\delta = 1/15$, Multi-Frequency

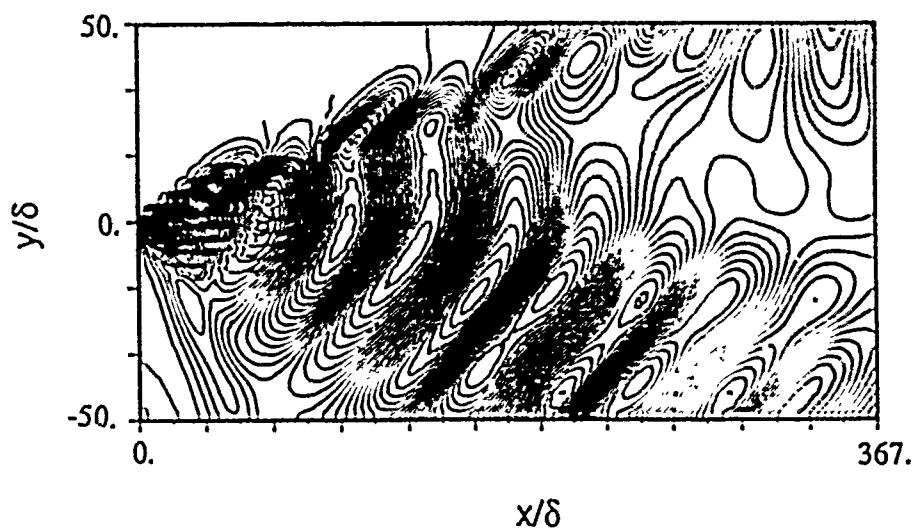


Fig. 3 Pressure Countours

$M_c = 1.2$, $M_1 = 5.0$, $M_2 = 1.3$, $a_1/a_2 = 2.3$, $\delta = 1.0$

INSTABILITIES IN SUPERSONIC TURBULENT MIXING LAYERS

ONR Contract No. N00014-87-K-0168

Principal Investigator: Saad A. Ragab
Graduate Research Assistant: Jeun-Len Wu

Department of Engineering Science and Mechanics
Virginia Polytechnic Institute and State University
Blacksburg, VA 24061.

SUMMARY

The objective of this research is to investigate the structures of instability waves of supersonic mixing layers and to determine the effects of certain flow parameters such as the Mach number, velocity ratio, and temperature ratio on the growth rates of these waves. Both viscous and inviscid linear analyses are used. For turbulent flows, the mean velocity profile is approximated by a hyperbolic-tangent profile and the temperature profile is determined from the Crocco-Busemann equation. Alternative mean flow profiles are obtained by solving the laminar mixing layer equations. Furthermore, in order to shed some light on the development of the two-dimensional and helical pairing modes, the three-dimensional secondary subharmonic instability of spatially and temporally periodic mixing layers are investigated using the Floquet theory.

TECHNICAL DISCUSSION

The mixing of two parallel supersonic streams is of primary importance to the designer of propulsive systems that employ supersonic combustion. It has been established experimentally and theoretically that the spreading rates (and hence entrainment and mixing) of supersonic free shear layers are substantially lower than the rates of subsonic layers (e.g. Ref.1-4). The objective of this research is to provide a detailed study of the effects of the velocity and temperature ratios on the instability characteristics of mixing layers. And to provide more detailed substantiation of the convective Mach number that is proposed by Bogdanoff (Ref.5) and Papamoscho and Roshko (Ref.2) as a compressibility parameter of mixing layers.

Effect of the Velocity Ratio: Using the Blasius-Lock profile and inviscid analysis, we computed the growth rates of 2D waves at a temperature ratio $T_2 = 2$ and for different Mach numbers. Sample results are shown in Fig.1. Only the incompressible case shows linear variation of the maximum growth rate with the velocity ratio. At higher Mach numbers the growth rate shows a maximum at a particular velocity ratio that depends on the Mach number. More details are given in Ref.6.

Effect of the Temperature Ratio: The maximum growth rates for the temperature ratios $T_2 = 0.5, 1,$ and 2 at $U_2 = 0$ are shown in Fig.2. For Mach numbers less than 1.5 heating the slow stream stabilizes the mixing layer. However, at higher Mach numbers the opposite effect is obtained. The effect of T_2 on the higher modes of instability is studied in Ref. 6.

Oblique Waves: The maximum growth rates of oblique waves are depicted in Fig.3. for $T_2 = 1$ and $U_2 = 0$. Oblique waves become more amplified as the Mach number increases; as one might expect.

Convective Mach Number M^+ : To isolate the compressibility effects on the spreading rate, Papamoschou and Roshko pointed out that the spreading rate σ for certain values of Mach number M_1 , velocity ratio U_2 and density ratio ρ_2 , must be normalized with respect to the spreading rate at zero Mach number and the same velocity and density ratio. They gave the expression for the spreading rate ratio R_σ as

$$R_\sigma = \frac{\sigma(M_1, U_2, \rho_2)}{\sigma(0, U_2, \rho_2)} = F(M^+)$$

In this work we use the maximum growth rate of the instability waves instead of the spreading rate in forming the growth rate ratio. The growth rate ratio is shown in Fig. 4. It is evident that the $R_\sigma - M^+$ is independent of the specific values of M_1 , U_2 and ρ_2 up to $M^+ = 0.7$. For higher M^+ oblique waves dominate, and that calls for a modified definition of M^+

Secondary Subharmonic Instability: This work is an extension to compressible flow of the work by Pierrhumbert and Widnall (Ref.7) and Santos and Herbert (Ref.8) concerning the subharmonic instability of a row of distributed vortices. The basic state is given by linear superposition of a steady mean flow, which is specified by the hyperbolic-tangent profile, and a neutral primary wave. In a frame of reference moving with the phase speed, the basic state becomes steady and spatially periodic. Such a state is shown in Fig. 5b for $\max(u_{rms}) = 0.1 U_1$ and $M^+ = 0.7$. Using the Floquet theory, we compute the growth rates of the 2D and 3D secondary subharmonic waves of that periodic flow. The results in Fig.6 show that the growth rates of the 2D waves (pairing mode) are enhanced by increasing the amplitude of the periodicity but at a decreasing rate as the convective Mach number increases. Assuming a subharmonic wave of amplitude $\max(u_{rms}) = 0.2 U_1$, vorticity contours of the basic state and subharmonic are shown in Fig.5c, while contours for the subharmonic in absence of the primary are shown in Fig.5a. The clockwise rotation of the vortices indicates the beginning of the pairing phase. The growth rates for the 3D waves are shown in Figs. 7 and 8. The results show that the most amplified subharmonic wave is a 3D helical mode. More details are given in Ref.9.

REFERENCES

- (1) N. Chinzei, G. Masuya, T. Komuro, A. Murakami, and D. Kudou, Phys. Fluids 29, 1345 (1986).
- (2) D. Papamoschou, and A. Roshko, AIAA Paper 86-0162 (1986).
- (3) D. Papamoschou, Ph.D. Dissertation, CALTECH, Pasadena, Cal., (1986).
- (4) H. Gropengiesser, NASA Technical Translations NASA TT F-12-786 (1970).
- (5) D. W. Bogdanoff, AIAA J. 21, 926 (1983).
- (6) S. A. Ragab, and J. Wu, accepted Phys. Fluids, to appear (1989).
- (7) R. T. Pierrhumbert, and S. E. Widnall, JFM 114, 59, (1982).
- (8) G. R. Santos, and Th. Herbert, Bull. Am. Phys. Soc., 31, 1718, (1986).
- (9) S. A. Ragab, and J. Wu, AIAA Paper 89-039 (1989).

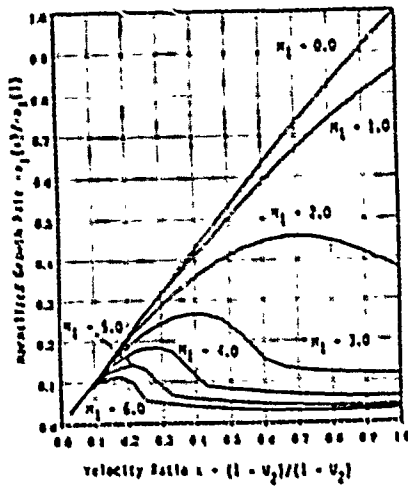


Fig. 1 Effect of the Velocity Ratio

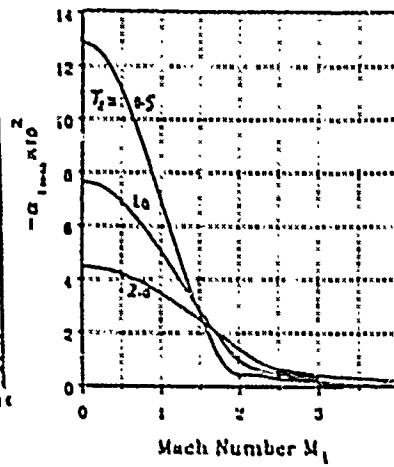


Fig. 2 Effect of the Temperature Ratio

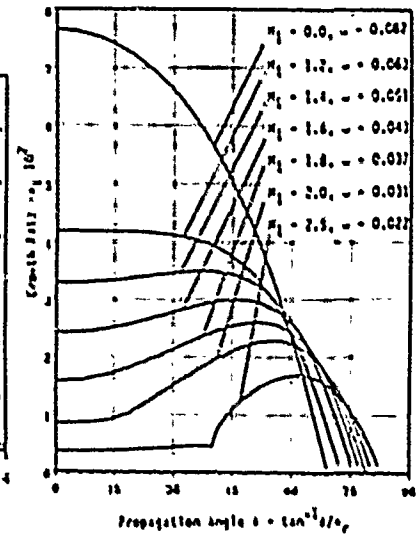


Fig. 3 Oblique Waves

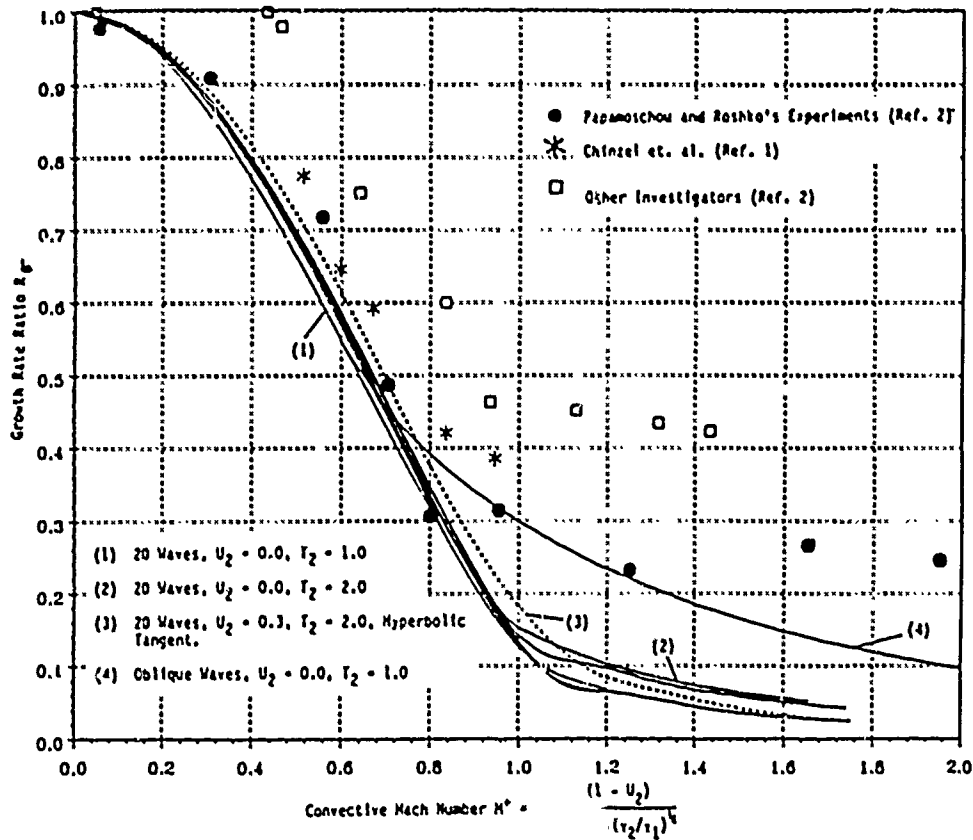
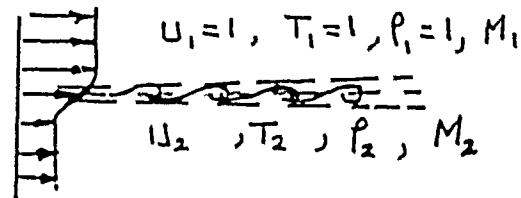


Fig. 4 Correlation with Co. h number

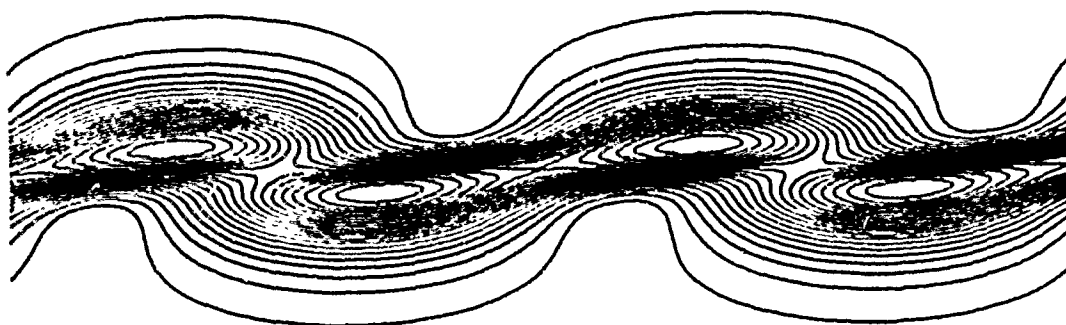


Fig.5a Vorticity Contour: Mean Flow + Subharmonic

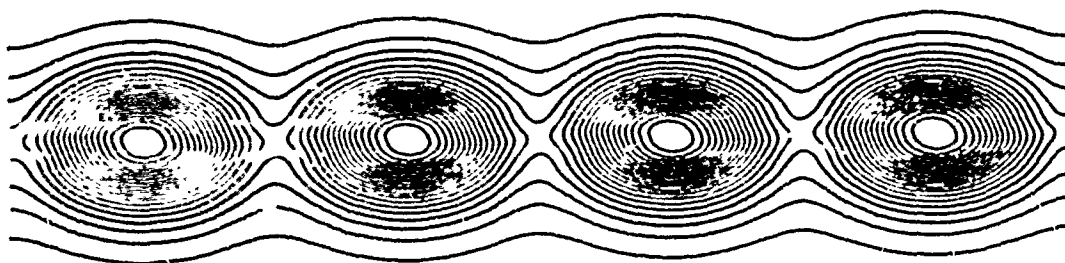


Fig.5b Vorticity Contour: Mean Flow + Primary

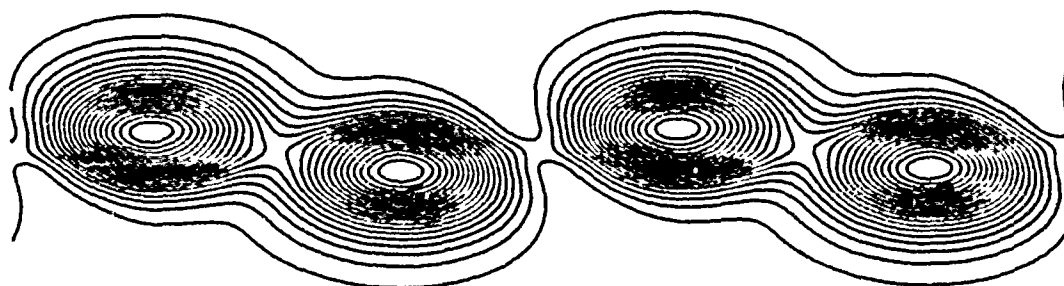


Fig.5c Vorticity Contour: Mean Flow + Primary + Subharmonic

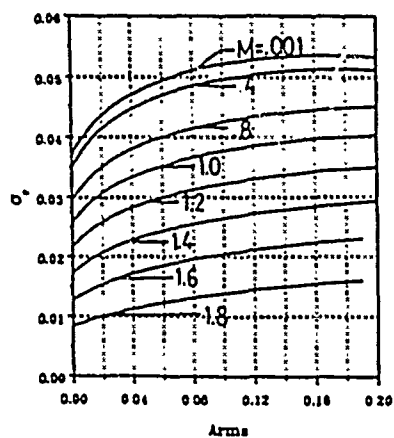


Fig.6 Growth Rates vs. Amplitude of primary

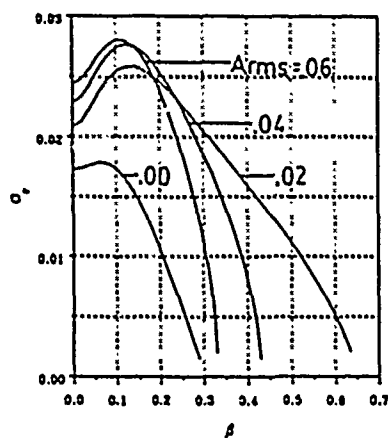


Fig.7 Growth Rates vs. β Different Arms at $M = 1.4$

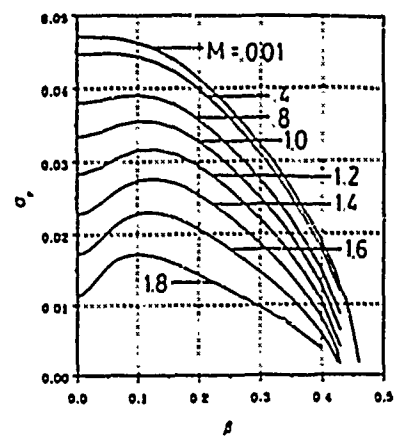


Fig.8 Growth Rates vs. β Different M at Arms = 0.04

DESTABILIZATION OF SUPERSONIC FREE SHEAR LAYERS BY PARAMETRIC EXCITATION

(ONR Grant/Contract No. N00014-87-J-1130)

Principal Investigator: Christopher K.W. Tam

Department of Mathematics
Florida State University
Tallahassee, Florida
32306-3027

SUMMARY/OVERVIEW:

The instability and acoustic wave models associated with a supersonic free shear layer inside a rectangular channel is investigated. It is found that because of acoustic reflections from the walls a thin shear layer at supersonic convective Mach numbers which is stable in an unconfined environment is now subjected to two families of instabilities. To enhance mixing in such a shear layer it is proposed that a periodic Mach wave system which penetrates through the shear layer may be effective. The Mach wave system can be generated by a wavy wall of the channel. Computations of flow instabilities show that new three dimensional modes are possible in the presence of the Mach wave system. The effectiveness of such parametric excitation on mixing enhancement is to be studied.

TECHNICAL DISCUSSION

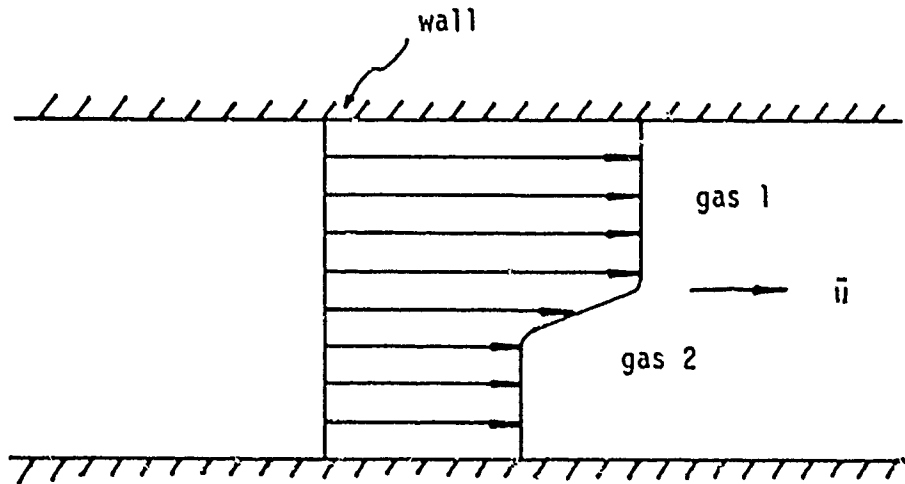
Two aspects of confined supersonic shear layers with a flow configuration as shown in figure 1 are investigated. First, the three dimensional instability waves/coherent structures and acoustic wave modes associated with these flows are studied. Second, the possibility of destabilizing such shear layers so as to enhance mixing by a Mach wave system generated by a wavy wall (figure 2) is examined computationally.

When confined inside a rectangular channel the motion of a supersonic shear layer is inevitably influenced by acoustic waves reflected off the walls. If the motion of the shear layer is in the form of a

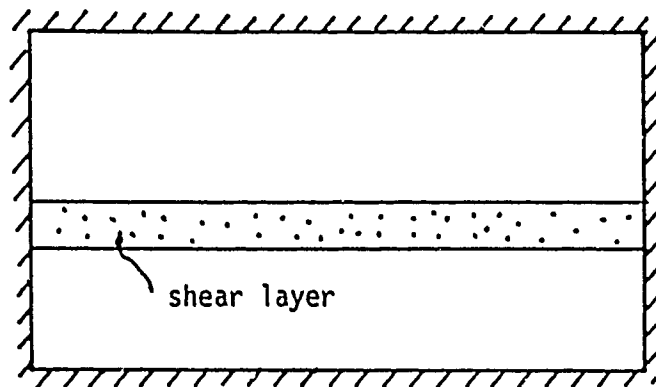
wave then it is advantageous to view the flow problem in a moving frame which is stationary with respect to the wave. The Mach numbers of the flow measured in the wave frame are referred to as convective Mach numbers. When the convective Mach numbers are supersonic two standing Mach wave systems one on each side of the shear layers are established between the shear layer and the (top and bottom) walls of the channel. For waves with appropriate wave lengths the unbalanced pressure distributions of the Mach wave system on the shear layer could be in phase with the vertical displacement of the shear layer and thus tend to increase its amplitude resulting in growth of the wave motion or instability. We have now shown that a thin supersonic shear layer which is stable in an unconfined environment becomes unstable when housed inside a rectangular channel due to the above Mach wave mechanism. A systematic study of the three dimensional instability and acoustic wave modes of such a confined two dimensional shear layer has been completed. For shear layers with supersonic convective Mach numbers two families of instability waves are found. Each of the wave family is associated with Mach wave reflections off one of the channel walls. In addition to the instability waves two principal families of neutral acoustic modes are found. Again each is associated with reflections off one of the walls. The study also examines the three dimensional modes due to reflections off the side walls. Finite shear layer thickness effects are also analyzed. A detailed report of this work will appear in a forthcoming article in the Journal of Fluid Mechanics.

To enhance mixing of supersonic shear layers inside a rectangular channel we propose to use a Mach wave system generated by a wavy wall as shown in figure 2. The Mach waves penetrate through the shear layer producing a flow periodic in the downstream direction. It is known from low speed transition work that a periodic mean flow can trigger highly unstable 3-D instabilities. We believe that a similar situation could arise in high speed shear flows. To prove that the Mach wave concept is worth pursuing it is necessary to demonstrate, first of all, that in the presence of the periodic Mach wave system new 3-D instabilities are now possible. To do so a computational study has been carried out. It is easy to show that 3-D instabilities in a periodic mean flow are governed by a system of partial differential equations with periodic coefficients. Eigenvalues of the system can be found in accordance with the Floquet theory. In the present work a Fourier-spectral expansion numerical method is used. The flow variables are expanded in Fourier series in the flow direction and in Chebyshev polynomials in the cross-stream direction. A special mapping is introduced to concentrate the Chebyshev collocation points in the shear layer. Because of the large number of

Fourier-Chebyshev coefficients required for convergence the resulting matrix eigenvalue problem can only be solved by a super computer (Cyber 205). New 3-D instability wave modes generated by the periodic Mach wave system have now been found. Future work is to optimize the parametric excitation to provide maximum destabilization.



(a) Side view.



(b) End view.

Figure 1. Confined two dimensional shear layer inside a rectangular channel.

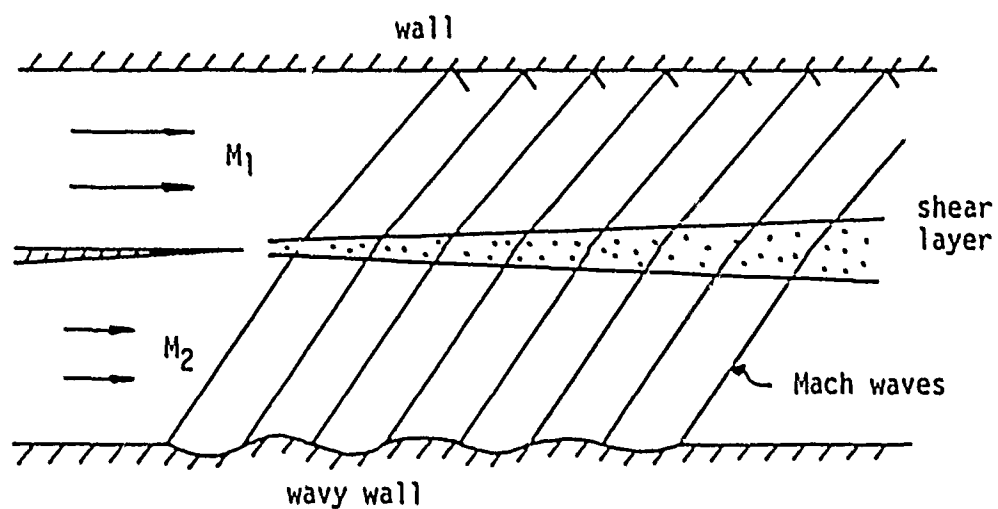


Figure 2. Parametric excitation of shear layer instabilities by a periodic Mach wave system.

MIXING IN SUPERSONIC SHEAR LAYERS

ONR Contract No. N00014-87-K-0169

Principal Investigator: Mo Samimy

The Ohio State University
 Department of Mechanical Engineering
 206 West 18th Avenue
 Columbus, Ohio 43210

OVERVIEW

The objectives of the present research are threefold. First, to investigate the effects of compressibility on the mixing in supersonic shear layers. Second, to explore different mixing enhancement techniques. Third, to explore the effects of large heavy particles on the mixing process. In the first category, our results show a significant reduction in both small and large scale mixing as the compressibility level is increased. In the second category, our preliminary results show that the bow shock/shear layer interaction does not change the mixing process judging from turbulence properties, the shear layer growth rate, and the flow visualizations. The research on the third category is in progress.

TECHNICAL DISCUSSION

In the past few years, the renewed interest in airbreathing hypersonic vehicles with supersonic combustion engine has resulted in more focused theoretical and experimental research on supersonic shear layers. A compressibility parameter has been identified which correlates well the growth rate of compressible shear layers. This parameter is the convective Mach number, a Mach number with respect to a frame of reference travelling with the average large scale structures in the flow. In a two-stream shear layer (Fig. 1), the convective Mach number of stream 1 is defined as $M_c = (U_1 - U_c)/a_1$ where $U_c = (a_1 U_2 + a_2 U_1)/(a_1 + a_2)$ is the convective velocity of the average large scale structures and a is the speed of sound [1]. The convective Mach number of stream 2 is the same if the specific heats ratios of both streams are the same. Experimental results show a good correlation between M_c and the compressible shear layer growth rate when nondimensionalized with the incompressible shear layer growth rate with the same density and velocity across the shear layers [2]. Also, linear stability analyses show a similar correlation between the ratio of maximum growth rates of stability waves and M_c based on a frame of reference travelling with the stability waves [3].

Most of the recent experimental research on supersonic shear layers has been focused on the effects of compressibility on the growth rate of shear layers with little or no work on the effects of compressibility on the turbulence characteristics. The objectives of the present work are threefold. First, to investigate the effects of compressibility on both the mean flow and turbulence characteristics. Second, to explore different mixing enhancement techniques. Third, to explore the effects of large particles on both small and large scale mixing in supersonic shear layers. We have obtained detailed results in the first category [2] and some preliminary results in the second category [4]. We will present some results from both categories in this note. The work on the third category is in progress.

Experimental Facility and Instrumentation. The experiments were conducted at the Ohio State University Aeronautical and Astronautical Research Laboratory. The test section of the high Reynolds number supersonic tunnel is 152.4x152.4x500 mm. The cold and dry air generated at 16.4 MPa (2400 psi) is stored in two storage tanks with 42.5 m³ (1500 ft³) capacity. The flow to both streams is independently controlled. The tunnel can be operated in a steady state mode from 1.5 minutes to over 5 minutes depending upon the run conditions. A two-component coincident LDV was used for mean velocity and turbulence measurements and a Schlieren system was utilized for flow visualizations.

Experimental Conditions. Five experiments were conducted; cases 1 to 5. Table 1 shows the flow conditions. Three levels of convective Mach numbers were used to determine the effects of compressibility on the mean flow and turbulence characteristics of shear layers; cases 1 to 3. For cases 4 and 5, the flow in case 1 was used and a 4.76 mm diameter cylindrical rod or a square rod with a 4.76 mm side was passed through the test section. In both cases, the rod was located 117 mm from the trailing edge of the splitter plate with its center at the splitter plate level and spanned the tunnel. The shear layer was 14 mm thick and was fully developed at this location [2]. In all five cases the incoming boundary layer was fully developed with the momentum and boundary layer thicknesses of approximately 0.6 mm and 8 mm for case 3 and 0.5 mm and 8 mm for the other cases.

Mean Flow Results. In characterizing the mean velocity of shear layers, $U_1 - U_2$ seems to be an appropriate velocity scale and $U^* = (U - U_2) / (U_1 - U_2)^{1/2}$ an appropriate nondimensional velocity. These two parameters have been used by many researchers in both subsonic and supersonic shear layers. Most of the researchers have used the local shear layer thickness, b , defined in a variety of ways such as the thickness between $0.1U^*$ to $0.9U^*$, as the shear layer lateral scale. Theoretical analyses show that the mean flow profile has significant effects on the shear layer results. The shear layer thickness is based on only two points at the edges of the shear layer and cannot correctly characterize the lateral scale. Therefore in search of a global lateral scale, we have examined $y^* = (y - y_{0.5}) / t$ where $y_{0.5}$ is the location of $0.5U^*$ and t is either the local momentum thickness, y_3^* , or the local vorticity thickness, y_2^* . Plotting U^* versus y_3^* , the mean flow velocity profiles for various convective Mach numbers collapse only when cy_3^* , instead of y_3^* , is utilized. In this linear transformation, c seems to be a linear function of convective Mach number at least for the available data for $0 < M < 1$; $c = 1 - 0.41M$ [2]. However, when the vorticity thickness is used, all the available data collapse without any transformation; Fig 2. In Figure 2, the solid curve is $U^* = 0.5(1 + \tanh(2.4y_2^*))$ and obtained by a least square curve fit to data. Therefore, the vorticity thickness seems to be a reasonable global lateral scale in turbulent free shear layers.

Shear Layer Spreading Rate. The shear layer growth rate characterized by the shear layer thickness, the momentum thickness, or the vorticity thickness growth rate showed a linear growth in the fully developed region of the shear layer [2]. The nondimensionalized values of the thickness growth rates and the vorticity thickness growth rates of the present experiments versus convective Mach number followed the trend established by other researchers [1-3].

Turbulence Results. The appropriate velocity and lateral scales established, now we use these scales to examine the effects of compressibility on the turbulence results. Figures 3 and 4 show the lateral turbulence intensities and the Reynolds stress results for the subsonic flow of Oster and Wygnanski [4] and the three convective Mach number cases of the present experiments. For each convective Mach number, the graphs shown are the averaged results over many stations in the fully developed region of the

flowfields[2]. As the compressibility is increased, the maximum level and the lateral extent of both transverse turbulence intensities and the Reynolds stress are decreased. Also, there seems to be a shift of the location of maximum values toward the lower edge of the shear layers. The streamwise turbulence intensities show similar trends[2]. Both small and large scale fluctuations contribute to the turbulence intensities. But, the main contribution to the Reynolds stress stems from large scale structures. Thus, the compressibility seems to suppress both the small and large scale mixing. Figure 5 shows the correlation coefficient. This seems to show that as the compressibility increases, the lateral extent of the structures is reduced significantly.

Mixing Enhancement. Vorticity is generated behind a bow shock due to curvature of the shock wave. Thus, one would anticipate that the interaction of a bow shock with a free shear layer would enhance the mixing. A simple way of generating a two-dimensional bow shock is to pass a rod through the shear layer. The flowfield in case 1 was utilized and either a cylindrical rod with 4.76 mm diameter or a square rod with 4.76 mm side was passed through the shear layer at 117 mm downstream of the splitter plate where the flow was fully developed and the shear layer thickness was about 14 mm. The measurements were carried out from approximately 19 to 53 cylinder diameters downstream of the rod location. Both the mean flow and the turbulence data collapsed reasonably well in this region. Therefore, the results were averaged over many stations. Figures 6 and 7 show the results for the transverse turbulence intensity and the Reynolds stress. The shear layer thickness, instead of the vorticity thickness is used as the lateral scale, because the velocity profiles did not have a well defined linear region due to the effects of the wake behind the rod. There seems to be little or no effect in either the turbulence intensity or the Reynolds stress on the high speed side of the shear layer where the bow shock was generated. However, the low speed side indicates significant increases in both parameters, especially the transverse turbulence intensity. The streamwise turbulence intensities also show similar effects. The correlation coefficient does not show any change in comparison with the undisturbed case. There was no bow shock on the low speed side, therefore, the changes are mostly due to the wake effects. The shear layer growth rate determined from both the Schlieren photographs and the mean velocity measurements did not show any changes from the undisturbed case.

REFERENCES

1. Papamoschou, D. and Roshko, A., "Observations of Supersonic Free Shear Layers," AIAA Paper 86-0162, 1986.
2. Samimy, M. and Elliott, G.S., "Effects of Compressibility on the Characteristics of Free Shear Layers," to appear in AIAA J., 1989.
3. Bogdannof, D.W., "Compressibility Effects in Turbulent Shear Layers," AIAA J., Vol. 21, No. 6, pp. 926-927, 1983.
4. Oster, D. and Wygnanski, I., "The Forced Mixing Layer Between Parallel Streams," JFM, Vol. 123, pp. 91-130, 1982.
5. Samimy, M. and Erwin, D.E., "Shock Wave/Free Shear Layer Interaction", AIAA Paper 89-2460, 1989.

Case No.	Table 1				
	M_1	M_2	M_c	U_2/U_1	ρ_2/ρ_1
1(free shear layer)	1.80	0.51	0.51	0.36	0.64
2(free shear layer)	1.96	0.37	0.64	0.25	0.58
3(free shear layer)	3.01	0.42	0.86	0.24	0.36
4(cylinder)	1.80	0.42	0.51	0.36	0.64
5(square)	1.80	0.42	0.51	0.36	0.64

Figure 1 Schematic of the flowfield.

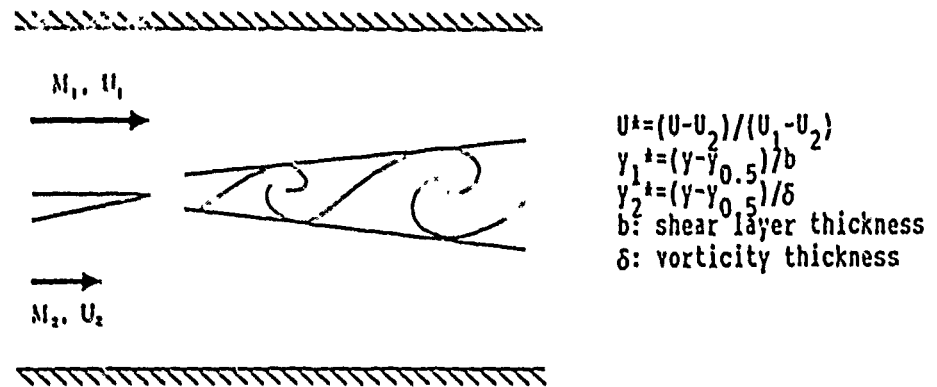


Figure 2 Axial mean flow profiles.

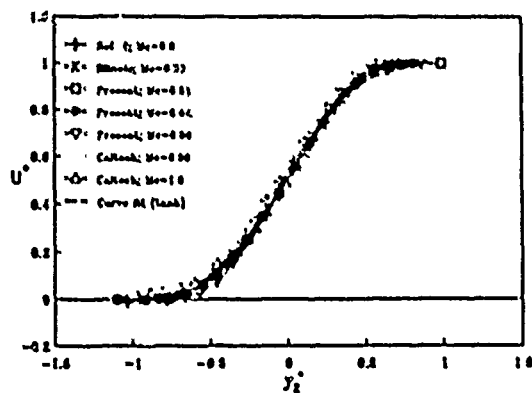


Figure 3 Lateral turbulence intensities.

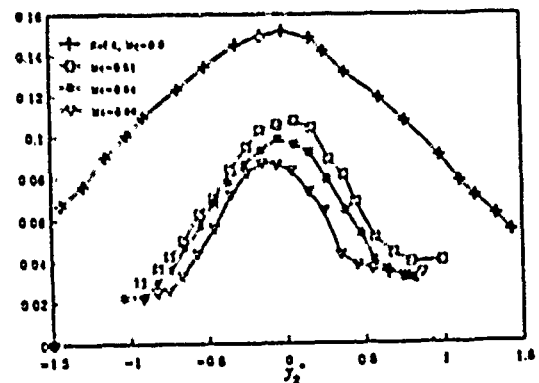


Figure 4 The Reynolds stress profiles.

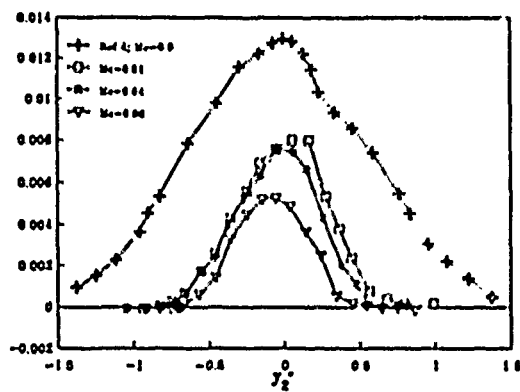


Figure 5 Correlation coefficient profiles.

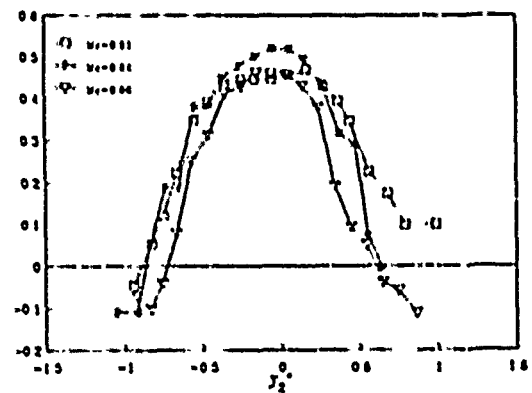


Figure 6 Lateral turbulence intensities.

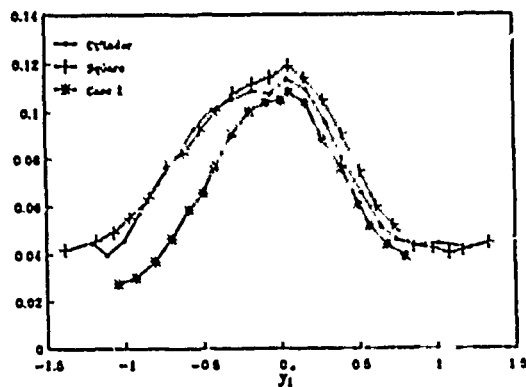
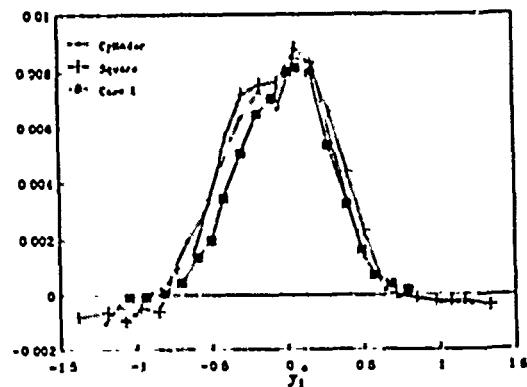


Figure 7 The Reynolds stress.



MIXING CONTROL IN SUPERSONIC SHEAR LAYERS

ONR Grant No. N00014-88-K-0242

Principal Investigators: P. J. Morris¹, D. K. McLaughlin¹ and G. S. Settles².

Departments of Aerospace Engineering¹
and Mechanical Engineering²
Penn State University
University Park, PA 16802

SUMMARY/OVERVIEW:

A combined experimental, analytical and computational program is underway to control and enhance the mixing of two supersonic streams. The experimental program involves both high Reynolds number studies of an axisymmetric shear layer and low Reynolds number studies of a two-dimensional shear layer. The analysis is based on the importance of large-scale coherent structures, modeled as instability waves, on the mixing process. Various mixing enhancement strategies are planned including acoustic shear layer excitation, shock shear layer interactions and periodic spatial forcing with Mach waves. The goals of this research are to gain a better understanding of the physics of supersonic mixing and to develop effective methods for supersonic mixing control and enhancement.

TECHNICAL DISCUSSION

The majority of the research this year has concentrated on describing the unforced shear layer. The high Reynolds number experiments have studied a helium-air mixing layer in a Mach 3 freestream. The low Reynolds number facility is in the final stages of construction. The analysis presented last year has been extended to compressible flows and axisymmetric layers.

I. High Reynolds Number Experiments (G. S. Settles)

As described in last year's abstract, an axisymmetric compressible mixing layer is being used to study the possibility of mixing enhancement and control by the manipulation of large-scale turbulent structures. Initial experiments have been conducted using an axisymmetric helium-air mixing layer in the supersonic wind tunnel facility of the Penn State Gas Dynamics Laboratory. This mixing layer is generated by injecting a helium stream through a swept strut into a cylindrical centerbody mounted along the wind tunnel axis. The 12mm dia. centerbody terminates in a replaceable, converging-diverging method-of-characteristics nozzle.

In principle, both the resulting helium stream and the wind tunnel freestream may be varied independently over the range of Mach 1.5 to 4.0. However, available pressure ratios and practical areas ratios for the axisymmetric nozzles limit this range somewhat. To date, all tests have been conducted with the wind tunnel freestream (air) at Mach 3, while the axisymmetric helium stream was injected at Mach

2.4, 3.5 and 4.3. (These cases were all chosen to yield theoretical convective Mach numbers above unity.) Both streams had near-ambient stagnation temperatures and stagnation pressures ranging from 7 to 24 atm in order to achieve a static pressure match for the various Mach number combinations studied. The typical mixing layer thickness in the region of observation was 3 to 4 mm.

Before attempting to manipulate the turbulence in this compressible mixing layer, we felt it necessary to first study its structure and phenomenology. Accordingly, high-speed schlieren observations have been made with a camera which uses the Cranz-Schardin principle of optical image separation. This camera takes 8 schlieren frames with a user-selectable interframe time interval from 0.1 μ s to 0.1 sec. For present purposes a 10 μ s interval, corresponding to an effective 100kHz framing rate, was found most appropriate. About 20 8-frame ensembles were shot at each of the 3 helium Mach numbers tested. The axisymmetry of the mixing layer provided a distinct advantage here, in that individual turbulent structures could be observed on the outer edge of the layer.

As an example, 3 consecutive schlieren frames from the Mach 3.5 helium/Mach 3 air mixing layer are shown in Figure 1. As indicated in the photographs, a particular turbulent structure on the outer edge (air side) of the shear layer can be followed from frame to frame. The 10 μ s time separation between frames and the distance travelled by the large-scale structure in this example yield a measured convective velocity of about 650 m/s. This is quite close to the velocity of the outer airstream (620 m/s), but far from that of the inner helium stream (1530 m/s). This trend is also seen in the other high-speed schlieren frames analyzed thus far.

For this example, the corresponding convective velocity from the isentropic theory is 945 m/s, much higher than what is actually observed. This discrepancy between the prevailing theory and experimental results has also been observed in planar mixing layers by Papamoschou(1989). It indicates that the actual phenomenon of large-scale turbulent motion in compressible shear layers is not properly described isentropically, and that an improved theoretical framework for convective Mach number is called for. The agreement of our results with those of Papamoschou(1989) strengthens this conclusion and also indicates no fundamental difference between our axisymmetric mixing layer and his planar case.

Qualitatively, the high-speed schlieren results show a mixing layer containing a broad range of turbulent scales (not unexpected at high Reynolds numbers). Large-scale coherent structures are imbedded in finer-scale "noise" and are not always identifiable. Both optical and digital image processing will be brought to bear on this problem in our continuing work. The collective observation from the results thus far is that the large scales are definitely evolving (changing shape) within our 70 s viewing "window." Whether or not this evolution involves classical vortex pairing is not obvious from the results to date.

In the near future we plan to use laser-beam deflectometry to obtain frequency spectra of the turbulence in our axisymmetric mixing layer. Laser-light-screen imaging will also be applied in an attempt to gain a better phenomenological view of the large-scale structure behavior. Having characterized the frequencies of these structures, we will then attempt to control the compressible mixing layer by "pumping" it with energy at these frequencies. Several schemes are in mind to accomplish this, including acoustic pumping and unsteady shock-wave motion. The effect on the overall mixing rate will be assessed both by optical observation and by probe surveys.

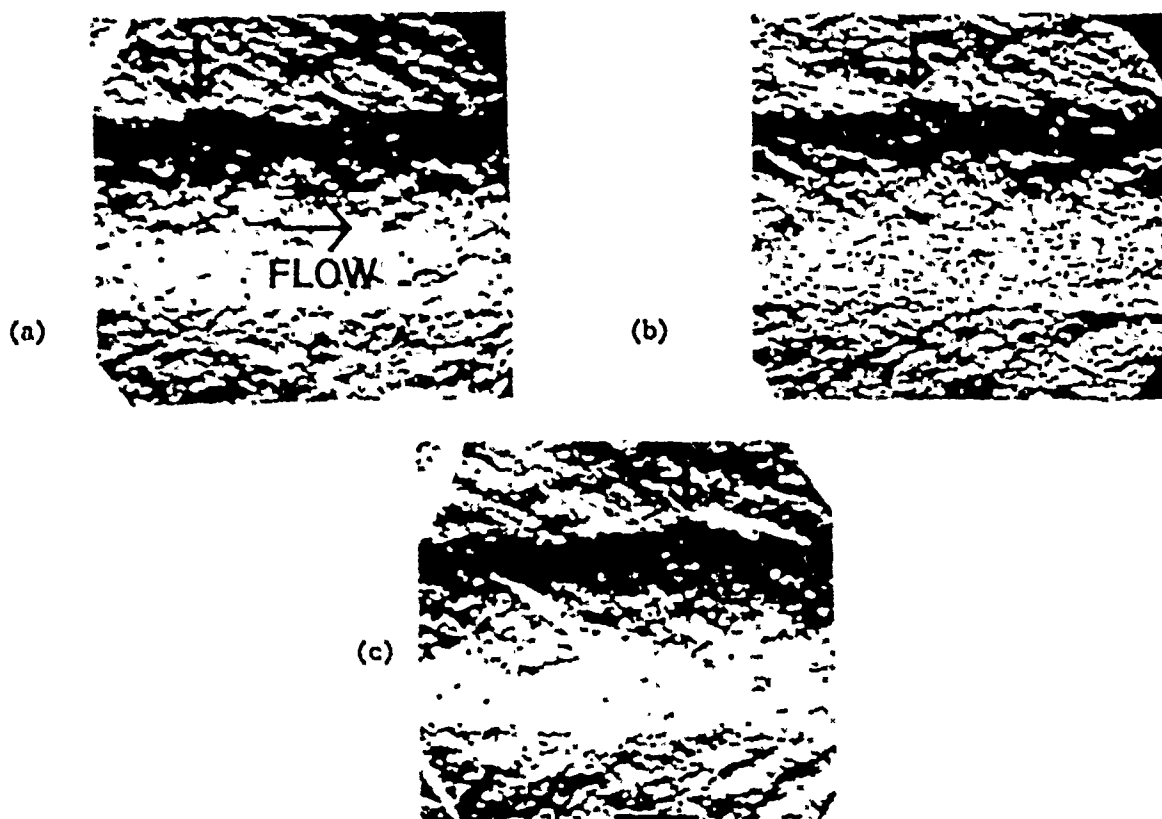


Fig.1 a-c. 3-Frame High Speed Schlieren Sequence Showing Motion of Large Scale Structures in Helium/Air Mixing Layer. $M_{He}=3.5$, $M_{Air}=3.0$, $\Delta t=10\mu s$.

II. Low Reynolds Number Experiments (D. K. McLaughlin)

During the past year the activity on this project has focussed on the final detailed design and fabrication of the low Reynolds number, two stream, supersonic shear layer facility. (See schematic diagram in Figure 2). Except for some of the instrumentation components, such as the probe traverse, the detailed design is virtually complete. The double sliding block nozzle system has been designed and fabricated using a CNC Mill. The test section shell has been fabricated and assembled (that includes the supersonic nozzles). The diffuser section has been fabricated. The vacuum pump and main vacuum tank are on hand, the secondary vacuum tank has been ordered; delivery is expected within 6 weeks. All vacuum piping, valves and controllers have been procured.

The computerized data acquisition system has been procured and facility monitoring and instrumentation data acquisition programs are being written. During the summer we will be assembling all purchased and fabricated components and conducting shakedown tests of our facility. These early experiments will include pitot pressure surveys and schlieren flow visualization of the shear layer, in a variety of combinations of Mach numbers of the two streams. The highest Mach number of the fast stream will be $M = 4$. The variation in spreading rate with Mach number combinations will be established at low to moderate Reynolds numbers.

Following the pitot pressure measurements, hot-wire surveys will be made to establish the characteristics of the large scale instability structure. Direct comparisons will be made with predictions of growth rates, etc., being made in the computation portion of this program. Comparisons will also be made with the high Reynolds number axisymmetric shear layer experiments.

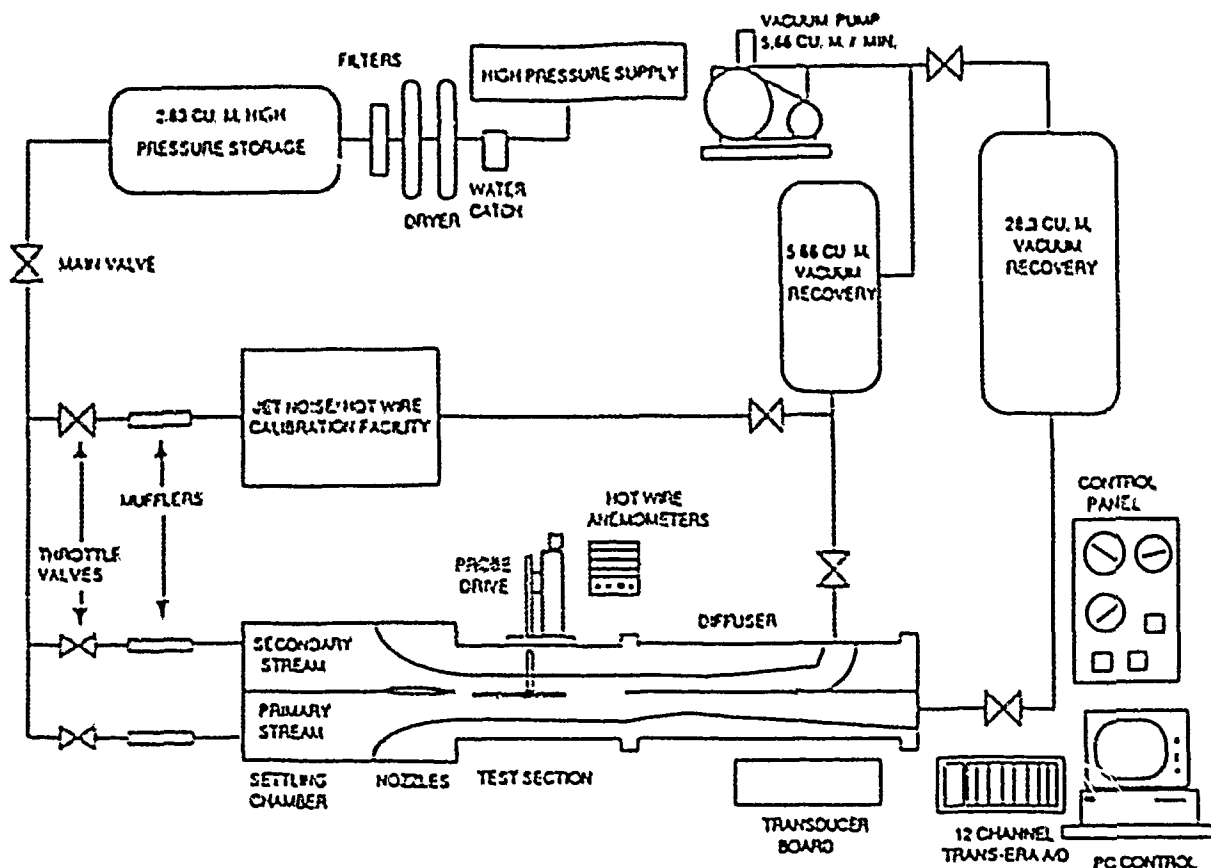


Fig. 2 Low Reynolds Number Supersonic Shear Layer Facility

III. Analysis and Computations (P. J. Morris)

In last year's abstract we presented a prediction scheme for two-dimensional shear layers where the large-scale coherent structures were modeled as instability waves. We also implemented the sub-harmonic evolution model to provide a single realization of the flow. There have been several extensions to this analysis.

The effects of compressibility have been included and predictions made for the spreading rate of two compressible shear layers. So far, only shear layers with subsonic convective Mach numbers for the instability waves have been considered. The agreement between prediction and experiment is very good. In addition we have extended the formulation to consider axisymmetric shear layers. This will provide the opportunity to determine the difference between the plane and axisymmetric shear layers and to compare with the axisymmetric shear layer experiments.

In addition to the sub-harmonic evolution model we have developed a model that describes the evolution of the wavenumber/frequency spectrum of the turbulence at the large scale. An initial "white noise" spectrum is introduced at the splitter plate and the spectrum is proposed to develop according to quasi-linear theory for each of the spectral components. Once again the predicted growth rate of the shear layer agrees well with experiments.

At present we are using the predictions of the large-scale unsteady flow field to determine the effects of compressibility on the turbulent structure. We are also extending the two-dimensional shear layer calculations to the supersonic convective Mach number range.

Reference:

Papamoschou, D., "Structure of the Compressible Turbulent Shear Layer," AIAA Paper 89-0126, Jan. 1989.

A REVIEW OF COMBUSTION INSTABILITIES IN PROPULSION SYSTEMS

F. E. C. Culick

California Institute of Technology

Abstract

Combustion of reactants in a confined volume favors excitation of unsteady motions over a broad range of frequencies. A small conversion of the energy released will produce both random fluctuations or noise, and, under many circumstances, organized oscillations generically called combustion instabilities. Owing to the high energy densities and low losses in combustion chambers designed for propulsion systems, the likelihood of combustion instabilities is high. The accompanying heat transfer to exposed surfaces, and structural vibrations are often unacceptable. This lecture is a brief review of combustion instabilities in solid propellant rockets and the three main types of liquid fueled systems: rockets, ramjets, and gas turbines, including afterburners.

Stability of combustion in a rocket motor was first treated by Malina and Karman in the late 1930's. They showed that to achieve stable burning of a solid propellant in a chamber having a choked nozzle, it is necessary that $n < 1$, where the linear burning rate is proportional to the pressure raised to the power n . That condition applied to very low frequency pulsations for which the pressure is nearly uniform within the chamber. While instabilities were encountered in both solid and liquid rockets in the early 1940's, extensive attention was not paid to the problem until after World War II. By 1950, instabilities had been encountered in all types of propulsion systems.

It is perhaps not surprising that until fairly recently, there has traditionally been relatively little communication between the communities of people concerned with combustion instabilities in the different systems. That situation has changed markedly in the past decade. Beginning in the early 1980's, increased concern with instabilities in dump combustors design for use in ramjet engines attracted the attention of many investigators who had previously been working primarily on solid rockets. Within the past two years or so, proposed development of new liquid rockets for the Advanced Launch System has further encouraged this trend.

One of the purposes of this lecture is to emphasize the common aspects of combustion instabilities found in the various systems. The chief physical reason for this property is that in all cases we are dealing with the excitation of acoustical motions by head addition or

by coupling between the unsteady motions and the average flow field. Thus it is possible to devise an analytical framework in which all cases may be accommodated. Differences in detail - which indeed can be significant - arise with differences in geometry and the fashion in which the reactants are introduced. Thus the essential mechanisms causing instabilities may be quite different. Nevertheless, appreciation of the more universal features is important to a sound understanding of the general problem.

Experimental results will be cited to support the development and conclusions of the formulation, but the emphasis here is on theoretical work, of which there are two sorts: analytical and numerical. By "numerical", we mean here results obtained by numerical solution of the partial differential equations governing the behavior of the system - that is, application of methods of computational fluid dynamics. Presently it is not possible to progress with exact formal analysis of those equations; "analytical" therefore implies some sort of approximate method. Both approaches are essential to a thorough treatment of instabilities; in this lecture we shall concentrate on approximate analysis, with only occasional reference to numerical results. The use of computational methods for treating problems of combustion instabilities is not widespread or highly developed.

The phenomena to be treated are extremely complicated, involving unsteady gas dynamics and the combustion of reacting flow systems which themselves cannot be described theoretically in all necessary detail. Hence the development of analytical methods must be guided at all stages by observational results. The theory is substantially a vehicle for organizing and interpreting experimental results. It is not possible to predict accurately the occurrence of instabilities from first principles. Nevertheless, with judicious melding of theory, measurements, and observations, we can construct a framework that provides the basis both for understanding the general behavior and for formulating simple statements succinctly summarizing the general characteristics. For practical purposes, achievements of the theory consist mainly in the ability to analyze, understand, and predict trends of behavior. The influences of geometrical characteristics and combustion processes can be assessed, but in any event some experimental data are required to provide quantitative results.

Owing to the semi-empirical nature of the theory, comparison with experimental results does not afford a sufficient basis for confirming the validity of any approximations. Thus an important function of numerical methods is to provide a means for checking the accuracy of approximate methods. Some recent results are given for elementary problems arising in solid propellant rockets.

The lecture will include a survey of the mechanisms that have been proposed during the

past fifty years to explain combustion instabilities in liquid and solid-fueled systems as well as summaries of the various analytical methods.

A PERTURBATION STUDY OF ACOUSTIC PROPAGATION IN A LOW MACH NUMBER SHEAR FLOW

(AFOSR Grant No. 89-0023)

Principal Investigator:

David.R. Kassoy

Mechanical Engineering Department, B-427
University of Colorado
Boulder, CO 80309

SUMMARY:

This study is focused on evaluating earlier work on acoustic wave propagation in shear flows. Traditional analyses are reformulated in terms of more formal perturbation methods, in order to be certain about the parameter ranges for which the solutions are valid. It is demonstrated that, (1) the refraction of traveling acoustic waves in a shear flow is strongly dependent upon the wave frequency, the wave amplitude and the mean flow Mach number; (2) the nonlinear effects are always weak; and (3) the earlier studies are valid only under limited conditions.

AUTHORS: Meng Wang and D.R. Kassoy

TECHNICAL DISCUSSION

Mathematical models for acoustic propagation in shear flows are traditionally formulated by a linearization technique (Pridmore-Brown, 1958, Mungur and Gladwell, 1969, Hersh and Catton, 1971). The linear acoustic wave equation for propagation in a fully-developed duct flow is given by

$$\frac{1}{c_0^2} p_{tt} = (1 - M^2) p_{xx} + p_{yy} - \frac{2M}{c_0} p_{xt} + 2\rho_0 c_0 M_y v_x, \quad (1)$$

where u , v , and p are acoustic horizontal velocity, vertical velocity and pressure, respectively. The sound speed of the mean state (p_0 , ρ_0 , T_0) is c_0 , and $M = M(y)$ is the mean flow Mach number. Both asymptotic and numerical solutions are obtained for unidirectional traveling waves in the above mentioned studies. When a plane wave travels downstream in a rigid-walled rectangular duct, the pressure distribution in the duct is severely distorted, and the acoustic pressure at the wall may reach very high values relative to that at the flow centerline. This phenomenon has received considerable attention in recent years due to its relevance to gasdynamic processes in rocket engines. Baum and Levine (1987) argue that the refraction-induced acoustic pressure enhancement or reduction on the solid propellant surface tends to alter its combustion characteristics. They conducted extensive numerical investigations of acoustic refraction phenomena based on Reynolds-averaged Navier-Stokes equations for compressible turbulent flow. The transient response of the gas to acoustic excitation at the inlet of the duct flow is considered. Results are compared qualitatively with those obtained by Pridmore-Brown and the other investigators mentioned above. A reduced refraction effect is observed in the numerical study, which is thought

to be attributable to nonlinear processes. However, the comparison is of limited value because the initial-boundary value problem considered by Baum and Levine is substantially different from the earlier work.

The goal of the present study is to gain more physical insight into acoustic refraction modeling by using a systematic rational approximation procedure. By examining the physical restrictions underlying the existing solutions, a common and consistent basis can be established for comparisons among those solutions. The parameter ranges for their validity are found. Results related to solid rocket engines are sorted out and analysed. This initial analysis is based on a laminar flow model for a viscous, heat conducting fluid. The concepts involved will be equally useful in gaining understanding of turbulent flows.

The complete dimensionless equations describing the compressible fluid motion in a planar duct can be written in the form,

$$p = \rho T, \quad (2)$$

$$\rho_t + M[(\rho u)_x + (\rho v)_y] = 0, \quad (3)$$

$$\rho[u_t + M(uu_x + uv_y)] = -\frac{1}{\gamma M} p_x + \frac{1}{\Omega R_c} \left(u_{yy} + \frac{1}{3} \Omega^2 u_{xx} + \frac{1}{3} \Omega^2 v_{xy} \right), \quad (4)$$

$$\rho[v_t + M(uv_x + vv_y)] = -\frac{1}{\gamma M \Omega^2} p_y + \frac{1}{\Omega R_c} \left(\Omega^2 v_{xx} + \frac{1}{3} v_{yy} + \frac{1}{3} u_{xy} \right), \quad (5)$$

$$\rho[T_t + M(uT_x + vT_y)] = -M(\gamma - 1)p(u_x + v_y) + \frac{\gamma}{\Omega P_r R_c} (T_{yy} + \Omega^2 T_{xx}) + M^2 \frac{\Phi}{\Omega R_c}, \quad (6)$$

where for convenience the thermophysical properties are assumed constant. The nondimensional variables are defined in terms of dimensional quantities by

$$(p, \rho, T) = \frac{(p', \rho', T')}{(p'_0, \rho'_0, T'_0)}, \quad u = \frac{u'}{U'_c}, \quad v = \frac{v'}{v'_R}, \quad t = \frac{t'}{t'_R}, \quad x = \frac{x'}{x'_R}, \quad y = \frac{y'}{d'}, \quad (7)$$

where p'_0 , ρ'_0 , and T'_0 are thermodynamic properties of the gas at mean state, d' is the half width of the duct and U'_c the mean velocity at the centerline. We will concentrate on acoustic waves of frequency ω' traveling in the x -direction, so that the inverse of ω' can be taken as the characteristic time of the system, $t'_R = 1/\omega'$. The other two characteristic variables are given by $x'_R = c'/\omega'$ and $v'_R = M\omega'd'$. The key parameters in (2)-(6) are:

$$M = U'_c/c', \quad \text{the maximum mean flow Mach number;} \quad (8)$$

$$R_c = c'd'/\nu', \quad \text{the acoustic Reynolds number;} \quad (9)$$

$$\Omega = \omega'd'/c', \quad \text{the normalized axial acoustic frequency.} \quad (10)$$

It should be noted that $MR_c = R_c$, the mean flow Reynolds number. Solutions are sought in the limit when $R_c \rightarrow \infty$ and $M \rightarrow 0$.

As in previous studies, the basic steady flow in the duct is assumed to be fully-developed. On the length scale x'_R the variation of p is negligibly small. The acoustic part of the Navier-Stokes equations in (2)-(6) is obtained by filtering out the mean flow equations. Since the acoustic Reynolds number is in general very large, it is observed from (2)-(6) that except for the extremely thin acoustic boundary layers adjacent to the solid surfaces, the wave motion in the core region is basically unaffected by transport effects. An $O(\epsilon)$ acoustic velocity is used to disturb the fully-developed flow, and it is shown that the thermodynamic variables are always $O(M\epsilon)$. Thus if

$u = U(y) + \varepsilon \tilde{u}$, $v = \varepsilon \tilde{v}$, then $\Psi = 1 + (M\varepsilon)\tilde{\Psi}$ where $\Psi = (p, \rho, T)$. The continuity equation (3) can be rewritten in terms of acoustic variables as

$$\dot{\rho}_t + \tilde{u}_x + \tilde{v}_y + MU(y)\dot{\rho}_x + M\varepsilon[(\dot{\rho}\tilde{u})_x + (\dot{\rho}\tilde{v})_y] = 0. \quad (11)$$

The momentum and energy equations are treated in the same way. From these equations one finds three distinct classes of acoustic motion in the core region:

1) $1 > M \gg O(\varepsilon)$; in the limit $\varepsilon \rightarrow 0$ M is treated as a constant, although it may be a small number. Since the effect of shear flow is retained in the leading order acoustic equations, strong acoustic refraction is expected. A combination of (11) with the corresponding momentum equations generates a leading order acoustic equation equivalent to (1). Thus one concludes that the previous analyses by Pridmore-Brown (1958), Mungur and Gladwell (1969), and Hersh and Catton (1971) are formally valid only for extremely small amplitude acoustics. These acoustic disturbances are too weak to be of relevance in rocket engine gasdynamic problems.

2) $M \ll O(\varepsilon)$; the basic acoustic equation describes wave propagation in a uniform field because the characteristic shear flow is so small. Acoustic refraction is observed only as a higher order effect.

3) $M = O(\varepsilon)$. This is the case most frequently encountered in an operating solid propellant rocket motor, which typically has an axial Mach number of $O(0.1)$ and a pressure oscillation of 1-2% of the mean value. Numerical studies by Baum and Levine (1987) are also concerned with this regime. We adopt Pridmore-Brown's solution form for traveling acoustic waves, $\dot{p} = F(\kappa, y)e^{i(\kappa x - t)}$, and seek plane-wave mode solutions. Both κ and the amplitude function F are expanded in terms of M . The boundary conditions are determined by requiring the vertical acoustic velocity to vanish at the wall ($y=1$) and the centerline of the flow field ($y=0$). It is found that when the wave frequency $\Omega \leq O(1)$,

$$\begin{aligned} F &= 1 + M(2\Omega^2) \left[\int_0^y \int_0^\eta U(\xi) d\xi d\eta - \frac{y^2}{2} \int_0^1 U(y) dy \right] + O(M^2), \\ \kappa &= 1 - M \int_0^1 U(y) dy + O(M^2). \end{aligned} \quad (12)$$

The above solutions agree with Hersh and Catton's (1971) perturbation results to $O(M)$. This shows that the *ad hoc* type of linearized solutions in the earlier literature are also valid to $O(M)$, for the case when $\varepsilon = M$. They are not valid at the next order, because nonlinear terms of $O(M^2)$ (cf. Eqn. (11)) are not included.

Equations (12) show explicitly the frequency dependence of the acoustic pressure distribution across the duct. The refraction induced pressure variation appears as an $O(M)$ correction term, which increases with increasing frequency of axial acoustic waves. For low frequency waves the refraction by the flow gradient becomes quite negligible. In a typical rocket motor of diameter $d' = O(1m)$, acoustic velocity $c' = O(10^3 m/s)$, and axial acoustic frequencies in the range 100-2000 Hz, the values of Ω are of order unity or less. The acoustic pressure distortion is small in general. Large refraction effects have been reported in the earlier literature for different parameter value ranges.

Asymptotic expansions in (12) become nonuniformly valid when $\Omega^2 \sim O(M^{-1})$. In this high frequency limit the problem is reformulated by using a scaled frequency, $\tilde{\Omega} = M^{1/2}\Omega$. The κ and F functions are shown to be $F(\kappa, y) = F_1(\kappa, y) + O(M)$ and $\kappa = 1 + M\kappa_2$, where F_1 and κ_2 are determined from the following eigenvalue problem,

$$\frac{d^2 F_1}{dy^2} = 2\tilde{\Omega}^2 [\kappa_2 + U(y)] F_1; \quad F_1'(0) = F_1'(1) = 0. \quad (13)$$

Obviously the acoustic refraction is greatly enhanced for higher frequency waves, as it now appears at the leading order term. Eqn. (13) is similar to but considerably simpler than the characteristic equation for wave amplitude in the earlier literature (e.g., Eqn. (7) in Pridmore-Brown's study, 1958). The latter is in fact not self-consistent when it is applied to the current situation ($\varepsilon = M$), because it contains higher order linear terms while ignoring nonlinear terms of the same order.

One important conclusion from our analysis is that nonlinear effects are always negligibly small during the low Mach number mean flow-acoustic interactions. The discrepancy between the classical linear acoustic theory and the numerical and experimental studies indicated by Baum and Levine (1987) may be caused by differences in flow conditions, especially the sensitive physical parameters such as the mean flow Mach number, the wave amplitude and the wave frequency.

The perturbation technique is also applied to study the thin acoustic boundary layer near the solid wall at $y = 1$. The boundary layer thickness is found to be $\delta \sim (\Omega R_c)^{-1/2}$, or $\delta' \sim (\nu'/\omega')^{1/2}$ in dimensional terms. If the acoustic variables are scaled properly, (2)-(6) can be simplified to

$$\begin{aligned} \gamma \bar{p} &= \bar{\rho} + \bar{T}, & \bar{\rho}_t + \bar{u}_x + \bar{v}_\eta &= 0, & \bar{u}_t &= -\bar{p}_x + \bar{u}_{\eta\eta}, \\ \bar{p}_\eta &= 0, & \bar{T}_t &= -(\gamma - 1)(\bar{u}_x + \bar{v}_\eta) + \frac{\gamma}{P_r} \bar{T}_{\eta\eta}, \end{aligned} \quad (14)$$

where $\eta = (1 - y)/\delta$ is the stretched boundary layer coordinate pointing away from the wall. The tilded acoustic quantities are defined by

$$u = M \bar{u}, \quad v = -(M\delta) \bar{v}, \quad \rho = 1 + M^2 \bar{\rho}, \quad p = 1 + M^2 \gamma \bar{p}, \quad T = 1 + M^2 \bar{T}. \quad (15)$$

The acoustic pressure is seen to be uniform across the boundary layer, equal to that at the edge of the layer. The viscous and thermal dissipation effects are responsible for acoustic energy losses. Eqns. (14) must satisfy no-slip condition and appropriate thermal conditions on the duct wall. The mean flow effects are exerted through the core solutions, that must be matched at the outer edge of the boundary layer. In particular, the equation for the horizontal acoustic velocity is decoupled from others because $\bar{p} \sim \bar{p}(x; t, y \rightarrow 1)$ is known. A separable solution form for traveling waves, compatible with that in the core, can be obtained.

Our analysis shows that in a quasi-static oscillatory acoustic system, the acoustic boundary layer is of constant thickness; and a self-similar horizontal velocity profile exists across the layer. The variation of boundary layer structure and the formation of new boundary layers observed by Baum and Levine (1987) are possibly only transient phenomena, of importance on the very short time scale for which their initial-boundary value problems are solved.

REFERENCES

- Baum, J.D. and Levine, J.N. 1987 Numerical investigation of acoustic refraction. *AIAA Journal*, Vol. 25, No. 12, 1577-1586.
- Hersh, A.S. and Catton, I. 1971 Effect of shear flow on sound propagation in rectangular ducts. *The Journal of the Acoustical Society of America*, Vol. 50, No. 3, 992-1003.
- Mungur, P. and Gladwell, G.M.L. 1969 Acoustic wave propagation in a sheared fluid. *J. Sound Vib.*, 9(1), 28-48.
- Pridmore-Brown, D.C. 1958 Sound propagation in a fluid flowing through an attenuating duct. *J. Fluid Mech.*, 4, 393-406.

NUMERICAL INVESTIGATION OF ENERGY EXCHANGE MECHANISMS BETWEEN THE MEAN AND ACOUSTIC FLOW FIELDS IN SOLID ROCKET COMBUSTION CHAMBERS

Principal Investigator: Dr. Joseph D. Baum
Science Applications International Corporation
McLean, VA 22102

SUMMARY:

This research effort is directed at understanding the energy exchange mechanisms between the mean and the acoustic flow fields in a solid propellant combustion chamber. A numerical investigation is conducted in which acoustic wave propagation in a tube in which the mean flow is injected through the lateral boundary, simulating the flow in a solid propellant rocket combustor, was modeled (Fig 1). The time-dependent compressible Reynolds-averaged Navier-Stokes equations were solved using a non-iterative Linearized Block Implicit scheme. Acoustic waves were initiated at the upstream boundary as downstream traveling compression waves. The traveling waves initially traversed the injection zone and then the hard wall zone of the tube. The computations utilized three different injection Mach numbers, simulating three different propellant burn rates, and three different acoustic wave frequencies.

Complex wave evolution phenomena were demonstrated as the wave propagated downstream near the injection surface. The acoustic signal propagated faster inside the acoustic boundary layer than outside. Consequently, the axial acoustic velocity transition near the injection surface occurred ahead of the transition outside the acoustic boundary layer, demonstrating a continuously varying phase relation between the axial acoustic velocity and the acoustic pressure near the injection surface (Fig 2). This phase difference varied with both injection Mach number and acoustic wave frequency. To complicate matters, it was shown that the flow in the acoustic boundary layer changed significantly with propagation distance from the upstream boundary (Fig 3). It is noted that the flow inside the acoustic boundary layer is controlled by the interaction between the mean and the acoustic flow fields, and that the mean flow varies with distance from the upstream boundary. It is thus concluded that a proper simulation of the interaction between the flow in a combustor and the combustion of the solid propellant, the so called velocity coupling effect, requires the coupling of the instantaneous local flow field with the propellant combustion model. The temporal and spatial evolutions of both the mean and the acoustic flow fields must be properly included. Thus, averaged or linearized models that do not model these processes, would yield erroneous solutions.

The rms acoustic boundary layer thickness at the same wavelength distance from the upstream boundary increased with blowing rate and decreased with frequency. The large

variation in acoustic boundary layer thickness (rms) as a function of propagation distance from the upstream boundary and the local mean flow demonstrate that it is impossible to obtain a unique acoustic boundary layer thickness value for any of these flows. Instead, it is necessary to compare acoustic boundary layer thicknesses under identical mean flow conditions.

The instantaneous axial acoustic velocity contours demonstrated significant mean velocity shifts that resulted in distortion of the initially harmonic acoustic signal. In addition, examination of the time averaged solution demonstrated large vorticity production and acoustic streaming phenomena. Results obtained demonstrated that while the instantaneous vorticity produced eddies near the wall which followed the local radial derivative of the axial acoustic velocity, the time averaged vorticity contours exhibit eddies which correspond to the interaction of the acoustic flow with the highest shear zones of the mean flow.

Finally, the time averaged axial energy flux values were integrated over radial planes to calculate the axial dissipation of acoustic energy as the wave propagated over the injection zone. The results demonstrated higher energy dissipation rates for upstream wave propagation than for downstream propagation, increased dissipation with frequency and with injection rates through the lateral boundary (Fig 4), and decreased dissipation rate with axial propagation distance (Fig 5). The results also showed that these higher dissipation rates resulted mainly due to higher viscous dissipation within the acoustic boundary layer, helping to pinpoint the source of the flow turning loss mechanism.

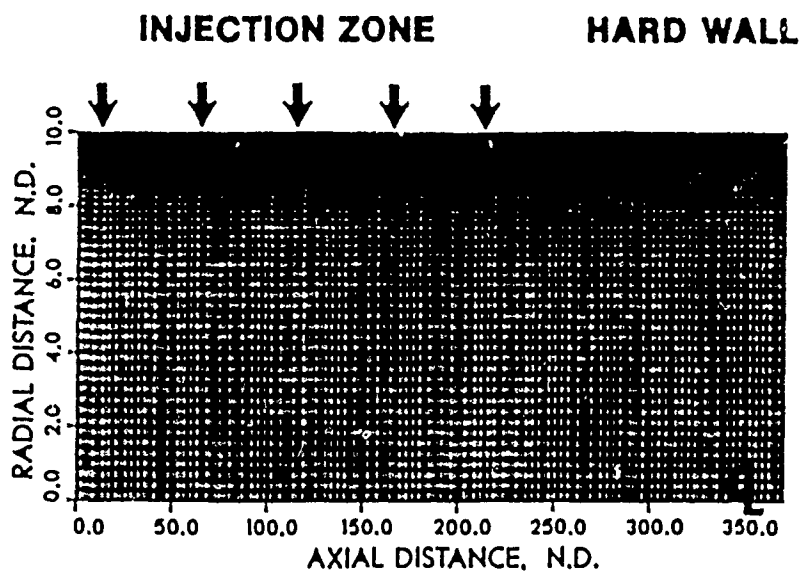


Fig 1. Computational Grid.

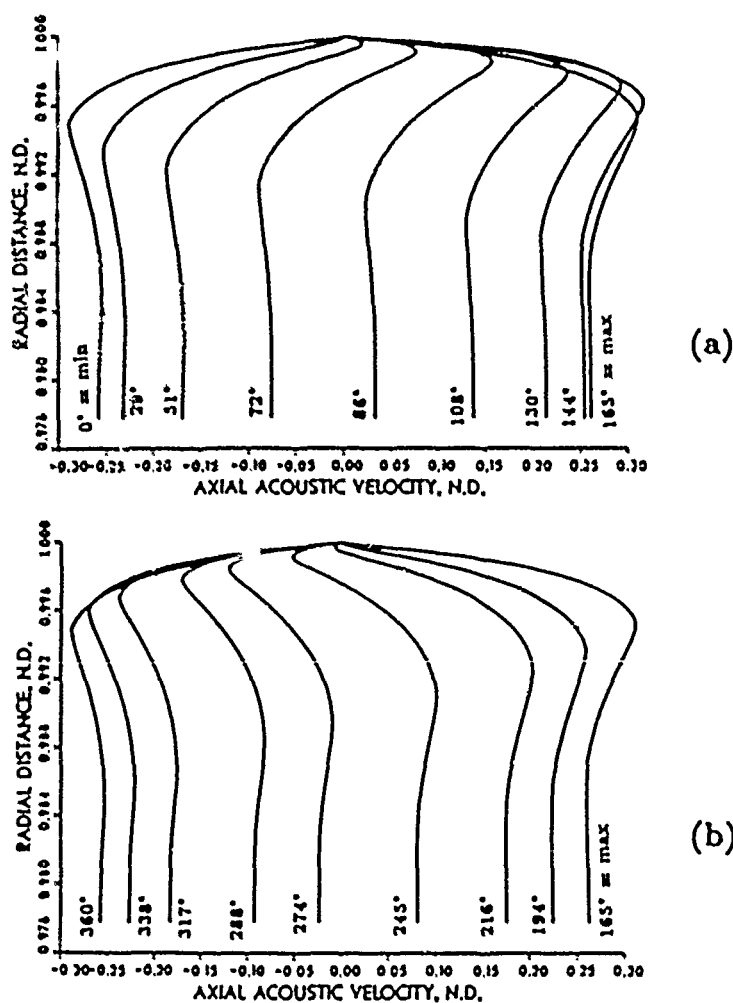


Fig 2. Time Evolution of Axial Acoustic Velocity Near the Injection Surface, $f=2000$ Hz, $M_{inj} = 0.0022$: a) Transition from Minimum to Maximum; b) Transition from Maximum to Minimum.

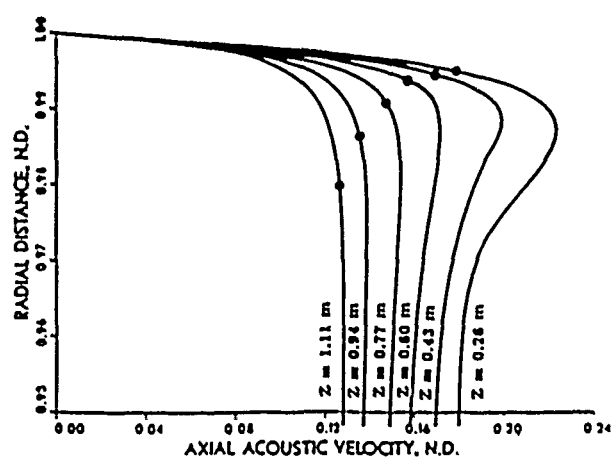


Fig 3. Axial Evolution of RMS Axial Acoustic Velocity Near the Injection Surface, $f=1000$ Hz, $M_{inj} = 0.0044$.

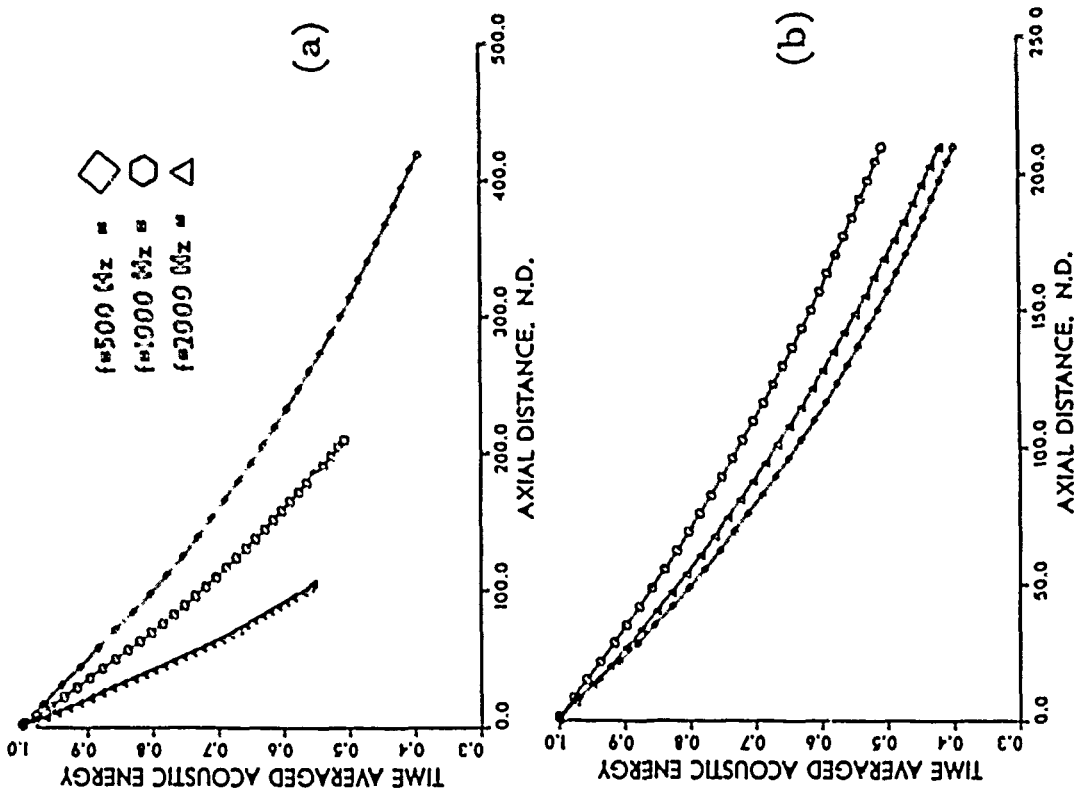


Fig 4. Comparison of the Axial Distribution of Time Averaged Acoustic Energy Flux: a) Injection Mach Number Dependence; b) Frequency Dependence.

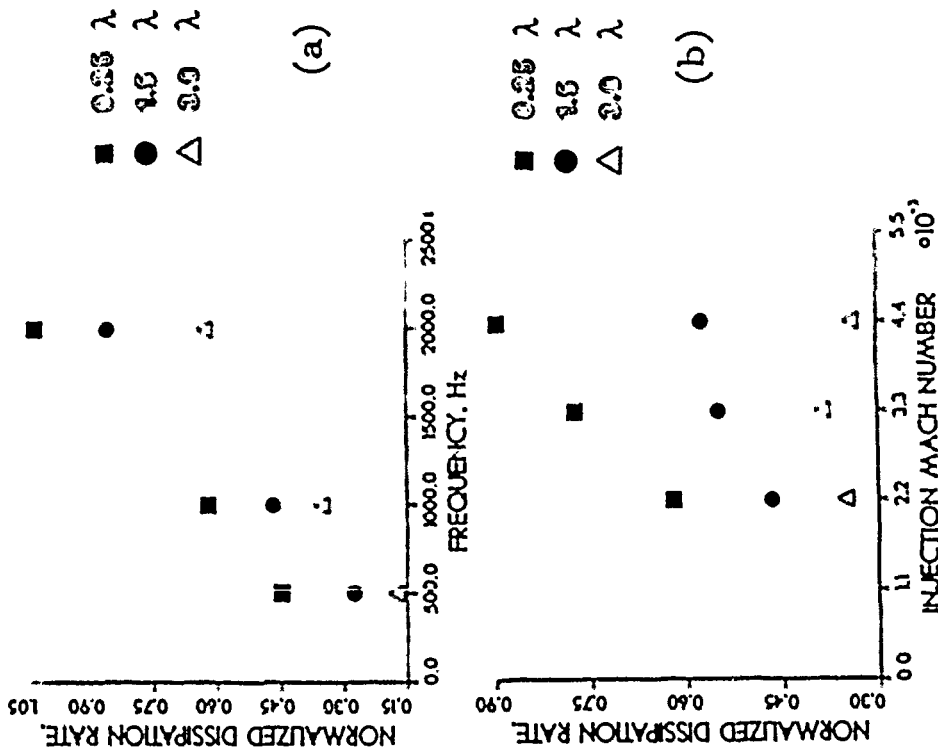


Fig 5. Comparison of the Axial Distribution of Time Averaged Acoustic Energy Flux Rates: a) Injection Mach Number Dependence; b) Frequency Dependence.

FLAME-ACOUSTIC WAVE INTERACTION DURING AXIAL SOLID ROCKET INSTABILITIES

(AFOSR Grant/Contract No. AFOSR-84-0082)

Principal Investigators: B.T. ZINN, B.R. DANIEL
and U.G. HEGDE

SCHOOL OF AEROSPACE ENGINEERING
GEORGIA INSTITUTE OF TECHNOLOGY
ATLANTA, GEORGIA 30332

Summary/Overview:

The objective of this study is to develop an understanding of the fundamental mechanisms through which axial instabilities in solid propellant rocket motors are driven by gas phase processes in the rocket combustion chamber. Laboratory simulations of unstable solid rocket motors, in which premixed and diffusion flames stabilized on the side wall of a duct are exposed to axial acoustic oscillations, have been investigated. To date, the manner in which the stabilized flames drive the acoustic oscillations has been clarified and theoretical models of this interaction have been developed. Future studies will investigate the effect of flow turning on the axial instabilities and determine its importance relative to the flame driving processes.

Technical Discussion:

Flow processes which occur near a propellant surface during unsteady burning are shown in Fig. 1. During an instability, unsteady heat transfer from the gas phase flame to the solid propellant results in an unsteady pyrolysis of the solid propellant. The latter produces an oscillatory flow rate of pyrolysis products which burn in a gas phase flame next to the propellant surface. The gas phase flame generally includes features of both premixed and diffusion flames. The velocity of the combustion products is, in most cases, almost completely radial. However, as these gases approach the combustor core flow, their flow direction changes from radial to axial.

The onset and maintenance of an axial instability depends upon the interaction between the acoustic motions and the above described processes. The gas phase flame drives the instability according to Rayleigh's criterion;¹ that is, unsteady heat release in phase with the acoustic pressure oscillations feeds energy into the acoustic motions. On the other hand, it has been argued² that flow turning would damp the instability since the unsteady axial momentum acquired by the gases, which leave the flame radially, is supplied by the axial acoustic field.

The present research program is concerned with elucidating the fundamental mechanisms involved in these driving and damping processes. Conceptually, the program may be divided into three parts. The first two parts deal with the problem of instability driving/damping by the gas phase flame, and the third part deals with the problem of flow turning. It has been noted that the gas phase flame has both premixed and diffusion flame characteristics. Therefore, Phase I deals with premixed flame - acoustic waves interaction and Phase II is concerned with diffusion flame - acoustic waves interactions. To date, the investigations under Phase I have been completed and the Phase II investigations are near completion. Phase III will commence shortly.

Laboratory investigations of these interactions have been studied in the specially developed experimental set up, see Fig. 2. It consists of a rectangular duct with a burner located on one of the side walls. The figure depicts the diffusion flame burner used for the Phase II studies. For Phase I investigations, a premixed flat flame burner was employed. During an experiment, the acoustic drivers excite an axial acoustic wave of desired frequency and amplitude in the duct. The interactions of the diffusion flames with the excited sound wave are then investigated.

Experimental efforts have included high speed cinematography, optical CH radiation and temperature measurements and LDV velocity measurements. These measurement systems have been utilized to determine the flame shapes, heat release rates and velocity field under a variety of excitation conditions. In addition, theoretical models of the unsteady flame behavior have been developed. The premixed flame (Phase I) studies have been described in detail in earlier reports³; here, the studies conducted to date with the diffusion flames are summarized.

A schematic of the developed diffusion flame is shown in Fig. 3. Fuel and oxidizer are injected through alternate slots and diffuse towards each other. A diffusion flame is formed at approximately the stoichiometric surface. The sidewall location is defined by $Y=0$ and the flame height is denoted by $Y = Y_f$.

From high speed shadowgraph visualizations, it was determined that the diffusion flames oscillate axially under the influence of a longitudinal acoustic field and the frequency of oscillation coincides with the frequency of the excited wave. Measurements of the CH radiation emitted by the flames have also been made as they are indicative of the heat release rates. Initially, the overall heat release rate oscillations were measured by measuring the CH radiation from the entire flame. It was found that the phase of the heat release rate with respect to the pressure oscillations was frequency dependent. Using Rayleigh's criterion, it was then shown that the flame driving/damping is also frequency dependent.

Next, the radiation from thin "slices" of the flame parallel to the X-axis (see Fig.3) was measured to determine the spatial distributions of the heat release rate. For example, Fig. 4 plots the real part of the cross spectrum between the radiation and pressure oscillations from thin slices of the flame at different Y locations for an excitation frequency of 500 Hz. When this quantity is positive, the unsteady heat release rate feeds energy into the acoustic motions and vice versa. Therefore, it may be seen that different regions of the flame may either drive or damp the oscillations.

Similar results have also been obtained from the developed theoretical model. It is based upon a modified Burke-Schumann type of analysis and it has also shown that different regions of the flame may either drive or damp the acoustic oscillations. This is described in Fig. 5. The plot shows the computed values of the real part of the cross spectrum between the normal velocity fluctuation, v' , and the pressure oscillations, p' , summed over the axial (X) extent of the flame region for different Y locations for simulated excitation conditions. In regions where this quantity increases (i.e., its slope with respect to Y is positive), energy is fed into the axial acoustic oscillations and vice versa.

Current studies are aimed at validating the model by comparing its predictions with experimental observations. Subsequently, the effects of flow turning on the axial instabilities will be investigated.

REFERENCES:

1. Lord Rayleigh, The Theory of Sound, Dover, 1945.
2. Culick, F.E.C., Comb. Sci. and Tech., Vol. 7, pp. 93-97, 1977.
3. Zinn, B.T., Hegde, U.G., Jagoda, J.I. and Daniel, B.R., Final Report, AFOSR Grant No. AFOSR-84-0082, March 1989.

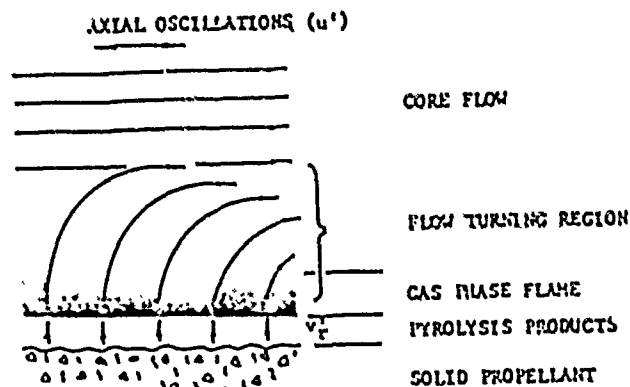


FIG. 1. FLOW PROCESSES IN THE VICINITY OF A BURNING SOLID PROPELLANT EXPOSED TO AXIAL OSCILLATIONS.

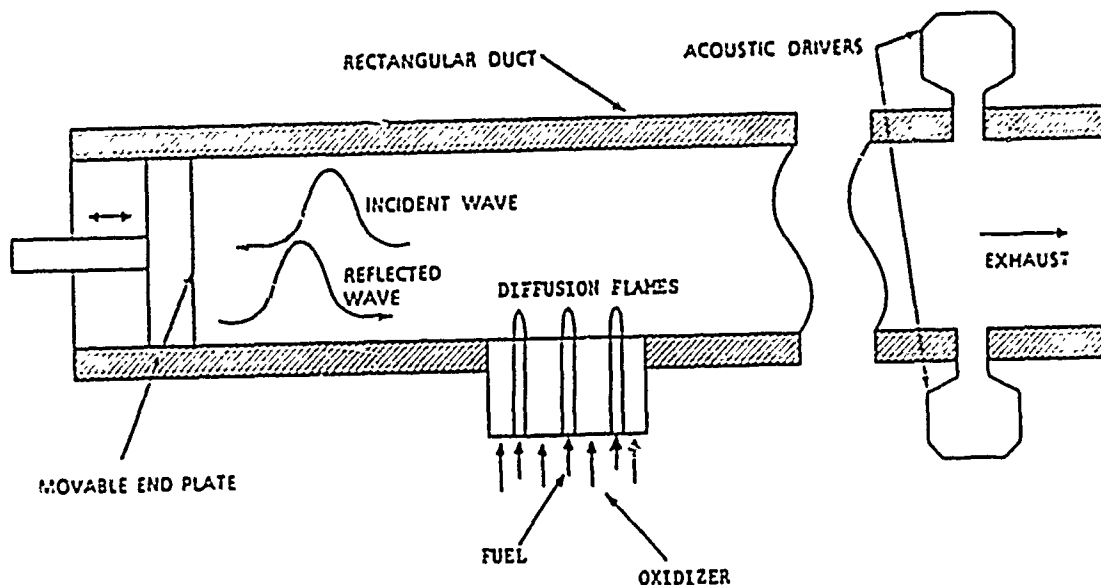


FIG. 2 SCHEMATIC OF THE DEVELOPED EXPERIMENTAL SET-UP TO INVESTIGATE THE INTERACTIONS BETWEEN GAS PHASE DIFFUSION FLAMES AND LONGITUDINAL ACOUSTIC FIELDS.

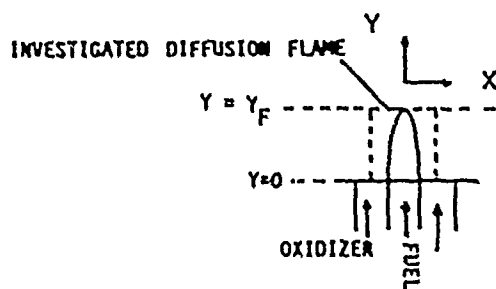


FIG. 3 A SCHEMATIC OF THE DEVELOPED DIFFUSION FLAME.

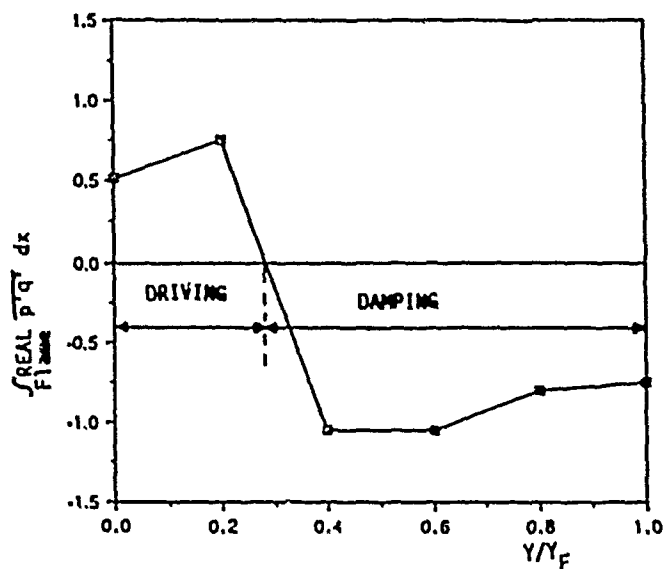


FIG. 4. MEASURED VALUES OF $\int_{Flame} REAL p'q' dx$ AS A FUNCTION OF FLAME HEIGHT FOR AN EXCITATION FREQUENCY OF 500 Hz.

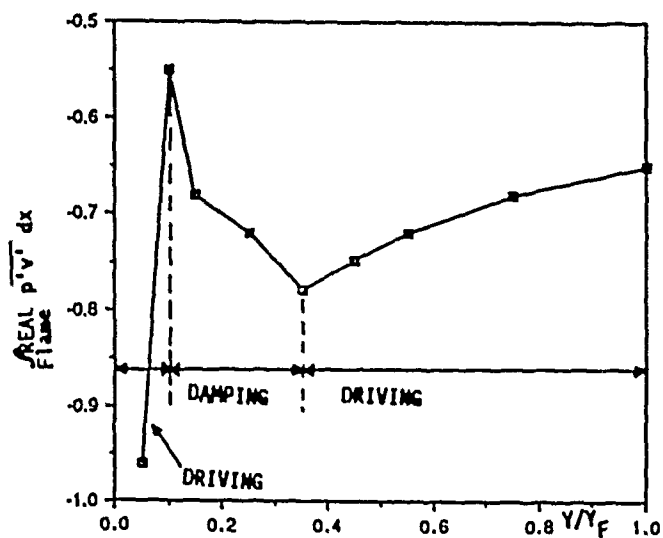


FIG. 5. COMPUTED VALUES OF $\int_{Flame} REAL p'v' dx$ AS A FUNCTION OF FLAME HEIGHT FOR SIMULATED EXCITATION CONDITIONS.

FRactal Image Compression of Rayleigh, Raman,
LIF and LV Data in Turbulent Reacting Flows

(AFOSR Contract No. 88-0001)

Principal Investigators: W. C. Strahle and J. I. Jagoda

School of Aerospace Engineering
Georgia Institute of Technology
Atlanta, GA 30332

SUMMARY/OVERVIEW

The objective of this study is to increase our understanding of, and to create a data base for, a complex, reacting, turbulent flow with recirculation. In addition, it is our goal to develop new methods for analyzing data obtained in experiments of short run times and with limited data rates. Furthermore, an analytical model of the flow field is being developed and compared with the data as they are being obtained. The reacting flow which is being investigated is that over a backward facing step with fuel injection through a porous plate which forms the floor behind the step. The diagnostics used include laser Doppler velocimetry, Rayleigh scattering and Raman spectroscopy. Laser induced fluorescence measurements will also be carried out. The data are being analyzed using fractal image compression techniques involving affine maps.

TECHNICAL DISCUSSION

The work under this contract can be divided into three interrelated parts: 1. to generate a data base of velocity, injectant concentration, temperature and OH radical concentration in a highly complex, turbulent, reacting flow field, 2. to compare the experimental data with the results from a modified k- ϵ model for this turbulent reacting flow and 3. to use fractal analysis to filter the noise from the data and to interpolate between a limited number of relatively widely spaced (in time) data points.

The need for the first two objectives is self-evident. This flow field was selected because it is similar to that encountered in the flame stabilization region of a solid fuel ramjet. However, the solid fuel has been replaced by the injection of hydrogen through the porous plate in order to generate the "clean" flow field necessary for optical diagnostics.

The need for the third objective arises when data can only be obtained at a finite rate for a limited time. This issue becomes critical if the time interval between data points exceeds the shortest characteristic time of the flow. The problem is further complicated if the treatment of joint properties of data is required. Such circumstances exist in the present investigation. The data rate of the Raman experiment is limited by the maximum firing rate of the pulse laser (5Hz). The rate is further decreased for simultaneous velocimetry - Raman measurements since laser triggering must await the arrival of a seed particle in the test region. In addition, run times are limited to a few minutes in order to avoid buckling of the porous plate in the presence of the high temperature flow. Nevertheless, a large number of data points are required at each location in order to fully characterize this highly turbulent flow field. A fractal reconstruction of the variation of the measured quantities

from a limited number of measured data points would, therefore, be of great assistance. Since covariances of different properties are also required to fully describe the flow, this problem lends itself to a full treatment of fractal reconstruction.

Velocity, concentration and their covariance in the cold (i.e. non reacting) flow were measured using combined LDV - Rayleigh scattering during a previous contract. During this time, a modified k- ϵ code was developed which was used to predict the flow field. Good agreement was obtained between the theoretical and experimental results. The results of this work were published in the open literature.

During the early stages of the present contract the measurements of covariance of velocity and concentration in the cold flow were improved and completed. In addition, preliminary velocity measurements were carried out in the axial direction of the flow field with combustion. Furthermore, the Raman system was readied for operation. On the theoretical side, work on the reacting turbulent flow code with finite reaction rates was continued. The results of this model were compared with the experimental data and with visual observations. Unfortunately two serious discrepancies were noted:

- the model predicted a shortening of the recirculation region upon the introduction of combustion while a lengthening was actually observed and measured.
- the model predicted a flame region close to the porous floor while a flame attached to the lip of the step was actually observed.

Additional work on the model was, therefore, called for.

During the first year of the present contract fractal based techniques were developed to interpolate between sparse data points in order to provide improved information on moments of pdf's. During the current year these techniques have been refined and applied to many data sets. An example of a fractal reconstruction of decimated data from a Rayleigh scattering measurement is shown in Fig. 1. Excellent results have been obtained when neighboring data points have some correlation with each other. However, when dealing with a Raman trace of uncorrelated data points, good results are not obtained. The root cause of this problem has been investigated and is believed to lie in the self-affine nature of the fractals used. That is, in Fig. 1 a magnified piece of the fractal fit is shown, and it contains some high frequency information which cannot exist on the true data trace. Its origin is in the mathematical mapping procedure used. Current work is attempting to overcome this problem by use of a more powerful technique known as hidden variable fractal interpolation.

Also accomplished during the past year was an investigation into the fractal character of the data traces used. Invented was the multifractal pdf which inquires into the distribution of fractal dimensions along a data trace. This information was compared with the multifractal spectrum, generated by inquiring into the generalized dimensions of the data traces. It was concluded that the multifractal pdf has some use in filtration of data but that the multifractal spectrum is not a particularly useful tool for gaining insight into the physical origin of the data.

During the current contract year the turbulent reacting flow field was mapped using Raman scattering. In addition, vertical mean velocities and

turbulence intensities were measured at different locations in the reacting flow. Hydrogen is used as a fuel since it results in a more one dimensional flame. In addition, hydrocarbon flames would emit a complicated spectrum, parts of which are known to interfere with the Raman Stokes and Anti-Stokes lines. The fuel flow was diluted with argon. In this way, the local nitrogen concentration in the flow field is indicative of the fraction of gas at that point which originated from the air inlet, i.e. of the degree of mixing.

The intensity of the rotational Stokes line of nitrogen was measured at different locations in the flow. This intensity is proportional to the number of nitrogen molecules in the test volume. The number density of nitrogen molecules is determined by two factors: 1. the local mixture fraction of nitrogen originating from the flow through the inlet and 2. the local temperature. In order to differentiate between the two effects, the argon diluent was replaced by nitrogen. Preliminary tests have shown that this did not measurably change the distribution of the nitrogen Stokes line intensities. It seems, therefore, that the observed changes in the number densities of nitrogen are predominantly due to the effects of temperature. For this reason, the results of the Raman Stokes measurements are presented in terms of temperature changes in this report.

Representative samples of the Raman results are shown in Fig. 2. The vertical distributions of mean temperature at various axial locations indicate the flame front (i.e. region of maximum temperature) is generally positioned about one half of one step height above the porous floor. This is in good agreement with visual observations but, as mentioned above, not with the results of the model. In addition, the mean temperature in the recirculation region becomes quite uniform in the downstream direction. At this particular station in the tunnel, the flame may have ceased at seven step heights downstream of the step. The vertical distributions of the RMS values of the temperature fluctuations at the corresponding axial locations are also shown in Fig. 2. The magnitudes of these RMS values are related to turbulent mixing of the cold reactants with the hot products, variations in heat transfer and, possibly, fluctuations in reaction rates. The regions of maximum temperature RMS values coincide with the areas of steep temperature gradients near the upper edge of the flame. In addition, temperature RMS values become quite small in the post reattachment region.

Vertical velocity profiles at three axial locations are shown in Fig. 3. Vertical mean velocities are generally downward. This is to be expected since the flow expands over the backward facing step. However, the relatively large magnitude of the downward component of the flow near the floor is somewhat surprising. Also, as expected, the magnitude of the downward component of velocity immediately behind reattachment is considerably smaller than that in the recirculation region. The RMS values of the vertical velocities are greatest in the vicinity of the flame region.

The discrepancies between the results of the model and the experimental observations were further investigated. Since the model does not account for heat losses to the floor, it was decided to compensate by slightly increasing the fuel flow rate. It was determined that if the fuel flow rate is doubled the flame front does, indeed, jump to the experimentally indicated position. The nature of this transition is currently being further investigated.

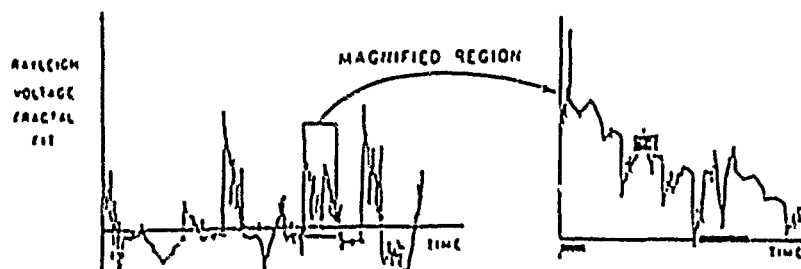


FIG. 1 - Fractal Fit of Density-Time Trace.

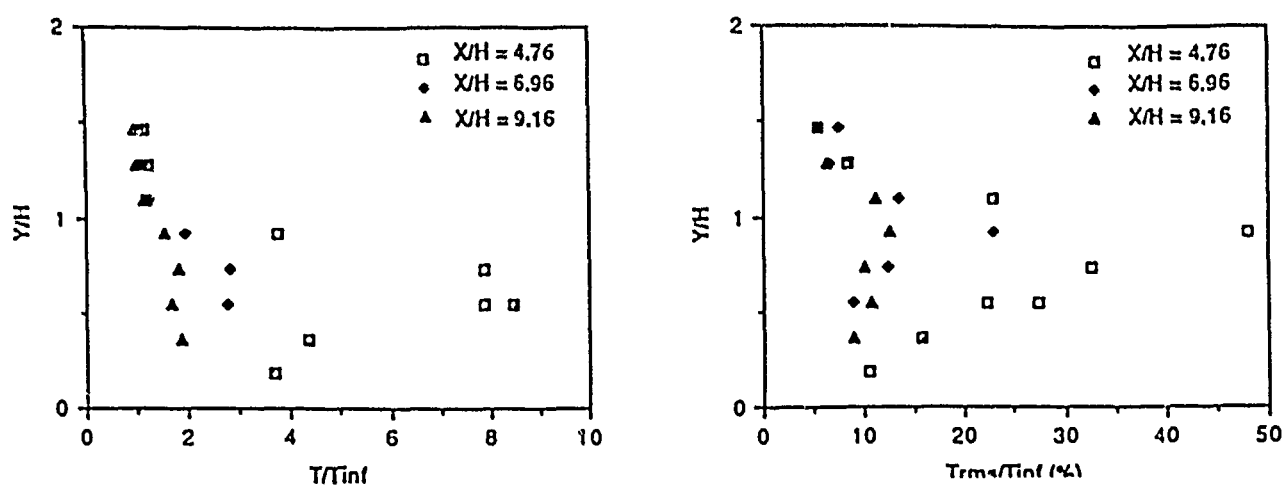


Fig. 2 - Normalized Temperature Distributions (mean-left, RMS-right)
 $T_{inj} = 298^{\circ}\text{K}$.

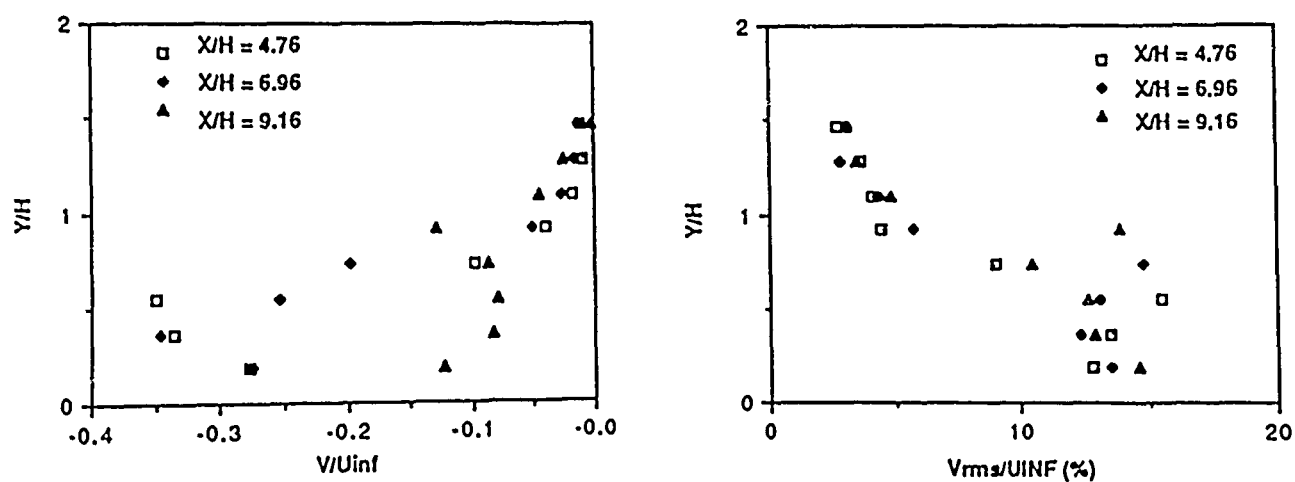


Fig. 3 - Normalized Vertical Velocity Distributions (mean-left, RMS -right)
 $U_{inj} = 60.2 \text{ m/s}$.

PLUME TECHNOLOGY

AFOSR Contract 2368/M²

Principal Investigators: D. P. Weaver and D. H. Campbell*

Astronautics Laboratory (AFSC)
Edwards Air Force Base, California 93521-5000

SUMMARY/OVERVIEW:

Investigations of the flowfield structure inside a rocket nozzle and in plume flow exhausting into a low density background, and the process of vibrational state relaxation of rocket exhaust plume effluents is being investigated using a variety of experimental and theoretical techniques. A high energy atmospheric simulator is also being developed to be used to investigate the interaction of high speed oxygen atoms with plume gases and spacecraft materials. A detailed understanding of the important physical processes responsible for the production of ultraviolet and infrared emission from high altitude liquid rocket motors is the primary goal of these studies. At present, the prediction of plume signatures relies on empirical assumptions about the flowfield structure and molecular excitation and relaxation processes. This research is aimed at delineating some of the most important basic flowfield and collisional processes in rarefied expansion flows.

TECHNICAL DISCUSSION:

In order to accomplish these stated goals, a series of investigation is being carried out to obtain information on the process of boundary layer expansion from nozzles into a low density background. The expansion of the boundary layer as the flow approaches the nozzle lip is a complex gas dynamic problem which can be complicated by the rarefaction of the flow to densities and temperatures at which the translational mode of the gas can become non-equilibrium. The gas that originates in the boundary layer is the primary source of flux into the higher angles ($>60^\circ$) which can (1) interfere with optical detectors on a spacecraft via radiation in the visible, UV, or IR, (2) contaminate spacecraft surfaces, or (3) collide with the high velocity freestream species to produce excitation of electronic, vibrational or rotational molecular energy levels which can then radiate. The chemical state of this boundary layer gas will depend critically on the structure of the flowfield inside and outside of the nozzle.

An experimental study is being conducted using a 0° halfangle nozzle (tube) inside a vacuum chamber. Optical diagnostics of the flowfield is being accomplished using the electron beam fluorescence technique. The boundary layer is being mapped at various positions inside the tube and immediately outside the tube exit plane. These results will be compared to theoretical predictions of the flow, using both continuum Navier-Stokes techniques and the direct simulation Monte-Carlo technique, which can predict flowfields when non-continuum conditions apply.

The other primary thrust of this work is an investigation of the process of vibrational relaxation of plume species in vacuum expansion flows. The basic phenomena of vibrational relaxation in expansion flows is being investigated via modeling and

* University of Dayton Research Institute On-Site Contractor

experimental work using free jets. To date, the flowfield and vibrational relaxation process have been investigated separately. Theoretical Monte-Carlo modeling results of the flowfield structure inside a stagnation region, out into tubes of various lengths, and finally in the free jet expansion have shown that the detailed geometry of the stagnation region and tube combination can have significant effects on the external flowfield. This is illustrated in Figs. 1 and 2, in which the velocity profile at the entrance to the orifice tube from the stagnation region and the total flux out of the orifice are shown for a range of orifice tube lengths for argon gas. The tube length is seen to have a significant effect on the magnitude and 2-dimensional profile of the gas velocity.

The vibrational relaxation work has used a rate equation modeling technique to track the vibrational levels of various gases with various starting population distributions expanding in a free jet. It has been demonstrated that the final "frozen" vibrational population distribution of plume gases can be highly non-equilibrium with a large amount of population in higher vibrational levels. Some of these results are shown in Fig. 3, where the final vibrational population distribution for a CO isentropic expansion after collisional relaxation in the vibrational levels has ended is shown for a series of stagnation densities and excitation positions in the jet (all population is initially in $v=1$). Experimental measurements of vibrational level populations of electric discharge heated gases in free jets are presently being conducted.

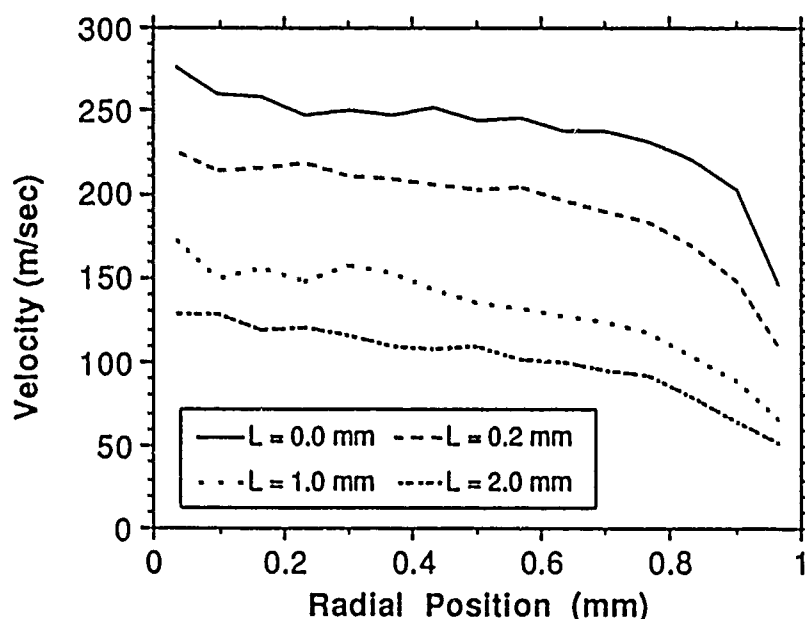


Fig. 1 Radial velocity distribution at stagnation region exit for various orifice tube lengths.

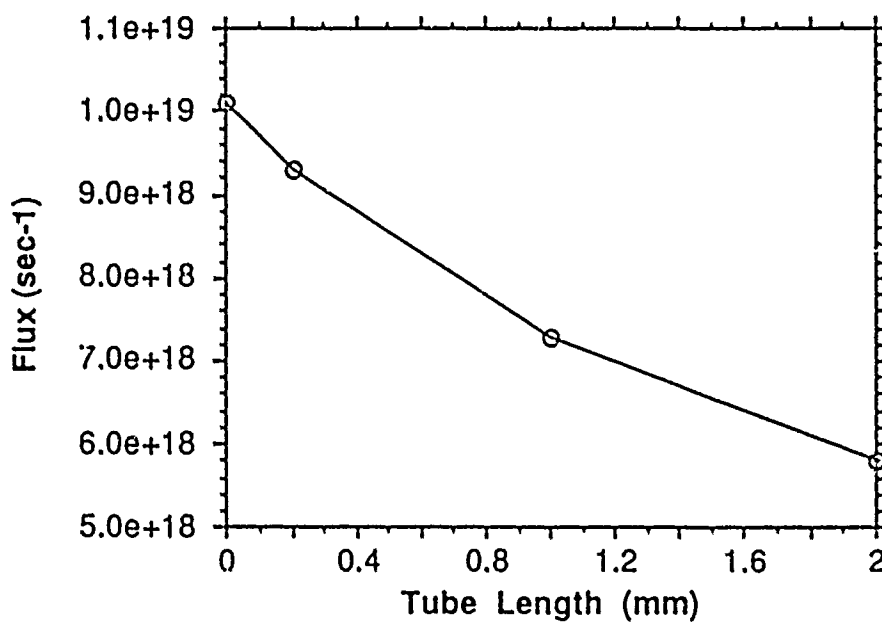


Fig. 2 Total flux through stagnation region exit plane for different tube lengths.

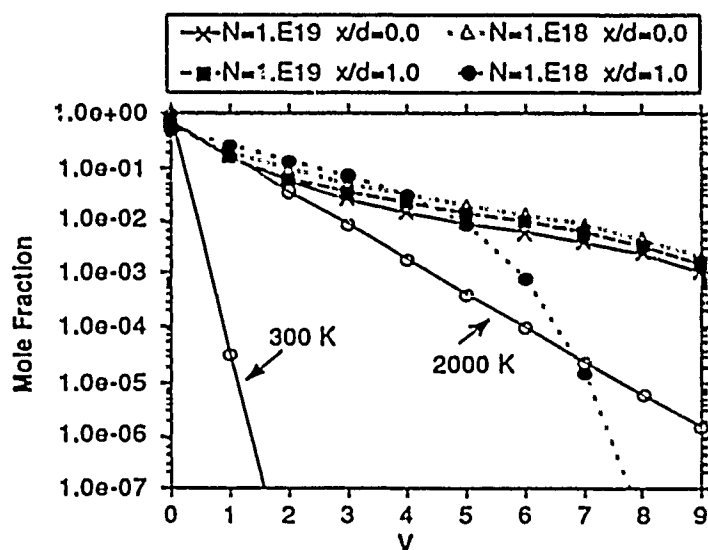


Fig. 3 Vibrational population distribution for isentropic CO expansion. Dependence on stagnation number density and position of initial excitation. Also shown is Boltzmann equilibrium distributions for 300 and 2000 K.

Robert Vondra
W J Schafer Associates

INTRODUCTION

Applied and self field MPD (magnetoplasmdynamic) thrusters will be covered in this report. Both thrusters consist of a cylindrical discharge chamber with a center mounted cathode and annular anode. Propellant gas is injected through a back plate. An arc discharge ionizes the gas and a $J \times B$ distributed body force (J is the current, B the magnetic field) provides the acceleration, although at low currents and high mass flows electrothermal forces become significant. The magnetic field can either be externally applied or self generated by the arc discharge.

Future DOD applications being considered for MPD thrusters include orbit raising heavy payloads (10s to 100s of thousands of kilograms) from low earth orbit to geosynchronous earth orbit. 100 kW to megawatts of electrical power are required to achieve transfer times of months. Electric propulsion systems will need total impulse capabilities of 10^7 to 10^8 N-s. Potential NASA requirements include multimegawatt cargo vehicle missions from earth to Mars, earth to Moon and Moon to Mars, with a total impulse requirement of 10^8 to 10^9 N-s.

THRUSTER OPERATION

Applied and self field MPD thrusters have been studied for over 20 years- quite extensively in the 1960s, at reduced levels in the 1970s and early 1980s, and again more extensively when the prospects of higher space power levels (10s kW, 100s kW, megawatts) and energetic orbit raising and planetary missions became a possibility.

In the electromagnetic mode, thrust is proportional to J^2 for self field thrusters, and $J \times B$ for applied field thrusters. Specific impulse is proportional to J^2 / \dot{m} (self field) and $J \times B / \dot{m}$ (applied field) where \dot{m} is the propellant mass flow rate. In self field thrusters, specific impulse is limited by a critical value of J^2 / \dot{m} called onset, above which arc column instabilities lead to a significant increase in cathode and insulator erosion. At low current levels, or more precisely low J^2 / \dot{m} , where electrothermal forces predominate, the above expressions for performance do not apply.

MPD propulsion has two foremost loss mechanisms. One is the anode fall loss and the other is the frozen flow loss. Thruster thermal efficiency is to first order determined by the relative magnitudes of the anode fall potential and the voltage across the plasma, hence efficiency tends to increase with power. Frozen flow losses include ionization, excitation and thermal losses, and represent power deposited in the plasma which is not recovered.

Applied Field

Applied field MPD thrusters have been operated over a range of a few 10's kilowatts to 100 kW+ power levels. The acceleration mechanism is quite complex, involving components of the applied magnetic field, self induced magnetic field, arc discharge current and Hall currents, which excite a number of thrust modes, including direct axial thrust (blowing), radial compression of the cathode tip, bulk plasma magnetic swirl, and electrothermal thrust. Applied magnetic fields enhance performance. The greatest enhancements occur at the lower power levels where self induced magnetic field strength is low. Applied magnetic fields are typically 0.1 to 0.2 Tesla, and enable low power engines to operate at specific impulses typical of megawatt level operation, i.e. a few thousand seconds. In some cases it has been shown that applied fields improve specific impulses of MW class engines, but more information is needed to determine if applied fields are necessary.

A typical performance range for hydrogen applied field thrusters range from 15% to 40% efficiency and 1500 to 3500 seconds specific impulse at low powers, and to 40% to 70% efficiency and 3500 to 8000 seconds specific impulse at high powers. Low powers are 20 to 80 kW, and high powers are 80 to 160 kW. Heavier propellants tend to have lower efficiencies and lower specific impulses.

Cathode erosion tends to be less of an issue with an applied field thruster than with a self field thruster because of lower currents. Also, there is evidence that an applied field enhances anode life by forcing the current to attach over a more diffuse region rather than in localized spots. The longest total impulse demonstrations to date have been 10^6 N-s for applied field operation, and 10^4 N-s for self field. Both performance levels are several orders of magnitude lower than DOD and NASA requirements.

Self Field

Self field MPD thrusters run at higher currents than applied field thrusters, in order to generate sufficient magnetic field strength; thrust $\sim J^2$. Current levels are typically several thousands to several tens of thousands amperes and power levels are several 100s of kilowatts to megawatts. The acceleration process is less complex than in applied field engines. There are effectively three components of thrust: direct thrust (blowing) due to the radial component of current interacting with the self induced azimuthal B field; radial compression (pumping) of the cathode tip, due to the axial component of current interacting with the self induced azimuthal B field; and electrothermal. At sufficiently high levels of J^2/Mdot , electrothermal contributions are negligible.

Self field MPD thrusters have operated at a few 100 kilowatts in steady state operation to megawatt levels in quasi-steady operation. At 100 kilowatt levels, J^2/Mdot is low,

indicative of electrothermal acceleration. As J^2/\dot{M} increases and acceleration changes from electrothermal to electromagnetic, performance improves. 100 kW operation has typically achieved 15 to 20% thruster efficiency and 1500 seconds specific impulse. Megawatt quasi-steady thruster operation has demonstrated efficiencies ranging from 20 to 40% with specific impulses from 2000 to 4000 seconds. 172

The operational life of self field MPD thrusters remains a central issue. High discharge currents take their toll on the cathode, either catastrophically with a cold cathode during quasi-steady operation, or more benignly with a hot cathode at thermionic emission temperatures typical of steady state operation. Erosion rates in the quasi-steady mode have ranged from 10^3 to 10^5 g/(kA-khr), and in the steady, hot mode, from 9 to 250 g/(kA-khr). Assuming a cathode mass of 1500 g, a discharge current of 10 kA, and cathode failure as 10% mass loss, the quasi-steady mode can be expected to operate reliably for no more than a few hours, 10^5 N-s total impulse. The steady mode of operation can be expected to operate reliably for a few hundred to a few thousand hours, 10^7 N-s total impulse. This is within range of DOD orbit raising applications.

PROGRAMS

The Air Force, SDIO, and NASA have initiated programs to develop high power electric propulsion. SDIO's thrust centers on 10 to 100 kW electrothermal arcjet technology. Since that does not include plasma propulsion it won't be discussed here. The Air Force and NASA are also developing arcjet propulsion, but in addition they are funding high power MPD development.

Air Force

The Air Force's Astronautics Laboratory (AL) is studying self field, steady state MPD propulsion at 0.5 MW and higher levels. This program is a continuation of their previous program with the University of Stuttgart which examined 100 kW MPD operation. Stuttgart evaluated different propellants, nozzles, chamber geometries, mass flow rates, etc, to find a design with desirable performance. Their work was guided by analytical models and research conducted by Stuttgart in other programs. At 100 kW levels, MPD performance was not stellar. Efficiency was 15 to 20% and specific impulses were in the mid 1000 to 2000 second range. Stuttgart found that increasing the mass flow rate and operating at higher current levels had the greatest impact on performance because electromagnetic thrust contribution became more significant. The goal of the present program is to demonstrate performance of 1500 to 3000 seconds specific impulse, with efficiencies greater than 30%, at powers above 500 kW.

The AL has a program at Princeton University to examine electrode and insulator erosion behavior using a real time measurement procedure developed by Princeton called the SLA (Surface Layer Activation) technique. It accommodates micron resolution depth measurements. Since Princeton's MPD thruster is operated quasi-steady, erosion rates are high compared to

Stuttgart's, and probably not representative of megawatt operation. Princeton is modifying their experiment to inductively heat the cathode electrode to temperatures sufficiently high for thermionic emission. Predictions of a simple erosion model based on evaporative mass loss will be compared with experimental measurements.

The Air Force Office of Scientific Research funds a number of programs addressing MPD issues. These are discussed in more detail elsewhere in these proceedings. Briefly, MIT and RDA are conducting a theoretical and experimental investigation of the physical processes in MPD thrusters, specifically the effects of electrode geometry on electrode current concentrations, and a description of the onset phenomena in terms of anode starvation and full single ionization of the plasma bulk. Stuttgart is looking at starting processes in MPD thrusters, an important consideration since the low pressure environment makes it difficult to start the engine. In previous AFOSR programs, Stuttgart developed theories, backed by experimental data, of arc column and arc attachment behaviors and their affects on onset and electrode mass loss. Ohio State is doing a theoretical study of MPD erosion, and RDA is studying MPD thrust chamber flow dynamics.

NASA

NASA's programs are primarily located at LeRC and JPL. Some work is funded at other institutions. LeRC and JPL are studying both applied and self field operation at the several hundred kW levels.

LeRC is examining the validity of using low power experiments to understand megawatt level MPD issues. Their approach is to determine the functional parameters that affect performance and then establish the relationship of those parameters to power level. Theoretical considerations indicate that MPD thruster performance (except for efficiency) is governed by local plasma and electrode characteristics, and not power.

LeRC is conducting applied and self field experiments at the low hundred kW level. The intent is to measure thrust on a thrust stand and make life measurements. In addition, LeRC is developing probe and nonintrusive diagnostics for determining and understanding MPD physical processes at low and high powers.

LeRC is developing a 2-D steady state, applied or self-induced magnetic field MPD simulation, adaptable to a variety of MPD geometries. The code includes viscous effects, and can be modified to include additional energy loss mechanisms. Ohio State is developing for LeRC non-intrusive diagnostics for quasi-steady state thrusters as well as computer codes to explore MPD physics fundamentals.

JPL has designed and built a subscale self field MPD thruster which they've operated at 60 kW, and will operate up to 250 kW. The goal is to understand cathode and anode erosion of steady state megawatt MPD operation by replicating pertinent

physical mechanisms at 100 kW. In addition, JPL is building an applied field thruster to verify performance and cooling schemes. The thruster will be radiation cooled. JPL is developing diagnostics to measure MPD exhaust velocities and magnetic fields, and are performing 2-D analysis of cathode and anode sheaths, and the arc discharge. 174

Princeton University, MIT, and Stuttgart have established experiments and analytical techniques for measuring and understanding the affects of MPD plasma wave instabilities on performance. Current driven instabilities, typical of electromagnetic plasma acceleration, strongly influence the efficiency and lifetime of electromagnetic accelerators. Turbulence dominates the processes of ionization and heating at all levels, especially when the plasma is fully ionized. At that point turbulence and loss processes are accentuated. Turbulence affects in all ranges of plasmas, particularly partially ionized, have dramatic implications for the performance of MPD thrusters.

ACKNOWLEDGEMENTS

I wish to thank the following people for their contributions to this report: John Barnett and Tom Pivirrotto (JPL), Roger Myers and Jim Sovey (LeRC), and Graeme Aston and John Brophy (Electric Propulsion Laboratory). Other information was taken from reports written by Arnold Kelly (Princeton) and Herbert Schrade (Stuttgart).

LASER THERMAL PROPULSION

AFOSR Grant No. AFOSR-86-0317

Principal Investigator: Dennis Keefer

Center for Laser Applications
University of Tennessee Space Institute
Tullahoma, TN 37388 - ph.:615 455-0631

The objective of this research is to develop an understanding of the basic physical processes that control the interaction of plasmas sustained by laser beams in a flowing propellant gas. Previous experimental and theoretical studies have provided a reasonable understanding of these processes in flowing plasmas sustained by continuous lasers, and have shown that the absorption efficiency and radiation losses can be controlled through a combination of optical geometry, pressure and flow configuration. Practical beamed laser propulsion systems may require laser powers greater than one megawatt, and current laser development for other applications suggest that lasers capable of delivering average powers at these levels will be free electron lasers (FEL). The power from these free electron lasers will be pulsed, rather than continuous, and we have successfully sustained quasi-steady argon plasmas using the RF linac free electron laser at Los Alamos National Laboratory (LANL). Although laser breakdown of argon was readily achieved, we were unable to obtain breakdown in either hydrogen or nitrogen.

In a plasma sustained by the absorption of power from a continuous laser, the power is absorbed primarily through inverse bremsstrahlung (free-free transitions in the electrons). The electrons are maintained in local thermodynamic equilibrium by electron-electron and electron-ion collisions, and the absorption coefficient can be accurately predicted using the Kramer-Unsöld theory. In free electron lasers, the pulse duration may be as short as a few picoseconds; a time similar to the electron collision time. Under these conditions it is unlikely that the electrons will maintain a Maxwellian distribution, and the absorption predicted by the Kramers-Unsöld theory may no longer apply. After the pulse terminates, the plasma will begin to decay from its nonequilibrium state through radiative and collisional processes, and may approach a local thermodynamic equilibrium prior to the arrival of the next pulse. If the time between pulses is sufficiently short, then subsequent pulses will be absorbed in the plasma remaining from the previous pulse, and a quasi-steady-state may be achieved, similar to plasmas sustained by continuous laser beams.

The RF linac free electron laser at LANL produces a burst of mode-locked micropulses having a duration of approximately 10 ps and a wavelength of 10.6 micrometers. These micropulses are spaced 46 ns apart in a burst (macropulse) lasting for 100 to 300 microseconds. The macropulses occur at rate of 1 Hz, and the average power in the macropulse is approximately 10 kW. This laser has a wavelength and an average power which are similar to those used for earlier experiments with continuous carbon dioxide laser sustained plasmas, and provides a nearly ideal source for experiments that can be compared with this earlier work.

The peak power in the micropulse was approximately 50 MW, and was sufficient to cause the argon plasma to self-ignite, in contrast to the continuous plasmas which must be initiated by some auxiliary means. The plasma initiated near the focal point and then migrated up the beam toward the lens as power was absorbed from subsequent pulses. The evolution of the argon plasma from initiation

through the 80 microsecond duration of the macropulse and its subsequent decay after the end of the macropulse is shown in Figure 1 as a sequence of high-speed images obtained using a Hadland Imacon 390 image converter camera. The framing rate was 100,000/s giving an interframe time of 10 microseconds. The plasma is observed to grow in size and intensity until near the end of the 80 microsecond macropulse, and then to decay over a time of approximately 50 microseconds. These plasmas were strong absorbers of the incident laser radiation. Measurements of the incident and the transmitted macropulse energy indicated that 80 to 96 percent of the incident laser radiation was absorbed by the plasma.

An interesting research issue was the rate of plasma decay during the 46 ns between the micropulses, and an optical multichannel analyzer (OMA) was used to observe the spectral emission of the plasma between pulses. The OMA was set to acquire a 10 ns time slice of the plasma, and the spectra from 10 successive macropulses was averaged and stored. The initial delay was then increased by 10 ns and the spectrum from the next 10 macropulses was averaged and stored. This process was repeated to scan a total of 60 ns. This data acquisition procedure insured that a spectral scan would include the full interpulse time and include at least one micropulse. Once a full 60 ns scan was obtained, the initial delay was increased by several microseconds and the 60 ns scan was repeated for a different portion of the macropulse.

Figure 2 is a composite of the six spectra taken at 10 ns intervals, and clearly shows that the plasma reaches a quasi-steady state during the 46 ns interpulse time. The spectrum consists primarily of the A II lines from the first ion of argon, and an estimate of the plasma temperature was obtained using the ratio of the intensities of the ion lines at 401.38 nm and 410.39 nm. The temperature is approximately 40,000 K during the early part of the macropulse, and then drops to about 35,000 K as the plasma expands in size. These temperatures are more than a factor of two larger than those we observed for continuous laser sustained argon plasmas, and reflect the much higher power that exists in the micropulses.

Attempts were made to initiate plasmas in both nitrogen and hydrogen using the same experimental procedures as for argon. These attempts were not successful, even though the pulse energy was an order of magnitude larger than our observed threshold for argon. This result is somewhat surprising since predicted breakdown thresholds for hydrogen and nitrogen are essentially the same as for argon using 10.6 micron wavelength and 10 ps duration pulses. This is because for such short pulses there is insufficient time for collisions to transfer the electron energy into the internal modes of the diatomic molecules. Thus, we have hypothesized that the argon plasma may not have broken down on the first micropulse, but may have accumulated electrons from subsequent pulses until breakdown occurred at some point several micropulses into the macropulse. Since we did not anticipate this effect, our measurements were unable to verify this hypothesis.

We have developed a theoretical model to investigate the question of breakdown threshold for the long wavelength, short pulse regime of our experiments. During the 10 ps duration of the laser pulse, there are only approximately 250 optical cycles and only approximately 10 electron-atom collisions. To study this process, we have developed a "square electron" model in which all elastic collisions result in a 90 degree change in direction. Preliminary results from this model indicate that electron energies of 60 eV are reached during the 10 ps micropulse, and that argon breakdown may occur after the eleventh micropulse. We will use this model to explore the differences in energy absorption and breakdown between argon and the diatomic gases, and to guide further experiments to be conducted both at UTSI and at LANL.

FIGURE 1

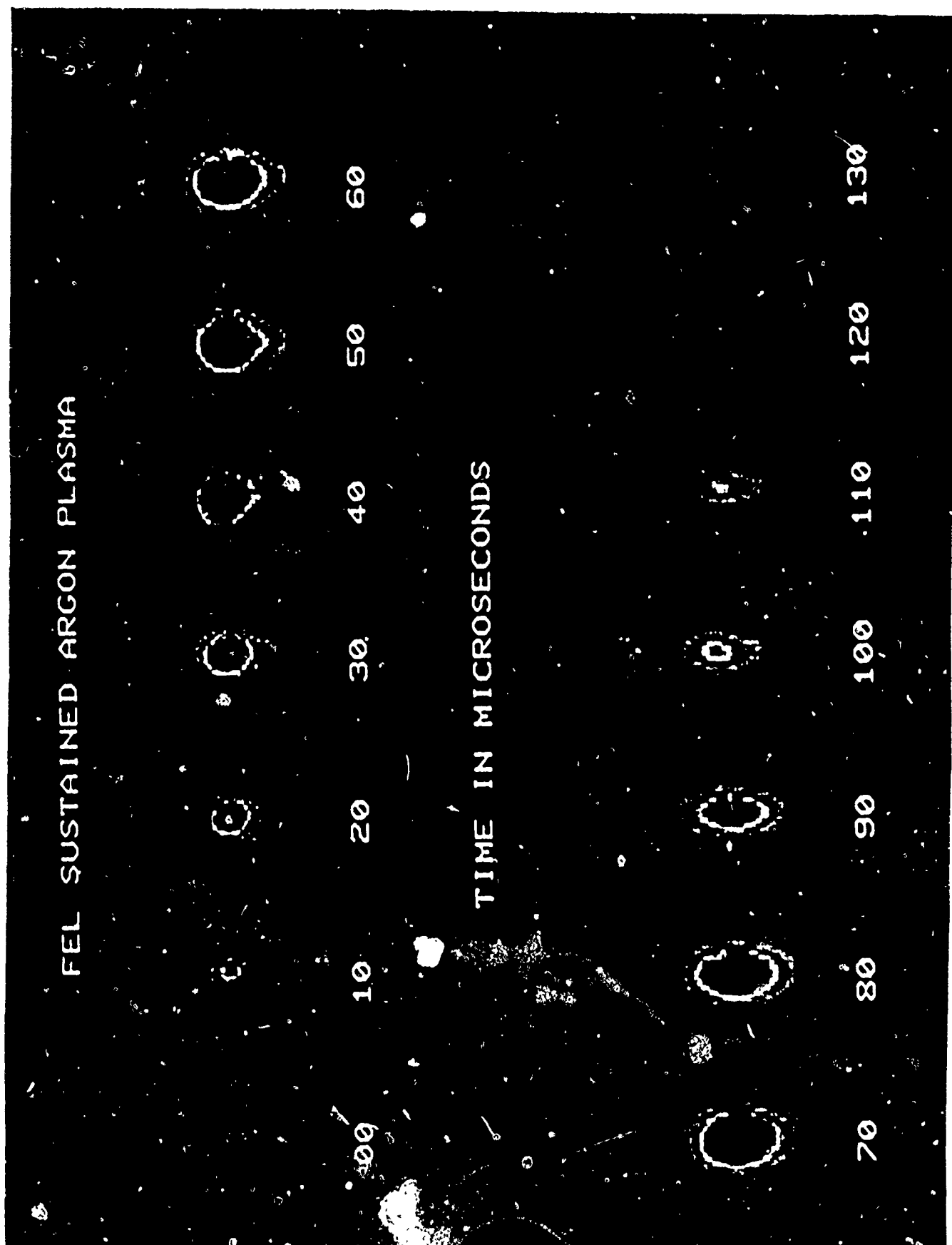
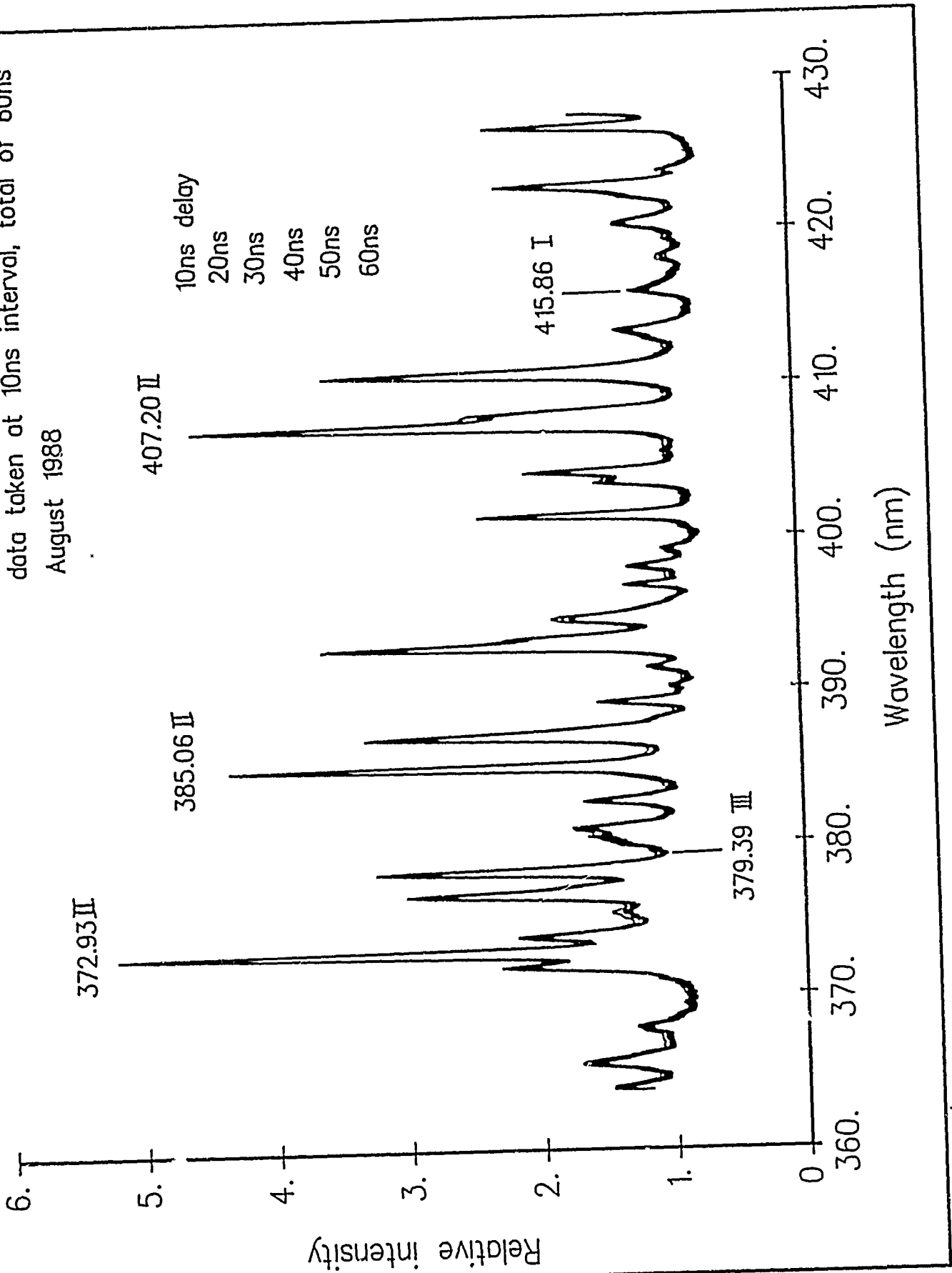


FIGURE 2

FEL sustained argon plasma spectrum
data taken at 10ns interval, total of 60ns
August 1988



PLASMA SCALING MECHANISMS FOR CONTINUOUS WAVE LASER PROPULSION

AFOSR Grant No. 88-0129

Principal Investigators: Herman Krier and Jyoti Mazumder

Department of Mechanical and Industrial Engineering
University of Illinois at Urbana-Champaign

SUMMARY/OVERVIEW:

This investigation focuses on the energy conversion mechanisms of multiple laser-sustained plasmas (LSP's) in pure flowing argon and single LSP's in argon/helium mixtures. Numerical modeling of the fully two-dimensional plasma flowfield is being used to scale experimental results and guide future experiments. Multiple plasma and argon/helium experiments have both resulted in thermal efficiencies greater than 50% for various flow conditions. Based on the high specific heat and low ionization potential of hydrogen, it is believed that pure hydrogen plasmas will produce thermal efficiencies higher than those possible using pure argon or an argon/hydrogen mixture. A spectroscopic imaging system is used to map plasma temperatures. Independent experimental determinations of electron temperature and electron number density are required in order to evaluate local thermal equilibrium which is needed in order to better interpret spectroscopic and numerical results. Rayleigh scattering is being experimented with as a means to accurately determine downstream plasma exhaust temperatures without the errors associated with thermocouples and gas heat loss to chamber walls.

TECHNICAL DISCUSSION:

Introduction

The key problem in the laser-sustained plasma rocket propulsion technique is the understanding and characterization of plasma energy conversion processes. These processes result in an increase in the thermal energy of the propellant gas. Various techniques are used to determine the fraction of the input laser energy absorbed by the plasma, how much is radiated to the plasma chamber environment, and finally how much is retained by the propellant gas as thermal energy. This gas thermal energy is the quantity used to determine thermal conversion efficiency by comparison to the input laser power.

Plasma temperatures are measured using a spectroscopic imaging system. With this system fractional laser absorption can be determined along with the amount of energy reradiated. The difference between these values is the energy retained by the gas. In addition laser absorption measurements are made with a water-cooled copper cone calorimeter, and gas temperature measurements are made with conventional type K thermocouples downstream of the plasma. These measurements provide independent determinations of global absorption and thermal efficiency. Rayleigh scattering thermometry is now being brought on line to eliminate errors associated with thermocouples and provide a more accurate method for measuring downstream gas temperature.

Much research has been done at our test facility involving the effects of varying mass flux, chamber pressure, laser power, and beam geometry on single pure argon plasmas. References 1-6 summarize much of our previous and ongoing work. Reference 7 is a paper on the quasi two-dimensional modelling of laser-sustained plasmas. A fully two dimensional model for single pure argon plasmas is being used to guide further experiments and will be used to scale results up to much higher laser powers. Experiments have been conducted with single and dual plasmas in pure argon and single plasmas in argon/helium gas mixtures.

Experimental Procedure

A plasma will form if sufficient power is focused into a gaseous medium ($\sim 10^9$ W/cm²), or onto a metallic target ($\sim 10^5$ W/cm²). In our experiment the laser is focused onto a tungsten rod which releases electrons through thermionic emission. This leads to avalanche breakdown and plasma initiation. At this point the tungsten rod is removed from the beam focus.

Figure 1 is a schematic of our test stand, current optical arrangement, and plasma initiation and flow chamber. The annular laser beam first strikes the flat copper mirror in the upper right portion of the figure and is reflected 90 degrees downward. The beam is then reflected across the bottom of the test stand and up through a plano convex zinc selenide lens which focuses the beam through a zinc selenide window into the chamber. Dual plasmas with an adjustable focal separation are achieved by splitting the beam at the second turning mirror by use of a micrometer adjustable split mirror which is shown schematically in Figure 2. Details of the experimental facility can be found in References 1, 3, 5, 6, and 8.

Efficiency and Absorption Measurements

The thermal efficiency of an LSP is defined as the ratio of the change in gas enthalpy flux to the laser power input to the plasma. Global absorption is the ratio of the total energy absorbed by the plasma to the input laser power. These quantities can be determined with both spectroscopic and conventional measurements.

Efficiencies presented in this abstract are based on bulk exhaust gas temperature measurements made with thermocouples in the chamber exhaust ports. The laser energy retained by the working gas is determined by calculating the change in enthalpy flux, ΔH , using $\Delta H = \dot{m} C_p (T_e - T_i)$ where \dot{m} is the measured mass flowrate, C_p is the specific heat of the gas, T_e is the measured bulk temperature of the exhaust gas, and T_i is that of the inlet gas.

Absorption percentages presented are based on calorimeter data. The calorimeter is mounted on top of the plasma chamber and collects the laser energy which is not absorbed by the plasma. The calorimeter is equipped with thermocouples which determine the difference in cooling water temperature as it absorbs the laser energy. This difference determines the amount of energy transmitted by the plasma and from this plasma absorption is calculated.

Figure 3 contains efficiency data from dual plasma experiments at 5 kW total input laser power (2.5 kW each), and single plasma experiments at 2.5 kW using only half a beam. These tests were done at 2.5 atmospheres gas pressure and with f/4 focusing optics. Efficiencies for the single half mirror represent an average of results from each of the half beams. Note that efficiency tends to increase with increasing mass flux for both the dual plasmas and for the single plasmas. Efficiencies are as high as 50.5 % for 5 kW total power dual plasmas depending on separation distance, and as high as 58.1 % for 3.5 kW total power dual plasmas depending on separation distance. It can be seen from the data in the figure that the dual plasmas have a higher thermal efficiency than single plasmas over most of the range of mass fluxes studied, and that the plasmas with 15 mm focal separation have the highest thermal efficiency. Since results from 3.5 kW total power dual plasmas show that 10 mm focal separation plasmas have the highest efficiencies over most of the mass fluxes studied, it is believed that the optimum focal separation distance for dual plasmas is a function of the input power. Further experiments at 7 kW total power and even greater focal separation distances will be conducted to study this effect.

Figure 4 contains absorption and efficiency data for helium/argon experiments conducted at 5 kW input laser power, at 2.5 atmospheres gas pressure and with f/4 focusing optics. Note that except for the low mole fluxes, the addition of helium to the mixture caused a decrease in global absorption. Thermal efficiencies for helium/argon mixtures were found to be as high as 56.1 % which is higher than any single pure argon plasma despite the fact that global absorption for helium/argon mixtures was lower than for single pure argon plasmas. This result indicates that helium/argon plasmas have a lesser radiation loss to the chamber walls than do pure argon plasmas. There appeared to be an optimum percentage of helium by volume for a fixed mole flux of helium, however it is believed that this optimum percentage may be a

function of mole flux, gas pressure, input power, and focusing geometry. As is discussed in Reference 8, the helium/argon experiments were performed as a preliminary guide to using pure hydrogen. Although it was found that helium did not significantly ionize in these experiments and its absorption and emission characteristics differ from that of hydrogen, the values of thermal conductivity and specific heat of helium are similar to those of hydrogen. It is believed that these similar thermodynamic properties will result in the production of still higher thermal efficiencies for pure hydrogen.

Progress is being made in implementing the fully two-dimensional single pure argon plasma numerical code. Most recent results indicate that for mass fluxes tested experimentally, model predictions for global absorption and thermal efficiency are within 10 % of experimental results.

REFERENCES:

1. McMillin, B.K., Zerkle, D.K., Glumb, R.J., Mazumder, J., and Krier, H., "Energy Conversion in Laser Sustained Argon Plasmas for Application to Rocket Propulsion," AIAA paper 87-1459; Presented at the AIAA Fluid Dynamics, Plasma Dynamics, and Lasers Conference, June 1987.
2. Mazumder, J., Rockstroh, T.J., and Krier, H., "Spectroscopic Studies of Plasma During CW Laser Gas Heating in Flowing Argon," Journal of Applied Physics, Vol. 66, No. 2, pp. 4712-4718, December 1987.
3. Krier, H., Mazumder, J., Rockstroh, T.J., Bender, T.D., and Glumb, R.J., "Continuous Wave Laser Gas Heating by Sustained Plasmas in Flowing Argon," AIAA Journal, Vol. 24, No. 10, pp. 1656-1662, October 1986.
4. Krier, H., Mazumder, J., Zerkle, D.K., Mertogul, A., and Schwartz, S., "Energy Conversion Measurements in Laser Sustained Argon Plasmas for Application to Rocket Propulsion," Technical Report, Department of Mechanical and Industrial Engineering, University of Illinois at Urbana-Champaign, UILU-ENG-88-4006, April 1988.
5. Mazumder, J., Krier, H., Rockstroh, T.J., Glumb, R.J., McMillin, B.K., Zerkle, D.K., and Chen, X., "Laser Sustained Plasmas for Application to Rocket Propulsion," Technical Report, Department of Mechanical and Industrial Engineering, University of Illinois at Urbana-Champaign, UILU-ENG-87-4002, March 1987.
6. Krier, H., Mazumder, J., Zerkle, D.K., Schwartz, S., Mertogul, A.E., and Chen, X., "Laser-Sustained Argon Plasmas for Thermal Rocket Propulsion," AIAA paper 88-2773, presented at the AIAA Thermophysics, Plasmadynamics, and Lasers Conference, June, 1988.
7. Glumb, R.J., and Krier, H., "Two-Dimensional Model of Laser Sustained Plasmas in Axisymmetric Flowfields," AIAA Journal, Vol. 24, No. 8, pp. 1331-1336, August 1986.
8. Krier, H., Mazumder, J., Mertogul, A.E., Schwartz, S., Chen, X., Eguiguren, J., and Zerkle, D.K., "Experimental and Numerical Studies of Laser Sustained Gas Plasmas," Final Technical Report, Department of Mechanical and Industrial Engineering, University of Illinois at Urbana-Champaign, UILU-ENG-89-4005, April 1989.

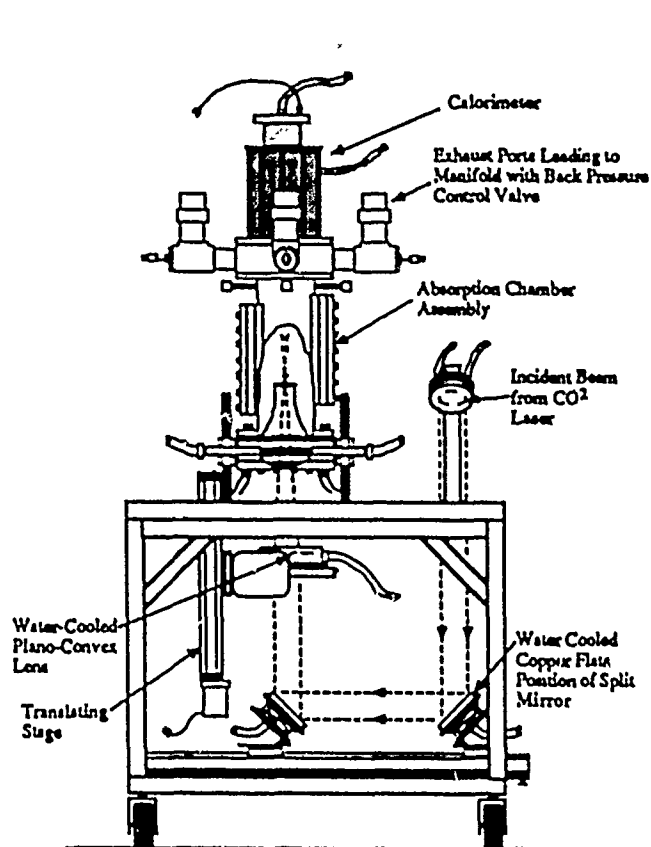


Figure 1 Schematic of test stand, current optical arrangement and plasma initiation and flow chamber.

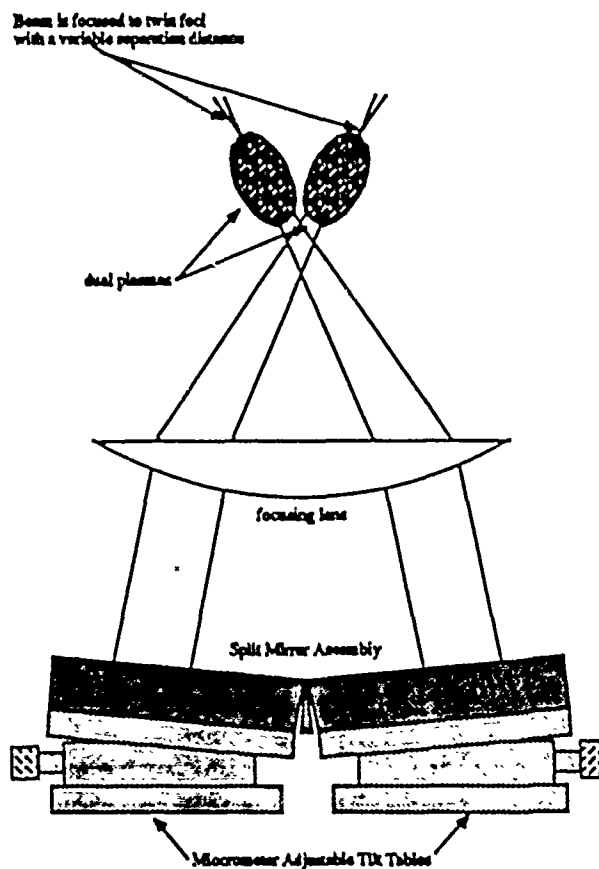


Figure 2 Schematic of adjustable split mirror assembly used to produce dual plasmas.

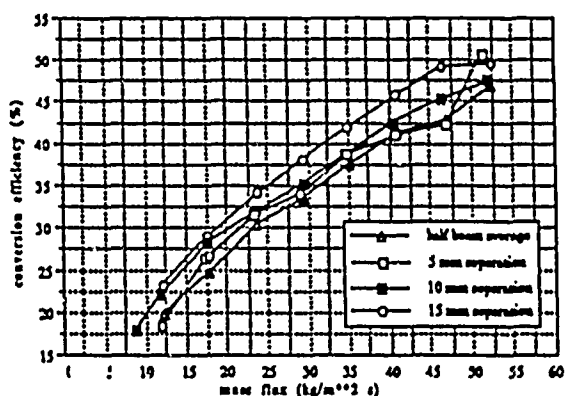


Figure 3 Comparison of thermal efficiencies of 5 kW total power dual plasmas and 2.5 kW single half-beam plasmas at 2.5 atmospheres gas pressure and 1/4 focusing geometry.

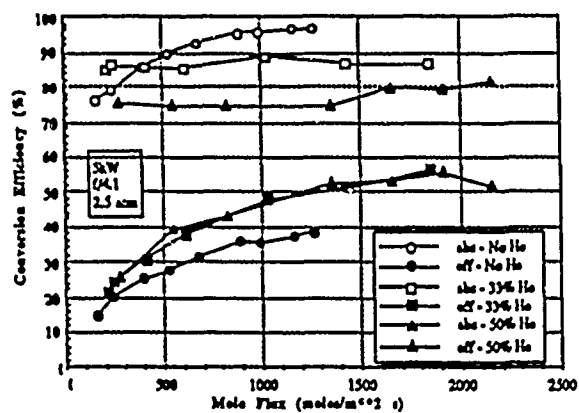


Figure 4 Comparison of global absorption and thermal efficiency for argon/helium mixtures at 5 kW, 2.5 atmospheres gas pressure, and 1/4 focusing geometry.

TRANSPORT PROCESSES IN BEAMED ENERGY PROPULSION SYSTEMS

(AFOSR Grant No. 89-0308)*

Principal Investigator:

Robert A. Beddini

University of Illinois at Urbana-Champaign
Urbana, IL 61801-2997

OVERVIEW

Concepts such as laser heated thrusters and microwave heated thrusters (Figure 1) employ controlled and directable energy addition to achieve a desired plasma zone with temperatures of the order 10^4 K. The plasma is then mixed with the outer flow and expanded through a nozzle. Of particular interest in such flows are turbulent convective and radiative heat fluxes, which distribute the deposited energy, and their effects on the system enclosure for chamber cooling requirements and evaluation of system efficiency. Research efforts are focused on the analysis of radiative and gas dynamic interactions in beamed-energy propulsion chamber environments.

TECHNICAL DISCUSSION

Specific topics have included the development of turbulence, incident radiative transport and reradiative transport¹⁻³. The following is a brief summary of the methodology being employed at present.

Incident laser radiation: A new transport equation for incident radiation was developed under this effort¹. Whereas prior analyses utilize ray-tracing techniques for the incident radiation, the new equation is of divergence form, and permits a strongly coupled solution with the hydrodynamic equations using contemporary finite volume techniques.

Incident microwave radiation: Maxwell's equations for a Transverse Electric or Magnetic mode breakdown in a waveguide have been order-of-magnitude analyzed on a term by term basis. A multidimensional equation system has resulted for which appropriate numerical solution techniques are presently being examined.

Plasma and chamber wall reradiation: The P_1 (first-order spherical harmonics) method is being utilized. Initial work has involved solving the coupled one-dimensional (radial) radiative heat flux equation employing a gray gas absorption coefficient². During the past year, a modified flux-form of the P_1 approximation has been developed and evaluated³ by comparisons with approximate and exact solutions of the transfer equation.

Numerical solution method: A new flux-split, non-factored, implicit finite volume method is being developed for the time-accurate solution of the axisymmetric Navier-Stokes equations (real gas) and coupled incident radiation field (the previously developed method¹ proved to be Courant-limited). This new technique borrows from a three-dimensional full Navier-Stokes (perfect gas) algorithm developed under a separate research effort⁴, and the method is not Courant limited.

Turbulence: Initial results have been obtained with an established second-order turbulence closure model. Future work will attempt a large eddy simulation of turbulence in the flow, though work on this topic has been suspended to address radiative transport issues as a priority.

* Supercomputing time on the Cray X-MP/48 provided by the National Center for Supercomputing Applications under grant *ilh*.

SUMMARY OF PROGRESS

It is known that by considering the P_1 approximation for net radiative flux (rather than intensity), the equation system and boundary conditions are well posed in the traditional optical depth coordinates and the radiative flux attains the correct optically thin limit. This limit characterizes the broadband radiative regime of interest. The use of optical coordinate mappings is conventional in the field of radiative transfer, but does not lend itself well to coupled numerical solution with equations describing the fluid dynamics of the problem, where more general coordinate mappings are often desired. In physical coordinates, an additional term occurs in the radiative transport equation due to the spatial inhomogeneity of the spectrally integrated broadband absorption/extinction coefficient β , i.e.

$$\nabla \nabla \cdot \vec{q}^r - (\nabla \ln \beta) \nabla \cdot \vec{q}^r - 3\beta^2 \vec{q}^r = 4\pi \beta \nabla I_b \quad (1)$$

The appearance of the $(\nabla \ln \beta)$ term can present numerical difficulties in optically thin regions of the computational domain. Moreover, its outright neglect can cause significant error, since the flows of interest have appreciable temperature and absorption coefficient gradients.

For regions of the computational domain in which $\Delta \tau \ll 1$, but $\nabla \ln \beta$ is large, an alternative form of equation (1) may be exploited. Specifically, if use is made of the optically thin relation for the net heat flux (valid independently of the differential approximation) in the second term of equation (1), there results

$$\nabla \nabla \cdot \vec{q}^r - 3\beta^2 \vec{q}^r = 4\pi \nabla (\beta I_b) \quad (2)$$

This form of the transfer equation has obvious advantages in optically thin regions containing radiative discontinuities, since the source term is in gradient or conservation form.

Figure 2 shows a comparison of the solutions obtained for the exact equation of radiative transfer, an analytic solution of the transverse component of equation (1) (obtained in optical space), and a computational (finite difference) solution of equation (2). The problem geometry represents a "planar" continuous laser supported plasma in a cool-wall chamber with an abrupt step in absorption coefficient and temperature profiles, and thus presents a difficult but realistic test of the P_1 approximation and its computational solution in physical coordinates. The accuracy of the computational solution of eq. (2) is limited only by the accuracy of the numerical differencing, i.e., radiative "shock" capturing.

The "generic" beamed-energy electrothermal thruster coupled radiative/flowfield calculations reported in² have been revised³ utilizing equations (1) and (2). Some results are shown in Figures (3) and (4). Figure (3) shows radial profiles of the normalized radial radiative heat flux at a specific axial location. Since broadband optical depths are < 0.05 for this configuration, good agreement is obtained between eq. (2) and the emission-dominated analytic solution for net intensity,

$$q_{ed}^r = \frac{4\pi}{r} \int_0^r (\beta I_b r) dr$$

Neglecting the inhomogeneous term in eqn (1) yields an approximate 40% underprediction of radiative flux.

Figure (4) shows the calculated radial radiative flux along the wall of the thruster, comparing eqn. (1) with the modified form (eqn. (2)). The instability caused by including the inhomogeneous absorption term in the computational solution of eqn(1) is particularly severe for this case, and demonstrates the advantage of utilizing eqn(2) in optically-thin grid segments.

While the new real-gas, two-dimensional, flux-split, non-factored, implicit finite volume method with coupled radiation fields is in development, preliminary calculations have been made with its three-dimensional perfect gas (full Navier-Stokes, high-order upwind) predecessor. The objective of these calculations is to assess the capability of the method in tracking the blast waves which can be produced by a pulsed laser detonation in an enclosed chamber. The initial conditions correspond to the instantaneous deposition of one Joule of energy (a laboratory laser pulse) in a 1 mm^3 cubical volume of stagnant atmospheric air. Since a perfect gas in LTE is assumed without

radiative transport, the initial conditions correspond to a pressure and temperature of 400 MPa and 1.1×10^6 K. The chamber is a cube with sides of 1.0 cm, and a uniformly spaced $(40)^3$ cell grid is employed. Transition from a cubical to spherical blast wave takes place in relatively short time (it is affected by the coarse grid). However, after this phase, spherical shock propagation is further affected by the nonspherical grid, such that a rhomboidal wave evolves. This problem is presently being examined, and results will be presented at the AFOSR/ONR Research Conference.

PLANNED RESEARCH

Development of the new two-dimensional, time-dependent method is anticipated to be completed within the year. However, preliminary results indicate that adequate resolution of all significant time-dependent three-dimensional phenomena will require significant, if not prohibitive, computational resources. The principal rationale for pursuing this area of research is that there are several propulsion problems of interest in which the optical axis of the beam is not aligned with the flow, leading to cross-beam, asymmetric discharges.

Another goal during the next year is to utilize the available experimental data and the results of computer simulations to assess the order-of-magnitude scaling of phenomena in the laser deflagration region. An example result of this work would be the production of a stability map for continuous laser discharges in true similarity variables.

REFERENCES

1. Beddini, R. A., Owano, T. G. and Kuo, S. -L., "Analysis of Gas Dynamic Interactions with Intense Optical Beams," AIAA paper no. 87-1455, AIAA 19th Fluid Dynamics, Plasma Dynamics and Laser Conference, Honolulu, Hawaii, June 1987.
2. Beddini, R. A. and Owano, T. G. "Analysis of Turbulent Convective and Radiative Heat Transfer in High Temperature Rocket Chamber Flows," AIAA paper no. 87-1770, 23rd Joint Propulsion Conference.
3. Beddini, R. A., Owano, T. G., and Meyer M. L. "Analysis of Convective and Radiative Energy Transport in High Temperature Rocket Chamber Flows," submitted to *J. of Thermophysics and Heat Transfer*.
4. Ridder, J. P. and Beddini, R.A.: "A Time Accurate Finite Volume Method for Propulsion System Chamber Flows," AIAA Paper no. 89-2554, to be presented at the 25th Joint Propulsion Conference, Monterey, CA, July, 1989.

ENERGY TRANSFER IN MICROWAVE THRUSTER CHAMBERS

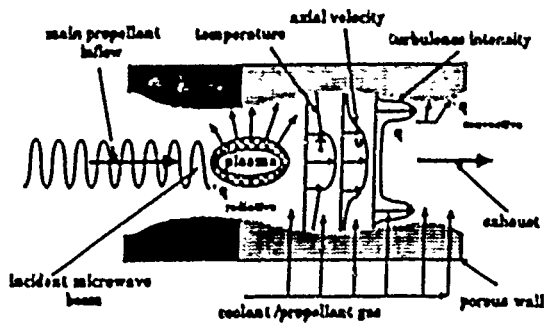


Figure 1

Radial Radiative Heat Flux Profiles

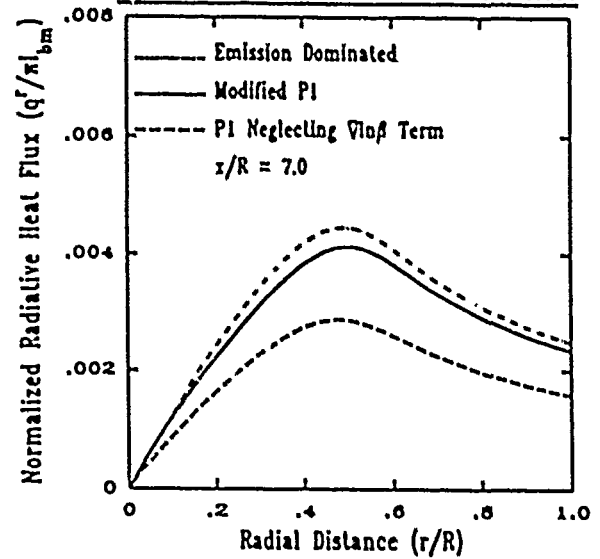


Figure 3

Comparison of Solutions For Normalized Radiative Heat Flux

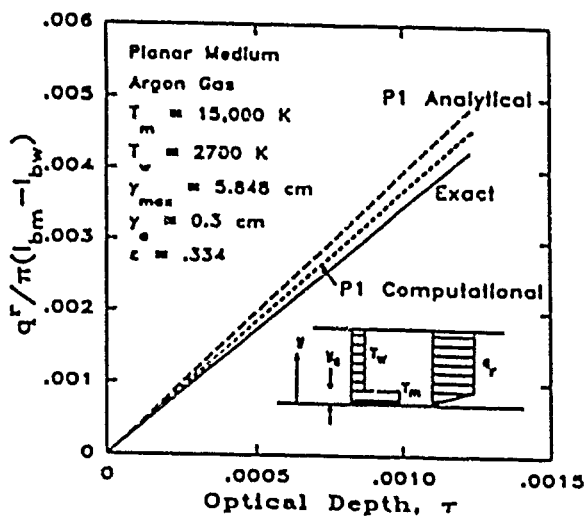


Figure 2

Radiative Heat Flux Along Chamber Surface

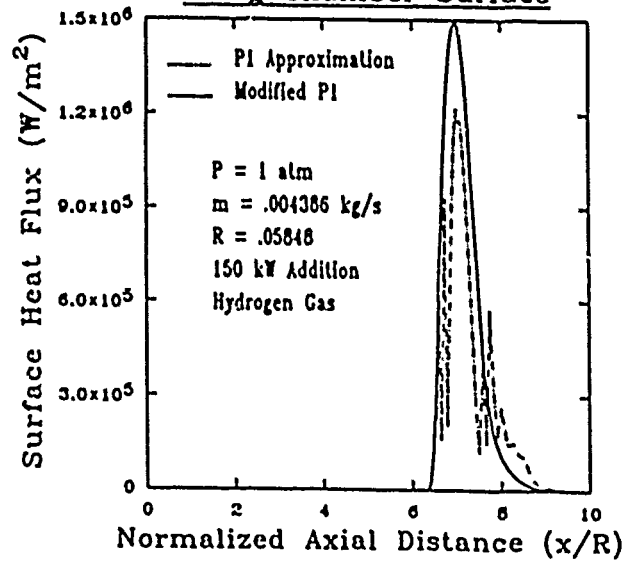


Figure 4

AFOSR Grant No. AFOSR-84-0048

Principal Investigator:

Dr. Michael M. Micci

The Pennsylvania State University
Department of Aerospace Engineering
University Park, PA

SUMMARY/OVERVIEW:

There is an understanding of the process of microwave energy addition to a high pressure gas for propulsive purposes for some of the available absorption modes but no unified comparison of all the modes in terms of absorption efficiency, maximum temperature, etc. Also there is little knowledge of the coupling of the absorbed energy to the gas dynamics required to obtain propulsive thrust. This research is the first experimental effort to examine and compare free floating filamentary and toroidal microwave absorbing plasmas and planar propagating plasmas in hydrogen gas as well as the first examination of the coupling of the energy absorption to the gas dynamics in order to convert internal thermal energy of the gas to directed kinetic energy by means of a nozzle expansion. The research will provide insight to the entire field of high temperature gas flows driven by radiation absorption.

TECHNICAL DISCUSSION:

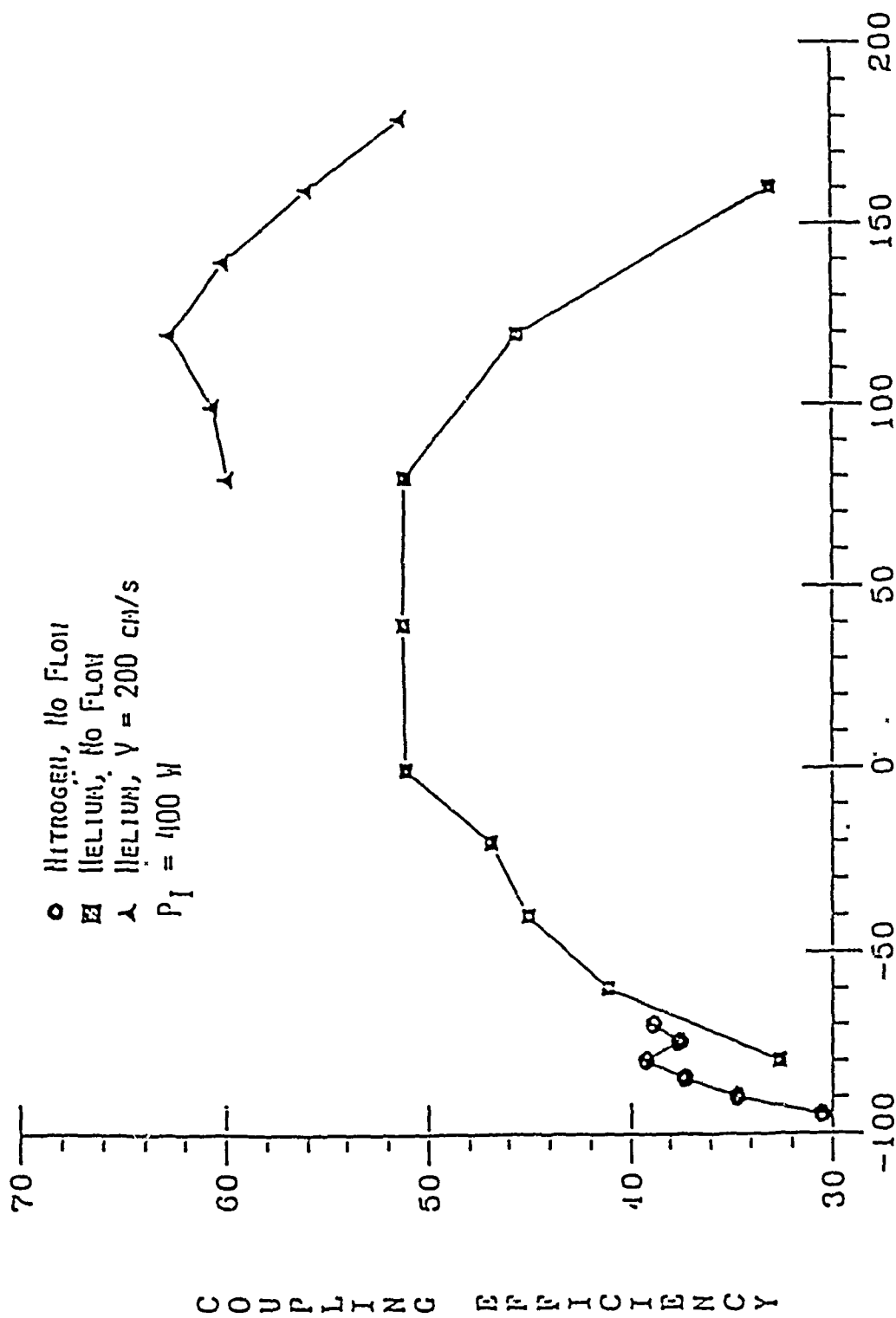
Free-floating spherical plasmas have been generated in stationary and flowing nitrogen and helium gas contained inside a 10.2 cm diameter spherical quartz vessel located within a cylindrical resonant cavity operated in the TM_{012} mode at a frequency of approximately 2.45 GHz. The plasmas are approximately two inches in diameter and are centered within the quartz sphere. Power coupled to the plasma was measured as a function of gas composition, flow rate and pressure and microwave power input to the cavity only for those conditions which resulted in the plasma being stabilized in the center of the quartz sphere away from adjacent walls.

The coupling efficiencies of helium and nitrogen plasmas were measured with no gas flow and an input power of 400 W. Similar measurements were made for a helium plasma with a gas flow rate of 1.056×10^{-4} kg/s and 400 W input power. Figure 1 shows the coupling efficiency versus pressure curves for the three cases considered. The coupling efficiency is defined to be the percentage of input microwave power actually absorbed in the gas. The most striking feature is the much greater range of operation of the helium discharges. The nitrogen discharge is limited to low pressure operation (less than 30 kPa (absolute)), whereas the helium discharges operate at well above 250 kPa (absolute). The helium discharges generally exhibit higher coupling efficiencies, with peak values of 51% (no flow) and 63% (with gas flow). In comparison, the nitrogen discharge exhibits a peak coupling efficiency of 40%.

A numerical model of the one-dimensional planar propagating microwave plasma in hydrogen, helium and nitrogen gas has been successfully formulated. This model numerically integrates the system of governing equations consisting of the one-dimensional steady energy equation and Maxwell's equation describing the propagation of the microwave energy. Due to thermal conduction of the cold gas ahead of it, the plasma propagates toward the microwave energy source at a velocity determined by the energy balance between the absorbed microwave power and the heated gas which is convected away downstream.

The two governing equations were numerically integrated using a fifth/sixth order variable step Runge-Kutta scheme. An iterative method was used to determine the propagation velocity eigenvalue, βu , similar to the method used by Kemp and Root to solve for the propagation velocity of a laser heated plasma. The propagation velocity, maximum temperature and percent power absorbed were calculated as functions of the input microwave power. The propagation velocity was found to rise with increased microwave power but the maximum gas temperature is constant for hydrogen and nitrogen because significant dissociation is occurring in this temperature range and is absorbing the additional absorbed power. The maximum gas temperature for helium, which is not dissociating, was found to rise with increasing input power. It was found that all of the input power was either reflected or absorbed with no power being transmitted through the plasma and that the present power absorbed for hydrogen decreases with increased input power while the percent power absorbed for helium and nitrogen remained fairly constant as a function of input microwave power. Radiative heat loss from the plasma was subsequently added to the model but was found to have no effect on the numerical results.

The results of the experiment are shown in Fig. 2 which gives the measured plasma velocities for helium and nitrogen at 1 atm together with the numerical predictions. For helium a reasonable agreement between numerical and experimental data could only be found towards lower power levels, however, an enormous deviation can be observed for power levels above 1550 W. It is believed that in this power range a change in the propagation mode takes place towards resonant radiation. Nitrogen doesn't show this kind of behavior and agrees reasonably well with the numerical model. The percentage absorbed power values for helium at 1 atm range from the mid 60 to the low 70 percent and for nitrogen from the low to mid 60 percent. These values were much higher than those predicted by the model.



PRESSURE KPa

Fig. 1 Microwave coupling efficiency as a function of gas pressure for nonflowing nitrogen and helium with a mass flow rate of 0.1 gm/s.

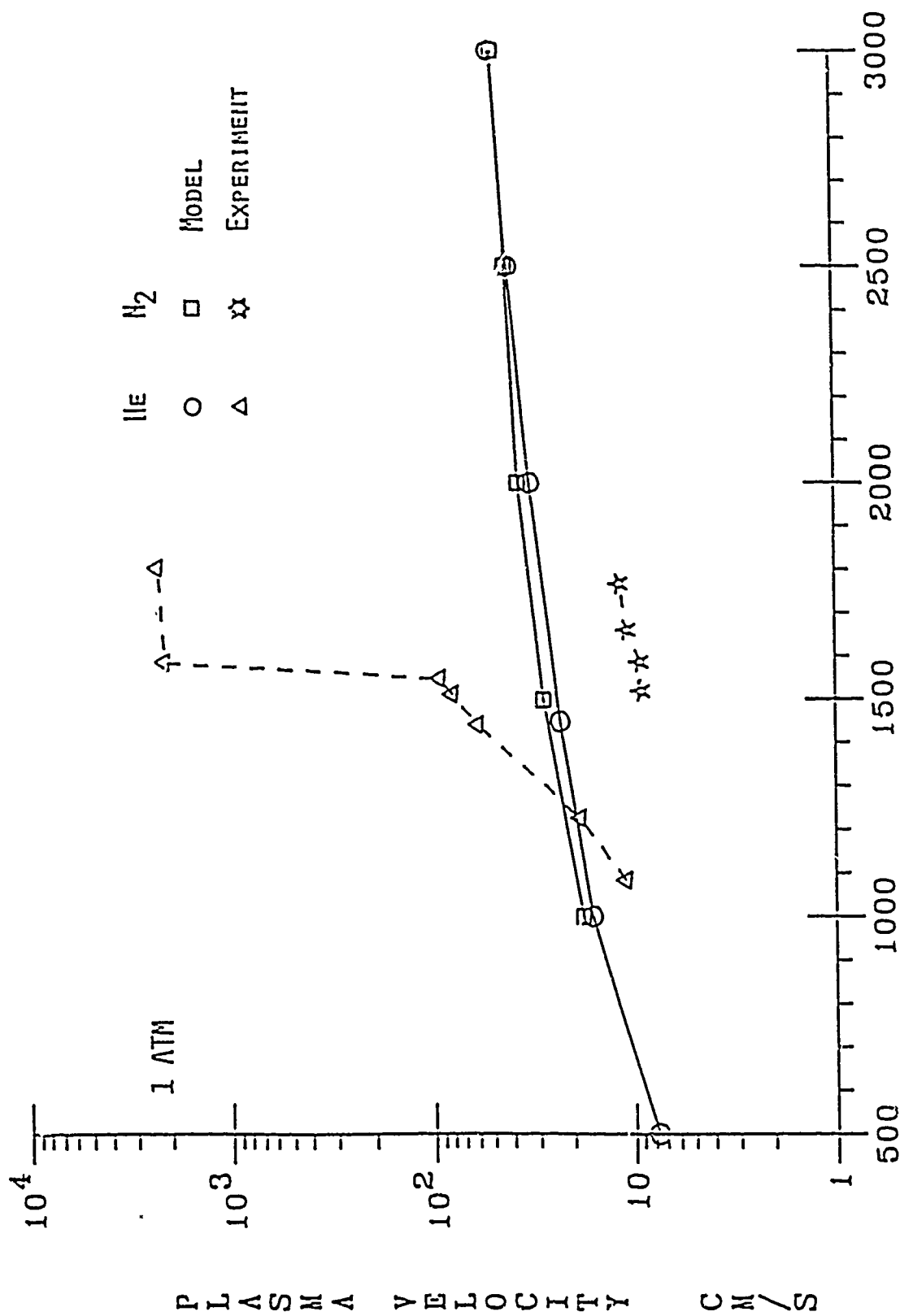


Fig. 2 Numerically and experimentally obtained values of plasma velocity as a function of incident power for helium and nitrogen at atmospheric pressure.

HEATING OF A LIQUID/VAPOR MIXTURE BY A PULSED ELECTRIC DISCHARGE

4/89

AFOSR Contract No. F49620-87-C-0061
Principal Investigator: Rodney L. Burton
Co-investigator: Brian K. Hilko

GT-Devices, Inc., Alexandria, VA 22312

SUMMARY:

Arc discharge heaters in the 5-1000 MW class, used for pulsed electrothermal propulsion and for hypersonic combustion research, are required to ingest their working fluid in solid or liquid form to keep working temperatures within the desired 6000-20,000°K range. This research effort seeks to understand the two-phase heating process for liquid water injected into a 5 MW, 100 atm. capillary-confined pulsed arc, for which the arc heating is roughly constant in time. The water is injected either as a straight jet or as an approximately mono-disperse droplet train, and is subjected to pulses of 15 or 30 μ secs duration. Voltage, current, pressure, photographic and arc spectral measurements suggest that the drops explode in the high dynamic pressure flowfield, creating a liquid-phase mist which causes the arc temperature to plummet, and the arc resistance and ohmic heating to rise rapidly. A 1-D, unsteady plasma flow numerical model explains the early droplet phase of the pulse, and a 2-D, unsteady model is being developed to understand the late-time, high-resistance phase.

TECHNICAL DISCUSSION:

A liquid fuelled pulsed electric discharge [1,2] is being studied to identify the energy exchange and mixing processes occurring between the liquid, vapor and plasma components. A variety of complex, inter-dependent phenomena can participate in the energy transfer and mixing (see Fig. 1). Plasma radiation, thermal conduction and convection

all contribute heat flux for evaporation of the liquid. Vapor-plasma mixing can occur in the fast flowfield as a steady surface erosion, or via instabilities leading to a more-or-less explosive breakup of the injected liquid. The goal of this research is to identify the mechanisms dominating the liquid-vapor heating and mixing processes occurring in the high pressure, high enthalpy

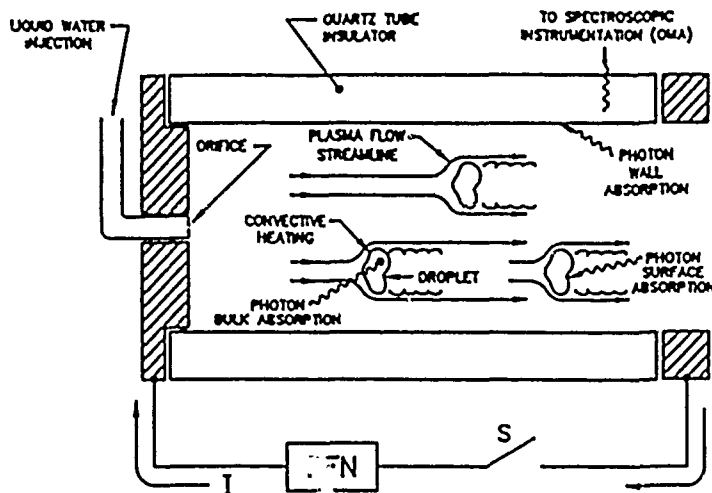


Figure 1

flow.

Over the first year we have developed an understanding of these unsteady discharges by the application of various diagnostic techniques for obtaining detailed measurements of the time-dependent plasma conditions (i.e. density, temperature, pressure) and of the liquid/vapor interface. Over the past (second) year of this program, emphasis has also been placed on modeling and numerical simulation of the discharge dynamics for comparison with the available experimental data.

The numerical method used for this study is an algorithm developed specifically for the solution of time-dependent flow problems containing steep gradients and shocks. The algorithm, called Flux-corrected Transport (FCT) [3,4], incorporates methods of general applicability to calculate accurately the dynamics of the fluid equations, and then correct the computed results to remove the numerical errors which are a byproduct of conventional finite-difference calculations. The FCT algorithm can provide a complete two-dimensional unsteady flow solution in the high density continuum regime, and potentially can also model the free-molecular regime.

At present, preliminary investigations of the discharge dynamics are being made with a simplified, 1-D description of this cylindrically symmetric, two phase flow problem. Power input to the capillary is obtained from a step pulse or from the experimental current pulse, assuming a Spitzer type plasma resistivity, $\eta(T) = (\text{const})T^{-3/2}$. Water is evaporated from the liquid surface area, S , by the heat flux q imposed by the local plasma conditions, thus providing the source of vapor mass \dot{m}_v from $\dot{m}_v = Sq/h_{\text{plasma}}$, where h_{plasma} is the enthalpy of the evaporated mass in the plasma. Using $q = \sigma T^4$ presumes that the plasma radiates as a pure blackbody, and that heat flux due to thermal convection or turbulent transport is negligible. In the 1-D description, radial dynamics are not considered, so that the ablated mass at each axial position is radially distributed, instantaneously and uniformly.

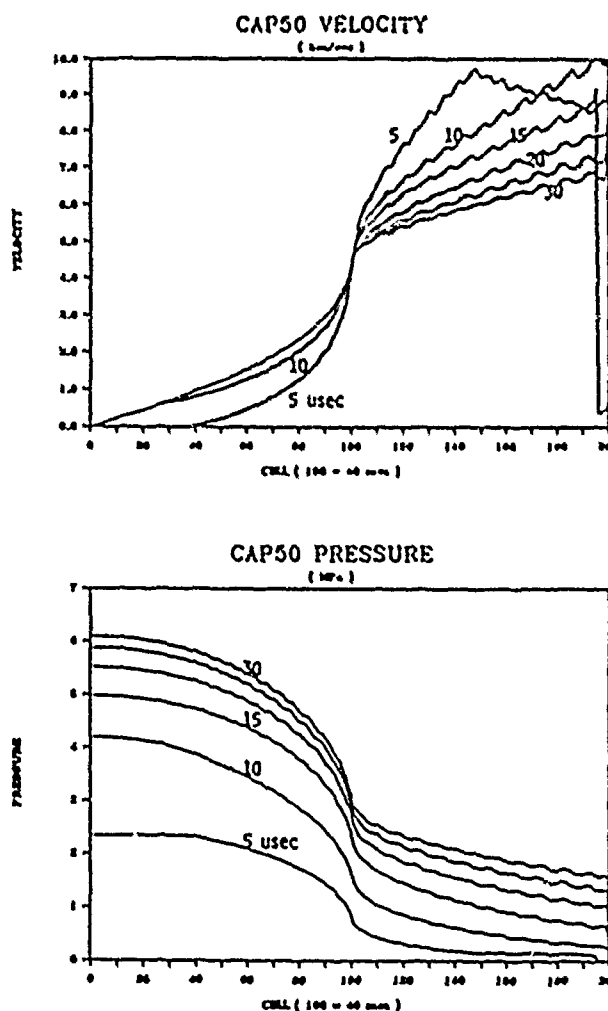


Figure 2

The model has been developed with increasingly complex physics to provide agreement with experimental results. Model output is plasma density, velocity, pressure and temperature, plotted versus axial distance for selected times during the pulse. The simple case of a step pulse in current is shown in Fig. 2, which shows profiles of the plasma flow velocity and pressure at 5 to 30 μsecs . The ohmically-heated capillary is a cylindrical, 40 mm long discharge chamber, occupying computational cells 1-100, and having a uniform coating of water on the 5 mm diameter inner wall. Boundary conditions at the capillary exit (cell 100) are simplified by venting the plasma into a second 5 mm pipe, occupying cells 101-200, in which the flow is supersonic and does not influence the capillary dynamics.

As shown in Fig. 3, the resistance calculated from the simple model gives approximate agreement to the resistance observed experimentally for the case of a water-wetted wall. However, the model does not predict the 33% increase in resistance observed between 5 and 20 μsecs . Other model predictions, such as temperature, pressure and density, also appear to follow the average trends of experimental results over a range of injection geometries and discharge parameters, though details of the dynamic behavior are likewise not well tracked. Initial results from the numerical simulations, though encouraging, show the need for an improved description of the evaporation and mixing processes.

In order to benchmark the computational results, it is essential to obtain good measurements of the plasma temperature. Qualitative indications of temperature and detailed density measurements have been obtained from previous, low resolution

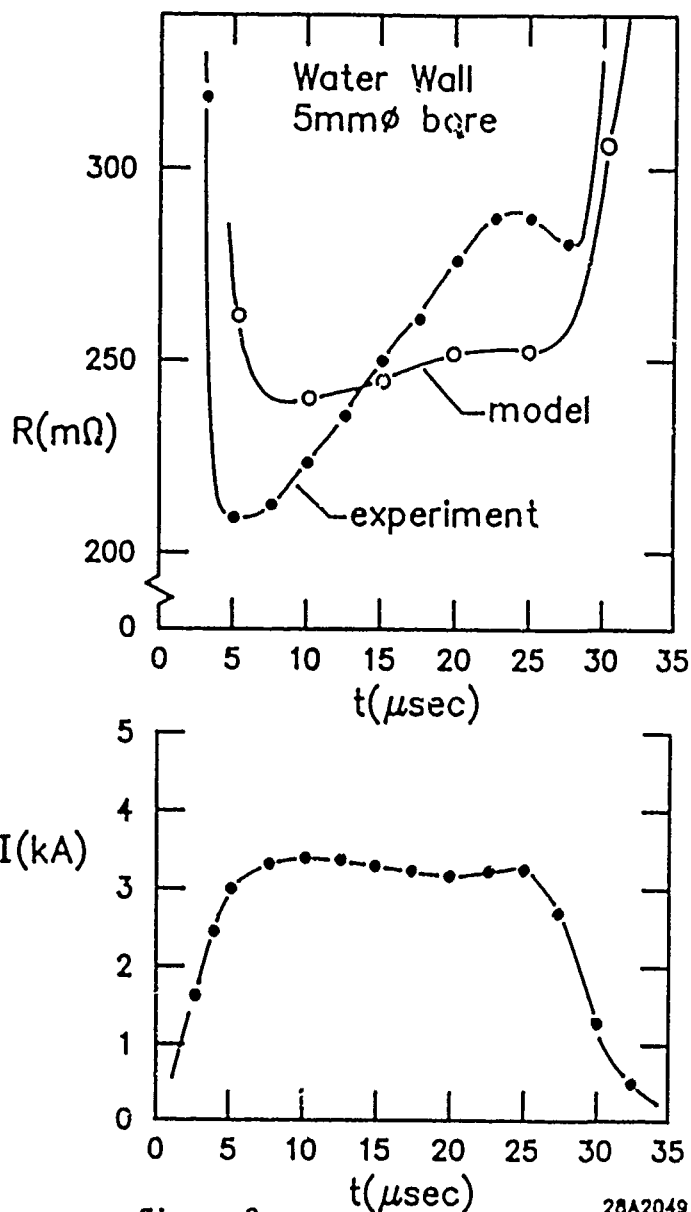


Figure 3

28A2049

spectroscopic surveys of the plasma emission on an OMA [2]. The presence of singly and doubly ionized oxygen line emissions has prompted a high resolution OMA study to see if a meaningful temperature can be extracted from these features. In principle, the line intensities within a given ionization stage will follow a Boltzmann distribution for the upper level populations; i.e., $I \sim \exp(-E_u/kT)$. Analysis of the line intensities vs. level energy can yield the temperature [5]. Additionally, the intensity ratio of lines from successive ionization states can give a sensitive measure of temperature, though the electron density must be independently established. The data and evaluation techniques are presently being examined.

It has previously been conjectured that droplet breakup and/or vapor expansion occurs to varying degrees in the fast, high density flow field. We have recently used nitrogen laser shadowgraphy at the capillary exit plane to observe that droplet shattering may be occurring within the 30 μ sec pulse time. At the closed end of the capillary (cell 0) the plasma is stationary, so that, in this region, evaporated water may simply be expanding as a cool, dense vapor with relatively minor mixing into the plasma component. Since the strongest axial flow gradients exist near the exit (cell 100), these can more strongly influence the droplet breakup, expansion, and mixing processes, i.e., the radial dynamics. Consequently, future efforts will be made to resolve the temperature and resistance axial variations for clues to the effects of these gradients.

REFERENCES

- [1] R. L. Burton, et. al., "Investigation of a Repetitive Electrothermal Thruster," GT-Devices, Inc., Report GTD 86-5, NASA CR-179464, NASA-Lewis Research Center, August 21, 1986.
- [2] R. L. Burton and B. K. Hilko, "Heating of a Liquid/Vapor Mixture by a Pulsed Electric Discharge," GT-Devices, Inc., Report GTD 88-8, AFOSR Contract No. F49620-87-C-0061, Annual Technical Report, July 31, 1988.
- [3] J. P. Boris and D. L. Book, "Flux-Corrected Transport I: SHASTA--A Fluid Transport Algorithm That Works," J. Comp. Phys. 11, 38, 1973.
- [4] R. L. Burton, N. K. Winsor, and F. D. Witherspoon, "Numerical Modeling of Fully Viscous Rocket Plume Flows," GT-Devices, Inc., Report GTD 88-9, Contract NAS3-25407, NASA-Lewis Research Center, August 26, 1988.
- [5] W. Lockte-Holtgreven, ed., Plasma Diagnostics, John Wiley & Sons, Inc., New York, 1968. pp. 180-183.

THE PHYSICS OF HIGH VOLTAGE SOLAR ARRAYS IN CONTACT WITH THE SPACE PLASMA

AFOSR GRANT-87-0340

Daniel E. Hastings

Dept of Aeronautics and Astronautics
MIT, Cambridge, MA 02139

1 Summary:

The physics of high voltage solar arrays in contact with the space plasma is under investigation. Such solar arrays suffer from enhanced current collection, enhanced drag and arcing. These problems are under study with a two and half dimensional particle in cell code so that the micro-physics of the plasma surface interaction can be studied. Previous work has clarified some of the underlying mechanisms behind the enhanced current collection. In the present work, the effect of magnetic field on the enhanced current collection and on the enhanced drag is studied. A better understanding of these interactions will lead to better design of solar arrays so as to alleviate these problems.

Technical Discussion

As space systems become larger and more complex, the power required to run them has increased. Simple calculations show that the power lost in a transmission line expressed as a fraction of the power generated scales as the current carried in the line. It is also easy to show the mass of the transmission line scales as the square of the current. From these considerations space engineers have tried to design high power systems to operate at high voltages rather than high currents since this minimizes the mass penalty. This has led to the development of high voltage solar arrays. The potential drop across these solar arrays may be several hundred volts. These solar arrays are

typically designed with the solar cells connected by metallic interconnects which are exposed to the space environment. The reason for this is to reduce the mass of the solar array by removing the insulation from the connector and because it is observed that the insulation erodes under the impact of the low energy ions found in low earth orbit and also because small defects in the insulation have been found to render it useless. Maxwell's equations applied to the whole solar array demand that the net plasma current to the solar array must be zero for the system to be in equilibrium. In order for this to be true what is found is that a part of the array will take a positive potential with respect to the environment (and attract electrons to the interconnects) while the rest of the array will float negatively with respect to space and collect ions to the interconnects. One observation for these high voltage solar arrays is that the positively biased interconnects collect anomalously large currents above a critical voltage. This voltage has been termed the "snapover" voltage from the shape (an S shape) of the current voltage curve for the conductor. Negatively biased surfaces undergo arcing below a critical voltage. The two phenomena are connected when both occur on a solar array in that once the positively biased end of the array undergoes snapover the area of the negatively biased end of the array increases to maintain current balance. This exposes an increased area of the array to negative arcing damage. In addition the negatively biased parts of the solar array have been found experimentally to have enhanced ion drag associated with them.

In previous work a theory was developed for the anomalous current collection observed on positively biased conductors surrounded by dielectric surfaces. This is seen on segments of high voltage solar arrays. It is proposed that the snapover seen in current collection to the conductor is the result of a transition from one stable root of the neighboring dielectric surface to the other stable root of the current balance relation. Two specific predictions of the theory that may be amenable to experimental test are first that the snapover voltage will be larger for conductor geometries that give planar current collection as opposed to conductor geometries that give spherical current collection. Secondly, the snapover voltage is a sensitive function of the material that the dielectric is composed of and depends most sensitively on the first unity crossing. Hence materials with the same maximum yield but different unity crossings can have substantially different snapover voltages.

The effect of the magnetic field on the snapover phenomenon has been studied. This is motivated by the use of solar arrays on spacecraft in polar orbits where the spacecraft will see a magnetic field which changes substantially over the orbit. The appearance of snapover results from the surface charge on the dielectric going from a large value to a small value, while the disappearance of snapover results from the surface charge on the dielectric going from a small value to a large value. The process of losing surface charge from the dielectric requires high energy electrons to leak through a potential barrier and initiate secondary emission. The process of gaining surface charge requires the dielectric to recapture the secondary electrons emitted by primary electrons.

Increasing the magnetic field suppresses the mechanisms for snapover. The appearance of snapover requires high energy electrons. A strong magnetic field prevents electrons from crossing field lines to reach areas of high energy. The reduced number of high energy electrons lowers the probability of snapover. Therefore, snapover is delayed until the conductor voltage reaches higher levels.

The disappearance of snapover occurs when electrons are unable to escape from the dielectric after being reemitted. Increasing the magnetic field strength shortens the gyroradius of the electrons. Electrons over the dielectric move in smaller circles, and a shorter radius will cause most of the electrons to fall back on the dielectric. More secondary emission is required to achieve the same escape level. Therefore, snapover also disappears at higher levels of the conductor voltage.

When the orientation of the magnetic field is parallel to the plane of the conductor and dielectrics, the collected current decreases, and the appearance of snapover occurs at a lower conductor voltage. Charged particles moving in the presence of a magnetic field orbit the field lines at their gyroradius. When the magnetic field is weak, the gyroradius is large enough for the electrons to reach the conductor. When the field is strong, the gyroradius decreases allowing only electrons with very high energies to reach the conductor. Thus, the collected current is reduced.

When the magnetic field is perpendicular to the electric field, the particles have a greater perpendicular velocity and thus a greater gyroradius. With the magnetic field perpendicular to the conductor, the conductor voltage must be higher in order to give the electrons the same gyroradius they have when the magnetic field is parallel to the plane. The appearance of snapover depends

upon the presence of high energy electrons. With the magnetic field parallel to the plane, sufficient numbers of high energy electrons can cross the magnetic field lines at a lower conductor voltage. Thus, snapover appears earlier.

These conclusions imply that spacecraft in polar orbit will be in a constant state of flux. When crossing above the tropical regions, high voltage solar arrays will be more likely to undergo snapover due to the weakness of the magnetic field. As the spacecraft crosses the polar regions, the strengthening of the magnetic field could cause snapover to disappear. Thus, the surface potential of any solar array on such a spacecraft will be changing constantly. Spacecraft in equatorial orbits will encounter constant magnetic fields, and the surface potential of their solar arrays will be constant as well. It is well documented that portions of solar arrays biased negatively with respect to the ambient plasma are subject to arcing damage. Spacecraft in equatorial orbits will be able to limit this damage to specific regions. For spacecraft in polar orbits, the constant change in the surface potential of their solar arrays means that a much larger portion of their arrays will be subject to arcing damage.

The enhanced ion drag on high voltage solar arrays was identified in experiments in Japan. The solar array was modelled as a conductive plate with one overlapping sheath structure. Numerical calculations with a particle tracking code verified the high ion drag and showed that it was primarily due to the reflected ions which had partially accommodated on the surface. In the present work the drag has been calculated with a particle in cell code. This enables us to study the effect of the magnetic field on the electrons as they participate in the process. In addition we study the effect of having a surface which does not have an overlapping sheath structure as realistic high voltage solar arrays will most likely have. We find that the PIC simulations reproduce the particle tracking results when they are both run on a conductive plate. However once a dielectric surface is included the drag coefficient is substantially changed. This is due to the fact that the ions and electrons can get to the dielectric surface so that the charge distribution on it may be quite different than the nearby conductor. When the ions accommodate and partially reflect the momentum transfer to the surface is changed from the conductor only case. We study these effects as a functions of the nondimensional parameters which govern the interaction.

FUNDAMENTAL RESEARCH ON THE ECR PLASMA THRUSTER

Grant No. AFOSR-87-0205

F. E. C. Culick and J. C. Sercei

California Institute of Technology
Pasadena, California 91125

SUMMARY/OVERVIEW:

The Electron-Cyclotron-Resonance (ECR) plasma thruster is an electrodeless electromagnetic device with the theoretical potential for very high specific impulse, long life, and high unit power handling capability. This research is directed at developing a quantitative scientific understanding of the operation of the ECR plasma thruster. To accomplish this objective, both analytical and experimental research is being conducted. In the analytical part of this program a quasi-one-dimensional, steady-state model of the acceleration process has been developed. Numerical calculations based on this model are being undertaken to provide quantitative predictions of physical parameters which can be tested experimentally. Experimental tests on a laboratory ECR plasma accelerator have been on-going. Several diagnostic tools, including a gridded energy analyzer, an ion collection cup current density analyzer, and emissive probes, have been used to measure physical parameters of interest in further developing a basic scientific understanding of this device.

TECHNICAL DISCUSSION:

Analytic Research The quasi-one-dimensional model of the ECR plasma acceleration process which has been developed under this effort is designed to determine the effects of the following physical processes: i) up-stream ambipolar diffusion, ii) cross-field radial diffusion, iii) various elastic scattering phenomena, iv) inelastic collision effects, and v) the electron-cyclotron, dipole-moment, grad-B accelerating force. To accomplish this objective, the model treats axial variation in the plasma properties using a constant-area plasma flow model. Certain parameters, such as the magnitude of the applied magnetic field (and its spatial derivative), and the spatial power density of the coupled microwave radiation are assumed constant in time with a specified axial variation. The basic equations of this model can be written as a plasma continuity equation, a plasma momentum equation, and two energy equations for the perpendicular and parallel components of the electron energy.

$$\text{continuity: } \frac{d(nu)}{dz} = S_p$$

$$\text{momentum: } m_i \left(\frac{d(nu^2)}{dz} - u_a S_p \right) = -m_i n n_a \sigma_{ia} (u - u_a)^2 - n \frac{W_{prp}}{B} \frac{dB}{dz} - m_e n n_a \langle v_e \sigma_{ea} \rangle (u - u_a) - \frac{dP_{par}}{dz}$$

$$\text{energy: } \frac{d(nu W_{prp})}{dz} = nu \frac{W_{prp}}{B} \frac{dB}{dz} + p_{ecr} + F_1 - W_{prp} F_2$$

$$\frac{d(nuW_{par})}{dz} = u \frac{dP_{par}}{dz} - F_1 - W_{par}F_2$$

Where the plasma source term is given by the following relationship.

$$S_p = nn_a \langle v_e \sigma_i \rangle - \frac{nkT_e}{8eBr^2}$$

Two additional functions which account for electron energy distribution due to collisions are defined as follows.

$$F_1 = n(W_{prp} - 2W_{par})(nQ_{iel} + n_a Q_{ael})$$

$$F_2 = \frac{nn_a(U_{ex}Q_{ex} + U_i Q_i) + n^2 U_{exi} Q_{exi}}{W_{prp} + W_{par}}$$

In this notation, n is the plasma electron number density (assumed equal to the ion number density), u is the plasma flow velocity, z is the axial coordinate, S_p is the plasma source term, m_i is the ion mass, u_a is the gas flow velocity, n_a is the gas number density, σ_{ia} is the cross section for ion-atom momentum exchange, W_{prp} is the mean electron energy perpendicular to field lines, W_{par} is the mean electron energy parallel to field lines, B is the magnitude of the local magnetic field, σ_{ea} is the cross section for electron-atom momentum exchange, P_{par} is the component of the electron pressure parallel to field lines, p_{ecr} is the density of microwave power assumed coupled to the electron motion, r is the radius of the plasma beam, and Q represents the various rate coefficients for electron scattering. Subscripts for the rate coefficients for electron scattering have the following meanings: *iel* is elastic scattering with charged species, *ael* is elastic scattering with atoms, *ex* is inelastic excitation scattering with atoms, *i* is ionization of atoms, and *exi* is inelastic excitation of ions. U indicates the energy level of the various inelastic scattering phenomena with the same meaning ascribed to subscripts as for the rate coefficients.

Due to space limitations only the most important assumptions made in the model are summarized here. The momentum equation stated above is derived by combining the ion and electron momentum equations using the ambipolar electric field under the assumptions of zero net axial electric current, quasi-neutrality, and neglecting the ion thermal motion. Electron mass is neglected in comparison to ion mass. The energy equations treat the two components of the electron thermal energy while neglecting the mean directed kinetic energy of the electrons. Treatment of the ion directed kinetic energy is implicit in the electron energy and plasma momentum equations. In the plasma source equation, the usual ionization term is present along with a worst-case loss term associated with cross-field Bohm diffusion. The unusual feature of the two functions which account for electron energy distribution due to collisions is the presence of a single excitation energy and an associated rate coefficient. This lumped approximation for the excitation process is similar to a technique which has been used successfully in modeling electrostatic ion engines.

Calculations based on this model using a finite differencing scheme are in progress. Appropriate boundary conditions and peripheral equations describing the flow of the neutral gas are also used in these calculations, the results of which will be predictions of measurable plasma parameters and thruster performance. The parameters the model is design to predict include plasma density, temperature, electrostatic potential, and velocity. Once the model is verified it will hopefully be useful in the design of much more efficient ECR thrusters and will form the basis of an important program of basic scientific research.

Experimental Research An experimental test bed has been developed as part of this program and is described in Ref. 2. Some of the diagnostic tools which have been developed include a gridded energy analyzer, an ion collection cup current density analyzer, and emissive probes for measuring plasma potential.

The gridded energy analyzer (shown in Figure 1) is a four grid device in which the first grid is a grounded attenuator with an open hole fraction of about 15 percent and a mesh size on the order of 10 μm . The second grid is an electron repeller which is held at a negative potential of 100 to 200 volts to remove the electrons from the ion stream. The third grid is the ion repeller screen whose potential is varied to obtain the characteristic. The fourth grid is the electron suppressor which prevents secondary electrons from obscuring the signal picked-up by a collector plate. By taking the slope of a plot of collector plate current against ion repeller grid voltage, the ion energy distribution can be determined. A typical ion energy distribution thus obtained is given in Figure 2.

The ion collection cup current density analyzer (shown in Figure 3) is a simple probe in which an ion collection tube is located inside a grounded Faraday cup with an aperture of known area. In use, the plasma stream is directed to pass through the aperture into the Faraday cup. Once inside the Faraday cup, electrons are removed from the ion beam by a negative potential of several hundred volts which is applied to the ion collection tube. The geometry of the ion collection tube is designed to ensure the suppression of secondary electrons. Beam density is calculated from the area of the collecting aperture and the magnitude of the ion current. Measured centerline beam densities obtained from this device at approximately 30 cm downstream of the thruster are 1.0 mA/cm² at mass flow rates of 7 sccm of argon and 1 kW_e input microwave power.

In addition to the above described instruments, an emissive probe has been used to measure the plasma potential at various locations in the plume. Typical measured steady-state accelerating potentials fall in the 60 to 100 volt range. A plot of measured plasma potential versus on-axis distance from the thruster is presented in Figure 4 along with the measured local magnetic field. In the absence of collisional losses, one would expect a linear relationship between magnetic field strength and plasma potential in reasonable agreement with experimental data shown in the figure. We have observed an oscillation in plasma potential at kilohertz frequencies with a typical variation of 25 percent of the peak potential. Further research is required to explain this oscillation.

Conclusion and Plans The on-going theoretical and experimental development as described above represents the basis for a meaningful scientific understanding of the ECR plasma acceleration process. Future effort will be directed toward obtaining numerical predictions of plasma conditions based on the present model and comparing these predictions with the results of a systematic implementation of the diagnostics developed thus far. High-speed video imaging of the ECR plasma is also planned to help gain insight into the unsteady aspects of its operation.

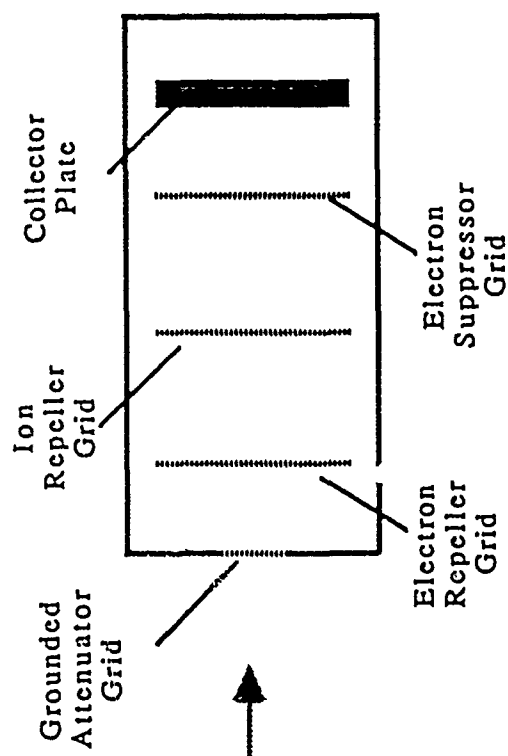


Figure 1 - Gridded Energy Analyzer Developed for ECR Plasma Thruster Diagnostics.

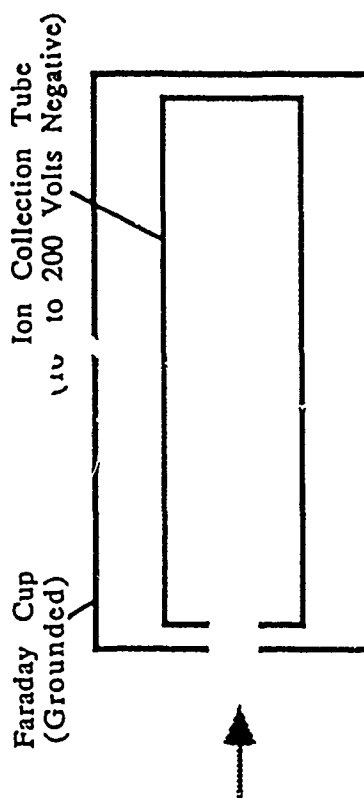


Figure 3 - Ion Collection Cup Current Density Analyzer.

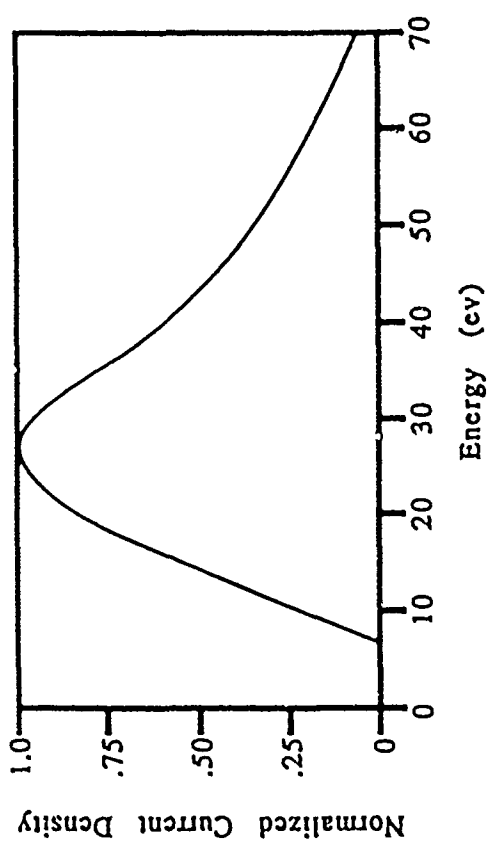


Figure 2 - Typical Ion Energy Distribution Found Using Gridded Analyzer.

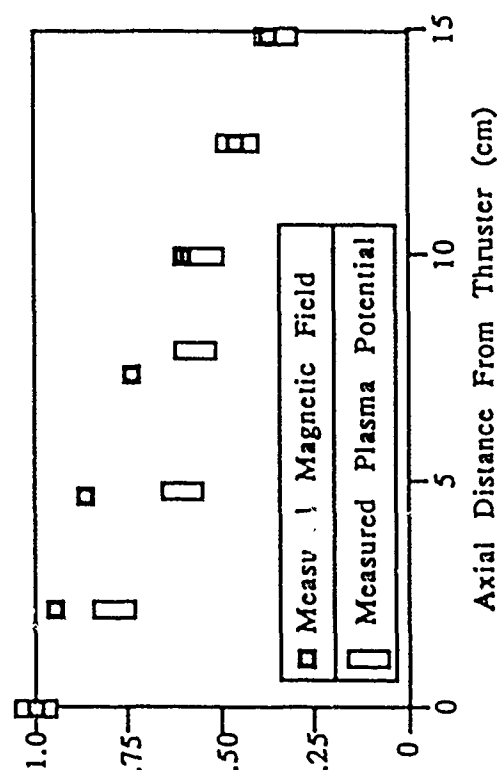


Figure 4 - Plasma Potential and Magnetic Field Versus On-Axis Distance Down-Stream.

BASIC PROCESSES OF PLASMA PROPULSION

(AFOSR Grant No. 86-0337)

Principal Investigator: Herbert O. Schrade

Institut für Raumfahrtsysteme
University of Stuttgart
Pfaffenwaldring 31
D-7000 Stuttgart 80
Federal Republic of Germany

OVERVIEW:

The proposed research addresses itself to the development of computer codes to predict the performance of arcjet and magneto-plasma dynamic thruster devices.

AUTORS: P.C. Sleziona and H.O. Schrade

TECHNICAL DISCUSSION:

1. Curvilinear Calculations of Discharge Equation

Up to now two different numerical codes have been used for the two main configurations of the MPD-thrusters (ZT1 and DT2) developed and investigated at the IRS [1,2,3]. Here a uniform solution method for the discharge equation, describing the magneto-plasmadynamic part of the MPD-thruster modellings, is presented. For this purpose the discharge equation is transformed from cylindrical coordinate to general curvilinear coordinates [4].

Contrary to [2] there are no terms neglected at the transformation of the discharge equation into curvilinear coordinates. That means the complete discharge equation is transformed into a curvilinear coordinate system, which gives the complete solution of numerical accuracy due to a correspondingly fine discretisation.

In the first two figures the solution of this discharge equation for two different geometries, represented by the current contour lines, is shown as an example. Both representations have been determined for a constant electron temperature of 10000 K and a pressure of 1000 Pa. The velocity hereby is taken zero all over the field.

In both cases the discharge equation has been iterated to a maximum local residuum, which is smaller than $\frac{1}{100}$ %. In the calculations of the two different geometries all there had to be done was a) to produce the different grids, and b) the different starting and ending positions of the electrodes had to be stated for the boundary conditions.

2. Cylindrical MPD-Thruster Calculations

The magnetoplasmadynamic calculations become more and more difficult the smaller the local densities of the plasma flow are. During the recent time we have calculated the cylindrical MPD-thruster with a fairly small mass flow rate of 2 g/s. These calculations require a detailed understanding of the flow and discharge program, since the structure of the program is very sensible against numerical errors. Typical results of such a calculation are presented in figure 3-5. The boundary conditions and initial distributions were the same as in [2].

3. Prospect for the Future

According to the solution of the discharge equation which is simple for different geometrical configurations, it is also necessary to form the solution of the flow equations. This requires a flow calculation program that is robust enough to enable flow calculation in complex geometry with fairly satisfying, curvilinear grids. An additional aspect is that the program with very big source terms in the impulse and energy equations has guarantee a stable computation. These source terms change the homogeneous differential equation system into a strong inhomogeneous differential equation system, and most of the solution methodes become instable.

The flow calculation program we have used up to now is a finite difference program which remains stable despite high source terms in the conservation equations, however requires high accuracy for the grid positioning in particular at the borders for the modelling of the boundary conditions. Due to that it is not suitable for geometrical changes. Presently we are investigating the stability of a modern finite volume procedure with high source terms, which easily enables a change of the geometrical configuration.

With such a program and the solution program for the discharge equation one only has to make the grid for a new MPD-thruster configuration, to place the electrode starting and ending positions and to state the inflow conditions in order to carry out a calculation in the scope of physical modelling.

- [1] Auweter-Kurtz, M., Kurtz, H.L., Schrade, H.O., Sleziona P.C.: Numerical Modeling of the Flow Discharge in MPD-Thrusters. Journal of Propulsion and Power, Vol. 5 No. 1, pp. 49-55, 1989.
- [2] Sleziona, P.C., Auweter-Kurtz, M., Schrade H.O.: Numerical Codes for Cylindrical MPD Thrusters. IEPC 88-043, 20th International Electric Propulsion Conference, Garmisch-Partenkirchen, 1988.
- [3] Auweter-Kurtz, M., Glaser, S.F., Kurtz, H.L., Schrade H.O., Sleziona P.C.: An Improved Code for Nozzle Type Steady State MPD Thrusters. IEPC 88-043, 20th International Electric Propulsion Conference, Garmisch-Partenkirchen, 1988.
- [4] Sleziona, P.C.: Vollständige Lösung der Entladungsgleichung in krummlinigen Koordinaten. Interner Bericht, 89-IB-1, IRS, Stuttgart, 1989.

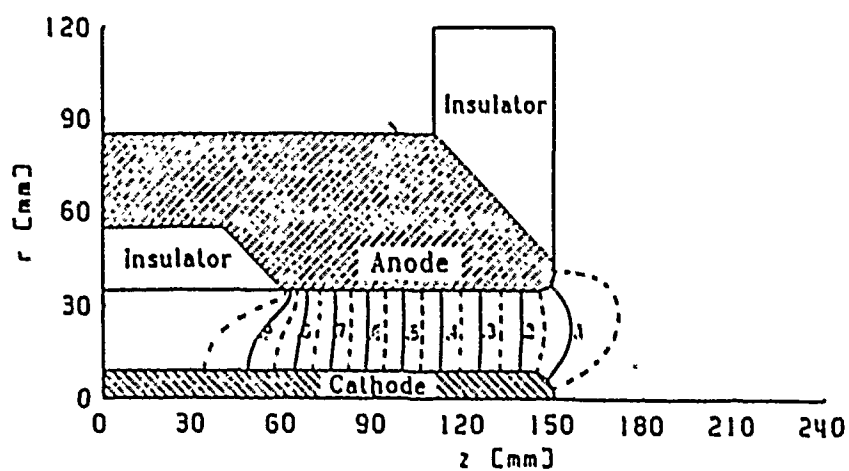


Figure 1: Current contour lines for the ZT1-IRS thruster.

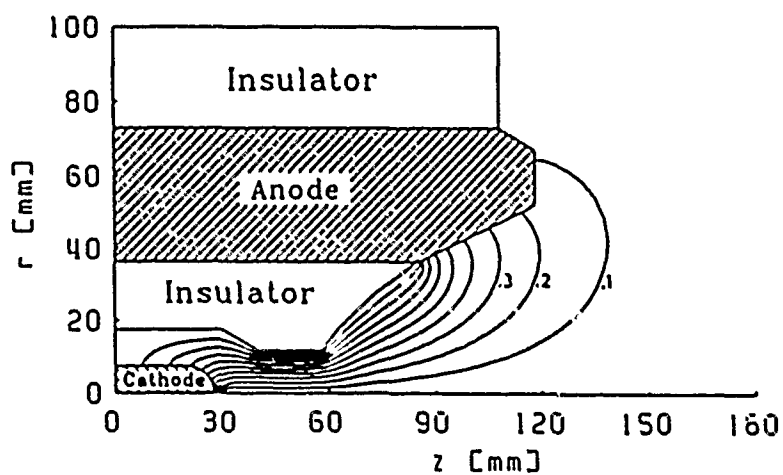


Figure 2: Current contour lines for the DT2-IRS thruster.

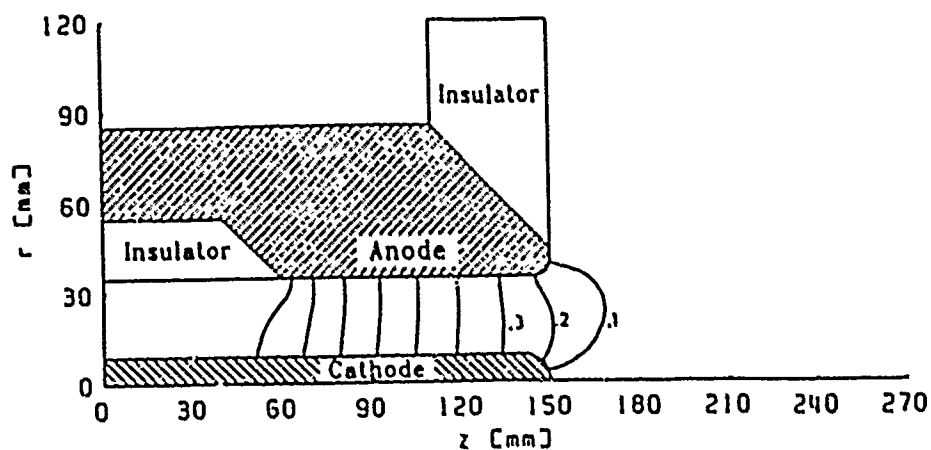


Figure 3: Current contour lines with a current of 2 kA and a mass flow rate of 2 g/s .

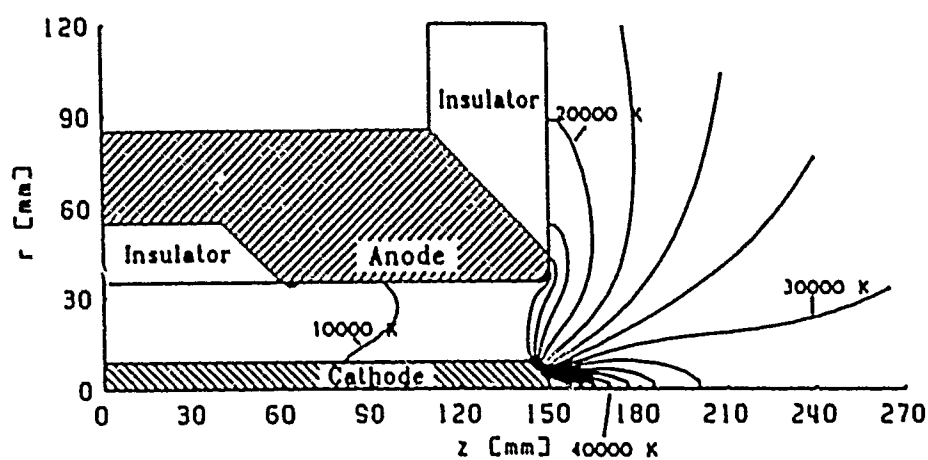


Figure 4: Temperature contour lines, current of 2 kA , mass flow rate of 2 g/s .

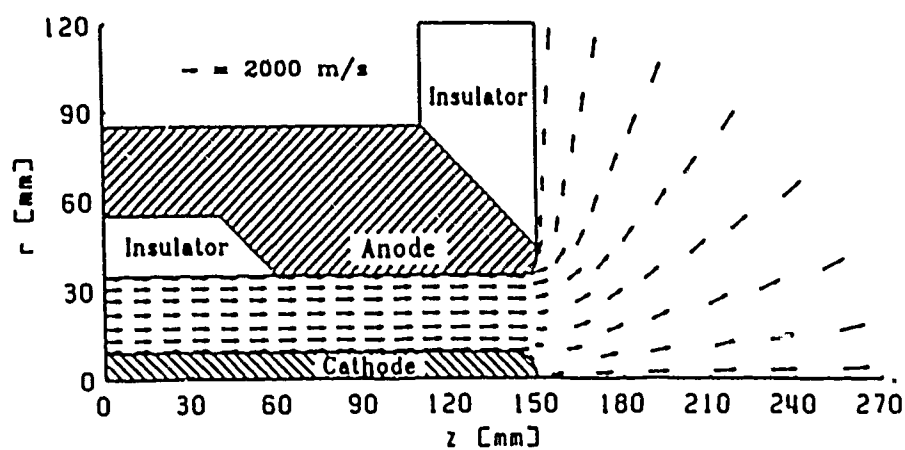


Figure 5: Velocity vector distribution, current of 2 kA , mass flow rate of 2 g/s .

Nonequilibrium and Radiation in MPD Plasmas: Two Fluid Numerical Simulations

AFOSR GRANT-86-0019

Manuel Martinez-Sanchez

Dept of Aeronautics and Astronautics

MIT, Cambridge, MA 02139

1 Summary:

Technical Discussion

A variety of different types of electric propulsion have been put forward as appropriate for space applications. One class of electric propulsion device is the magnetoplasmadynamic, or MPD, thruster. MPD thrusters use the Lorentz force produced by charged particles moving in an electric field to accelerate the propulsive fluid and produce thrust.

MPD channels, although simple to construct, are hard to analyze because of the complex interaction between the magnetic field and the fluid. One way to model these devices and to predict their performance is to simulate them numerically. Some numerical work has already been done with MPD thrusters. Martinez [5] and Kuriki [3] study a one fluid, fully ionized model of a steady quasi one dimensional flow. Minakuchi [6] includes the effect of axial heat conduction in his steady, one fluid, quasi one dimensional model. Subramaniam [7] and Lawless [4] worked with both the one fluid model and a partly ionized two fluid model. Heimerdinger [1] also works with a partly ionized, thermal equilibrium model, which includes viscosity. Other work has been done with two dimensional models.

This research uses a quasi one dimensional two fluid model. The model consists of fluid equations for the total density, the ionization fraction, the axial velocity, the electron temperature, and the heavy species temperature, as well as a magnetic field equation derived by combining Maxwell's equations with Ohm's law. It is assumed that all the particles have the same axial velocity, and that the ion and neutral temperatures are the same.

A number of source terms are used to model various phenomena in the flow. The electron temperature equation includes axial heat conduction. A number of source terms are used to model various phenomena in the flow. The Hinov-Hershberg model is used to determine the ionization and recombination at each axial location. Ambipolar diffusion is included by assuming a parabolic number density distribution across

the channel. The contribution of viscosity to the momentum and the heavy species temperature equations is also included by assuming a parabolic velocity distribution. Collisional energy transfer between electrons and heavy species is also modeled. The electrical conductivity at each axial location is computed using the Spitzer-Harm formula. The viscosity and heat conduction coefficients are also computed at each axial location. All of the equations are written in their unsteady forms, and the numerical method is an unsteady method, although only steady state results have been examined so far.

The numerical method used is a combination of various schemes. This is due to the different types of equations and their different time scales. The magnetic field equation and the heat conduction term in the electron temperature equation are integrated using McCormack's method a number of times for each step of the other equations. The remaining equations are stepped using either the Donor Cell method or a modified Rusanov method.

A number of the inlet boundary conditions of the flow are determined by the physical characteristics of the flow, the mass flow per unit area, the applied current, and the total inlet enthalpy. The inlet ionization fraction is physically zero, but, because of the limitations of the model, the inlet ionization fraction is set to some small number. The inlet heavy species temperature is set to room temperature. For cases with heat conduction, the electron temperature gradient at the inlet is set to zero. For cases without heat conduction, the inlet density is computed using a downwind difference.

The exit boundary conditions for supersonic flow are zero gradient in all variables except the magnetic field, which is set to zero at the exit, and the heavy species temperature, which is chosen so that there is zero gradient in the sum of the fluid and magnetic pressures. For subsonic flow the pressure is set to some small external pressure, and the other variables are chosen so that there is zero gradient in the Riemann invariants.

The method was tested by simplifying the equations to be the unsteady analogue of the equations used by Martinez [5]. Running the simulation to steady state provided results similar to those found by Martinez for a number of different magnetic Reynolds numbers and for both constant and variable area channels.

The full set of equations were then used to examine the effect of various phenomena on the flow and performance characteristics of the thruster. The thruster was taken to be 20 cm long with an electrode separation of 2 cm. The inlet ionization and total enthalpy were chosen to be small enough so that their effect on the flow was negligible.

First ambipolar diffusion was added to the baseline case, then viscosity, and finally, heat conduction. As shown in Table 1, ambipolar diffusion and heat conduction had little effect on performance. Viscosity however played a major role in determining thruster performance and flow characteristics. Viscosity causes the heavy species temperature to increase rapidly to levels of 1 to 10 eV and causes the flow to be frictionally

Case	R_{mag} or B_0	ambipolar diffusion	viscosity	heat conduction	channel	E_z V/m	\bar{T} N/m^2	η
1-fluid	20	no	no	no	CAC	345	4370	0.69
1-fluid	4.9258	no	no	no	CAC	433	4630	0.62
2-fluid	0.1	no	no	no	CAC	399	4256	0.57
2-fluid	0.1	yes	no	no	CAC	401	4180	0.55
2-fluid	0.1	yes	yes	no	CAC	258	2100	0.21
2-fluid	0.1	yes	yes	yes	CAC	287	2300	0.23
2-fluid	0.15	yes	yes	yes	CAC	519	4550	0.33
2-fluid	0.2	yes	yes	yes	CAC	860	6980	0.33
2-fluid	0.1	yes	yes	yes	FFC	340	3053	0.34

Table 1: Thrust and Efficiency for All Cases

choked with exit velocities on the order of 5000 meters/second .

It was also desired to determine the effect of increasing the total current supplied to the thruster, and hence the inlet magnetic field. Increasing the total current from 80 kAmp/meter-depth to 120 kA/m caused the flow to develop a large current concentration at the exit, with a corresponding increase in the exit electron temperature and ionization. Increasing the total current to 160 kA/m caused this concentration to become so large that the simulation did not converge to a steady state. As shown in Table 1, increasing the total current to 120 kA/m resulted in an increase in the thruster efficiency.

It is possible that the large exit current concentrations in the higher total current cases is due in part to the static instability described by Heimerdinger [2]. Physically this instability would first appear near the inlet and then travel down the channel. When the current buildup reaches the exit, the current would bend out of the channel and the concentration would dissipate . The current concentration would then reappear at the beginning of the channel. However, in a one dimensional model with zero exit current, the instability is forced to remain at the exit.

The last effect examined was the effect of area variation. The results for the full model at the 80 kA/m current for a constant area channel were compared to the results for a parabolic channel with an throat area of 2 cm², an inlet to throat area ratio of 1.5, and an exit to throat area ratio of 2. Area variation alleviated the exit current buildup somewhat and resulted in an increase in performance.

As detailed earlier, a model with a one dimensional magnetic field which goes to zero at the channel exit is problematic. To alleviate these problems, a two dimensional magnetic field simulation, coupled with a quasi one dimensional fluid calculation, was developed. This simulation allows the current to bend at

the exit. However, the quenching of the exit current has not yet been simulated numerically.

Some work has also been done in an attempt to combine the one dimensional MPD simulation with a model of anomalous dissipation in MPD thrusters. The dissipation arises due to the presence of a modified two stream instability in the plasma. The one dimensional code produces the parameters at each axial location needed by the dissipation model to determine if the instability exists and what its effect will be, in terms of a modified conductivity and electron and ion heating rates. The one dimensional code will then take into account the effects of the instability. By iterating this process a number of times, a steady state should be reached.

References

- [1] D.J. Heimerdinger, "Fluid Mechanics in a Magnetoplasmdynamic Thruster", Doctoral Thesis, Massachusetts Institute of Technology, Jan. 1988
- [2] D.J. Heimerdinger and M. Martinez Sanchez, "Fluid Mechanics in a Magnetoplasmdynamic Thruster", IEPC-88-039, DGLR/AIAA/JSASS 20th International Electric Propulsion Conference, West Germany, Oct. 1988
- [3] K. Kuriki, Y. Kunii, and Y. Shimizu, "Idealized Model for Plasma Acceleration in an MHD Channel", AIAA Journal, Mar. 1983, Volume 21, Number 3
- [4] J.L. Lawless and V.V. Subramaniam, "Theory of Onset in Magnetoplasmdynamic Thrusters", Journal of Propulsion and Power, Vol. 3, No. 2, Mar., Apr. 1987
- [5] M. Martinez-Sanchez, "The Structure of Self Field Accelerated Plasma Flows", AIAA/DGLR/JSASS 19th International Electric Propulsion Conference, May 1987
- [6] H. Minakuchi and K. Kuriki, "Magnetoplasmdynamic Analysis of Plasma Acceleration", IEPC-84-06, AIAA/DGLR/JSASS 17th International Electric Propulsion Conference
- [7] V.V. Subramaniam and J.L. Lawless, "Onset in Magnetoplasmdynamic Thrusters with Finite- Rate Ionization", Journal of Propulsion and Power, Vol. 4, No. 6

Fundamental Research on Erosion in Magnetoplasmadynamic Thrusters

(AFOSR Grant No. 87-0360)

Principal Investigators:

V. V. Subramaniam and J. W. Rich

Department of Mechanical Engineering
The Ohio State University
Columbus, Ohio 43210

SUMMARY/OVERVIEW:

The purpose of this research is to understand and quantify the mechanisms responsible for erosion in steady state magnetoplasmadynamic (MPD) thrusters. This is an important step in being able to predict thruster lifetimes. A major if not dominant erosion mechanism in the diffuse mode, is evaporation. This analytical work aims to understand this mechanism in particular, its limits, and to provide quantitative models in order to estimate the electrode lifetimes.

TECHNICAL DISCUSSION

Erosion processes depend on a complex coupling between plasma discharge characteristics, plasma-wall interactions, and electrode phenomena. In particular, erosion rates depend on whether the current conduction is through localized spots, or via a diffuse (distributed) mode. Spots are detrimental to the electrode material because of their high erosion rates. Therefore, it is important to understand how and under what conditions they may be formed, and exactly when diffuse mode behaviour ends. Much of the focus of this research is on the cathode, although the anode has also been studied. The thermal response of the electrodes at steady state is discussed next, followed by a brief summary of ongoing and planned research.

The anode will be discussed first. A recent theory predicts two operating modes for the anode.¹ One of these is a stable steady state, while the other results in a thermal runaway. The transition of the stable diffuse mode to the unstable thermal runaway occurs as the current density increases. For low current densities, the anode sheath attracts plasma ions and repels plasma electrons. The anode is at a negative potential with respect to the plasma at the sheath edge, under these operating conditions. As the current density continuously increases, the magnitude of the anode "fall" decreases, goes through zero, and assumes positive values (i.e. the anode reaches positive values of the potential with respect to the plasma, at high current densities). This sheath reversal has been observed experimentally.² In our anode theory, we show that a thermal runaway occurs prior to the sheath reversal. This thermal runaway which occurs at a critical value of the anode "fall", is caused by a positive feedback between electron bombardment and thermionic emission. Consider the anode operation at low current density. A small decrease in the absolute value of the anode sheath drop results in an increase in electron bombardment. This results in local heating of the surface leading to higher temperatures and hence increased thermionic emission. The increased surface electron emission current then causes a further decrease in the sheath drop in order to conserve overall current. This process then repeats itself until the surface is regeneratively heated and has locally melted. This thermal runaway can be delayed by external cooling and may explain the occurrence of anode spots under MPD conditions.

The thermal response of the cathode under steady diffuse conditions has also been considered.³ As in the case of the anode, two operating modes are found. One is stable, while the other results in the previously discussed thermal runaway due to excessive electron bombardment. The thermal runaway leads to eventual local melting of the cathode surface, and may be a precursor to spot formation at the cathode. The stable steady state is also

strongly influenced by discharge and electrode parameters. While the anode is affected by the thermal runaway at high current densities, the cathode is affected by the same at low current densities. The steady diffuse mode operation of the cathode is also limited at high current densities however, because of excessive ion bombardment. This theory yields the following sufficient condition for the cathode sheath voltage drop in order to have stable diffuse mode operation:

$$V_c \geq \frac{kT_-}{2e} \ln \left[\frac{2m_i}{\pi m_e} \right] \quad (1)$$

where T_- is the plasma electron temperature, m_i is the ion mass, and m_e is the electron mass. As long as the voltage drop across the cathode sheath is approximately larger than the right hand side of equation (1), a thermal steady state at the cathode can be maintained indefinitely even in the presence of fluctuations in the MPD discharge. In other words, the thermal runaway due to electron bombardment will not occur as long as equation (1) is satisfied. A more accurate expression for this sufficient condition is given in ref. [3]. A stability criterion such as (1) may also be derived for the anode:

$$V_A \geq -\frac{kT_-}{e} \ln \left[\frac{j_- + O(2\epsilon\sigma_{SB}T_o^3T_i^2/2\phi_A T_-)}{en_-(kT_-/2\pi m_e)^{1/2}} \right] \quad (2)$$

where $O(\)$ signifies the order of magnitude of the term in parentheses, ϵ is the emissivity of the outer anode surface, σ_{SB} is the Stefan-Boltzmann constant, j_- is the net plasma current density, T_o is the anode outer surface temperature, T_i is the anode inner surface temperature, ϕ_A is the anode material work function, and n_- is the charged particle number density at the anode sheath edge. Equation (2) may be interpreted in the same manner as equation (1) for the cathode.

Following these earlier simple theories, a more detailed two-dimensional axisymmetric steady thermal model of the cathode has been developed in order to better understand the influence of the plasma flow and external cooling on electrode processes. In this model, the cathode temperature satisfies the two-dimensional heat conduction equation including ohmic heating:

$$\frac{1}{r} \frac{\partial}{\partial r} \left[r\lambda \frac{\partial T}{\partial r} \right] + \frac{\partial}{\partial x} \left[\lambda \frac{\partial T}{\partial x} \right] + \frac{j^2}{\sigma} = 0 \quad (3)$$

where λ is the thermal conductivity, σ is the electrical conductivity of the cathode material, and j is the current density through the cathode. The boundary conditions are:

$$-\lambda \frac{\partial T}{\partial x}(x=0) = h(T(x=0) - T_{cool}),$$

$$-\lambda \frac{\partial T}{\partial x}(x=L) = \epsilon\sigma_{SB}T^4(x=L),$$

$$\frac{\partial T}{\partial r}(r=0) = 0 \text{ for a solid cathode,} \quad (4)$$

$$\text{and } -\lambda \frac{\partial T}{\partial r}(r=r_c) = j_i(V_c + e_i - \phi) + j_e(\phi + \frac{2kT_-}{e}) - j_E(\phi + \frac{2kT_-}{e})$$

where h is the heat transfer coefficient between the cathode base and an external coolant at T_{cool} , ϵ is the emissivity of the cathode tip, L is the cathode length, r_c is the cathode radius, j_i is the ion current density from the plasma, j_e is the electron current density from the plasma, j_E is the emitted electron current density which in general can depend on the surface temperature and the surface electric field, ϕ is the cathode work function, V_c is the cathode sheath voltage drop, T_- is the plasma electron temperature, and e_i is the ionization potential of the propellant gas. The boundary conditions (4) contain plasma as well as sheath variables. This is how the electrode is coupled to the plasma discharge. The sheath voltage drop and electric field at the cathode surface must be determined from overall current conservation and from the solution of Poisson's equation. The plasma variables (such as the charged particle number density and electron temperature distributions) at the sheath edge are determined from earlier ionizing quasi one-dimensional and boundary layer theories.⁴⁻⁷ Thus, given a total propellant mass flow rate, total current, cathode length, cathode diameter, and external cooling conditions, the plasma and electrode behaviour can be predicted. In this manner, the plasma discharge and electrode can be coupled so that their combined behaviour can be understood. As an illustration, the calculated axial cathode surface temperature profile is displayed in Fig. 1 for a 5 cm. long tungsten cathode, argon flow rate of 0.5 g/s, and

a total current of 5000 A.

Although the present theory is a first to attempt at truly coupling the plasma flow and electrode processes, it suffers from several weaknesses. First, this theory does not account for the pre-sheath and ionization in the pre-sheath caused by electrons emitted from the cathode surface. Although this is a complicated problem, it must be addressed since there are MPD conditions where the electrodes are "starved". In this situation, there are an insufficient number of charge carriers in the electrode-adjacent plasma to carry the current that is being driven. Therefore, the diffuse mode cannot exist unless there is an increase in the charged particle number density in the sheath and pre-sheath due to ionization by the emitted electrons. Second, radiative heating from the plasma has not been considered. Finally, the models used here for the plasma flow do not include the Hall effect which could affect the characteristics of the electrode-adjacent boundary layer in some MPD thruster designs. Future research is therefore aimed at removing these deficiencies.

References

- (1) V. V. Subramaniam, and J. L. Lawless, "Thermal Instabilities of the Anode in an MPD Thruster", *J. Propulsion & Power* (in press).
- (2) H. Hugel, "Effect of Self-Magnetic Forces on the Anode Mechanism of a High Current Discharge", *IEEE Trans. Plasma Sci.*, Vol. PS-8, No. 4, December 1980.
- (3) K. S. Hoyer, V. V. Subramaniam, and J. L. Lawless, "Limits on Steady Diffuse Mode Operation of the Cathode in an MPD Thruster", submitted to *J. Propulsion & Power*.
- (4) J. L. Lawless, and V. V. Subramaniam, "Theory of Onset in Magnetoplasmadynamic Thrusters", *J. Propulsion & Power*, Vol. 3, No. 2, pp. 121-127, March-April 1987.
- (5) V. V. Subramaniam, and J. L. Lawless, "Onset in Magnetoplasmadynamic Thrusters with Finite Rate Ionization", *J. Propulsion & Power*, Vol. 4, No. 6, pp. 526-532, November-December 1988.
- (6) V. V. Subramaniam, and J. L. Lawless, "An Integral Method for Two-Temperature Ionizing Laminar Boundary Layers", *Phys. Fluids*, Vol. 31, No. 1, pp. 193-200, January 1989.
- (7) V. V. Subramaniam, and J. L. Lawless, "Electrode-Adjacent Boundary Layer Flow in Magnetoplasmadynamic Thrusters", *Phys. Fluids*, Vol. 31, No. 1, pp. 201-209, January 1988.

Temperature Profiles

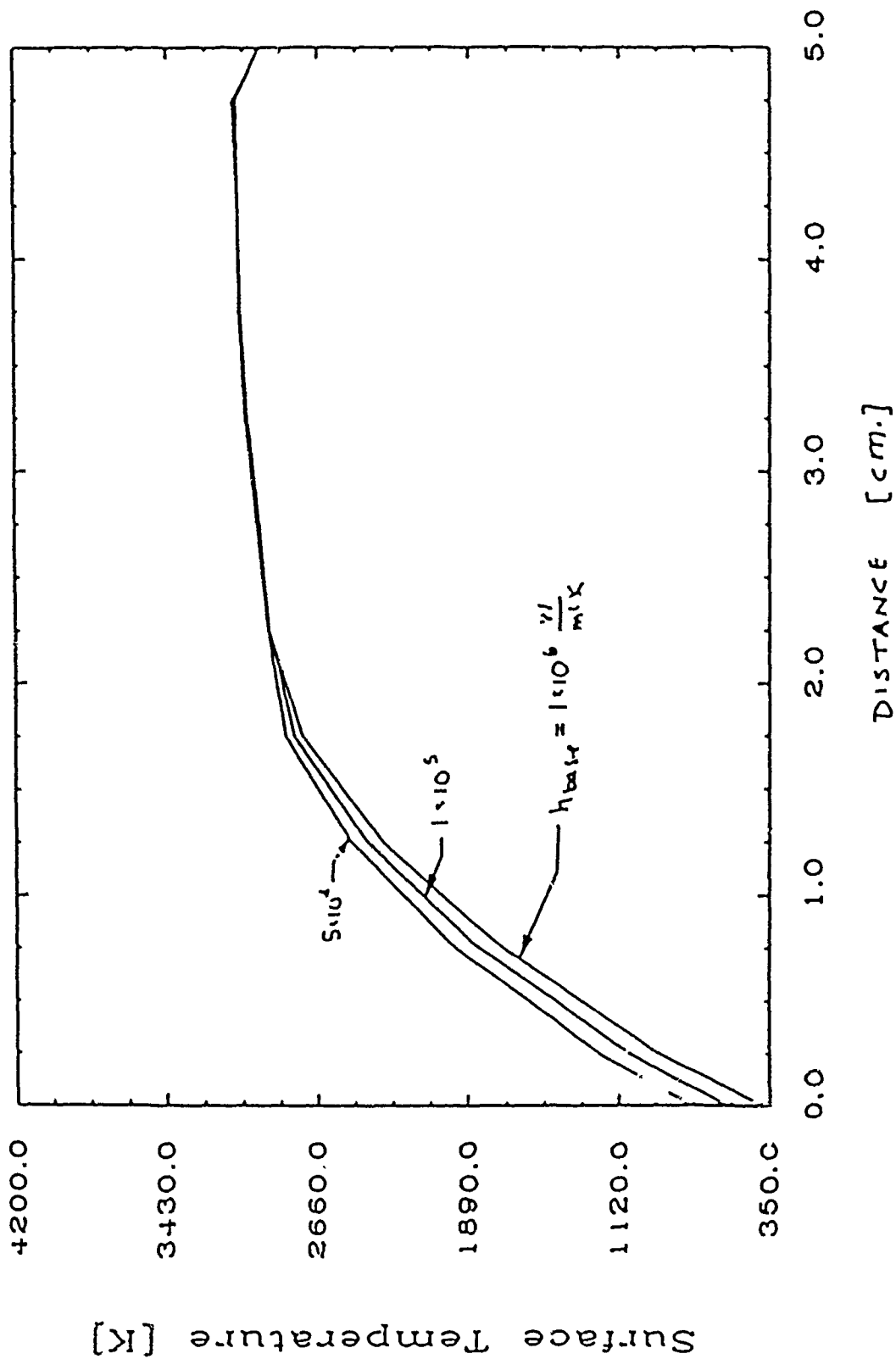


Fig. 1: The cathode surface temperature is shown here versus distance along the cathode, for typical values of the heat transfer coefficient for external cooling at the base of the cathode. The cathode is 5 cm. long, 1.75 cm. in diameter, and is made of tungsten. The total argon mass flow is 0.5 g/s and the total current to the thruster is 5000 A.

Propulsion Research on the Hybrid Plume Plasma Rocket

Contract No. AFOSR-84-0190

T. F. Yang, F. R. Chang-Diaz*, X. Yao, S. Y. Peng, W. A. Krueger, J. Urbahn

Plasma Fusion Center
Massachusetts Institute of Technology
Cambridge, Massachusetts 02139

Summary

The major achievement for the current year has been the completion of the construction of the tandem mirror device and its successful operation at low power levels. The hydrogen plasma has been created with microwave breakdown. The experiment of heating the plasma with rf power is underway. The results on the measurements of density and temperature of the plasma will be presented. On the computational study of the plasma exhaust a parameter scan of the region of interest has been undertaken using the time dependent $2 - \frac{1}{2}D$ three fluid MHD code. Details of the study will also be presented.

Technical Discussion

As reported previously, the purpose of this work is to study hybrid plume plasma propulsion using the hot plasma exhaust of a tandem mirror magnetic confinement device. A compact tandem mirror device has been assembled with the components built last year which consists of eight central cell coils, four mirror coils and booster coils, a vacuum chamber and structure.

Figure 1 shows the completed assembly of the device mounted on a stand. Shown in the picture there is a vacuum pumping system on the left end. An identical vacuum pumping system is on the other end. The feed through and transmission line for 2 kW;

*Astronaut Office, NASA Johnson Space Center, Houston, Texas.

2.4 GHz microwave power can be seen at the middle of the plug on the left. On the back of the device, there is feed through, frequency match box and transmission line of the rf power and a laser fluorescence diagnostic system. A two half loop antenna is inside the vacuum. Ultra-high vacuum of 5×10^{-8} Torr and microwave discharge of hydrogen gas at 10% of the field were obtained early during the fall of last year. The power supply for energizing the magnetic coils to full field, the rf antenna, and the power transmitter were installed and became operational recently.

Currently we are carrying out the experiment to study the plasma with microwave discharge as well as the low power and short pulse rf heating. The Langmuir probe is our only diagnostic at present. The microwave unit is a pulsed system with pulse length of 4 ms at 270 cycles per second. Therefore the plasma is a pulse mode at the same frequency and the temperature cannot be determined with probe measurement. The density is estimated to be $5 \times 10^{12} \text{ cm}^{-3}$. The rf heating experiments are carried out at a power level of 10 kW and pulse length of 10 ms for hydrogen pressure ranged from 5×10^{-5} to 5×10^{-3} Torr and for maximum field ranged from 1 kG to 6 kG. A typical probe measurement is shown by the bottom trace in Figure 2. The top trace is the input microwave pulse. Although temperature has not been determined at this moment, there is strong indication of heating. This is a survey study to find the optimal operating conditions. The probe measurement of the plasma properties will be analyzed, and results will be presented.

The experiment with low power, short pulse at 50% of the designed field will be conducted to obtain the full understanding of the plasma properties and rf heating process. The power level, pulse length and field strength will be increased gradually in the future.

On the computational side, the emphasis has been on the study of the development and formation of the hybrid plume. To understand the physical mechanism involved in the development of the hybrid plume, a parameter scan of the region of interest has been undertaken. The parameter scan allows one to change the specifications that one has control over in an actual device (e.g., plasma exhaust temperature or density, neutral gas density, and jet location). From the runs one can see which parameters are the most critical to the proper formation of a hybrid plume design and give insight to the physical mechanisms involved. Details of the parameter scan and current results will be presented.

References

1. Chang, F. R., Fisher J. L., Nuclear Fusion, 22, No.8 (1982).
2. Chang, F. R., Krueger, W. A., Yang, T. F., AIAA/DBLR/JSASS International Electric Propulsion Conference, paper AIAA-85-2049, Alexandria, VA, September 1985.
3. Yang, T. F., Miller, R. H., Wenzel, K. W., Krueger, W. A., AIAA/DBLR/JSASS International Electric Propulsion Conference, paper AIAA-85-2054, Alexandria, VA, September 1985.
4. Chang-Díaz, F. R., Yang, T. F., Krueger, W. A., Peng, S., Urbahn, J., Yao, X., and Griffin, D., AIAA/DBLR/JSASS International Electric Propulsion Conference, paper AIAA-88-126, Garmisch-Partenkirchen, W. Germany, October 3-6, 1988.
5. Chang, F.R., Krueger, W. A., Yang, T. F., "Numerical Modeling of the Hybrid Plume Plasma Rocket," AFOSR/AFRPL Chemical Rocket Research Meeting, paper 30, Lancaster, CA, September 1986.
6. Chang, F. R., Krueger, W. A., Yang, T. F., Fisher, J. L., "Plasma-Gas Interaction Study in a Hybrid Plume Plasma Rocket," AFOSR/AFRPL Chemical Rocket Research Meeting, paper 51, Lancaster, CA, March 1985.

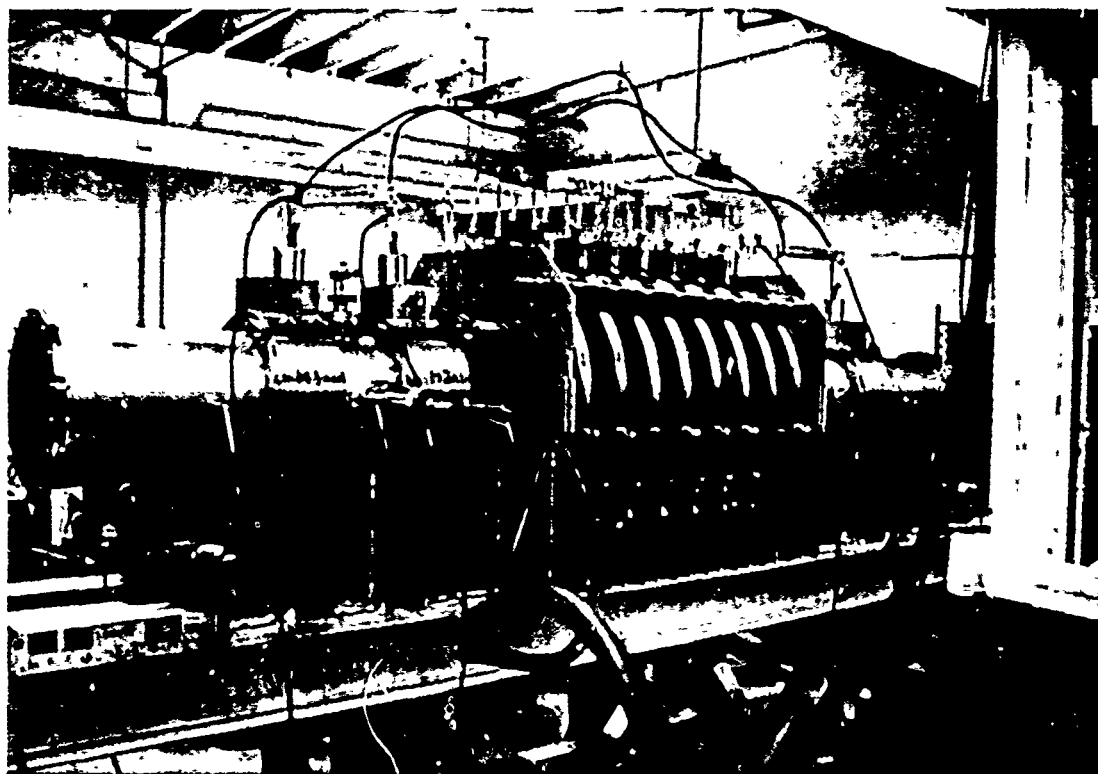


Fig. 1: Tandem mirror plasma propulsion experimental device.

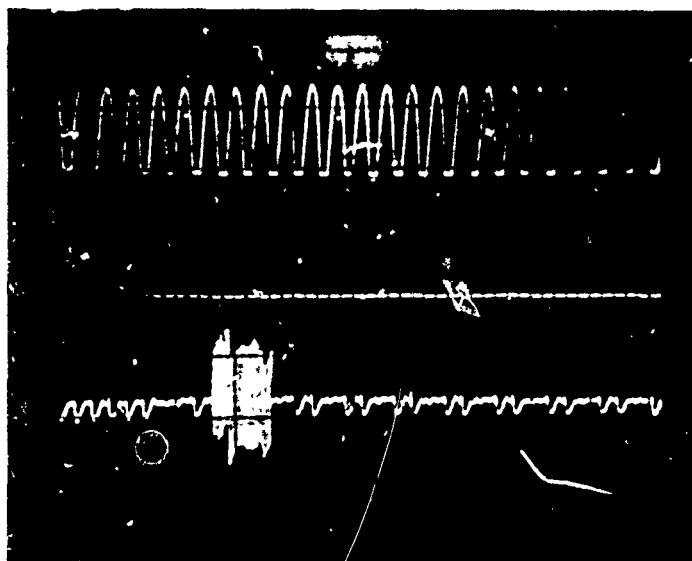


Fig. 2: Langmuir probe measurement of the plasma with microwave discharge and low power rf heating. The pulse width is 10 ms.

MPD THRUST CHAMBER FLOW DYNAMICS

AFOSR Contract No. F49620-86-C-0117

Principal Investigator: P.J. Turchi*

Co-Investigators: J.F. Davis*, and N.F. Roderick**

*R & D Associates, Washington Research Laboratory
Alexandria, VA 22314**University of New Mexico
Albuquerque, NM

SUMMARY:

In order to understand and improve the performance characteristics of MPD arcjets, it is necessary to determine the electromagnetic discharge and flow structures within the thrust chamber and their relationship to the arcjet design and operating conditions. The present research program is directed toward diagnosing an MPD thrust chamber by measurement of the electromagnetic field distributions, particle densities and velocities in the thrust chamber flow. A new technique was developed to unfold the emission distribution and profile and to estimate thermal, radial and (in-plane) turbulent velocity components of the thrust chamber flow. The results indicate that the plasma within the present MPD arcjet has a strong radially-inward flow with a substantial increase in hydrodynamic turbulence near the cathode. Such flow can have important consequences for thruster efficiency. Changes in the total current and mass flow with fixed thruster geometry would be expected to change the radial versus axial flow and would substantially affect the thruster performance for reasons that cannot be inferred from simple scaling relationships based on electromagnetic thrust and total mass flow.

TECHNICAL DISCUSSION:

The MPD arcjet used in the present study is a cylindrical coaxial device with a brass outer anode 8.41 cm ID and a copper-tungsten alloy cathode 3.81 cm OD. The channel length is 5 cm from a boron nitride insulator backplate to the exit plane. Argon-hydrogen mixtures are delivered to the arcjet through 16 choked orifices in the insulator at mid-radius of the channel gap. Current is delivered to the arcjet from a pulse forming network with a pulse width of 0.8 ms and current of 20 kA. The arcjet breech voltage attains a quasi-equilibrium value of 50 V for approximately 0.4 ms at 0.2 ms after current initiation for a gas flow rate of 6 g/s (argon with 1.5 percent added hydrogen). Figure 1 shows the measured enclosed current contours in the arcjet at these operating conditions from internal magnetic probes. Note that the current distribution is basically retained within the thrust chamber, with less than 5 percent of the total current beyond the exit plane. The $\mathbf{j} \times \mathbf{B}$ forces on the plasma have significant radial components toward the cathode indicating the potential for radial velocity components and subsequent increases in plasma density towards the cathode.

A computer-controlled, time- and spatially-resolved spectrographic system is used for measurement of line emission profiles to infer plasma temperature, velocity components and electron density. In order to make measurements within

the arcjet thrust chamber, a slit 1.6 mm wide was machined in the outer conductor as shown schematically in Figure 2, which allows chordal observation between the cathode and anode perpendicular to the arcjet axis. Time-integrated line profile measurements are made of the argon ion 434.80 and the 696.28 nm line of hydrogen (H_α) which yield digital data of observed intensity versus wavelength and versus spatial position (along the slit) simultaneously. The raw data is digitally filtered versus wavelength using a low frequency bandpass filter with frequency cutoff determined by the allowable spectral frequencies from the spectrograph instrument profile.

The observed intensity at any wavelength is the line integral across a cord of observation. If the plasma is optically thin and axisymmetric, then, generally, a normal Abel inversion technique can be applied at each wavelength to yield the local emission coefficient versus radius of a volume element at that radius and at that wavelength. Repeating the Abel inversion process for a sufficient number of wavelengths yields the local line emission profile versus radius. By assuming a thermal velocity distribution of the particles, a fit to a Gaussian profile yields the (heavy) particle temperature. Earlier application of this technique to the observed 434.8 nm argon ion emission and to the H_α emission implied argon ion temperatures of 12.5 to 17 eV and hydrogen temperatures of 0.5 to 0.85 eV. The discrepancy between the argon and hydrogen temperatures, and the rather high value for argon temperature throughout the thrust chamber suggest that radially-directed flow and/or hydrodynamic turbulence contribute to the observed line width.

If the plasma has velocity components along the chord of observation, then a Doppler shift away from the natural line center will occur. Figure 3 shows schematically the observation geometry and illustrates the contributions to the observed intensity profile from an emission element at r' at two different chordal positions, y and y' . If there are velocity components from a volume element dV along the line of sight that are due to radial plasma motion, then the observed intensity at y and λ from dV will be shifted to $\pm \lambda_0 V_r \sin \theta / c$ at y' . Consequently, a standard Abel inversion techniques cannot be applied. The local emission profile of a thermal plasma with radial velocity V_r is therefore not only a function of r and λ but y (through $\sin \theta$):

$$e(r, \lambda) = \frac{I_t}{\pi^2 \Delta \lambda_D} \exp \left[- \left(\frac{\Delta \lambda \pm \lambda_0 \frac{V_r \sin \theta}{c}}{\Delta \lambda_D} \right)^2 \right] \quad (1)$$

where $\Delta \lambda_D = \langle v \rangle \lambda_0 / c$; $\langle v \rangle = [2kT/M]^{1/2}$ is the most probable velocity of the emitters, θ is the angle from vertical to the velocity vector at r and y . I_t is the integral of the local emission coefficient over all wavelengths. In order to determine the true local emission profile at $\theta = 0$ from the observed chordal intensity, the effects of the radial velocity components from outer volume elements ($|\theta| > 0$) must be subtracted. If in Figure 3, dV at y represents the outermost emission element, the observed emission profile will have no shifted components due to the radial velocity ($\sin \theta = 0$) and a fit to Equation 1 will determine $\Delta \lambda_D$. The observed profile at $y-dy$ can then be fit to a sum of two exponentials where, in the first, $\Delta \lambda_D$ at $y-dy$ is an unknown (but $V_r \sin \theta \approx 0$) and, in the second, $V_r \sin \theta$ at y is an unknown (but $\Delta \lambda_D$ is already known). This process is then repeated (starting from the largest radius and working inward) to yield $\Delta \lambda_D$ and V_r versus radius.

The results of applying this technique to the argon and hydrogen emission data, indicate a radial velocity component to the flow with velocities on the order of 10 km/s (Figure 4a). If the turbulent velocity distribution in the

x-y plane produces a Gaussian or near-Gaussian emission profile then the unfolded emission profile represents the convolution of two Gaussians, (one thermal and one turbulent) and the parameter $\Delta\lambda_D$ is related to the thermal and turbulent components by

$$\Delta\lambda_D^2 = \left(\frac{\lambda_0}{c} \langle v \rangle_{tr} \right)^2 + \left(\frac{\lambda_0}{c} \sqrt{\frac{2kT}{m}} \right)^2 \quad (2)$$

If the argon and hydrogen have a common temperature and a common turbulent velocity component, then equation 2 gives a system of two equations that can be solved for T and $\langle v \rangle_{tr}$ from the unfolded values of $\Delta\lambda_D$ for argon and hydrogen versus radius. These results, shown plotted in Figure 4b indicate a particle temperature (upper curve) of approximately 0.5 eV in the arcjet midplane to anode with an approximate 50 percent rise in temperature toward the cathode. The hydrodynamic turbulent velocity, (lower curve) shows a much more dramatic rise of nearly 300 percent from values of 1500 to 2500 m/s from the midplane to anode region to approximately 7000 m/s near the cathode.

The measured radial mass flow and development of hydrodynamic turbulence would have important consequences for thrust efficiency since shock and viscous losses near the cathode surface would be expected. It may also be expected that the relative strength of the radial (versus axial) flow can change significantly as the total current and mass flow values are varied with fixed electrode configuration and injection geometry. Such change in flow direction can substantially affect the MPD thruster performance for reasons that cannot be inferred from simple scaling relationships based on electromagnetic thrust and total mass flow. Examination of MPD performance by variation of operating current and mass flow rate, (i.e. external parameters) with a fixed device geometry will thus be an inaccurate procedure for assessing the potential of MPD thrusters. Instead, it will be necessary to vary the arcjet geometry and/or mass-inlet ratios as the current is changed. To guide the combination of geometry, current and mass flow toward an optimum design, two-dimensional calculations are required.

In addition to the experimental effort, a short series of numerical simulations were successfully carried out to investigate the use of a two-dimensional time dependent magnetohydrodynamic (MHD) code for flow field and thruster calculations to evaluate application of this code to MPD thruster problems. The MHD code MACH2 is a one-temperature, single fluid code with three magnetic field components. It includes an Arbitrary-Lagrangian-Eulerian (ALE) mesh with adaptive grid control, perfect gas or tabular equations of state, thermal and magnetic field diffusion, radiative emission, and the Hall effect. The initial calculations were made with coarse zoning and gave reasonable agreement with the experimental magnetic field measurements. Additional work is required to adjust the conditions for onset of anomalous resistivity to the regime of MPD thruster operation.

FUTURE DIRECTIONS:

With the experimental and theoretical techniques now available, it will be possible to examine and compare details of the MPD arcjet internal flow over a range of operating conditions and geometries. These studies should yield a better understanding of the performance characteristics and capabilities of MPD thrusters. Further work is required to develop diagnostic techniques for directly determining axial velocity distributions within the thrust chamber and for examining structures very near the mass flow injectors and backplate.

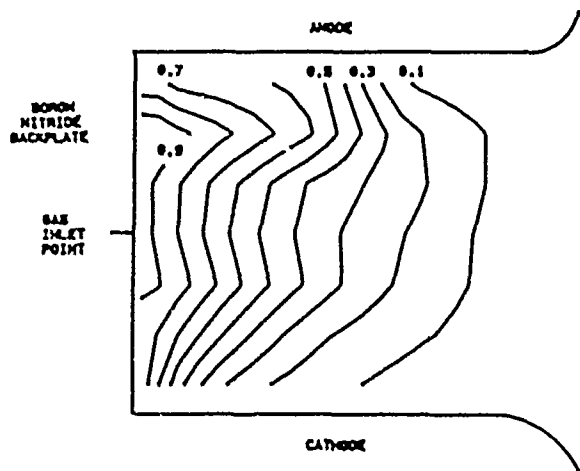


Figure 1: Enclosed current contours from B-probe measurements indicate that the current is largely retained within the thruster chamber and has radial components of $\mathbf{j} \times \mathbf{B}$ force toward the conductor walls.

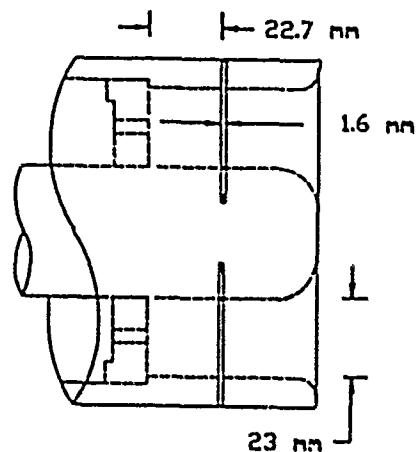


Figure 2: Schematic of arcjet showing slit in outer conductor at the midplane allowing spectroscopic measurements of internal flow dynamics.

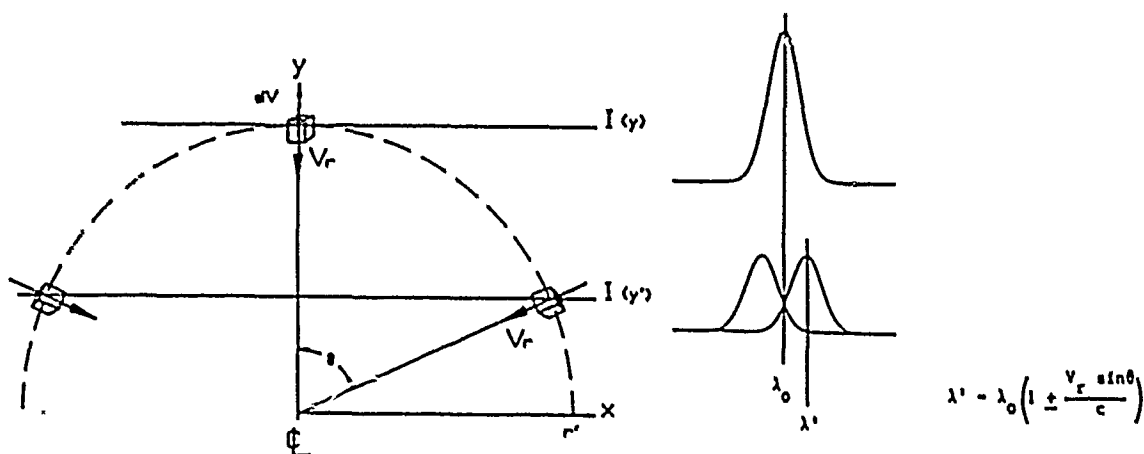
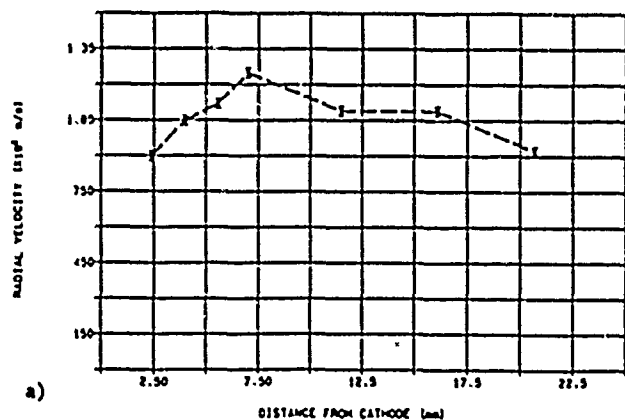
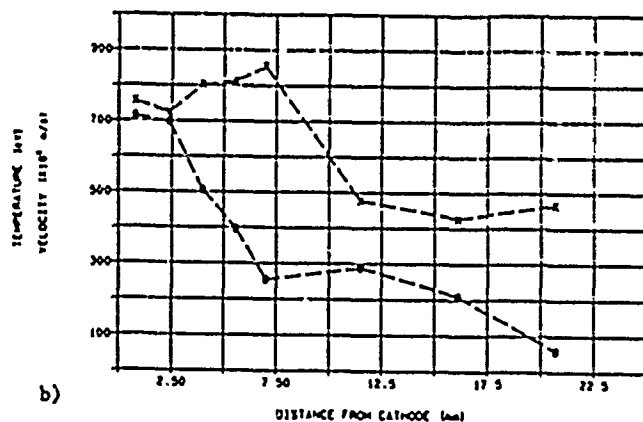


Figure 3: Emission from a volume element dV at r' viewed along chord y has a symmetrical emission profile. The equivalent volume elements at y' will consist of two Doppler shifted emission profiles due to radial velocity components.



a)



b)

Figure 4: Particle temperature, radial velocities and hydrodynamic turbulent velocities can be inferred from observed argon and hydrogen emission profiles; a) radial velocities versus radius, b) upper curve is particle temperature and lower curve is hydrodynamic turbulent velocity versus radius.

THE MODELING OF DROP-CONTAINING TURBULENT EDDIES

(AFOSR Contract No. NASA 7-918 Task Order RE182 Amendment 480)

Principal Investigator:

J. Bellan
Jet Propulsion Laboratory
California Institute of Technology
4800 Oak Grove Drive
MS 125-214
Pasadena, CA 91109

SUMMARY/OVERVIEW

The development of a mathematical model describing the behavior of a drop-containing turbulent eddy is made with the goal of initiating a theory describing the interactions of several drop-containing eddies during evaporation, ignition and combustion of liquid fuels injected into combustors. Specifically, the approach taken here is that it is reasonable to take a first step towards such a description by formulating the description of the behavior of a cluster of single component fuel, monodisperse, uniformly-distributed drops contained in a turbulent eddy. Since this model is thought to be utilized as a subscale or subgrid model in more elaborate calculations, the interest is focussed on the global rather than the detailed aspects of behavior. These global aspects are in many cases sufficient to characterize regimes of specific behavior and also to identify the parameters that control various phenomena in each particular regime.

TECHNICAL DISCUSSION

In this study we seek to develop a subgrid model that is general enough to be useful both close to and further downstream from the atomizer. For this reason it is important that the formulation be valid for both dense and dilute clusters of drops.

Our previous studies (1,2,3,4) have shown that: (1) turbulence in the flow surrounding clusters affects differently, dense and dilute clusters of drops and (2) there is a non-negligible amount of fuel vapor that escapes from the cluster, especially for small clusters of drops evaporating in high turbulence surroundings, even in the absence of vortical motion inside the cluster.

On the basis of the above information, a new model was formulated. In this new model a cluster of drops is embedded into a cylindrical vortex which is infinite in the longitudinal direction, z . Moreover, it is assumed that there is uniformity in the z direction, and thus it is sufficient to study only a cross section of the cylinder. Both gas and drops are assumed to have radial and

tangential velocities. Assuming that the collection of drops is monodisperse and that all drops behave identically, the momentum behavior is described by four equations, two for the drops and two for the gas. Momentum transfer between drops and gas is taken into account. Each velocity component is assumed to be the sum of a vortex motion term and a solid-body rotation term. By averaging both radial momentum equations, and the terms describing momentum transfer between phases, solutions can be obtained for the four momentum equations. Mass, species and energy conservation are formulated in a manner similar to that of the evaporation model in Ref. (2).

The calculations discussed below have been performed for n-decane at atmospheric pressure, ambient gas temperature of 1000K, initial drop temperature of 350K, initial drop radius of 2×10^{-3} cm, initial outer cluster radius of 1 cm and initial inner cluster radius of 0.25 cm. The results show that, due to the centrifugal force, the cluster of drops evolves into a cylindrical shell with an inner and an outer radius different from the initial one. Both the inner and outer surfaces of the cluster are tracked as a function of time and boundary conditions at these surfaces are part of the model. Due to the inviscid assumption for the gas, only simplified boundary conditions for the momentum equations must be satisfied.

The formulation is valid for Stokes numbers less than or equal to order unity. The code solving the model equations was run for a variety of initial conditions. Preliminary analysis of the results shows several interesting features.

The evaporation time of the drops is a decreasing function of the air/fuel mass ratio, and it is also a function of the initial conditions for the velocities.

In the dilute regime (defined as that where the initial drop number density $n^0 \leq 10^3 \text{ cm}^{-3}$) the evaporation time is controlled by the initial gas velocity rather than the initial drop velocity when the drops have either only initial solid body rotation or only initial vortex motion. For the same initial gas vortex motion, the evaporation time decrease as the initial solid body rotation of the gas increases.

In the dense regime ($n^0 \geq 10^4 \text{ cm}^{-3}$) the evaporation time depends upon the initial drops velocity. For the same initial gas velocity, the evaporation time increases when the drops have initially only vortex motion rather than only solid body rotation. In fact, at the same initial air/fuel mass ratio, saturation before complete evaporation can be obtained with the first condition, whereas complete evaporation is obtained for the second condition. Thus, the addition of initial solid body rotation to the drops can make the drops evaporate faster for the same initial drops number density. The solid body rotation promotes expansion of the cluster with the result that there is more engulfing of the surrounding hot air by the cluster, resulting in a decrease of the evaporation time.

When the initial conditions for the drop vortex motion and the gas vortex motion are kept the same, but both gas and drops have solid body rotations, the evaporation time decreases. A larger decrease is observed in the dense regime consistent with the observation that the initial drop velocity becomes important in the dense regime.

The ratio between the final cluster volume and the initial cluster volume is a decreasing function of the initial air/fuel mass ratio. For dilute clusters of drops when both gas and drops have only vortex motion and no initial solid body rotation, the volume ratio is unity; for dense clusters of drops with these initial conditions for the velocities, the volume ratio increases at most to 1.8. For smaller values of the air/fuel mass ratio, and thus larger values of n^0 , saturation is obtained before complete evaporation. The results show that in the dilute regime the volume ratio is controlled by the initial vortex motion of both phases whereas in the dense regime it is controlled by the initial solid body rotation of the two phases, but most particularly by the initial solid body rotation of the drops.

The ratio between the difference between the final outer and inner cluster radii, and the difference between the initial outer and inner cluster radii, is a decreasing function of the initial air/fuel mass ratio. This ratio is usually less than unity, in both dilute and dense regimes. However, for large initial solid body rotation for the drops, the ratio is larger than unity. In the dilute regime the value of this ratio is determined by the initial gas vortex motion and initial drop solid-body rotation. A decrease by half in the initial drop solid body rotation affects only slightly the value of this ratio; however, no initial drop solid body rotation substantially affects the ratio in the dilute regime. In the dense regime, the initial drop vortex motion becomes important: when the drops have initial vortex motion in addition to solid body rotation, the ratio between the final and the initial shell thickness decreases. This is due to the fact that vortex motion tends to move the inner radius more than the outer radius, resulting in a thinner shell. When the initial solid body rotation of the drops is increased, without changing the initial drop and gas vortex motion, the ratio between the final and the initial shell thickness increases. This is because the solid body rotation tends to move the outer radius more than the inner radius, resulting in a thicker shell.

The above results pertain only to four parametric runs. A total of eighteen parametric runs have been performed so far, and the results are still being analyzed.

REFERENCES

1. Bellan, J. and Harstad, K., "Turbulence Effects During Evaporation of Drops in Clusters", Int. J. Heat Mass Transfer, 31, 8, 1655-1668, 1988.
2. Harstad, K. and Bellan, J., "Electrostatic Dispersion of Drops in Clusters", Combust. Sci. and Tech., 63, 4-6, 169-172, 1989.
3. Bellan, J. and Harstad, K., "Transport-Related Phenomena for Clusters of Drops", Int. J. Heat Mass Transfer, in press.
4. Bellan, J. and Harstad, K., "Evaporation, Ignition and Combustion of Non Dilute Clusters of Drops", Combust. and Flame, in press.

FUEL ADDITIVE EFFECTS IN SOOTING FLAMES

(AFOSR Contract No. F49620-86-C-0054)

Principal Investigator: P. A. Bonczyk

United Technologies Research Center
East Hartford, CT 06108

SUMMARY/OVERVIEW

Fuel additives have been used in the past to suppress soot formation in both laboratory and practical flames. Since, however, the mechanism of suppression has not been established as yet, there are no criteria for additive selection and evaluation. The purpose of this research is to clarify the nature of additive behavior in relation to soot control.

TECHNICAL DISCUSSION

Under AFOSR support of this research, an extensive effort has been made to document the sooting behavior of hydrocarbon/air diffusion flames with and without additives present. In one case, experiments were performed to clarify the role of alkaline-earth and other metal additives in suppressing soot formed in a nearly two-dimensional C_2H_4 /air flame emanating from a symmetric Wolfhard-Parker burner. Soot size, number density and volume fraction were determined from Mie scattering, whereas metal species concentrations and flame temperature were determined by other appropriate means. The alkaline-earth metals suppressed soot principally via number density reduction, and a conclusion was reached which strongly implicated charged MOH^+ (M-Ba, Sr, Ca) species as responsible for suppression (Refs. 1, 2). In succeeding work, emphasis was given to ferrocene added to an axisymmetric diffusion flame fueled by prevaporized iso-octane. Ferrocene was observed to suppress a visible soot plume completely and, from a Mie analysis, was observed to reduce both soot size and number density at a late combustion stage, suggesting that ferrocene enhances the oxidative burn-out of soot. Hydrocarbon species concentrations were determined as well in the latter flame using quartz probe sampling and chromatographic analysis. Of the roughly twenty species detected, most were unaffected by the ferrocene. Exceptions were C_2H_2 and H_2 which showed a decrease and increase, respectively, with ferrocene seeding.

During the latter term of this contract our attention has turned to a study of metal additive effects in premixed flames. More specifically, emphasis is being given to alkali and alkaline-earth metals added to $C_2H_4/O_2/N_2$ mixtures. The methodology in use is similar to that above; namely, Mie scattering and quartz probe sampling are being used for soot and hydrocarbon species analysis, respectively. Most of this work has been completed, with only the probe sampling requiring some additional effort. Some of the details of the premixed flame work are outlined below.

Premixed Flame Measurements

In all of our additive measurements to date, it has proven to be nontrivial to arrive at a burner design consistent with the operation of a flame which remains physically stable and unperturbed thermochemically for additive injection in sufficient quantity to effect soot perturbation. This problem was equally difficult for the premixed flame case. In our final burner design, the premixed gases enter a cylindrical chamber and exit through 357 equally spaced 1 mm diam. holes drilled through a 16 mm thick brass plate (Ref. 3). The hole spacings are such that the transverse flame dimension is about 57 mm diam. The brass plate (disk) is enclosed by a sintered bronze annulus which is water-cooled and through which cold N_2 flows to shroud the flame from external air. The metals enter the flame via pneumatic aspiration of their respective salts using a Jarrell-Ash 90-790 cross-flow fixed nebulizer which requires a very modest flow of Ar as the nebulizing gas. The burner, as described, does not produce a stable flame. To this end, an uncooled steel plate is held parallel to and roughly 28 mm above the exit of the burner (Refs. 4, 5). In addition, a cylindrical glass tube is located external to and concentric with the bronze annulus to further shroud the flame from room air disturbances. The design above yields a cylindrical flame of nearly constant diameter with a stability which is adequate.

For earlier measurements in diffusion flames, our approach has been to characterize soot size from the angular dissymmetry of Mie scattered laser light. For our current measurements, however, this approach was not possible since the observed dissymmetry was too slight to permit accurate particulate sizing. Accordingly, a combination of 160° scattering and extinction were used to determine soot parameters with and without additives. Following Rayleigh calibration of the light scattering apparatus, size was determined from the ratio of scattering to extinction, number density from the extinction, and volume fraction from the calculated product of number density times the equivalent spherical particulate volume. Although the particulates were small ($D < 500 \text{ \AA}$) we did not use a Rayleigh size analysis, but rather chose to use the uncompromisingly more accurate Mie approach. The particulate sizes were calculated assuming a zeroth-order logarithmic size distribution (Ref. 6). It was used since a nearly identical lognormal distribution has been shown to describe actual soot sizes satisfactorily (Ref. 7), and also because it is very similar to the self-preserving size distribution which many coagulating aerosols fit (Ref. 8).

In carrying out the premixed flame measurements, we have limited ourselves to alkali and alkaline-earth inorganic salts added to $C_2H_4/O_2/N_2$ sooting flames. This choice of additives served to complement our earlier diffusion flame studies (Ref. 1). Also, conscious of the fact that dissimilar metals may, and most probably do have dissimilar soot suppressing mechanisms, limiting the study to a few similar additive species seemed prudent. Since there is no forceful reason to anticipate a dependence of additive behavior on either fuel type or equivalence ratio (Ref. 9), our measurements up to now have been limited to the single ethylene flame above at a fixed stoichiometry. On the other hand, conscious of the potential importance of metal cations in suppressing soot (Ref. 1), and the pronounced dependence of their concentration on flame temperature, the role of the latter parameter has been studied systematically in this work.

Representative examples of the results we have obtained are given in

Tables I and II. Table I gives the measured soot parameters as a function of vertical position in the flame. For this flame, $C/O = 0.72$, $O_2/(O_2 + N_2) = 0.33$, and the calculated (Ref. 10) adiabatic flame temperature is $2195^\circ K$. These data display the well known size and volume fraction increase with residence time, along with a concomitant decrease in number density for the coagulating aerosol. As such these data are not new (Ref. 9); they serve principally to confirm the validity of our sizing approach, and to identify the stage of soot evolution at which our additive measurements were made. In this regard, we were unable to assess additive behavior at $z < 10$ mm; additive effects in the latter zone were too small to determine with any meaningful accuracy. Table II gives the effect of various metal additives on soot at $z = 15$ mm for the same flame appropriate to Table I. The data clearly show that perturbation of the soot is greatest for metals with smallest ionization potentials, i.e., K, Rb and Cs, which is a result very similar to that obtained by us and others in diffusion flames (Refs. 1, 11, 12) and by others in premixed flames (Ref. 9). Measurements similar to those in Table II were made at $z = 10$ mm. They confirm the general trends in Table I, except that the magnitude of the soot perturbation is reduced. Other $C/O = 0.72$ flames have been studied at reduced temperatures. Here again the more readily ionizable additives are effective, but the magnitude of their perturbation is reduced relative to Table II. We conclude therefore that the mode of action of readily ionizable additives in diffusion and premixed flames do not essentially differ. The metal cations suppress coagulation which leads to more rapid soot burn-out.

Quartz Probe Measurements

To complete these measurements, we are in the midst of quartz probe sampling and gas chromatographic analysis of hydrocarbon precursor species present in the flame with and without additives present. As in our earlier ferrocene seeded diffusion flames, we do not anticipate reporting dramatic additive induced perturbations; but as of the time of preparation of this abstract the work is not sufficiently complete to permit final conclusions.

REFERENCES

1. Bonczyk, P. A., *Combust. Sci. Technol.* **59**, 143 (1988).
2. Bonczyk, P. A., *Combust. Flame* **67**, 179 (1987).
3. Homann, K. H., and Strofer, E., in Soot in Combustion Systems and its Toxic Properties (J. Lahaye and G. Prado, Eds.), Plenum Press, New York, 1983, p. 217.
4. D'Alessio, A., Beretta, F., and Venitozzi, C., *Combust. Sci. Technol.* **5**, 263 (1972).
5. Ritrievi, K. E., D.Sc. Thesis, Massachusetts Institute of Technology, 1984, p. 101.
6. Kerker, M., The Scattering of Light and Other Electromagnetic Radiations, Academic Press, New York, 1969, p. 356.
7. Prado, G., and Lahaye, J., in Particulate Carbon Formation During Combustion (D. C. Siegla and G. W. Smith, Eds.), Plenum Press, New York, 1981, p. 143.
8. Friedlander, S. K., Smoke, Dust and Haze - Fundamentals of Aerosol Behavior, Wiley, New York, 1977.
9. Haynes, B. S., Jander, H., and Wagner, H. Gg., Seventeenth Symposium (International) on Combustion, The Combustion Institute, Pittsburgh, 1979, p. 1365.

10. Reynolds, W. C., "STANJAN", Interactive Computer Programs for Chemical Equilibrium Analysis, Stanford University, 1981.
11. Bonczyk, P. A., Combust. Flame 51, 219 (1983).
12. Bulewicz, E. M., Evans, D. G., and Padley, P. J., Fifteenth Symposium (International) on Combustion, The Combustion Institute, Pittsburgh, 1974, p. 1461.

TABLE I

Dependence of soot size (D_o), number density (N_o), and volume fraction (f_o) on vertical position for zero aspiration rate of the 0.1 molar metallic salt solution.

<u>z(mm)</u>	<u>$D_o(\text{\AA})$</u>	<u>$N_o(\text{cm}^{-3} \times 10^{-9})$</u>	<u>$f_o(\times 10^7)$</u>
6	42	903	0.35
7	84	159	0.49
8	135	48	0.61
9	172	23	0.88
10	222	16	0.94
11	264	11	1.08
12	295	9	1.16
13	312	8	1.33
14	329	8	1.46
15	348	7	1.52

TABLE II

Soot parameters in a metal seeded flame (D , N , f) relative to those for water injection alone (D_w , N_w , f_w) at 15 mm height. For water alone: $D_w = 336 \text{\AA}$, $N_w = 8 \times 10^9 \text{cm}^{-3}$, $f_w = 1.63 \times 10^{-7}$. Aspirated solutions: 1/10 molar MCl ($M = \text{Li, Na, K, Rb and Cs}$) and $\text{MCl}_2 \cdot n\text{H}_2\text{O}$ ($M = \text{Ca, Sr and Ba}$).

<u>Additive</u> <u>Metal</u>	<u>D/D_w</u>	<u>N/N_w</u>	<u>f/f_w</u>
Li	1.02	0.95	1.01
Na	0.92	1.23	0.97
K	0.43	10.03	0.81
Rb	0.39	12.79	0.74
Cs	0.32	23.30	0.78
Ca	1.02	0.94	0.99
Sr	1.01	0.97	0.98
Ba	0.99	1.06	1.04

COMPUTER MODELING OF SOOT FORMATION
COMPARING FREE RADICAL AND IONIC MECHANISMS

231

(AFOSR Contract No. F49620-88-C-0007)

Principal Investigator: H. F. Calcote

AeroChem Research Laboratories, Inc.
P. O. Box 12
Princeton, NJ 08542

SUMMARY/OVERVIEW:

The main objective of a joint program between AeroChem and Penn State (Principal Investigator: Michael Frenklach) is to compare the relative importance of the free radical and ionic mechanisms of soot formation in flames. The two mechanisms will be compared using computer simulations carried out at Penn State; their work is reported separately. The free radical mechanism has been previously formulated for computer simulation; the ionic mechanism is being formulated in this program. This involves developing thermodynamic information for both neutral and ionic species; developing ambipolar diffusion coefficients for the ions; and developing the mechanism and reaction rate coefficients for large ion-molecule and large ion-electron recombination reactions.

TECHNICAL DISCUSSION

The strategy is to first compare each model with the "well-studied" acetylene/oxygen flame for species up to mass 300 amu to confirm the validity of the models, and to perform sensitivity analysis to eliminate unnecessary reactions; then to extend the molecular weight of the species treated to about 600 amu, the extent of the available ion species data in this flame. Once the two models have been demonstrated to be consistent with the experimental data, we will extend them to masses approaching soot particle inception and compare the carbon mass fluxes of the two models with the carbon mass flux required to produce soot particles. We will next compare the relative effectiveness of the two models in correlating soot formation in other flame systems. It may, of course, become clear at an early date that one mechanism is not capable of accounting for soot formation.

The "well-studied" flame is the acetylene/oxygen flame burning on a flat flame burner at a pressure of 2.67 kPa and a linear unburned gas feed rate of 50 cm/s. In previous work,¹ we duplicated the burner Bittner and Howard² used to obtain neutral species concentrations, and we measured ion concentration profiles with this burner so the ion and neutral profiles would be from the same system. We also compared the data obtained by a number of other researchers on nearly the same flame; and showed that there was amazing agreement among several laboratories.

The thermodynamic quantities, C_p^0 and S^0 , for 45 hydrocarbon ions up to $C_{24}H_{13}^+$, mass 301 amu, and for 14 neutral species, were calculated using thermodynamic methods. These data will be extended to 600 amu ions.

Because the pressure for the standard flame is less than one atmosphere and we have experimentally demonstrated the importance of diffusion,¹ it is necessary to include the diffusion coefficients for ions. Experimental ion mobilities, μ (measured in N_2 at STP), for a wide mass range of PCAH ions^{3,4} were extrapolated to the higher mass range required for this program. This gave μ vs. ionic mass which paralleled the results obtained from a calculation using the Langevin ion mobility equation^{5a} thus giving confidence in the procedure. The ion mobility was then calculated for each ion in each of the flame gas components. Using Blanc's mixing law the ion mobility was then calculated for the flame gas mixture, with appropriate corrections for temperature and pressure.

We assume that the negative species in the flame is the free electron, although there is evidence that there are large negative ions present.^{6,7} The ambipolar diffusion coefficient (D_a) for a specific ion was calculated from the ion mobility, μ , using the relationship^{5b}: $D_a = 2kT\mu/e$, where k is Boltzmann's constant, T is temperature, and e is the elementary charge.

A set of ion-molecule reactions was developed in which the reactant and product ions were only those which have been observed in flames, and in which the neutral reactants are C_2H_2 , C_4H_2 , and C_3H_4 . When available, experimental rate coefficients were used, but these are available only for small ions. In general, experimental rates are very close to the rate calculated by the average dipole orientation, ADO, theory⁸

$$k = \frac{2\pi e}{\mu^{1/2}} \left[\alpha^{1/2} + c\mu_D \left(\frac{2}{\pi kT} \right)^{1/2} \right] \quad (1)$$

where, μ is the reduced mass, α is the polarizability of the neutral reactant, c is a locking constant determined from experimental data, and μ_D is the dipole moment of the neutral reactant. For nonpolar species such as the neutral growth species in our ionic model, except for propyne, Eq. (1) reduces to the Langevin equation which does not have a temperature coefficient.

Equation (1) accounts only for the number of collisions (it does not include collision efficiency) and fits most room temperature experimental rate coefficient data. There is considerable evidence that the rate of ion-molecule reactions is directly dependent upon the exothermicity of the reaction, $\Delta H(\text{react})$ and we will use such correlations to estimate the collision efficiency for this set of reactions.

The temperature dependence for ion-molecule reactions is not well known, but they generally have negative temperature coefficients so we assume a T^n dependence with $n = -1/2$. There are complex means of estimating n which we will consider later. Since entropy makes a large contribution to $\Delta G(\text{react})$ at flame temperatures we are seeking a means of using the entropy of reaction to estimate n ; this is not straightforward without estimating the structure of the collision complex, and for the number of reactions involved and the time constraint this is out of the question.

One of the major problems in working with large ions, is their identification; mass spectrometry gives mass only. The number of carbon and hydrogen atoms has been determined by use of isotopes. Thus for a given molecular formula there can be several structures. We thus include several isomers for some ions when their free energies of formation are close; we seek a rational means of reducing this to "one isomer" per ion, probably by weighting the thermodynamic quantities, ΔH and C_p , appropriately and by mechanistic considerations. In some cases the experimental data on flame ion profiles furnishes a clue. For example, the ion 165 amu, $C_{13}H_9^+$, is a dominant flame ion which we have always represented as a three-member ring. Inspection of the formation and removal reactions of this ion does not suggest a large concentration. Further consideration indicates that the three-membered ring cation, $C_{13}H_9^+$, is antiaromatic, so we should choose a more stable two-ring aromatic structure with a side chain.

The ions disappear by ion-electron recombination reactions, neglecting the presence of negative ions^{6,7} for the time being. We estimate the rate of ion recombination, α , by the equation for the rate of collision of electrons with particles⁹

$$\alpha = \frac{\pi d^2}{4} \left(\frac{8kT}{\pi m_e} \right)^{1/2} \left(1 + \frac{e^2}{(2\pi\epsilon_0 d)kT} \right) \quad (2)$$

in which d = the ion diameter, m_e = the electron mass, and ϵ_0 = dielectric constant of free space. The ion diameters were calculated from ion mobilities, see above, by use of the Langevin equation for ion mobilities. Equation 2 gives a $T^{-1/2}$ temperature dependence which compares favorably with experiments of Ogram et al.¹⁰ for H_3O^+ . The values calculated by Eq. (2) were about twice the measured values of Ogram, so we divide Eq. (2) by 2. Inclusion of negative ions, which could be formed by electron attachment to large molecules,⁶ would reduce the rate of ion recombination.

Another major problem incurred in developing the ionic mechanism relates to the need for better estimates for the neutral reactions forming electronically excited CH and C_2 . These species are the precursors of the chemiions formed in the flame which initiate the ionic mechanism of soot formation.

The development of a realistic set of reaction rate data to use in the computer simulations has taken longer than anticipated, but we are now in a position to move ahead with computer simulation studies.

Dr. Robert J. Gill has worked closely with the principal investigator on this program and his contribution is gratefully acknowledged.

REFERENCES

1. Calcote, H.F. and Keil, D.G., "Ion-Molecule Reactions in Sooting Acetylene-Oxygen Flames," *Combust. Flame* 74, 131 (1988).
2. Bittner, J.D. and Howard, J.B., "Pre-Particle Chemistry of Soot Formation," in Particulate Carbon: Formation During Combustion, D.G. Siegl and G.W. Smith, Eds. (Plenum, New York, 1981) p. 109.
3. Griffin, G.W., Dzidic, I., Carroll, D.I., Stillwell, R.N., and Horning, E.C., *Anal. Chem.* 45, 1204 (1973).
4. Hagen, D.F., *Anal. Chem.* 51, 870 (1980).
5. McDaniels, E.W., Collision Phenomena in Ionized Gases, (Wiley, New York, 1964) (a) p. 432-433; (b) p. 512.
6. Keil, D.G., Gill, R.J., Olson, D.B., and Calcote, H.F., "Ionization and Soot Formation in Premixed Flames," Twentieth Symposium (International) on Combustion (The Combustion Institute, Pittsburgh, 1985) p. 1129.
7. Homann, K.H. and Stroefer, E., "Charged Soot Particles in Unseeded and Seeded Flames," in Soot in Combustion Systems, J. Lahaye and G. Prado, Eds. (Plenum Press, New York, 1981) p. 217.
8. Su, T. and Bowers, M.T., in Gas Phase Ion Chemistry, M. T. Bowers, Ed. (Academic Press, New York, 1979), Ch. 3.
9. Sodha, M.S. and Guha, S., *Adv. Plasma Phys.* 4, 219 (1971).
10. Ogram, G.L., Chang, J.-S., and Hobson, R.M., "Dissociative Recombination of H_3O^+ and D_3O^+ at Elevated Electron and Gas Temperatures," *Phys. Rev.* 21, 982 (1980).

DETERMINATION OF RATE-LIMITING STEPS DURING SOOT FORMATION

AFOSR Contract No. F49620-88-C-0051

Principal Investigator: Meredith B. Colket, III

United Technologies Research Center
E. Hartford, CT 06108

SUMMARY/OVERVIEW:

A variety of hydrocarbons are being pyrolyzed and/or oxidized in a single-pulse shock tube. End gases are being collected and then analyzed using capillary gas chromatography. Real time data will be collected using a time-of-flight mass spectrometer directly coupled to the end wall of the shock tube. Data will be used to identify rate-limiting steps during soot formation and to assist in the development and/or verification of chemical models describing formation of products and soot-precursors. A focus of the work is to obtain time-dependent data and to collect and analyze multi-ringed species (C10-C16 hydrocarbons) which are believed to be pre-cursors of soot. In addition, simplified modeling concepts have been examined in order to describe soot production in flames. Reasonable success has been achieved by using a recent version of the MAEROS code.

TECHNICAL DISCUSSION

Eight separate series of single-pulse shock tube experiments have been completed. For each series, a hydrocarbon or a mixture of a hydrocarbon and oxygen were shock-heated in argon over an approximate temperature range of 1100K to 2000K. Total pressures were about five to ten atmospheres and dwell times were about 500 microseconds. Gas samples were collected automatically at the end wall of the shock tube and then were analyzed quantitatively using gas chromatography. Measured species include C1 to C14 hydrocarbons, carbon oxides, hydrogen, and oxygen. Hydrocarbons pyrolyzed (or oxidatively pyrolyzed) include toluene, benzene, dicyclopentadiene and cyclopentadiene.

Experimental modifications have been directed towards detecting the presence of high molecular weight species (>128 grams/mole). Specifically, the gas sampling system has been modified (new valves, heating tapes, etc.) to operate at temperatures of 100 to 150C. Other new experimental efforts include the coupling of a time-of-flight mass spectrometer to the end wall of the shock tube for measurement of species profiles in real-time. Data obtained from this facility will reduce some ambiguities regarding species whose concentrations peak during the shock or are effected by finite quenching in the rarefaction wave. Due to delays in delivery of the mass spectrometer, this latter work has been delayed.

One of the first mixtures analyzed for this program was 1% toluene, since several previous runs with this mixture have been performed and provide a reference set of data. The newly obtained data is in excellent agreement with the results presented previously for the lower molecular weight compounds

(<128 g/mole). Aromatic compounds produced from pyrolysis of 1% toluene are shown in Fig 1. Profiles of toluene, benzene, indene, and naphthalene shown in Figure 1 agree well with the earlier data. The remaining profiles are new information. The low temperature formation of bibenzyl is from recombination of benzyl radicals, some of which may occur in the quenching waves. Other products shown in Figure 1 represent a relatively small portion of the total number of high molecular weight species, although the mass contained in the selected species represents about 75% or more of the total mass of the species observed. Possible reactions describing the production of selected species are proposed in Ref. 2. The result that PAH's are produced very rapidly at 1400 to 1500K is consistent with concepts developed from diffusion flames which indicate inception occurs at 1300 to 1500K.

The oxidation of benzene was also examined during this past year. As reported³, benzene decay and light product formation (acetylene, diacetylene, cyclopentadiene, and vinylacetylene) are consistent with the mechanistic arguments proposed⁴ for benzene oxidation. Low molecular weight and polyaromatic hydrocarbons produced during the rich oxidation of benzene have been measured. Dominant PAH products are similar to those observed during pyrolysis of toluene. In both cases, both five- and six-membered rings are observed. The presence of species containing five-membered rings is not surprising based on previous studies in flames; however, existing models for PAH growth and soot formation neglect the potential importance of these species.

Dicyclopentadiene was selected as a reactant since it is a convenient source of cyclopentadiene. However, preliminary experiments on the dimer led to uncertain interpretation of the data. Subsequently, dicyclopentadiene was thermally decomposed in a flask and the monomer extracted. Pyrolysis and oxidation of cyclopentadiene yields polyaromatic species in concentrations similar to those produced from toluene and/or benzene. Preliminary interpretations of the data indicate that principle growth mechanisms do not include benzene or toluene as an intermediate. The very rapid production of polyaromatics support arguments for growth routes involving five-membered carbon rings.

Several different simplified models² have been developed for describing soot formation in premixed flames. Varying degrees of success have been attained with the models. Perhaps the most successful is one based on a recent version of an aerosol dynamics code, MAEROS⁵ which has been modified for application to the soot growth problem. Surface growth is assumed to occur primarily through acetylene deposition, using the Harris-Weiner growth rate expression.⁶ The most important (and speculative) approximations have been to set the lower limit of size range at the approximate size (0.5 nm) of a benzene molecule and to extrapolate the Harris-Weiner surface growth rate expression to this size class. The nucleation rate for this size range was taken to be the local benzene production rate⁷ in the rich, premixed ethylene flame and the nucleation rate is set equal to zero for all other size classes. The calculated soot size distribution is shown in Fig. 2 for times up to 20 milliseconds. Calculated soot volume fractions for several different coalescence sticking probabilities are compared to experimental values for a similar flame in Fig. 3. The excellent agreement is perhaps fortuitous but

lends strong support to arguments indicating that a rate limiting step to soot formation is the formation of the first one or two aromatic rings.

REFERENCES

1. M. B. Colket, and D. J. Seery, "Mechanisms and Kinetics of Toluene Pyrolysis", poster presentation at the Twentieth Symposium (International) on Combustion, Ann Arbor, MI, 1984.
2. M. B. Colket, R. J. Hall, J. J. Sangiovanni, D. J. Seery, "The Determination of Rate-Limiting Steps During Soot Formation", United Technologies Research Center, UTRC 89-13, Annual AFOSR Report, April 1989.
3. M. B. Colket, "The Role of Oxidative Pyrolysis in Preparticle Chemistry". Presentation to the Eastern Section of the Combustion Institute, Dec. 5-7, 1988.
4. C. Venkat, K. Brezinsky, and I. Glassman, Nineteenth Symposium (International) on Combustion, The Combustion Institute, Pittsburgh, PA, p. 143, 1982.
5. F. Gelbard, MAEROS User Manual, NUREG/CR-1391, (SAND80-0822) 1982. The version of the code which we use is "MAEROS2X".
6. S. J. Harris and A. M. Weiner, Combustion Science & Technology, 131, 155 (1983).
7. S. J. Harris, A. M. Weiner and R. J. Blint, "Formation of Small Aromatic Molecules in a Sooting Ethylene Flame", from preprints of papers presented at 194th National Meeting of American Chemical Society, Div. of Fuel Chemistry, New Orleans, LA, 31 August - 4 September 1987, Vol. 32, p. 488.

Figure 1

Formation of Selected Aromatic Products SPST Pyrolysis of 1% Toluene

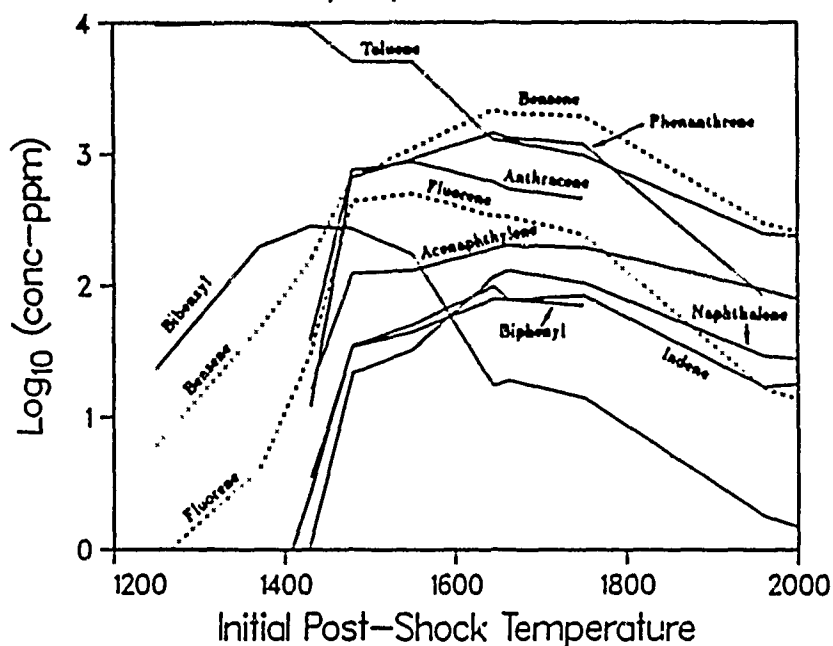


Figure 2

Calculated Evolution of Soot Size Distribution
Coagulation & Surface Growth from Maeros Code
Harris Surface Growth Rate and Flame Conditions

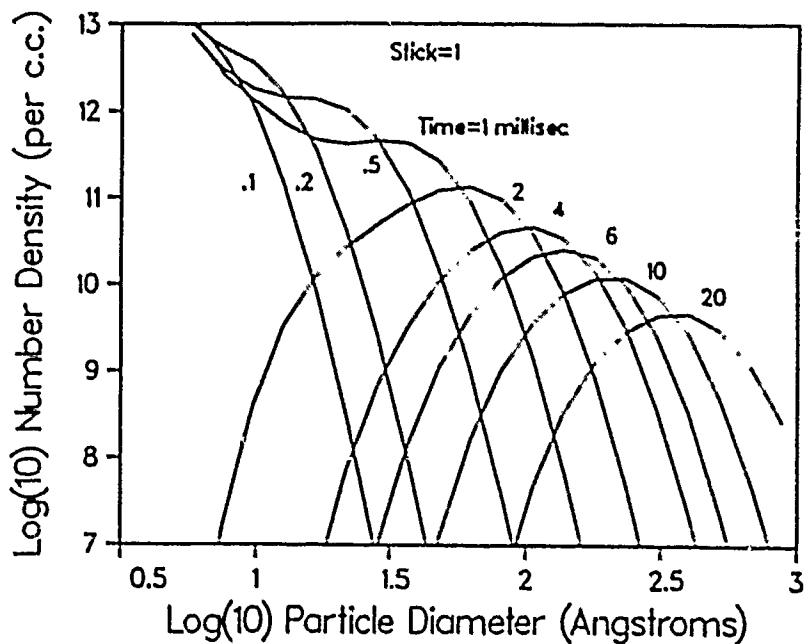
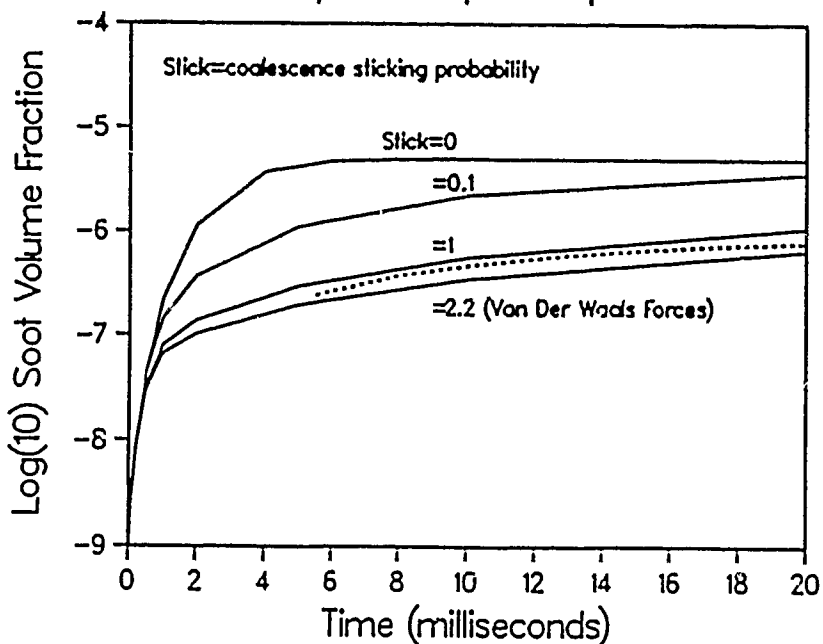


Figure 3

Calculated Soot Volume Fraction
Harris Flame Conditions
Acetylene Vapor Depletion



DENSE-SPRAY STRUCTURE AND PHENOMENA

(AFOSR Grant No. 85-0244)

Principal Investigator: G. M. Faeth

217 Aerospace Engineering Building
The University of Michigan
Ann Arbor, Michigan 48109-2140

SUMMARY/OVERVIEW

Three aspects of dense sprays are being studied: turbulent dispersion, turbulence modulation and the structure of pressure-atomized sprays. Major findings include: successful predictions of turbulent dispersion, highlighting effects of self-induced particle motions; successful predictions of continuous-phase properties by extending methods used to analyze noise; and proof that dense sprays are actually dilute flows dominated by processes of breakup rather than collisions.

TECHNICAL DISCUSSION

Introduction. The near-injector dense-spray region is not well understood which hampers understanding of sprays since it is an initial condition for the rest of the flow (Faeth 1987, 1989). Thus, aspects of dense sprays are being studied using homogeneous particle-laden flows and large-scale pressure-atomized sprays. Parthasarathy and Faeth (1987, 1988), Parthasarathy et al. (1988) and Ruiff et al. (1988, 1989) have reported aspects of the work.

Homogeneous Particle-Laden Flows. Turbulent dispersion and turbulence modulation are being studied in homogeneous particle-laden flows involving a uniform flux of particles falling in a stagnant water bath. Measurements include motion-picture shadowgraphs, Mie scattering, and two-point phase-discriminating laser velocimetry. Stochastic methods are used for predictions: statistical time-series techniques for turbulent dispersion (Box and Jenkins, 1976); and summing properties of particle wakes by extending methods used to analyze noise for turbulence modulation (Rice, 1954).

Some typical results appear in Figs. 1 and 2. Figure 1 is an illustration of predicted and measured streamwise and crosstream particle velocities plotted as a function of dissipation — which is the main variable characterizing continuous-phase properties. Mean particle velocities are predicted quite well. Predictions of velocity fluctuations must account for two effects: variations of terminal velocities that influence streamwise velocity fluctuations significantly even for the narrow size distributions of present tests; and self-induced motion (denoted SIM) due to effects of eddy shedding at higher particle Reynolds numbers and irregularities of the shape of the particles, that dominate crosstream velocity fluctuations for the largest particles. The comparison between predictions and measurements is quite good, after accounting for these effects; however, the results highlight the need for more information on self-induced motion which contributes to crosstream velocity fluctuations that cause turbulent dispersion.

Figure 2 is an illustration of predicted and measured velocity fluctuations of the continuous phase. These velocity fluctuations are proportional to the square-root of dissipation, are relatively independent of particle size, and are strongly anisotropic — all these properties are represented reasonably-well by the predictions. The large anisotropy is especially interesting since it shows the relative importance of mean and fluctuating properties in the particle wakes. In particular, the large mean streamwise velocity in the wake dominates streamwise velocity fluctuations while wake

turbulence dominates the crosstream velocity fluctuations because mean velocities in the crosstream direction are small. Since the mean streamwise velocities are greater than the rest, the streamwise velocity fluctuations are largest: an effect that tends to increase anisotropy as particle Reynolds numbers, and thus wake turbulence levels, increase.

Measurements and analysis for this phase of the study are complete and current efforts are devoted to preparing reports of the work. The next phase of the study will involve measurements and predictions of the phase properties of grid-generated turbulent particle-laden flows.

Large-Scale Jets. Large-scale (10 mm diameter) pressure-atomized sprays are being studied to find the structure and mixing properties of dense sprays. Measurements include: gamma-ray absorption, phase-discriminating laser velocimetry, and double-flash holography. Analysis is limited to the locally-homogeneous flow (LHF) approximation (Faeth 1987, 1988).

Some recent measurements of drop properties in the drop-containing mixing layer near the injector exit, using double-flash holography, appear in Figs. 3-5. Each figure includes plots of ellipticity (roughly the volume-weighted average of the ratio of the major to the minor dimensions of liquid elements), the Sauter mean diameter (SMD) and velocities of various drop sizes, as a function of radial distance normalized by distance from the jet exit. The position of the surface of the all-liquid core (a potential core-like region along the axis) is also indicated on the plots.

Figure 3 is an illustration of drop properties close to the injector for fully-developed turbulent flow at the jet exit. Both the ellipticity and the SMD are large near the liquid surface, reflecting the presence of large and irregularly-shaped liquid elements in this region. As the edge of the flow is approached, however, ellipticities approach unity and the SMD becomes relatively small, implying the presence of small round drops. Velocities vary significantly with drop size, this implies that the LHF approximation is not valid for this flow and the predictions are poor. Assuming that the velocities of the small drops approach gas velocities, the results indicate that gas velocities remain surprisingly low as the liquid surface is approached; this behavior follows since the layer is actually quite dilute and contains large liquid elements that don't transfer momentum very effectively (Ruff et al. 1989).

Figure 4 is an illustration of the same results for a streamwise position near the downstream end of the drop-containing mixing layer, also for fully-developed turbulent flow at the jet exit. In this region as well, large irregular liquid elements having velocities much higher than the gas are found near the liquid surface. However, the outer region, containing relatively-small round drops, clearly has grown in extent. Comparing Figs. 3 and 4 it is evident that the drop-containing mixing layer involves large liquid elements being ejected from the all-liquid core and subsequently breaking up into smaller drops and spreading by turbulent dispersion to the edge of the flow. Thus, the mixing layer is a relatively dilute flow, dominated by breakup; rather than a dense flow, dominated by collisions, as suggested by some workers in the past (see Faeth, 1987, 1989).

Finally, Fig. 5 is an illustration of the same results for a streamwise position near the upstream end of the drop-containing mixing layer but for nonturbulent slug flow at the jet exit. The structure clearly differs from fully-developed flow at the jet exit for the same injector flow rate (see Fig. 3). In particular, both ellipticities and SMD are smaller, and the mixing-layer is thinner, for slug flow. This indicates that turbulence in the liquid phase promotes the formation of large liquid elements from the all-liquid core, and that these elements penetrate the flow laterally, due to their inertia, before breaking up into relatively small drops near the edge of the flow. This provides the mechanism for faster mixing as turbulence levels at the jet exit are increased (see Ruff et al. 1988).

Current work is concentrating on studies of gas-phase properties in the drop-containing mixing layer, using phase-discriminating laser velocimetry; as well as effects of the density ratio of flow, using gamma-ray absorption measurements of liquid volume fraction distributions for sprays in air at elevated pressure.

- Box, G.E.P. and Jenkins, G. M. (1987) *Time Series Analysis*, Revised Edition, Holden-Day, San Francisco, pp. 47-84.
- Faeth, G. M. (1987) Mixing, transport and combustion in sprays. *Prog. Energy Combust. Sci.* 13, 293-345.
- Faeth, G. M. (1989) Turbulent multiphase flows. *Proceedings of the U.S.-France Workshop on Turbulent Reacting Flows* (S.N.B. Murthy and R. Borghi, eds.), Springer-Verlag, Berlin, pp. 784-814.
- Parthasarathy, R. N. and Faeth, G. M. (1987) Structure of particle-laden turbulent water jets in still water. *Int. J. Multiphase Flow* 13, 699-716.
- Parthasarathy, R. N. and Faeth, G. M. (1988) Homogeneous turbulence in dilute particle-laden flows. 41st Annual Meeting, APS Division of Fluid Dynamics, Buffalo, N.Y.
- Parthasarathy, R. N., Ruff, G. A. and Faeth, G. M. (1988) Turbulence modulation and dense-spray structure, Annual Report, Grant No. AFOSR-85-0244, Department of Aerospace Engineering, The University of Michigan, Ann Arbor, MI.
- Rice, S. O. (1954) Mathematical analysis of random noise. *Noise and Stochastic Processes* (N. Wax, ed.) Dover Publications, Inc., New York, pp. 133-294.
- Ruff, G. A., Sagar, A. D. and Faeth, G. M. (1988) Structure and mixing properties of pressure-atomized sprays. AIAA Paper No. 88-0-2376; also, *AIAA J.*, in press.
- Ruff, G. A., Bernal, L. P. and Faeth, G. M. (1989) Structure of the near-injector region of non-evaporating pressure-atomized sprays. AIAA Paper No. 89-0050; also *AIAA J.*, submitted.

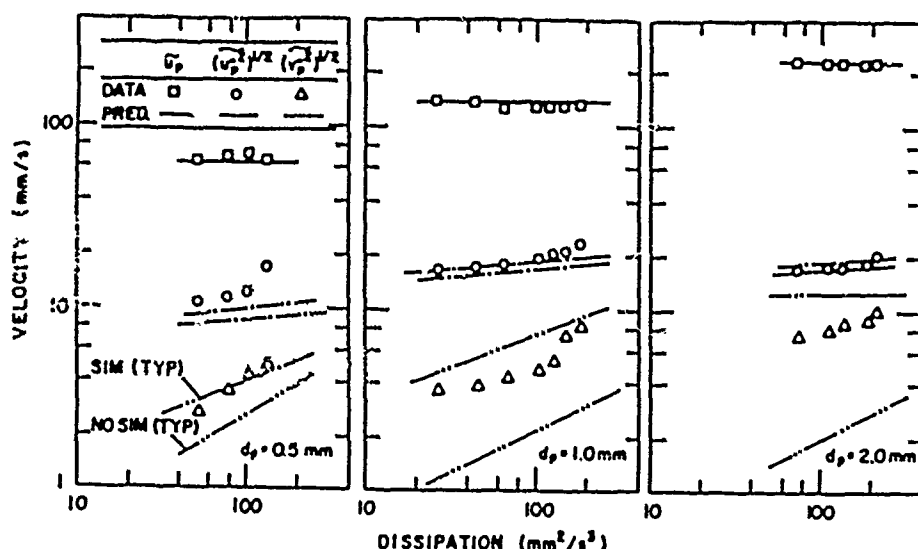


Fig. 1 Particle velocity fluctuations in a homogeneous particle-laden flow.

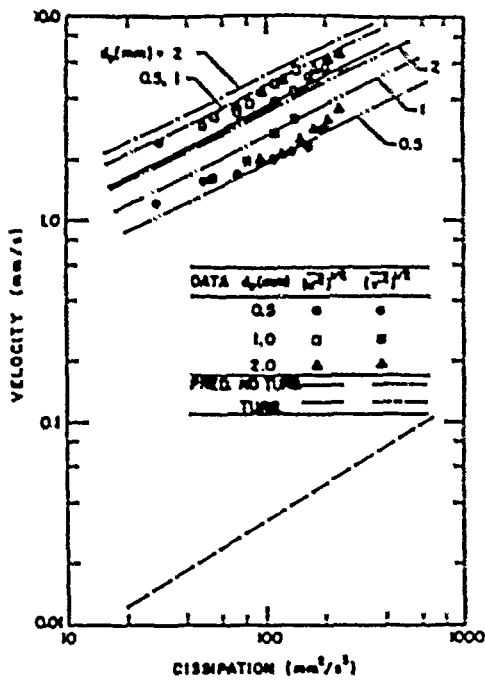


Fig. 2 Continuous-phase velocity fluctuations in a homogeneous particle-laden flow

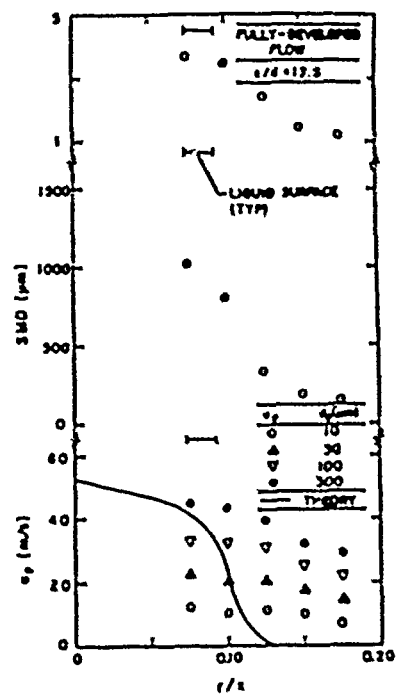


Fig. 3 Dispersed-phase properties in a pressure-atomized spray with fully-developed jet exit conditions ($x/d = 12.5$).

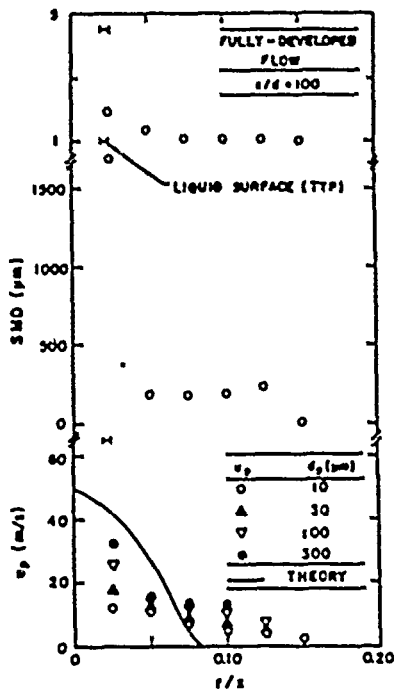


Fig. 4 Dispersed-phase properties in a pressure-atomized spray with fully-developed jet exit conditions. ($x/d = 100$).

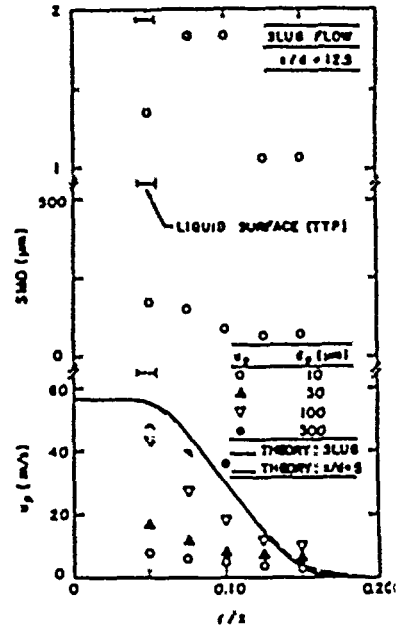


Fig. 5 Dispersed-phase properties in a pressure-atomized spray with slug flow jet exit conditions ($x/d = 12.5$).

IGNITION AND MODIFICATION OF REACTION BY ENERGY ADDITION:
KINETIC AND TRANSPORT PHENOMENA

AFOSR Contract No. F49620-87-C-0081

Principal Investigators: Francis E. Fendell, Mau-Song Chou and
Tmitri J. Zukowski

Systems Technology Laboratory, TRW Space and Technology Group
One Space Park, Redondo Beach, CA 90278

SUMMARY/OVERVIEW

Increased activity in high-speed air-breathing combustion systems puts a premium on the complete release of chemical energy during the relatively brief residence time of reactants within combustors of practical length: mixing, ignition, and chemical reaction must be achieved in a relatively short time. We address, from a fundamental chemical-dynamics and fluid-transport point of view, the use of both alternative, photochemical ignition (by laser irradiation) and ignition-promoting additives, in order to alter chemical-reaction pathways to achieve rapid ignition and enhanced combustion rate. We plan ultimately to address the influence of mixture inhomogeneity, and of departure from stoichiometric proportion in fuel/air mixtures, on the processes of ignition, flame development, and flame propagation. Chemical systems of particular interest include hydrogen/air and methane/air, often with trace amounts of carefully selected sensitizers. We seek to identify optimal circumstances [minimal input energy, minimal amount of sensitizer(s), etc.] for achieving ignition and burnup with currently available optical sources by irradiating premixtures flowing faster than the adiabatic flame speed, and by carrying out supporting approximate analyses of these experiments.

TECHNICAL DISCUSSION

Experiment - We have conducted experiments on laser ignition of H_2/O_2 using NH_3 as a sensitizer. A Lambda Physik EMG150 excimer laser operated at 193 nm (ArF) is used as an ignition source. The beam converges above the surface of a 6.0 cm diameter flat-flame burner, with beam dimensions of 2.5 mm x 10.5 mm at the burner leading edge, and 1.6 mm x 6.6 mm at the burner trailing edge as determined from film burns for an estimated irradiated volume of 1.1 cc. The premixed flow of hydrogen/oxygen/ammonia from the burner has a maximum flow velocity of 2.2 cm/sec. The typical ammonia mole fraction value is 6.1×10^{-3} , which gives an average energy absorption of 68%. An energy ratiometer is used to measure the incident and absorbed energy. A McPherson 0.3 m monochromator (with a photomultiplier recorded on an oscilloscope) and an EG&G OMA time-gated reticon array spectrometer are used to measure emissions near the center of the irradiated volume.

A primary distinctive feature of the laser ignition in these experiments is that it is not a thermal process resulting from plasma formation or heat addition. To establish this, numerous observations were made with the OMA gated for a short time (~ 1 s) after the laser pulse, to investigate initial

events. The major emissions observed are the NH band at 336 nm, NH_2 at 550 nm, and OH at 308 nm and 283 nm. No atomic or ionic emission lines indicative of plasma formation are observed, suggesting that no plasma formation occurs. The estimated initial temperature rise is approximately 40 K assuming all the residual energy is completely thermalized, for the case where the absorbed energy was 190 mJ/cc (maximum value for ignition cases).

Figure 1 is a plot of successful ignition events at various equivalence ratios. The absorbed energy values are calculated from the measured relative fraction of laser energy transmitted through the gas flow, and are the average for the irradiated volume. Uncertainties with respect to both axes are about 10% (not indicated on the Figure). Of particular importance is the approximate lower limit for ignition in terms of absorbed energy per unit volume, which has a minimum near stoichiometry.

Figure 3a shows typical OH emission during and immediately following the laser pulse for approximately 50 ns, suggesting that such initial OH emission may be due to the reaction of fast atomic hydrogen from the photolysis with molecular oxygen. Figure 3b is a typical profile showing a relatively long induction time for the rise of OH emission from ignition. Figure 2 is a plot of induction time based on OH emission at different absorbed energy values for four events at equivalence ratio 0.35.

The following table lists ignition threshold values of absorbed energy for several ammonia mole fractions at an equivalence ratio of 1.00:

NH_3 mole fraction:	6.1×10^{-3}	6.0×10^{-3}	5.5×10^{-3}	5.1×10^{-3}
Absorbed energy:	92 mJ/cc	106 mJ/cc	>137 mJ/cc	>150 mJ/cc

The threshold values appear to increase with decreasing ammonia concentration. For ammonia mole fraction less than 5.5×10^{-3} , ignition was not achieved, suggesting that ammonia is needed as a sensitizer for ignition.

We have successfully demonstrated ignition by non-intrusive energy deposition in hydrogen/oxygen flows at room temperature and atmospheric pressure using ammonia sensitizer. We have also measured the ignition threshold and induction time variation for several fuel/oxygen equivalence ratios.

Analysis - The analysis seeks to provide the answers to the key questions about flame propagation and stabilization in the aftermath of a rapid (photochemical) conversion of a single small "blob" of reactive gases to product gases.

One helpful sequence of analytical studies to complement the "blob" experiment is to proceed as follows. Consider the steady uniform streaming at supercritical speed (i.e., at a speed in excess of the adiabatic flame speed) of a homogeneous premixture, characterized by large Arrhenius activation energy. If one formed a flame in such a premixture, it would be blown off, because upwind diffusion of heat and radicals is ineffective for bringing fresh mixture to the reactive temperature. One may stabilize a flame in such a premixture by the continuous nonintrusive deposition of energy; in effect, this is a "continuous ignition" achieved by nonintrusive energy addition. For a planar concentrated source (say, a Dirac delta function), one finds (by treatment of a modified version of the classical steady one-dimensional formulation of laminar flame propagation) that a relatively broad, convective-diffusive preheating zone precedes a thin reactive-diffusive zone,

and that this two-zone flame structure lies upwind of the site of the energy deposition. This supercritical-flame-stabilization problem is tractable for monopropellant decomposition and bipropellant reactions at general Lewis-Semenov number. What one finds is that the energy-deposition requirement is appreciable because the entire preheating must be furnished by the continuous nonintrusive source to every flowing element of premixture, in order to maintain a planar flame.

It is informative to postulate a continuous nonintrusive cylindrical or point source of energy in a uniform supercritical stream of premixture, in order to define the "downwind-bent" configuration of the flame locus. For asymptotically large lateral distances from the plane or axis of symmetry (on which the source is situated), the flame locus becomes a parabola (in two dimensions) or cone (in three dimensions), with the flame locus so situated that the component of the freestream velocity normal to the flame locus is the adiabatic flame speed. Closer to the axis of symmetry, heat from the source modifies the asymptotic configuration, which is based on the flame exothermicity only; in fact, on the axis of symmetry, the previously discussed, one-dimensional (planar) problem assures that the flame locus lies at a finite distance upwind of the heat source. Execution of this analysis indicates that, because only those flowing elements of premixture which pass the source in the vicinity of the source need be preheated, the heat-addition requirement is reduced from that of the planar-flame case, but is still appreciable.

For more modest enthalpy-addition requirements of the nonintrusive source, one turns to the intermittent irradiation of spherical "blobs" within the supercritically flowing premixture. One could vary the geometry of the irradiated volumes, but this seems of perturbational consequence; if ignition is achieved, two successive downwind-translating blobs will spawn outwardly propagating, mutually approaching flames that will eventually convert all the intervening nonirradiated premixture to product within a domain suggested by the above-discussed, continuous-point-source solution. One need add only enough energy to convert quickly a small fraction of the flowing premixture, because the exothermicity evolved from each resulting quick conversion to product via an alternate chemical path can then spawn a conventional, outwardly propagating flame.

Thus, by subtracting out the convective transport of the blob in the stream, there arises the classical hot-blob-ignition problem (in which relaxation, by radial diffusion of heat from the hot spot, competes in time with the rate of chemical exothermicity, to determine whether a flame develops). In the pulsed-irradiation context, we ask: what localized mass of premixture (i.e., what localized volume of flow) must undergo rapid conversion to product owing to instantaneous energy deposition to ensure that a spherical flame propagation ensues? (The emphasis on realistic localized energy deposition is noteworthy; energy deposition such that a completely burned-out hot spot is enveloped by entirely unreacted mixture, or such that the energy deposition integrated over all space is unbounded, poses an academic problem.) The essential point is the volume of the annulus of flame differs from the volume of the annulus of premixture being preheated, and this geometry challenges the sustaining of burning of ignited small blobs. The interplay of off-stoichiometric conditions, differing diffusivities for each reactant species and for heat, and flame curvature can lead to flame-propagation rates distinct from those found in the same premixture in planar flames. These phenomena have been elucidated quantitatively by identification of a convenient quasisimilarity.

The rate of radially outward propagation of the reaction front of a

successfully irradiated blob is characterized by the magnitude of the laminar flame speed. This highly subsonic speed is typically much less than the speed of the oncoming stream of premixture in many practical aerodynamic contexts. A very large number of energy-deposition sources, situated transverse to a stream of fast-flowing premixture, would be required to span that stream with flame, within a modest distance downwind of the plane containing the sources. For practical purposes, therefore, attention is turned to the use of nonintrusive energy deposition in a supersonically flowing mixture, not to initiate a flame propagation, but rather to initiate a detonation. Practical considerations are (1) one would not want to initiate so strong a detonation that it propagated upwind; and (2) one would not want the intermittent incidence of a strong pressure wave to pose problems for material surfaces in a combustor. Because so many fewer energy-deposition sources are required to span a supersonic stream of premixture with flame within a modest distance downwind of the source-containing plane if the sources initiate detonation waves, this phenomenon is now under analytic investigation.

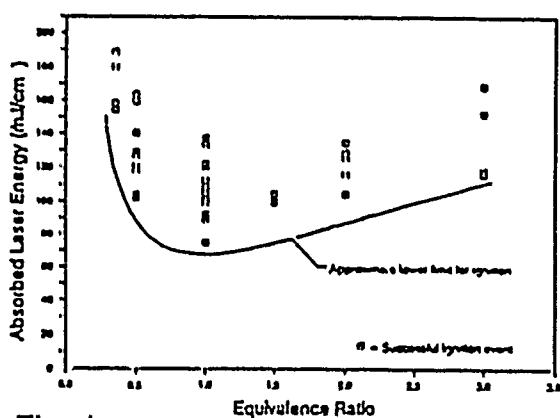


Fig. 1

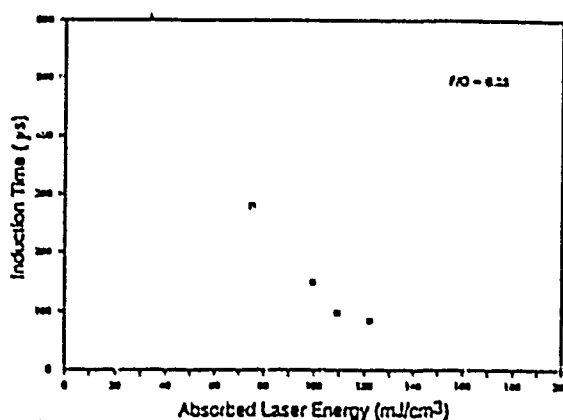


Fig. 2

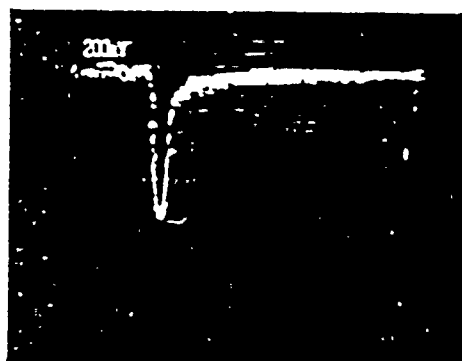


Fig. 3A

100 ns

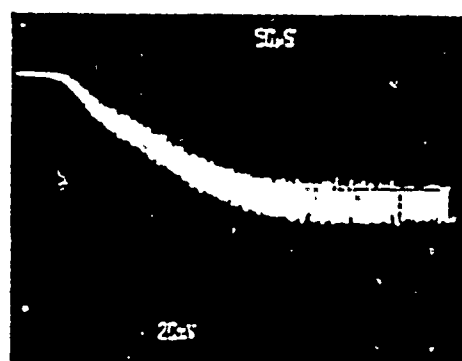


Fig. 3B

50 μs

Carrier, G. F., Fendell, F. E., and Sheffield, M. W. 1989 Stabilization of a premixed planar flame by localized energy addition. AIAA J., to appear.

Carrier, G. F., Fendell, F. E., Kung, E. Y., and Sheffield, M. W. 1989 Stabilization of an axisymmetric premixed flame by localized energy addition. Comb. Flame, in review.

Carrier, G. F., and Fendell, F. E. 1989 Spherical flame propagation: effects of stoichiometry, differing diffusivities, and flame curvature. In preparation.

COMPUTER MODELING OF SOOT FORMATION COMPARING FREE RADICAL AND IONIC MECHANISMS

(AFOSR Grant No. 88-0072)

Principal Investigator: M. Frenklach

Fuel Science Program
Department of Materials Science and Engineering
The Pennsylvania State University
University Park, PA 16802

SUMMARY/OVERVIEW:

This is a part of a joint program between The Pennsylvania State University and AeroChem (Principal Investigator: Dr. H. F. Calcote) in which the main objective is to compare the relative importance of the free radical mechanism and the ionic mechanism of soot formation in flames. The approach undertaken is that of experimenting with chemical kinetic models: to test and analyze computationally the ionic mechanism advocated and developed by AeroChem, and to compare the results with those obtained for the free-radical mechanism. The Penn State computational results obtained to date are reported below, those of AeroChem on the details of the ionic mechanism used in the computer simulations are reported separately.

There are basically two places in the soot formation process where ions can compete with neutrals: first, in the formation and growth of polycyclic aromatics, and second, in the coagulation of these aromatics into soot particles. The computational results indicate that the formation of polycyclic aromatic species via the ionic mechanism is much slower than that via the pathway involving neutral radicals.

TECHNICAL DISCUSSION

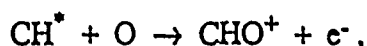
At the last-year AFOSR meeting we reported the computational analysis of the ionic reaction mechanism under the conditions of shock-tube experiments on soot formation. Now we report the results obtained in simulation of "well-studied" laminar premixed flames. The computations were performed using the Sandia burner code¹ installed on a CRAY XMP/48 at the National Center for Supercomputing Applications at Urbana, Illinois, and on an IBM 3090/400E VF at the Penn State Center for Academic Computing.

As there is no single flame reported for which there are measurements available of all the chemical species of interest to this study, two flames were chosen to represent a "well-studied" flame. As the primary focus of this study is on the ionic species, the main flame — referred to as Flame 1 — is the flame for which ion concentration profiles were measured by Calcote and co-workers:² 52.9 % C₂H₂ – 44.1 % O₂ – Ar ($\phi = 3.0$), pressure 20 torr, cold gas velocity 50 cm/s. Since, however, Calcote and co-workers did not measure the concentrations of neutral species in this flame, a second flame, that of Delfau and Vovelle³ — referred to as Flame 2 — was chosen to test the predictions of the present simulations for the major neutral species. The stoichiometry, pressure and cold gas velocity of this flame are exactly the same as those of Flame 1. The mixture used by Delfau and Vovelle did not contain any argon, whereas that of Calcote and Keil had 3 % argon. Also, the reported temperature profiles of Flames 1 and 2 are slightly different from each other. Temperature profile is a critical input parameter for the flame simulations and even small differences in the given profile data cause significant changes in computed profiles of minor (e.g., PAHs) species.

The results of the flame simulations indicate that the concentrations of major species are predicted well — as good as the present state of the art in the knowledge of chemical reactions, their rates and thermochemistry, the accuracy of numerical techniques, and quality of experimental measurements allow. The agreement is worse for the minor ionic species compared to the agreement seen for the major species. In the computer simulation as opposed to the experiment, the positions of the concentration peaks are shifted towards the burner and the decay in some of the concentration profiles is much steeper (Fig.1). This behavior was seen in computer simulations of an acetylene flame with the radical mechanism.⁴ The reasons for this are discussed in the cited work. It is important to note, however, that the peak values of the ion concentrations are predicted reasonably well, taking into account the uncertainty in the input reaction data and in the experimental measurements — many of them are computed within an order of magnitude of the experimental numbers. It should be pointed out that the current ionic mechanism does not contain oxidation reactions of aromatic species. Therefore, the computed concentrations of neutral aromatic molecules with the ionic mechanism constitute the upper limit values. However, the corresponding measured concentrations of the neutral PAHs⁵ are higher by about an order of magnitude compared to these predictions.

Although the analysis of the results obtained in the flame simulations is not entirely completed, the following conclusion, based on both the shock-tube and flame simulations, seems to emerge: the ionic mechanism produces polycyclic aromatic hydrocarbons (PAHs) at significantly lower rate than does the free-radical mechanism. This result is illustrated in Fig.2, where the concentrations of selected aromatics computed with the ionic mechanism are compared to those computed with the free-radical mechanism at the same conditions. As can be seen from this comparison, the production of aromatics via free radicals is much faster than that via ions (the difference between the two cases increases with the switching off oxidation reactions in computer simulations with the free-radical mechanism). An extensive sensitivity and rate analysis performed so far found no conceivable adjustments in the parameter values that would change this conclusion.

There are two basic factors identified in the present analysis to be responsible for the low rate of PAH production via the ionic mechanism tested. First is the relatively low rate of ion production. The reaction initiating the formation of primary ions under conditions of the "well-studied" flame was identified to be



in agreement with a recent report of Eraslan and Brown.⁶ The second factor limiting the rate of PAH production via the ionic mechanism is the reversibility of the principal reaction steps. The computer simulations indicated that the forward and reverse reactions of these steps are tightly balanced, i.e., are in partial equilibrium, similar to the situation identified for the free-radical growth.⁷ However, compared to the free-radical mechanism, the ionic mechanism does not have an equivalent of the H-abstraction reactions and irreversible cyclization steps that provide the kinetic driving force for the molecular growth.⁸

REFERENCES

1. Kee, R. J., Grcar, J. F., Smooke, M. D., and Miller, J. A., Sandia Report No. SAND85-8240, December 1985.
2. Calcote, H. F. and Keil, D. G., *Combust. Flame* 74, 131 (1988).
3. Delfau, J.-L., Vovelle, C., *Combust. Sci. Technol.* 41, 1 (1984).
4. Frenklach, M. and Warnatz, J., *Combust. Sci. Technol.* 51, 265 (1987).
5. Bitner, J. D. and Howard, J. B., in *Particulate Carbon: Formation during Combustion* (D. C. Siegla and G. W. Smith, Eds.), Plenum: New York, 1981, p. 109.
6. Eraslan, A. N. and Brown, R. C., *Combust. Flame* 74, 19 (1988).
7. Frenklach, M., Clary, D.W., Yuan, T., Gardiner, W.C., Jr., and Stein, S.E., *Combust. Sci. Technol.* 50, 79 (1986).
8. Frenklach, M., *Twenty-Second Symposium (International) on Combustion*, in press.

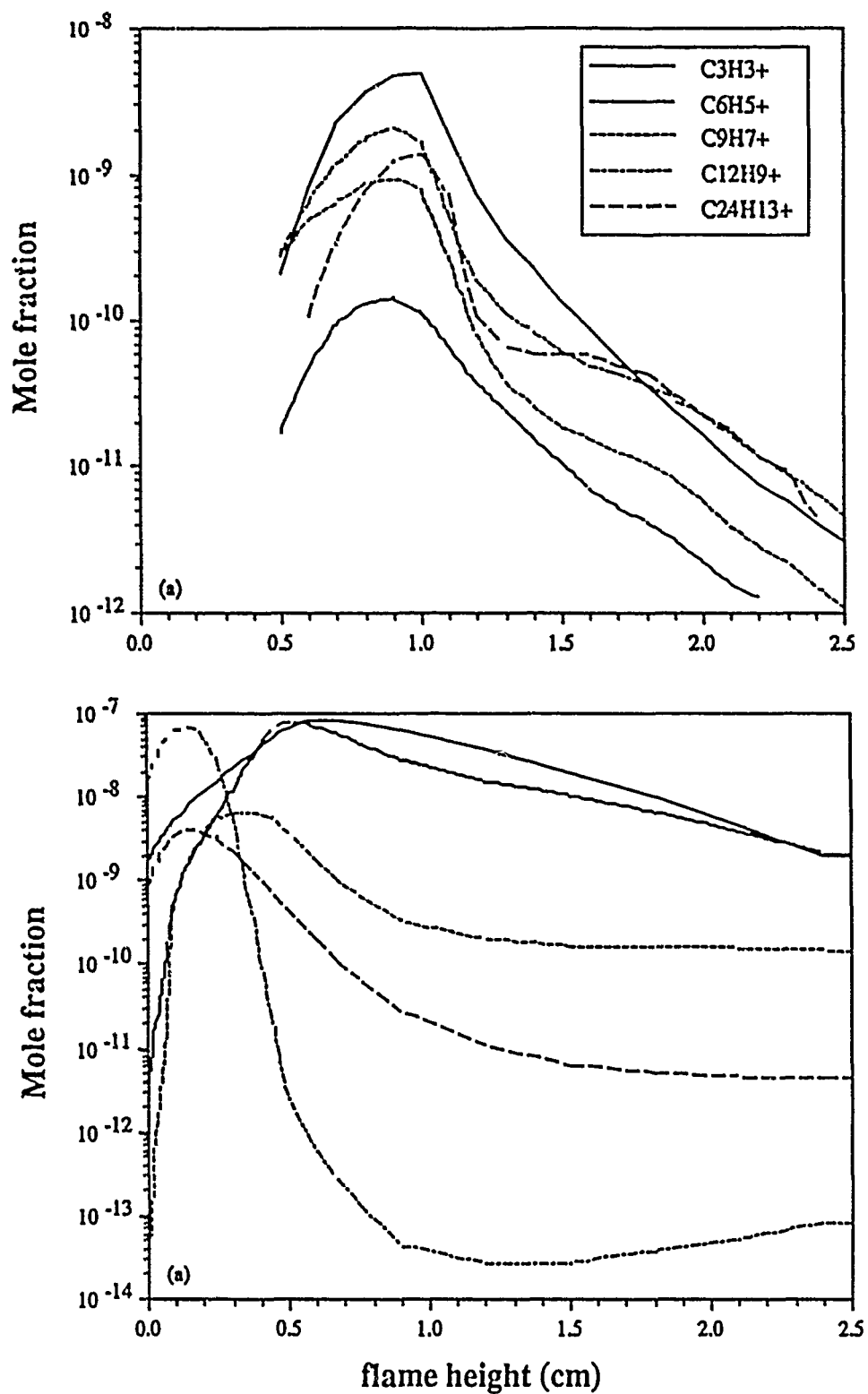


Figure 1. The profiles of selected ions: (a) experimental results from Ref. 2; (b) computed. The line identification applies to both (a) and (b).

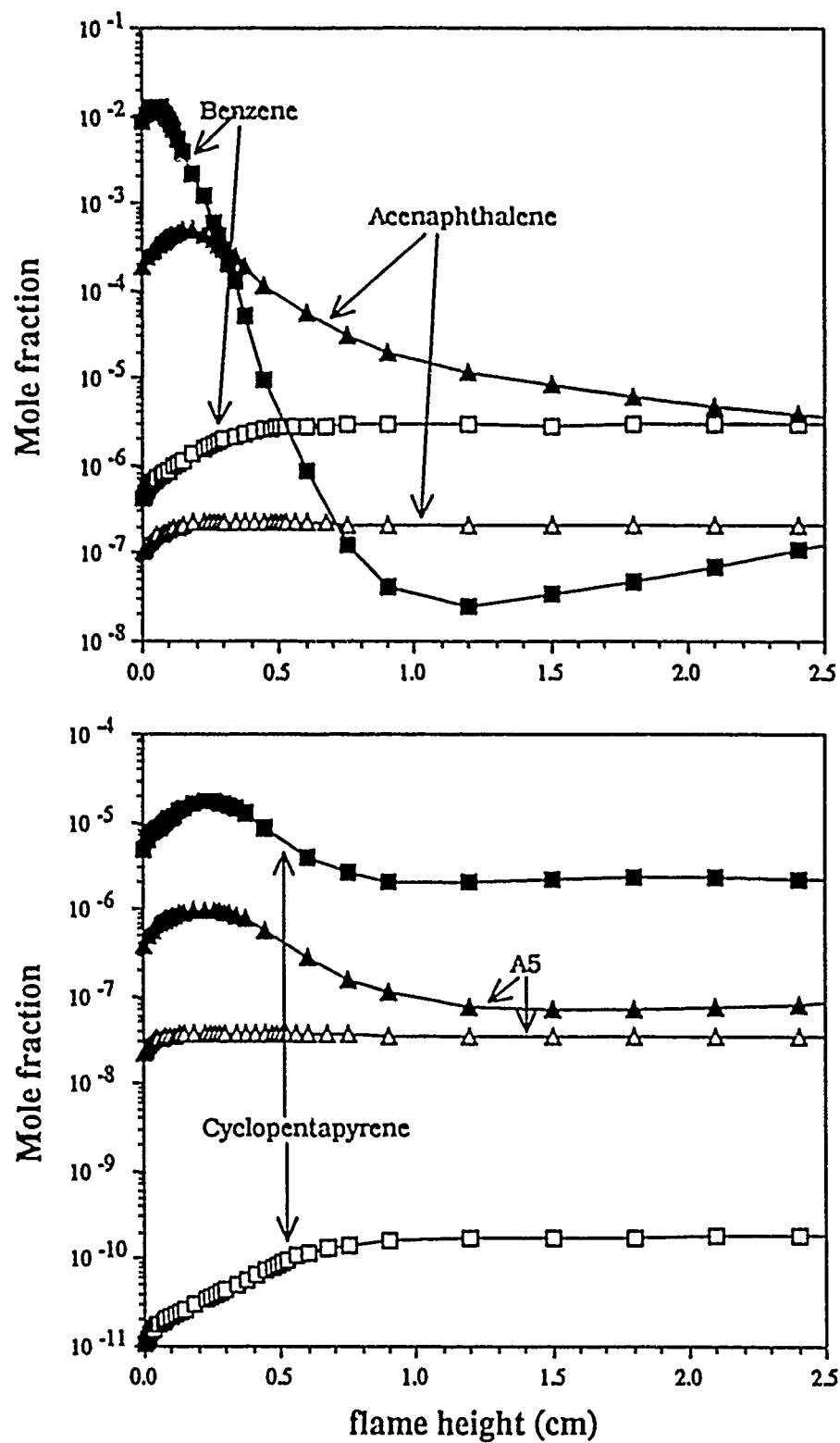


Figure 2. Profiles of selected aromatic hydrocarbons computed with radical (filled symbols) and ionic (open symbols) mechanisms.

KINETIC STUDIES OF METAL COMBUSTION IN PROPULSION

AFOSR Grant No. 89-0086

Principal Investigator: Arthur Fontijn
Research Collaborator: Aleksander G. Slavejkov

High-Temperature Reaction Kinetics Laboratory
Department of Chemical Engineering
Rensselaer Polytechnic Institute
Troy, NY 12180-3590

SUMMARY

The transfer of engineering data, on rocket chamber and plume combustion, from present to advanced propulsion systems is hampered by a lack of understanding and knowledge of individual A1 and B species reactions. Experiments with our unique HTFFR (high-temperature fast-flow reactor) technique have shown a wide variety of ways by which temperature affects the rate coefficients. Current theory, such as used for hydrocarbon-fuel combustion reactions, has been found to be inadequate to either predict or adequately explain these observations.¹⁾ This emphasizes the need for accurate measurements on further A1 and B reactions, which need to be included in rocket combustion models. Here we report on five reactions and discuss some of the implications.

TECHNICAL DISCUSSION

Technique

HTFFR is a unique method, which can provide accurate kinetic measurements on reactions of refractory species, such as A1 and B, over the 300 to 1900 K temperature range. The elementary reactions are studied in isolation in a heat bath. With traditional high-temperature techniques such isolation is usually impossible to achieve; as a result, data on any given reaction depend on the knowledge of other reactions occurring simultaneously, leading to large uncertainties. In the HTFFR shown in Fig. 1, BCl₃ in Ar bath gas is passed through a microwave discharge to produce BCl. The pyrolysis tube removes any remaining BCl₃. The BCl radicals are then mixed with the oxidant, e.g., CO₂. The relative BCl concentration is measured by laser-induced fluorescence, LIF, as a function of oxidant concentration for several pressures, reaction times and average gas velocities, to yield a rate coefficient k . "Arrhenius" plots of $\ln k(T)$ vs. T^{-1} are then obtained from similar measurements at various temperatures.

Results and Discussion

Over the past year we have made a series of measurements on reactions of AlO, AlCl, and BCl. The following $k(T)$ data, in $\text{cm}^3\text{molecule}^{-1}\text{s}^{-1}$, have been obtained:

- (1) $\text{AlO} + \text{Cl}_2 \rightarrow \text{OAlCl} + \text{Cl}$ $T = 460 \text{ to } 1160 \text{ K}$
 $k(T) = 3.0 \times 10^{-10} \exp(-1250 \text{ K}/T)$
- (2) $\text{AlO} + \text{HCl} \rightarrow \text{see below}$ $T = 440 \text{ to } 1590 \text{ K}$
 $k(T) = 5.6 \times 10^{-11} \exp(-139 \text{ K}/T)$
- (3) $\text{AlCl} + \text{HCl} \rightarrow \text{AlCl}_2 + \text{H}$ $T = 1330 \text{ to } 1610 \text{ K}$
 $k(T) = 1.1 \times 10^{-11} \exp(-13100 \text{ K}/T)$
- (4) $\text{BCl} + \text{CO}_2 \rightarrow \text{OBCl} + \text{CO}$ $T = 770 \text{ to } 1830 \text{ K}$
 $k(T) = 1.8 \times 10^{-31} T^{5.6} \exp(-1190 \text{ K}/T)$
- (5) $\text{BCl} + \text{HCl} \rightarrow \text{BCl}_2 + \text{H}$ $T = 1250 \text{ to } 1620 \text{ K; T-range}$
 $k(T) = 1.2 \times 10^{-10} \exp(-1200 \text{ K}/T)$ is currently being extended.

The product paths shown are the only reasonable on thermochemical grounds. For reaction (2) there are three possible sets of potential products, $\text{OAlCl} + \text{H}$, $\text{AlCl} + \text{OH}$ and $\text{AlOH} + \text{Cl}$. For this and some other reactions, studied previously, mass spectrometry as well as LIF will be used to determine the actual products, branching ratios and their temperature dependences.

Figure 2 shows an individual reaction data set over a wide temperature range, i.e., that for $\text{BCl} + \text{CO}_2$. In Fig. 3 we summarize the rate coefficient measurements made thus far on reactions of the Al/Cl/O system. (Reaction (3) is not shown as its rate coefficients are off-scale, $< 1 \times 10^{-15}$, for most of the temperature range investigated.) The figure illustrates the wide variety of $k(T)$ vs. T^{-1} dependences that occur. In addition to further Al-species reactions, a major current effort concerns the comparison between like boron and aluminum species reactions. Figure 4 shows the beginning of a set of B-species reactions, similar to that for Al in Fig. 3.

Figures (3) and (4) allow several observations and comparisons. Thus, the activation energies of exothermic reactions leading OAlCl are small ($E_A/R \leq 1250 \text{ K}$) for $\text{AlO}(X^2\Sigma)$ as the precursor, but considerably larger ($E_A/R \geq 3500 \text{ K}$) for $\text{AlCl}(X^1\Sigma)$ as the reactant. The difference may be attributable to the unpaired electron of the former. The BCl reactions with O_2 , CO_2 , and HCl are significantly faster over the observed temperature ranges than their AlCl counterparts. The differences in curvature in the Arrhenius plots of these two monochlorides with O_2 and CO_2 , respectively, show that predictions from Al to B species would not be reliable, notwithstanding the position of B directly above Al in the periodic table. The zero to slightly negative temperature dependences of $k(T)$ for the $\text{Al} + \text{O}_2$, $\text{AlO} + \text{O}_2$, $\text{AlO} + \text{CO}_2$ reactions can be explained in the usual way as being due to formation of an intermediate complex, which preferentially dissociates to reactants rather than products. However, the very slight positive temperature dependence of the $\text{AlO} + \text{HCl}$ reaction (2) is surprising, most likely it reflects strong dipole-dipole interaction; this then would suggest $\text{AlCl} + \text{OH}$ as a major product path.

The practical uses for our measurements have recently been illustrated by Kolb, *et al.*²⁾ They used three of our papers³⁻⁵⁾ in a fairly accurate prediction of the strength of the AlCl absorption feature of a rocket plume. An aluminized propellant with ammonium perchlorate oxidizer was used for this test.

References

1. D.F. Rogowski, P. Marshall and A. Fontijn, "High-Temperature Fast-Flow Reactor Kinetics Studies of the Reactions of Al with Cl₂, Al with HCl and AlCl with Cl₂ Over Wide Temperature Ranges," J. Phys. Chem. **93**, 1118 (1989).
2. C.E. Kolb, S.B. Ryali and J.C. Wormhoudt, "The Chemical Physics of Ultraviolet Rocket Plume Signatures," SPIE Proceedings, **932**, Ultraviolet Technology II, 2 (1988).
3. D.F. Rogowski and A. Fontijn, "An HTFFR Kinetics Study of the Reaction Between AlCl and CO₂ from 1175 to 1775, Chem. Phys. Lett. **132**, 413 (1986).
4. D.F. Rogowski and A. Fontijn, "An HTFFR Kinetics Study of the Reaction Between AlCl and O₂ from 490 to 1750 K," Twenty-first Symposium (International) on Combustion (The Combustion Institute, Pittsburgh, 1988), p. 943.
5. D.F. Rogowski and A. Fontijn, "The Radiative Lifetime of AlCl A¹Π," Chem. Phys. Lett. **137**, 219 (1987).

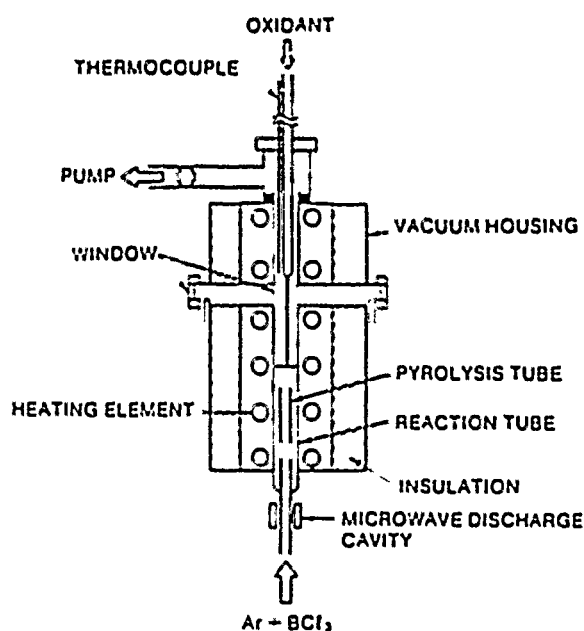


Figure 1. Schematic of an HTFFR, as used for the BCl + CO₂ Reaction.

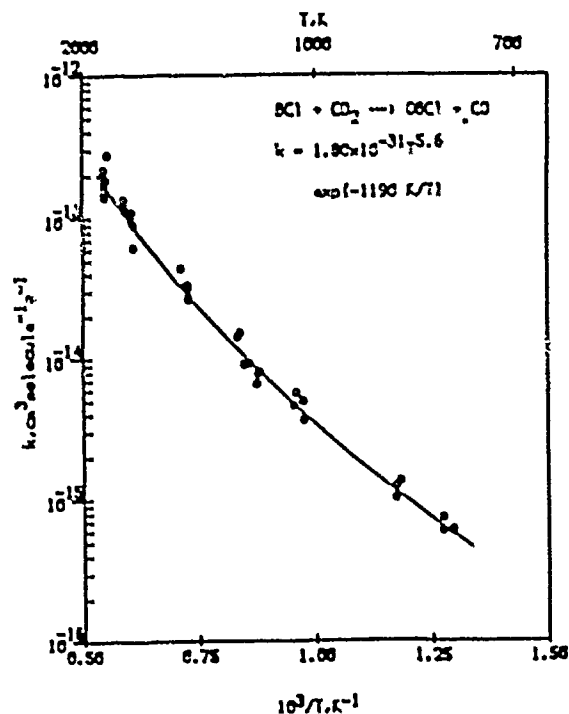


Figure 2. Arrhenius Plot of the Rate Coefficients of the $\text{BCl} + \text{CO}_2$ Reaction.

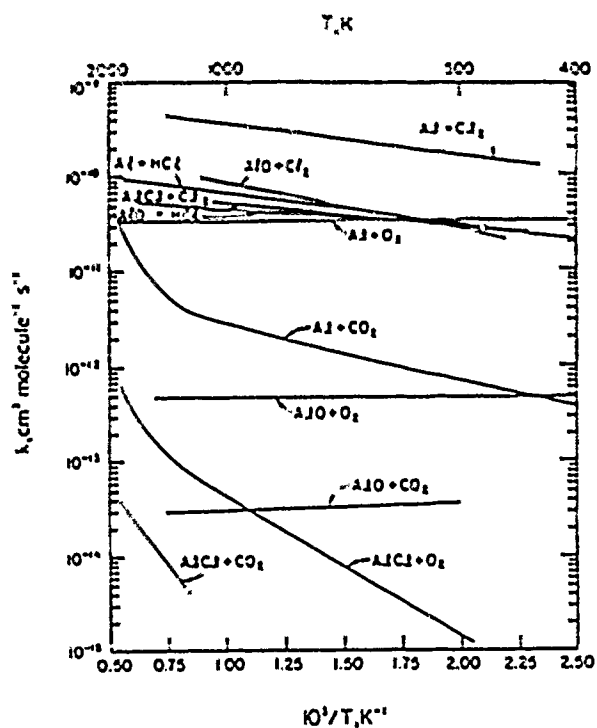


Figure 3. Summary of HTFFR Rate Coefficient Measurements for Al/Cl/O Reactions.

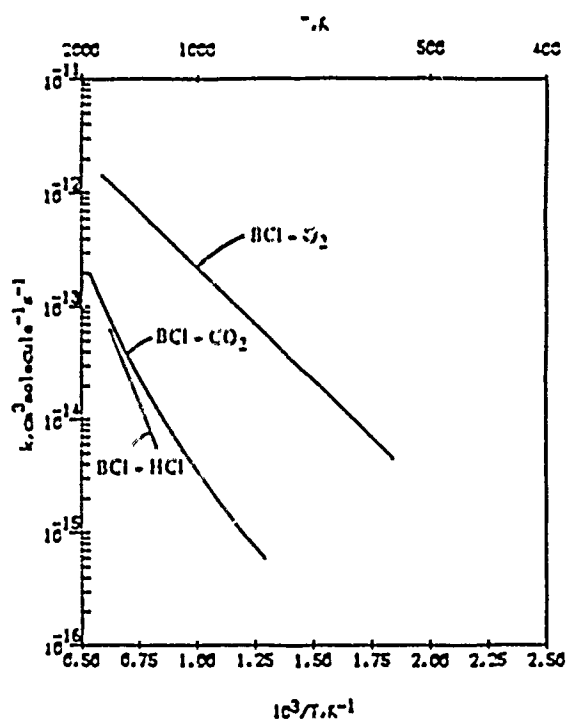


Figure 4. Summary of HTFFR Rate Coefficient Measurements for B/Cl/O Reactions.

FUELS COMBUSTION RESEARCH

(AFOSR Grant-89-0034)

Principal Investigators: I. Glassman and K. Brezinsky

Department of Mechanical and Aerospace Engineering
Princeton University
Princeton, New Jersey 08544

SUMMARY/OVERVIEW

Little had been known about the processes which control the formation of soot in combustion systems and the effect of fuel type, particularly aromatics. By use of pre-mixed and both co-flow and counter-flow diffusion flame systems in which temperatures are controlled, it has been possible to achieve a limiting temperature and to determine the relative effects of flame temperature, equivalence ratio, and C/H ratio in premixed systems and temperature, additives (particularly O_2) and fuel structure in diffusion controlled systems. Corresponding studies of the high temperature oxidation and pyrolysis mechanisms of aromatic, naphthenic and paraffinic fuels using the Princeton turbulent flow reactor are not only providing important kinetic data and mechanisms for those modeling combustion, but also fundamental information necessary to understand the controlling processes in soot formation.

TECHNICAL DISCUSSION

The understanding of the chemistry of aromatic fuel oxidation has been the driving force for our past and present research. A description of the results of experimental work on the high temperature oxidation of p-xylene (1,4-dimethylbenzene) was described previously (1). The experiments were conducted, as usual, in the Princeton Adiabatic Flow Reactor and gave time resolved profiles of the fuel and intermediate products. From those results it was possible to estimate the contribution of various reactions to the fuel's decay early in the oxidation of the xylene. An important result was that abstraction of the benzylic H by the radicals O, OH and H consumed about 75% of the fuel. It was estimated that abstraction by O_2 was not a major fuel consumption step. This result was similar to results obtained by previous workers from our laboratory on the oxidation of toluene (methylbenzene).

Recent work has concentrated on improving the experimental data and modeling the oxidation kinetics of aromatic fuels. Preliminary results from the modeling of toluene have indicated that even though abstraction of the benzylic H by O_2 may not be the primary fuel consumption route, it does play a major role in the oxidation of the fuel through production of the HO_2 molecule.

The modeling work has been initiated with the goal being to determine the reactions that require further study and to develop a set of reactions and rate constants that characterize the oxidation chemistry of aromatic fuels. The experimental results obtained from flow reactor studies will be used to guide the modeling effort and verify the model predictions. Very little work has been performed in the past on aromatic oxidation modeling and most of this

previous work has concentrated on reproducing only one specie profile. The advantage of the flow reactor data is apparent in that it allows one to verify a model using all of the major intermediate products present.

Because the desire is to understand the aromatic chemistry, a 28 reaction $H_2/O_2/CO/CO_2$ mechanism from a verified H_2/CO model developed at Princeton was used as a fixed starting point (2). Aromatic rate data in the literature are most abundant for toluene, so this fuel was modeled first. Because of the methyl sidechain present, methyl radicals play a role in the chemistry and hence a 23 step methyl sub-mechanism from a recent methanol model developed at Princeton was incorporated into the reaction set (3). With these 51 reactions as a solid basis, steps specific to toluene were added.

Only in the last five years have reaction rates important to aromatic combustion become available in the literature. With the published rate data and by estimating unknown rates using thermodynamics, a set of 30 reactions have currently been selected to represent the aromatic oxidation steps up to the point of ring break up. Preliminary results have been obtained for selected species and the present reaction scheme. Comparisons have been made with the experimental data from a toluene oxidation run in the flow reactor at 1188K and an equivalence ratio of 0.63 (4). At the present we are attempting to model only that portion of the oxidation in which ring break up is minor. This approach is feasible due to the stability of the ring structure. Good agreement was obtained with the experimental profiles of the fuel and benzaldehyde, but improvement is required for predicting the experimental profiles of the intermediates benzene and cresol ($HOC_6H_4CH_3$). Very little is known about cresol oxidation chemistry and the experimental data do not give any indication of products unique to cresol consumption. It is worth noting that recent work in this laboratory has shown that cresol does not play a major role in the oxidation of toluene, however, experiments will be performed in the near future to determine the manner of cresol breakdown so that its chemistry can be incorporated into the model (5).

As mentioned, the abstraction of a hydrogen atom by O_2 to form HO_2 has been found to be more important than originally thought. The relatively unreactive HO_2 builds up in concentration and can react with the benzyl radical (also relatively unreactive) in the branching reaction $C_6H_5CH_2 + HO_2 \rightarrow C_6H_5CH_2O + OH$ followed by $C_6H_5CH_2O \rightarrow C_6H_5CHO + H$. Here the benzyl radical and the HO_2 are converted to benzaldehyde and the very reactive H and OH radicals. The modeling work has shown that the abstraction route is a major producer of HO_2 even compared to the well known $H+O_2+M \rightarrow HO_2+M$ reaction. One goal of the modeling effort was to determine which reactions are important in aromatic chemistry and deserving of further research attention. We see here an example of this approach in that H abstraction from the fuel by O_2 may be minor, but the resulting HO_2 is very important.

Work will continue on the modeling with better estimation of unknown rate constants and the eventual addition of ring break up steps. It is also hoped that the applicable temperature range of the model can be extended beyond flow reactor temperatures (around 1200 K) by considering other data from such sources as shock tube studies. As the temperature rises ring break up will become increasingly important. Finally, the xylene experimental work will be concluded and the toluene model extend to this and other dialkylated benzenes.

Our various experiments designed to gain further understanding of soot formation processes has yielded some very important physical insights. In the

work with our opposed jet diffusion flame in which the equivalence ratio of the oxygen doped fuel was varied from infinity to values that would normally be considered within premixed flammability limits, it was discovered that at all conditions under which premixed flames can operate, fuel structure plays no role in the sooting tendency of the fuel (6). That is, one cannot operate a premixed flame so rich that there will be an effect on the sooting tendency directly related to the original fuel characteristics.

In the coflowing diffusion flame apparatus in which laser extinction and scattering measurements were made, results were obtained which indicated that along the centerline of a fuel jet the temperature at which soot particles (inception) were found was always around 1400 K regardless of the fuel used or the amount of nitrogen dilution of the fuel (7).

These results were emphasized in a review paper by the senior co-principal investigator presented last summer at the International Combustion Symposium (8). Preparing this paper was a considerable effort and has commanded tremendous interest as evidenced by the fact there have been over two hundred requests for pre-publication copies. An important outgrowth of the insights of this paper was that as one examined the results of other investigators, one could find similar results that had gone unappreciated. We have concluded from these results that there is a controlling critical step (or steps) which has a high activation energy. The fact that there is a narrow range of temperature around 1400 K is evidence of the ability of H radicals to diffuse into the pyrolysis zone and subsequently incipient particle formation is initiated. There is, however, some variation around 1400 K corresponding to the type of experiment. In fact, analysis of shock tube experimental results, where there can be no H atom diffusion, shows the characteristic temperature to be higher, somewhat above 1600 K (9).

This concept of a critical temperature range commanded much attention at a recent soot workshop in Goettingen. Indeed the Goettingen group repeated our early premixed flame experiments on a flat flame burner (10). They varied the temperature over a greater range than in our original work. They found that the critical sooting equivalence ratio decreased as the flame temperature decreased - sooting tendency increased as flame temperature decreased. Then around 1500°K, the tendency sharply inverts itself and sooting tendency practically stops. We believe that again the critical pyrolysis step to form soot becomes so slow that sooting under this premixed condition essentially stopped.

This concept reflects strongly on the probability of the various detailed mechanisms that are being proposed. We have contended for a long time that the formation of the first aromatics from C_4 aliphatic species and allene were the controlling steps to incipient soot formation and the critical step that gives the characteristic temperature is involved in the formation of these species (11). Others have been proposing that the growth of the larger ring structure may be controlling.

An experiment that would resolve the controversy would be to measure the critical sooting equivalence ratio of premixed flames to which a halogen compound such as a freon has been added. In diffusion flames, we established early that addition of freon substantially increased the sooting tendency of the fuel by accelerating the early pyrolysis steps (12). We have further argued that in premixed flames all fuels break down to acetylene due to extensive oxidative pyrolysis and that the acetylene builds up to the

polynuclear aromatic structures. Since pyrolysis is already extensive in premixed flames, we predict no effect of the halogens. If large ring growth is the controlling element, then halogens should have the same strong effect in premixed flames as they do in diffusion flame. Thus we propose to perform these premixed flame experiments in the near future.

The critical temperature results obtained by various investigators came from the examination of only a limited number of fuels. Thus we decided to try to obtain results without extensive laser diagnostic measurements, for many other fuels by diluting a fuel jet to an extent that all soot luminosity disappears. The experimental conditions at which this loss of luminosity occurs were then used to calculate the adiabatic flame temperature. The temperatures calculated for ethane and propane at a respectable flame height revealed that because heat losses to the burner rim were not too great, a common temperature of about 1900 K is obtained. The actual experimental temperature would be somewhat lower than 1900 K, but higher than the 1400-1500 K range. A full explanation of this higher temperature is not at hand, but the belief is that the extensive nitrogen dilution required could have a strong concentration effect and the associated larger convective velocities may have altered the hydrogen diffusion sufficiently to prevent soot formation. Further attention could be directed to these unusual results.

References

1. Emdae, J.L., Brezinsky, K., and Glassman, I., "The Oxidation of Para-Xylene at 1160-1183K," Eastern States Section/Combustion Institute Paper No. 19, 1988.
2. Yetter, R.A., Dryer, F.L., and Rabitz, H., "A Comprehensive Reaction Mechanism for CO/H₂/O₂ Kinetics," to be submitted to CST (1989).
3. Norton, T.S. and Dryer, F.L., "Some New Observations on Methanol Combustion Chemistry," Combust. Sci. Tech. 63, 107 (1989).
4. Brezinsky, K., Litzinger, T.A., and Glassman, I., "The High Temperature Oxidation of the Methyl Side Chain of Toluene," Int. Jour. Chem. Kin., 16, 1053 (1989).
5. Brezinsky, K., Lovell, A.B., and Glassman, I., "The Oxidation of Toluene Perturbed by NO₂," Combust. Sci. and Tech., in review.
6. Hura, H.S. and Glassman, I., "Soot Formation in Diffusion Flames of Fuel/Oxygen Mixtures," 22nd Symp. (Int'l.) on Combustion, in press.
7. Gomez, A., Littman, M.G., and Glassman, I., "Comparative Study of Soot Formation in the Centerline of Axisymmetric Laminar Diffusion Flames," Comb. and Flame 70, 225 (1987).
8. Glassman, I., "Soot Formation in Combustion Processes," 22nd Symp. (Int'l.) on Combustion, in press.
9. Frenklach, M., Clary, D.W., and Ramachandra, M.K., NASA Report No. CR-174880 (1985).
10. Bohm, H., Hesso, D., Jarde, H., Bluers, B., Pietscher, J., Wagner, H. Gg. and Weiss, M., "The Influence of Pressure and Temperature on Soot Formation in Pre-mixed Flames," 22nd Symp. (Int'l.) on Comb., in press.
11. Glassman, I., "Phenomenological Models of Soot Processes in Combustion Systems," AFOSR TR-79-1147 (1979).
12. Schug, K.P., Mannheimer-Timnat, Y., Yaccarino, P., and Glassman, I., "Sooting Behavior of Gaseous Hydrocarbon Diffusion Flames and the Influence of Additives," Combust. Sci. and Tech., 22, 235 (1980).

THE COMBUSTION OF HYDROGEN AND HYDROCARBONS IN FLUORINE

AFOSR 84-0196

Myron Kaufman

Emory University
Atlanta, GA 30322

SUMMARY/OVERVIEW

Our program is directed towards increasing understanding of combustion processes in general, as well as advancing the application of fluorine-supported combustion in areas such as propulsion and chemical lasers. Since fluorine is monovalent, combustion in fluorine is simpler than combustion in oxygen. Experiments in H_2 - F_2 flames to which very small amounts of CH_4 have been added are particularly revealing and indicate that the most likely mechanism for explaining luminescence from CH and CHF radicals in these flames involves vibrational-to-electronic energy transfer from highly vibrationally excited HF . C_2 emission probably results from the $CH + CH \rightarrow C_2^* + H_2$ reaction.

TECHNICAL DISCUSSION

Flame studies

In order to identify the mechanisms leading to chemiluminescence from F_2 -hydrocarbon flames, we have been investigating such systems by the method of very dilute flames.¹ In this technique, very low concentrations of hydrocarbons (less than 2%) are added to F_2 - H_2 flames while monitoring luminescence from carbon-containing species, such as CH , C_2 and CHF . Measurements of HF rotational temperature and photography with infrared-sensitive film help to define the properties of the H_2 - F_2 flames to which CH_4 is added. At very low additions of hydrocarbons, the basic flame parameters, such as flame shape and burning velocity and the concentration of H and F atoms are determined by the well-understood hydrogen-fluorine kinetics, which is not altered by small additions of hydrocarbon. Thus, the dependence of the intensity of CH , C_2 and CHF emission can be studied as a function of the concentration of hydrocarbon radicals in the flame at constant flame parameters, and the flame parameters can be varied at constant concentrations of hydrocarbon radicals.

CH and C_2 emission are well known in hydrocarbon- O_2 combustion. However, we have previously shown that CH emission is an intrinsic property of hydrocarbon- F_2 combustion and is not dependent on O_2 impurity in F_2 .² Mechanisms can probably be more easily determined in

fluorine than in oxygen-supported combustion, since combustion in monovalent fluorine is simpler, not being complicated by species analogous to aldehydes, peroxides, etc.. In addition, since there are no compounds with bond energies comparable to CO in fluorine-supported combustion, in general there are fewer energetically permissible routes for generating particular excited states.

In very dilute flames, CH, C₂ and CHF emissions show very different dependence on flame parameters. For example, CH and CHF intensities increase linearly with CH₄ added to the flame, while C₂ intensity shows close to a square dependence (Figure 1a). CH and C₂ intensities peak for lean flames and decrease rapidly as the equivalence ratio of the flame increases, while CHF intensity decreases much slower with equivalence ratio (Figure 1b). As pressure is increased, CH and C₂ intensity increases rapidly, while CHF intensity decreases (Figure 1c). These observations have been explained using a mechanism involving the following reactions for populating the emitting states:

- 1) $\text{CH} + \text{HF}^* \longrightarrow \text{CH (A and B states)} + \text{HF}$
- 2) $\text{CHF} + \text{HF}^* \longrightarrow \text{CHF (A state)} + \text{HF}$
- 3) $\text{CH} + \text{CH} \longrightarrow \text{C}_2 \text{ (A state)} + \text{H}_2$

The proposed mechanisms for producing the emitting species provide interesting possibilities for diagnostics in fluorine-supported combustion. For example, from reaction (1) and (3), $I_{\text{CH}}/[\text{CH}] \propto I_{\text{CH}}/(I_{\text{C}_2})^{1/2}$ is proportional to the concentration of HF molecules with sufficient vibrational energy to result in electronically excited CH. Since superthermally vibrationally excited HF represents wasted energy in propulsion, the latter diagnostic might be useful in the exhaust of H₂-F₂ propulsion systems to which small additions of CH₄ have been added as a probe. It may also be of use in HF lasers, where highly vibrationally excited HF is desirable. In the coming year we propose to extend these studies in dilute CH₄-F₂ flames to bands of CF and CF₂ in the ultraviolet and to investigate dilute F₂ flames of the fuels C₂H₂, C₂H₆, NH₃ and N₂H₄.

A modulated cw dye laser system has been prepared for monitoring intermediates in fluorine-supported combustion. This laser has been optimized for the detection of CHF by laser-induced fluorescence using radicals generated by the F + CH₃F reaction in a flow system.

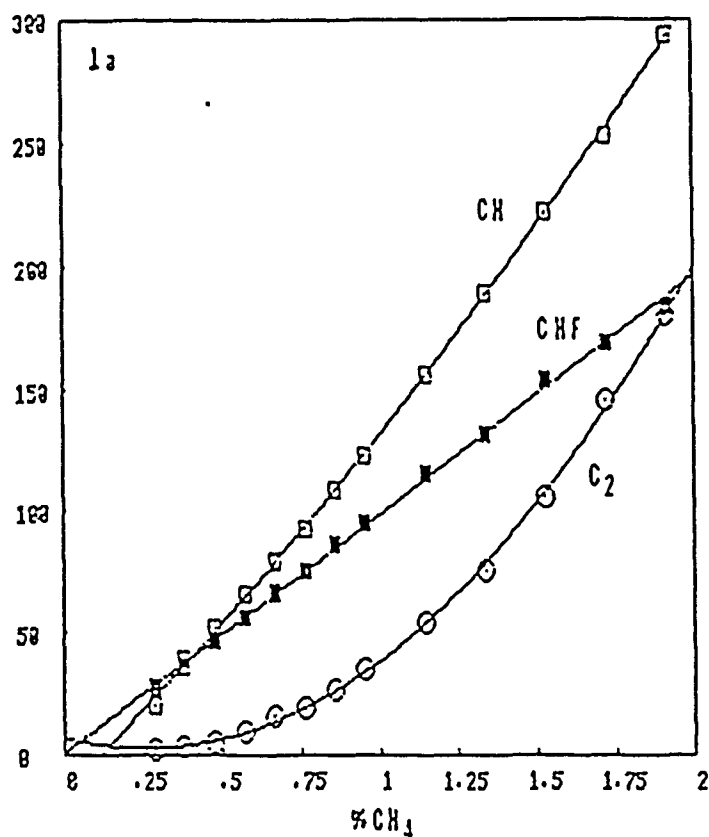
Kinetics studies

We have previously shown that the equivalence points of titrations in bimolecular reactions can be defined kinetically as the ratio of concentrations of reactants that

provide the greatest persistence of the reaction. This results from the fact that only at the equivalence point do the reactants decay in a second-order fashion, while at any other ratio of concentrations the decay eventually becomes pseudo-first order. In order to obtain rate constants from kinetic titrations, detailed fitting to the shape of the titration curve is necessary. For accurate results, we have modified our numerical treatment of the shape of titration curves to include axial diffusion. The theory has been verified by good agreement with titrations of the $O_3 + NO$ reaction, monitored by chemiluminescence at long times in a flow reactor.³

References

1. C. Moore, M. Erickson and Myron Kaufman, technical report, AFOSR 84-0196, May 1989
2. D. Jones and M. Kaufman, *Comb. Flame* **67**, 217 (1987)
3. Myron Kaufman, submitted to the *Journal of the American Chemical Society*



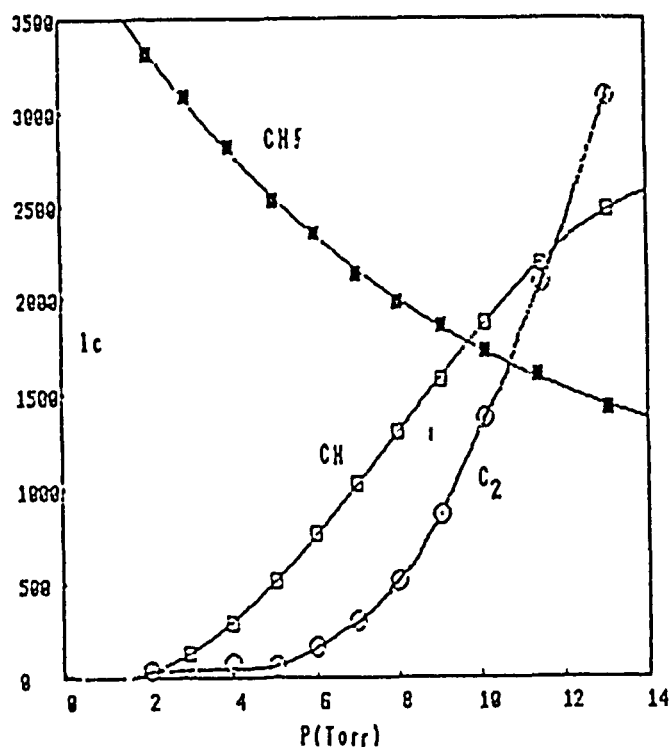
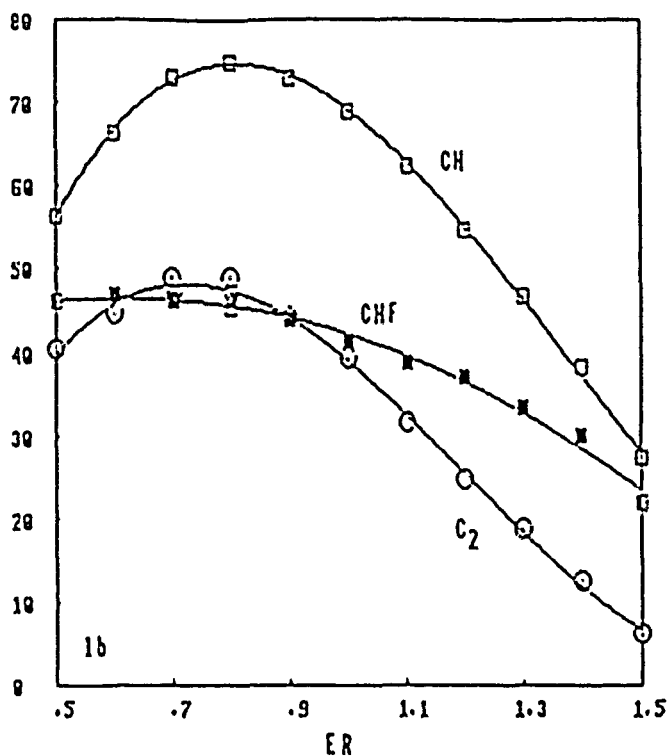


Figure 1. Emission intensity of CH (431nm), C₂ (516nm) and CHF (518nm) emissions from F₂/H₂/CH₄ flames as a function of % CH₄ in fuel (1a), equivalence ratio (1b) and pressure (1c). Intensities of the different emissions are not comparable.

ASYNCHRONOUS OPTICAL SAMPLING FOR LASER-BASED COMBUSTION DIAGNOSTICS IN HIGH PRESSURE FLAMES

AFOSR Grant No. AFOSR-84-0323

Galen B. King
Normand M. Laurendeau
Fred E. Lytle

Flame Diagnostics Laboratory
School of Mechanical Engineering
Purdue University
West Lafayette, IN 47907

SUMMARY/OVERVIEW:

This research is concerned with the development and subsequent testing of a new laser-based combustion diagnostic for the quantitative measurement of both major and minor species concentrations in high-pressure flames. The technique, called Asynchronous Optical Sampling (ASOPS), is a state-of-the-art improvement in picosecond laser spectroscopy. ASOPS is a pump/probe method which will allow determination of both electronic quenching and state-to-state relaxation rates. Such information is necessary for quantitative application of both laser-induced and laser-saturated fluorescence at high-pressures. The specific goal of the project is to develop and prove the viability of the ASOPS technique as a practical, quenching independent diagnostic. This will be achieved through measurements of atomic sodium and the hydroxyl radical in simple flames.

TECHNICAL DISCUSSION

Pump/probe methods are commonly employed to measure subnanosecond excited state processes in liquid and gas phase systems.^{1,2} Asynchronous Optical Sampling (ASOPS) is a newly-developed pump/probe method that will potentially allow the determination of number densities and relaxation rates in turbulent, high-pressure flames. In addition, ASOPS should yield a signal-to-noise ratio comparable to that for laser-induced fluorescence in practical combustion environments. The ASOPS method utilizes a coherent, signal-carrying beam and thus requires no more optical access than LDV measurements.

In conventional pump/probe instruments the pump and probe lasers operate at identical repetition rates, and an optical delay line is used to control the relative timing between pulses from the two lasers. Moreover, some type of mechanical or electro-optical chopping scheme is generally employed to induce an amplitude modulation on the signal which facilitates the use of synchronous detection.³ In contrast, the ASOPS instrument employs pump and probe lasers operating at slightly different repetition rates. This induces a repetitive phase walk-out between the pump and probe pulse trains.

¹ G. R. Fleming, *Adv. Chem. Phys.* 49, 1 (1982).

² F. E. Lytle, R. M. Parrish, and W. T. Barnes, *Appl. Spectrosc.* 39, 444 (1985).

³ G. R. Fleming, *Chemical Applications of Ultrafast Spectroscopy*, Oxford University Press, New York, NY, 1986.

The ASOPS process is illustrated in Fig. 1a, which shows the excited state population produced by several pump pulses over which the temporal positions of several probe pulses have been superimposed. Each successive probe pulse is delayed in time relative to the pump pulse train by a constantly increasing duration which is determined by the beat frequency of the system. Thus each probe pulse samples the excited-state population at a slightly later time than the immediately preceding pump pulse. This is equivalent to varying the optical delay in a conventional pump/probe instrument. The entire process of Fig. 1a repeats itself when the cumulative delay equals the period of the pump laser. Hence any modulation of the probe beam, resulting from the creation and subsequent decay of the excited state, repeats at the beat frequency of the system. Therefore, in contrast to a conventional pump/probe instrument, there is no need to amplitude modulate either beam to employ synchronous detection.

Figure 1b illustrates the change in probe intensity which occurs owing to stimulated emission from the excited-state population shown in Fig. 1a. The net effect of the ASOPS technique is that a small amplitude waveform, which is directly related to the fluorescence decay of the species under study, is impressed onto the probe laser intensity. In essence, a temporal transformation of the excited-state decay is performed with the time scaled by the factor $[(f_{\text{pump}}/(f_{\text{pump}} - f_{\text{probe}}))]$, where f is the repetition rate of the two lasers. The ASOPS technique is thus an optical analog of the sampling oscilloscope.

A block diagram of the basic ASOPS instrument is shown in Fig. 2. The pump and the probe beams are derived from dye lasers, which are synchronously-pumped by frequency-doubled, mode-locked Nd:YAG lasers. The mode-locking frequencies are generated by two frequency synthesizers operated in a master-slave (i.e. phase-locked) configuration to minimize drift in the beat frequency of the system. The pump and the probe beams cross at an included angle of $\sim 5^\circ$ in the flame. The probe beam intensity is monitored by a photodiode subtraction circuit the output of which is amplified and directed to the signal processing system. Triggering of the latter for synchronous detection at the beat frequency is accomplished by frequency doubling and electronically mixing the synchronous voltage output from each synthesizer.

In previous papers,^{4,5} we reported initial ASOPS studies of Rhodamine B in methanol. We have now extended the ASOPS technique to measurement of the relative number density of atomic sodium in an atmospheric $\text{CH}_4/\text{O}_2/\text{N}_2$ flame.^{6,7} Fig. 3 shows a typical ASOPS signal for sodium. The pump beam is set to the sodium D_2 ($3\text{S}_{1/2} \rightarrow 3\text{P}_{3/2}$) transition (589.0 nm) while the probe beam is set to the $3\text{P}_{3/2} \rightarrow 5\text{S}_{1/2}$ transition (616.1 nm). Thus, the ASOPS signal monitors the population of the $3\text{P}_{3/2}$ state, which modulates the probe beam intensity through excited-state absorption.

The decay curve in Fig. 3 was obtained by averaging over 256 separate single-decay curves. For alkali atoms such as sodium, the decay of the $3\text{P}_{3/2}$ state is not a true exponential, but is governed by a second-order decay incorporating the quenching rate ($3\text{P}_{3/2} \rightarrow 3\text{S}_{1/2}$) and the doublet mixing rates

⁴ P. A. Elzinga, F. E. Lytle, Y. Jiang, G. B. King, and N. M. Laurendeau, *Appl. Spectrosc.* **41**, 2 (1987).

⁵ P. A. Elzinga, R. J. Kneisler, F. E. Lytle, Y. Jiang, G. B. King, and N. M. Laurendeau, *Appl. Opt.* **26**, 4303 (1987).

⁶ G. J. Flechtner, Y. Jiang, G. B. King, N. M. Laurendeau, R. J. Kneisler and F. E. Lytle, *Twenty-Second Symposium (International) on Combustion*, The Combustion Institute, Pittsburgh, PA, in press.

⁷ R. J. Kneisler, F. E. Lytle, G. J. Flechtner, Y. Jiang, G. B. King and N. M. Laurendeau, *Opt. Lett.* **14**, 260 (1989).

($3P_{3/2} \rightarrow 3P_{1/2}$).^{8,9} A curve fit to the data with a .05% standard error is shown in Fig. 4, resulting in a $3P_{3/2} \rightarrow 3S_{1/2}$ quenching time of 830 psec and a $3P_{3/2} \rightarrow 3P_{1/2}$ mixing time of 500 psec. This compares to lifetimes of 710 psec and 330 psec reported by Takubo *et al.*⁹ for sodium in a propane-air flame.

The results of Fig. 3 represent a factor of 2.5 improvement in peak signal-to-noise ratio over initial measurements using the ASOPS technique. This takes place despite the 2056 samples required to obtain the initial results, in comparison to the 256 samples of the present data. Furthermore, the pump and probe beams of the initial results were tuned to the D_2 transition, which has an Einstein coefficient for absorption that is approximately 12 times larger than that of the $3P_{3/2} \rightarrow 5S_{1/2}$ transition in resonance with the probe beam in the present experiments. The resulting increase in SNR by a factor of ~ 100 is attributed to the new trigger arrangement, a new detection circuit, and improved dye laser operation.

Based on the sodium experiments, we conclude that the ASOPS method has great potential for use in high-pressure, turbulent flames. Although visible pump and probe beams are used in the above experiments, the ASOPS technique can eventually be extended to ultraviolet wavelengths to monitor molecular species such as the OH radical.

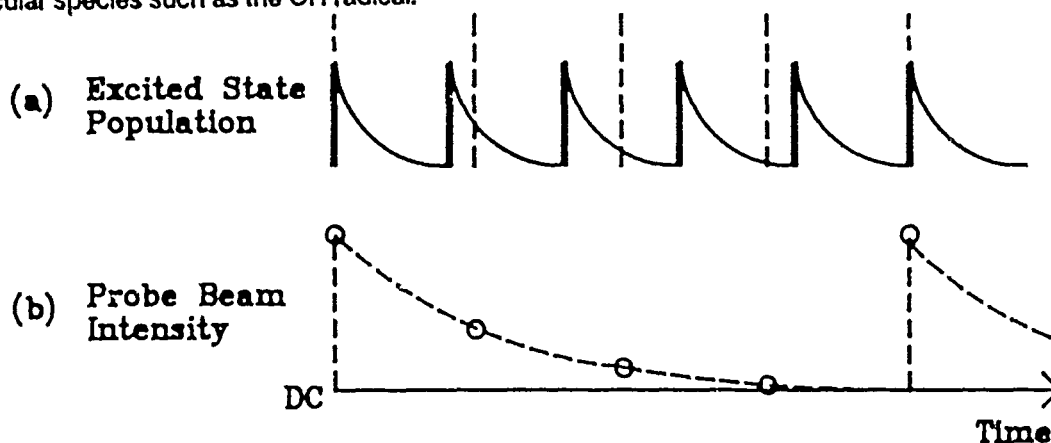


Figure 1. ASOPS timing diagram showing (a) excited state population and (b) probe beam intensity. The probe pulses in (a) are indicated by the vertical dashed lines.

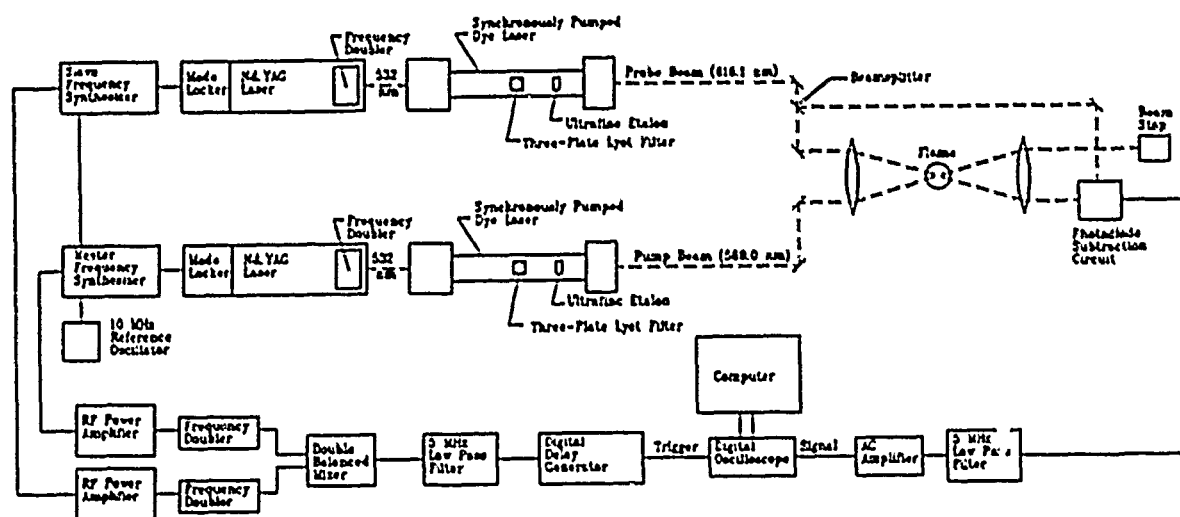


Figure 2. Block diagram of the ASOPS instrument.

⁸ R. A. Beaman, A. N. Davies, A. J. Langley, W. J. Jones, *Chem. Phys.* 101, 127 (1986).

⁹ Y. Takubo, T. Okamoto and M. Yamamoto, *Appl. Opt.* 25, 740 (1986).

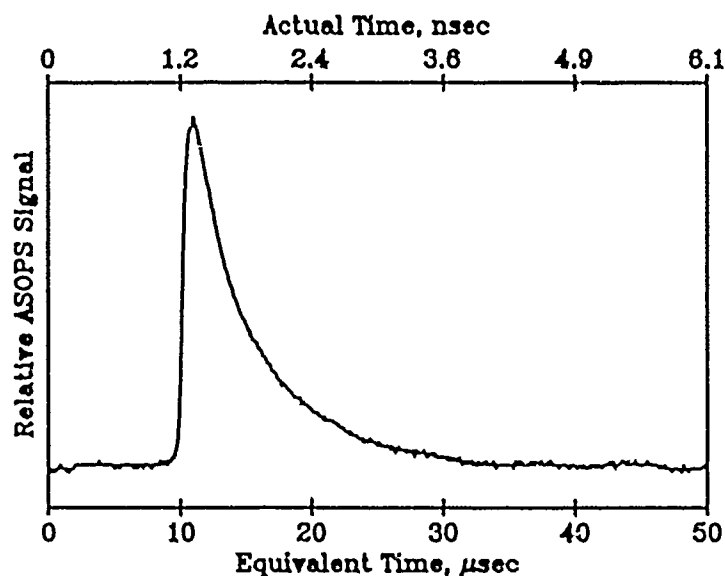


Figure 3. Temporal decay for atomic sodium obtained with a 589.0-nm pump beam (120 mW) and a 616.1-nm probe beam (3 mW). The lower scale gives the equivalent time displayed on the oscilloscope, while the upper scale gives the actual time.

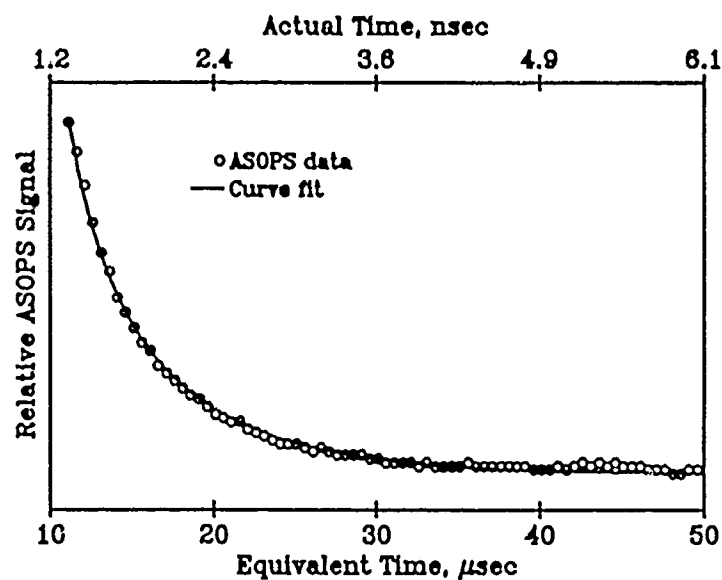


Figure 4. Second order curve fit to the decay of Fig. 3. A $3P_{3/2} \rightarrow 3S_{1/2}$ quenching rate of $1.2 \times 10^9 \text{ sec}^{-1}$ and a $3P_{3/2} \rightarrow 3P_{1/2}$ doublet mixing rate of $2.0 \times 10^9 \text{ sec}^{-1}$ result in a fit (indicated by the solid curve) with .05% relative error from the experimental results (data points indicated by circles). To distinguish the curve fit from the experimental data, only every fifth data point is plotted.

TWO- AND THREE-DIMENSIONAL MEASUREMENTS IN FLAMES

AFOSR Grant No. 88-0100

Marshall B. Long (Co-Principal Investigator)

Yale University
Department of Mechanical Engineering and Center for Laser Diagnostics
New Haven, Connecticut 06520-2157

SUMMARY/OVERVIEW

Laser diagnostic techniques are being developed that are capable of two- and three-dimensional mapping of scalars of interest in turbulent flames. Several light-scattering techniques are being utilized including Rayleigh, fluorescence, and spontaneous Raman scattering. The availability of quantitative data on the spatial and temporal characteristics of structures in turbulent reacting flows will aid in understanding the interaction of chemical reactions with the turbulent motion. A better understanding of this key interaction is important for testing assumptions of existing models of turbulent combustion as well as for suggesting new models.

TECHNICAL DISCUSSION

Turbulent flows are inherently three-dimensional and one aspect of our diagnostics work has been to extend our species concentration mapping techniques into three dimensions. The basis of our volume-measuring techniques is to synthesize a three-dimensional flow measurement by assembling a series of two-dimensional measurements from closely-spaced parallel sheets. The two-dimensional measurements are obtained by sweeping a thin laser illumination sheet through the flow and recording the scattered intensity distributions corresponding to different sheet locations. Figure 1 shows an example of data from a series of planes which make up a three-dimensional data set. With this approach, we have succeeded in making instantaneous 3D measurements in nonreacting jets using Rayleigh and Lorenz-Mie scattering^{1,2} and in flames using fluorescence.³

A significant problem related to three-dimensional measurements is the difficulty of representing the large amount of data obtained with these techniques. We have continued to develop new and more efficient means of conveying the information contained in the data.⁴ Although the concentration distributions shown in Fig. 1 give a complete representation of the three-dimensional data, they do not provide much insight into the topology of the flow structures. One approach that we have used is to represent constant concentration surfaces, which are analogous to lines of constant concentration in a two-dimensional plot. The leftmost surface shown in Fig. 2 shows a constant gas concentration surface obtained from the data set represented by the set of slices shown in Fig. 1. The representation of the species data obtained in these measurements as constant concentration surfaces coincides quite well with one of the current models of turbulent combustion. According to the flame sheet model of combustion, chemical reactions in flames occur in thin sheets located in those regions where the proper mixture of fuel and oxidizer exists. In this model, the data shown in Fig. 2 could correspond to the flame sheet in a turbulent flame. The availability of three-dimensional data allows the investigation of the topology of the flame structures.

The most difficult aspect of obtaining instantaneous three-dimensional data is the requirement that the measurement be made in a time during which the flow is essentially stationary. To relax this constraint, measurements can be performed in forced flows. By causing the flow to evolve in a repeatable fashion, the constraint of making very rapid measurements is replaced with the condition that the measurement be made at the right phase of the repeatable flow. Since the flow is repeatable, many instantaneous shots can be accumulated to integrate weak signals and sequential measurements of several different quantities such as temperature, species, and velocity are also possible. Another advantage of using forced flows is realized by varying the relative phase of the perturbation and the measurement. In this way, the evolution of the three-dimensional structures can be recorded. It is then possible to construct an animated sequence to visualize the development of the three-dimensional surfaces of constant concentration. Figure 2 shows a sequence of surfaces obtained at different phase delays relative to an acoustic perturbation. The convection and evolution of the structures is evident in this four dimensional measurement.

Another advance made during the last year was the development of a new technique for visualizing the mixing structures in supersonic jet flows. This work, which was the result of a collaboration with Dr. R. Dibble at Sandia National Laboratories and Prof. G. Mungal at Stanford, involves the use of Rayleigh scattering from a thin sheet and was demonstrated in an underexpanded air-into-air jet. In the supersonic flow, a low level of humidity was present in both the nozzle and ambient air causing the formation of very small condensed-phase water droplets. Because the Rayleigh signal increases as r^6 (r is the radius of the scattering particle), the presence of even very small particles produces a large elastically-scattered signal. Figure 3 shows a composite of two different instantaneous pictures covering different downstream locations. The Mach disk and triple-point shock structures are clearly visible as are large-scale structures near the edge of the jet and along the slip discontinuity. The relationship of the signal intensity to the flow properties is complex since the temperature, pressure, number density of scatterers, and condensed-phase size distribution all affect the elastically-scattered light intensity. However, the ability to visualize regions of violent mixing shown in the data is of critical importance to the development of supersonic combustors. Work is currently underway to more fully understand the mechanisms of the elastically-scattered signal generation and to ascertain what quantitative information can be extracted from data such as that shown in Fig. 3.

REFERENCES

1. M.B. Long, B. Yip, M. Winter, and J.K. Lam, "Measurement of the Topology of Large-Scale Structures in Turbulent Reacting Flows," in *Turbulent Reactive Flows*, R. Borghi and S. N. B. Murthy, eds. (Springer-Verlag, New York, 1989), p. 1.
2. M.B. Long and B. Yip, "Measurement of Three-Dimensional Concentrations in Turbulent Jets and Flames," *Proceedings of the Twenty-Second Symposium (International) on Combustion*, The Combustion Institute, in press.
3. B. Yip, R.L. Schmitt, M.B. Long, "Instantaneous Three-Dimensional Concentration Measurements in Turbulent Jets and Flames," *Opt. Lett.* 13, 96 (1988).
4. M.B. Long, K. Lyons, and J.K. Lam, "Acquisition and Representation of Two- and Three-Dimensional Data from Turbulent Flows and Flames," *Computer*, in press.

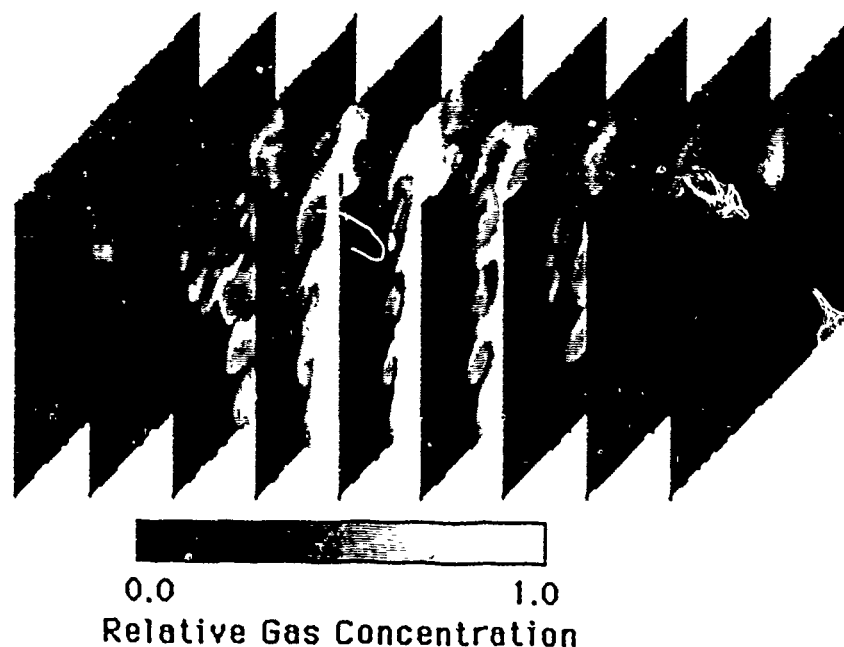


Figure 1

A series of flow planes in an acoustically forced jet, represented by gray-scale mapped concentration contours. The concentration was determined from the intensity of Lorenz-Mie scattering. The region imaged is 1.8 cm in the streamwise direction and centered 2.4 cm downstream of a 0.3 cm diameter nozzle. The frames correspond to planes spaced 0.8 mm apart.

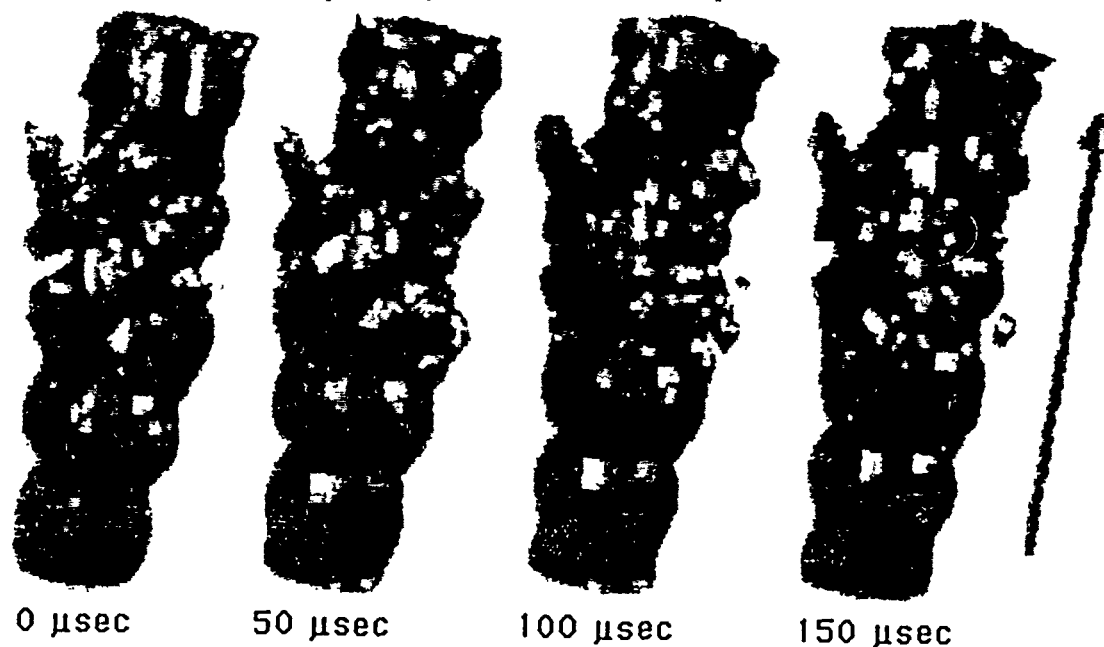


Figure 2

Three-dimensional time evolution of an acoustically forced jet. This series of three-dimensional surfaces was obtained by delaying the phase of the measurement relative to the acoustic forcing. The phase was varied at 50 μ s intervals in order to produce a "movie" sequence. The flow is from bottom to top and the nozzle exit velocity is 8 m/sec. The leftmost surface was obtained from the flow planes shown in Fig. 1.

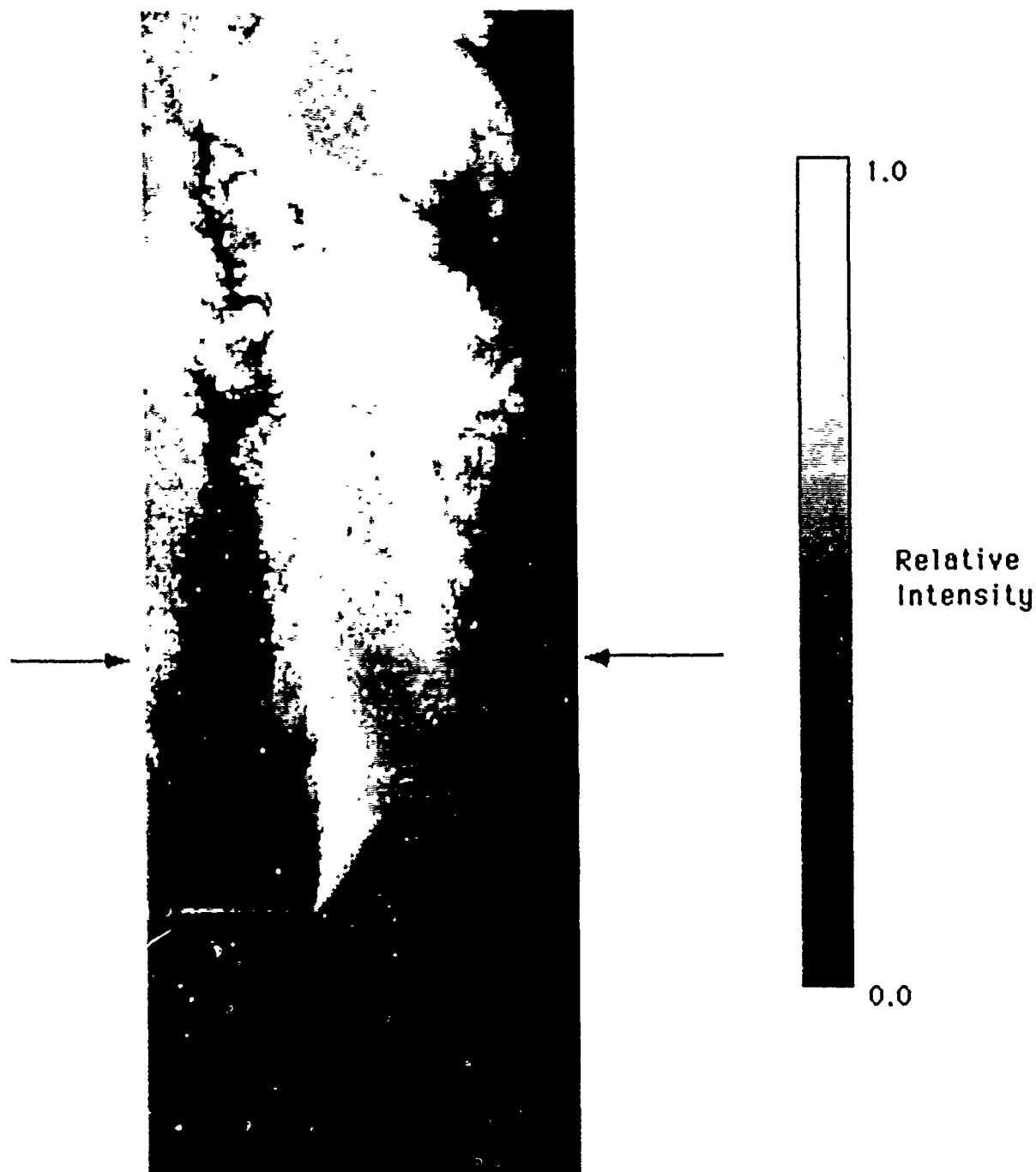


Figure 3

Visualization of a supersonic underexpanded jet (pressure ratio 7) by Rayleigh scattering. The figure is a composite of two instantaneous shots with the arrows indicating the location at which two independent realizations were joined. The nozzle diameter is 8.8 mm. The images were obtained using a pulsed, doubled Nd:YAG laser (10 ns pulse duration) and an unintensified CCD detector.

INVESTIGATION OF COMBUSTION IN LARGE VORTICES

AFOSR Grant No. AFOSR-84-0286

Principal Investigators: Frank E. Marble and Edward E. Zukoski

Jet Propulsion Center

California Institute of Technology

Pasadena, CA 91125

Summary/Overview:

The time available for mixing and combustion in hypersonic engines must be limited to a few milliseconds to keep the mass of the engine and its cooling requirements within bounds. Shock enhanced mixing, suggested by Marble (1986), utilizes the strong vorticity induced by the interaction of weak shock waves with the large density differences of hydrogen and air to enhance the mixing rate between these gases. The strong vorticity produced by this interaction produces strong vortices in the hydrogen, and consequently combustion will take place in these vortical structures. Combustion in such vortices is being investigated in an experimental program. We are also investigating with numerical computations the flow field produced by an injection system which utilizes shock enhanced mixing.

Technical Discussion:

The aim of the experimental work is to develop an understanding of the influence of vorticity on the combustion which takes place in a vortex. We cause vortices to be shed from a rearward facing step which is immersed in a flow of a mixture of fuel and air; see Figure 1. In the absence of vortex shedding, a flame develops in the shear layer between the fuel air mixture flowing over the step and a strongly recirculating flow of hot burnt-gas sheltered behind the step. Pressure oscillations in the frequency range 180 to 500 hz, forced by a siren or naturally present as self excited acoustic oscillations, cause vortices to be shed from the step, and we are studying the heat release process in these vortices formed in the burning shear layer.

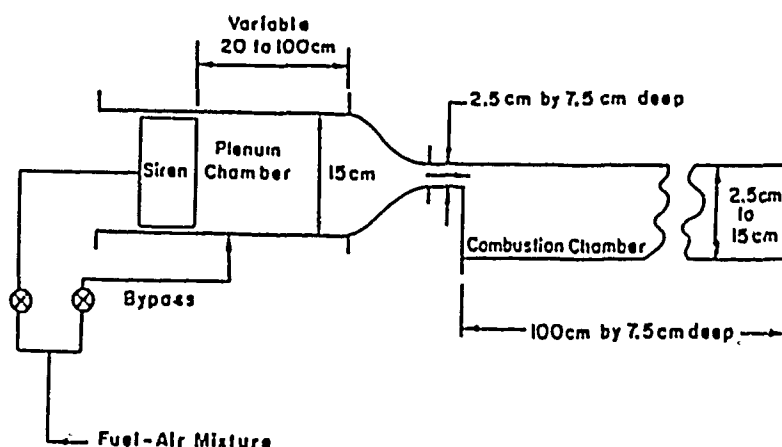


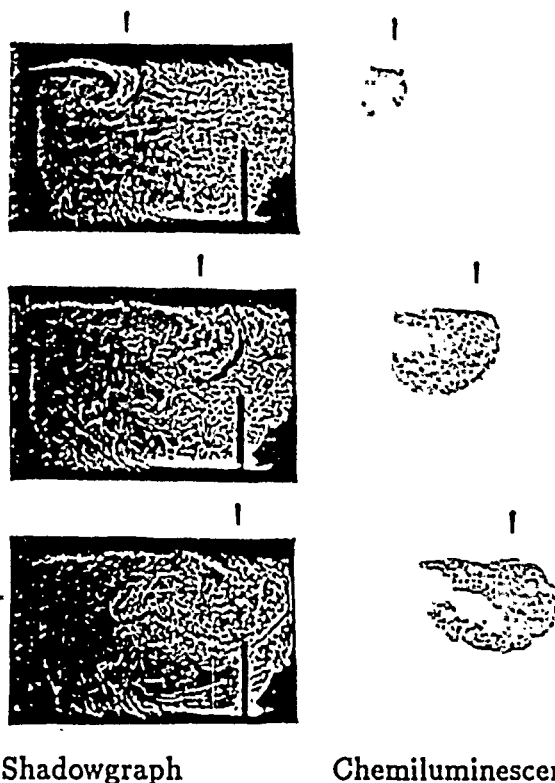
Figure 1. Diagram of Experimental Facility.

The experimental investigation of combustion in a vortex is being carried out in the system illustrated in Figure 1. The lower wall of the combustion chamber can be moved vertically to allow a variation in height of the chamber from 2.5 to 15 cm. Moving the wall allows us to avoid in most cases interference between the burning vortex and the lower wall of the duct. The siren is used to produce a controlled pressure perturbation in the system at frequencies between 100 and 1000 hz, and the bypass system allows control over the amplitude of the disturbance.

Instrumentation includes time resolved measurements of pressure, velocity, and ionization, and shadowgraphs of the density field. An intensified video camera is used to obtain time resolved photographs of the chemiluminescence produced by combustion in the vortices which gives a measure of the volumetric heat release rate in this premixed fuel-air mixture. Exposure times as small as 5 microseconds are used to obtain time resolved data; however, spatial resolution is limited by the 240 by 380 pixel array of the camera, and the experimental technique which involves averaging light across the 7.6 cm width of the combustion chamber. Although the vortices appear to be nearly two-dimensional, this averaging process limits the spatial resolution severely.

Because the repetition rate of the video camera is no faster than 30 frames per second, a form of phase averaging is required to obtain the evolution of a single vortex. At present we are using the pressure signals to determine the phase of the vortices. Our ability to obtain shadowgraph and the video camera photographs within a few microseconds of each other aides in our interpretation of the individual frames.

Control of chemical parameters is achieved by using a range of mixtures of methane and hydrogen gas as the fuel.



Shadowgraph Chemiluminescence
Figure 2. Shadowgraph and Chemiluminescence Photographs.

Spark shadowgraph photographs and intensity contour maps of chemiluminescence

intensity obtained in a typical experiment are shown in Figure 2 and correspond to other data shown as function of the time in Figure 3. In Figure 2, the vertical face of the step flame holder is near the left side of the shadowgraph and vertical lines above both sets of data are at the same physical location. The vertical rectangle on the lower right side of the shadowgraphs is a ionization probe.

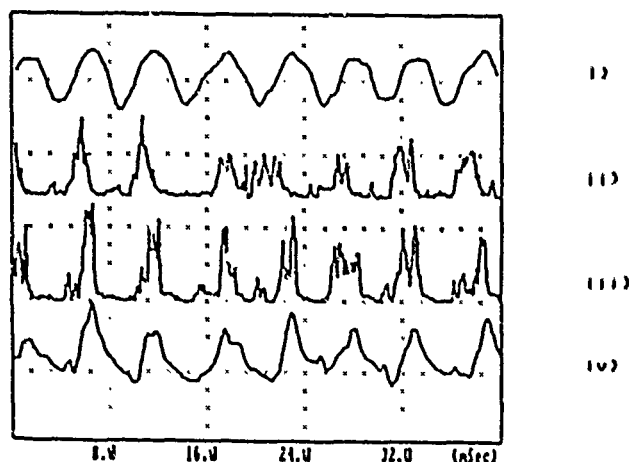


Figure 3. Transducer Signals for a Number of Cycles.

For this experiment, vortices were produced behind a 8 cm high rearward facing step and methane was used as the fuel. The data channels illustrated in Figure 3 show the amplitudes of signals i.) the pressure transducer, ii.) and iii.) ionization gages at 5 and 10 cm downstream of the step, and iv.) the photomultiplier tube which views a thin vertical slice of the combustion chamber.

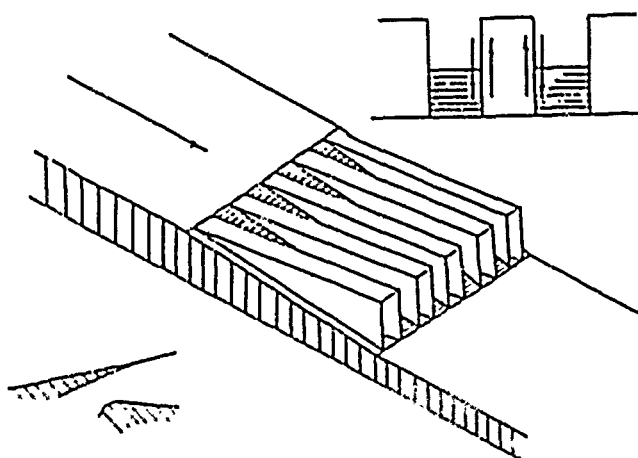
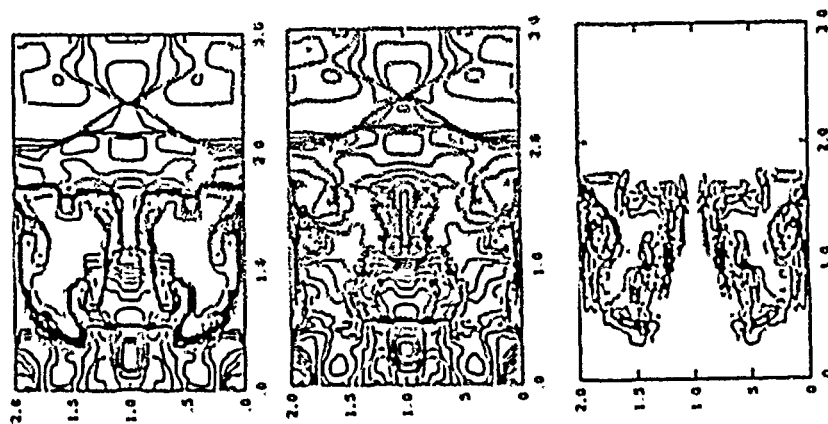


Figure 4. Configuration of Proposed Hypersonic Hydrogen Injector.

We are now in the process of gathering data of this type for a range of parameters including the amplitude and frequency of the oscillations, and a chemical relaxation time which is fixed by the fuel-air ratio and the ratio of hydrogen to methane in the fuel.



a.) Density

b.) Pressure

c.) Vorticity

Figure 5. Field Contours 6" Downstream from Injector Discharge.

A second part of this project involves using an Euler code to examine the vortices formed in an injector system designed to take advantage of shock enhanced mixing. The proposed injector, shown in Figure 4, consists of alternating ramps and expansion troughs placed along one wall of the combustor with their long axis parallel to the flow. Air flowing down the troughs generates a shock wave as it is turned at the bottom of the trough. This shock wave interacts with the hydrogen which is injected at the downstream surface of the ramps and produces a longitudinal vortex, discussed elsewhere. The Euler code is used to generate maps in the cross plane of the pressure, species concentration and vorticity. These maps have been of great aid in the design of a wind tunnel model and we expect will be crucial in the interpretation of the experimental data obtained in windtunnel tests.

A set of these maps obtained in a Mach 6 flow over the injector is shown in Figure 5 at a plane located six trough width-spacings downstream of the nozzle exits. The vortex like distortion of the hydrogen is clearly shown in the density plot and the horizontal line in the density and pressure plots near the center of the jet is a secondary shock wave. At this position, the process has forced a flow of air to penetrate completely through the center of the hydrogen jet.

References:

- Marble, F. E. (1986) "Investigations into the Shock-Induced Enhancement of Mixing and Combustion in Supersonic Burners," Proposal submitted to AFOSR under URI Program, California Institute of Technology.
- Marble, F. E., Hendricks, G. J. and Zukoski, E. E. (1987) "Progress Toward Shock Enhancement of Supersonic Combustion Processes," AIAA Paper No. AIAA-87-1880, 23rd Joint Propulsion Conference, June 29-July 2, 1987, San Diego, California.

INVESTIGATIONS OF THE APPLICATIONS OF
LASER-INDUCED EXCIPLEX FLUORESCENCE
TO FUEL SPRAY AND SINGLE DROPLET VAPORIZATION

ARO Contract No. DAAL03-97-1-0120

Principal Investigator: Lynn A. Melton

Department of Chemistry
University of Texas at Dallas
Richardson, TX 75083-0688

SUMMARY/OVERVIEW:

Laser induced fluorescence methods have been applied to two distinct studies of isolated droplets. First, the quenching of naphthalene fluorescence by molecular oxygen has been used to demonstrate the existence of internal circulation within 300-500 micron diameter falling droplets. Second, exciplex thermometry has been used to measure the surface temperatures of isolated droplets which have fallen through a known heated zone. These diagnostic developments/applications are part of long range program to measure the heat transfer and/or vaporization properties of isolated droplets so that (1) computational models for single droplets can be tested and (2) accurate representations of the heat transfer and/or vaporization of single droplets can be used in full spray simulations.

TECHNICAL DISCUSSION:

The imaging of internal circulation patterns within isolated droplets has been carried out under subcontract at United Technologies Research Center, East Hartford, CT, with Dr. Michael Winter and Dr. G. M. Dobbs as the principal scientists. The measurements of droplet surface temperatures has been carried out at the University of Texas at Dallas. These two experiments will be discussed in separate subsections.

A. Imaging of Internal Circulation Patterns

The detection of internal circulation within decane droplets makes use of the quenching of electronically excited naphthalene molecules by molecular oxygen. Nitrogen and decane are completely inert as quenchers, and therefore the contrast ratio, defined as the ratio I_0/I of the naphthalene fluorescence intensity in the absence of oxygen, I_0 , to that measured in the presence of oxygen, I , depends only on the oxygen concentration in the liquid. For air-saturated cyclohexane the contrast ratio is 6.4, and it is expected to be quite similar for decane.

The liquid from which the droplets are generated can be purged of dissolved oxygen by bubbling nitrogen through it for several minutes. The naphthalene/decane droplets are then allowed to fall into a chamber which contains room temperature nitrogen or air. If the chamber contains air, then oxygen molecules absorb into the surface liquid and quench the naphthalene fluorescence there. Compared to the oxygen-free liquid, this oxygen-

containing liquid appears dark, and as it is convected into the droplet, a dark zone appears in the otherwise generally uniform naphthalene fluorescence.

The fourth harmonic of a Nd:YAG laser at 266 nm was focused into a thin sheet, approximately 50 microns wide, and this sheet was used, as nearly as possible, to illuminate an equatorial section of a 300-500 micron diameter droplet. The fluorescence at right angles was magnified and imaged onto a two-dimensional vidicon camera, such that a resolution of 5 microns per pixel was obtained. The images obtained in this fashion require correction for background in the detector, for the distribution of excited states within the droplet, and for refraction of the fluorescence by the front half of the droplet. The first correction requires a simple subtraction. The second correction is achieved by calculating, pixel by pixel, the ratio of the background corrected image obtained for a droplet falling into oxygen to the background corrected image obtained for an identically arranged droplet falling into nitrogen. The third correction has not yet been applied; the general effect of the refraction is that elements of the uncorrected image appear displaced toward the surface, i.e., penetration of oxygen-containing fluid toward the droplet center appears to be less than it actually is. Figure 1 shows the result obtained. The dark lobes are oxygen-containing liquid which has been convected from the surface of the droplet into the droplet.

These studies are believed to be the first experimental demonstration that internal circulation occurs in droplets whose sizes approach the sizes of droplets within sprays. However, it has not yet been proven that these internal circulation patterns are the result of aerodynamic shear forces, since the process of droplet ejection from the nozzle may also cause internal circulation. Work is underway to separate these effects.

5. Measurement of Surface Temperatures

Exciplex thermometry has been demonstrated previously by Melton and coworkers.¹ Recent work by Stufflebeam has confirmed that spatially precise temperature measurements, accurate to approximately 1 °C, can be obtained.² By measuring the temperature-dependent ratio of the monomer fluorescence intensity to that of the exciplex and comparing this ratio to laboratory calibrations, the temperature of a droplet can be determined non-intrusively. In addition, if the exciplex thermometry system is compounded with strongly absorbing molecules at relatively high concentrations, the optical density can be sufficiently high that virtually all of the incident laser beam is absorbed within a few microns of the surface. Since the diagnostic fluorescence then originates only at the surface, the temperature so determined is a "surface temperature".

In the experiment described here, a single droplet containing 7×10^{-3} M pyrene falls 9.0 cm through a heated brass cylinder and is intercepted by a laser beam at an optical port, approximately 150 msec after entering the cylinder. The droplet generation rate is set sufficiently low that the hot nitrogen purge gas (linear velocity approximately 0.1 m/sec) purges the fall path between droplets. The resulting fluorescence is imaged onto an OMA III detector, and by comparison with standard spectra obtained from the same solution in a capillary at known temperatures, the surface temperature can be determined. For excitation of 7×10^{-3} pyrene with a nitrogen laser at 337 nm, 90% of the incident light is absorbed within 26 microns of the surface of the 230 micron diameter droplet, i.e., within roughly one-fifth of the radius.

The possibility of perturbation of the droplet temperature by energy absorbed from the probe laser was tested by comparing droplet temperatures measured with the unfocused nitrogen laser beam (normal operation) and with a modestly focused (approximate 10x increase in intensity) laser beam. These temperature measurements were consistently within 1-2 °C.

In addition to the exciplex thermometry measurements, the diameter of the droplet, immediately after leaving the droplet generator, D_{gen} , and at the optical port, D_{port} , was determined by standard photomicroscopy techniques with stroboscopic backlighting and a standard reticle..

In early experiments with hexadecane (BF 287 °C) as the solvent substantial evaporation (approx. 40% volume loss) was observed with ambient temperatures as low as 150 °C. Subsequently, Dow Corning 200 heat transfer fluid (viscosity 5 cp at 25 °C, boiling range 320-380 °C at 1 atm. was used in order to obtain data in which droplet heatup might be more clearly distinguished from droplet evaporation. Table I summarizes the data obtained thus far in what is believed to be the first non-intrusive determination of droplet surface temperatures.

Table I
Surface Temperatures and Evaporation of DC-200 Drops

T_{ambient} (°C)	T_{surface} (°C)	D_{gen} (microns)	D_{port} (microns)	Volume Loss (%)
24	24	230 ± 5	230 ± 5	0
155	122	221 ± 4	224 ± 4	0
209	145	223 ± 3	223 ± 3	0
252	200*	225**	176 ± 4	53

* Extrapolated beyond calibration of exciplex thermometer.

** Reliably estimated.

This preliminary data show several interesting elements. Substantial evaporation can occur at ambient temperatures well below the liquid boiling point. The surface temperature, even after 150 msec, is well below the ambient temperature. The volume loss through evaporation seems to begin quite abruptly. These and other effects will be pursued through more detailed experiments. In addition, in the near future, the apparatus will be modified to allow observation of the droplet at any point in the path, i.e., to allow determination of the surface temperature as a function of time in the heated zone.

REFERENCES

1. A. M. Murray and L. A. Melton, "Fluorescence Methods for Determination of Temperature in Fuel Sprays", Appl. Opt., 24, 2783 (1985).
2. J. H. Stufflebeam, "Exciplex Fluorescence Thermometry of Liquid Fuel", Appl. Spectroscopy, 43, 274 (1989).

$$F_O(X, Y) - B(X, Y)$$

$$F_N(X, Y) - B(X, Y)$$

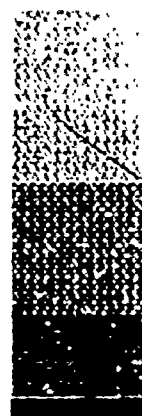
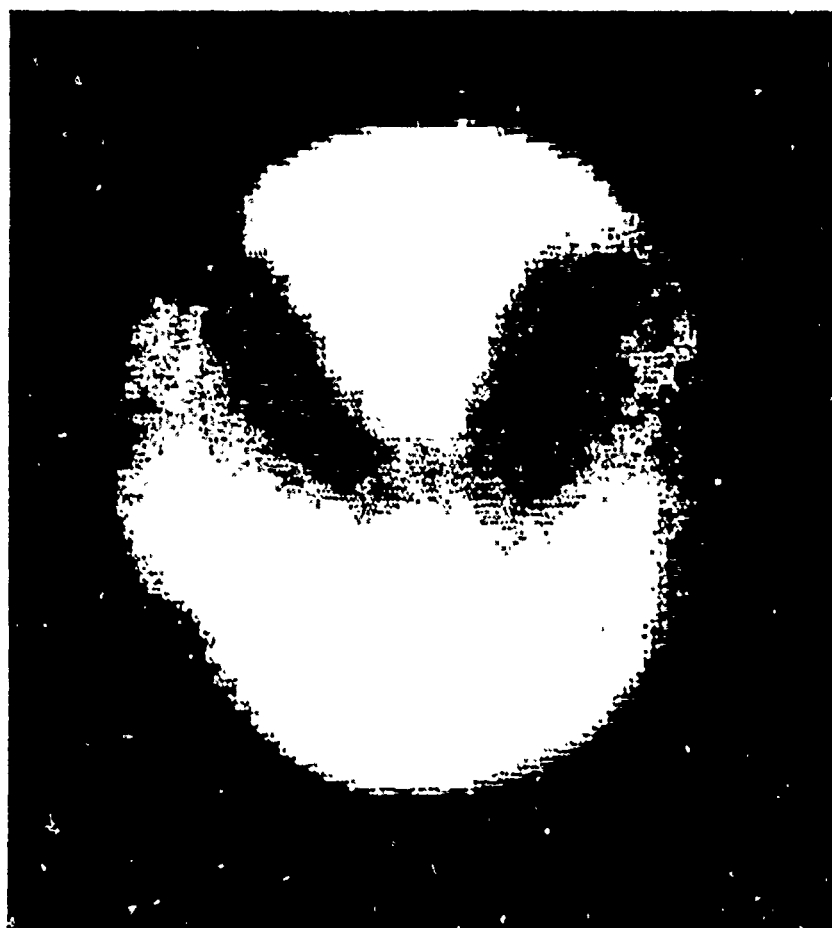


Figure 1

COUPLING BETWEEN GASDYNAMICS AND MICROWAVE ENERGY ABSORPTION

279

(AFOSR Grant No. 89-0312)

Principal Investigator: Charles L. Merkle

Department of Mechanical Engineering
104 Research Bldg. Bigler Rd.
University Park, PA 16802

SUMMARY/OVERVIEW:

A comprehensive analytical model of the microwave-gasdynamic interaction is being developed based on numerical techniques. A coupled solution of Maxwell's equations and the Navier-Stokes equations is being used to determine the characteristics of the resulting plasma and its controllability, absorption efficiency, and potential for propulsion applications. This represents the first two-dimensional model ever attempted and is to be used in conjunction with companion experiments to ascertain the scientific feasibility of microwave propulsion.

TECHNICAL DISCUSSION

Microwave energy promises to provide capability for obtaining attractive propulsion performance, but detailed questions concerning its scientific feasibility must first be addressed. The present effort, in connection with the comparison experimental effort by Micci, represents a program to provide information upon which these feasibility assessments can be made. In this regard, it is appropriate to compare the issues in the feasibility of microwave propulsion with those for laser and solar thermal propulsion.

Of the three systems, laser propulsion has seen the most concerted research efforts. The prospects on the basis of scientific feasibility are also very good. The high energy fluxes in a focussed laser beam ensure near complete energy transfer in very short distances. The flexibility provided by optical wavelength radiation means the location, shape and size of the absorbing volume can be easily controlled by lenses and fluid mechanical considerations. Major drawbacks of laser propulsion lie with the development, and efficiency of large size lasers and with the availability of necessary pointing and tracking accuracy.

Solar propulsion differs from laser propulsion in that the energy is currently being beamed to locations of interest. Further, there is no cost associated with its generation. The major question regarding the feasibility of solar thermal propulsion concerns the capability for coupling the radiation energy into the directed motion of the working fluid. Thermodynamic limits restrict

the maximum energy fluxes to which solar energy can be focussed. These levels are considerably below the intensities needed for sustaining a densely absorbing plasma in pure hydrogen. Addition of trace alkali species may be sufficient to realize efficient coupling, but the final verdict awaits additional experimental evidence.

The primary question concerning microwave propulsion centers around the degree to which the location of the absorbing plasma can be controlled so as to prevent arcing to the wall and wall erosion. The longer wavelength of microwave energy ensures complete absorption at low power levels. Representative peak temperatures ($< 10,000\text{K}$) suggest lower wall heat loading than in the laser case, and the efficiency and relative compactness of microwave sources also represent advantages. The present analytical effort is directed at studying the detailed characteristics of microwave plasmas, and at addressing the questions concerning the controllability of the heating volume as well as scale-up issues.

The coupled Maxwell and Navier-Stokes equations are being solved simultaneously by numerical means to provide understanding of the details of the interaction. To date calculations have included cases with specified heat absorption to understand the basic nature of the flow in the experimental apparatus and cases in straight ducts with fully coupled microwave-gasdynamic interactions. To date buoyancy and re-radiation losses have been ignored, but these are to be added soon. Comparison of predicted temperature profiles with experimental measurements which are just getting underway will be made to check the accuracy of the model.

Representative results for the uncoupled calculation (specified energy absorption) are shown in Fig. 1 for a geometry and flow conditions corresponding to the experimental effort. As can be seen, the spherical bulb on the flow tube gives rise to a recirculation region. Parametric studies concerning the location and strength of the heat absorption region show the size of this recirculation zone changes dramatically with flow conditions. The sensitivity of the flow field to this uncoupled problem demonstrates the importance of knowing details of the flow in the absorption regime if appropriate flow passage geometries and imposed fields are to be determined.

Corresponding results from calculations of the fully coupled problem with electrical conductivity given as a function of temperature are shown in Fig. 2. Perhaps the most striking aspect of this calculation is the degree to which the electric field is restructured by the conducting medium. The flow conditions for this calculation are chosen to match experimental conditions and the power absorption of 270 Watts is also representative of experimental conditions. Peak temperatures here are probably somewhat overstated because of the use of constant specific heats. The streamlines show the expected deviation around the heating zone, and the downstream cooling caused by thermal conduction is also noted.

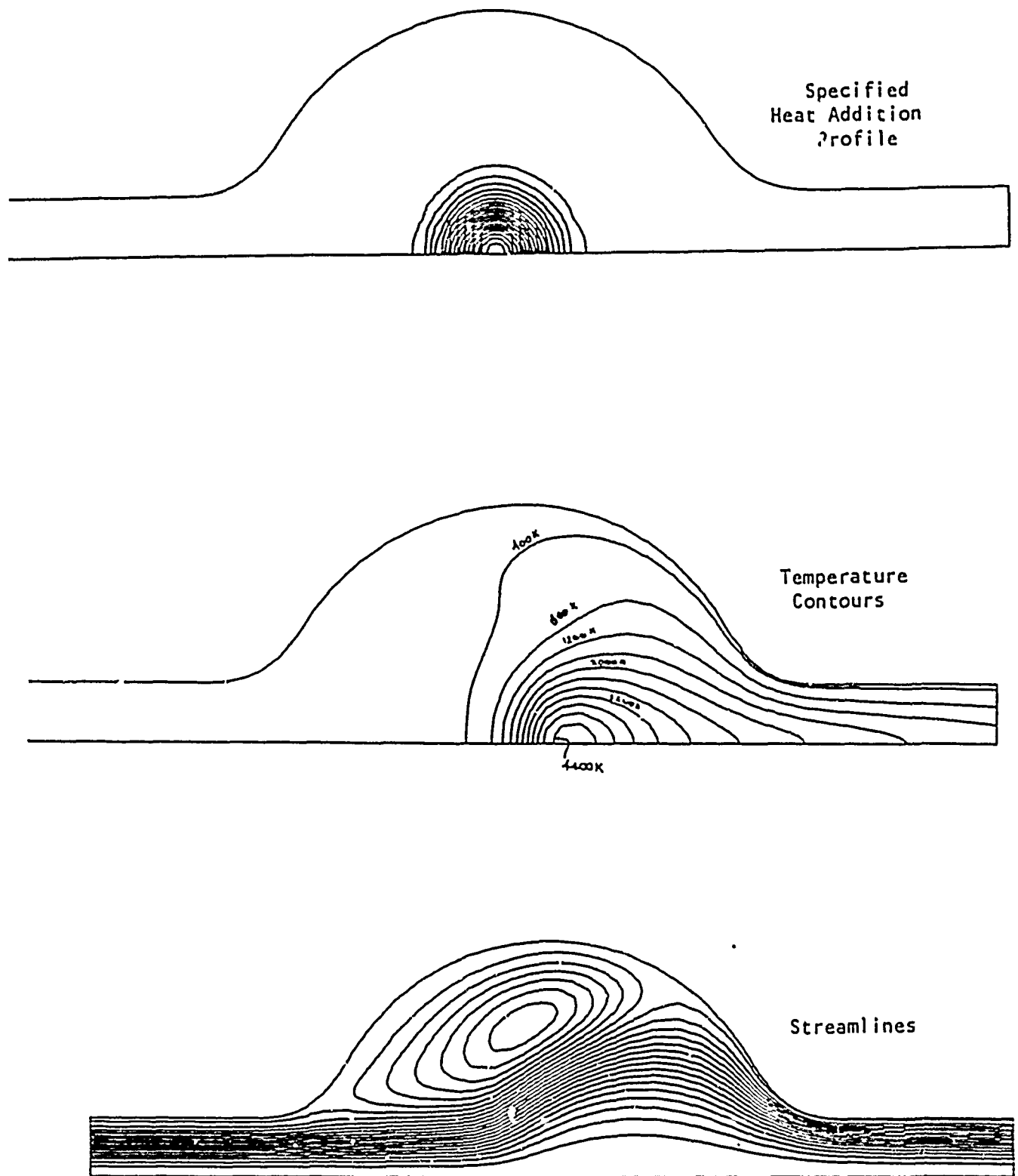
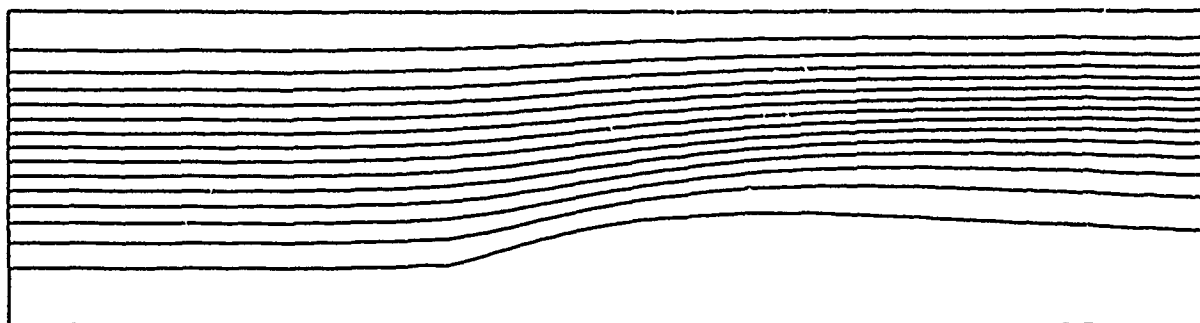


Fig. 1 Effect of specified heat addition on flow through sphere-cylinder combination.
 $Re = 80$; $Q = 300W$.

(a) Streamlines



(b)

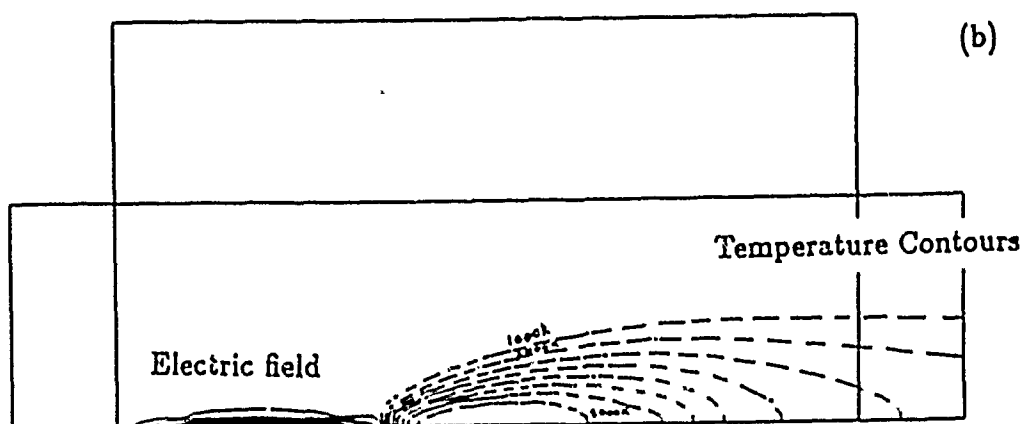


Fig. 2 Predictions of the fully coupled problem for microwave absorption in flowing gas in a circular pipe showing (a) streamlines and (b) temperature contours with superimposed electric field (E^2). $Re = 450$; $Q = 270W$.

IGNITION AND COMBUSTION ENHANCEMENT BY MULTIPHOTON PHOTOCHEMICAL MEANS

(AFOSR Contract No. 89-0017)

Principal Investigators: Andrzej W. Miziolek
Brad E. Forch
Associate Investigator: Clifton N. Merrow*

U. S. Army Ballistic Research Laboratory
Aberdeen Proving Ground, MD 21005-5066

SUMMARY/OVERVIEW:

Our research involves the use of uv laser photochemistry (single or multiphoton) for the purpose of enhancing ignition and steady-state combustion of reactive gases related to air-breathing propulsion systems as well as for using it as a tool to better understand the details of the relevant heat-release chemical processes. Our approach has been to investigate the underlying physical phenomena which govern the ignition behavior of reactive gases upon irradiation by focussed uv laser light as well as to study the photochemical mechanisms that are involved. Our attention is focussed on reactive systems relevant to hypersonic propulsion, i.e. H_2/O_2 and H_2/air , and on laser systems such as the ArF excimer laser (193 nm), which might possibly be used in a practical application. Recent work has demonstrated that the laser ignition properties of these gases is strongly influenced by atmospheric attenuation of the ArF laser beam, although the reasons for this effect are not yet clear. In addition, we have uncovered preliminary indications that spin-orbit effects in the oxygen atom may be significant in ArF laser studies of O_2 -containing flows and may play an important role in high-speed low pressure reactive flows.

TECHNICAL DISCUSSION

A. UV Laser Ignition Studies

Last year we reported that a broadband ArF excimer laser (193 nm) was capable of igniting a premixed flow of H_2/O_2 quite efficiently (less than 1 mJ pulse energy required), a behavior similar to our previous observations at other wavelengths, i.e. 226 nm (O-atom two-photon resonance) and 243 nm (H-atom two-photon resonance). We speculated at that time that efficient generation of "seed" electrons in the laser focal volume which lead to microplasma formation may have been the result of multiphoton ionization (MPI) of O_2 via the Schumann-Runge (S-R) bands (1+1 process), or from MPI of H_2 via the E,F states (2+1 process), or both. Definitive experiments to resolve this question await the arrival of a tunable ArF laser system in our laboratory in the near future. However, in the course of this work we became concerned that the values for the incident laser energy (ILE) that we were measuring may depend on the distance of the ignition site from the laser due to beam attenuation by atmospheric gases, i.e. O_2 absorption in the S-R bands. In order to determine the severity of this potential problem we measured the spectral profile of the transmitted ArF laser beam as propagated through 20 feet of helium gas as compared to 20 feet of air (Fig. 1). The He data shows the expected broadband ArF laser spectral profile¹ except for the strong self-absorption feature near 193.1 nm.² The air profile, in comparison, clearly shows a number of O_2 absorption line features¹ with the laser beam attenuation measured around 65%. However, the impact of the atmospheric attenuation of the laser beam on the ignition behavior of a premixed H_2/O_2 flow appears to be quite dramatic (Fig.

2). The data in Figure 2 suggest that laser radiation within the O_2 absorption spectrum must be important in the ignition process otherwise one would not expect to see such a dramatic difference. Clearly, this phenomenon where laboratory air acts as an "active optical filter" needs to be properly accounted for in ArF laser experiments that are wavelength specific.

B. Photochemical Studies/Spin-Orbit Effects/Diagnostics Development

Figure 3 shows a graphic illustration of the uv laser photochemical effect in a H_2/O_2 flame where the laser is set at 225.6 nm corresponding to the two-photon excitation process in atomic oxygen.³ Similar types of results where the apparent O-atom concentration was found to be progressively higher as the laser pulse energy was increased or the focal length shortened have been observed previously and attributed to single-photon photolysis of O_2 in the hot region of the postflame gases.⁴ These results underscore the photochemical potential of uv lasers in this wavelength region and strongly suggest that lasers operating in the 200-250 nm range may enhance combustion chemistry in fast reactive flows, such as found in scramjet engines, where the temperature of the shock-heated air will be much higher than that of the ambient air.

When photons from an ArF laser beam are absorbed by O_2 , the excited molecules predissociate very rapidly such that more than 99% of these excited molecules break apart to form oxygen atoms in the ground electronic state ($2p^4\ ^3P$). However, this O-atom state is split into three spin-orbit J states which give rise to the frequently seen spectral "triplet" in fluorescence/ionization excitation scans or ignition spectral scans around 226 nm. Very little attention has been paid to the nascent distribution of these oxygen atoms into the different spin-orbit states upon photolysis or as reaction products, but this could be important in air-breathing combustion applications, particularly in low pressure/high flow speed conditions where there may not be sufficient time/collisions to "thermalize" these three states. The reason for this is that a substantial difference in the elementary reaction rate constants for the three different O-atom spin-orbit states may exist even for such important combustion reactions as $O(^3P_{2,1,0}) + H_2 \rightarrow$ products. Such spin-orbit state specific rate constant differences have been previously observed in atoms like Br, F, I, Ca, and Sr (typically factors of 2-10) with extreme cases showing 5 orders of magnitude differences.⁵ Figure 4 shows a clear case of non-statistical behavior in the photolysis of O_2 by the ArF laser.

We have completed an initial study related to laser diagnostic development for transient species such as the H_2CN radical which are important in flames involving oxides of nitrogen.⁶ We are using the photolysis/probe technique to detect such radicals starting with stable parent molecules in the gas phase. Figure 5 shows the nascent OH radical distribution resulting from photolysis of the parent acetaldoxime molecule $H(CH_3)CNOH$.

* NAS/NRC Postdoctoral Research Associate

1. M.P. Lee and R.K. Hanson, JQSRT, **36**, 42 (1986).
2. T.R. Loree, et al., Appl. Phys. Lett., **33**, 171 (1978).
3. B.E. Forch, J.B. Morris, and A.W. Miziolek, Book Chapter in "Laser Based Approaches in Luminescence Spectroscopy", ASTM, (in press).
4. J.E.M. Goldsmith, Appl. Opt., **26**, 3566 (1987).
5. P.J. Dagdigian and M.L. Campbell, Chem. Rev., **87**, 1 (1987).
6. P.J. Dagdigian, W.R. Anderson, R.C. Sausa, and A.W. Miziolek, J. Phys. Chem., (in press).

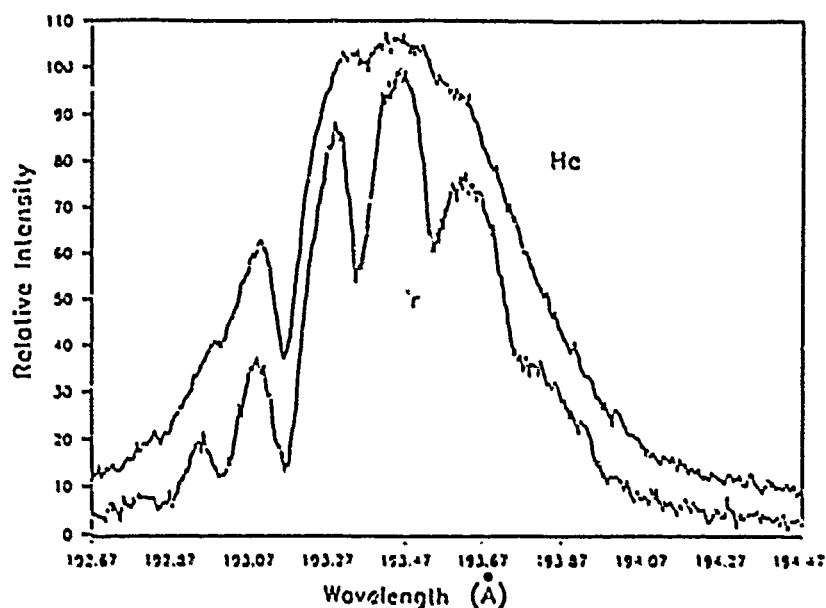


Figure 1. Transmitted broadband ArF laser intensity through He and Air. Pathlength = 20 feet.

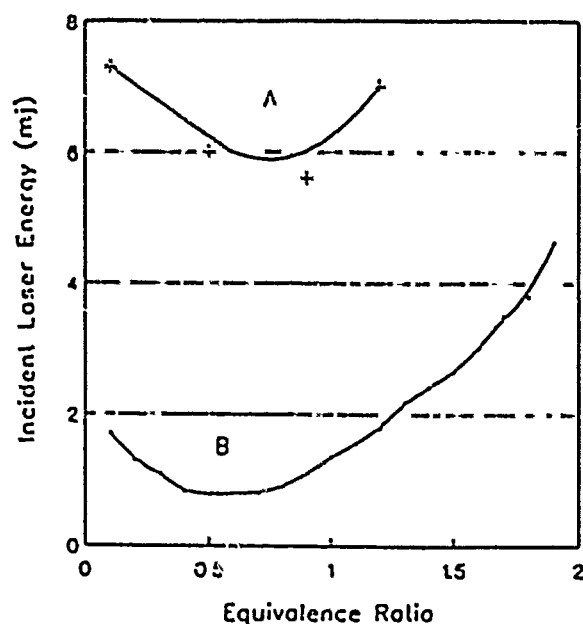


Figure 2. Effect of ArF laser attenuation by laboratory air on ignition of H_2/O_2 premixed gases. A) Pathlength=20 feet, B) Pathlength=1 foot.

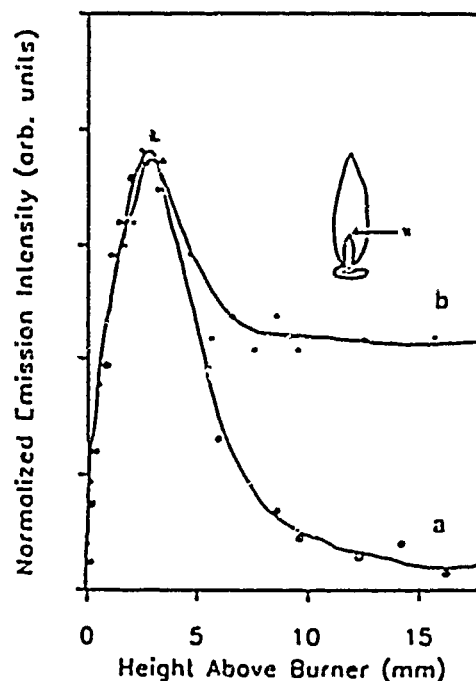


Figure 3. O-atom profile in a fuel-lean H_2/O_2 flame (laser = 225.6 nm). a) laser pulse energy=0.35 mJ, focal length=300 mm, b) laser pulse energy=0.8 mJ, focal length=100 mm.

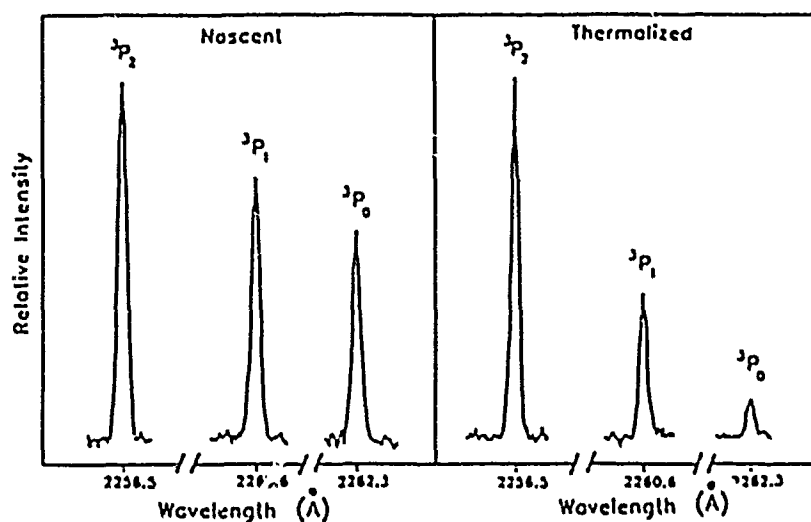


Figure 4. O-atom spin-orbit state distribution from ArF laser photolysis of O_2 . Nascent conditions: $O_2=160$ mtorr, 40 nsec delay. Thermalized conditions: $O_2=300$ mtorr, $N_2=8$ torr, 40 nsec delay.

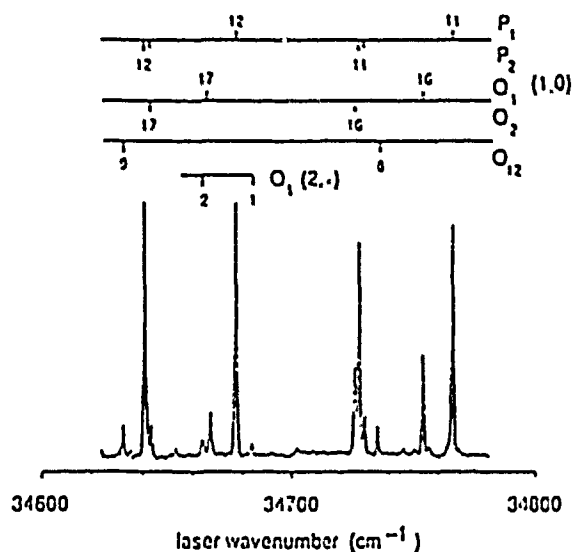


Figure 5. Excitation spectrum near OH A-X (2,1) band origin for photodissociation of acetaldoxime under nascent conditions. Lines of the (1,0) band and of the (2,1) Q_1 branch are marked. The pressure and pump/probe delay were 4 mtorr and 3 μ sec, respectively.

COMBUSTION ENHANCEMENT BY HIGH ENERGY ELECTRON IMPACT PROCESSES

NSF Grant No. CBT-8713328

Principal Investigator: Richard B. Peterson

Department of Mechanical Engineering
Oregon State University
Corvallis, Oregon 97331

SUMMARY/OVERVIEW:

Non-traditional means of attaining combustion initiation and augmentation, referred to here as enhancement, may find an important application in the field of supersonic combustion as it relates to SCRAMJET engine research. As part of a larger project funded by both NSF and AFOSR, gas phase processes induced by high energy electron impacts are being studied. The salient feature of this research involves the in-situ creation of a dilute, non-thermal plasma having a high concentration of free radicals. These species, when formed in gaseous reactants such as H_2 /air and CH_4 /air, initiate the chain branching reactions leading to ignition of the reactants. This research is expected to provide a greater understanding of the various mechanisms associated with combustion enhancement. Progress on the experimental and analytical aspects of the project are described below.

TECHNICAL DISCUSSION:

This project is conveniently divided into three parts: (1) development of a 1 kW electron beam facility for use in combustion enhancement experiments, (2) development also of a diagnostic technique for the detection of free radicals such as H, O, and N atoms, and (3) modeling of electron transport through a gas. These topics are discussed below.

ELECTRON BEAM FACILITY

The beam facility has been design, constructed, and is now undergoing preliminary testing at low power (in the 100 W range). In the course of developing the apparatus, modification of the original facility design (as described in last year's report) has occurred. The addition of a pre-chamber connected to a 2 cubic meter vacuum reservoir was necessary for providing the large mass flow rates experienced by the vacuum/air aperture. With this modification, experimental run time is limited to approximately 10 seconds by the pressure rise (to 10 Torr) in the vacuum tank. However, this period of time is much longer than is required for conducting experiments. Another change is concerned with the powering of the filament of the diode gun. An oil insulated isolation transformer outside the vacuum chamber was developed and is now in use along with a new DC power supply capable of supplying 8 mamps of current at 120 kV. Thus the capability now exists to conduct experiments with 120 keV electrons directed into various gases at pressures up to one atmosphere.

DIAGNOSTIC APPARATUS

Figure 1 is a schematic diagram of the apparatus and instrumentation we are using to detect atomic free radicals. It is an intrusive, direct sampling technique employing resonant absorption for the detection of H, O, and N atoms in a jet of gas expanding into a vacuum chamber. The presence of a particular atomic species is detected by a reduction in the amount of transmitted radiation at the resonant frequency. Because the wavelengths involved in this study are in the vacuum ultraviolet region of the spectrum, an evacuated monochromator is required. Signal detection is by way of a PMT and recording is accomplished with a dual

channel digital storage scope. Currently, the apparatus is being used for quantitative analysis of H atoms originating from closed volume combustion of stoichiometric H_2 /air mixtures. For this analysis both the lamp emission temperature and degree of self absorption are needed. Figure 2 shows two lamp emission profiles for the hydrogen line obtained with a 315 gr/mm Eschelle grating used in 47th order. Lamp doppler broadening and self absorption can easily be determined from such data. Two signals recorded at different lamp self absorption levels are shown in Figure 3. They demonstrate the potential of the technique for providing a relatively simple diagnostic technique for atomic free radicals. Analysis of these signals will yield quantitative measurements of the concentrations during combustion.

ELECTRON TRANSPORT MODELING

The third part of the project is nearly complete with the development of a computer code to predict the trajectory of high energy electrons passing through a gas. The method used is a single scattering Monte Carlo routine utilizing an energy loss relation that can be change depending on the type of gas under consideration. Figure 3 shows two contour plots of probability density for electron passage through two downstream locations from the "vacuum/air" aperture. These plots are a result of following the paths of 10,000 electrons with an initial energy of 100 keV as they pass through an atmosphere of helium at standard conditions. From such data, we have gain a better understanding of the behavior of high energy electrons as they pass through a gaseous medium. Future use of this model will be in the analysis of data from combustion initiation experiments. The computer code is capable of handling gases with variable composition and density. Energy required to initiate combustion can be obtained by making only a few experimental measurements and then using the code to provide the detailed information about the energy deposition process.

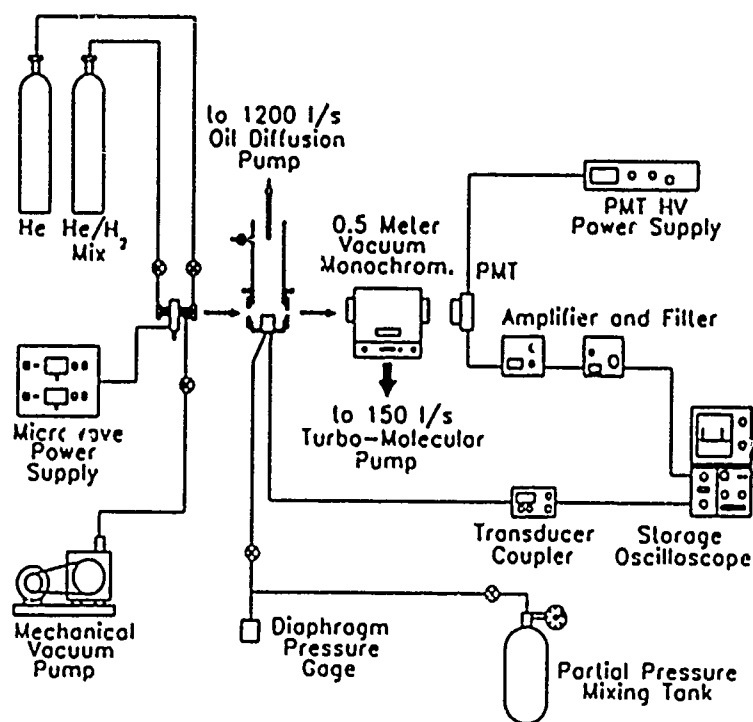


FIGURE 1

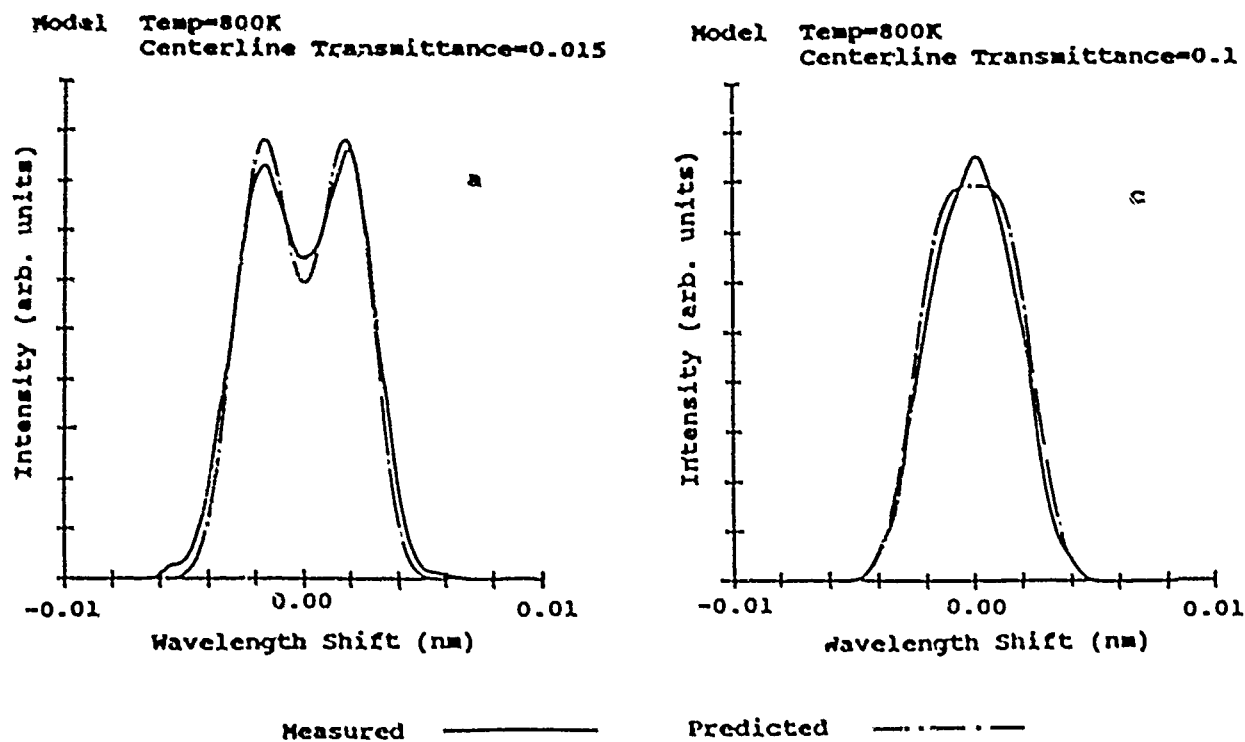


FIGURE 2

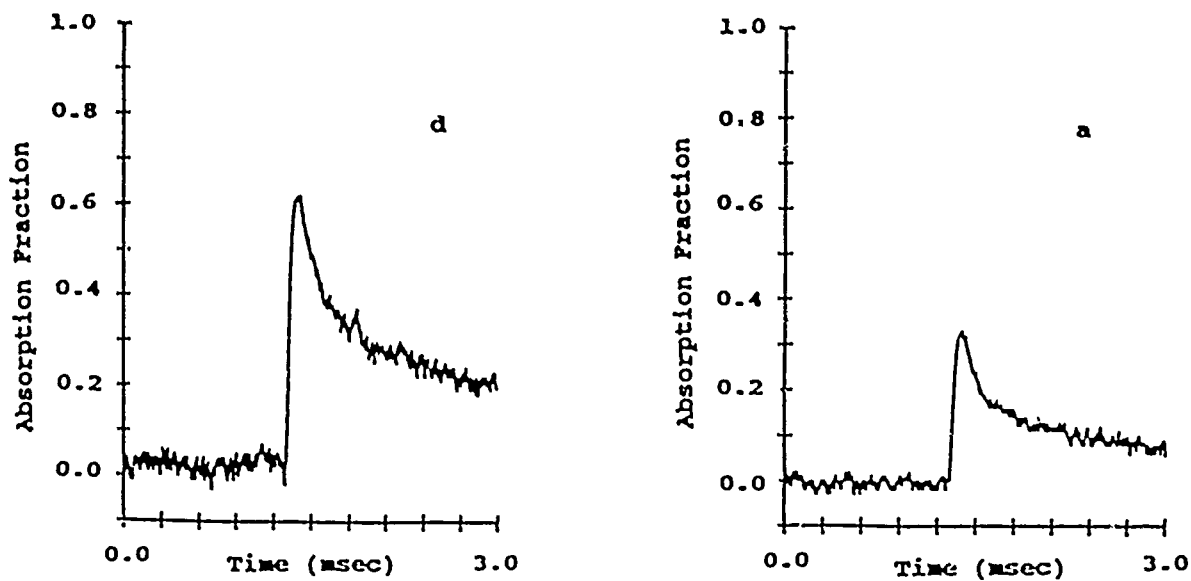


FIGURE 3

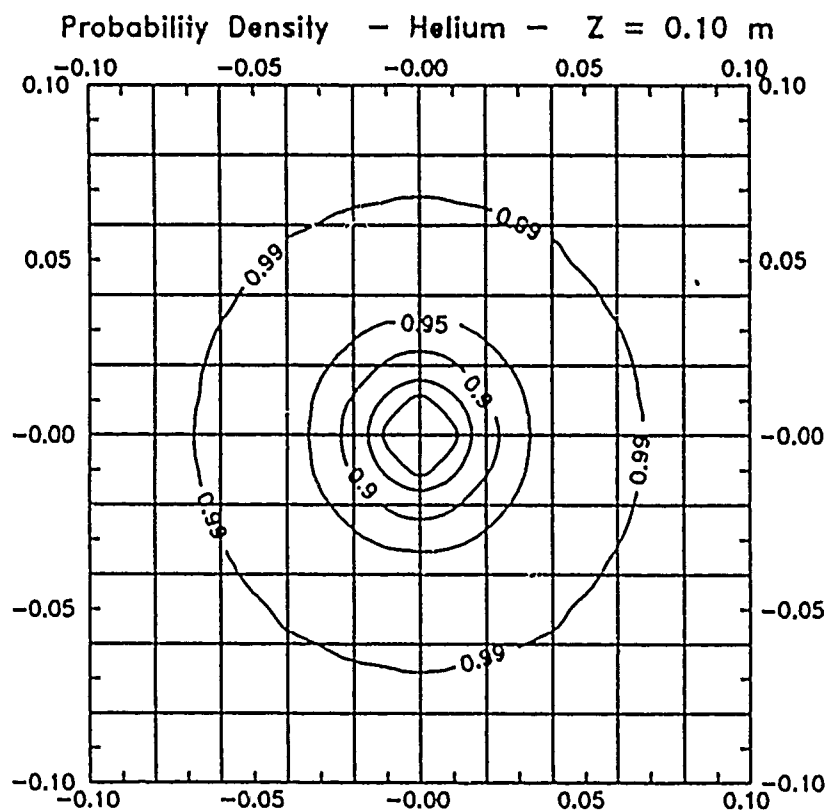
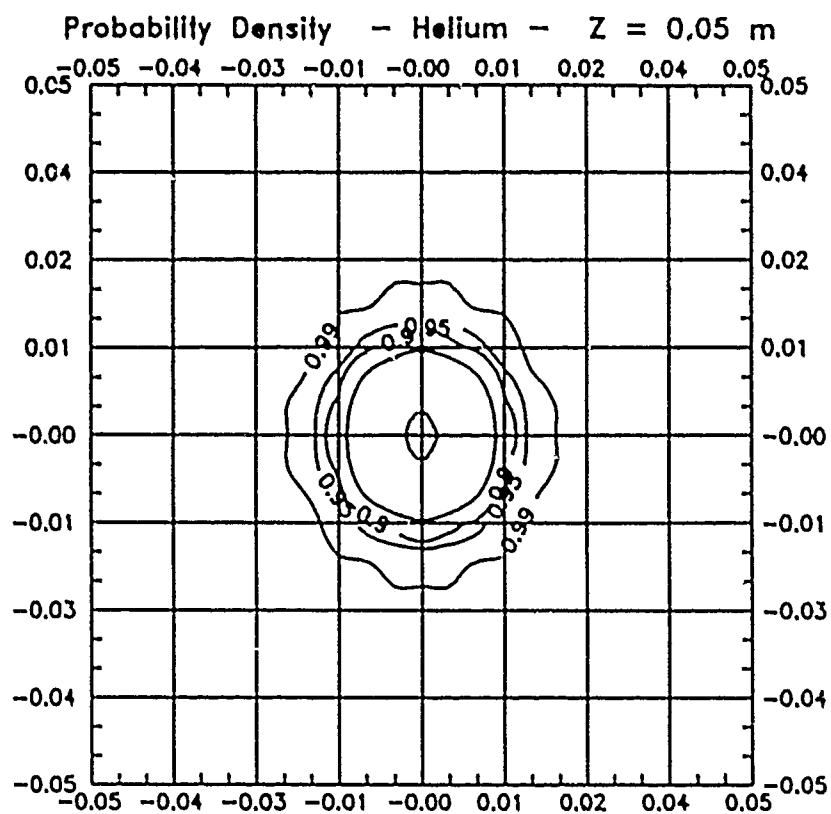


FIGURE 4

A SYSTEMATIC APPROACH TO COMBUSTION MODEL REDUCTION AND LUMPING

AFOSR Grant #AFOSR-89-0070

Principal Investigators:

Herschel Rabitz
Department of Chemistry
Princeton University
Princeton, NJ 08544-1009

Fred Dryer
Department of Mechanical and
Aerospace Engineering
Princeton University
Princeton, NJ 08544-1009

SUMMARY OVERVIEW:

This research is concerned with the development and application of new techniques for reducing the complexity of kinetic schemes arising particularly in combustion systems. Advanced techniques from sensitivity analysis, formal system lumping and Lie Group theory are being adapted for this purpose. The emphasis in this work is on the systematic aspects of model reduction including the assessment of whether a given system may be reduced successfully and the development of practical means for doing so. This work is being carried out in collaboration with Dr. R. Yetter at Princeton and Dr. G. Wulfman at the University of the Pacific.

TECHNICAL DISCUSSION:

Realistic combustion systems inevitably involve complex chemical reactions as well as transport processes. An important goal of combustion measurements and theory is the achievement of practical models ultimately for design purposes. Serious limitations will arise if it becomes necessary to include the full complexity of the chemical processes as well as transport. This realization has motivated a number of attempts to generate lumped or reduced combustion mechanisms. These latter efforts have largely been guided by intuition, and the present research is concerned with the development and application of a systematic means for this purpose. The overall problem is a complex one and several approaches are being simultaneously pursued as described below.

A. Application of local sensitivity analysis for model reduction. This work has been concerned with the calculation of local sensitivity gradients and their utilization as indicators of model reduction. In particular, we have studied laminar premixed flames involving complex mechanisms. Calculations were performed on H_2 -Air systems. Sensitivity functions were evaluated and studied for the diffusion-free situations, both isothermal and adiabatic, as well as for steady premixed flames. In the diffusion-free cases, most reactions of the 38-step mechanism were shown to be influential in a distinct fashion. The form of the sensitivity functions was, however, radically changed and rendered self-similar by simultaneous thermal coupling and diffusion that introduced strong nonlinear coupling among the variables. Due to self-similarity within the sensitivity coefficients, the mechanism was reduced to 15 reactions while keeping the temperature profile and the mass fraction profiles of the molecular species almost unchanged in the flame calculations. Furthermore, there existed an invariant subspace in the space

of kinetic parameters such that large parameter perturbations along any vector in the subspace resulted in relatively small changes in the component flame properties. It was thus possible to identify a sequence of reduced models. It was found that the existence of these reductions depended critically on the presence of molecular and thermal diffusion.

B. A general analysis of approximate lumping in chemical kinetics. This research is based on applying formal matrix projection techniques to the kinetic equations with an emphasis on establishing the rigorous criteria for system lumping. These criteria have now been utilized to establish a general analysis for approximate lumping. Under the constraint that the lumped equations have the same general form as the original set, this analysis can be applied to any reaction system with n species described by $dy/dt = -f(y)$, where y is an n -dimensional vector and $f(y)$ is an arbitrary n -dimensional function vector. We considered lumping by means of a rectangular constant matrix M (i.e., $\hat{y} = My$, where M is row-full rank matrix and \hat{y} has dimension \hat{n} not larger than n). The lumped kinetic equations have the same form $d\hat{y}/dt = -Mf(My)$ as that for an exactly lumped one, but depend on the choice of the generalized inverse \bar{M} of M . When the lumping matrix M satisfies the restriction $MM^T = I_{\hat{n}}$, M^T is a good choice of the generalized inverse of M . The equations to determine the approximate lumping matrices M have been developed. These equations can be solved by iteration. An approach for choosing suitable initial iteration values of the equations was illustrated by several examples. The overall utility and limitations of this approach are being explored.

C. Lie group techniques for global kinetic analysis. This work, particularly in contrast to that of paragraph A above, is based on determining and analyzing global sensitivity behavior of kinetic systems. This work is being carried out by means of special Lie groups. We have been able to establish a number of properties of the transformation groups that map elementary kinetic equations into new elementary kinetic equations with locally altered rate constants. The chemical significance of these transformations has been assessed by applying them to nonlinearly coupled kinetic systems. Twelve distinct groups of mappings were identified. Some of the mappings were effective in making changes in input/output fluxes on concentrations and their compensation by changes in other rate constants. A number of mappings will transform nonlinear kinetic equations into approximately linear kinetics valid in regions larger than those obtained by standard methods. In special cases the linearization is globally exact. Some mappings may also create lumped concentration variables to systematically simplify the number of kinetic equations. The global mappings may be characterized by the functions of rate constants and concentrations that they leave invariant. Although the mappings can produce large changes in the rate constants and concentrations, none of these mappings change the topology of the concentration phase plots as they map a phase plot determined by one set of initial conditions and rate constants into that determined by transformation of initial conditions and rate constants. Current work with these Lie techniques is focused towards developing better approximations as well as establishing practical means for wider use of these techniques.

TRANSPORT PHENOMENA AND INTERFACIAL KINETICS IN MULTIPHASE COMBUSTION SYSTEMS†

AFOSR Grant No. 89-0223

Principal Investigator: Daniel E. Rosner‡
High Temperature Chemical Reaction Engineering Laboratory
Department of Chemical Engineering, Yale University
P.O. Box 2159 YS; New Haven, CT 06520

SUMMARY/OVERVIEW

The performance of ramjets burning slurry fuels (leading to condensed oxide aerosols and liquid film deposits), gas turbine engines in dusty atmospheres, or when using fuels from non-traditional sources (e.g., shale-, or coal-derived), depends upon the formation and transport of small particles across non-isothermal combustion gas boundary layers (BLs). Even airbreathing engines burning "clean" hydrocarbon fuels can experience soot formation/deposition problems (e.g., combustor liner burnout, accelerated turbine blade erosion and "hot" corrosion). Moreover, particle formation and transport are important in many chemical reactors used to synthesize or process aerospace materials (turbine blade coatings, optical waveguides, ...). Accordingly, our research is directed toward providing chemical propulsion systems engineers and materials-oriented engineers with new techniques and quantitative information on important particle- and vapor-mass transport mechanisms and rates.

An interactive experimental/theoretical approach is being used to gain understanding of performance-limiting chemical-, and mass/energy transfer-phenomena at or near interfaces. This includes the development and exploitation of seeded laboratory flat flame burners (Section 1), flow-reactors (Section 3), and new optical diagnostic/spectroscopic techniques. Resulting experimental rate data, together with the predictions of asymptotic theories, are then used as the basis for proposing and verifying simple viewpoints and effective engineering correlations for future design/optimization studies.

TECHNICAL DISCUSSION

1. SEEDED FLAME EXPERIMENTS ON SUBMICRON PARTICULATE TRANSPORT RATES

As described in recent years, we have developed and exploited seeded, atmospheric pressure flat flame burner techniques combined with laser optical probing of chemically inert, reflective targets (e.g., Pt ribbons) and diffusion boundary layers to study rates of chemical vapor deposition, submicron particle deposition and condensate evaporation (e.g., $B_2O_3(l)$, $Na_2SO_4+K_2SO_4(l)$) under well-characterized conditions amenable to theoretical investigation (Section 2) and systematic physicochemical model development. During this past year our emphasis has been on the development of a $TiCl_4(g)$ -seeded low strain-rate counterflow diffusion flame technique (Fig. 1) for determining the thermophoretic diffusivity, $(\alpha_T D)_p$, of flame-generated submicron $TiO_2(s)$ "soot" particles. Our diffusivity inference is based on the existence of an easily measured thermophoretically-induced particle-free ("dark") zone on either side of the diffusion flame sheet. Earlier we reported (Gomez *et al.*, 1988) that inferred $(\alpha_T D)_p$ -values based on *observed* dark-zone thicknesses and *observed* (thermocouple) temperature gradients, but *computed* gas velocities were within 10% of values expected using a Waldmann's kinetic theory approach for spherical particles. By using LDV (radial) velocity measurements on N_2 -diluted flames we have now confirmed these earlier estimates and are studying the dependence of the inferred $(\alpha_T D)_p$ on carrier gas momentum diffusivity (using helium substitution). The ability to

† AFOSR/ONR Contractors Meeting on Propulsion Ann Arbor, MI, 19-23 June, 1989

‡ For research collaborators consult REFERENCES

reliably measure and ultimately predict thermophoretic diffusivities of flame-generated particles (carbonaceous soot, Al_2O_3 , SiO_2 , TiO_2 , ...) will be important to many technologies, including chemical propulsion, materials fabrication, and hot gas "clean-up".

2. MULTIPHASE TRANSPORT THEORY

Because of increasing interest in the Soret diffusion of large, highly nonspherical molecules (e.g., polycyclic aromatic soot precursors and large metal-organic vapors used to deposit thin films with useful optical properties) and the thermophoretic transport of nonspherical submicron particles (e.g., long soot aggregates) we are continuing our work on predicting the *shape*- and orientation-dependence of their thermal diffusion velocities (Garcia-Ybarra & Rosner, 1989), including the implications of these effects for agglomeration rates (Park & Rosner, 1989a). Of course, particle size and shape also affect Brownian diffusivities, and we are simultaneously developing useful engineering methods for predicting total mass deposition rates from 'coagulation-aged' *distributions* of particles — including 'fractal' agglomerates (see, e.g., Rosner, 1989; and Rosner & Tassopoulos, 1989). For convective-diffusion deposition Fig. 1 shows the predicted ratio of the *actual* mass deposition rate to the (reference) rate corresponding to the hypothetical case of all particles in the population having the average size (volume), $\bar{v} = \bar{v}_p/N_p$, as a function of the spread of the (lognormal) particle size (volume) distribution function.

The competition between particle *inertia* and particle thermophoresis has also been clarified, especially for the case of axisymmetric laminar impingement flows toward overheated (or undercooled) solid surfaces (Park & Rosner, 1989b). Figure 2 shows the predicted dependence of the "critical" Stokes number ($\tau_p/\tau_{\text{flow}}$) for inertial impaction on the wall temperature-ratio and particle mass loading. In the presence of appreciable *radiation* energy fluxes, photophoretic ("radiometric") effects can also become important for intermediate size absorbing particles. Castillo *et al.* (1989) have shown that this effect, like inertia (Fig. 2) can drive 'illuminated' particles on to an "overheated" surface. For undercooled surfaces ($T_w/T_g=0.7$) Fig. 3 shows the predicted dependence of mass transfer coefficient on carbonaceous particle radius (in multiples of the gas mean free-path) and the radiation/Fourier (conduction) heat flux ratio (i.e. the curve marked zero corresponds to the radiation-free (reference) case). In situations where the radiative fluxes to the wall are comparable to the 'convective' (conductive-) fluxes (i.e. $q_R/q_F = O(1)$) we anticipate (Castillo *et al.*, 1989) a noticeable (ca. 10%) increase in the deposition rates of such particles.

3. GASIFICATION KINETICS OF SOLID BORON AND PYROLITIC GRAPHITE

Because of the energetic potential of boron as solid fuel (or fuel additive) and the likely role of *surface* reactions involving the gaseous oxidants $\text{O}_2(\text{g})$ and $\text{B}_2\text{O}_3(\text{g})$ in the processes of fine boron-particle ignition, combustion and extinction, we are obtaining new flow reactor measurements of the intrinsic kinetics of the gasification of $\text{B}(\text{s})$ at surface temperatures between about 1300K and 2100K (Zvuloni *et al.*, 1989a). Some of the propulsion implications of these measurements can be demonstrated with the help of a diagram (Fig. 4) of (log) particle diameter vs (log) chamber pressure, which not only displays the onset of non-continuum behavior but also the locus of expected particle *extinction* due to "passivation" associated with the kinetically-controlled onset of condensed B_2O_3 at the gas/solid interface.

To make rapid-response gas/solid reaction rate measurements over a large temperature range, we have recently been improving and exploiting a sensitive spectroscopic technique called *microwave-induced plasma excitation* (MIPE) in which characteristic line emissions from atoms in the gaseous product species of a gas/solid reaction are monitored in a low pressure flow reactor (Fig. 5). This is a modified version of our transonic, vacuum flow reactors developed earlier under AFOSR-support for studying important gas reactions with refractory solids (metals, semi-metals, ceramics). The reaction *product* vapor species are dissociated and photon emission from the resulting boron (or carbon)-atoms is caused by interaction with the products of a microwave discharge plasma before leaving the reactor. The oxidant $\text{B}_2\text{O}_3(\text{g})$ is generated from an upstream electrically heated folded metal "boat" (vaporization) source. Our results for the inferred reaction probability, ϵ , over the broad surface temperature range from ca. 1300K to 2050K are displayed in Fig. 6. Note that above about 1400K (at the stated reactant pressure level) this gas/solid

chemical reaction is remarkably efficient — more so than boron gasification by $O_2(g)$, $O(g)$, $H_2O(g)$ or $CO_2(g)$. This implies that $OBOBO(g)$ is able to efficiently chemisorb over a broad temperature interval, thereby delivering an O-atom to form the expected gaseous product molecules (BO_2 and BO). Also of considerable interest is the location of the "low temperature break" in the Arrhenius diagram — i.e. the surface temperature below which the kinetics reveals oxide-layer 'protective' behavior at the prevailing oxidizer and water vapor partial pressure.

Apart from studying the (surprisingly modest) effects of the simultaneous presence of $H_2O(g)$ on the abovementioned surface reactions (Zvuloni *et al.*, 1989b), we have initiated mass-loss measurements of the remarkably efficient gasification of pyrolytic graphite by $OBOBO(g)$ (Zvuloni *et al.*, 1989c). Indeed, we report experimental and thermochemical evidence that at surface temperatures near 2000K, not only is each arriving $OBOBO(g)$ molecule able to chemisorb, but each of its three O-atoms is able to form a CO molecule which desorbs from the surface (along with 2 "naked" B-atoms). These measurements, which are continuing with AFOSR support, may have important implications for boron-containing systems in which suspended organic soot, and/or pyrolytic graphite containment walls, are present.

CONCLUSIONS, FUTURE RESEARCH

In the OSR-sponsored Yale HTCRES Lab research during 1988-1989, only briefly described here, we have shown that new methods for rapidly measuring vapor- and particle-mass transfer rates, combined with recent advances in convective mass transfer theories, provide useful means to incorporate important, but previously neglected, mass transport phenomena in many propulsion engineering and materials engineering design/optimization calculations. We are now extending our work on the potentially important effects of new "phoretic" phenomena, high local particle mass loading, 'polydispersed' particle populations, non-negligible particle inertia, and highly nonspherical particles, aggregates (or molecules). To shed light on boron particle ignition, quasi-steady combustion and extinction, we are studying the remarkably efficient $B_2O_3(g)/B(s)$ reaction and its $B_2O_3(g)/C(s)$ analog in the broad temperature interval: 1300K-2100K, both in the absence and presence of $H_2O(g)$. We are also supplementing these gasification kinetic studies with preliminary experimental/theoretical studies of the *condensation* kinetics of $B_2O_3(g)$.

REFERENCES

- Castillo, J.L., Mackowski, D.W., and Rosner, D.E., "Photophoretic Contribution to the Transport of Absorbing Particles Across Combustion Gas Boundary Layers", presented at ACS 197th Annual Meeting — *Symposium on Ash Deposition*, Dallas, 9-14 April (1989); *Progress in Energy and Combustion Science* (to appear).
- Garcia-Ybarra, P., and Rosner, D.E., "Thermophoretic Properties of Small Nonspherical Particles and Large Nonspherical Molecules," *AIChE J.*, 35, [1], 139-147 (1989).
- Gomez, A., and Rosner, D.E., "Applications of Counterflow Diffusion Flames to the Determination of Particle Thermophoretic Diffusivities", (poster) *22nd Int. Combustion Symposium*, Seattle, WA (August, 1988).
- Park, H.M., and Rosner, D.E., "Dopant Redistribution Across Aerosol-Laden Laminar Non-Isothermal Boundary Layers", *Chem. Engrg. Sci.* 44, [3], 603-617 (1989a).
- Park, H.M., and Rosner, D.E., "Combined Inertial and Thermophoretic Effects on Particle Deposition Rates in Highly Loaded Dusty Gas Systems", *Chemical Engrg. Science*, (in press 1989b)
- Rosner, D.E., and Tassopoulos, M., "Mass Deposition Rates from Streams Containing 'Polydispersed' Particle Populations of Arbitrary Spread", *AIChE J.* (in press, 1989)
- Rosner, D.E., "Total Mass Deposition Rates from 'Polydispersed' Aerosols", *AIChE J.* 35, [1], 164-167 (1989)
- Zvuloni, R., Gomez, A., and Rosner, D.E., "Direct Measurements of the High Temperature Kinetics of Solid Boron Gasification by its Higher Oxide $B_2O_3(g)$: Chemical Propulsion Implications", *A.I.A.A. J. Propulsion and Power* (submitted, 1989a)
- Zvuloni, R., Rosner, D.E., and Gomez, A., "Role of Water Vapor on the Gasification Kinetics of Solid Boron by its Higher Oxide $B_2O_3(g)$ ", (in preparation, 1989b)
- Zvuloni, R., Rosner, D.E., and Gomez, A., " $OBOBO(g)$ as a Gasifier of Graphite: Measurements and Implications", (in preparation, 1989c)

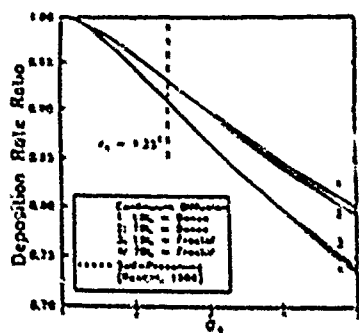


Figure 1. Deposition rate ratio, R_d , vs the standard deviation σ_g of the aerosol (%) for continuum diffusion of dense or dilute particles through laminar (L) or turbulent (T) boundary layers.

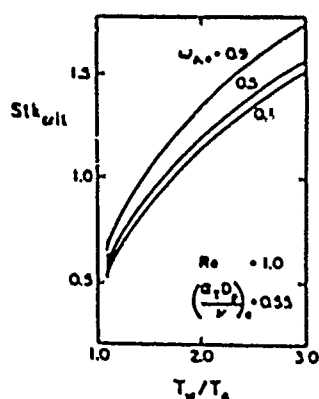


Figure 2. Variation of the critical Stokes number for particle impaction with "overheat" temperature ratio, T_w/T_0 , at several feed stream particle mass loadings, $\omega_{p,e}$ ($Re_p = 1$, $(\alpha_T D_p / \nu)_0 = 0.55$).

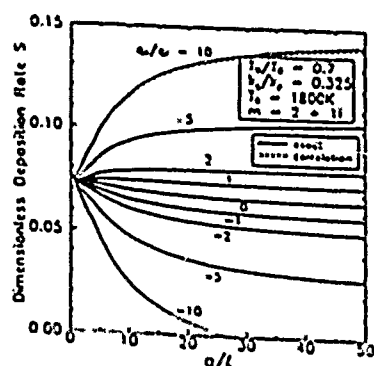


Figure 3. Predicted dimensionless deposition rates S for char-like particles as a function of the particle size parameter a/l , for a heat exchanger surface maintained at $T_w/T_0 = 0.7$ and different ratios of the radiative to conductive heat flux at the surface.

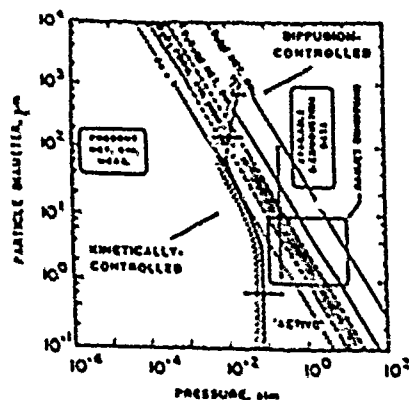


Figure 4. Boron particle combustion "map" displaying expected: 1) diffusion-controlled or kinetically-controlled regimes for $B_2O_3(g)$ and $O_2(g)$ reactions with the surface, 2) transition to non continuum behavior, 3) domains of present and past experimental investigations and principal safety interest, and 4) extinction due to surface passivation.

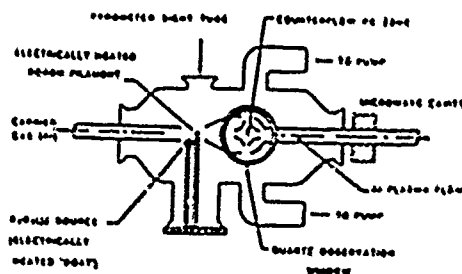


Figure 5. Flow reactor configuration for kinetic studies of gas/solid reactions using product detection via Microwave Induced Plasma Emission Spectroscopy (MIPES). Configuration shown includes "boar" source of $B_2O_3(g)$ reactant vapor upstream of transverse boron filament.

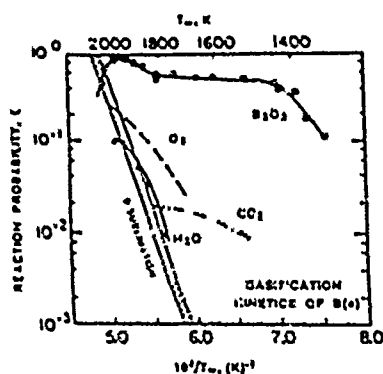


Figure 6. Experimental results (Arrhenius diagram) showing inferred reaction probabilities for gasification kinetics of solid boron by $B_2O_3(g)$, $O_2(g)$, $H_2O(g)$, and $CO_2(g)$ at reactant pressure of the order of 10^{-2} Pa.

(AFOSR Contract No. AFOSR-87-0145)

Principal Investigator: Robert J. Santoro

Department of Mechanical Engineering
The Pennsylvania State University
University Park, PA 16802

SUMMARY/OVERVIEW:

The objective of the present study is to provide a fundamental understanding of soot formation processes under conditions applicable to gas turbine operation. Specifically, the effects of fuel molecular structure and operating pressure have been selected for study using a laminar diffusion flame apparatus. Measurements of particle inception and surface growth have been of primary interest for studies conducted during the past year. Detailed measurements of the particle and velocity fields allow examination of the evolution of the soot particle field to obtain specific rate information. A primary goal of the study is to provide quantitative understanding of soot formation phenomena suitable to allow appropriate model development. These results are deemed important to remedy current shortcomings in our present understanding of such phenomena. This understanding will impact development of future gas turbine technology where operation involves burning broader specification fuels at higher pressures.

TECHNICAL DISCUSSION

During the past year, studies have concentrated on several areas of the soot formation problem. Both atmospheric and high pressure laminar diffusion flames have been investigated. A coannular diffusion flame arrangement has been used for both studies because of its demonstrated capability to produce stable flames over a range of operating conditions [1]. The measurement approaches used in these studies have emphasized non-intrusive optical diagnostic techniques, such as laser light scattering and laser anemometry. These approaches have been widely applied to the study of particle formation in several flame systems with great success [2]. The fuel molecular structure studies have been conducted in a series of flame in which the fuel of interest is added to a well characterized ethene or methane flame. This approach allows the study of fuel structure effects independent of flame size effects [3,4].

A brief summary of the accomplishments and current status of the program is given below. Following this summary, a more detailed presentation of selected aspects of the work is presented. Specifically the following tasks have been accomplished:

1. In order to begin to better understand the relationship between the soot precursor chemistry and the inception of soot particles, an investigation of the early particle formation region has been undertaken. Using laser light scattering measurements for soot particle characterization and laser fluorescence measurements for large hydrocarbon species determination, a comparison of the particle inception region for a series of fuels has been investigated. The fuels investigated include butane, 1-butene and 1,3 butadiene introduced into a methane baseline flame. The results of these studies clearly show a strong correlation between the fluorescence observed from gas phase species and the early soot particle inception and growth rates. It is hoped that these results will form a basis of comparison of these laminar diffusion flame results with detailed chemical kinetic models of soot formation.
2. In these same flames, comparisons between the specific surface growth rates for the C_4 fuels studied have been made. These studies show that when the available surface area of the soot particles is taken into account, the specific surface growth rate constant is similar

for all of the flames. This result further emphasizes the importance of the inception process, since initial surface area determines the subsequent growth of the soot particles.

3. In the studies described above, a detailed determination of the velocity field is required in order to determine the particle paths in the flame. Presently, measurements obtained in a similar ethene/air diffusion flame have been used to complete the analysis. Although these results represent a good first approximation to the velocity field, it is desirable to have the velocity field for the specific flame under study. To this end, velocity measurements in the butane/methane and 1-butene/methane flames have been obtained. Comparisons between the velocity fields for the two fuels studied, as well as for the previously measured ethene flame are presently being made. The results of these comparisons will determine the need for detailed velocity measurements in other flames to be studied.
4. A series of studies in the high pressure diffusion flame facility have been completed. In these experiments, ethene/air flames have been studied over a pressure range of one to seven atmospheres. The results of these studies are being used to examine the pressure dependence of the soot formation process and for a comparison with previous work [5].
5. Modeling efforts for these laminar diffusion flames have been initiated during the past year. Separate comparisons with models developed by R. Davis of the National Institute of Standards and Technology and C. Merkle in the Mechanical Engineering Department at Penn State have demonstrated good agreement with the measurements in terms of velocity and temperature fields for the ethene/air and methane/air flames studied.

Soot Particle Inception and Surface Growth

The early particle formation region has been extensively investigated for butane, 1-butene and 1,3 butadiene fuels which were added to a methane baseline flame. In addition to light scattering/extinction and velocity measurements, a series of fluorescence measurements were also obtained. For these measurements the fluorescence, excited by an argon ion laser tuned to the 488 nm laser line, was monitored at 514.5 nm. Fluorescence signals observed using this approach have often been attributed to large hydrocarbon species which may represent soot precursor species. The objective of these experiments was to investigate the region where soot particles are first observed and to relate fuel structure effects to changes in the soot production processes. Additionally, information on the surface growth rates under these conditions was also of interest, particularly in the region immediately following particle inception.

Although measurements were obtained throughout the flame, data in the region where the maximum soot formation occurred will be examined here. Figure 1 shows the soot volume fraction and fluorescence measurements as a function of residence time obtained along the particle path which displayed the maximum soot volume fraction. From these results it is clear that the fluorescence and soot volume fraction increase similarly as a fuel's propensity to soot increases. Additionally, the fluorescence signals are observed to precede soot particle inception and increase rapidly during the early part of soot production. Comparisons along individual particle paths indicate that between 20% and 70% of the soot growth occurs prior to fluorescence achieving a maximum value depending on the particle path location in the flame. This point raises the question of participation of these large hydrocarbon species in the early soot surface growth process. This question will be addressed below.

The combination of these fluorescence and soot particle measurements indicate that the species detected using fluorescence give a good qualitative indication of the sensitivity of the soot formation process to fuel structure effects. When combined with appropriate temperature measurements, relative comparisons between comprehensive chemical kinetic models and these measurements may serve as a test case for extending these models to diffusion flame conditions.

It is equally interesting to determine the effect of fuel molecular structure on the surface growth process for soot particles formed in diffusion flames. As mentioned above, it is also of interest to examine the role that large hydrocarbon species may have in the early surface growth process. In order to address these two questions, the soot particle growth rate has been examined. The analysis has been carried out along the same particle path for which measurements are shown in figure 1. The present approach to the analysis is to represent the soot mass growth rate as

$$\frac{dm}{dt} = k S [C_x H_y]$$

where m is the mass of soot (g/cm^3), k is the surface growth rate constant ($\text{g/cm}^2\text{-s-atm}$), S is the specific surface area (cm^2/cm^3) and $[C_x H_y]$ is the species concentration reacting with the surface to add mass [atm]. In the present experiments, the product of k and $[C_x H_y]$ can be determined since S and dm/dt can be determined from the combined light scattering and velocity measurements. This product, $k[C_x H_y]$, is termed the specific surface growth rate constant. The specific surface area is calculated from the particle diameter and number density measurements while the soot mass growth rate can be found from the measured soot volume fraction assuming the density of soot particles is 1.8 g/cm^3 . Figure 2 shows the specific surface growth rate constant for the present C_4 fuels studied. The behavior for each fuel is similar. Shortly after the particles are formed, the specific surface growth rate is close to $2 \times 10^{-4} \text{ g/cm}^2\text{-s}$. After a period for which this rate constant is approximately constant, the surface growth rate drops rapidly. It should be pointed out that the present analysis has been limited to the region of the flame before the soot volume fraction reaches a maximum. Thus, regions where soot particle oxidation dominates have been excluded from consideration.

From these extensive studies, it is clear that the surface growth process is similar in all the flames studied here. Furthermore, since accounting for the differences in available surface area substantially explains differences in the growth processes for flames of widely differing soot concentrations, the value of the initial surface area is critical to subsequent surface growth. Additionally, comparisons along the centerline of these flames show that similar values of specific surface growth rate are found throughout the flame for the fuels studied.

Before making further observations concerning the present status of the understanding in the area of soot particle surface growth, some discussion of the effect of the fluorescing species in this process is appropriate. Clearly, if the initial surface area is important in all subsequent growth, species involved in the first stages of surface addition should be carefully examined. To quantify the contribution of large hydrocarbon species attributed as the source of the observed fluorescence, a series of highly spatially resolved radial profiles of the soot particle field were obtained for closely spaced intervals along the axis of the flame. These profiles correspond to the earliest data points shown in figures 1 and 2. No systematic increase in the specific surface growth rate constant is observed. Thus, the present data does not support a model in which the species observed in the fluorescence measurements contribute extensively to the surface growth in the region immediately following particle inception. These species may contribute to the particle inception process.

The experiments described in the last two sections have identified some key questions for consideration. The surface growth process has been shown to be similar for a variety of fuel structures and sensitive to the initial surface area available for growth. Thus, a quantitative understanding of the relationship between the soot precursors and this initial surface area is required for a more complete description of soot formation. The present approach of concentrating on the initial particle inception region is sound, but it needs to be expanded in terms of diagnostic approaches and quantities measured.

REFERENCES

1. Santoro, R. J., Yeh, T. T., Horvath, J. J. and Semerjian, H. G., *Combustion Science and Technology*, 53, 89 (1987).
2. Santoro, R. J., "Fuel Molecular Structure Effects on Soot Particle Growth in Diffusion Flames," Twentieth Fall Technical Meeting of the Eastern Section of the Combustion Institute, Gaithersburg, MD, Nov. 2-5, 1987.
3. Richardson T. F. and Santoro, R. J., "Soot Growth in Diffusion Flames Burning Fuel Mixtures," 1988 Fall Technical Meeting of the Eastern Section of the Combustion Institute, Clearwater Beach, FL, Dec. 5-7, 1988.
4. Santoro, R. J., "Optical Measurements of Soot Particles in Flames," *Mat. Res. Soc. Symp. Proc.* vol. 117, p. 157 (1988).

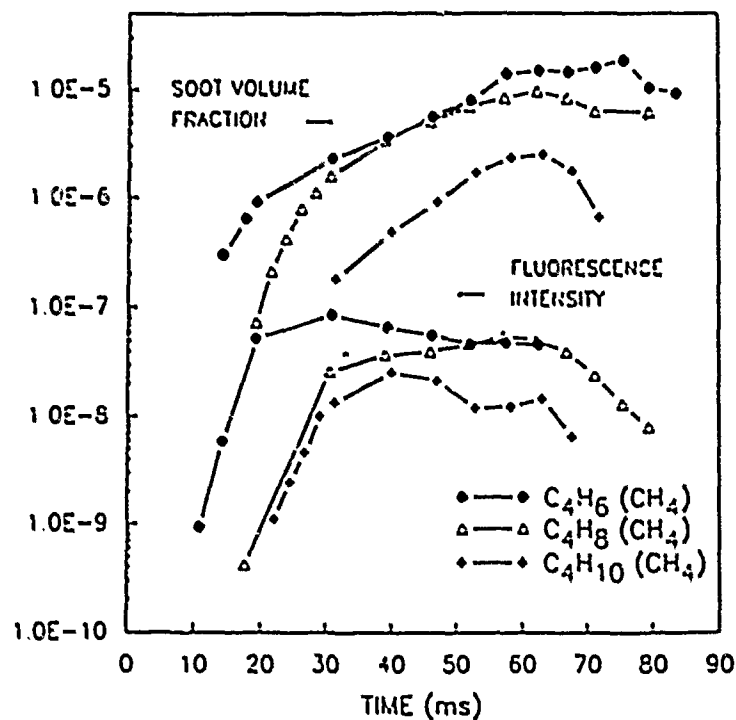


Figure 1 The soot volume fraction and fluorescence measurements along the particle paths of maximum soot concentration in the annulus region.

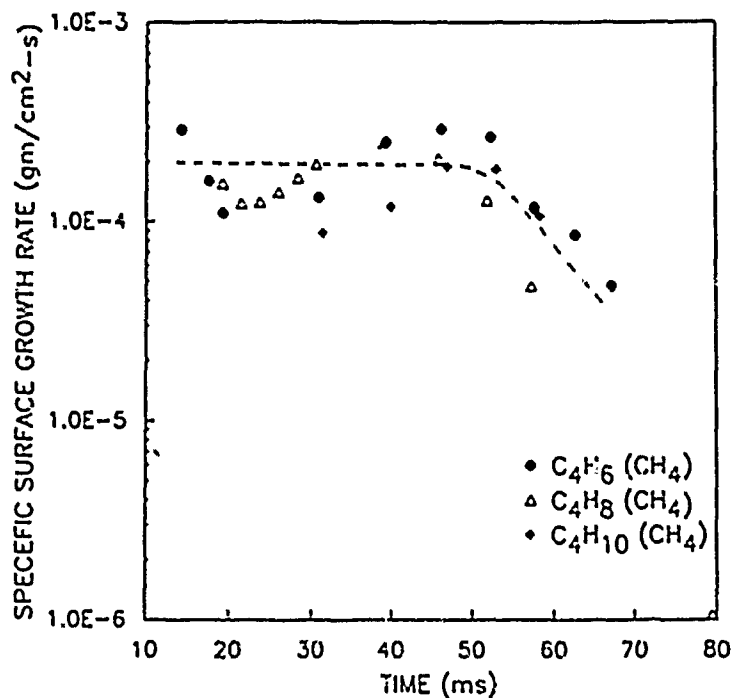


Figure 2 The specific surface growth rate vs. time for the butane, 1-butene and 1,3 butadiene addition studies to the methane baseline flame. Results along the particle path containing the maximum value for the soot volume fraction.

CHEMICAL KINETIC DATA BASE FOR PROPELLANT
COMBUSTION

(AFOSR CONTRACT-issa-89-0052)

Principal Investigator: Wing Tsang

Chemical Kinetics Division
National Institute of Standards and Technology
Gaithersburg, Maryland 20899

Summary:

This work is aimed at the development of an evaluated chemical kinetic data base of single step reactions for use in the computer simulation of propellant combustion. Our initial efforts are aimed at the gas phase reactions involved in RDX decomposition. All of the possible reactions involving 28 of the most likely compounds that are present in such decomposition systems are considered. The work involves the collection and evaluation of mechanistic and rate information in the literature and the use of various methods for the estimation of rate data where information does not exist. The conditions to be covered will range from 500-2000 K and 10^{17} - 10^{20} particles/cm³. This work is part of a general effort and is also supported by ERL, AFAL and ONR and was initiated during the current year.

Technical Discussion:

Quantitative understanding of the detailed chemical kinetics of propellant combustion can have important impacts on the formulation of such mixtures, the optimization of currently operating systems and the design of new combustors. An important complicating factor has been the scores of rate constants of elementary processes that are needed to give a complete description of the process. For many years, the necessary experimental tools and theoretical understanding were not available for the development of such a chemical kinetic information base. Furthermore, until recently, accompanying such understanding is also the necessity of identifying key reactions and developing sufficiently simple mechanisms. This is not an easy task. With these two major impediments, it is not surprising that much work in this area, as far as the chemistry is concerned, has been empirical in nature. This implies the necessity of constant physical testing. The expense of such efforts is a severe limitation on innovative efforts in this area.

This work is aimed at developing a chemical kinetic data base aimed at applications in propellant combustion. The major impetus for such an effort is the confluence of a number of exciting technological developments. These include;

a) Rapid progress in computational capabilities, so that the simulation of increasingly realistic physico-chemical systems are well or will be within our capabilities. Thus the information in a chemical kinetic data base can be immediately used.

b) Development of experimental and theoretical capabilities in chemical

kinetics, so that the needed rate constants can be measured or estimated.

c) Extensive applications of powerful modern diagnostic techniques to laboratory systems, so that we are developing much better pictures of the micro-structure in both a physical and chemical sense of combustion systems. The interpretation and the projection of such results to real systems is however crucially dependent on the existence of a correct detailed model. Given the large number of parameters one can always "fit" a particular experimental observation. Only the model with the correct inputs can be expected to project results to real systems.

In the course of a recent survey, there appear to be a general consensus that the most useful propellants to be studied are the "double base" nitrocellulose/nitroglycerine types, nitramines, ammonium perchlorate and ammonium nitrate. It is our intention to cover in time the gas phase reactions pertinent to the decomposition of all these substances and with appropriate binders. The work aims to develop a data base that will permit the simulation of many aspects of RDX combustion. Note that many of the species and reactions to be considered will actually be components of the data base dealing with double based propellants or ammonium nitrate. Indeed addition of Cl, HCl and the chlorine oxides will bring in ammonium chloride. Connecting the propellant and hydrocarbon data base will permit us to include binder chemistry.

The physical conditions to be covered are 500-2000 K in temperature and $10^{17} - 10^{20}$ particles/cm³. The lower temperature limit is slightly lower than the boiling point of RDX.

The compounds that we will consider are listed in the reaction grid in Figure 1. There can be little question regarding the inclusion of the small species (4 atoms or less) in the listing. Indeed they include practically all the possibilities. Many of these species have been detected in experiments involving RDX. Other are natural precursors or products of these compounds.

The selection of the larger fragments is more speculative. Most of these have not been detected and the possibilities are considerably larger than the number of species that we have chosen. Mechanistic considerations enter in the selection and the following represents our rationale. First, note that the only none six-membered ring species are H₂CNNO₂ and H₂CNH. The former may well be an important initial product and is certainly an important secondary product. The latter is the result of the displacement of the NO₂ group from the former. It can also be formed from H₂CN* attack on a hydrogen containing species. We have not included H₂CNNO. The N-N bond energy in this compound is 18 kcal. This will imply a lifetime of the order of 0.1 microsec or less at 500K. In the course of this analysis we will generally use an activation energy for unimolecular reaction below 20 kcal as a cut off. At or below this number we will regard rate as essentially instantaneous.

In the following we review briefly how we proceed with our evaluations. Having decided on the species to be included in the data base we begin by determining the thermodynamic properties. For many of the stable species the existing JANAF data base is accepted. The properties of the unstable

	0.	1.	2.	3.	4.	5.	6.	7.	8.	9.	10.	11.	12.	13.	14.	15.	16.	17.	18.	19.	20.	21.	22.	23.	24.	25.	26.	27.	28.
0. H		H																											
1. H ₂		H ₂																											
2. H ₂ O		H ₂ O																											
3. O*		O*																											
4. H*		H*																											
5. OH*		OH*																											
6. HCHO		HCHO																											
7. CHO*		CHO*																											
8. CO		CO																											
9. NO		NO																											
10. NO ₂		NO ₂																											
11. HNO		HNO																											
12. HNO ₂		HNO ₂																											
13. HCN		HCN																											
14. N ₂ O		N ₂ O																											
15. CN*		CN*																											
16. HCCO		HCCO																											
17. NCO*		NCO*																											
18. H ₂ CN*		H ₂ CN*																											
19. H ₂ CNH		H ₂ CNH																											
20. H ₂ CNNO ₂		H ₂ CNNO ₂																											
21. NO ₃ *		NO ₃ *																											
22. HNO ₃		HNO ₃																											
23. RDX		RDX																											
24. RDX-NO ₂ *		RDX-NO ₂ *																											
25. RDX-NO ₂ +H		RDX-NO ₂ +H																											
26. RDX-HNO ₂		RDX-HNO ₂																											
27. RDX-NO*		RDX-NO*																											
28. RDX-O		RDX-O																											

Figure 1: Reaction Grid

A: From Hydrocarbon Combustion Data Base

B: Current Work (x represent data sheets being prepared)

C: Next years work

species, many of them radicals, are subject to many uncertainties. For many of these cases we have carried out our own analysis. These are usually based on the existing kinetic data, since it is our experience that for unstable species the most reliable results are obtained from rate data in both directions, thus leading to an equilibrium constant. Since the entropies of most larger organic molecules can in general be calculated with a high degree of confidence, the heats of formation can then be deduced with high accuracy.

There is at present no standard method for carrying out data evaluation in chemical kinetics. Our experience in these matters has led to the following procedure. First preference is given to experimental determinations where the mechanism is clear-cut. Frequently, this is from direct determinations of the rate of disappearance or appearance of reactants or intermediates in real time. We have also found that in a complex (or apparently complex) situation where care and complete final (stable) product analysis are carried out very useful results can be achieved. In many cases these may not be individual rate constants, but very accurate ratios of rate constants. In this manner we are frequently able to generate a very accurate network of reactions. In the absence of kinetic data, thermodynamic considerations in the form of detailed balance are used. In other cases, rate constants are assigned on the basis of analogy or thermokinetic information. In all cases we assign an uncertainty value to

our recommendations. It should be realized that this is a subjective number. It is based on the intercomparison of data sets, considerations imposed by related reaction mechanisms and the constraints imposed by thermodynamics and theory. Quantitatively, it means that the user of the data should feel free to adjust the rate constant in his models within these limits.

Rate theory is used in these evaluations purely as a method of extrapolation. For metathetical reactions involving H-atoms the Bond-Energy and Bond Order method of Johnston was used to derive the transition state structure or alternatively the curvature of the Arrhenius plots for these reactions. We have found with others that the BEBO method does not lead to accurate absolute values of the rate constants. However the transition state structures are reasonable. It is interesting to note that the resulting curvature varies from T^2 to T^4 range, where the smaller values are characteristic of atoms and the larger values that of polyatomics. Unfortunately there is a distinct lack of data covering large temperature ranges so that we do not really have the definitive evidence that our predictions are absolutely reliable.

Unimolecular reactions in the broadest sense, including not only decompositions and isomerizations but also combination and chemical activation processes, are rendered more complex than metathesis reactions by their dependence not only on temperature but also on the nature of the bath gas. There is at present a fully developed calculational method, the RRKM procedure, which provides a framework for projecting data over all relevant pressure and temperature ranges. We have applied this technique for a large number of reactions. The results have proven to be very satisfactory in correlating in a wide variety of data. The consistencies in the collisional efficiencies that we have derived have led us to use the general method for predictive purposes.

The reaction grid in Figure 1 is divided into a number of blocks. Block A consists of the reactions involved with formaldehyde oxidation. We have already prepared data sheets for these reactions. Block B contains reactions involving the smaller nitrogenated species. It is the target of current work. With its completion it should be possible to model HCHO-NO_2 combustion systems. Block C contains reactions to be considered during the next fiscal year. It will permit us to model HCN combustion systems. We have therefore the means of validating the data during the course of the work. It is expected that the overall process will involve continuous iteration between data evaluators, modelers and experimenters. A similar procedure have worked with marked success for the stratospheric ozone problem.

DIAGNOSTICS FOR RESEARCH IN ATOMIZATION AND TURBULENT TWO-PHASE FLOWS

(AFOSR Contract no. F49620-86-C-0078)

Principal Investigator: William D. Bachalo

Aerometrics, Inc.
Sunnyvale Technology Center
894 Ross Drive, Unit 105
Sunnyvale, CA 94089

SUMMARY/OVERVIEW:

Experimental research in atomization and the interaction of the dispersed particles with the turbulence is being supported by the development of the instrumentation and measurement techniques. The basic light scattering theories are being advanced to enable the optimization of the available techniques and to aid in the development of new methods, as well as to respond to the contradictory results of others. Because of the complex behavior associated with the interaction of the particle field and the turbulent continuous phase flow, methods have been developed to extend the available information on these phenomena.

TECHNICAL DISCUSSION:

Advances in the Phase Doppler Method:

The phase Doppler method which is capable of measuring the particle size and velocity, number density, flux, and temporal behavior of the particles, in addition to the continuous phase mean velocity and turbulence parameters, is relatively mature in its development. However, because of its importance and wide application in spray combustion research, the remaining questions on the light scattering phenomena needed to be resolved. Theoretical analyses by others [1] have indicated that the application of the phase Doppler method, under certain optical configurations, will lead to large errors and that the resolution may be insufficient to separate the gas phase and dispersed phase velocity measurements [2]. These results were in contradiction to our theoretical and experimental observations.

During the last period, the geometrical optics approach was extended to include all of the light scattering components as well as the effects of the nonuniform illumination of the particle due to the Gaussian beam. Furthermore, the light scattering theory has been developed to account for the particle trajectory through

Although the geometrical optics theory produced results that were in excellent agreement with the experiments [3], the question regarding the minimum size sensitivity required the development of the Lorenz-Mie theory for the phase Doppler configuration. In general, the Lorenz-Mie theory is used for particles $< 20 \mu\text{m}$ for which the assumption of uniform particle illumination holds. The models differ only in the manner in which the scattering amplitude functions, $S_{mn}(\theta_n)$ are computed. In both cases, the scattering amplitude functions are computed at points forming a mesh over the receiver lens aperture. The amplitude functions are complex and are related to the complex electric field, E_{mn} by

$$E_n = \frac{t}{k_n r} e^{-i(k_n r + \omega t)} \cos \phi_n S_{1n}(\theta_n)$$

assuming that the incident electric field is linearly polarized. In the equation, k_n and ω_n are the wave number and frequency, respectively, of the scattered light for the n th incident beam and r is the distance from the probe volume to the respective point (x', y') on the receiver lens. The scattered light from each of the two beams will interfere at the plane of the receiver to yield a light intensity that varies temporally at the Doppler difference frequency ω_d and spatially as a result of the phase shift produced by the particle. The scattering intensity is expressed as

$$I_m(x', y') = (|E_{m1}|^2 + |E_{m2}|^2)/2 + |E_{m1}||E_{m2}|\cos(\omega_D t + \beta_{m2} - \beta_{m1}) \quad (3)$$

for $m=1,2$

The terms β_{m1} and β_{m2} are the phases of the scattered light fields. Integration of the scattered light intensity over the segments of the receiver lens through which the light reaches the respective detectors produces the resulting intensity seen by the photodetectors as

$$T_j = \frac{1}{A_j} \sum_{x'y'} \sum_{m=1}^2 I_m(x', y') \Delta x' \Delta y' \quad (4)$$

$$= D_j + C_j \cos(\omega_D t + \eta_j) \quad \text{for } j=1,2,3$$

where A_j is the area of the segment over which light is received for the j th detector, $\Delta x'$ and $\Delta z'$ are the integration mesh sizes, m indicates the polarization direction, and D_j and C_j are the dc and ac levels of the output of the j th detector.

Direct comparisons between the geometrical optics approach and the Lorenz-Mie theory are shown in figure 1. It is interesting to note that the linear fit is in excellent agreement with the simple geometrical optics theory first posed by Bachalo [4]. However, the detailed theories are necessary to show the oscillations in the response function which serves to define the theoretical resolution limits on the

method. Modifications to the optical system to improve the resolution were derived using the Lorenz-Mie theory. Figure 2 shows that a resolution to within $0.3\ \mu\text{m}$ is possible for particles as small as $0.3\ \mu\text{m}$. This capability is important in discriminating the velocity of the gas phase from that of the dispersed phase. Previous predictions [2] implied that the resolution was limited to 2 to $3\ \mu\text{m}$. Our predictions have been verified by experiments. Figure 3 shows the results for a mixture of 5 different particle sizes. The measurements agreed to within $0.5\ \mu\text{m}$ but the system was not fully optimized.

The capability to perform temporal analyses on the two-phase flow data was developed. Particle time of arrival is measurable to within $0.6\ \mu\text{s}$. This capability is fundamental to the evaluation of velocity and concentration bias errors. In addition, the time of arrival information has provided insights to the interaction of fuel sprays with large scale turbulent eddies [5]. As an example, figure 4a shows the formation of drop clusters in a swirl stabilized spray flame with local number densities, an order of magnitude greater than the long time average. The Fourier analyses were applied to reveal the characteristic shedding frequency, figure 4b.

An alternate approach to the phase Doppler method is being evaluated. This method requires only a single focused laser beam, figure 5. The receiver is configured to produce the interference. Light reaching different segments of the receiver lens will have a Doppler shift frequency and phase that depend upon the size and velocity of the particle, respectively and the angle of observation. Light passing through different segments of the lens is combined to form the interference fringe pattern. This method lends itself to the possibility of using novel signal processing techniques, minimizes the errors due to individual beam attenuations, and may solve problems associated with the use of single mode polarization preserving fibers.

The ratiometric method described in the previous report is undergoing testing and promises to provide a reliable means for the in situ characterization of irregular-shaped particles.

Preliminary tests on the Lagrangian method have revealed some difficulties with the array detector sensitivity. Other laser sources and enhanced detectors are being considered.

References:

1. S.A.M. Al-Chalabi, Y. Hardalupas, A.R. Jones, and A.M.K. Taylor, Optical Particle Sizing, editors G. Gouesbet and G. Grehan, Plenum Press, 1987.
2. M. L. Yeoman, L.E. Drain, D.M. Livesley, and S.R. Martin, 4th Int'l Symposium on Applications to Fluid Mechanics, Lisbon, 1988.
3. W.D. Bachalo and S.V. Sankar, IBID.
4. W.D. Bachalo, Applied Optics, Vol.19, No. 3 p363, 1980.
5. R.C. Rudoff, A Brena de la Rosa, and W.D. Bachalo, AIAA-89-0052, Reno, 1989.

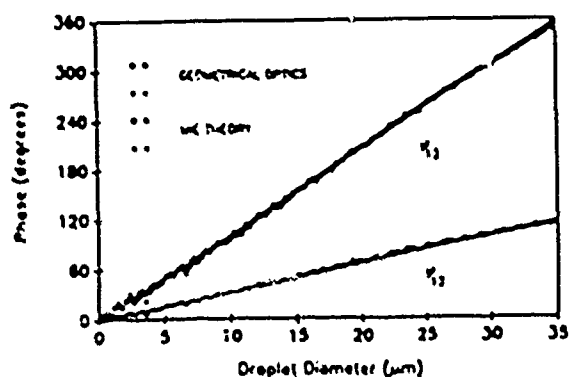


Figure 1. Comparison of the Instrument Response Function Computed Using the Geometrical Optics and The Lorenz-Mie Theories.

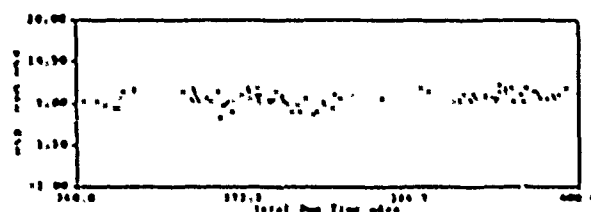


Figure 4a. Time of Arrival Record for Reacting Kerosene Interacting with Large Scale Turbulent Eddies Showing Cluster Formation

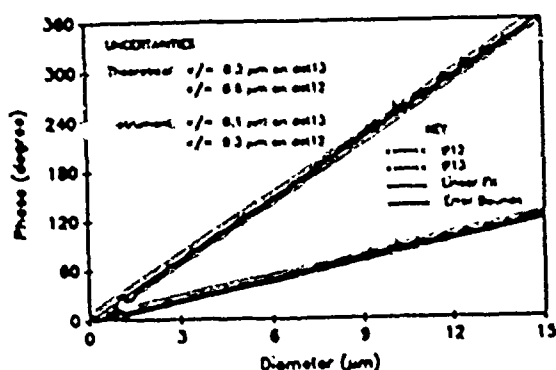


Figure 2. Predictions Showing the Effects of the Optical Parameters on the Instrument Resolution

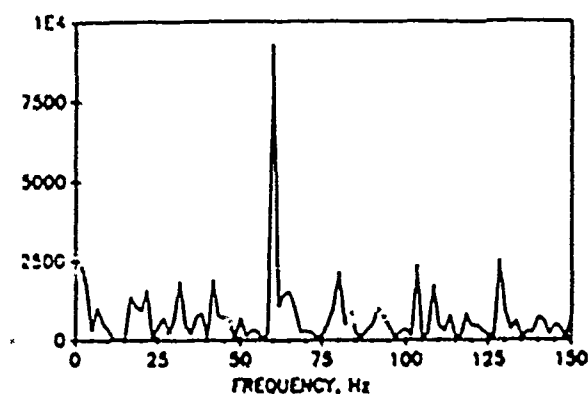


Figure 4b. FFT Analysis Showing a Predominant Shedding Frequency

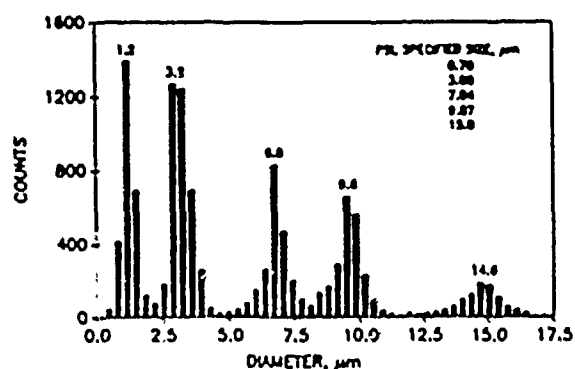


Figure 3. Measured Size Distribution of a Mixture of Classified Particles

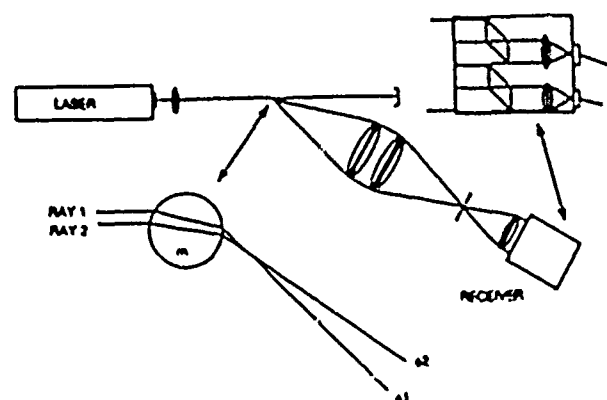


Figure 5. Schematic Showing the Heterodyne Phase Doppler Approach.

NONLINEAR SPECTROSCOPY OF MULTICOMPONENT DROPLETS

AFOSR Grant No. 88-0100

Richard K. Chang (Co-Principal Investigator)

Yale University
Section of Applied Physics and Center for Laser Diagnostics
New Haven, Connecticut 06520-2157

SUMMARY/OVERVIEW

Nonintrusive in-situ optical diagnostic techniques are needed to determine the chemical species and physical properties of multicomponent liquid droplets in a spray combustor. Our research is directed toward the understanding of nonlinear optical effects from individual droplets which retain their spherical shape after irradiation by a high-intensity laser beam. Further, our research is directed toward the understanding of laser-induced breakdown and vaporization mechanisms that lead to plasma formation, explosive vaporization, droplet shattering and deformation, and droplet propulsion.

TECHNICAL DISCUSSION

The spherical liquid-air interface on the illuminated side of a droplet acts as a lens to concentrate the incident plane wave just within the droplet shadow face and to focus the incident wave just outside the droplet shadow face. For most organic liquid and water droplets (with radius $< 60 \mu\text{m}$) which are transparent at the incident laser wavelength, the maximum of the internal intensity located just within the droplet shadow face causes laser-induced breakdown (LIB). The LIB-generated plasma rapidly develops during the initial portion of the input laser pulse and is initially confined just within the droplet shadow face. Subsequently, this internal plasma is ejected from the droplet shadow face and propagates toward the droplet illuminated face. At high input intensities, the internal plasma can strongly absorb the remaining portion of the laser pulse and become a laser-supported optical detonation wave, which rapidly propagates toward the droplet illuminated face and then out of the illuminated face toward the laser. The following speeds of the plasma waves have been determined: (1) ejection speed of the plasma from the shadow face; (2) propagation speed of the plasma from the droplet shadow face toward the illuminated face; and (3) ejection speed of the plasma out of the illuminated face.¹ A paper reviewing the LIB mechanisms in droplets has been published.²

For organic liquid and water droplets which are absorbing at the incident laser wavelength, the laser beam can directly heat the droplet. Four processes are known to occur after the laser pulse (2 μsec in duration) is off: (1) rapid vaporization, usually from either the droplet shadow or illuminated face; (2) droplet deformation; (3) droplet propulsion as a result of the recoil from the material ejection; and (4) droplet shattering resulting in numerous smaller droplets. A recently published book on the optical properties of small particles contains a chapter on laser-induced droplet heating.³ We have been developing a fluorescence imaging technique which can provide a clear distinction between the ejected material (either in the vapor or liquid phase) and the remaining droplet. After irradiation by

a pulsed CO_2 laser beam (with $\approx 3 \text{ J/cm}^2$), the temporal evolution of a linear stream of water droplets ($a \approx 50 \mu\text{m}$) containing Rhodamine 6G dye is shown in Fig. 1. Note that the photos reveal the four above-mentioned processes.

For organic liquid and water droplets which are transparent at the incident laser wavelength, the internal high-intensity regions just within the droplet shadow and illuminated faces give rise to a large gradient of the intensity (∇I) and thus cause laser-induced electrostriction. Photographs showing the bulging of the droplet resulting from laser-induced electrostrictive forces have been published.⁵ Physical properties of the droplet can be deduced by noting how the surface-tension restores the deformed droplet into a spherical droplet. The oscillation frequency of the droplet between a spheroid and a sphere is proportional to the square root of the dynamic surface tension and the decay of the distortion amplitude is inversely proportional to the kinematic viscosity.

The spherical liquid-air interface of a droplet also acts as an optical cavity for the internally generated radiation, such as spontaneous Raman scattering, spontaneous Brillouin scattering, and fluorescence. Stimulated oscillations will occur if the gain is greater than the loss as the internal radiation propagates around the droplet rim. During the input laser pulse, the spontaneous Raman scattering will turn into intense stimulated Raman scattering (SRS), the spontaneous Brillouin scattering will turn into intense stimulated Brillouin scattering (SBS), and the fluorescence will turn into laser emission. We have measured with a streak camera the growth time of the first-order Stokes SRS starting from the spontaneous Raman scattering which acts as the input noise of an oscillator. Furthermore, we measured the growth time of the second-order Stokes SRS starting from the parametrically generated signal resulting from the four-wave mixing process between the laser field and the field of the first-order Stokes SRS.⁴ The growth time of the third- and fourth-order Stokes SRS was noted to behave the same way as the second order Stokes SRS, i.e., the third- and fourth-order Stokes SRS start from the parametrically generated signal resulting from the four-wave mixing processes of the laser field and the fields of the second- and third-order Stokes SRS, respectively.

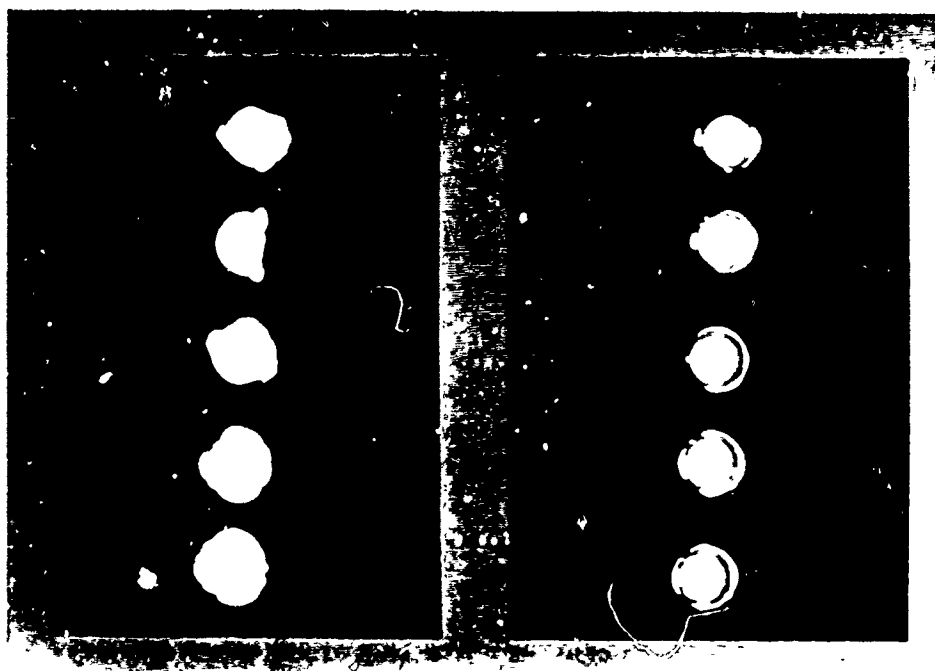
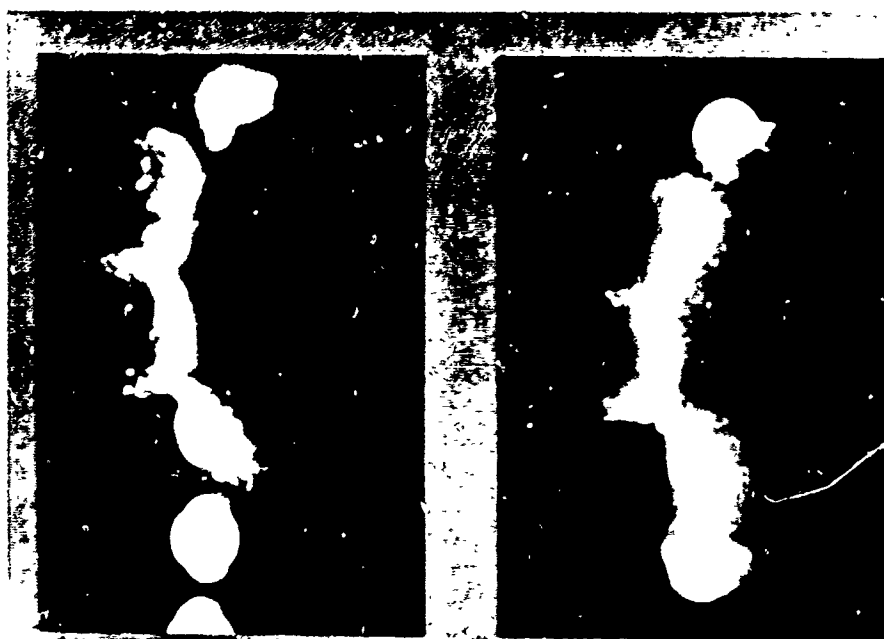
The frequency shift of the first-order Stokes SRS from the input laser frequency is equal to the molecular vibration frequency and, thus, can provide chemical species identification of the multicomponent liquid droplet. In principle, the relative intensities among the various SRS peaks also contain quantitative information of the relative concentration of the multicomponents. However, we have noted that large fluctuations exist in the ratios of SRS intensities, causing big uncertainties in the concentration ratios. We have started to investigate the cause of such intensity fluctuations. Our first finding is that the SRS is not directly pumped by the incident laser beam but is pumped by the SBS generated by the incident laser beam. The most striking feature which we have observed thus far is that the temporal profiles of the SRS and the SBS pulses are correlated, i.e., the valleys of the SBS pulses correspond to the peaks of the the SRS pulses. The implication of such temporal correlations between the SRS and SBS pulses is that the fluctuations in the SRS may be partially caused by the fluctuations in the SBS. Work in understanding and ultimately reducing intensity fluctuations in the SRS is continuing.

REFERENCES

1. J.-B. Zheng, W.-F. Hsieh, S.-C. Chen, and R.K. Chang, "Temporally and Spatially Resolved Spectroscopy of Laser-Induced Plasma from a Droplet," *Opt. Lett.* **13**, 559 (1988).
2. R.K. Chang, J.H. Eickmans, W.-F. Hsieh, C.F. Wood, J.-Z. Zhang, and J.-B. Zheng, "Laser-Induced Breakdown in Large Transparent Water Droplets," *Appl. Opt.* **27**, 2377 (1988).
3. P.W. Barber and R.K. Chang, eds., Optical Effects Associated with Small Particles (World Scientific Publ. Co., Singapore, 1988).
4. W.-F. Hsieh, J.-B. Zheng, and R.K. Chang, "Time Dependence of Multiorder Stimulated Raman Scattering from Single Droplets," *Opt. Lett.* **13**, 497 (1988).
5. J.-Z. Zhang and R.K. Chang, "Shape Distortion of a Single Water Droplet by Laser-Induced Electrostriction," *Opt. Lett.* **13**, 916 (1988).

FIG. 1:

Fluorescence images of a linear stream of water droplets (radius = 50 μm) containing Rhodamine 6G dye and irradiated by a pulsed CO_2 laser beam which is propagating from the left to the right and has the intensity maximum imaged either on the third or fourth droplet from the top of each photograph. The time delays between the CO_2 laser pulse and the detection of the fluorescence images are as follows: (1) top row, 1 μsec and 3 μsec ; (2) middle row, 7 μsec and 10 μsec ; and (3) bottom row, 12 μsec and 15 μsec .



LASER SPECTROSCOPY OF A FLAME ASSISTED PLASMA

AFOSR Grant 86-0067

John W. Daily

Department of Mechanical Engineering

University of Colorado at Boulder

Boulder, CO 80303

May 24, 1989

1 SUMMARY

The purpose of our work has been to develop advanced laser spectroscopy methods to diagnose partially ionized plasmas. We have focused on methods that are based on observing the Doppler shift in ionic spectra due to the presence of an ion drift velocity. Two particular methods we are working with are Velocity Modulated Laser Spectroscopy (VMLS) and Two Beam Doppler Shift Laser Spectroscopy (TBDSLS). This work like any other development of a diagnostic tool for plasma applications proved to be complicated by the difficulties of understanding the plasma structure itself and creating the ideal experimental conditions under which the diagnostic methods would work. Therefore, we have focused on devising a theory for our plasma model and validating it experimentally in the hopes that the best and optimum conditions would be found for the demonstration of principle of the Doppler shift methods.

2 TECHNICAL DISCUSSION

The scientific goal of our work is to increase understanding of the role of flow non-uniformities and plasma-wall interactions in plasma devices by making in-situ measurements of electric field strength, ion mobilities, concentrations and temperatures in a non-intrusive fashion that allows point, one, and two dimensional imaging. The scientific approach is to use laser induced fluorescence to probe ion absorption line profiles. If there is an electric field present, the ions will experience a net force and undergo drift, resulting in a shift in the position of the line profile. If the ion mobility is known, then the electric field component along the probe direction can be calculated. If the electric field driving

the plasma is modulated, one will observe an oscillating shift in the line profile that arises because of the oscillating force imposed on the ions. The shift may be related to the ion mobility, thus conductivity. Temperature and concentrations may be recovered by conventional laser spectroscopic means. The methods are species and state selective, allowing one to make measurements on more than one species and to study the effect of internal mode nonequilibrium. The merit of the methods lies in their ability to provide simultaneous measurements of important parameters in plasmas. The methods are well suited to multi-dimensional imaging. One may use an array detector to image lines and planes in addition to the more conventional point configuration. During the first year of the program, the theoretical basis of the method was developed and our experimental facility modified for the purpose of demonstrating its effectiveness. During the second year we have worked mostly on understanding the global behavior of the plasma model that we have chosen to use in the demonstration of principle experiments. Then, during the past year, data on the line profile of the ionic species were obtained by using LIF. After that several attempts were made to observe a Doppler shift in the line profile. However, this proved to be very difficult and unsuccessful due to the high decrease in ion number density in the plasma when an adequate electric field strength, needed for the methods to operate, is present. Thus a more detailed spatial and temporal description of the plasma was due to locate the optimum position in the plasma where a high enough electric field is present and an LIF signal is still within the detectability limit. LIF supported with some probe measurements was used for spatial profiling of the number density and electric field strength in the plasma. Also, the plasma equations were solved numerically and comparison between the theory and experiment can be made.

3 THEORETICAL BASIS

The basis of the Doppler shift methods is Coulomb's law which states that the force felt by a charged particle is directly proportional to the imposed electric field

$$\vec{F} = q\vec{E} \quad (1)$$

where \vec{E} is the electric field, q the charge, and \vec{F} the force. For a collisionally dominated, partially ionized plasma, the net Doppler shift for D.C. and A.C. fields respectively is

$$\frac{d\nu}{\nu_0} = \frac{\mu_i E}{c} \quad (2)$$

or

$$\frac{d\nu}{\nu_0} = \left(\frac{\left(\frac{\mu_i E}{c} \right)}{1 + i(\omega/\nu_c)} \right) E_0 \exp(i\omega t) \quad (3)$$

For a Doppler broadened line, the modulation depth (peak depth for an A.C. field) is

$$\frac{d\nu}{d\nu_D} = \left(\frac{\pi q}{8Q\sqrt{\ln 2}} \right) \left(\frac{E}{P} \right) \quad (4)$$

The coefficient of E/P is of the order unity in typical plasmas for electric field in volts/meters and pressure in Pascals. Thus one can obtain significant modulation depths at moderate values of E .

4 PLASMA THEORY

The advantage of utilizing a collisionally dominated plasma is that the theoretical description of the plasma is simplified considerably. Such a simplified description has been formulated by Lawton and Weinberg expressly for flames. Our approach has been to use their theory in conjunction with experiments to ensure that we have a reasonable understanding of the plasma conditions. The Lawton and Weinberg theory is based on the assumption that diffusion of ions and electrons can be neglected in comparison with drift. Under this assumption and assuming that the plasma is one-dimensional with uniform properties, the governing equations display simple limiting solutions. These are the zero field limit, the saturation limit, and the sub-saturation limit. The current-voltage relationship takes on the form

$$\frac{I}{I_s} = 1 - \exp\left(-a \frac{V}{V_s}\right) \quad (5)$$

where the subscript *s* indicates saturation conditions, and *a* is a constant whose value depends on the definition of the saturation condition. Very good agreement between the theory and experiment were found. However, under the best of conditions where we reach saturation and the electric field is high enough to detect any Doppler shift, the ion number density decreases significantly making the signal to noise ratio in the LIF signal very low. Water cooling was added to the electrode plates to delay saturation voltages and extend the saturation plateau. Still under these conditions spacial profiling of the ion number density by LIF measurements showed that SNR goes to one as saturation conditions are established. In our final report comparison between experimental and numerical calculations for spatial profiling will be presented as well as some recommendations for increasing SNR and/or the use of the more powerful pulsed dye laser system with broadband excitation and a different arrangement for proof of principle of the Doppler shift methods.

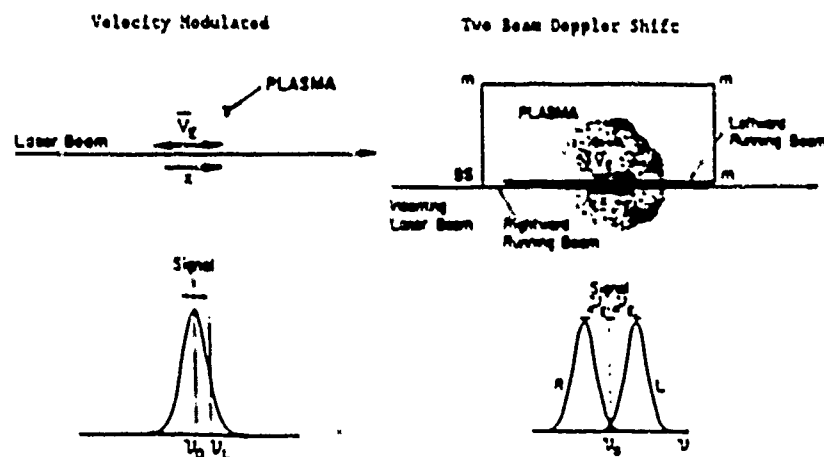


Figure 1: Measurement Configurations

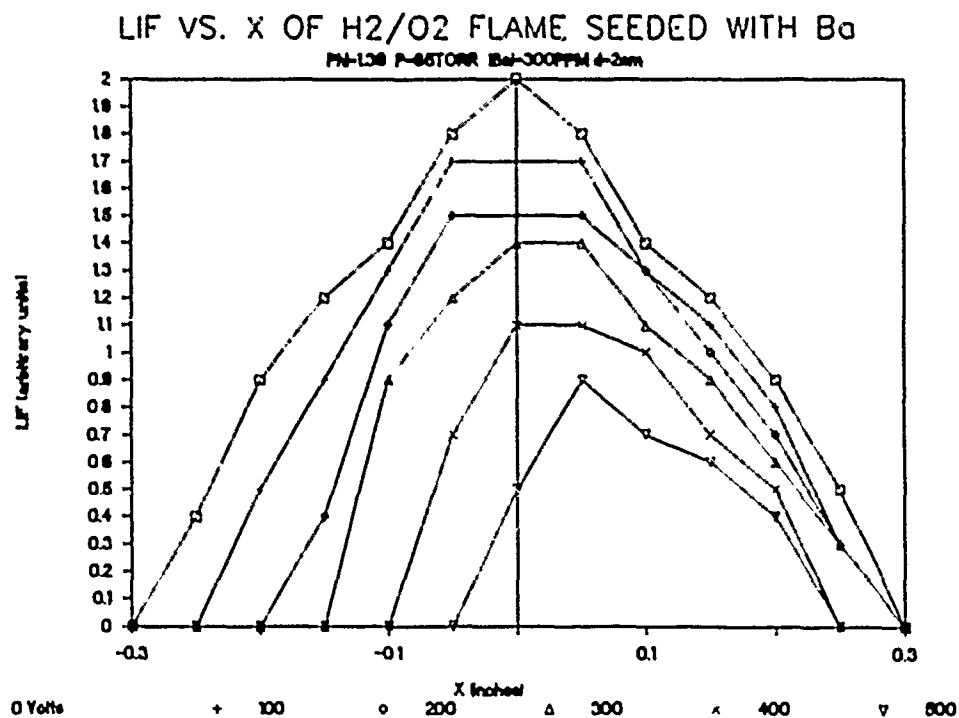
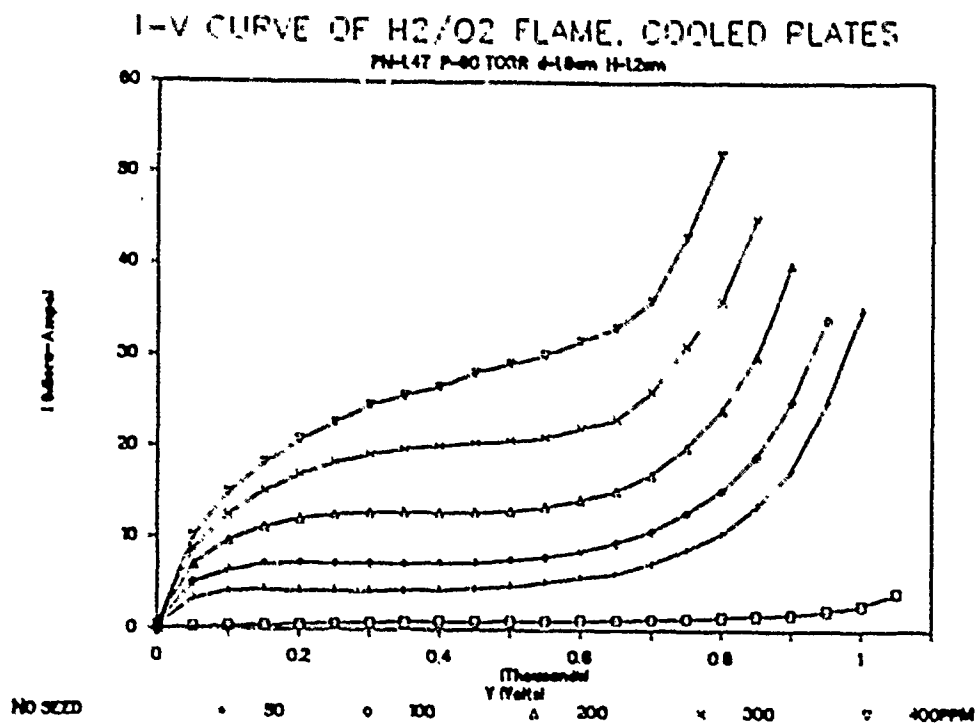


Figure 2: Experimental Results

DETECTING MICROWAVE EMISSIONS FROM TERRESTRIAL SOURCES:
A FEASIBILITY STUDY

AFOSR GRANT/CONTRACT No. 88-0257

Principal Investigators: Thomas C. Ehlert & Thomas K. Ishii

Marquette University, Milwaukee, WI 53233

SUMMARY: Calculations based on the radiative transfer equation predict that modern conventional microwave equipment is capable of detecting the energy emitted as a result of rotational state changes in a hot, polar gas. To test this prediction, experiments to detect the 22.235 GHz radiation from H_2O are underway.

AUTHOR: Thomas C. Ehlert

TECHNICAL DISCUSSION: Although the use of microwave absorption spectroscopy for observing rotational state changes in polar gases is well known, the use of microwave emission spectroscopy for this purpose is not, save for radioastronomy and certain laboratory experiments which require a perturbing electric field. Yet it can be shown that modern microwave equipment is capable of detecting the energy emitted by hot, polar gases under laboratory conditions. According to the radiative transfer equation, at frequency ν the radiation intensity expressed as brightness temperature seen by a receiver looking at a uniform source of length l without any intervening medium is given by

$$T_R = T_B \exp(-\alpha_\nu l) + T_s [1 - \exp(-\alpha_\nu l)]$$

where T_R is the brightness temperature seen by the receiver looking at a source of length l , volume absorption coefficient α and brightness temperature T_s against a background of brightness temperature T_B . A Dicke-type receiver is being constructed to detect the 22.235 GHz emission from water vapor at 373° K and 1 millibar in a 10 meter length of waveguide. By Van Vleck's equation for α , this source should give a T_s 2°K greater than that of a reference source. Potential applications include a) determination of rotational properties of molecules which are difficult to study by absorption spectroscopy, b) studies of the role of rotation in energy transfer, and c) remote, passive detection of processes which produce hot, polar gases such as H_2O , CO , and NO , e.g. jet and rocket plumes.

ADVANCED DIAGNOSTICS FOR REACTING FLOWS

AFOSR-89-0067

Ronald K. Hanson
High Temperature Gasdynamics Laboratory
Mechanical Engineering Department
Stanford University, Stanford, CA

SUMMARY/OVERVIEW

This research is directed toward innovation of advanced diagnostic techniques applicable to combustion gases and plasmas, including hypersonic flows. Emphasis is placed on laser-induced fluorescence methods suitable for digital 2-d and 3-d imaging of species concentrations, electron density, mass density, temperature, velocity and pressure. This approach can provide non-invasive, simultaneous measurements at 10^4 – 10^6 points, useful for studies of propulsion, aerothermodynamics, and combustion sciences. Other research topics include: laser-wavelength modulation spectroscopy, laser photolysis in shock-heated gases for kinetics/spectroscopy studies, and laser ignition of combustion gases.

TECHNICAL DISCUSSION

In the following paragraphs we highlight primary activities of the past year.

Plasma Diagnostics

Two new plasma facilities are now operational: a 3 kW RF-powered plasma torch suitable for benchtop studies of diagnostic concepts, and a 75-kW RF-powered torch which yields higher enthalpies and allows study of practical plasmadynamic behavior. Both torches operate at atmospheric pressure on a range of gases. One recent project involved development of a new method for measuring electron number density in an Ar plasma. The scheme utilized a tunable cw ring dye laser to probe fully resolved, Stark-broadened H-atom lineshapes. The use of laser-induced fluorescence detection (time-averaged) of the H-alpha transition (656 nm), in particular, led to high sensitivity and spatial resolution for electron densities of 10^{14} – 10^{16} cm⁻³. Current work is aimed at establishing methods of monitoring C-atom densities in Ar-hydrocarbon plasmas using PLIF imaging with a tunable ArF laser source.

Laser-Wavelength Modulation Spectroscopy

A significant development during the past year was the extension of the wavelength operating range of our tunable cw ring dye laser well into the UV. By increasing the UV power of the argon pump laser and by use of a custom intracavity frequency doubler based on BBO, we've managed to generate about 1 mW of tunable output at wavelengths of 215-235 nm, a region well below the 260 nm cut-off of commercial systems. This new laser can be scanned at multiple-kHz rates to allow rapid recording of fully resolved absorption lines of several species, including NO, O₂, CH₃ and several other hydrocarbon radicals. Current work is aimed at exploiting this new laser source for fundamental spectroscopy and reaction kinetics studies in flame and shock tube environments.

PLIF Imaging in Shock Tube Flows

Shock tubes and tunnels provide a convenient means of studying a variety of nonequilibrium gasdynamics problems and of simulating conditions relevant to advanced air-breathing and electric propulsion systems. Our objective in this project is to establish capabilities for PLIF imaging in such flows. This requires, for example, an intensified solid-state camera system

which can be triggered precisely during the short test times of a shock tube. At present we are investigating PLIF imaging of O_2 , NO and OH in several shock tube flows, including flow over a wedge, shock reflection from a nonplanar wall, shock wave-boundary layer interactions, injection and mixing/combustion of H_2 in supersonic air flows, and nonequilibrium hypersonic flows in a shock tunnel. An example of current work is illustrated in Fig. 1, which shows a single-shot PLIF image of shock reflection from a nonplanar wall in a NO(0.5%)/ N_2 mixture. A tunable ArF laser at 193 nm was used to excite a specific group of lines in the $D \leftarrow X$ system of NO originating from $v'' = 1$. This scheme provides sensitive imaging of NO at high temperatures, and it should be quite useful for studies of vibrational nonequilibrium in supersonic flows. Note that the images clearly reveal a change in the shape of the shock with distance from the wall. The spatial resolution possible with PLIF suggests that this approach will work well in flows which contain three-dimensional structure not observable with conventional flow visualization techniques.

High Resolution PLIF Imaging

We have continued work to acquire high-resolution PLIF data on mixing in turbulent non-reacting round jets. The experiment involves exciting combined fluorescence/phosphorescence of biacetyl seeded into a jet of N_2 which flows into a slow co-flow of pure N_2 ; the experiment is conducted at atmospheric conditions. The scattered light is recorded on an astronomy grade, unintensified large format (384x576 pixels) CCD camera. Our objective is twofold: to explore the use of imaging cameras with a very large number of pixels; and to generate a high quality data set useful in addressing the physics of this fundamental flowfield. The underlying hypothesis of the effort is that 2-d image data of the jet mixture fraction, of a quality suitable for digital image processing, will provide critical tests of mixing models and stimulate new insights regarding such flows. An example of recent data is shown in Fig. 2 for the case of a Reynolds number = 8500 jet. The figure provides a false-color display of the instantaneous mixture fraction, six histograms of the distribution at discrete axial locations, and corresponding data for rms fluctuations based on a 25 image data set. It is clear that such data should be useful in answering questions regarding: (1) differences between instantaneous and time-averaged fields; (2) the role of organized structures; (3) regions of high dissipation; (4) details of scale sizes and character; and (5) various issues of correlations and statistics.

Velocity Imaging

A specific objective in our research is the establishment of imaging concepts for velocity which utilize molecular constituents of gaseous flows. During the past year we made good progress on the development of a PLIF scheme based on pulsed, broadband laser excitation. This new approach (see ref. 1) should enable true single-shot determinations of two velocity components in a plane, and it has the potential for enabling simultaneous measurements of velocity, temperature and species. The underlying concept of the measurement is the Doppler effect, which influences the absorption of a gas moving in the direction of incident laser light. The subsequent fluorescence is simply a measure of the absorption. An example of recent work carried out in a supersonic underexpanded jet of N_2 seeded with a low level of NO is shown in Figs. 3 and 4; Fig. 3 presents raw PLIF data while Fig. 4 presents processed data for the axial and radial velocity components at one axial location ($x/D=3$). This scheme is particularly promising for probing hypersonic flows at reduced densities.

Laser-Photolysis Shock Tube

During the past year we have continued development of a shock tube which combines gasdynamic heating with excimer laser photolysis as a means of generating controlled levels of free radical species at elevated temperatures. Such a device provides new capability for fundamental studies of reaction kinetics and spectroscopy in species of interest in combustion and plasma sciences. A critical adjunct to the new shock tube is the continued development of sensitive species detection schemes based on both atomic resonance lamps and tunable dye lasers. As an example application of a new high-performance microwave-discharge resonance

lamp which operates at 119.9 nm for N-atom detection, Figs. 5 and 6 illustrate raw data and rate coefficients obtained in laser photolysis experiments with NO in Ar. The 193 nm excimer photons are used to produce a few ppm of N (and an equal amount of O) which subsequently reacts via $N + NO \rightarrow O + N_2$. The decay rate of N by the pseudo-first order reaction leads directly to the only data for this rate coefficient at temperatures of 1400-3500K. The data are in excellent agreement with a previous determination of the reverse rate in this laboratory by another shock tube method.

Other Projects

Other projects currently underway include. (1) quantitative imaging of Mie scattering from sheet-illuminated sprays to obtain instantaneous particle size distributions, (2) development of detailed absorption/fluorescence spectroscopy codes for O_2 , OH and NO, (3) laser ignition of combustion gases; (4) multi-photon PLIF imaging of H_2 and N_2 , and (5) development of advanced solid-state camera systems.

REFERENCES

1. P. H. Paul, M. P. Lee and R. K. Hanson, Optics Letters, May 1, 1989.

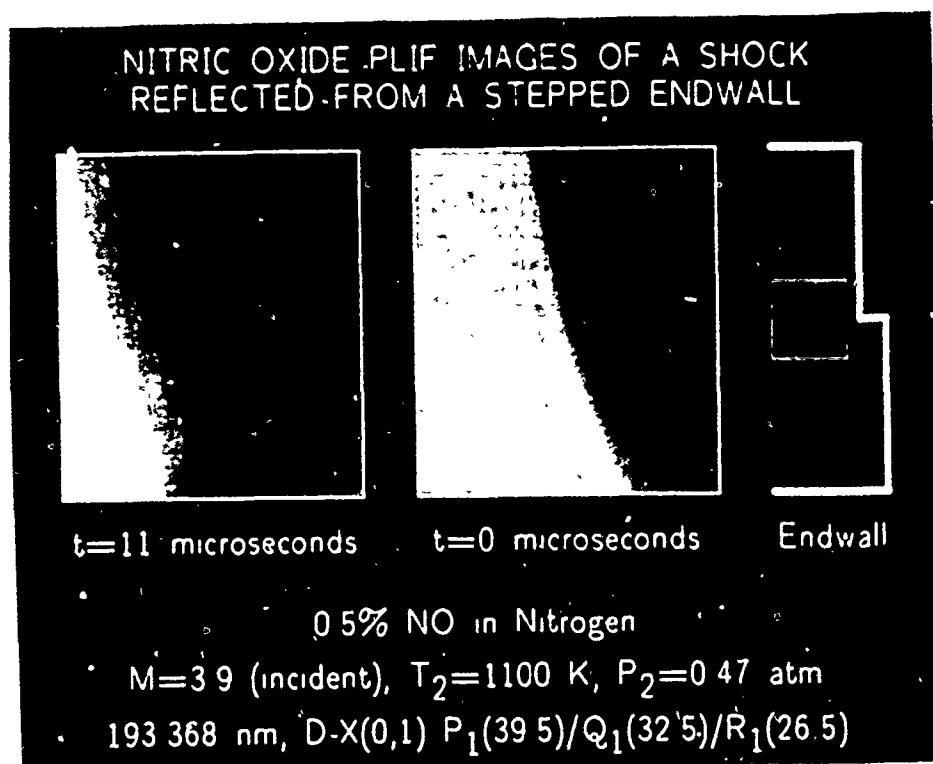


Fig. 1 Single-shot PLIF images at two discrete times following shock reflection from a stepped end wall. The gray scale is: black (max signal) and white (min signal). Thus the black-white boundary marks the reflected shock wave location and shape.

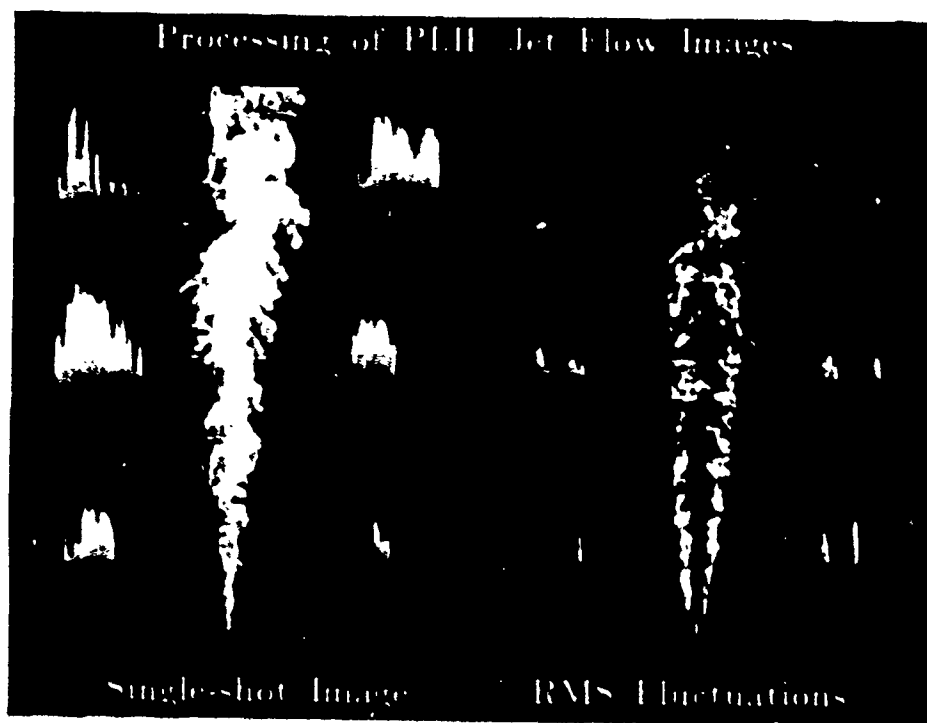


Fig. 2. PLIF data for turbulent jet.
 $Re \approx 8500$



Fig. 3. PLIF velocity data.

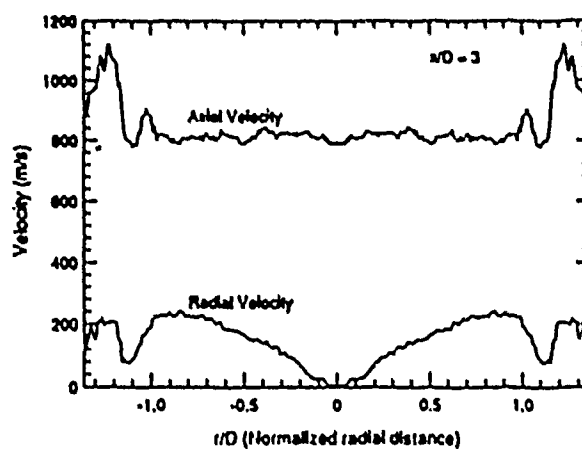


Fig. 4. Axial/radial velocity at $x/D=3$.

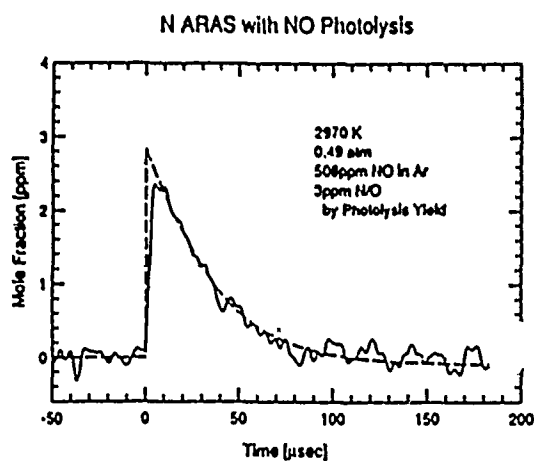


Fig. 5. Photolysis Shock Tube data.

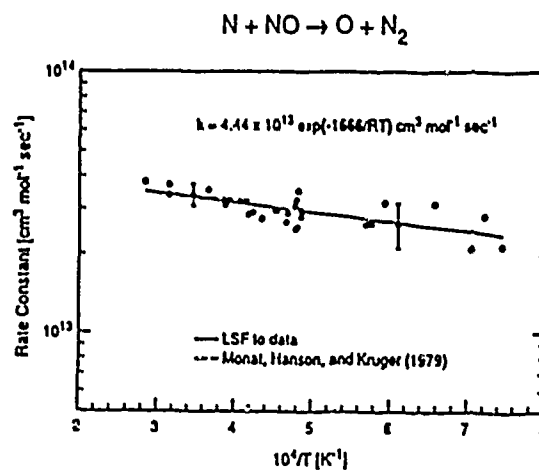


Fig. 6. Rate coefficient results.

MULTIPLE SCATTERING AND THE INVERSE FRAUNHOFER DIFFRACTION PARTICLE SIZING PROBLEM

AFOSR Grant No. 84-0187

Principal Investigator: E. Dan Hirtleman

Mechanical and Aerospace Engineering Department
Arizona State University
Tempe, AZ 85287

SUMMARY/OVERVIEW:

The phenomenon of multiple scattering significantly complicates the analysis of radiation transfer through particulate-laden media. Nonintrusive diagnostics for reacting flows depend on an understanding of light scattering and propagation, and for that reason can unfortunately not be used in the many important systems and applications involving optically thick media. The long term objective of this research is the development of methods for nonintrusive characterization of optically thick aerosols which could, in turn, allow calculation of the effect of the multiple scattering on other diagnostics techniques. Specifically, we are continuing research on diagnostic methods and the supporting theoretical models to permit on-line characterization of the size distribution of optically thick aerosols of large particles using multi-angle interrogation and multi-angle scattering measurements.

TECHNICAL DISCUSSION:

One of the most difficult problem areas for future work in optical diagnostics involves measurements in optically thick media. The overall objective of this research is to develop methods to perform inverse scattering measurements of particle size distributions under conditions where multiple scattering is significant. The research involves work in the following four areas: development of an experimental facility for multiple scattering research; verification of a new multiple scattering scaling law; research on inverse multiple scattering algorithms; and research on strategies for "active interrogation" of multiple scattering media.

In the last period of this research we have concentrated on verifying the performance of a new technique for solving the inverse scattering problem for optically thick sprays. Fig. 1 is a schematic of the proposed optical system for making laser diffraction measurements in thick sprays. The key difference between Fig. 1 and conventional single scattering Fraunhofer instruments is the presence of a programmable mask in the front focal plane of the transmitter lens. The programmable mask has annular ring apertures which can be individually switched on (transmitting) or off (absorbing or opaque). A ring of light in the front focal plane of an ideal transmitter lens produces a hollow cone of light of constant angle θ passing through the spray or particle sample volume. By switching open the various rings, a sequence of hollow cones of probe radiation is created. The fraction of the incident energy in the cones which is not scattered by the medium is redirected by the transform lens to a ring on the detection plane which matches the ring in the programmable mask (assuming the focal lengths of the transmitting lens and the transform lens are equal). Light which is scattered by particles in the spray leaves at some angle different than the cone angle and ends up at another radial position (i.e. a different detector ring) on the detector plane. A conventional photodiode array ring detector or a matched programmable mask followed by a field lens and detector as reported by Dellenback and Hirtleman [1,2] can be used.

The inverse scattering problem for *single* scattering requires n measurements (effectively n equations) to solve for n unknowns, where the unknowns are the quantity of particles in n size classes. The n measurements involve a sampling of the scattering signature, and are the amounts of light scattered into various scattering angles and which eventually strike associated detectors.

The incident beam must be narrow and well-defined both spectrally and in angular distribution to allow credible inversions. Conventional diffraction systems use a collimated (incident angle of zero) input or interrogation laser beam, but we have pointed out that any angle could in fact be used. The optical system of Fig. 1 generates incident beams of various angles, and for each incident cone n scattering measurements could be made. Thus, the system in Fig. 1 could theoretically provide enough measurements to support n independent solutions to the n by n single scattering system.

In optically thick media, the inverse problem becomes more complex because the light which eventually reaches the detectors has, in general, undergone more than one scattering event. In other words, the single scattering signature (which can be modeled relatively easily) is perturbed or altered by the additional (multiple) scattering events which occur after the light leaves the first scattering event on its way to a detector. Additional unknowns are thereby introduced, specifically variables which determine or predict the expected fate of light which would have reached each of the various detectors if not for the thick medium. Now since light originally traveling at a scattering angle corresponding to say the j th detector could be rescattered into n other detectors, there are n^2 unknowns necessary to model the n -angle scattering behavior of an optically thick medium. In contrast, the single scattering medium required only n equations and unknowns. Clearly then additional measurements are needed to characterize a multiple scattering medium, and the system in Fig. 1 can provide n^2 independent measurements (each of n incident light cones scattered to n detectors). After the n^2 measurements are taken via Fig. 1, an n^2 by n^2 system of equations must effectively be solved to determine the particle size distribution.

This n^2 by n^2 system of equations which represent the inverse problem is based on the successive-order discrete-ordinates multiple scattering model of Hirleman [3]:

$$S_m = \exp(-b) \cdot \exp(a_f b \cdot H) \cdot S_0 \quad (1)$$

where S_m is a vector representing the scattering signature for a general medium of arbitrary optical depth (the first element corresponds to zero degree scattering, the second to the smallest detector scattering angle, etc.), S_0 contains the angular distribution of the incident radiation (S_1 would therefore be identical to the scattering signature for an optically thin medium), H is the single scattering redistribution matrix, b is the optical depth, and a_f is defined as the forward scattering albedo. The first column of H is proportional to the scattering signature that would be obtained with a conventional diffraction system using collimated incident radiation onto a thin medium. In conventional laser diffraction systems then, the first column of H is effectively used in an inversion to obtain the size distribution.

Now consider a multiple scattering redistribution matrix H_m defined using Eq. (1):

$$S_m = H_m \cdot S_0 \quad (2)$$

$$H_m = \exp(-b) \cdot \exp(a_f b \cdot H) \quad (3)$$

Now a conventional diffraction system under multiple scattering conditions will measure a signature proportional to the first column of H_m , and only for small b are H and H_m equivalent. But H can be determined from measured H_m using:

$$H = \exp(b) / (a_f b) \cdot \ln (H_m) \quad (4)$$

The n^2 terms of H_m are measured using Eq. (2) by illuminating the medium using n different S_0 vectors and measuring the scattering signature on n different detectors for each incidence case. Then H is obtained from Eq. (4) which in effect amounts to "reaching into the medium" and determining the scattering signature that is present after just one scattering event has taken place. Once the single scattering properties of the medium are known, the inverse problem can be solved using an array of methods discussed by Koo [4].

Some numerical and experimental studies of the proposed inverse scattering algorithm have been performed. NBS standard reference material 1003A has been used as the particle size distribution for this work. The first results involve a numerical study of the inversion. In this study the theoretical H matrix was calculated for SRM 1003A using published methods [3], and then H_m calculated for a series of values of the optical depth parameter b using Eq. (3). The calculated elements of H_m were perturbed by adding a simulated random noise contribution. A numerical simulation of the measured H matrix was then determined from Eq. (4), and the first column of the resulting H is plotted in Fig. 2 for a typical noise level. The first column of H obtained in this manner is an estimate of the single scattering signature, and could be used in a conventional single scattering inversion. Errors of the order shown in Fig. 2 do not degrade significantly the inverse scattering algorithms for obtaining particle size distributions as discussed by Koo [4]. Some experimentally measured columns of H_m obtained using cone illumination as discussed above are shown in Fig. 3. The results show that the new method is feasible for measuring size distributions in optical depths up to $b = 6$ (99.75% extinction).

References

1. E. D. Hirleman and P. A. Dellenback, "Faraday-effect Light Valve Arrays for Adaptive Optical Instruments", pp. 6-11, in *Optical Methods in Flow and Particle Diagnostics*, Vol. 63, Laser Institute of America, 1988.
2. Dellenback, P. A. and Hirleman, E. D. "Adaptive Fraunhofer Diffraction Particle Sizing Instrument Using a Spatial Light Modulator", Proceedings, OSA Meeting on Spatial Light Modulators, Lake Tahoe, NV, June, 1988. Under review for inclusion in a special issue of *Applied Optics*.
3. E. D. Hirleman, "Modeling of Multiple Scattering Effects in Fraunhofer Diffraction Particle Size Analysis," *Particle and Particulate Systems Characterization*, V. 5, pp. 57-65, 1988.
4. J. H. Koo, "Particle Size Analysis using integral transform techniques on Fraunhofer diffraction patterns", Ph.D. dissertation, George Washington University and Arizona State University, 1987.

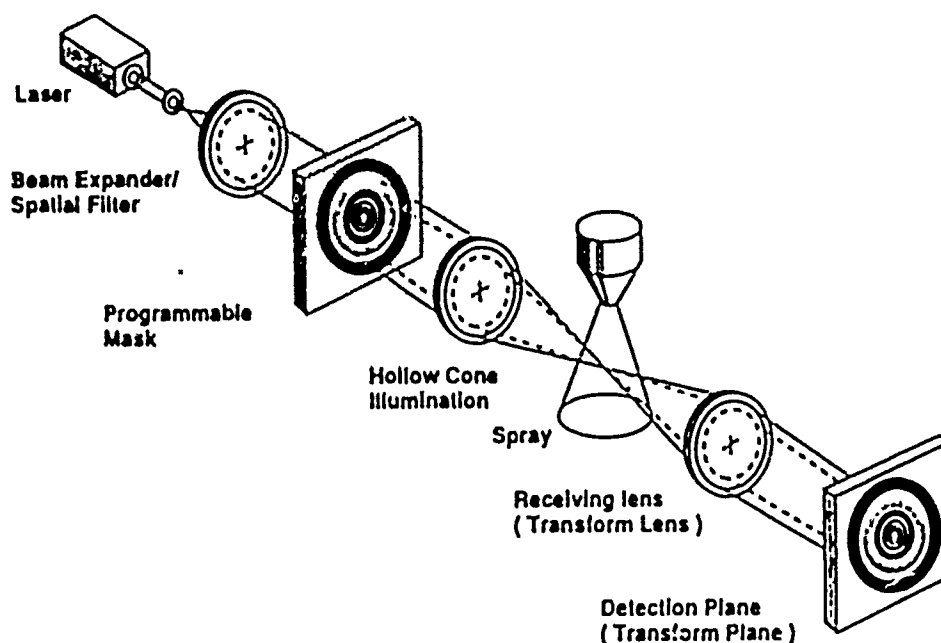


Fig. 1. Schematic of a next-generation laser diffraction particle sizing instrument which allows multi-angle interrogation and multi-angle scattering measurements. The programmable mask creates annular ring of light which are converted into cone of light of varying angles to illuminate the particle field.

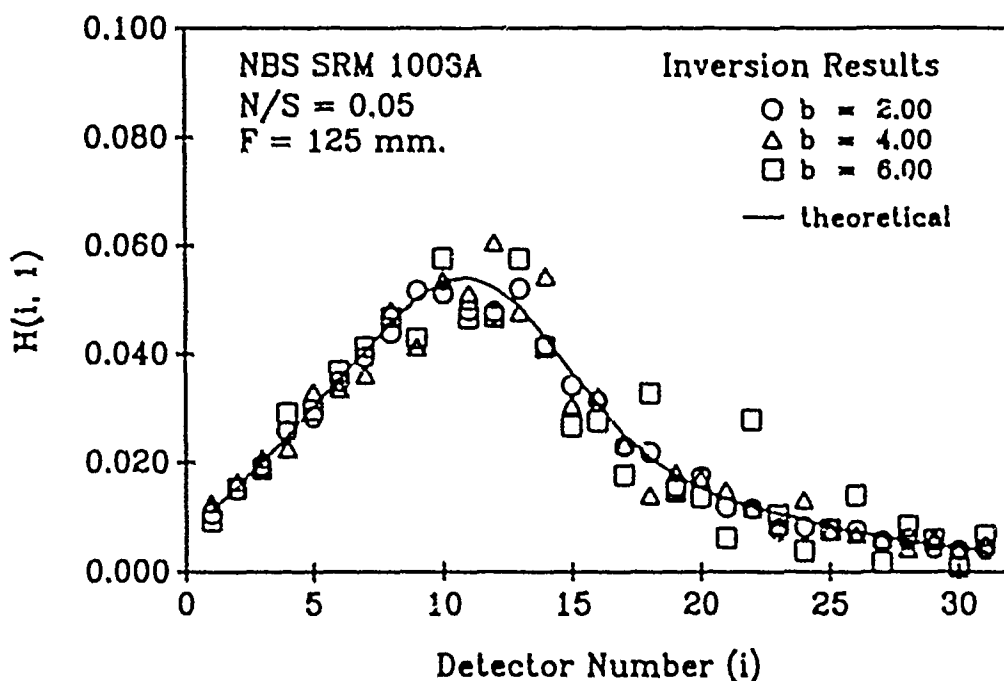


Fig. 2. Plot showing the first column of the single scattering redistribution matrix H reconstructed in a numerical experiment using an inversion of synthetic scattering data. The assumed optical system had an RI Inc. ring detector and a $f = 125 \text{ mm}$ transform lens. The calculated elements of the H_m matrix were perturbed with simulated Gaussian noise of 5%.

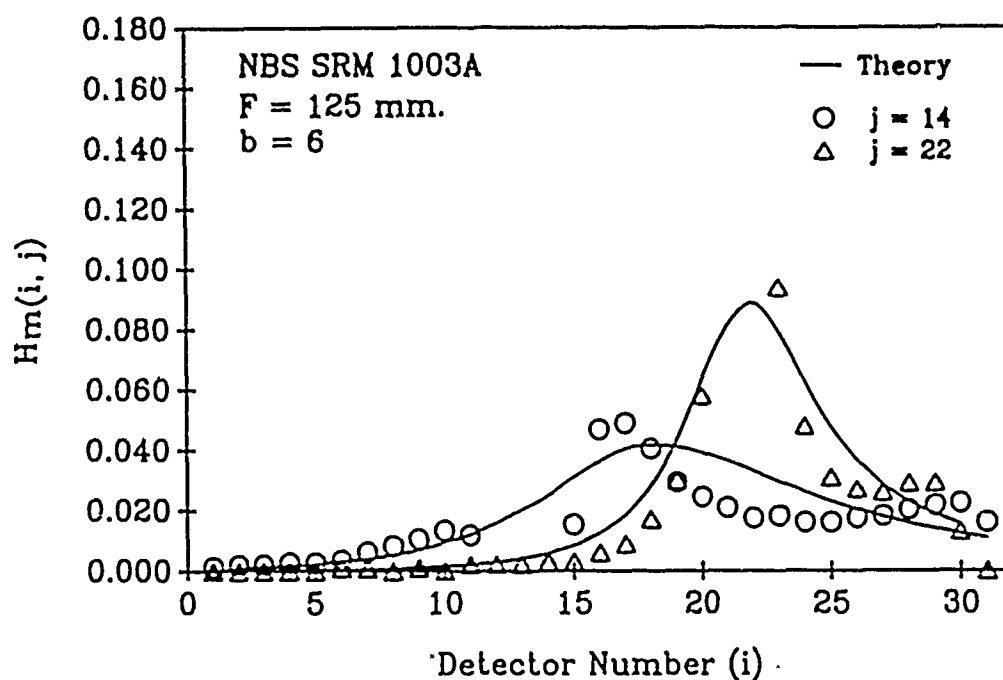


Fig. 3. Measured and predicted data for two columns of the multiple scattering redistribution matrix H_m . The data are for NBS SRM 1003A for a laser diffraction system with an RSI Inc. ring detector and a transform lens with $f = 125 \text{ mm}$. The j values correspond to ring detector numbers (0.0162 and 0.0434 rad for rings 14 and 22 respectively).

MULTIPHOTON DETECTION TECHNIQUES FOR F AND F₂

(AFOSR Contract No. F49620-88-K-0003)

Principle Investigator: David L. Huestis

Collaborating Staff: Gregory W. Faris, Mark J. Dyer, William K. Bischel,
and Roberta P. Saxon

SRI International
Molecular Physics Laboratory
333 Ravenswood Avenue
Menlo Park, CA 94025

SUMMARY/OVERVIEW:

New quantitative remote detection techniques for atomic and molecular fluorine that have high sensitivity, coupled with good temporal and spatial resolution, are needed for such diverse applications as semiconductor manufacturing and laser development. The goal of this project is to develop quantitative detection techniques based on two-photon excitation of atomic or molecular states followed by the detection of fluorescence or ionization. In this paper we report the first observation of fluorescence from two-photon excitation of the $F^1\Pi_g$ and $f^3\Pi_g$ states of F₂. Using a vacuum spectrometer, we have shown that the fluorescence corresponds to the 157 nm F₂ laser transition.

TECHNICAL DISCUSSION

At the 1988 AFOSR Contractors Meeting we reported the two-photon resonant, three-photon ionization spectroscopy of molecular fluorine, probing the $F^1\Pi_g(v'=0,1,2)$ and $f^3\Pi_g(v'=3)$ states. Since that time, we have observed fluorescence from the $F^1\Pi_g(v'=2)$ and $f^3\Pi_g(v'=3)$ states. Emission spectra of the $F^1\Pi_g(v'=2)$ state and high resolution fluorescence excitation spectra of both the $F^1\Pi_g(v'=2)$ and $f^3\Pi_g(v'=3)$ states have been obtained. In addition to providing a means of detecting the ground state of F₂, this fluorescence is the first optical pumping of the important F₂ laser transition in the VUV.

The experimental arrangement for two-photon excitation of F₂ is shown in Figure 1. The light from an excimer-pumped dye laser is frequency doubled in a β -BaB₂O₄ crystal to give about 200 μ J at 207 nm. This light is focused with a 5-cm lens into a cell containing a mixture of fluorine and helium. Fluorescence light is collected and collimated with a 5-cm MgF₂ lens, focused with a 25-cm MgF₂ lens onto the input slits of a vacuum spectrometer, and detected with a CsI solar blind photomultiplier at the exit slits. Imaging the focal volume of the laser onto the slits enhances the contrast between the fluorescence and the scattered laser light. The 207-nm light passes through the cell either passes through a calibration cell containing NO or onto a photometric energy meter. The 1+1 REMPI signal from the $B^2\Pi \leftarrow X^2\Pi(3,0)$ band in NO is used as a wavelength calibration.

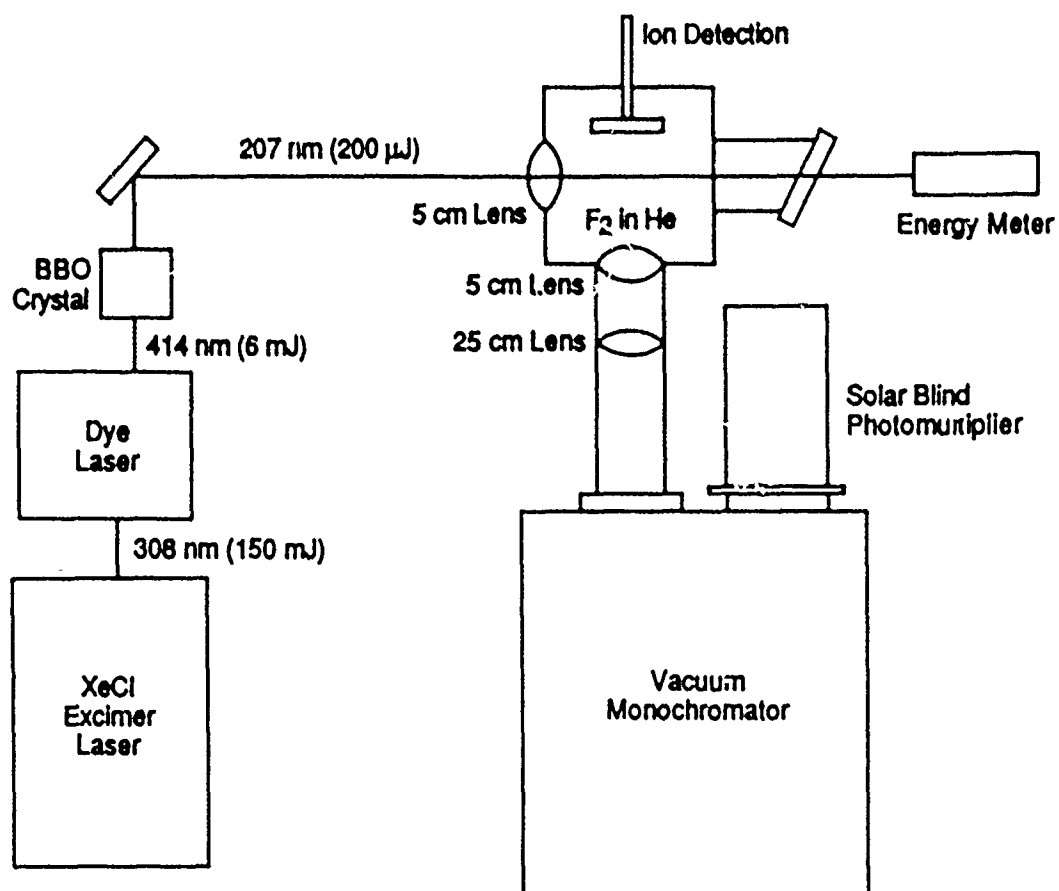
We have calibrated this NO band against iodine fluorescence by operating the dye laser at about 621 nm, doubling the frequency in a KDP crystal, and mixing the doubled and fundamental beams in the same β -BaB₂O₄ crystal. Part of the remaining fundamental beam was directed to an iodine cell, while the mixed beam passed through the NO cell.

High resolution fluorescence excitation spectra have been obtained of both the $F^1\Pi_g(v'=2)$ and $f^3\Pi_g(v'=3)$ states. A fluorescence emission spectrum obtained using the vacuum spectrometer when exciting the $F^1\Pi_g(v'=2)$ state is shown in Figure 2. This spectrum agrees very well with those observed in electron excited F₂-rare gas mixtures.^{1,2} Thus we conclude that our initially excited $F^1\Pi_g$ levels are being collisionally transferred to the upper level of the F₂ laser, believed to be the outer well of the $f^3\Pi_g$ state. This discovery is important because it establishes with high certainty the origin of the F₂ laser transition (about which there has been some controversy).³ In addition, because this state can now be accessed optically, the kinetics of the laser may be studied in an environment which can be controlled much better than that of electron beam or discharge excitation.

Detection of atomic fluorine was demonstrated under the previous AFOSR contract (No. F49620-85-K-0005).⁴ This scheme involves two-photon excitation with 170-nm light followed by detection of fluorescence at 776 nm. In the previous experiments the 170-nm light was generated as the sixth-order anti-Stokes Raman wave in H₂/N₂ of a doubled Nd:YAG pumped dye laser, which yielded only about 10 μ J at 170 nm. To increase the sensitivity of the detection technique, which depends on the square of the pump laser intensity, we have designed and constructed a new apparatus for generating intense narrow-band 170-nm radiation by Raman shifting an ArF laser. By Raman shifting in HD gas, the tuning range of the second anti-Stokes wave of ArF covers the two-photon transition in atomic fluorine. We hope to obtain 100 times more energy than was available previously. If successful, this would be an important advance in making the two-photon excited fluorescence detection of atomic fluorine simpler and more sensitive.

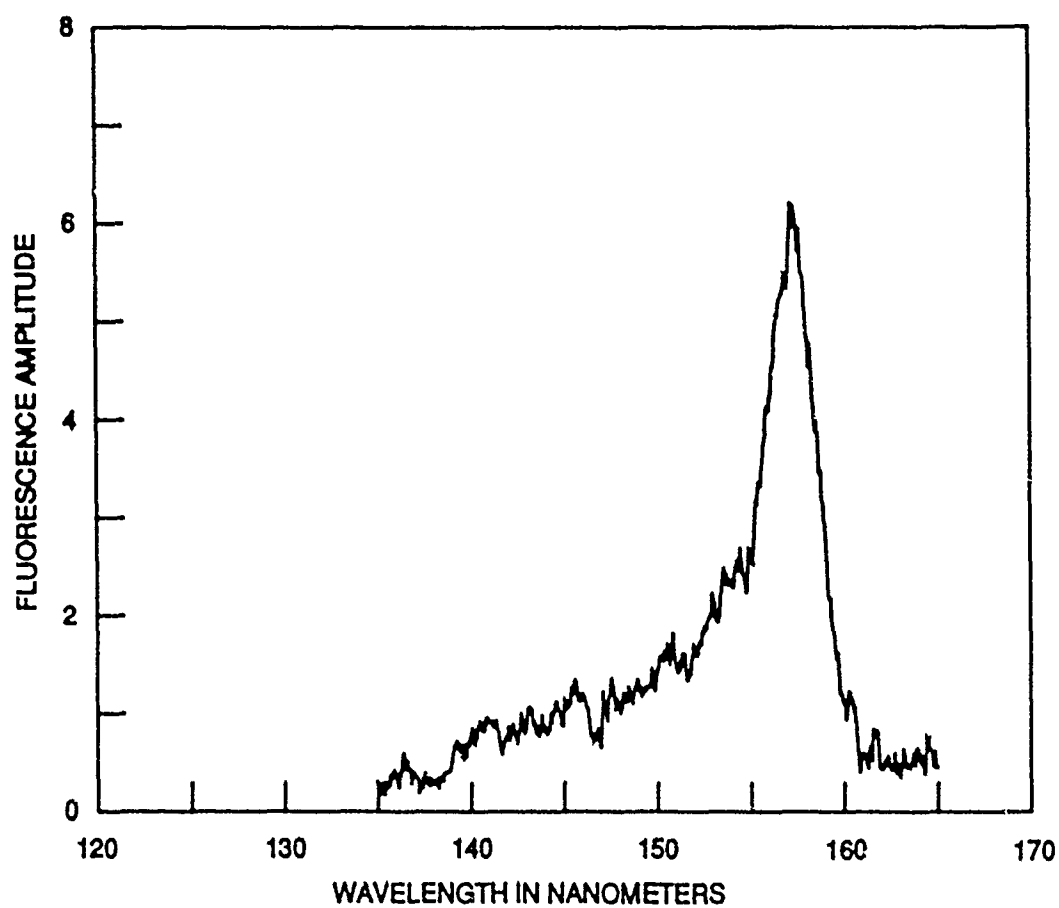
REFERENCES

1. J. K. Rice, A. K. Hays, and J. R. Woodworth, *Appl. Phys. Lett.* **31**, 31 (1977).
2. M. Dieglelmann, "Untersuchungen an molekularen Halogenlasern: Fluoreszenzspektroskopie, Reaktionskinetik und Laserexperimente," Dissertation, Ludwig-Maximilians-Universität, Munich (1980).
3. T. Sakai, K. Tanaka, A. Murakami, H. Iwaki, H. Terashima, and T. Shoda, *J. Phys. B.* **21**, 229 (1988).
4. G. C. Herring, M. J. Dyer, L. E. Jusinski, and W. K. Bischel, *Opt. Lett.* **13**, 360 (1988).



RA-6066-2

Figure 1. Experimental schematic for F₂ detection.



RA-6066-5

Figure 2. VUV emission on excitation of the $F_2 F^1\Pi_g (v' = 2)$ state.

SURFACE THERMOMETRY OF ENERGETIC MATERIALS BY LASER-INDUCED FLUORESCENCE

AFOSR Grant/Contract No. F49620-87-C-0040

Principal Investigators: Michael E. Post and Larry P. Goss

Systems Research Laboratories, Inc.
A Division of Arvin/Calspan
2800 Indian Ripple Road
Dayton, OH 45440-3696

SUMMARY/OVERVIEW: The objective of this research was to continue the development and application of the thermal-phosphor LIF technique for temperature measurement on reacting surfaces. During this program, the technique has been extended from a point to a two-dimensional measurement, developed for measuring thermal depth profiles of reacting materials, and applied to ceramic and composite materials for heat-transfer studies. During the past year a major effort has been underway to develop a fiber-optic probe based on the LIF technique and to extend the LIF method to the simultaneous measurement of velocity and temperature.

TECHNICAL DISCUSSION

The thermal-phosphor LIF technique lends itself naturally to the development of a fiber-optic probe. The advantages of such a probe over thermocouples include increased signal-to-noise ratio, ability to survive harsh flame and chemically reacting environments, and natural immunity to optical and electronic interference. The experimental arrangement of the fiber-optic probe developed for study is shown in Fig. 1. The probe consists of a 200- μm sapphire rod to which a single Dy:YAG crystal is bonded using a high-temperature ceramic adhesive. Sapphire was chosen for this purpose because of its high melting temperature and chemical inertness. The sapphire rod is coupled to a quartz fiber-optic cable which serves not only to transmit the 355-nm light from a Nd:YAG laser which excites the Dy:YAG crystal but also to receive the resulting fluorescence signal from the crystal. Because the probe is single ended, it can be employed in minimum-optical-access applications such as internal combustors and turbo-machinery. The 355-nm beam is coupled into the quartz fiber by a beam splitter which reflects the UV beam and transmits visible wavelengths. The fluorescence signal from the crystal exits the quartz fiber, where it is collimated and split into two equal paths which are fed into green (496-nm) or blue (467-nm) filters and detected by photomultipliers. The integrated signals from both photomultipliers are digitized and stored in a computer for analysis. Data reduction consists of ratioing the blue and green signals to determine the probe temperature.

Calibration of the fiber-optic probe was conducted with a platinum coiled oven over the temperature range 300 - 1700 K. Because of the size of the sapphire probe, its temporal response is limited. Thus, the main applications of the probe are associated

with average-temperature measurements. By isolating the thermally sensitive phosphors from the sapphire tip (dispersing the crystals in the material to be studied), however, the response can be greatly increased. Applications of this probe to gaseous and solid combustion processes are presently underway.

A substantial portion of the effort during the past year has been devoted to extension of the thermal-phosphor LIF technique to a method for simultaneous two-dimensional measurement of velocity and temperature. The concept involves combining the unique capabilities of the LIF technique in determining temperature with the capabilities of particle-image-velocimetry (PIV) techniques to enable measurement of both temperature and velocity in a combustng flowfield. The extended technique consists of seeding a flowfield with Dy:YAG particles, exciting fluorescence within the particles from which the local gas temperatures can be determined, and then exposing the particle field a second time to determine the spatial displacement of the particles between laser pulses. The double exposure of the particle field can be achieved by utilizing a double-pulsed Nd:YAG laser. This laser is capable of producing two laser pulses separated by a 25 - 250 μ s interval. By controlling the time separation between laser pulses, the spatial resolution of the velocity measurement can be adjusted to ~ 1 mm for flows up to 40 m/s.

The double-exposed particle-field image is captured either with a digitizing camera or on film. The resulting image is then analyzed to determine the coordinates of the particles and to match displaced-particle image pairs of the double-pulsed image. This analysis is a two-step process which involves 1) construction of a correlation map from which average-velocity displacements can be determined and 2) use of a particle tracker which employs the average-displacement information to find particle pairs. With the combined correlator-tracker, $\sim 1 - 3$ min. is required to determine the velocity vectors over a 384 x 576 pixel image. As with most other double-pulsed velocimetry techniques, this method displays a 180-deg. directional ambiguity, associated with the initial pulse being indistinguishable from the second pulse. However, since the direction of velocity flow in most cases is well known, this does not present a problem. Results from measurements made on a cold flowing jet from a 5-mm tapered nozzle are presented in Fig. 2. The measured exit velocity of the cold jet was 35.5 m/s, which agreed well with the 33.7 m/s velocity based on the mass flow of the jet.

The experimental arrangement for combining the LIF and PIV techniques is shown in Fig. 3. A double-pulsed Nd:YAG laser will be used to produce a 355-nm laser sheet for particle fluorescence and to produce a 532-nm laser sheet for Mie scattering for the PIV technique. Two CCD cameras--an intensified one for the LIF technique and a non-intensified one for the PIV technique--are required for combining the techniques. The flowfield to be studied will be seeded with Dy:YAG crystals which will not only fluoresce when excited by the 355-nm laser light, allowing the temperature to be determined, but also act to scatter the 532-nm laser light (Mie scattering) to pinpoint individual particle positions for velocity determination. Experiments are presently underway to apply the combined technique to the study of simple jet diffusion flames.

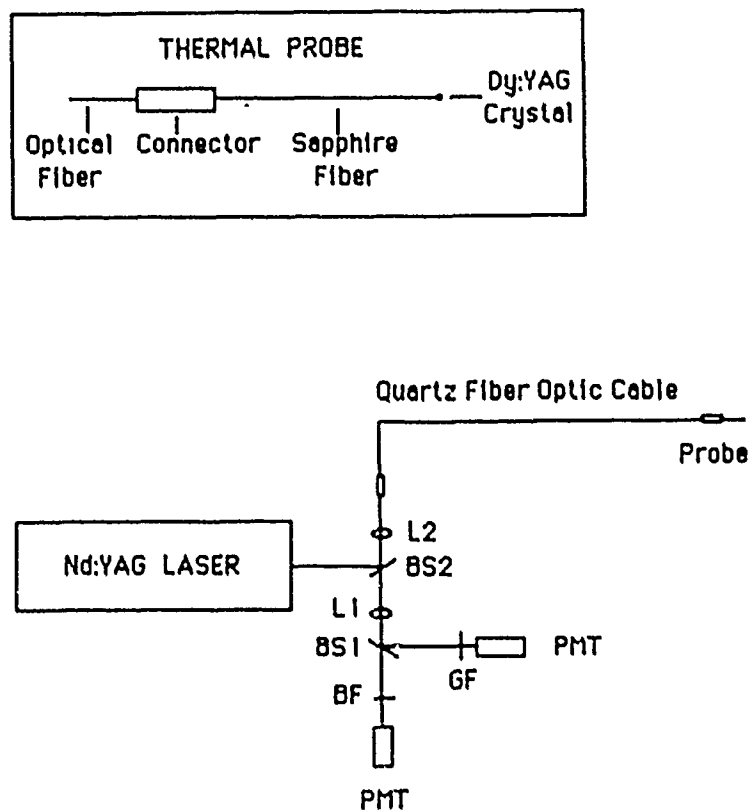


Figure 1. Schematic Diagram of Thermal-Phosphor LIF Fiber-Optic Probe. L1 and L2 are lenses; BS1 is 50/50 beam splitter; BS2 is UV beam splitter; BF is blue filter; GF is green filter; PMT is photomultiplier.

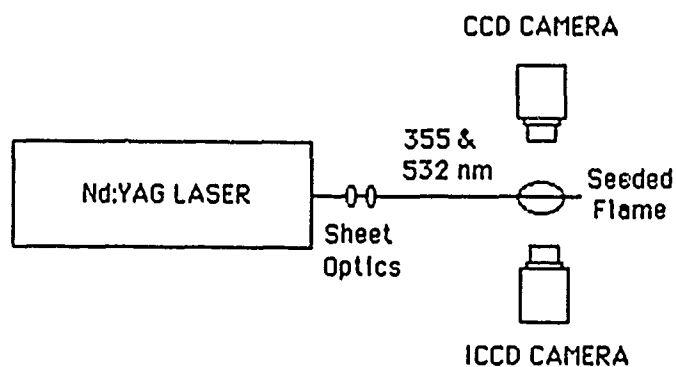


Figure 3. Schematic Diagram of Experimental Layout for Combined Temperature (LIF) and Velocity (PIV) Measurements.

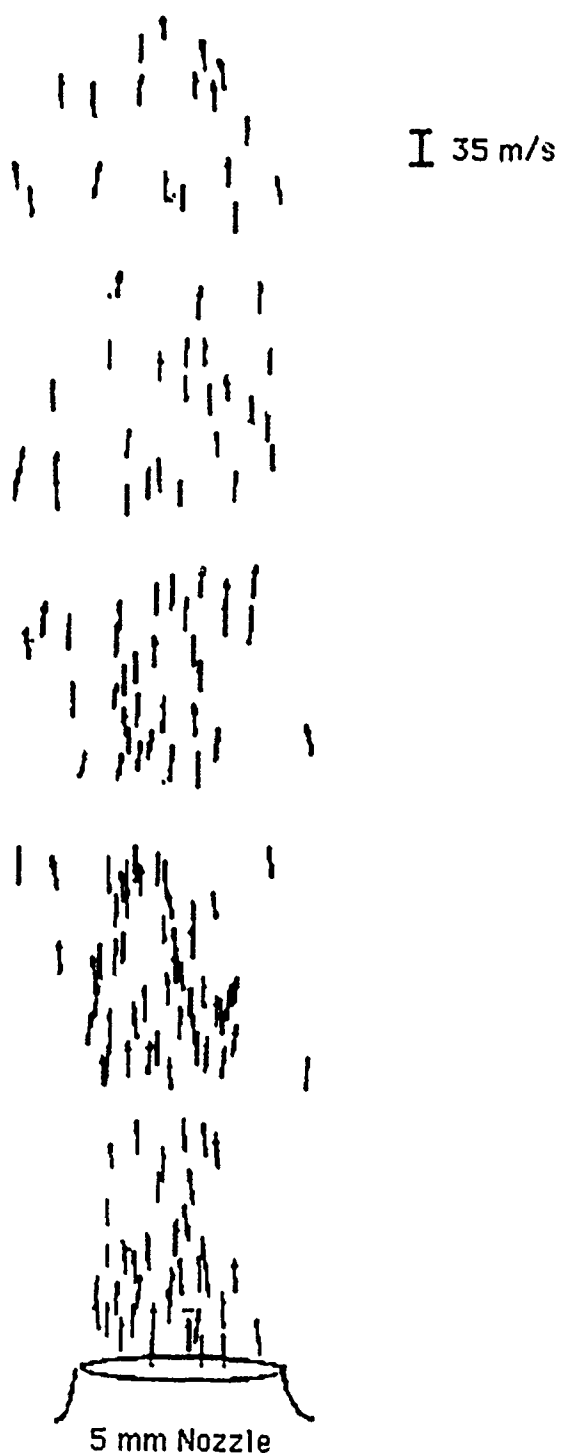


Figure 2. Measured Velocity Vectors from a 5-mm Jet. Average speed was determined to be 35.5 m/s. Data were reduced with correlator-tracker software.

(AFOSR Grant No. 89-0297)

Principal Investigator: Dr. Thomas M. York

Chairman and Professor
Aeronautical and Astronautical
Engineering Department
328 CAE Bldg., 2036 Neil Avenue
The Ohio State University
Columbus, Ohio 43210
(614-292-2691)

SUMMARY/OVERVIEW:

The research will involve diagnostic studies of plasma thrusters. These devices generate ionized gases which are accelerated at thermal and electromagnetic modes. The research effort will use the new, high resolution diagnostic techniques that will determine electron densities, local magnetic fields and density fluctuations indicating anomalous transport. A long wavelength carbon dioxide laser which allows more sensitive measurements, with its long wavelength, will be used. The laser will be coupled with a Far Infrared Laser System capable of generating beams around ten milliwatt power levels, and provide a diagnostic study that has not yet been used in thruster plasma diagnosis.

TECHNICAL DISCUSSION:

Description and Capabilities of Laser Source

The laser system that will be the heart of the diagnostic arrangements is a CO₂ source (Model 570, Apollo Lasers, Chatsworth, CA). This is a tunable system with an output of 30 Watts minimum at 50 or more wavelengths, TEM₀₀. It is capable of 65 W output CW or 200 W pulsed. This laser can also be used to pump an FIR laser (Model 122, Apollo Lasers, Chatsworth, CA). Using methanol, this can operate between 70 μm and 500 μm ; at 118.8 μm power levels on the order of 100 mW CW or 200 mW pulsed are available; beam diameter is 10 mm. These wavelengths and power levels are appropriate for diagnosing the plasmas of interest in the exhaust of plasma thruster, as will be discussed below. Along with the laser, modulating and mixing components in the optical train are critical, as well as detectors at the various wavelengths.

Plasma Properties in the Thruster Exhaust Field

The plasma being ejected from MPD type device has been categorized by a number of research studies. In 1971, NASA-Lewis reported Thomson scattering measurements in the exhaust of a nitrogen MPD: at 20kA, and 11.2kA 30 cm from the exit plane $N_e \approx 8 \times 10^{13} \text{ cm}^{-3}$, $T_e \approx 5 \text{ eV}$. With argon, a propellant, a spatial variation of properties was reported by E.M. Campbell (Princeton EPL) in 1977, who used Langmuir probes: at 4kA with 12g/Sec, $N_e = 6 \times 10^{14} \text{ cm}^{-3}$ to $2 \times 10^{13} \text{ cm}^{-3}$ between 0 and 30 cm on axis while $T_e = 12,000^\circ\text{K}$ to $4,000^\circ\text{K}$ between 0 and 30 cm. In 1985, an MPD operated at AFAL was diagnosed with Langmuir probes developed by the principal investigator and indicated $T_e = 2 \text{ eV}$ at 25 cm, while $N_e = 4.48 \times 10^{15}$ at 20 cm and $N_e = 1.9 \times 10^{15}$ at 30 cm.

Based on the above evaluations, it is anticipated that source plasma generated by 4kA will produce plasmas with $N_e \approx 10^{15} \text{ cm}^{-3}$, 4eV and will expand to $N_e = 10^{14} \text{ cm}^{-3}$, $T_e \approx 2 \text{ eV}$ at 30 cm. These are critical values when designing a diagnostic system.

PROPOSED RESEARCH STUDIES

The effort to be carried out will involve three different diagnostic measurements with the CO_2 laser based system: (1) multi-beam interferometry; (2) Faraday-rotation measurements of local B-field; and (3) fluctuation studies. Each of these has its own inherent difficulty; i.e., this is not an application of off-the-shelf type techniques, but the application of recently reported, physically proven techniques which will require careful experimental design and unique components to produce useful results. Generally, the list above is indicative of increasing difficulty. A one year effort, especially with a significant percentage being carried by a (new) graduate student researcher, must concentrate on the simpler techniques in order to optimize results. Accordingly, some techniques (2 and 3) will receive careful and complete evaluation with respect to experimental design, while emphasis will be directed to accomplishing measurements with the multi-beam interferometer.

Multi-beam Interferometer

This technique generally utilizes a Mach-Zender configuration. A measurement of phase shift (ϕ) allows determination of electron density as

$$\phi = 2.82 \times 10^{-12} \lambda_0 \int_{Z_1}^{Z_2} N_e(Z) dZ \quad (\text{Cg5 units})$$

When λ_0 is the laser wavelength, Z is the path variable through the plasma. In the above, measurement of \oint indicates the integrated line density.

Clearly, one can see the importance of CO_2 radiation at $10\mu\text{m}$ as compared to say, red light at 6973\AA . Also, the unfolding of an axisymmetric profile of Ne requires a large number (2-5) of interferometer channels. Successful applications of this technique with CO_2 lasers have produced time histories of profiles of $\text{Ne}(r)$ over a period of 20 ms with $\text{Ne} \approx 10^{15} \text{ cm}^{-3}$ and $l \approx 10 \text{ cm}$. Considerable care will have to be exercised in detector selection to be successful. The use of a Bragg cell to modulate the beam has proven successful and that technique will be pursued. Care will have to be taken with the beam deflection (α) due to gradients, as $\alpha \sim M_0 \lambda_0^2$, and this could cause problems in location of detector windows. Another advantage of large λ_0 is that the sensitivity to mechanical vibration decreases; specifically, when $\lambda_0 > 4 \times 10^5 [\Delta\epsilon/r_0 n_0]$ where $\Delta\epsilon$ is vibration induced path change and r_0 is plasma radius.

Faraday Rotation Measurements of B field - Polarimetry

The determination of local, unperturbed magnetic field is quite difficult; all experimenters use physical loops placed in the plasma. This disturbs the signal, cools the plasma, and alters current conduction path. So, a nonintrusive technique is quite valuable. Through Maxwells' equation, the local current density can also be determined.

The basic principle of this measurement is that the plane of polarization of a laser beam will be rotated proportional to B , as

$$\theta \text{ (deg)} = 1.5 \times 10^{-12} \lambda_0^2 \int_0^l \text{Ne} B_{11} (\text{kG}) dl$$

Clearly, a large λ_0 will allow significant θ to be generated even though B_{11} (the component of B along propagation) will be small. Specifically with $\text{Ne} \approx 10^{15} \text{ cm}^{-3}$ and $l \approx 10 \text{ cm}$, the θ with CO_2 radiation would be very difficult to

measure. However, using $118.8 \mu\text{m}$ will produce a rotation of greater than 1 degree. It can be seen that the signal involves the product, $N B_{11}$, so the results from the CO_2 measurement of $N(r)$ will be critical to accurate determination of $B_{11}(r)$ profiles.

Measurement of Electron Density Fluctuations

This technique is based upon the principles of Thomson scattering -scattering from free electrons and ions. The ability to measure fluctuations, which are extremely important because they generate anomalous transport, is related to a number of factors. The characteristic parameter for Thomson Scattering is $\alpha = 1/k\lambda_D = \lambda_0/4\pi\lambda_D \sin(\theta_s/2)$ where λ_D is the Debye length and θ_s is the scattering angle. The range, $\alpha \ll 1$, defines normal Thomson Scattering for Te, Ne. When $\alpha \gg 1$ plasma waves and thermal ion fluctuations may be studied and ion temperature determined.

Wave scattering can result in large enhancements in the scattered power, well above those achieved with thermal motion, as scattered power is

$$P_s = k P_i r_e^2 \lambda_0^2 (N)^2 L_v$$

Where P_i is incident power, r_e is electron radius, λ_0 is incident wavelength, N is defined by $N = \omega_{pe} / (kZ - \omega)$ and L_v is the length of the scattering volume. CO_2 lasers with 10-100 W can be used, but also, FIR lasers generating $119 \mu\text{m}$ at 10-100 mW output power levels have been sufficient to perform scattering measurements with good signal-to-noise ratios. One critical element in the type of measurement is a low-noise fundamental mode mixer. Fluctuation measurements over a range of frequencies have been made with plasmas similar to those expected in MPD exhaust flows.

AFOSR/ONR CONTRACTORS' MEETING ON COMBUSTIONInvitees

Dr. Scott L. Anderson
Department of Chemistry
State University of New York
Stony Brook NY 11794-3400
(516)632-7915

Dr K Annamalai
Mechanical Engineering Dept
Texas AM University
College Station TX 77843-3123

Dr Kurt Annen
Aerodyne Research, Inc.
45 Manning Road
Manning Park Research Center
Billerica MA 01821-3976
(508)663-9500

Dr Simon H Bauer
Department of Chemistry
Cornell University
Ithaca NY 14853-1301

Dr. S. L. Baughcum
Spectra Technology
2755 Northrup Way
Bellevue WA 98004-1495
(206)828-3517

Dr. H. R. Baum
National Institute of
Standards and Technology
Center for Fire Research
Gaithersburg MD 20899
(301)975-6668

Dr John Bdzil
Los Alamos National Laboratory
Los Alamos NM 87545

Dr. H. L. Beach
NASA Langley Research Center
MS 168
Hampton VA 23665-5225
(804)865-3772
(804)865-2658

Dr. Josette Bellan
Applied Technologies Section
Jet Propulsion Laboratory
4800 Oak Grove Drive
Pasadena CA 91109
(818)354-6959

Dr. Paul A. Bonczyk
United Technologies Research
Center
Silver Lane
East Hartford CT 06108
(203)727-7162

Dr Kevin G Bowcutt
Rockwell International
Mail Code WA40
2770 East Carson Street
Lakewood CA 90712
(213)420-0317

Dr. C. T. Bowman
Department of Mechanical
Engineering
Stanford University
Stanford CA 94305-3032
(415)723-1745

Dr Robert E Breidenthal
Department of Aeronautics and
Astronautics
University of Washington, FS10
Seattle WA 98195
(206)545-1098

Dr. J. E. Broadwell
Graduate Aeronautical Labs
California Institute of
Technology
Pasadena CA 91125

Dr Garry L Brown
Aeronautical Research Labs
506 Lorimer St, Fishermen's Bn
Box 4331, P. O.
Melbourne, Victoria AUSTRALIA 3001
03-647-7511

Dr R C Brown
Aerodyne Research, Inc.
45 Manning Road
Manning Park Research Center
Billerica MA 01821-3976
(508)663-9500

Dr Dennis Bushnell
NASA Langley Research Center
Mail Stop 168
Hampton VA 23665
(804)865-4546

Dr Ron Butler
WRDC/POSF
Wright-Patterson AFB OH 45433-6563

Dr. T. D. Butler
Group T-3
Los Alamos National Laboratory
Los Alamos NM 87545
(505)667-4156

Dr. H. F. Calcote
AeroChem Research Laboratories
Inc.
P. O. Box 12
Princeton NJ 08542
(609)921-7070

Dr. B. J. Cantwell
Department of Mechanical
Engineering
Stanford University
Stanford CA 94305-3032
(415)723-4825

Dr. T Charalampopoulos
Mechanical Engineering Dept.
Louisiana State University
Baton Rouge LA 70803
(504)388-5792
(504)388-5799

Capt Wayne Chepren
HQ AFESC/RDV
Tyndall AFB FL 32403-6001
(904)283-4234
AV523-4234

Dr. Robert E. Childs
Nielsen Engineering and
Research, Inc.
510 Clyde Avenue
Mountain View CA 94043-2287
(415)968-9457

Dr S Y Cho
Department of Mechanical and
Aerospace Engineering
Princeton University
Princeton NJ 08544-5263

Dr M-S Chou
Building R1, Room 1044
TRW Space and Technology Group
One Space Park
Redondo Beach CA 90278
(213)535-4321

Mr. R. W. Claus
NASA Lewis Research Center
21000 Brookpark Road
Cleveland OH 44135-3127
(216)433-5869

Dr. M. B. Colket
United Technologies Research
Center
Silver Lane
East Hartford CT 06108
(203)727-7481

Dr. S. M. Correa
General Electric - Corporate
Research and Development
P. O. Box 8
Schenectady NY 12301
(518)387-5853

Dr. E. T. Curran
WRDC/CA-P
Wright-Patterson AFB OH 45433-6563
(513)255-2246
AV785-2246

Dr Werner J A Dahm
Department of Aerospace
Engineering
The University of Michigan
Ann Arbor MI 48109-2140
(313)764-4318

Dr. R. W. Dibble
Combustion Research Facility
Sandia National Laboratories
Livermore CA 94550
(415)294-2825

Mr Lee G Dodge
Southwest Research Institute
P O Drawer 28510
San Antonio TX 78284
(512)684-5111
Ext 3251

Mr Steven Clouser
Research and Technology Group
Naval Air Propulsion Center
Trenton NJ 08628
(609)896-5752
AV442-7752

Mr Stephen Corda
Applied Physics Laboratory
Johns Hopkins University
Johns Hopkins Road
Laurel MD 20707-6099
(301)953-5000
Ext 4654

Dr Clayton T Crowe
Department of Mechanical
Engineering
Washington State University
Pullman WA 99164-2920
(509)335-3214

Dr Eli K Dabora
Mechanical Engineering Dept
University of Connecticut
Box U-139 ME
Storrs CT 06268
(203)486-2415
(203)486-2189

Lt Col Larry P Davis
AFOSR/NC
Bolling AFB DC 20332-6448
(202)767-4963
AV297-4963

Dr. P. E. Dimotakis
Graduate Aeronautical Labs
California Institute of
Technology
Pasadena CA 91125
(818)356-4456

Dr David Dolling
Department of Aerospace Engrg
and Engineering Mechanics
University of Texas at Austin
Austin TX 78712
(512)471-4470
(512)471-7593

Dr. M. C. Drake
Physical Chemistry Department
General Motors Research Labs
Twelve Mile and Mound Roads
Warren MI 48090-9055

Dr. Fredrick L. Dyer
Department of Mechanical and
Aerospace Engineering
Princeton University
Princeton NJ 08544-5263
(609)452-5206

Dr C Dutton
Department of Mechanical and
Industrial Engineering
University of Illinois
Urbana IL 61801

Dr. H. A. Dwyer
Department of Mechanical
Engineering
University of California
Davis CA 95616

Dr Raymond B Edelman
WC 70
Rocketdyne
6633 Canoga Avenue
Canoga Park CA 91304
(805)371-7196

Ms Charlotte Eigel
WRDC/POSF
Wright-Patterson AFB OH 45433-6563
(513)255-5106
AV785-5106

Dr Phillip Emmerman
Harry Diamond Laboratories
Attn. SLCHD-ST-RD
2800 Powder Mill Road
Adelphi MD 20783-1197
(301)394-3000

Dr. K. C. Ernst
Pratt and Whitney Aircraft
Group
Government Products Division
West Palm Beach FL 33402

Dr. G. M. Faeth
Department of Aerospace
Engineering
University of Michigan
Ann Arbor MI 48109-2140
(313)764-7202

Dr. Francis E. Fendell
TRW Space and Technology Group
Building R1, Room 1022
One Space Park
Redondo Beach CA 90278
(213)812-0506

Capt Nannette Founds
AFWL/ARDF
Kirtland AFB NM 87117-6008
(505)844-0196
AV244-0196

Dr Michael Frenklach
202 Academic Projects Building
The Pennsylvania State
University
University Park PA 16802
(814)865-4392

Mr Jack Fultz
WRDC/POPR
Wright-Patterson AFB OH 45433-6563
(513)255-2175
AV785-2175

Dr David E Fyfe
Laboratory for Computational
Physics
Naval Research Laboratory
Washington DC 20375
(202)767-6583
AV297-6583

Dr Alon Gany
 Department of Aeronautical Eng
 Technion-Israel Institute of
 Technology
 32000 Haifa, ISRAEL
 04-292308

Dr. A. F. Ghoniem
 Department of Mechanical
 Engineering
 MIT
 Cambridge MA 02139
 (617)253-2295

Mr. R. Giffen
 General Electric Company
 Aircraft Engine Group
 Neumann Way
 Cincinnati OH 45215

Dr. P. Givi
 Department of Mechanical
 and Aerospace Engineering
 State University of New York
 Buffalo NY 14260

Dr. Irvin Glassman
 Department of Mechanical and
 Aerospace Engineering
 Princeton University
 Princeton NJ 08544-5263
 (609)452-5199

Dr Frederick C Gouldin
 Department of Mechanical and
 Aerospace Engineering
 Cornell University
 Ithaca NY 14853-1301

Dr F Grinstein
 Laboratory for Computational
 Physics
 Naval Research Laboratory
 Washington DC 20375
 (202)767-

Dr William Grosshandler
 National Science Foundation
 Chemical and Process Eng. Div.
 1800 G Street, N. W.
 Washington DC 20550
 (202)357-9606

Dr Ephraim Gutmark
 Research Department
 Code 3892
 Naval Weapons Center
 China Lake CA 93555-6001
 (619)939-3745
 AV437-3745

Dr Robert J Hansen
 Office of Naval Research
 Code 1215
 800 North Quincy Street
 Arlington VA 22217-5000
 (202)696-4715

Dr Stephen J Harris
 Physical Chemistry Department
 General Motors Research Labs
 30500 Mound Road
 Warren MI 48090-9055
 (313)986-1305

Capt Henry Helin
 AFOSR/NA
 Bolling AFB DC 20332-6448
 (202)767-0471
 AV297-0471

Mr Norman Hirsch
 WRDC/POPR
 Wright-Patterson AFB OH 45433-6563
 (513)255-2175
 AV785-2175

Mr Robert E Holland
 United Technologies Chemical
 Systems Division
 P O Box 49028
 San Jose CA 95161-9028
 (408)224-7656

Mr. Dale A. Hudson
WRDC/POTC
Wright-Patterson AFB OH 45433-6563
(513)255-5974
AV785-5974

Dr A K M F Hussain
Department of Mechanical
Engineering
University of Houston
Houston TX 77004
(713)749-4444

Dr. T. A. Jackson
WRDC/POSF
Wright-Patterson AFB OH 45433-6563
(513)255-6462
AV785-6462

Mr Gordon E Jensen
United Technologies Chemical
Systems Division
P O Box 49028
San Jose CA 95161-9028
(408)365-5552

Dr Sheridan C Johnston
Combustion Sciences
Sandia National Laboratories
Livermore CA 94550
(415)294-2138

Dr. W-H Jou
Flow Industries, Inc.
21414 68th Avenue South
Kent WA 98031
(206)872-8500

Dr. Ann R. Karagozian
Mechanical, Aerospace and
Nuclear Engineering Department
University of California, LA
Los Angeles CA 90024
(213)825-5653

Dr. Arnold A. Kelly
Department of Mechanical and
Aerospace Engineering
Princeton University
Princeton NJ 08544-5263
(609)452-5221

Dr. John T. Kelly
Altex Technologies Corporation
650 Nuttman Road
Suite 114
Santa Clara CA 95054
(408)980-8610

Dr Ian M Kennedy
Mechanical Engineering Dept
University of California,
Davis
Davis CA 95616
(916)752-2796

Mr. M. Kenworthy
General Electric Company
Aircraft Engine Group
Neumann Way
Cincinnati OH 45215

Dr. J. A. Kezerle
Gas Research Institute
8600 West Bryn Mawr Avenue
Chicago IL 60631
(312)399-8331

Dr. G. B. King
Department of Mechanical
Engineering
Purdue University
West Lafayette IN 47907
(317)494-2713

Mr. R. Kirby
Garrett Turbine Engine Company
111 South 34th Street
P. O. Box 5217
Phoenix AZ 85010

Dr Charles E Kolb
Aerodyne Research, Inc.
45 Manning Road
Manning Park Research Center
Billerica MA 01821-3976
(508)663-9500

Dr Wolfgang Kollmann
Mechanical Engineering Dept
University of California,
Davis
Davis CA 95616
(916)752-1452

Mr. Gil Kraemer
Combustion Section, D-12
AVCO-Lycoming
550 South Main Street
Stratford CT 06497
(203)385-3283

Dr C R Krishna
Department of Nuclear Energy
Brookhaven National Laboratory
Upton NY 11973

Dr Kenneth K Kuo
Department of Mechanical
Engineering
Pennsylvania State University
University Park PA 16802
(814)865-6741

Dr. Marshall Lapp
High Temperature Interfaces
Division
Sandia National Laboratories
Livermore CA 94550
(415)294-2435

Dr. John C. Larue
Department of Mechanical
Engineering
University of California
Irvine CA 92717

Dr. A. Laufer
Office of Energy Research
U. S. Department of Energy
1000 Independence Avenue, N.W.
Washington DC 20585
(202)353-5820

Dr. N. M. Laurendeau
Department of Mechanical
Engineering
Purdue University
West Lafayette IN 47907
(317)494-2713

Dr. Moshe Lavid
ML Energia, Inc.
P. O. Box 1468
Princeton NJ 08540
(609)799-7970

Dr. C. K. Law
Department of Mechanical and
Aerospace Engineering
Princeton University
Princeton NJ 08544-5263
(609)452-5271

Dr Stan Lawton
McDonnell Douglas Research Lab
McDonnell Douglas Corporation
PO Box 516
St Louis MO 63166-0516
(314)233-2547

Dr J Carl Leader
McDonnell Douglas Research Lab
McDonnell Douglas Corporation
PO Box 516
St Louis MO 63166-0516
(314)232-4687

Dr C C Lee
Environmental Protection
Agency
Cincinnati OH 45268
(513)569-7520

Dr Spiro Lekoudis
Office of Naval Research
Mechanics Division, Code 432
800 North Quincy Street
Arlington VA 22217-5000
(202)696-4406

Dr. Anthony Leonard
Graduate Aeronautical Labs
California Institute of
Technology
Pasadena CA 91125
(818)356-4465

Dr. R. S. Levine
National Institute of
Standards and Technology
Center for Fire Research
Gaithersburg MD 20899
(301)921-3845

Dr. Erwin A. Lezberg
NASA Lewis Research Center
21000 Brookpark Road
Cleveland OH 44135-3127
(216)433-4000
Ext. 6161

Dr. P. A. Libby
Dept. Of. Appl. Mech. and
Engrg. Sci.
University of California
La Jolla CA 92093
(619)534-3168

Dr. Wilbert Lick
Department of Mechanical and
Environmental Engineering
University of California
Santa Barbara CA 93106

Dr. Hans W. Liepmann
Graduate Aeronautical Labs
California Institute of
Technology
Pasadena CA 91125
(818)356-4535

Dr. F. E. Lytle
Department of Chemistry
Purdue University
West Lafayette IN 47907
(317)494-5261

Dr Andrej Macek
National Institute of
Standards and Technology
Physics Building, B-312
Gaithersburg MD 20899
(301)975-2610

Dr James Madson
McDonnell Douglas Research Lab
McDonnell Douglas Corporation
PO Box 516
St Louis MO 63166-0516

Dr. Edward T. Mahefkey
WRDC/POOC-5
Wright-Patterson AFB OH 45433-6563
(513)255-6241
AV785-6241

Dr Oscar Manley
US Department of Energy
Office of Energy Research
1000 Independence Avenue, SW
Washington DC 20585

Dr. Nagi N. Mansour
Computational Fluid Mechanics
Branch, M/S 202A-1
NASA Ames Research Center
Moffett Field CA 94035
(415)694-6420

Dr. F. E. Marble
Engrg. and Appl. Sci. Dept.
California Institute of
Technology
Pasadena CA 91125
(818)356-4784

Dr John C Marek
NASA Lewis Research Center
21000 Brookpark Road
Cleveland OH 44135-3127

Mr. C. R. Martel
WRDC/POSF
Wright-Patterson AFB OH 45433-6563
(513)255-7431
AV785-7431

Dr Bruce Masson
AFWL/ARDF
Kirtland AFB NM 87117-6008
(505)844-0208
AV244-0208

Dr. James McDonald
Code 6110
Naval Research Laboratory
Chemistry Division
Washington DC 20375
(202)767-3340
AV297-3340

Dr D K McLaughlin
233 Hammond Building
Pennsylvania State University
University Park PA 16802
(814)865-2569

Dr James McMichael
AFOSR/NA
Bolling AFB DC 20332-6448
(202)767-4936
AV297-4936

Dr A M Mellor
Mech Matls Eng Department
Station B, Box 6019
Vanderbilt University
Nashville TN 37235
(615)343-6214

Dr. Lynn A. Melton
Programs in Chemistry
University of Texas, Dallas
P. O. Box 668
Richardson TX 75080
(214)690-2913

Dr. R. Metcalfe
Department of Mechanical
Engineering
University of Houston
Houston TX 77004
(713)749-2439

Dr D L Mingori
Mechanical, Aerospace and
Nuclear Engineering Dept
University of California
Los Angeles CA 90024
(213)825-1265

Dr. Andrzej W Miziolek
Ignition and Combustion Branch
Interior Ballistics Division
Ballistic Research Laboratory
Aberdeen Proving Gnd MD 21005-5066
(301)278-6157

Dr Parviz Moin
Center for Turbulence Research
Stanford University
Stanford CA 94305-3032
(415)725-2081

Dr. H. Mongia
General Motors Corporation
Allison Gas Turbine Operations
P. O. Box 420
Indianapolis IN 46206-0420
(317)242-5945

Dr Peter A Monkewitz
Mechanical, Aerospace and
Nuclear Engineering Dept
University of California
Los Angeles CA 90024
(213)825-5217

Dr P J Morris
233-L Hammond Building
Pennsylvania State University
University Park PA 16802
(814)863-0157

Dr. E. J. Mularz
Aviation Res. and Tech. Activ.
NASA Lewis Res. Ctr., MS 5-11
21000 Brookpark Road
Cleveland OH 44135-3127
(216)433-5850

Dr. M. G. Mungal
Department of Mechanical
Engineering
Stanford University
Stanford CA 94305-3032
(415)723-1745

Dr Arje Nachman
AFOSR/NM
Bolling AFB DC 20332-6448
(202)767-5028
AV297-5028

Dr. Abdollah Nejad
WRDC/POPT
Wright-Patterson AFB OH 45433-6563
(513)255-9991
AV785-9991

Dr Herbert Nelson
Code 6110, Chemistry Division
Naval Research Laboratory
Washington DC 20375
(202)767-3686

Dr. David Nixon
Nielsen Engineering and
Research, Inc.
510 Clyde Avenue
Mountain View CA 94043-2287
(415)968-9457

Dr. G. B. Northam
NASA Langley Research Center
MS 168
Hampton VA 23665-5225
(804)865-2803

Dr. R. C. Oldenberg
Chemistry Division
Los Alamos National Laboratory
Los Alamos NM 87545
(505)667-2096
(505)667-3758

Dr. A. K. Oppenheim
Department of Mechanical
Engineering
University of California
Berkeley CA 94720
(415)642-0211

Dr. E. S. Oran
Laboratory for Computational
Physics
Naval Research Laboratory
Washington DC 20375
(202)767-2960

Dr Simon Ostrach
Case Western Reserve Univ
Department of Mechanical and
Aerospace Engineering
Cleveland OH 44106

Dr Richard B Peterson
Department of Mechanical
Engineering
Oregon State University
Corvallis OR 97331-6001
(503)754-2567

Dr. W. M. Pitts
National Institute of
Standards and Technology
Center for Fire Research
Gaithersburg MD 20899
(301)975-6486

Dr. Robert W. Pitz
 Department of Mechanical and
 Materials Engineering
 Vanderbilt University
 Nashville TN 37235
 (615)322-0209

Dr. C. L. Proctor II
 Department of Mechanical
 Engineering
 University of Florida
 Gainesville FL 32611
 (904)392-7555

Dr Saad Ragab
 Engrg Sci Mechanics Dept
 Virginia Polytechnic Institute
 and State University
 Blacksburg VA 24061
 (703)231-5950

Dr. R. G. Rehm
 National Institute of
 Standards and Technology
 Center for Fire Research
 Gaithersburg MD 20899

Dr David Reuss
 Fluid Mechanics Department
 General Motors Research Labs
 30500 Mound Road
 Warren MI 48090-9055
 (313)986-0029

Dr James J Riley
 Mechanical Engineering Dept
 University of Washington
 Seattle WA 98195
 (206)543-5347

Dr. W. M. Roquemore
 WRDC/POSF
 Wright-Patterson AFB OH 45433-6563
 (513)255-6813
 AV785-6813

Dr. S. B. Pope
 Department of Mechanical and
 Aerospace Engineering
 Cornell University
 Ithaca NY 14853-1301
 (607)255-4314

Dr. Herschel Rabitz
 Department of Chemistry
 Princeton University
 Princeton NJ 08544-5263
 (609)452-3917

Dr. S. R. Ray
 National Institute of
 Standards and Technology
 Center for Chemical Engrg
 Gaithersburg MD 20899

Dr M Renksizbulut
 Department of Mechanical
 Engineering
 University of Waterloo
 Waterloo, Ontario CN N2L 3G1
 (519)885-1211
 Ext 3977

Dr. W. C. Reynolds
 Department of Mechanical
 Engineering
 Stanford University
 Stanford CA 94305-3032
 (415)723-3840

Dr. U. S. Rohatgi
 Department of Nuclear Energy
 Brookhaven National Laboratory
 Upton NY 11973
 (516)282-2475

Dr. Anatol Roshko
 Graduate Aeronautical Labs
 California Institute of
 Technology
 Pasadena CA 91125
 (818)356-4484

Dr. D. E. Rosner
Department of Chemical
Engineering
Yale University
New Haven CT 06520
(203)432-4391

Dr John Ross
Department of Chemistry
Stanford University
Stanford CA 94305-3032
(415)723-9203

Dr Gabriel Roy
Office of Naval Research
Mechanics Division, Code 1132
800 North Quincy Street
Arlington VA 22217-5000
(202)696-4405

Dr Leonidas Sakell
AFOSR/NA
Bolling AFB DC 20332-6448
(202)767-4935
AV297-4935

Dr Mohammad Samimy
Ohio State University
Mechanical Engineering Dept
206 West 18th Street
Columbus OH 43210-1107
(614)422-6988

Dr. G. S. Samuelsen
Department of Mechanical
Engineering
University of California
Irvine CA 92717
(714)856-5468

Mr. John Sanborn
Garrett Turbine Engine Company
111 South 34th Street
P. O. Box 5217
Phoenix AZ 85010
(602)231-2588

Dr. B. R. Sanders
Thermofluids Division, 8363
Combustion Research Facility
Sandia National Laboratories
Livermore CA 94550
(415)294-3113

Dr. J. J. Sangiovanni
United Technologies Research
Center
Silver Lane
East Hartford CT 06108
(203)727-7328

Dr Lakshmi Sankar
School of Aerospace Engrg
Georgia Institute of
Technology
Atlanta GA 30332
(404)894-3014

Dr. Domenic Santavicca
Department of Mechanical
Engineering
Pennsylvania State University
University Park PA 16802
(814)863-1863

Dr. R. J. Santoro
Department of Mechanical
Engineering
Pennsylvania State University
University Park PA 16801
(814)863-1285

Dr Klaus Schadow
Naval Weapons Center
Code 3892
China Lake CA 93555-6001
(619)939-6532
AV437-6532

Dr. John W. Schaefer
Energy and Environmental Div.
Acurex Corporation
555 Clyde Ave., P. O. Box 7555
Mountain View CA 94039

Dr W H Schofield
Aeronautical Research Labs
506 Lorimer St, Fishermen's Bn
Box 4331, P O
Melbourne, Victoria AUSTRALIA 3001

Dr. D. J. Seery
United Technologies Research
Center
Silver Lane
East Hartford CT 06108

Dr. H. G. Semerjian
National Institute of
Standards and Technology
Center for Chemical Engrg
Gaithersburg MD 20899
(301)975-2609

Dr. K. Seshadri
Dept. Of. Appl. Mech. and
Engrg. Sci.
University of California
La Jolla CA 92093
(619)534-4876

Dr G S Settles
309 Mechanical Engrg Building
Pennsylvania State University
University Park PA 16802
(814)863-1504

Dr Robert W Shaw
Division of Chemical and
Biological Sciences
U S Army Research Office
Research Triangle Park NC 27709-2211
(919)549-0641

Mr. Harold C. Simmons
Parker Hannifin Corporation
Gas Turbine Fuel Systems Div.
17325 Euclid Avenue
Cleveland OH 44143
(216)531-3000
Ext 2309

Dr. W. A. Sirignano
School of Engineering
University of California
Irvine CA 92717
(714)856-6002

Dr Bernard Spielvogel
U S Army Research Office
P O Box 12211
Research Triangle Park NC 27709-2211

Dr David S Stewart
Department of Theoretical and
Applied Mechanics
University of Illinois
Urbana IL 61801

Dr. F. D. Stull
WRDC/POPS
Wright-Patterson AFB OH 45433-6563
(513)255-5210
AV785-5210

Dr B Sturtevant
Engrg and Appl Sci Dept
California Institute of
Technology
Pasadena CA 91125

Dr G Sullins
Applied Physics Laboratory
Johns Hopkins University
Johns Hopkins Road
Laurel MD 20707-6099
(301)953-5000

Dr. Dexter Sutterfield
National Institute for
Petroleum and Energy Research
Post Office Box 2128
Bartlesville OK 74005
(918)337-4251

Dr. L. Talbot
Department of Mechanical
Engineering
University of California
Berkeley CA 94720
(415) 642-6780

Dr Christopher Tam
Department of Mathematics
Florida State University
Tallahassee FL 32306-3027
(904) 644-2455

Julian M. Tishkoff
AFOSR/NA
Bolling AFB DC 20332-6448
(202) 767-0465
AV297-0465

Dr. T. Y. Toong
Department of Mechanical
Engineering
MIT
Cambridge MA 02139
(617) 253-3358

Dr Michael Trenary
Department of Chemistry
The University of Illinois
Chicago IL 60680

Dr Timothy R Troutt
Department of Mechanical
Engineering
Washington State University
Pullman WA 99164-2920

Dr. C. J. Ultee
United Technologies Research
Center
Silver Lane
East Hartford CT 06108

Dr A D Vakili
University of Tennessee
Space Institute
Tullahoma TN 37388

Dr. S. P. Vanka
Department of Mechanical
and Industrial Engrg
University of Illinois
Urbana IL 61801

Dr. P. J. Waltrup
Applied Physics Laboratory
Johns Hopkins University
Johns Hopkins Road
Laurel MD 20707-6099
(301) 953-5000
Ext. 4186

Dr. C. K. Westbrook
Lawrence Livermore National
Laboratories
P. O. Box 808
Livermore CA 94550

Dr. R. W. Whitehead
Office of Naval Research
Mechanics Division, Code 432
800 North Quincy Street
Arlington VA 22217-5000
(202) 696-4404

Dr James Whitelaw
Department of Mechanical Engrg
Imperial College of Science
and Technology
London SW7 2BX UK

Dr. Forman A. Williams
Department of Applied Mech and
Engineering Science
University of California
La Jolla CA 92093
(619) 534-5492

Dr. Francis Wodarczyk
AFOSR/NC
Bolling AFB DC 20332-6148
(202)767-4960
AV297-4960

Dr J M Wu
University of Tennessee
Space Institute
Tullahoma TN 37388

Dr Richard A Yetter
Department of Mechanical and
Aerospace Engineering
Princeton University
Princeton NJ 08544-5263

Mr Fred Zarlingo
Code 3246
Naval Weapons Center
China Lake CA 93555-6001
(619)939-7395
AV437-7395

Dr. E. E. Zukoski
Engrg. and Appl. Sci. Dept.
California Institute of
Technology
Pasadena CA 91125
(818)356-4785

AFOSR ROCKET PROPULSION CONTRACTORS' MEETINGInvitees

Mr. Robert Acree
AFAL/DYCC
Edwards AFB CA 93523-5000
(805)275-5598
AV525-5598

Dr George F. Adams
USA-BRL
AMXBR-18D
Aberdeen Proving Gnd MD 21005-5006
(301)278-6168
(301)278-6783

Mr Ranney Adams
AFAL/PA
Edwards AFB CA 93523-5000
(805)275-5465
AV525-5465

Dr. Horst Adolph
Synthesis and Formulations Br
Naval Surface Weapons Center
10901 New Hampshire Avenue
Silver Spring MD 20903-5000

Dr William S. Anderson
United Technologies/CSD
P.O. Box 50015
San Jose CA 95150-0015
(408)778-4302

Mr W. C. Andrepont
P.O. Box 431
858 W. Jackman
Suite 111
Lancaster CA 93534
(805)942-5098

Lt John L. Andreshak
AFAL/LKLR
Stop 24
Edwards AFB CA 93523-5000
(805)275-5194
AV525-5194

Dr Ron Atkins
Naval Weapons Center
China Lake CA 93555-6001
(619)939-1630
AV437-1630

Dr Carl Aukerman
NASA/Lewis Research Center
21000 Brookpark Road
Cleveland OH 44135
216-433-2441

Dr John Bahns
AFAL/LKCS
Stop 24
Edwards AFB CA 93523-5000

Dr William F Bailey
AFIT/ENP
Wright-Patterson AFB OH 45433-6583
(513)255-4498
AV785-4498

Dr Joseph D. Baum
SAIC
1710 Goodridge Drive
P.O. Box 1303,
McLean VA 22102
(703)827-4952

Dr Roger J. Becker
KL-462
Research Institute
University of Dayton
Dayton OH 45469
(513) 229-3938

Mr Charles Beckman
AFAL/MKPA
Stop 24
Edwards AFB CA 93523-5000
(805) 275-5487
AV525-5487

Dr Merrill Beckstead
Dept of Chemical Engineering
Brigham Young University
Provo UT 84602
(801) 378-6239

Dr Robert Beddini
Univ of Illinois
AAE Department
104 South Mathews Avenue
Urbana IL 61801-2997
(217) 333-4239

Dr Clifford Bedford
SRI International
Chemistry Laboratory
Menlo Park CA 94025
(415) 859-4449

Dr S. J. Bennett
Adv Technology Projects Div
Morton Thiokol, Inc, Wasatch
Box 524
Brigham City UT 84302
(801) 863-2980

Dr Oscar Biblarz
Department of Aeronautics
Naval Post Graduate School
Monterey CA 93943-5100
(408) 646-2972
AV878-2972

Mr Robert A. Biggers
AFAL/XXR
Stop 24
Edwards AFB CA 93523-5000
(805) 275-5241
AV525-5341

Dr S Binkley
Combustion Research Facility
Sandia National Laboratories
Livermore CA 94550

Dr Mitat A Birkan
AFOSR/NA
Bolling AFB DC 20332-6448
(202) 767-4938
AV297-4938

Dr Arthur Bracut
ARDC
LCWSL
Dover NJ 07801
(201) 724-3788
AV880-3788

Dr Mel Branch
Mechanical Engineering Dept
University of Colorado
Boulder CO 80309-0427
(303) 492-6318
(303) 492-7151

Dr John E Brandenburg
Mission Research Corporation
8560 Cinderbed Road
Suite 700
Newington VA 22122
(703) 339-6500

Dr Tom Brill
University of Delaware
Department of Chemistry
Newark DE 19716
(302) 451-2466

Dr Bruce M. Broline
PO Box 3999
M/S 82-23
Boeing Aerospace
Seattle WA 98042
(206)773-5846

Dr Robert S. Brown
United Technologies Corp
Chemical Systems Division
P. O. Box 49028
San Jose CA 95161-9028
(408)778-4680

Dr James T. Bryant
Naval Weapons Center
China Lake CA 93555-6001
(619)939-7206
AV437-7206

Dr Rodney L. Burton
Director, Space Applications
GT Devices, Inc
5705A General Washington Drive
Alexandria VA 22312
(703)642-8150

Mr David Byers
NASA Lewis Research Center
MS 500-219
21000 Brookpark Road
Cleveland OH 44135-3127
(216)433-2447

Dr George Caledonia
Physical Sciences Inc
PO Box 3100
Andover MA 01810
(617)475-9030

Dr David Campbell
AFAL/DYC
Stop 24
Edwards AFB CA 93523-5000

Dr Robert Cassel
Naval Sea Systems Command
Code 62D
Washington DC 20362
(202)692-8635

Dr Robert J. Cattolica
Sandia National Laboratories
Division 9351
Livermore CA 94550

Dr Leonard Caveny
OSD/SDIO/IST
Pentagon
Washington DC 20301-7100
(202)693-1530

Dr Yunus Ali Cengel
University of Nevada-Reno
Dept of Mechanical Engg
Reno NV 89557-0030

Dr May Chan
Naval Weapons Center
China Lake CA 93555-6001
(619)939-7519
AV437-7519

Dr Franklin R Chang-Diaz
Lyndon B Johnson Space Center
Code CB
Houston TX 77058
(713)483-2321

Dr Robert Chapman
AFAL/LKLR
Stop 24
Edwards AFB CA 93523-5000
(805)275-5416
AV525-5416

Dr Malcolm Chase
Center for Chemical Physics
National Inst of Stds Tech
Building 222, Room A158
Gaithersburg MD 20899
(301)975-2526

Dr Won-Ho Choe
214 Nuclear Engineering Lab
University of Illinois
103 South Goodwin Avenue
Urbana IL 61801
(217)333-2821

Dr Karl Christe
Rocketdyne Division
Rockwell International
6633 Canoga Ave
Canoga Park CA 91304
(818)710-3268

Dr T. J. Chung
University of Alabama
Huntsville AL 35801
(205)895-6394

Dr George M. Clark
Aerojet Tactical Systems
PO Box 13400
Building 0525
Sacramento CA 95813
(916)988-6919

Dr William Clark
Naval Weapons Center
Code 3895
China Lake CA 93555-6001

Dr Norman Cohen
Aerospace Corporation
PO Box 92957
M/S 747
Los Angeles CA 90045
(213)648-7427

Dr Norman S. Cohen
Professional Services
141 Channing St
Redlands CA 92373
(714)792-8807

Dr Ronald Cohen
The Aerospace Corporation
PO Box 92957
Mail Stop M5-754
Los Angeles CA 90009
(213)336-5946

Dr Cliff Coon
Lawrence Livermore National
Laboratories
Livermore CA 94550
(415)422-6311

Cpt Edward N. Coppola
AFAL/MKPA
Stop 24
Edwards AFB CA 93523-5000
(805)275-5534
AV525-5534

Mr Robert Corley
AFAL/DYC
Stop 24
Edwards AFB CA 93523-5000
(805)275-5353
AV525-5353

Dr L. Cottle
RARDE, Fort Halstead
Knockholt
Matternrks Kent UK

Dr F E C Culick
Engrg and Appl Sci Dept
California Institute of
Technology
Pasadena CA 91125
(818)356-4470

Dr C L Dailey
TRW Space and Technology Group
Applied Technology Division
One Space Park
Redondo Beach CA 90278
(213)536-1874

Dr B R Daniel
School of Aerospace Engrg
Georgia Institute of
Technology
Atlanta GA 30332

Dr William D Deininger
Jet Propulsion Laboratory
California Inst. of Technology
4800 Oak Grove Drive
Pasadena CA 91109
(818)354-7765

Mr S T Demetriades
STD Research Corp
P.O. Box C
Arcadia CA 91006
(818)357-2311

Col. Alan J. Driscoll
AFOSR/CC
Bolling AFB DC 20332-6448
(202)767-5017
AV297-5017

Dr Joel Dubow
Materials Science
Univ of Utah
2008B Mechanical Engrg Bldg
Salt Lake City UT 84112
(801)581-8388

Dr. J. T. Edwards
AFAL/DYCR
Stop 24
Edwards AFB CA 93523-5000
(805)275-5656
AV525-5656

Dr John Eisch
Department of Chemistry
State University of New York
Binghamton NY 13901
(607)798-3994

Dr Allan J Ferrenberg
Manager, Advanced Comb. Device
Rocketdyne Div, Rockwell Int.
Mail Stop IR06, 6633 Canoga Ave
Canoga Park CA 91303
(818)718-3713

Dr John Fischer
Code 3853
Naval Weapons Center
China Lake CA 93555-6001
(619)939-1641
AV437-1641

Dr J. E. Flanagan
Rocketdyne
6633 Canoga
Canoga Park CA 91304
(818)710-2466

Dr Jim Fong
Aerojet Tech Systems
P O Box 13222
Sacramento CA 95813

Dr Arthur Fontijn
Chemical Environmental
Engineering Department
Rensselaer Polytechnic Inst.
Troy NY 12180-3590
(518)266-6508

Dr Milt Frankel
Rocketdyne
6633 Canoga Avenue
Canoga Park CA 91304
(818)710-4803
(818)710-5088

Dr R A Frederick
Sverdrup Technology, Inc
Mail Stop 900
Arnold AFB TN 37389-9998
(615)454-3130

Dr Sheilah K. Fultz
Naval Weapons Center
China Lake CA 93555-6001
(619)939-7521
AV437-7521

Mr Robert Geisler
AFAL/YS
Edwards AFB CA 93523-5000
(805)275-5230
AV525-5230

Dr Eugene Gerber
Univ of Dayton Research
Institute
KL465
Dayton OH 45419
(513)229-3221

Dr. Robert Ghirardelli
U.S. Army Research Office
P.O. Box 12211
Research Triangle Pk NC 27709-2211
(919)549-0641
AV935-3331

Lt Col Fred T Gilliam
EOARD
Box 14
FPO NY 09510-0200
AV235-4505

Dr David Golden
SRI International
333 Ravenswood Avenue
Menlo Park CA 94025-3696
(415)859-0811

Dr B. B. Goshgarian
AFAL/MKPB
Stop 24
Edwards AFB CA 93523-5000
(805)275-5183
AV525-5183

Dr William H Graham
Morton Thiokol, Inc
Huntsville Division
Huntsville AL 35807-7501
(205)882-8397

Dr Alten Grandt
Department of Aeronautics
and Astronautics
Purdue University
West Lafayette IN 47907

Dr John Guimont
Chemistry Division
United Technologies Corp
P. O. Box 50015
San Jose CA 95150-0015

Mr Eugene Haberman
AFAL/MK
Stop 24
Edwards AFB CA 93523-5000
(805)275-5420
AV525-5420

Dr V E Haloulakos
Advanced Propulsion
McDonnell Douglas
5301 Bolsa Avenue
Huntington Beach CA 92647
(714)896-3456

Dr Elmer Hansen
Department of Mechanical
Engineering
University of Florida
Gainesville FL 32611
(904)392-0802

Dr Kenneth Harstad
 Jet Propulsion Laboratory
 4800 Oak Grove Drive
 Pasadena CA 91109

Dr David Hastings
 Department of Aeronautics
 and Astronautics
 Massachusetts Inst of Tech
 Cambridge MA 02139

Dr Clark Hawk
 AFAL/LK
 Stop 24
 Edwards AFB CA 93523-5000
 (805) 275-6530
 AV525-6530

Dr Rich Hollins
 Naval Weapons Center
 China Lake CA 93555-6001
 (619) 555-1650
 AV437-1650

Maj E S Huston
 AFAL/LKC
 Edwards AFB CA 93523-5000
 (805) 275-5476
 AV525-5476

Dr H R Jacobs
 Mechanical Engg Bldg, 208
 Penn State University
 University Park PA 16802

Dr J.I. Jagoda
 Aerospace Engineering Dept
 Georgia Institute of
 Technology
 Atlanta GA 30329
 (404) 894-3060

Dr Donald Jassowski
 Aerojet Technical Systems Co
 PO Box 13222
 Sacramento CA 95813
 (916) 355-2849

Dr Jay B. Jeffries
 Molecular Physics Lab
 SRI International
 333 Ravenswood Avenue
 Menlo Park CA 94025-3696
 (415) 859-6341

Dr S M Jeng
 University of Tennessee
 Space Institute
 Tullahoma TN 37388

Dr Robert Jensen
 Rockwell/Rocketdyne Division
 6633 Canoga Ave
 Canoga Park CA 91303

Mr Arch Johnston
 AFAL/DYC
 Stop 24
 Edwards AFB CA 93523-5000
 (805) 275-5441
 AV525-5441

Dr Abraham Kadish
 Earth and Space Sciences Div.
 Atmospheric Sciences Group
 Mail Stop D466, LANL
 Los Alamos NM 87545

Dr Jordin Kare
 Building 197, Room 1020
 Lawrence Livermore Nat'l Lab
 P O Box 808
 Livermore CA 94550
 (415) 423-8300

Dr David R Kassoy
 Dept of Mechanical Engineering
 University of Colorado at
 Boulder, Campus Box 427
 Boulder CO 80309
 (303)492-2991
 (303)492-7694

Dr Dennis Keefer
 University of Tennessee
 Space Institute
 Tullahoma TN 37388
 (615)455-0631

Dr Sue Kim
 California State University
 6000 J Street
 Sacramento CA 95819
 (916)454-6712

Dr Merrill K. King
 Atlantic Research Corp
 5390 Cherokee Ave
 Alexandria VA 22312
 (703)642-4217

Dr James J. Komar
 Atlantic Research Corp
 5390 Cherokee Avenue
 Alexandria VA 22312
 (703)642-4473

Prof M Kristiansen
 P.W. Horn Professor
 Dept of Electrical Engg, MS3102
 Texas Tech University
 Lubbock TX 79409-4439
 (806)792-3007

Dr Bill Larsen
 AFAL/YSC
 Edwards AFB CA 93523-5000
 (805)275-5657
 AV525-5657

Dr Myron Kaufman
 Department of Chemistry
 Emory University
 Atlanta GA 30322
 (404)727-6619

Dr Philip Kessel
 AFAL/LSCF
 Edwards AFB CA 93523-5000

Dr David King
 Mail Stop 125-224
 Jet Propulsion Laboratory
 4800 Oak Grove Drive
 Pasadena CA 91103
 (818)354-3315

Dr Kenneth Kolouko
 Morton Thiokol
 Wasatch Division
 P.O. Box 524
 Brigham City UT 84302
 (801)863-4220

Dr Herman Krier
 Dept of Mechanical and
 Industrial Engineering
 University of Illinois
 Urbana IL 61801
 (217)333-0529

Dr Warren A. Krueger
 167 Alvana Street, NW16-160
 Massachusetts Institute of
 Technology
 Cambridge MA 02139
 (617)253-0236

Dr Jack Lawless
 Space Power, Inc.
 1977 Concourse Drive
 San Jose CA 95131
 (408)434-1671

Dr Miller Layton
AFAL/LKLR
Stop 24
Edwards AFB CA 93523-5000

Dr Ja H Lee
NASA Langley Research Center
M/S493
Hampton VA 23665
(804)865-4332

Mr Edward L Lee
Special Projects Leader
P.O. Box 808, L-368
LLNL-University of California
Livermore CA 94550
(415)422-1316

Mr Jay Levine
AFAL
Code LSCF
Edwards AFB CA 93523-5000
(805)275-5366
AV525-5366

Dr George A. Lo
Lockheed Palo Alto Research
Laboratory
3251 Hanover St, 8204-93-50
Palo Alto CA 94304
(415)424-2514

Dr Geoffrey Main
School of Mechanical Engrg
Georgia Institute of
Technology
Atlanta GA 30332-0420
(404)894-3242
(404)951-8058

Dr David M. Mann
Army Research Office
P.O. Box 12211
Research Triangle Pk NC 27709-2211
(919)549-0641
AV935-3331

Professor Alan P Marchand
Dept of Chemistry
North Texas State Univ
NTSU Station, Box 13767
Denton TX 76203-5068
(817)565-3823

Dr Stephen B Margolis
Combustion Research Facility
Sandia National Laboratories
Livermore CA 94550
(415)294-

Dr Manuel Martinez-Sanchez
Aeronautics and Astronautics
Massachusetts Inst of Tech
Building 37-401
Cambridge MA 02139
(617)253-5613

Dr Peter Mattern
Combustion Sciences
Sandia National Laboratories
Livermore CA 94550

Dr Anthony J. Matuszko
AFOSR/NC
Bolling AFB DC 20332-6448
(202)767-4963
AV297-4963

Dr Jyotirmoy Mazumder
Department of Mechanical and
Industrial Engineering
University of Illinois
Urbana IL 61801
(217)333-1964

Dr John McVey
Rasor Associates, Inc
253 Humboldt Court
Sunnyvale CA 94086
(408)734-1622

Dr Franklin Mead
AFAL/LK
Edwards AFB CA 93523-5000
(805)275-5540
AV525-5540

Dr Carl F. Melius
Sandia National Laboratories
Livermore CA 94550
(415)294-2650

Dr Charles L. Merkle
205 ME
Pennsylvania State University
University Park PA 16802
(814)863-1501

Dr Claude Merrill
AFAL/MKPL
Stop 24
Edwards AFB CA 93523-5000
(805)275-5169
AV525-5169

Dr Michael M. Micci
233 Hammond Building
Pennsylvania State University
University Park Pa 16802
(814)863-0043

Dr Richard S. Miller
Office of Naval Research
Mechanics Division, Code 432
800 North Quincy Street
Arlington VA 22217-5000
(202)696-4403

Dr Charles Mitchell
Dept. of Mechanical Engineering
Colorado State University
Fort Collins CO 80523

Dr. Robert Moriarty
University of Illinois
(Chicago Circle)
Department of Chemistry
Chicago IL 60680
(312)996-2364

Dr Marlow D. Moser
AFAL/DYCC
Stop 24
Edwards AFB CA 93523-5000
(805)275-5442
AV525-5442

Dr Kenneth G Moses
Plasma Technology Division
JAYCOR
3547 Voyager Street, Suite 104
Torrance CA 90503-1667
(213)542-3800

Dr Philip Muntz
Dept. of Aerospace Engineering
University of Southern
California
Los Angeles CA 90089

Dr S N B Murthy
Dept of Mechanical Engineering
Purdue University
West Lafayette IN 47907
(317)494-1509
(317)494-5639

Dr Subhash Narang
Chemistry Laboratory
SRI International
333 Ravenswood Avenue
Menlo Park CA 94025-3696

Dr Lori A. Newhouse
AFAL/DYCC
Stop 24
Edwards AFB CA 93523-5000
(805)275-5305
AV525-5305

Dr Arnold T. Nielsen
Naval Weapons Center
China Lake CA 93555-6001
(619)939-1614
AV437-1614

Mr Randy T Nishiyama
R/E/WPS
US Dept of Commerce
NOAA, 325 Broadway
Boulder CO 80303-3328

Col James R Nunn
AFAL/CC
Edwards AFB CA 93523-5000

Dr Douglas B. Olson
AeroChem Research Laboratories
Inc.
P. O. Box 12
Princeton NJ 08542
(609)921-7070

Dr Tae-Woo Park
AFAL/TODP
Stop 24
Edwards AFB CA 93523-5000
(805)275-5196
AV525-5196

Ms Dorothy L Pecker
The John Hopkins Univ/APL
John Hopkins Rd
Laurel MD 20707

Dr Kenneth Philippart
AFAL/DYCC
Stop 24
Edwards AFB CA 93523-5000
(805)275-5419
AV525-5419

Dr Leanne Pitchford
GTE Laboratories
40 Sylvan Road
Waltham MA 02254
(617)466-2704

Lt Col Homer Presley
AFAL/LK
Edwards AFB CA 93523-5000
(805)275-6530
AV525-5630

Dr Edward Price
School of Aerospace Engrg
Georgia Institute of
Technology
Atlanta GA 30332-0420
(404)894-3063

Dr Richard Priem
Priem Consultants
13533 Mohawk Trail
Cleveland OH 44130
(216)845-1083

Dr Lawrence P Quinn
AFAL/DYC
Edwards AFB CA 93523-5000
(805)275-5353
AV 525-5353

Dr Russell Reed
Naval Weapons Center
China Lake CA 93555-6001
(619)939-7296
AV437-7296

Dr Robert A Rhein
Research Chemist
Code 3244
Naval Weapons Center
China Lake CA 93555-6001
(619)939-7392
AV 437-7310

Dr J W Rich
 Department of Mechanical
 Engineering
 The Ohio State University
 Columbus OH 43212-1194
 (614) 292-6309

Dr Frank Roberto
 AFAL/MKP
 Stop 24
 Edwards AFB CA 93523-5000
 (805) 275-5430
 AV525-5430

Dr Stephen Rodgers
 AFAL/LKLR
 Stop 24
 Edwards AFB CA 93523-5000
 (805) 275-5416
 AV525-5416

Mr Wayne Roe
 AFAL/XXR
 Stop 24
 Edwards AFB CA 93523-5000
 (805) 275-5206
 AV525-5206

Dr David Rosen
 Physical Sciences Inc.
 Dascomb Research Park
 Andover MA 01810
 (617) 475-9030

Dr S D Rosenberg
 P O Box 13222
 Sacramento CA 95813
 (916) 355-2609

Dr David S Ross
 Director, Physical Organic Chem
 SRI International
 333 Ravenswood Avenue
 Menlo Park CA 94025-3696
 (415) 859-2430

Dr Kevin Rudolph
 Martin Marietta Corporation
 Mail Stop S8071
 PO Box 179
 Denver CO 80201
 (303) 977-3681

Dr. Michael J. Salkind
 AFOSR/NA
 Bolling AFB DC 20332-6448
 (202) 767-0467
 AV297-0467

Dr Robert Schmitt
 Chemistry Lab
 SRI International
 333 Ravenswood Avenue
 Menlo Park CA 94025-3696
 (415) 859-5579

Dr Keith Schofield
 Quantum Institute
 University of California,
 Santa Barbara
 Santa Barbara CA 93106

Dr Herbert Schrade
 Institut Fur Raumfahrtantriebe
 Universitat Stuttgart
 Pfaffenwaldring 31
 D-7000 Stuttgart GE
 7116-852-383
 or 375

Dr Gary I. Sega
 Aerospace Corp
 P.O. Box 92957
 MS/747
 Los Angeles CA 90004
 (213) 648-6501

Maj Scott A Shackelford
 F J Seiler Research Laboratory
 United States Air Force Acad
 Colorado Springs CO 80840
 (719) 472-2655

Dr Pam Sherretz
Naval Weapons Center
China Lake CA 93555-6001
(619)939-7392
AV437-7392

Dr R Shoureshi
School of Mechanical
Engineering
Purdue University
West Lafayette IN 47907
(317)494-5639

Prof Jean'ne M. Shreeve
Dept of Chemistry
University of Idaho
Moscow ID 83843
(208)885-6552

Ms Elizabeth Slimak
AFAL/LSCF
Edwards AFB CA 93523-5000

Lt Col LaRell Smith
EOARD/LRC
Box 14
FPO NY 09510-0200
AV235-4505

Dr Warren Strahle
School of Aerospace Engrg
Georgia Institute of
Technology
Atlanta GA 30332
(404)894-3032

Dr V V Subramaniam
Department of Mechanical
Engineering
The Ohio State University
Columbus OH 43212-1194
(614)292-6096

Dr. Mostafa Talukder
AFAL/LKLR
Edwards AFB CA 93523-5000
(805)275-5416
AV525-5416

Dr James Tien
Case Western Reserve
University
Glennan Building, Room 415
Cleveland OH 44106
(216)368-4581

Professor William C Trogler
Department of Chemistry
University of California, San
Diego
LaJolla CA 92093
(619)452-6175

Dr Wing Tsang
National Institute of Standard
and Technology
Chemical Kinetics Division
Gaithersburg MD 20899
(301)975-3507

Dr Peter Turchi
RD Associates
301 S West Street
Alexandria VA 22314
(703)684-0333

Mr Gary L. Vogt
AFAL/DYCR
Stop 24
Edwards AFB CA 93523-5000
(805)275-5258
AV525-5258

Dr Robert Vondra
PO Box 596
Wrightwood CA 92397
(619)249-3451

Dr Nzoo Vu
Naval Weapons Center
China Lake CA 93555-6001
(916)939-7392
AV437-7392

Dr R H Woodrow Waesche
Atlantic Research Corporation
7511 Wellington Road
Gainesville VA 22065

Dr Peter Wayner
Dept of Chemical and
Environmental Engineering
Rensselaer Polytechnic Inst
Troy NY 12180-3590
(518)266-6199

Dr David P Weaver
AFAL/DYCR
Edwards AFB CA 93523-5000
(805)275-5657
AV525-5657

Dr Jim Weber
Rocketdyne Division
Rockwell International Corp.
6633 Canoga Ave
Canoga Park CA 91303
(818)710-5558

Dr Richard Weiss
AFAL/CA
Edwards AFB CA 93523-5000
(805)275-5622
AV525-5622

Dr Rodney Willer
Morton Thiokol Inc
Elkton Division
P.O. Box 241
Elkton MD 21921
(301)398-3000
(301)398-4440

Dr D O Woolery
Rocketdyne
6633 Canoga Avenue
Canoga Park CA 91304

Dr Ted F. Yang
Massachusetts Institute of
Technology
167 Albany Street
Cambridge MA 02139
(617)253-8453

Dr Vigor Yang
Department of Mechanical
Engineering
Pennsylvania State University
University Park PA 16802

Dr Thomas M York
AERO/ASTRO Engineering
328 CAE Building
Ohio State University
Columbus OH 43210
(614)292-2691

Dr Ben T. Zinn
School of Aerospace Engrg
Georgia Institute of
Technology
Atlanta GA 30332
(404)894-3033

Cpt Joseph Zirrolli
FJSRL/NC
United States Air Force
Academy
Colorado Springs CO 80840
(303)472-2655

Mr Robert L Zurawski
Program Manager
Propulsion Technology Programs
NASA HQA, OAST-MAIL CODE RP
Washington DC 20546
(202)453-2261

Invitees

Mr. Leonard Angello
Electric Power Research
Institute
3412 Hillview Avenue
Palo Alto CA 94303
(415)855-2873

Dr. W. D. Bachalo
Aerometrics, Inc.
P. O. Box 308
Mountain View CA 94042
(415)965-8887

Dr Edward J Beiting
Aerophysics Lab, Prop Env Sc
The Aerospace Corporation
P O Box 92957, M5/754
Los Angeles CA 90009-2957
(213)336-7035

Dr William K Bischel
Coherent, Inc.
3210 Porter Drive
Palo Alto CA 94304
(415)858-7639

Dr. Richard K. Chang
Electrical Engineering Dept.
P. O. Box 2157, Yale Station
Yale University
New Haven CT 06520
(203)432-4272

Dr. Wai K. Cheng
Department of Mechanical
Engineering
MIT
Cambridge MA 02139
(617)253-4531

Dr. David R. Crosley
Molecular Physics Department
SRI International
333 Ravenswood Avenue
Menlo Park CA 94025-3696
(415)326-6200

Dr. John W. Daily
Center for Combustion Research
Mechanical Engineering Dept
University of Colorado
Boulder CO 80309
(303)492-7151

Dr. Gregory Dobbs
United Technologies Research
Center - Mail Stop 90
Silver Lane
East Hartford CT 06108
(203)727-7145

Dr. Joel Dubow
Materials Science Department
University of Utah
2008B Mechanical Engrg. Bldg.
Salt Lake City UT 84112
(801)581-8388

Dr. A. C. Eckbreth
United Technologies Research
Center
Silver Lane
East Hartford CT 06108
(203)727-7269

Dr Thomas Ehlert
Department of Chemistry
Marquette University
Milwaukee WI 53233
(414)224-7066

Dr. Richard Field
U. S. Army Armament RD Center
DRSMC-LCA-G(D)
Building 382-S
Dover NJ 07801
(201)724-5844
(201)724-5682

Dr. Bish Ganguly
WRDC/POOC-3
Wright-Patterson AFB OH 45433
(513)255-2923
AV785-2923

Dr. Alan Garscadden
WRDC/POOC-3
Wright-Patterson AFB OH 45433-6563
(513) 255-2923
AV785-2923

Dr. Larry P. Goss
Research Applications Division
Systems Research Labs, Inc.
2800 Indian Ripple Road
Dayton OH 45440-3696
(513) 252-2706

Dr. R. K. Hanson
Department of Mechanical
Engineering
Stanford University
Stanford CA 94305-3032
(415) 723-1745

Dr. D. L. Hartley
Combustion Sciences
Sandia National Laboratories
Livermore CA 94550

Dr. L. Hesselink
Department of Aeronautics and
Astronautics
Stanford University
Stanford CA 94305-3032
(415) 723-3466

Dr. E. D. Hirleman
Department of Mechanical and
Aerospace Engineering
Arizona State University
Tempe AZ 85287
(602) 965-3895

Dr. Donald J. Holve
Insitec
28 Bobbie Court
Danville CA 94526
(415) 837-1330

Dr David Huestis
SRI International
333 Ravenswood Avenue
Menlo Park CA 94025
(415) 859-3464

Dr Thomas K Ishii
Department of Electrical
Engineering
Marquette University
Milwaukee WI 53233
(414) 224-1593

Dr. Roman Kuc
Department of Electrical
Engineering
Yale University
New Haven CT 06520
(203) 432-4891

Dr. Marshall B. Long
Department of Mechanical
Engineering
Yale University
New Haven CT 06520
(203) 432-4229

Dr. Bruce G. MacDonald
Research Applications Division
Systems Research Labs, Inc.
2800 Indian Ripple Road
Dayton OH 45440-3696
(513) 252-2706

Dr. Timothy Parr
Naval Weapons Center
Code 3893
China Lake CA 93555
(619) 939-2521

Dr. S. S. Penner
Dept. Of. Appl. Mech. and
Engrg. Sci.
University of California
La Jolla CA 92093
(619) 534-4284

Dr Emil Pfender
Department of Mechanical Engrg
125 Mechanical Engineering
The University of Minnesota
Minneapolis MN 55455

Dr. John P. Renie
Department of Mechanical and
Industrial Engineering
University of Illinois
Urbana IL 61801
(217)333-6199

Dr Won B Roh
Department of Engrg Physics
Air Force Institute of
Technology
Wright-Patterson AFB OH 45433-6583

Dr Gregory P Smith
Department of Chem Kinetics
SRI International
333 Ravenswood Avenue
Menlo Park CA 94025
(415)859-3496

Dr. Alan C. Stanton
Southwest Sciences, Inc.
1570 Pacheco Street
Suite E-11
Santa Fe NM 87501
(505)984-1322

Dr. James D. Trolinger
MetroLaser
18004 Skypark Boulevard
Suite 254
Irvine CA 92714-6428
(714)553-0688

Dr. John A. Vanderhoff
Ballistic Research Laboratory
DRSMC-BLI(A)
Aberdeen Proving Ground MD 21005
(301)278-6642

Dr. James F. Verdick
Rockwell International
Rocketdyne Div, M/S FA26
6633 Canoga Avenue
Canoga Park CA 91303
(818)700-4709

Dr. Joda Wormhoudt
Aerodyne Research, Inc.
45 Manning Road
Manning Park Research Center
Billerica MA 01821-3976
(508)663-9500